Medical Radiology
Diagnostic Imaging
A.L. Baert
M.F. Reiser
H. Hricak
M. Knauth

Jürgen Hennig
Oliver Speck
Editors

High-Field MR Imaging

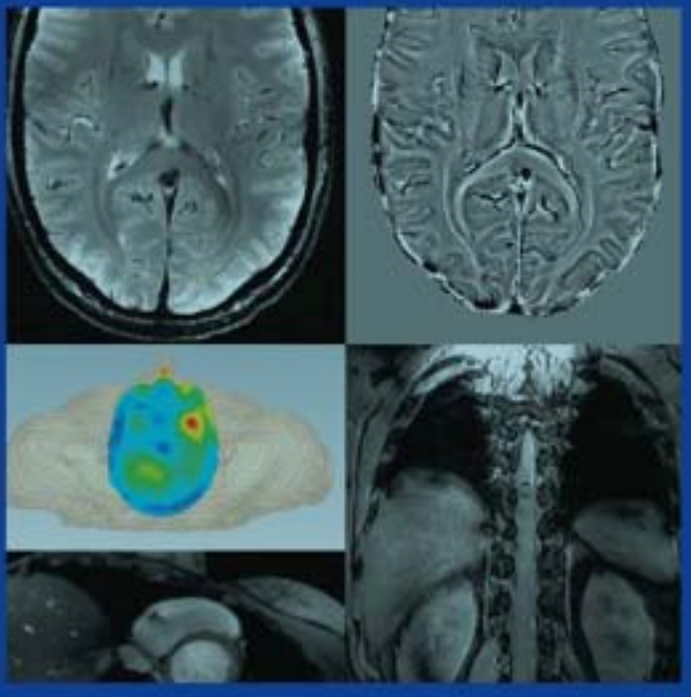

Springer

Medical Radiology

Diagnostic Imaging

For further volumes:
http://www.springer.com/series/4354

Jürgen Hennig • Oliver Speck
Editors

High-Field MR Imaging

Foreword by
Albert L. Baert

Springer

Editors
Prof. Dr. Jürgen Hennig
Radiologische Klinik
Universitätsklinikum Freiburg
Abt. Chir./Kernspintomographie
Breisacherstr.60a
79106 Freiburg
Germany
e-mail: Juergen.Hennig@uniklinik-freiburg.de

Prof. Dr. Oliver Speck
Inst. Experimentelle Physik
Otto-von-Guericke Universität Magdeburg
Abt. Biomedizinische Magnetresonanz
Leipziger Str. 44
39120 Magdeburg
Germany
e-mail: oliver.speck@ovgu.de

ISSN 0942-5373
ISBN 978-3-540-85087-8 e-ISBN 978-3-540-85090-8
DOI 10.1007/978-3-540-85090-8
Springer Heidelberg Dordrecht London New York

Library of Congress Control Number: 2011935747

Cover design: eStudio Calamar, Berlin/Figueres

Printed on acid-free paper

Springer is part of Springer Science+Business Media (www.springer.com)

Foreword

Clinical and scientific applications of high-field MRI are now rapidly expanding due to recent technical improvements in hardware design and new software and method developments.

It is my great pleasure and privilege to introduce this fascinating new volume of our series dealing with this hot issue in medical radiology.

This book offers MRI users in depth but transparent information on the physical background and the theoretical concepts of high field MRI, necessary for a better understanding of the morphological and functional findings including contrast applications and essential guidelines on safety issues.

In addition, this volume covers comprehensively the most recent and best performing clinical applications of high-field MRI in diverse organs of the human body.

The editors: J. Hennig and O. Speck are internationally widely acknowledged leaders by virtue of their original and innovative previous contributions on new technological breakthroughs in the field of medium- and high-field MR. The chapters on clinical applications of high-field MRI are written by scientists, that have extensive personal expertise in the diverse organ applications as proven by their outstanding scientific publications and lectures on the topic.

This superb book will be of great value to guide and to assist radiologists in their daily clinical work. It will also be helpful to referring physicians from diverse clinical disciplines, that are interested in high field MR imaging such as neurosurgeons, neurologists, orthopedic surgeons, and oncologist for a better clinical management of their patients.

I am convinced that it will encounter great success with our readership.

Albert L. Baert
Leuven

Preface

When we were approached by Springer about the project for this book we were somewhat doubtful at first. The extremely rapid development of the field of ultra high field MR seemed to be more appropriate for a transient and fleeting medium like a blog rather than a solid and static publication like a book. Trying to catch the essence of the ongoing research in all relevant aspects—technologies, methods, research and applications—seemed like trying to nail a pudding to a wall. But on second thought and as the chapters came in and the book evolved and took shape, we became more and more aware and convinced, that this does make sense after all. Yes, there will be newer results, newer applications, and better images at the time the book hits the shelves and there may even be breakthroughs in some of the problem areas elaborated in the text. New solutions will have been found, but the basic facts—opportunities as well as challenges—are here to stay. New technologies may and will help to bring the potential of UHF-MR to fruition, but the basic physics will remain the same. Thus, with all the elusiveness of details we hope that the essence of the substance matter will remain valid for some time to come. We also hope that the readers of this book will learn new aspects whether their background is engineering, physics, medicine or similar. Perhaps, they will even be able to share some of our enthusiasm for MR in general and high field in particular.

We want to thank our authors for the effort and dedication they took in preparing their chapters. With all the commitments to write and review papers, articles, and grant applications—not to mention the research that we would all want to spend most of our time with—this is far from being a given. All friends and colleagues, who we approached, spontaneously agreed to contribute and most of them delivered their text on time to make sure that the materials in this book are as fresh as they can be. This is a book, not an encyclopedia, therefore although we have aimed to cover all schools of thought this is by far not and not meant to be complete. We are proud and happy to have enlisted leading scientists in the field as authors, but needless to say, there are others of no lesser status who we were not able not include in order to keep the volume manageable. The attentive reader will note a bias of the geographic allocation of our authors towards Europe. Although this is not by accident it is certainly not meant in any way to be Euro-chauvinistic. The UHF-MR community is truly international. It comprises scientists from all over the world, including not only the old world on both sides of the Atlantic but having made already a running start in several Asian countries as well. If anything the European focus is meant to reflect the currently ongoing intense activities in Europe to establish and renew research infrastructures as UHF-MR has been identified as one of the

key technologies within the newly established ESFRI (European Science Forum for Research Infrastructures)-initiative EuroBioImaging. Substantial investment into UHF-MR has already been made or is underway in many European countries. Given the fact, that so far no clear 'killer application' has been found, the amount of funding already invested into UHF-systems is truly astounding. A key element to bring this investment to success will be whether funding will also become available to hire, educate and train the scientists and clinicians necessary to translate technologies into useful applications in research and clinics. With all fascination for new technologies it is people who at the bottom line really count.

Jürgen Hennig
Oliver Speck

Contents

Introduction

Jürgen Hennig and Oliver Speck

The prehistoric area of ultra high field MR (UHF-MR) began in the late 1980s, when 4T systems were introduced and installed in Birmingham (Alabama), at NIH and at the Centre for Magnetic Resonance Research in Minnesota (CMRR). For more than a decade, the research teams working on these systems produced a constant stream of papers on the benefits, and the challenges of high field MR. Some of the early work—most notably early results on fMRI at 4T produced by CMRR—showed a very clear and distinct advantage of UHF-MR compared to the then common 1.5T systems, particularly for functional brain imaging and spectroscopy. Nevertheless the enthusiasm for these huge systems didn't really catch on, and the rest of the MR community was quite happy to stand by and watch the affluent few struggling along and fighting all the challenges coming with the higher field.

Then came the large-scale introduction of 3T-systems, which automatically raised the bar for what should be called UHF-MR. In 1998, a first 8T human system was installed at Ohio State University, followed by a 7T system at CMRR. Both these systems were experimental devices assembled with considerable effort and skill by various researchers and companies, and in part these systems were based on homebuilt components. The current area of UHF-MR started, when the leading manufacturers of clinical MR systems—Siemens, Philips, and GE—introduced their first 7T systems. The first two such systems were installed at MGH and NIH in 2002. These were still experimental devices meant to test the technological limits and the expectancy that 7T would become a valid market was rather low. First results demonstrated the advantages of the higher field in terms of SNR and improved sensitivity for fMRI, but they also clearly showed the challenges especially with respect to the radiofrequency fields. At 300 MHz—the Larmor frequency of protons at 7T—the wavelength in tissue is shortened to around 14 cm. In this regime the near-field approximation still valid at lower fields breaks down. Radiofrequency transmission and reception can no longer be treated by the reasonably straightforward laws of electromagnetic induction. Maxwell equations with all ensuing complexities of spatiotemporal variations of the electromagnetic fields take over. As a consequence, B_1 fields (and therefore excitation and refocusing flip angles) show considerable variations across the field of view leading to variations in SNR and—even worse—contrast behaviour across the image. On top of that, the electrical field component is now an inherent part of the excitation process leading to severe challenges regarding patient safety by the increased specific absorption rate (SAR). The first results at 7T were—in comparison to the respective state-of-the-art—on a similar level as the first 4T results, more than a decade ago. The perception was however markedly different. This time UHF-MR caught on in a big way.

J. Hennig (✉)
Universität Freiburg, Abt. Roentgendiagnostik,
Breisacherstr.60a, 79106 Freiburg, Germany
e-mail: juergen.hennig@uniklinik-freiburg.de

O. Speck
Department of Biomedical Magnetic Resonance,
Otto-von-Guericke-University Magdeburg, Leipziger Str. 44, Haus 65, 39120 Magdeburg, Germany
e-mail: oliver.speck@ovgu.de

J. Hennig and O. Speck (eds.), *High-Field MR Imaging,* Medical Radiology. Diagnostic Imaging,
DOI: 10.1007/174_2011_161, © Springer-Verlag Berlin Heidelberg 2011

Rather than watching the elected few struggling along, 7T centres started to spring up all over the world and sometimes at rather unlikely places, quite remote from where one would suspect appropriate MR expertise to be available. At the time of writing this introduction, there are already around fifty 7T systems in operation or at least under construction, several 9.4T systems are around. At the time of this book going to print, there will be one 11.7T human magnet at NIH and magnet builders have construction plans for 14T in their drawers, only waiting to find financial support. One may speculate, why UHF-MR is such a runaway success this time, when it—at least in terms of market impact—so miserably failed with the first-generation 4T systems more than a decade ago.

The most crucial factor is the fact that this time, the systems were built by established vendors rather than being assembled on site from various components. Although systems were and still are experimental devices under constant development, the effort now is supported by the full momentum, know-how and expertise of the development teams in the companies' R&D centres. UHF-MR still is far away from being a push-button modality and a first class team of MR physicists in close collaboration with application oriented researchers is still mandatory to run and operate a 7T system in any meaningful way. Still the on-site experts today can focus on specific issues (most of which relate to RF) and one can trust that the nuts and bolts of system integration of the multiple components are taken care of by the vendors. A second factor for today's enthusiasm relates to the overall status of development in the field. In the 1980s and early 1990s, most of the methodological and technological effort in the field was related to the development of new sequences utilising the continuously improving gradient performance. Nowadays, sequence development has very much decreased, there is a perception, that all basic sequences are known and sequence development is more or less reduced to how to make acquisition faster and more efficient by clever variations of k-space acquisition schemes, in combination with parallel imaging or other reduced sampling schemes. It would be imprudent to comment on the veracity of this perception, it is too reminiscent of the statement that all major inventions have been made already, which is attributed to the commissioner of the United States Patent Office, a Mr. Charles Duell, back in 1899. But justified or not, 7T MR came around at a time, when the MR community was looking for new challenges and was and is therefore embraced with lots of enthusiasm. This has led to an influx of expertise into UHF-MR increasing the momentum of the development and thus yielding new and exciting results, creating even more enthusiasm and so on—a stampede would ensue were it not for the still exorbitant costs involved in construction of a 7T facility. Setting up a 7T requires not only the already costly system itself, it currently invariably comes with several hundreds of tons of iron for shielding. This package then requires some substantial real estate for housing. So getting a 7T operational within the notoriously cramped spacing in medical centres and universities is an enormous financial effort and it is quite astounding, that UHF-MR proliferation in times of financial stringency is still rampant at least in some parts of our world. In some respects, UHF-MR has even benefitted from the financial crisis of 2008/2009: The stimulus packages set up in the US and Europe contained significant amounts of funding for large infrastructures. They were therefore destined for acquiring big instruments, so the market was pushed rather than decelerated. (A foreseeable but unforeseen side-effect of this focus on large scale infrastructure was the fact that large companies, who by their global market orientation were least affected by the financial crisis, were the big winners, whereas small and medium enterprises, which constitute the backbone of innovation and local/national market force went away more or less empty handed—politicians just love to cut those red ribbons at the opening of grand project schemes).

This book is an attempt to catch and display the state-of-the-art in this rapidly developing field. We are well aware, that due to the tremendous pace of the ongoing development, many of the specific examples will become out-dated quickly. We have therefore made an effort to not only show the state-of-the-art of current results, but to provide insight into the fundamental facts, challenges, and opportunities of UHF-MR. New solutions to existing challenges are produced everyday, and the highlights of today are likely to become either a matter of course or obsolete quickly. The fundamental facts remain, so we are quite confident, that this book will remain to be useful for a while.

There is a continuous and rather monotonous change in key parameters affecting image formation. SNR, relaxation parameters, susceptibility effects,

chemical shifts, RF power issues—all of these show a more or less pronounced dependency on field strength. The overall combination of these effects may lead to rather complex and sometimes unexpected field dependency for given applications, but the field dependant scaling moves on a continuum. In spite of the monotony of the physical parameters involved, the application value in many cases shows a rather sharp threshold effect. Some applications, which just didn't work out well enough at some stage of development suddenly turned into valid and robust tools after some moderate improvement. This threshold effect has been observed before, notable examples are the introduction of fast, shielded gradients in the early 1990s, which suddenly enabled breath hold imaging and thus changed the world of cardiac and abdominal MR. More recently 3T has converted fMRI from a handicraft for those with sufficient skills to pick out real signals from an exorbitance of noise into a stable and robust tool for day-to-day use. The most notable example for such a threshold effect at 7T is susceptibility weighted imaging (see Chaps. 6 and 10). Susceptibility varies only linearly with field strength and in fact, most of the basic phenomena observed at 7T can also be demonstrated at 3T. Most interesting findings are however only seen at high spatial resolution and are obscured at 3T by the increased noise level. Therefore, this is one application which can be said to be unique for 7T. This translation of a monotonous variation into a threshold phenomenon unfortunately also works the other way round: some applications become impractical above a certain level. This is (at least currently) true for all methods requiring lots of RF-pulses and/or high flip angles—this most notably affects balanced SSFP and especially TSE. These sequences are extremely useful and popular up to 3T, at 7T their usage becomes severely limited (see Chap. 6). The problem is even exacerbated by the use of multiple transmitters used to homogenize the B_1-field. So 7T really poses a new challenge to sequence developers—how to realise the well appreciated contrast variability of MRI with low flip angle sequences. This task is in continuation of the work of many creative sequence designers that invented new sequences only to then modify those sequences to yield the established T_1 or T_2-contrasts that radiologists have been trained to interpret. It is important to limit the complexity of a modality on one hand in order to allow safe and reliable application in daily routine. On the other hand, the user has to adapt to the new possibilities, develop an understanding and perhaps even intuition for the new challenges and opportunities in order to find the best use for it.

UHF-MR has made tremendous progress over the last few years. Originally 7T-systems were acquired mainly for use in neuroscience. With the increasing feasibility of cardiac and abdominal imaging, driven by the ongoing development of RF-coils, the field is continuously broadening and UHF-MR is raising increasing attention, also for clinical applications. Currently there is no clear 'killer application' for clinical use, but the quality of results steadily increases the level of confidence, that it will be only a matter of time until such a 'killer application' develops. Given the still high cost of UHF-MR, it is quite safe to expect, that it will not suffice for an indication to be merely diagnostic. Even if it works perfectly, a UHF-MR examination will only be justifiable, if it has a direct impact on therapy and patient outcome. UHF-MR in oncology and especially at a disease stage, where it really matters, is therefore a very likely candidate field for UHF-MR to become clinical. Given the horrendous cost of many oncological treatments, the cost of an UHF-MR exam is close to be negligible if it can be shown to make a difference. The results presented in Chap. 10 indeed show some very real and already more than just promising developments indicating that this may become a clinical reality in the very near future. However, proof of superior performance of an imaging modality in terms of patient outcome has not been the focus of many clinical studies. The reason may be that such studies are difficult, costly, and long lasting. There have only been few such studies for lower field strength and yet 3T has taken a major market share. A similar development may be seen for 7T if prices come down due to higher production volume and the introduction of self shielded magnets reducing siting requirements.

UHF-MR of the brain shows high resolution images of staggering quality. Subtle microstructural changes have been observed in several pathologies (neurodegeneration, Alzheimer, multiple sclerosis, Parkinson disease). So far, however, the clinical impact of these findings is still unclear, especially since so far there is no clear therapeutic consequence.

UHF-MR currently is on the verge of taking a big step ahead with the imminent introduction of self-shielded magnets. This will not only reduce the overall cost in spite of the increased price of the magnet itself. Being able to place a 7T-system onto the footprint of a current 3T installation, will enable to integrate 7T into the clinical workflow and thus tremendously increase the pace of clinical development compared to today's installations, which—even when they are within a hospital—often are more or less isolated islands of research.

The basic structure of this book aims at a balance between introductions into the fundamentals of the physics, technologies and methodologies, and an overview of the current status of applications in different fields. The technological chapters on magnets (Chap. 2), gradients (Chap. 3) and RF coils (Chap. 4) strive to give sufficient solid information, to be of interest to specialists while still being understandable to non-Ph.D. readers. Safety (Chap. 5) is—as already mentioned—an overriding concern at 7T, finding robust and reliable solutions especially regarding prediction of RF-induced tissue heating will be crucial for the development of the field. Chaps. 6 and 7 present the basic concepts on the relevant differences for the use of key sequences at 7T. After the introduction of the technological and methodological basics, Chaps. 8–11 give an overview on the status of different fields of applications. The allocation of specific topics into 4 chapters is rather broad, reflecting the current lack of breadth of experience. Clinical UHF-MR is still at a toddler stage, but—as shown by the examples—this toddler is very alive and kicking and holds great promise.

Chapter 12 is dedicated to how the advantages of the higher field lead to improvement of spectroscopy. The final Chap. 13 builds a linkage from human MR to animal research and illustrates the importance of UHF-MR in translational research, bridging the gap between pre-clinical research and clinical application.

Given the rapid development of the field there are some omissions to be noted even now in the final stages of preparing the book. To note just a few, recent developments show the use of translating the phase/amplitude information of susceptibility weighted imaging into susceptibility maps. There are still problems to be solved in the stability and robustness of the algorithms and the distinction of susceptibility effects from other mechanisms like chemical shift, but this may well be the way to go to translate the current nice images into stable parametric maps. Similary, the development of even faster acquisition schemes promises that routine fMRI acquisitions with isotropic 1 mm resolution (or even higher) covering the whole brain in two to three seconds are within reach. A further omission relates to the ongoing rapid development of new concepts for accelerated imaging based on an inverse imaging approach with iterative reconstruction using prior knowledge (like image sparsity). This extremely lively development has not quite reached the world of UHF-MR but will likely have a future impact similar to parallel imaging trading SNR for speed. There will always be a chance to fill these gaps in a future second edition.

High-Field Superconducting Magnets

Holger Liebel

Contents

Abstract

Over the past 30 years, magnetic resonance imaging (MRI) and magnetic resonance spectroscopy (MRS) have developed into the key technologies assisting medical diagnosis and many kinds of scientific research. MRI and MRS, however, remain fields characterized by a great deal of innovation. The main goal of this innovation is the improvement in the basic signal to noise ratio. One way whereby the signal to noise ratio can be improved is by increasing the strength of the main magnetic field, and this has initiated a lot of development in the field of magnet technology. The exploitation of superconductivity is the only practical and economic way of reaching higher magnetic field strengths. This paper will describe the basic principles of superconducting magnet design starting with the generation of magnetic fields and the handling of the associated forces. MRI and MRS applications pose considerable demands on the homogeneity and stability of such magnets. These demands are reflected in the design of the magnet coil windings, and the superconducting materials that are used in magnet construction. Furthermore, methods for the fine adjustment of the magnet homogeneity (often referred to as shimming) are described. For operational and economic reasons superconducting coil structures need to be well thermally insulated and therefore the cryostat technology is also described with particular reference to active and passive cooling technologies. Finally, different specifications

H. Liebel (✉)
Bruker BioSpin MRI GmbH, Rudolf-Plank-Str. 23, 76275 Ettlingen, Germany
e-mail: Holger.Liebel@bruker-biospin.de

H. Liebel
Bruker BioSpin, 34 rue de l'industrie – BP 10002, 67166 Wissembourg Cedex, France

J. Hennig and O. Speck (eds.), *High-Field MR Imaging,* Medical Radiology. Diagnostic Imaging,
DOI: 10.1007/174_2010_100, © Springer-Verlag Berlin Heidelberg 2011

and parameters for existing High-Field Superconducting MRI magnets are presented beginning with 7 T magnets for human applications and ending with 11.7 T human systems that are currently in the design phase. For each magnetic field strength typical specifications and parameters for small animal MRI superconducting magnets used in pre-clinical research are also described.

1 Introduction

Magnetic resonance imaging (MRI) has become a unique tool for both scientific research and medical diagnosis since its first invention in the early 1970s (Lauterbur 1973; Mansfield and Grannell 1973; Damadian 1971). MRI methods generate in a non-invasive manner images from inside the body of humans or animals that not only demonstrate the exact status of the internal organs but also can even be used to visualize their functions. A major advantage for MRI methods, in contrast to methods that use X-ray, is the utilization of non-ionizing radiation to scan the subjects under investigation.

Clinical MRI studies first appeared in 1979, and the first commercial MRI scanner was manufactured by Fonar in 1979 based on a heavy permanent magnet. Other early entries into the MRI market were based on higher field strength air-core resistive electromagnets that indeed were lighter in weight but required ~40 kW of electrical power (Morrow 2000).

Further innovation led to the development of air-core superconducting magnets and since MRI and magnetic resonance spectroscopy (MRS) performance is determined ultimately by the signal to noise ratio the higher field strength provided higher signal to noise ratios that in turn allowed more detailed images to be constructed. Consequently, the market was soon dominated by unshielded superconducting air-core magnets. However, these unshielded systems had a large dipole moment and thus a relatively large stray field. The stray field of these superconducting magnets posed significant difficulties when being sited in a hospital environment. In the late 1980s, Hawksworth et al. (1987) proposed and realized the utility of an electromagnetic self-shielding concept that eliminated the need for the heavy iron yoke or room shields previously required for siting high-field magnets.

The practical and economic operation of superconducting MRI/MRS magnets requires the development of cryogenic systems with very low thermal losses. The evolution of such MRI cryostats has been significant over the past 25 years, and they have developed from simple liquid helium, liquid nitrogen shielded reservoirs with relatively high cryogen evaporation rates to single or multi-cryocooled cryostats providing nominally zero-boil-off conditions (Williams 2001).

Recently, the typical requirements for a whole body imaging magnet include a central field uniformity of a few ppm (mostly in a spherical volume of around 45 cm) and a temporal field stability of better than 0.05 ppm/h. The self-shielding concept is applied routinely up to 4 T for human whole body systems and is currently being introduced also for 7 T systems. The magnet system is housed normally in a low loss cryostat using pulse tube (PT) or Gifford–McMahon (GM) refrigeration technology to provide nominally zero boil-off conditions.

In this chapter, the design aspects of MRI/MRS magnet systems will be described and an overview about currently available systems will be given.

2 Design Principles

2.1 Basic Principles of Nuclear Magnetic Resonance as Related to Magnet Design

Magnetic resonance imaging and nuclear magnetic resonance (NMR) methods are only applicable to nuclei having an angular momentum $\vec{J} \neq 0$. The relationship between the angular momentum and the magnetic moment $\vec{\mu}$ of a nucleus is given by $\vec{\mu} = \gamma * \vec{J}$, where γ is the gyromagnetic ratio. If an external uniform magnetic field, usually denoted as $\vec{B}_0$, is applied a splitting of the energy levels occurs (see Fig. 1); $\vec{B}_0$ is of course a magnetic flux density but will be denoted as magnetic field or magnetic field strength in the following description. By convention $\vec{B}_0$ is defined as pointing in the z-direction only ($\vec{B}_{0z}$), and it is assumed that protons only are exposed to the magnetic field. The proton may assume one of two equilibrium positions under these conditions viz: either with the z-component of the magnetic moment

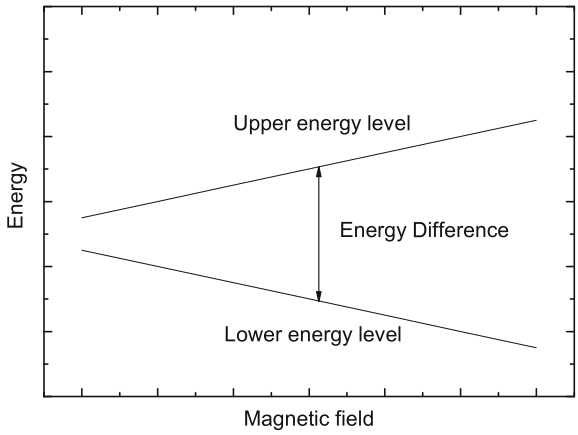

Fig. 1 Splitting of energy levels as caused by the application of a static magnetic field

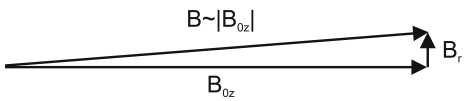

Fig. 2 Vectorial addition of different components of the magnetic field

aligned with the external field or with the z-component of the magnetic moment opposed to the external field. Between these energy levels, transitions in the radiofrequency range can be induced and detected thereby making NMR and MRI possible. The transition frequency is given by $\omega = \gamma * B_{0z}$ (see, e.g., Jin 1999). When carrying out MRI/MRS experiments relative frequency changes of less than one part in 1 million need to be detected and this requirement defines important aspects of the magnet design viz: homogeneity and temporal stability of the magnet systems.

In designing MRI/NMR magnets, it is usual to take advantage of cylindrical symmetry. Hence, only radial B_r and axial B_z components have to be taken into account. Having a very homogenous field in z-direction (B_{0z}) results in very small contributions from radial components B_r. As shown in Fig. 2, these radial components add vectorially to the main component, and thus, the radial contribution to the total field can be neglected. Therefore, the measured frequencies are practically determined by the axial component B_{0z}. Thus, for homogeneity purposes magnet designers can focus on B_{0z} alone.

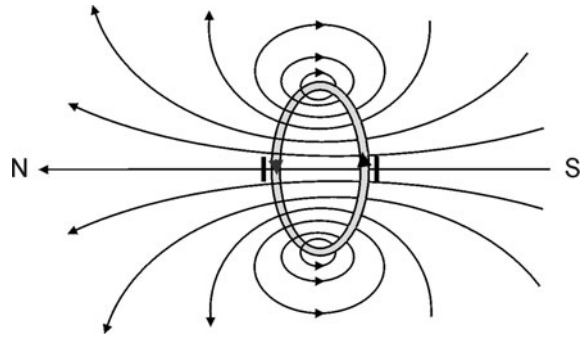

Fig. 3 Magnetic field lines surrounding a current-carrying loop

2.2 Generation of Magnetic Fields and Forces

Magnetic fields can be generated in a number of ways:

1. using an assembly of previously magnetized structural elements (a permanent magnet);
2. passing a current through an electrical conductor at room temperature;
3. passing a current through an electrical superconductor at low temperature.

For several MRI/MRS applications permanent magnets can be used to generate the homogenous main magnetic field; however, the achievable field strength and bore sizes are rather restricted. For the highest field strength and largest bore size, current-carrying superconducting structures need to be used.

Magnetic fields surround any current-carrying conductor in concentric rings. The magnet field strength at a given location is inversely proportional to the distance from the conductor. Bending a current-carrying conductor into a loop concentrates the magnetic field inside the loop and weakens it outside (see Fig. 3).

Such a current-carrying loop is the basic "building" block of typical MRI magnet structures. The properties of a current-carrying loop can be calculated using the Biot–Savart law, and it can be shown that for a single loop of whole body dimensions carrying a current of 300 A the field on-axis will be 0.4 mT (see Fig. 4). As a result, several thousand loops will be needed to achieve field strengths in the range of a few Tesla.

A current-carrying structure will produce an associated magnetic field and in multi-element structures there will be an interaction between the

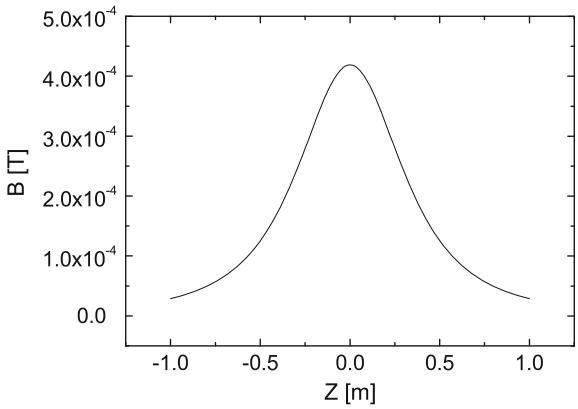

Fig. 4 Magnetic field of a wire loop. The radius $r = 0.45$ m and $I = 300$ A correspond to a typical values of high-field whole body systems

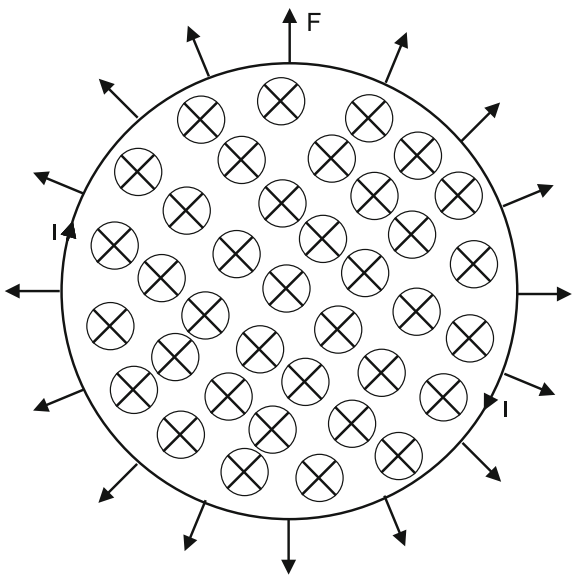

Fig. 5 Current-carrying loop in a homogenous magnetic field. The current I is interacting with the external field and is leading to tensile forces F

conductors and the magnetic fields that will result in the conductors experiencing a net force. A current-carrying loop located inside a homogenous magnetic field with its axis parallel to the magnetic field, will experience tensile forces as shown in Fig. 5 or compression forces depending on the direction of the magnetic field.

As can be seen in Fig. 3, a current-carrying loop does not only produce magnetic fields that are directed in the axial direction (parallel to axis) but also produces magnetic field components that are in the radial direction (perpendicular to the axis). Such radial components lead to forces that tend to compress the current-carrying wire packages.

Fig. 6 Equivalent electrical circuit of a magnet system

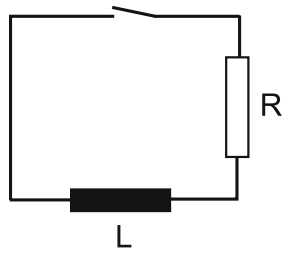

As already stated, several thousands of current-carrying wire loops are required to build a magnet that for whole body dimensions and typical currents is able to generate field strengths in that range of a few Tesla. Such a huge number of current-carrying loops form basically an equivalent electrical circuit shown in Fig. 6. The electrical circuit consists of a huge inductance L (typically in the range of hundreds or thousands of Henry) and a resistance R. A superconducting magnet has of course a resistance extremely close to 0 Ω, and if it is assumed that a circulating current is established and the switch closed then this is equivalent to a representation of a persistent magnet. Such a system shows a current decay according to $I(t) = I_o e^{-(R/L)t}$. The time constant L/R for superconducting magnets is typically in the range of a thousand or more years.

2.3 Superconductor

The practical operation of MRI systems using a central field $B_0 > 0.4$ T relies on a magnet design based on superconductivity. The key important features of a superconductor are described by three parameters viz: the critical current density j_c, the critical magnetic field strength B_c, and the critical temperature T_c. All three parameters are interdependent. If one of these thresholds is exceeded superconductivity breaks down. Both the critical current and the critical field of the early superconductors were small. Consequently, although the discovery was made in the early twentieth century, the practical basis for producing strong magnetic fields was not achieved until much later (Sekulic and Edeskuty 2001). For many years, superconductors based on NbTi are now being and are

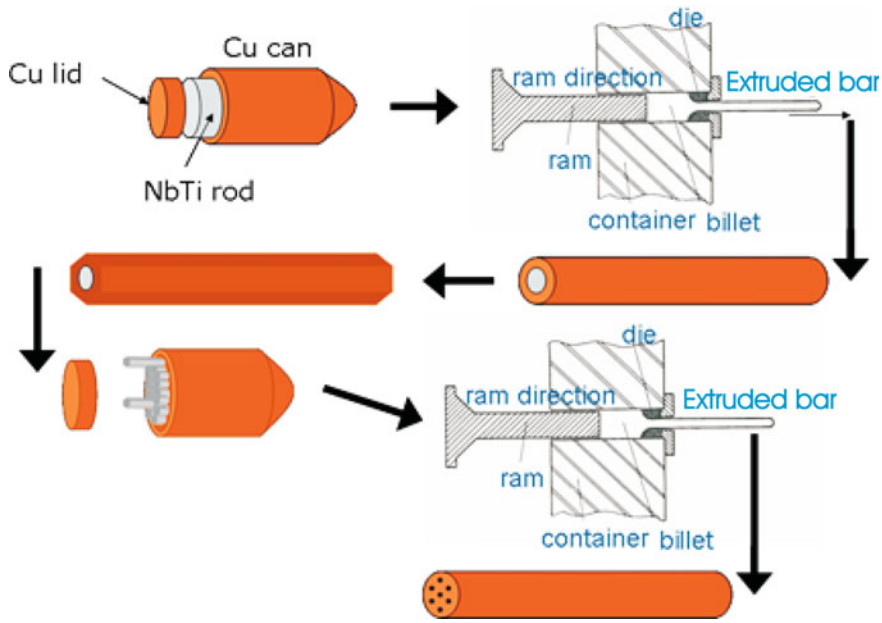

Fig. 7 Typical manufacturing process for NbTi multifilament wire

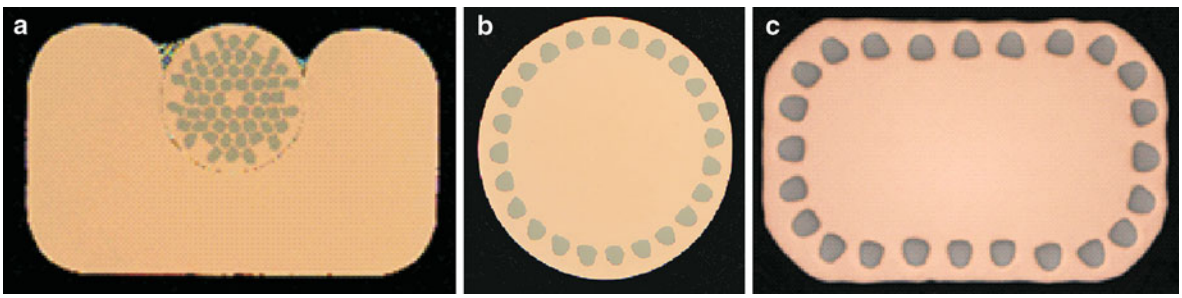

Fig. 8 Conductor types used in MRI magnets **a** wire-in-channel, **b** round, and **c** rectangular monolith conductor

the most widely used superconductors for applications below 9.4 T and, respectively, 11.7 T (Krauth 1988). MRI remains the largest consumer of superconducting materials and wire with ~100,000 km being produced annually (Lvovsky and Jarvis 2005). Cost and quality are the drivers for the development and industrial production process. Figure 7 illustrates a typical manufacturing process for NbTi wire.

A NbTi rod is inserted into a Cu can, the can is evacuated, covered with a lid and welded. This monofilament billet is then hot extruded. The extruded rod is cold drawn down to smaller diameters and shaped into a hexagonal cross-section, that is then stacked to a multifilament billet. The multifilament billet is then again extruded and drawn down to the desired wire diameter.

Three typical configurations with dimensions in the millimeter range are shown in Fig. 8. All are highly optimized with respect to the magnet requirements. Selection of the overall current density and the Cu/NbTi ratio are influenced by stress considerations and issues related to stability (Lvovsky and Jarvis 2005). Operation at 50–60% of I_c provides a temperature margin of ~1 K or higher and provides sufficient stability regarding field drift that needs to be typically less than 0.05 ppm/h for MRI applications. Usually, the current densities for MRI applications below 9.4 T are in the range of several 100 A/mm^2.

At present, MRI scanners using magnets with bore sizes of ≥68 cm are not commercially available above 11.7 T. However, there are analytical NMR systems operating at up to 23.5 T (Bhattacharya 2010) and dedicated small bore (animal) MRI systems on the market operating at field strength up to 17.2 T. The critical current density of NbTi decreases above 10 T considerably (see Fig. 9) when operating it at 4.2 K.

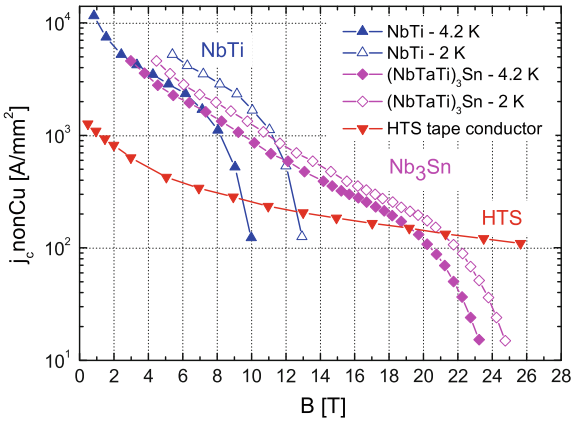

Fig. 9 Critical current density versus magnetic field for NbTi, Nb_3Sn, and typical HTS tapes

By a reduction of the temperature to 2 K, NbTi can be used up to 11.7 T, but this is the limit for this conductor. However, above 11.7 T Nb_3Sn-based superconductors are widely used up to 23.5 T. Currently, it is expected that high-temperature superconductors (HTS) will pave the way toward operating field strengths above 23.5 T, although issues relating to superconducting joint technology and handling remain to be resolved.

The first low-field whole body MRI demo magnet system based on HTS conductors ($B = 0.2$ T; $T_{op} = 20$ K) was built by Oxford Magnet Technology Oxford Instruments and Siemens in the late 1990s (Steinmeyer et al. 2002). In 2001, it was reported that MgB_2 exhibited superconductivity up to 39 K (Nagamatsu et al. 2001). Magnesium diboride has the potential for improved ease of manufacture, lower cost and better short sample lengths. The increase in operating temperature compared to that for low-temperature superconductors (LTS) provides an advantage for higher conductor stability due to the increased enthalpy margin. High enthalpy margins are an essential for innovations that would lead eventually to cryogen-free magnets and long endurance and tolerance in the event of cryocooler malfunction (Lvovsky and Jarvis 2005).

High-temperature superconductors and MgB_2 wire technology with their application for MRI magnets are currently in progress, e.g., (Xu et al. 2009; Alessandrini et al. 2008). However, for the present, the commercial superconducting MRI systems are normally wound for economic reasons using LTS NbTi or for applications above 11.7 T with Nb_3Sn.

2.4 Magnetic Field Homogeneity

The shaping of magnetic fields having a specific spatial variation over a localized region is a problem that arises in several areas of research but notably in the use and application of MRI (Reméo and Hoult 1984). One of the boundary conditions is the bore size of the magnet and is given by the object under investigation in combination with the configuration of radio-frequency (RF) and gradient coils. The construction of a high-homogeneity MRI magnet system develops in three stages:

1. A winding array is designed based solely on the analysis of the axial variation of the field of compensated solenoids or a multiple coil configuration.
2. The magnet is wound and the spatial variation of its actual field is measured.
3. The unwanted errors in the field arising from manufacturing imperfections are removed by shimming.

The basis for the design of a winding array that can shape a static magnetic field is given by the Maxwell equation in the magneto static case. Solutions of the Maxwell equations are often given by rather complicated expressions, e.g., the Biot–Savart law. However, as already stated MRI/NMR magnet design is usually based on cylindrical and mirror symmetric structures. For such structures, the resulting magnetic field can often be described along the rotation axis using a Taylor series shown below:

$$B = B_{oz} + A_{2,0} * z^2 + A_{4,0} * z^4 + A_{6,0} * z^6 + A_{8,0} * z^8 + A_{10,0} * z^{10} + O(z^{12}) \tag{1}$$

(NB: The odd orders vanish because of mirror symmetry of the magnetic structure.)

The goal of the MRI magnet design is to ensure that the coefficients $A_{n,0}$ vanish for small n. This is achieved by using different sub-coils and adjusting their positions relative to each other. The simplest example is a two-wire loop arrangement shown in Fig. 10. In Fig. 11, the field of each separate loop (lower curve) and the resulting superposition, i.e., the

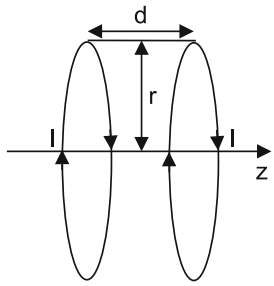

Fig. 10 Typical two-wire loop arrangement. The distance between the coils is given by the distance d and the radius by r. The current I flows in the same direction in both coils

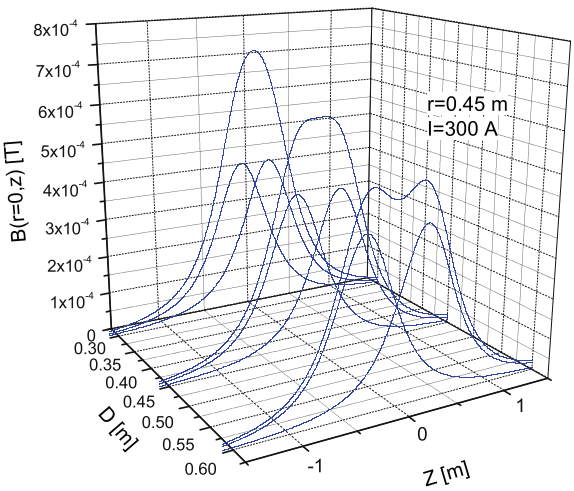

Fig. 11 Field profile of a two loop structure on-axis for different distances between loops

final field (upper curve) is shown for three different distances between loops. For each arrangement, the magnetic field on the z-axis for both of the two coils is shown (lower curves) and the resulting sum (upper curve). The configuration with $d = 0.3$ m is characterized by a distance smaller than the radius of the loops. For the set-up with $d = 0.6$ m, the distance between the loops is larger than the radius. The configuration in the middle shows a plateau. The distance between two coils is in that case chosen in such a way that it is equal to the radius. The consequence is that $A_{2,0}$ vanishes and a plateau emerges. This is called the Helmholtz configuration and provides a homogenous area very close to the center of the loops.

According to Eq. 1, the following situation exists $B = B_{0z} + O(z^4)$, i.e., the deviations from homogenous magnetic field are of the order z^4. Such a configuration is called a fourth order system. The system is described for small distances by a parabola of fourth order with the size of the homogenous volume being comparably small. In order to increase this volume, additional degrees of freedom (i.e., more compensating coils) are required that can provide compensation for the higher orders, i.e., $A_{4,0} = A_{6,0} = 0$, etc.

The description above has been mainly reduced to a problem along the z-axis of the system. However, MRI magnet systems for human application have usually bore sizes in the range of $\leq$90 cm. Therefore the homogeneity off-axis must also be considered. This changes dramatically the complexity and scale of the mathematical formulation of the solution but does not change the principles already described.

More details of such an approach are shown below, but readers who are not interested in these mathematical descriptions may omit this section.

The Laplace equation $\nabla^2 B_z = 0$ is valid for regions without current sources. The most convenient way of solving this equation for cylindrical magnet design is to employ spherical polar coordinates (r, θ, ϕ).

The solution of the Laplace equation without current sources is given as an expansion in a series of spherical harmonics described by:

$$\begin{aligned} B_Z = B_{0z} &+ \sum_{N=1}^{\infty}\sum_{M=0}^{N} r^n P_N^M(\cos(\theta)) \\ &\cdot \left[A_{N,M}\cos(M\phi) + B_{N,M}\sin(M\phi)\right] \\ &+ \sum_{N=0}^{\infty}\sum_{M=0}^{N} \frac{1}{r^{N+1}} P_N^M(\cos(\theta)) \\ &\cdot \left[C_{N,M}\cos(M\phi) + D_{N,M}(\sin(M\phi)\right] \end{aligned} \quad (2)$$

P_N^M are the so-called associated Legendre functions. As already noted for homogenous MRI magnets, the radial component B_r is very small compared to the component in z-direction (B_Z) within the field of view, i.e., inside the bore close to the magnetic center, and thus, the analysis can be restricted to B_Z only.

Equation 2 is a general solution. Boundary conditions have to be taken into account. One boundary condition is that the solution needs to be finite for $r = 0$. The first series is finite at $r = 0$ and so it is valid inside the bore and thus $C_{N,M}$ and $D_{N,M}$ are regarded as zero. For MRI magnet design purposes Eq. 2 can be further simplified by taking advantage of the cylindrical symmetry that results in $M = 0$.

The associated Legendre functions P_N^M now become Legendre polynomials P_N and only coefficients $A_{N,0}$ need to be considered. As already shown when looking at the simplified picture on the z-axis the goal of MRI magnet design is to find current distributions perhaps in combination with shim solutions that cancel out all $A_{N,0}$ except B_{0Z} (Lvovsky and Jarvis 2005; Reméo and Hoult 1984; Sauzade and Kan 1973; Garrett 1951).

In Eq. 2, the second series remains finite for $r \to \infty$ $(N > 0)$ and is thus defined outside of the magnet where $A_{N,M} = B_{N,M} := 0$. $C_{N,0}$ represent the external moments of the magnetic system. $C_{2,0}$ being a dipole and $C_{4,0}$ a quadrupole moment. The external moments can be used to describe the stray field behavior of the magnet.

It is not only a uniform field of specific magnitude that is required but also this should be combined with other criteria. For instance, it could be accompanied by the requirement for the smallest magnet (i.e., the minimum length of conductor), or by a specified limit to the acceptable peripheral field strength. In order to achieve these idealized solutions, optimization techniques are used. The field strength for a set of current coils can be computed at points along the axis, and if the peripheral field strength is included in the optimization process then fields outside the immediate vicinity of the system can also be calculated.

Magnetic resonance imaging magnet manufacturers at present use mainly two distinct approaches for achieving magnetic designs with high uniformity viz: the multiple coil (or multicoil) and the compensated solenoid approach.

2.4.1 Multicoil Approach

The multicoil design is based on a set of discrete multiple coils being placed in a strategic way to achieve a balanced field of the required uniformity. Multicoil designs allow true conductor optimization within a given envelope hence lower cost. The challenges presented by this approach are higher magnetic field peak values and higher intracoil and intercoil forces.

In an attempt to alleviate patient claustrophobia and improve patient comfort (in effect this means a bore length of $\sim$1.5 m), the multicoil design has been adopted for all clinical magnets up to 3 T (Lvovsky and Jarvis 2005).

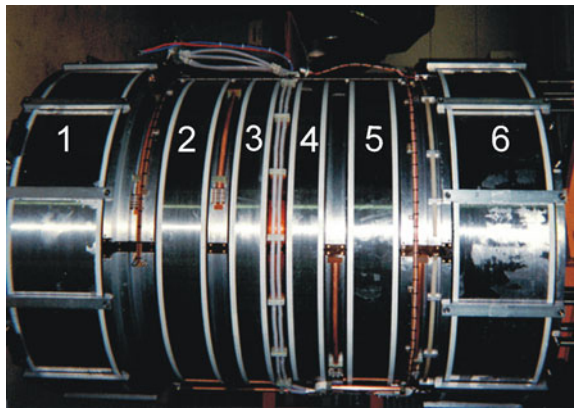

Fig. 12 Coil profile of a 3 T unshielded MRI magnet illustrating typical coil placement. The discrete multiple coils are denote by numbers in the picture

A typical example of this approach is illustrated for a non shielded 3 T whole body MRI magnet coil built by Bruker in the 1990s in Fig. 12.

The dimensions of the winding packages of the six-coil system are listed in Table 1.

The coil shown above is designed in such a way that it is compensated up to tenth order. The first uncompensated order is 12th order. The inhomogeneity is less than 10 ppm on a sphere of 45 cm DSV. As already mentioned multiple coils have disadvantages regarding intra- and intercoil forces. Thus for field strength higher than 4 T, the compensated solenoid approach is becoming favorable.

2.4.2 Compensated Solenoid Approach

The axial field of a solenoid decreases in a non-linear fashion as a function of distance from the center of the magnet (see, e.g., Sauzade and Kan 1973), and thus, inhomogeneities are created. The compensation of these inhomogeneities is usually performed using optimized compensation coils wound outside of the solenoid. The advantages compared with the multicoil approach are the low B_{Peak}/B_0 and the better-controlled stresses as a result of the solenoid being sectioned into several windings for reinforcement and conductor grading. The impact of manufacturing tolerances on the homogeneity of compensated solenoidal design is usually less pronounced compared to those for a multicoil approach. Compensated solenoids are also characterized by providing more field generating volume but only at the expense of requiring larger amounts of conductor because of the longer

Table 1 Example of an unshielded 3 T whole body MRI magnet

Coil number	Inner radius (mm)	Outer radius (mm)	Left end (mm)	Right end (mm)	Number of turns
1	568.3	617.7	−910	−585.8	7,380
2	566.3	600.8	−410.1	−239.4	2,700
3	566.3	600.8	−158.4	−35.1	1,950
4	566.3	600.8	35.1	158.4	1,950
5	566.3	600.8	239.4	410.1	2,700
6	568.3	617.7	585.8	910	7,380

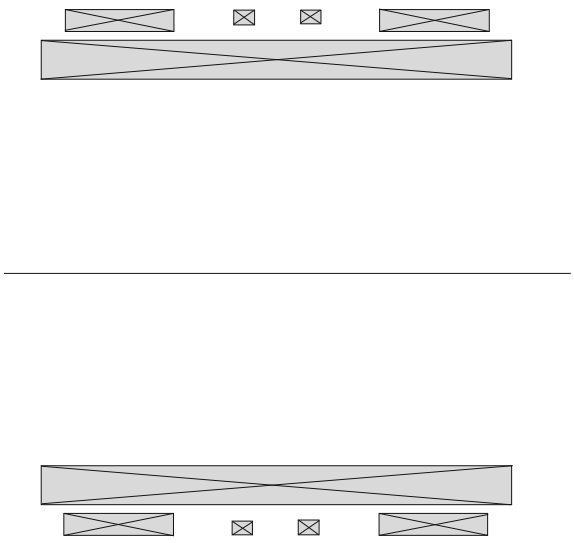

Fig. 13 Coil structure of a compensated solenoid. The compensation coils are the rectangular sections shown above and below the main section represented by the large rectangle

lengths that are required. However, the advantage of lower B_{Peak}/B_0 and less interfaces (intracoil and intercoil) compared to a multicoil design are the primary reasons for choosing solenoidal designs for fields above 4 T (Lvovsky and Jarvis 2005). A sectional drawing of a typical solenoid design with compensation coils is shown in Fig. 13.

2.4.3 Split Coil Open Approach

Split-type open superconducting systems are limited to field ranges around 1 T and are thus not the main focus of this work. However, these systems play a considerable role when considering HTS MRI magnet systems. The reader can find details about those systems in the following references (Lvovsky and Jarvis 2005; Ackermann et al. 1999; Razeti et al. 2008).

2.4.4 Active Shielding Approach

Owing to the large dipole moment of an MRI magnet, the unshielded peripheral field can extend several meters outside the cryostat. The minimization of the external stray field and thus the design of actively shielded systems is important for the siting and installation of MRI systems. Active shielding of whole body MRI magnets with central fields up to 4 T is now almost universal. Above 4 T passive shielding using hundreds of tons of iron was, for a long time, the only way to effectively reduce the extent of the peripheral field. Such amounts of iron dramatically increase the difficulties in siting these magnets and also the overall costs.

The basic theoretical idea of active shielding is to include two reverse polarity coils in the coil array. Typically, the diameter of the shielding coil is twice that of the main coil and the shielding coils use normally over one-third (1/3) of the total length of conductor. The negative ΔB_0 coming from the shielding coils wound on a larger radius has to be compensated by additional ampere-turns in the main coil itself. The effect of shielding on the harmonics of the central field must be included in the design of the compensation coils. Actively shielded magnets require considerably more conductor (typically about a factor of two) and normally exhibit higher stress than unshielded magnets of the same magnetic field and the same homogeneity (Williams 2001; Lvovsky and Jarvis 2005). However, the strongly diminished stray field and thus considerable reduction in siting costs more than outweighs these possible drawbacks.

In Fig. 14, the coil arrangement of an actively shielded 4.7 T Bruker system with a room temperature bore diameter of 40 cm is shown. The magnet system consists of a multicoil arrangement complete with shielding coils (shown on the ends of the coil arrangement in silver color). In Fig. 15, the 0.5 mT

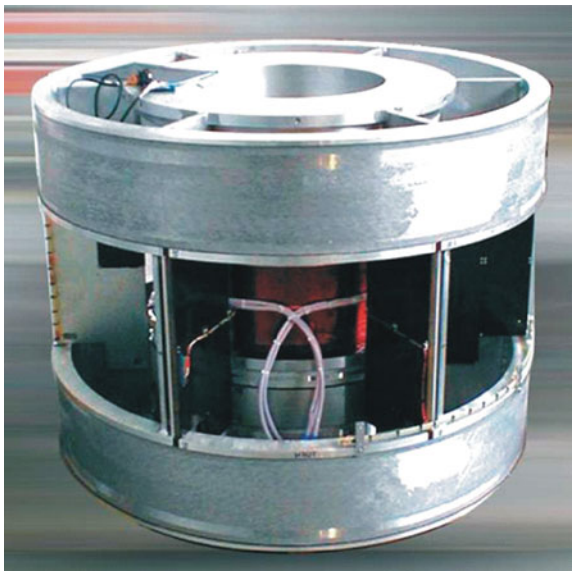

Fig. 14 Coil arrangement of an actively shielded 4.7 T with a warm bore size of 40 cm. The shielding coils are shown on the top and the bottom of the coil

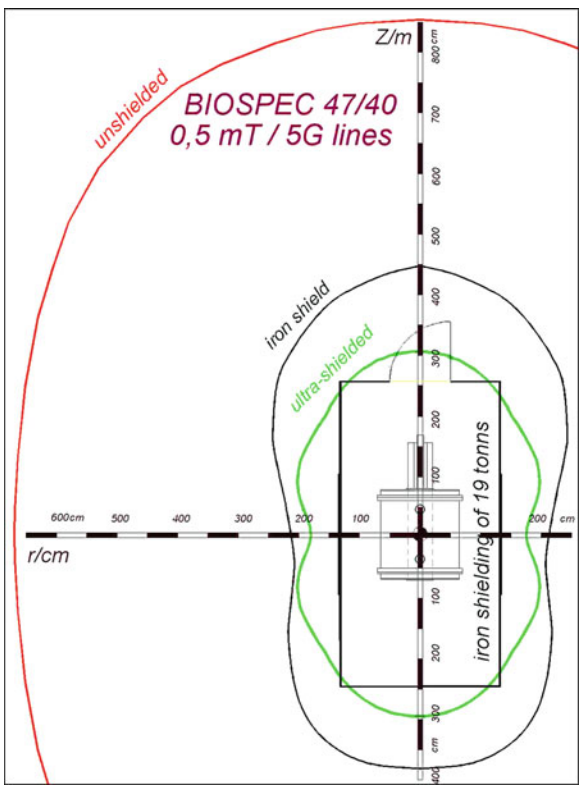

Fig. 15 Comparison of a non-actively shielded 4.7 T with 40 cm bore with and without passive shielding with an active shielded one

(5 Gauss) stray field line of a non-actively shielded 4.7 T with 40 cm bore is shown using no passive shielding and also using 19 t of shielding iron. This is then compared with a 4.7 T actively shielded system with the same bore size. As can be seen the new 4.7 T achieves a stray field that is even superior to those of the old system using 19 t of shielding iron.

2.4.5 Design Criteria

As already indicated magnetic field homogeneity is an exceedingly important aspect of coil design. However, force criteria also need to be applied to qualify any design. If the force and thus the stress exceed certain limits, the superconducting coil will be irreversibly damaged. As we have seen already there are radially acting tensile forces and compression forces which tend to compress the winding package in axial direction. The simplest calculation of hoop stresses (radially acting) is based on the assumption that each turn acts independently of its neighbors and therefore develops an overall hoop stress of $\sigma = j \cdot B_{oz} \cdot r$ (Wilson 1983) where j is the current density and could be typically in the range of 200 A/mm^2; B_{0z} can be 3 T and the typical radius r is for a whole body system in the range of 0.5 m. Thus, the resulting tensile stress in such a case amounts to about 300 MPa which significantly exceeds the yield strength of pure copper and is thus harmful for a single loop of superconducting material.

As referred to before the magnetic fields do not only point in the axial but also in the radial directions leading to axial compression of the winding packages. Axial compression forces lead to intra coil forces but could also lead to interaction with parts of the coil formers, i.e., interfaces (inter coil forces). For intra coil forces and also for inter coil forces design criteria showing upper limits need to be applied.

Another important design criterion is the maximum allowable current density in the superconductor. That criterion is strongly influenced by field drift and thus field stability considerations.

2.4.6 Shimming

The expression "shimming" refers to the need to compensate the central field and eliminate inhomogeneities arising from intrinsic design features, manufacturing tolerances, and thermal contractions of the magnet plus any magnetic disturbances produced by the site. Thus, the simplification (i.e., mirror

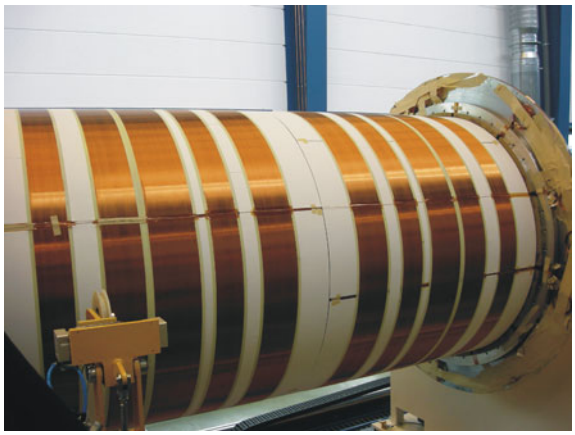

Fig. 16 Zonal shims mounted on a solenoid coil

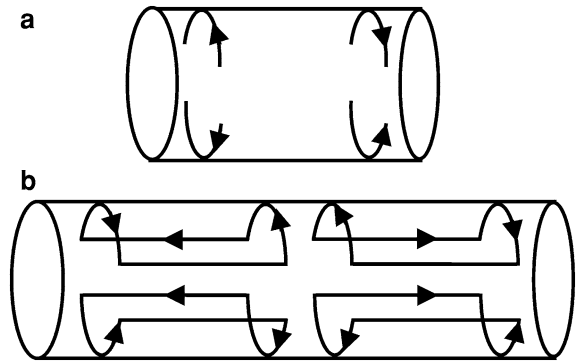

Fig. 17 Current arcs. The basic building block of tesseral shims is shown in **a**. However, the current loops are evidently not closed. Thus, additional wiring in z-direction is needed to complete the loop (currents in z-direction do not produce a field in z-direction and thus do not affect the MRI experiments). The resulting current arc for the first-order radial terms is shown in **b**

symmetry) is to some extent violated and Eq. 1 is no longer valid in such a simple form on the z-axis. Odd orders have to be taken into account. The cylindrical symmetry is also to a small extent violated and therefore off-axis terms depending on ϕ appear. Thus, Eq. 2 needs to be taken into account. The errors of a magnet are usually divided into purely axial variation (zonal harmonics that depend on the elevation θ from the z-axis and are independent of ϕ) and radial variations called tesseral harmonics that depend on ϕ (ϕ being the angle of azimuth in the x–y plane). In order to compensate for the presence of various unwanted harmonic errors in the central field of the as-built coils, additional current-carrying coils (room temperature or superconducting) or passive ferromagnetic shim elements capable of generating the opposite (and compensating) harmonics are introduced into the magnet systems (Morrow 2000; Williams 2001).

The process of shimming takes place after the superconducting magnet has been built and a field plot obtained. Based on the analysis of the coefficients of the field plot, the corresponding currents are put into the shim coils or the corresponding ferromagnetic shim distribution is loaded to compensate for the unwanted deviations from a homogenous magnet. When using ferromagnetic shims, more terms can be addressed (typically 8th–10th order). Some manufacturers deal with ferromagnetic shims only whilst others rely on a combination of superconducting shims for lower orders (up to the 4th order zonal; 3rd order tesseral) and ferromagnetic shims to compensate for the higher orders.

Superconducting shims. The basic mathematics for shim design has been described extensively in (Reméo and Hoult 1984; Sauzade and Kan 1973). In brief, the circular coil is the basic building block of zonal design. The goal of the design is now to combine the building blocks in such a way that a single harmonic order only is created and at the same time the other harmonic orders are suppressed. In Fig. 16, the zonal shims mounted on a solenoid coil are shown.

The current arc is the basic building block of tesseral shim design (Reméo and Hoult 1984; Sauzade and Kan 1973; Bobrov and Punchard 1988) (see Fig. 17). The goal of tesseral shim design is of course the same as that for zonal design (the desired harmonic is created and the undesired ones are suppressed as far as feasible). However, the radial shims are more complex than those for purely axial harmonics. For a linear shim coil with ($n = m = 1$) (linear term) a possible solution is shown in Fig. 17. More about optimum design of tesseral shim coils can be found in the literature (Bobrov and Punchard 1988).

The superconducting shims are fixed usually around the outside of the main windings. The relatively large radius reduces the effective strength of the harmonics generated by the superconducting shims. Placing the windings closer to the center of the coil would lead to increased costs for superconductor for the main coil and would require the use of superconducting material with a higher critical field for the shim coil that would also add to the total expense.

Fig. 18 Set-up for passive shimming a magnet

Additional information about the manufacturing process of superconducting shims can be found in the literature (Bobrov et al. 1987).

Ferromagnetic shims. The principle invoked in this kind of shimming is different from that used for superconducting shim coils. Shims take the form of discrete pieces of ferromagnetic material and are usually placed inside the bore of the magnet. The pieces of steel are exposed to an axial magnetizing field at a position sufficient to saturate the pieces. In turn, this generates a field at a point in space that is a function of the mass of the shim and its saturation magnetization with little dependence on its shape (Williams 2001). The field B caused by the ferromagnetic shim contains both axial and radial components. The axial component B_z is the field required and it adds arithmetically to the field of the magnet. The radial component adds vectorially to the field and produces negligible change in the magnitude of the axial field.

Hoult and co-workers have presented comprehensive details of ferromagnetic shimming together with the basic equations and solutions (Reméo and Hoult 1984; Hoult and Lee 1985).

The first step in a shim iteration is to carry out a field plot at a number of points. Then, the influence matrix of the shim fields at the same point is calculated and the required masses of the shims determined (Williams 2001). In an MRI magnet, the shims are steel plates or something equivalent and are fixed in shim trays. A typical mechanical setup for this method of shimming a magnet is shown in Fig. 18. Each of the pockets is filled with a certain amount of iron plates with different thicknesses to compensate for the corresponding inhomogeneities.

2.5 The Cryostat

As previously mentioned, the practical and economic operation of MRI systems with a central field $B_0 > 0.4$ T requires the use of a magnet system based on superconductivity. Superconducting magnet systems require a configuration that provides nearly perfect thermal insulation between the cold coil volume (typically at helium temperature $\sim$4.2 K) and the surrounding environment which is at room temperature ($\sim$300 K). Vessels satisfying these requirements are called cryostats.

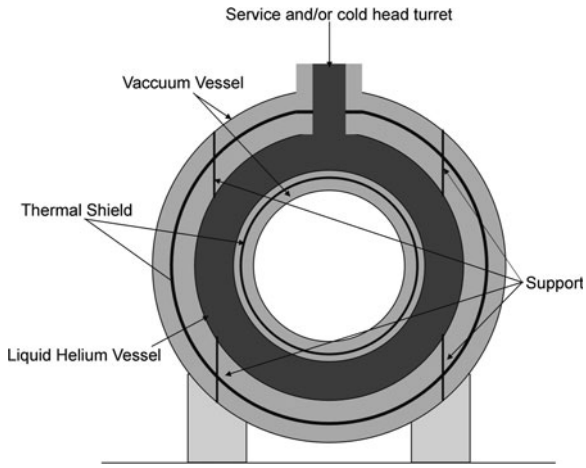

Fig. 19 Schematic of a cryostat for an MRI magnet system operating at 4.2 K

2.5.1 Cryostat Design

In Fig. 19, a schematic of a cryostat for an MRI magnet system is shown. Cryostats consist typically of an arrangement of two vessels. The MRI magnet coil is situated within the liquid helium vessel (the vessel shown in dark gray in Fig. 19). That vessel is supported within the outer vessels (shown in light gray) by structures made from material with very low thermal conductivity. For stability reasons, the coupling between the outer and inner vessel needs to be rigid. The space between the outer vessel and the liquid helium vessel is evacuated and equipped with thermal shield(s) and thermal insulation. The thermal shields/insulations are in connection with an appropriate cooling reservoir to minimize thermal losses caused by thermal radiation. An ultra high vacuum between the helium vessel and the outer vessel is essential for the reduction of heat transfer caused by residual gas atoms and molecules.

Passive cooling. In the early days of MRI cryostat design, one of the thermal shields was cooled by evaporating nitrogen. The helium vessel itself and a possible further shield were cooled by

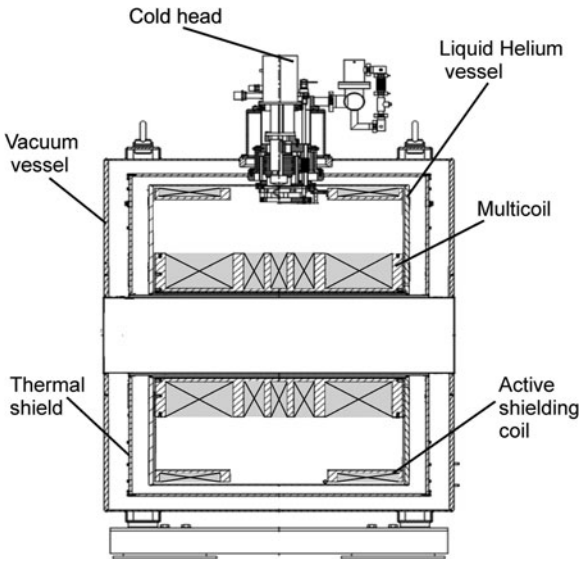

Fig. 20 Cryostat of a PT-refrigerated system

evaporating helium. The consumption of liquid helium was typically 0.5 and 1 l/h of liquid nitrogen (Schwall 1987).

Active cooling. The adaption of two stage GM refrigerators to the cryostat's thermal shield cooling around 1985 has eliminated the need for an expensive and bulky liquid nitrogen vessel within the cryostat (Morrow 2000; Ackermann et al. 1999). Since then the use of liquid nitrogen for cooling, the thermal shield of whole body MRI magnet systems has become more and more obsolete and the consumption of liquid helium was reduced well below 0.1 l/h (Morrow 2000). Further progress in the field of cryocoolers around 1996 made it possible to design the first zero boil-off systems (i.e., systems that recondense the evaporating helium and thus work in a closed cycle). All this innovation has led to a reduction in the operating costs and system down time for cryogen loading.

The use of PT refrigerator technology is becoming more and more popular. PTs induce much less vibration compared to the standard GM coolers. Thus, the interfacing between cold head and cryostat can be simplified. Less vibration also leads to an improvement in MRI short-term stability and thus better MRI/MRS quality. In Fig. 20, a pulse tube refrigerated cryostat for a 7 T with 30 cm bore is shown.

Cryogen-free cryostats in which all heat loads are removed by a cryocooler have been an important field for developments since the middle of 1990 (Steinmeyer et al. 2002; Ackermann et al. 1999; Razeti et al. 2008; Laskaris et al. 1995). However, cryostats using multiple cryogens also are a progressing field especially when looking at HTS (Stautner et al. 2009).

3 High-Field Superconducting Magnet Systems

The design aspects for magnets from the MRI user's point of view are:
high MRI/MRS performance;
efficient siting;
long term stability;
user friendly;
cost efficient.

Superior MRI/MRS performance is proportional to high signal to noise (SNR) ratio. The signal to noise ratio increases with the strength of the main magnetic field thereby leading the trend toward higher operating field strengths. However, MRI/MRS quality also requires a highly uniform main magnetic field accompanied with excellent temporal field stability. The field uniformity is defined by the layout and manufacturing of the magnet coil and the application of appropriate shimming procedures. High temporal field stability is usually achieved by operating the magnet in a persistent mode using high current-carrying superconducting switch technology. The connections between the superconducting wires (the joints) need also to be superconducting. In addition, measures have to be implemented to reduce perturbations caused by time dependent external magnetic fields. Efficient siting of an MRI magnet system is achieved by applying active shielding technology and restricting the stray field, the weight and the outer dimensions to an absolute minimum. For patient comfort, the maximum possible access should be provided keeping the magnet as short as possible. The design needs to provide long-term reliability and a cost efficient way for transport and installation of the system.

The cryostat system should be practically invisible for the user (e.g., providing zero boil-off) thus reducing costs and down time to an absolute minimum. However, all these features should be provided at a very low and competitive price. These are the drivers for MRI magnet development.

Table 2 Magnet parameters of an unshielded 7 T whole body scanner manufactured by Varian/Magnex and an actively shield head scanner

Specifications/ manufacturer	Magnex/Varian (Warner 2008; D. Houlden 2010, private communication)	Magnex/Varian (D. Houlden 2010, private communication)
Central field (T)	7	7
Bore size (cm)	90	68
DSV/field uniformity (cm/ppm)	45/5	30/5
Drift rate (ppm/h)	0.05	0.05
Stored energy (MJ)	78.7	
Stray field axial × radial (m × m) 5 G	22.5 × 17.8	6.4 × 3.3
Coil design type	Compensated solenoid	Compensated solenoid
Shim type	Superconducting + passive	Superconducting + passive
Magnet length (m)	3.37	2.2
Magnet diameter (m)	2.38	2.7
Magnet weight (t)	32	24
Service height (m)		
Helium hold time (days)	>100	Infinite, zero helium boil-off
Nitrogen hold time (days)	n/a	n/a

Standard clinical MRI scanners are still operating at 1.5 T and below. However, in recent years, the 3 T market has evolved rapidly reaching market penetration between 30 and 40%. The 4 T market has not become a standard and consequently the next higher field strength supported by three of the main manufacturers of MRI systems (GE, Philips, and Siemens) is 7 T. The first 7 T whole body (90 cm bore) was installed in 1999 (Warner 2008). The installed base of 7 T human systems amounts today (middle of 2010) to around 40 units. The standard 7 T configuration up to the end of 2009 used passive shielding. However, Varian has manufactured the first actively shielded 7 T with a bore diameter around 82 cm, and Bruker will soon launch a similar version. The actively shielded 7 T approach may very well open the market for an expanded range of applications and clinical opportunities.

An 8 T head scanner (at that time 80 cm) was manufactured in 1998 (Warner 2008), however, that field strength also has not developed into a standard.

The first 9.4 T head scanner (65 cm bore) was manufactured in 2003 by Magnex Scientific Ltd, a company that was later acquired by Varian, Inc. In the same year, GE installed a 9.4 T system with 80 cm bore. In 2006, Varian delivered a 9.4 T with 82 cm bore to a customer site and 2 years later a 9.4 T with a 90 cm bore was added to their product line. All 9.4 T magnets are passively shielded. At present Varian, Inc. is manufacturing a 10.5 T whole body and an 11.7 T head scanner. 11.7 T whole body scanners are at present not available on a commercial basis, however, a research program is on its way with the goal to realize such a system in 2012.

For some time, small animal MRI has played a vital role in the investigation of diseases and in the development of medication. Animal MRI focuses in many cases on smaller animals and thus bore sizes between 16 and 40 cm are large enough to accommodate the gradient coil, the RF Coil, and the animal handling. Horizontal axis animal MRI magnets are nowadays available up to 17.2 T with an entry level field strength of around 4.7 T.

The main manufacturers of such dedicated animal magnet systems are Bruker, Varian, and JASTEC.

In the following section, clinical MRI magnet systems with field strengths $\geq$7 T from different manufacturers will be discussed. In addition, the corresponding small animal MRI magnets are presented.

3.1 7 T MRI Magnets

The first 7 T system with a bore size of 90 cm (whole body system) was brought to the market in 1999 (Warner 2008). The increase in field strength led

Table 3 Magnet parameters of a 7 T 30 cm animal MRI magnet system manufactured by Bruker

Specifications/manufacturer	Bruker
Central field (T)	7
Bore size (cm)	30
DSV/Field uniformity (cm/ppm)	18/10
Drift rate (ppm/h)	0.05 ppm/h
Stored Energy (MJ)	5.4
Stray field axial × radial (m × m) 5 G	3 × 2
Coil design type	Multicoil approach
Shim type	Passive
Magnet length (m)	1.49
Magnet diameter (m)	1.65
Magnet weight (t)	5.2
Service height (m)	2.85
Helium hold time (days)	Infinite, zero helium boil-off
Nitrogen hold time (days)	n/a

finally to considerable improvements in image quality, although significant improvements in non-magnet related hardware and software still had to be achieved. The progress in the field of 7 T might have been less pronounced if the main manufacturers had not begun to implement 7 T in their respective product portfolios. At present, about 40 systems based on the Magnex/Varian magnet design shown in Table 2 have been installed. The market for 7 T whole body MRI systems is currently dominated by Siemens followed by Philips, GE, and Varian. From a magnet point of view, the peripheral field of these unshielded systems is currently regarded as the biggest restriction. A 7 T with 90 cm bore as shown in Table 2 typically requires a shielded room using about 200–400 t of steel to control the peripheral field. Steel cages are expensive and require a lot of site planning effort so that building costs can sometimes out-weight the magnet costs (Warner 2008). As already explained actively shielding considerably reduces the peripheral field and thus the siting costs, but increases the magnet price and the complexity of the system. The first actively shielded 7 T magnet for human applications was a dedicated head scanner with 68 cm bore size installed in 2006. Progress in gradient technology in recent years has made it possible to reduce the bore size of a human whole body

Fig. 21 The 9.4 T 90 cm MRI magnet from Magnex/Varian (D. Houlden 2010, private communication) being craned into a building

magnet system from 90 cm to about 82 cm. That reduction in diameter has also a very positive impact on costs and feasibility of an actively shielded 7 T human whole body MRI system. Varian has manufactured a 7 T MRI magnet with 83 cm bore size. The details about the design principle of Bruker's 7 T can be found in Neuberth and Westphal (2009).

For smaller systems, i.e., dedicated animal MRI systems with bore sizes well below 68 cm the actively shielding approach has been used since the end of the 1990s. As an example, the features of a Bruker 7 T magnet system with a 30 cm bore are displayed in Table 3. Similar systems are available from Varian and JASTEC also.

3.2 9.4 T MRI Magnets

Until 2008, the highest commercially available magnet system for human applications operated at 9.4 T. As can be seen in Table 4, there is a wider variety of bore sizes on the market compared to the 7 T whole body systems. It began with 65 and 80 cm bore systems in 2003. In 2006, the 9.4 T human MRI magnet family was extended by a 82 cm system, which could nowadays become a human whole body system. Two years later, the first 9.4 T with 90 cm was installed. All of these magnet systems are not actively shielded. The increase of the magnet and siting costs of such systems seems to have hampered their spread in the research market. A picture of a 9.4 T with a bore diameter of 90 cm when being craned into a building is shown in Fig. 21.

Table 4 Magnet parameters of 9.4 T head or whole body scanners

Specs/ manufacturer	Magnex/Varian (Warner 2008; D. Houlden 2010, private communication)	GE (Lvovsky and Jarvis 2005; P. Jarvis and P. Feenan 2010, private communication)	Magnex/Varian (Warner 2008; D. Houlden 2010, private communication)	Magnex/Varian (Warner 2008; D. Houlden 2010, private communication)
Central field (T)	9.4	9.4	9.4	9.4
Bore size (cm)	65	80	82	90
DSV/field uniformity (cm/ppm)	30/5	40/5	40/5	45/5
Drift rate (ppm/h)	<0.05	0.05	<0.05	<0.05
Stored Energy (MJ)	78	140	152	182
Stray field axial × radial (m × m) 5 G	20.2 × 16.0	25.1 × 20.0	25.9 × 20.5	27.6 × 21.8
Coil design type	Compensated solenoid	Compensated solenoid	Compensated solenoid	Compensated solenoid
Shim type	Superconducting + passive	Superconducting + passive	Superconducting + passive	Superconducting + passive
Magnet length (m)	3.15	3.6	2.56	3.72
Magnet diameter (m)	2.38	2.4	3.70	2.96
Magnet weight (t)	30	45	47	57
Service height (m)		4.5		
Helium hold time (days)	>180	90	>100	>90
Nitrogen hold time (days)	n/a	n/a	n/a	n/a

Animal scanners are considerably smaller, and thus, active shielding is a standard for such magnet systems. Typical specifications are shown in Table 5. A similar system is available from Varian also.

3.3 11 T MRI Magnets

As we have seen in the section about superconductivity, Niobium titanium conductor is not suitable for field strengths greater than about 10 T when operating at a temperature of 4.2 K. There are at present two ways to overcome that obstacle, by using Nb_3Sn superconductor or by reducing the operating temperature of the NbTi conductor by suitable measures to about 2 K making field strengths up to 11.7 T possible. Nb_3Sn is about a magnitude more expensive than NbTi so that the latter alternative is usually preferred when considering the design and manufacture of 11 T magnets for human applications.

Varian is currently working on a dedicated non-actively shielded head scanner operating at 11.7 T. Specifications of the system are displayed in Table 6. In brief, the big difference compared to systems at $\leq$9.4 T is that it will operate at about 2.4 K so that conventional NbTi superconductor technology can be used. The reduced operating temperature is achieved using a pump running continuously on the helium reservoir (Warner 2008). As a part of the French–

Table 5 Magnet parameters of an actively shielded 9.4 T animal MRI scanner

Specifications/manufacturer	Bruker
Central field (T)	9.4
Bore size (cm)	30
DSV/field uniformity (cm/ppm)	18/10
Drift rate (ppm/h)	0.05 ppm/h
Stored energy (MJ)	13.1
Stray field axial × radial (m × m) 5 G	2.3 × 3.3
Coil design type	Compensated solenoid approach
Shim type	Passive
Magnet length (m)	2.01
Magnet diameter (m)	1.70
Magnet weight (t)	11.5
Service height (m)	2.90
Helium hold time (days)	Infinite, zero helium boil-off
Nitrogen hold time (days)	–

Table 7 Magnet parameters of a 11.7 T Bruker system for animal applications

Specifications/manufacturer	Bruker
Central field (T)	11.7
Bore size (cm)	16
DSV/field uniformity (cm/ppm)	6/4
Drift rate (ppm/h)	0.05
Stored energy (MJ)	3.4
Stray field axial × radial (m × m) 5 G	3 × 2
Coil design type	Compensated solenoid
Shim type	Passive
Magnet length (m)	1.46
Magnet diameter (m)	1.65
Magnet weight (t)	7
Service height (m)	2.85
Helium hold time (days)	Infinite, zero helium boil-off
Nitrogen hold time (days)	n/a

Table 6 Magnet parameters of 11.7 T for human applications

Specifications/manufacturer	Magnex/Varian (D. Houlden 2010, private communication)	CEA/Dapnia/Irfu (Vedrine et al. 2008; Schild et al. 2010; Vedrine et al. 2010; Brédy et al. 2010)
Central field (T)	11.74	11.75
Bore size (cm)	68	90
DSV/field uniformity (cm/ppm)	30/5	10/0.05
Drift rate (ppm/h)	0.05	<0.05
Stored energy (MJ)	186	338.5
Stray field axial × radial (m × m) 5 G	27.0 × 21.4	13.5 × 10.5
Coil design type	Compensated solenoid	Double pancake
Shim type	Superconducting + passive	Cryoshims
Magnet length (m)	3.66	5.2
Magnet diameter (m)	2.73	5
Magnet weight (t)	<60	132
Service height (m)		
Helium hold time (days)	>365	
Nitrogen hold time (days)	n/a	

German research project Iseult/INUMAC the design and manufacture of an actively shielded 11.7 T with a 90 cm bore is advancing (Vedrine et al. 2008 and references therein; Schild et al. 2010). The magnet system will be built by CEA/Dapnia/Irfu. The concept shows considerable differences compared to the already presented designs. The main coil is built up from an arrangement of modules of double pancake windings. This configuration allows direct contact of the superconductor with super fluid helium

($T = 1.8$ K) and thus the system benefits from cryo-stabilization (Vedrine et al. 2008; Schild et al. 2010). As shown in Table 6, the magnet will store about 340 MJ when operating at about 1,500 A. Owing to the high operating current, the number of inter-double pancake joints and the high stored energy the magnet will operate in a non-persistent mode using a highly stabilized power supply permanently connected to the magnet (Vedrine et al. 2008).

The development of 11 T whole body magnets is an attractive field for magnet designers so that a new concept study was published recently (Wada et al. 2010).

In Table 7, the parameters of a small bore actively shielded small animal MRI system is shown. At bore diameters of, e.g., 16 cm, the price increase caused by additional cooling technology for operation at about 2 K can out-weight the additional costs for Nb_3Sn superconductor, which is required when operating at normal pressure and thus 4.2 K. Similar systems are advertised by Varian also.

Acknowledgments The author is grateful to Dr. M. Westphal for his useful comments and interesting discussions. Furthermore, the author thanks Dr. H. Post, Dr. R. E. Gordon, Dr. K. Schlenga, and G. Neuberth for their support. Contributions from our competitors are gratefully acknowledged.

References

Ackermann RA, Herd KG, Chen WE (1999) Advanced cryocooler cooling MRI systems. In: Ross RG Jr (ed) Cryocooler 10. Kluwer Academic, New York

Alessandrini M, Putman P, Majkic G et al (2008) Winding and testing of large bore solenoids, and study of quench propagation in short coils made with multifilament MgB_2 tape. IEEE Trans Appl Supercond 18(2):945–948

Bhattacharya A (2010) Breaking the billion-hertz barrier. Nature 463(4):605–606

Bobrov ES, Punchard WFB (1988) A general method of design of axial and radial shim coils for NMR and MRI magnets. IEEE Trans Magn 24(1):533–536

Bobrov ES, Pillsbury RD Jr, Punchard WFB et al (1987) A 60 cm bore 2.0 Tesla high homogeneity magnet for magnetic resonance imaging. IEEE Trans Magn 23(2):1303–1308

Brédy P, Bélorgey J, Chesny P et al (2010) Cryogenics around the 11.7 T MRI Iseult magnet. IEEE Trans Appl Supercond 20(3):2066–2069

Damadian RV (1971) Tumor detection by nuclear magnetic resonance. Science 171:1151–1153

Garrett MW (1951) Axial symmetric systems for generating and measuring magnetic fields. Part I. J Appl Phys 22: 1091–1106

Hawksworth DG, McDougall IL, Bird JM et al (1987) Considerations in the design of MRI magnets with reduced stray fields. IEEE Trans Magn 23(2):1309–1314

Hoult DI, Lee D (1985) Shimming a superconducting nuclear-magnetic resonance imaging magnet with steel. Rev Sci Instrum 56(1):131–135

Jin J (1999) Electromagnetic analysis and design in magnetic resonance imaging. CRC Press, Boca Raton

Krauth H (1988) Recent developments in NbTi superconductors at Vacuumschmelze. IEEE Trans Magn 24(2):1023–1028

Laskaris ET, Ackermann T, Dorri B et al (1995) A cryogen-free superconducting magnet for interventional MRI applications. IEEE Trans Appl Supercond 5(2):163–168

Lauterbur PC (1973) Image formation by induced local interactions: examples employing nuclear magnetic resonance. Nature 242:190–191

Lvovsky Y, Jarvis P (2005) Superconducting systems for MRI—present solutions and new trends. IEEE Trans Appl Supercond 15(2):1317–1325

Mansfield P, Grannell PK (1973) NMR "diffraction" in solids? J Phys C Solid State Phys 6:L422–L426

Morrow G (2000) Progress in MRI magnets. IEEE Trans Appl Supercond 10(1):744–751

Nagamatsu J, Nakagawa N, Muranaka T et al (2001) Superconductivity at 39 K in magnesium diboride. Nature 410:63–64

Neuberth G, Westphal M (2009) Kompakte supraleitende Magnetanordnungen mit aktiver Abschirmung, wobei die Abschirmspule zur Feldformung eingesetzt wird. German patent DE 10 2008 020 107 A1

Razeti M, Angius S, Bertora L et al (2008) Construction and operation of cryogen free MgB_2 magnets for open MRI systems. IEEE Trans Appl Supercond 18(2):882–886

Reméo F, Hoult DI (1984) Magnetic field profiling: analysis and correcting coil design. Magn Reson Med 1:44–65

Sauzade MD, Kan SK (1973) High resolution nuclear magnetic resonance spectroscopy in high magnetic fields. Adv Electron Electron Phys 34:1–93

Schild T, Abdel Maksoud W, Aubert G et al (2010) The Iseult/INUMAC whole body 11.7 T MRI magnet R&D program. IEEE Trans Appl Supercond 20(3):702–705

Schwall RE (1987) MRI-superconductivity in the marketplace. IEEE Trans Magn 23(2):1287–1293

Sekulic DP, Edeskuty FJ (2001) Cryogenic stabilization. In: Lee PJ (ed) Engineering superconductivity, 1st edn. Wiley, New York

Stautner W, Xu M, Laskaris ET et al (2009) The cryogenics of an MRI demonstrator based on HTS technology with minimum coolant inventory technology. IEEE Trans Appl Supercond 19(3):2297–2300

Steinmeyer F, Retz AW, White K et al (2002) Towards the invisible cryogenic system for magnetic resonance imaging. In: Breon S et al (ed) Advances in cryogenic engineering: proceedings of the cryogenic engineering conference, vol. 47. pp. 1659–1666

Vedrine P, Aubert G, Beaudet F et al (2008) The whole body 11.7 T MRI magnet for Iseult/INUMAC project. IEEE Trans Appl Supercond 18(2):868–873

Vedrine P, Aubert G, Beaudet F et al (2010) Iseult/INUMAC whole body 11.7 T MRI magnet status. IEEE Trans Appl Supercond 20(3):696–701

Wada H, Sekino M, Ohsaki H et al (2010) Prospect of high-field MRI. IEEE Trans Appl Supercond 20(3):115–122

Warner R (2008) Advances in high field magnets. Abstract ISMRM high field systems & applications: what's special about 7 T+? Workshop Rome

Williams EC (2001) Magnets for magnetic resonance analysis and imaging. In: Lee PJ (ed) Engineering superconductivity, 1st edn. Wiley, New York

Wilson MN (1983) Superconducting magnets. Clarendon Press, Oxford

Xu M, Laskaris T, Budesheim E et al (2009) Experimental layer-wound mock-up coil for HTS MRI magnet using BSCCO tape. IEEE Trans Appl Supercond 19(3): 2309–2312

Gradients in Ultra High Field (UHF) MRI

Peter Dietz, Franz Schmitt, and Jürgen Hennig

Contents

Abstract

The gradients are one of the three magnetic field generating units that are necessary to make MRI work. While the other two types of fields are directly affected by the strength of the main magnet—the static magnetic field, B_o, and the RF (radio frequency) fields by the Larmor frequency depending linear on the static magnetic field strength—the same set of gradients is able to work at any static field strength. The principle design goals for gradients in UHF are the same as in standard MRI. Nevertheless, it is advisable to adapt the gradient system to the challenging working conditions in an UHF environment.

1 Gradients in the MRI World

1.1 Function

The gradient system is supposed to deliver dynamically changing magnetic fields that allow spatial encoding inside the field of view.

A standard solution is a set of three fields that are orthogonal to each other and can be switched on and off separately. The name "gradient" is derived from the most common configuration which uses fields with a certain spatial characteristic.

The field component parallel to the direction defined by the static magnetic field (called B_z by definition) describes a linear increase in one of the Cartesian directions, but is otherwise constant. For example, the X-gradient will produce a field mathematically described as

P. Dietz · F. Schmitt (✉) · J. Hennig
Siemens AG H IM MR, University Freiburg, Freiburg, Germany
e-mail: franz.schmitt@siemens.com

J. Hennig and O. Speck (eds.), *High-Field MR Imaging,* Medical Radiology. Diagnostic Imaging,
DOI: 10.1007/174_2011_200,

$$B_z(r) = G * x \quad (1)$$

with G being the gradient strength given in mT/m.

Besides the gradient strength, nonlinearity and slew rate (or rise time) are the most important parameters to characterize the properties of a gradient field.

Nonlinearity is a figure, expressed in percentage, to identify the deviation of the shape of the real gradient field from the ideal (linear) gradient field at a certain distance from the center describing the linearity volume.

Slew Rate, measured in T/m/s, describes the capability to change the gradient field with time. A higher slew rate enables faster switching and is identical to a shorter rise time up to a certain gradient strength.

1.2 Components

The gradient system is divided into several subsystems: The gradient coil, the driving gradient power amplifier (GPA) and the interconnecting parts such as cables, filters, connectors etc. Also considered as part of the gradient system are shim coils and passive shims as long as they are built into the gradient coil. Some of these gradient system contributing parts are described below, others are not considered as they are not Ultra High Field (UHF) relevant.

1.2.1 Gradient Coil (GC)

All existing UHF systems are of the cylindrical MRI type. In such a configuration the gradient coil is also a cylinder concentrically positioned inside the magnet bore. This potted cylinder (Fig. 1 at left) contains several parts including its main components, the three separate gradient coil windings, representing the X-gradient, the Y-gradient (Fig. 1 at right) and the Z-gradient. Each gradient coil winding consists of an inner primary layer and an outer secondary layer, which shall reduce the stray field of the gradient coil towards the magnet and so define the shielding characteristics of the GC (Chapman 2006; Turner 1986a, b, 1988, 1993a, b; Roemer et al. 1986; Mansfield et al. 1985; Crozier et al. 1994).

The wire pattern of the X-and the Y-gradient will look similar, but is rotated 90° to each other. Often the term "transversal" gradient is used to describe the characteristics that X-and Y-gradient have in common.

A standard Z-gradient consists of wires running in loops on a cylindrical shell, most easily described by an axially symmetric representation (Fig. 2).

In an electrical sense the main properties of the gradient coil windings are resistance (typically <150 mΩ for DC currents) and inductance (typically <1,000 μH).

1.2.2 Gradient Power Amplifier (GPA)

Today's gradient power amplifiers fit into one cabinet located at the periphery of the MR system, packed with electronics to supply high voltages (~2,000 V) to drive the dynamic currents (up to 900 A) through the gradient coil and to permanently supervise the accuracy of these currents (Mueller et al. 1991; Ideler et al. 1992; Schmitt et al. 1998).

Pulse Width Modulation (PWM) technique amplifiers are standard these days as they provide high power at low loss and high fidelity. Very short (~20 μs) voltage packages (400 V) are applied. The on/off ratio of these packages is modified in order to provide the needed total voltage and current to the gradient coil (Schmitt et al. 1998). This can be best seen in Fig. 3.

High performance amplifiers incorporate a cascade of several amplifying stage. Such an architecture allows for overall output voltages in the range of 2,000 V and maximum currents up to 900 A.

1.2.3 Additional Components

Other MR-components are physically attached to the gradient coil, and therefore, can be considered to be a part of the gradient system.

1.2.3.1 Shim

The process of shimming incorporates all the measures to homogenize the static magnetic field, B_o (Koch et al. 2009; Chen and Hoult 2005; Neuberth and US patent 2005; Hoby 2010; Gruetter and Boesch 1992; Gruetter 1993; Shen et al. 1999).

Three different types of shims, i.e. superconductive, iron or passive and resistive shims exist. Two of them are usually integrated into the gradient coil. Typically all UHF magnets have super conducting shims implemented, which is not the case for clinical magnets at 3 T and below. The superconducting shims are located inside the main superconductive magnet and are not considered further. The passive or iron shim tries to mend the inhomogeneities

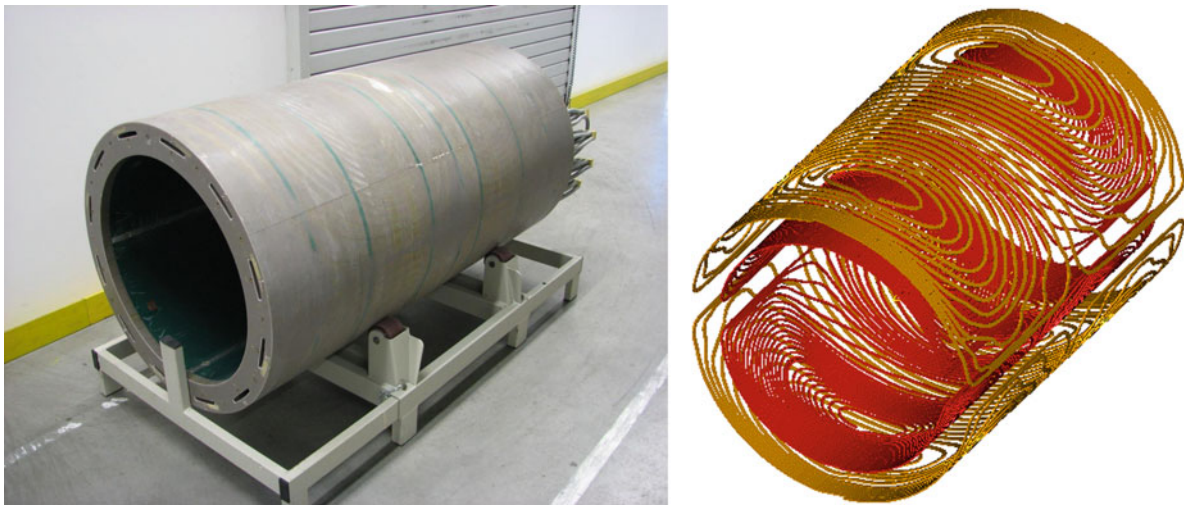

Fig. 1 *Left*: a gradient coil cylinder potted with resin incorporating the gradient windings. *Right*: A typical wire path for a transversal gradient—primary layer in *red*, secondary in *orange*

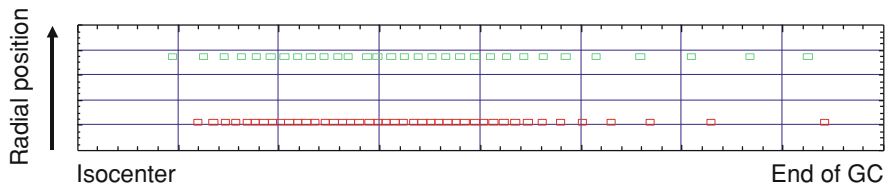

Fig. 2 Typical distribution of the wire positions of the loops forming half a Z-gradient winding. Primary layer in *red*, secondary in *green*

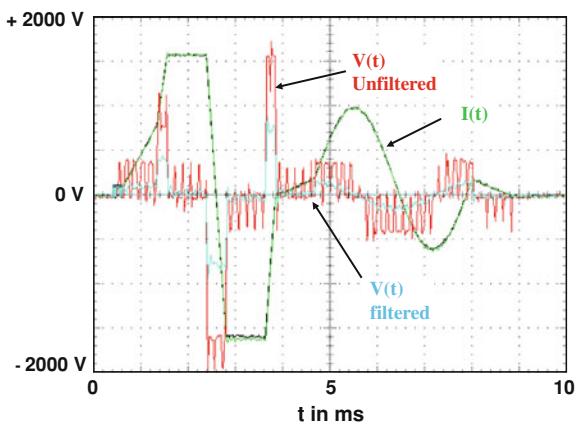

Fig. 3 Oscilloscope trace displaying the gradient current in *green* and the GPA output voltage: unfiltered in *red*, filtered in *blue*

introduced by magnet manufacturing tolerances and site influences (Koch et al. 2009; Chen and Hoult 2005), the same task is also tackled by the superconductive shim. Sometimes this shim iron is positioned inside slots of the GC, which can be seen on the front face of the GC in Fig. 1.

The resistive or also called electrical shim is another component to homogenize the static magnetic field introduced by individual human body magnetic inhomogeneities, particularly through susceptibility changes of human tissue.

This capability is reached through the use of independent coils, each driven by an individual electric power supply, the shim power supply, S-PSU. Sometimes these coils are positioned in a separate structure, but mostly they are incorporated in the gradient coil, making use of the potentially unused space between primary and secondary windings.

A standard embodiment is a series of coils producing spatial static field distributions representing

spherical harmonics. Field shapes that show a significant influence on the bulk of the field of view, FOV, are described by low order spherical harmonics. Higher order spherical harmonics are best suited to describe complex shapes close to the surface of the field of view.

"Zeroth order" describes a constant field which is the goal of the whole procedure. No new coils need to be designed for the three linear (first order) harmonics, since the three gradient windings can do this job, using a constant current. An additional set consisting of all five second order shim coils is standard today. Even higher harmonic coils become more important especially to homogenize the field at ultra high field systems (Hetherington et al. 2010).

1.2.3.2 Cooling

In order to assure continuous operation of the gradients, efficient cooling of both the gradient coil and the gradient amplifier is essential. Cooling with water flowing through both components is the standard. Altogether thermal energy up to ~50 kW needs to be transported away from the gradient system.

To keep the maximum temperatures as low as possible, it is desirable to get the cooling fluid in close contact to the heat sources. Despite such efforts hot spot temperatures of up to 100°C may occur under extreme usage of the gradient system.

2 Special Topics For Gradients at Ultra High Field

As already pointed out at the beginning of this chapter, gradients are not directly affected by ultra high field. However, some effects originating in the gradients can have serious consequences. These effects can all be traced to the higher static magnetic field.

The main challenges can certainly be attributed to the stronger Lorentz forces created by the interaction between gradient wire currents and gradient produced eddy currents with the static magnetic field. The most obvious disadvantage is the increase in acoustic noise by +6 dB each time the static magnetic field strength is doubled.

Due to its position inside the magnet, the gradient coil is the one component of the gradient system that experiences the strongest influence of UHF, whereas GPA and cooling are virtually unaffected.

The main driver for UHF imaging is the linear increase in signal to noise (SNR) with increasing magnetic field. Therefore, what was hidden in the noise floor at lower fields is now detectable at UHF. The expectation on the quality of the gradient fields is, therefore, increasing as well.

2.1 Effects of Higher B_o

2.1.1 Vibrations

Already at conventional static magnetic field strength of 1.5 T and 3 T, vibrations due to Lorentz forces are one of the main disadvantages. As soon as a current is flowing nonparallel to the magnetic field lines Lorentz forces are generated (Haiying and Junxiao 1996; Chapman and Mansfield 1995). These forces will move the current in a direction perpendicular to both the current and the magnet field.

Mathematically this behavior is expressed by the vector product of the orientation dependent current, $\underline{I}$, and the magnetic field, $\underline{B}$.

$$\underline{F} = \underline{I} \times \underline{B} \tag{2}$$

Field strength of whole body UHF systems will reach up to $B_o = 11.7$ T and maximum gradient currents up to $I_{\max} = 900$ A. With over $l = 200$ m of wire for each gradient winding running inside the GC, an impressive amount of force needs to be tamed at UHF systems. The major part of the total force summing up to 2.000.000 N—equivalent to a weight of 200 tons—is balanced internally. Only a small proportion can be experienced as movement or vibration of the gradient coil.

2.1.1.1 Low Frequency Vibrations

Low frequency movements—that can easily be experienced as shaking—are restricted to frequencies up to 100 Hz and have not yet been a major problem at UHF systems. This is due to the fact that (older types of) UHF magnets are extremely long and not actively shielded. These constraints always lead to magnet designs characterized by a very homogeneous magnetic field, not only in the area of the field of view, but almost everywhere inside the magnet inner bore. So the whole bulk of the gradient coil is sitting in an area with almost constant magnetic field.

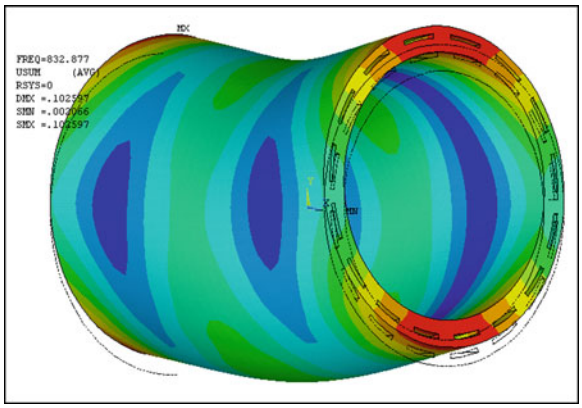

Fig. 4 The so-called "banana" resonance mode of the gradient coil cylinder. Calculation result with maximum displacements shown in *red*, stationary parts shown in *deep blue*

Now each gradient coil winding forms a closed loop, beginning and ending approximately at the same location. This means that every bit of current producing a local Lorentz force will definitively find its counterpart somewhere else on that same loop: In a homogeneous field no net forces apply.

Mechanically the cylinder of the gradient coil is only able to perform steady state movements (no bending or flexing movements) in the low frequency range. Since such steady state movements can only be excited by net forces, there will not be much movement in the low frequency range.

This situation is different with the second generation of UHF magnets, being actively shielded. With magnetic field inhomogeneities at the GC wire positions increasing by factors, force compensation is mandatory for the gradient wire design to avoid shaking of volunteers, damage to the system and vibration artifacts in images.

2.1.1.2 High Frequency Vibrations

As described above, high local Lorentz forces are produced along the wires of the gradient windings independent from the frequency of the driving current.

At frequencies >500 Hz the gradient coil cylinder mechanically starts to move following the shape of its eigen-modes. Bending resonances like the so-called "banana" vibration mode now dominate the movement (see Fig. 4). At such resonance frequencies even small gradient currents can cause high vibration amplitudes.

The main difference to standard MRI systems is simply the sheer amount of vibration energy that needs to be managed. Maximum vibration amplitudes of gradient coils still "only" reach 150 μm at 1,000 Hz. Considering a mass of typically 700 kg for the gradient coil cylinder, it becomes obvious that very strong internal bonds are necessary to prevent the gradient coil cylinder from falling apart. The choice of special resin material and the use of special vacuum casting techniques to avoid delamination are essential.

2.1.1.3 Vibration of Connector Cables

All parts attached to the gradient coil cylinder as well as the magnet need to withstand the brute force of gradient coil vibrations and need to be fixed carefully.

Vulnerable components are the cables connecting the GPA and the GC. These cables are not only attached to the heavily vibrating gradient coil, but they are also producers of Lorentz forces in their own rights, since their dedication is the transfer of the gradient currents through the magnetic field zone to the GC.

Firmly keeping these two strands together as tight as possible, so that Lorentz forces balance them self continuously, is the best way to handle this challenge.

2.1.2 Acoustic Noise

One of the most obvious consequences of the high frequency vibrations of the gradient coil is the acoustic noise generated (Hedeen and Edelstein 1996).

Conventional MRI systems are able to reach maximum noise levels in the range of 120 dB. Raising the magnetic field strength from 1,5 T to 11,7 T adds about 18 dB to the acoustic noise when using the same gradient coil and current. Therefore, for UHF systems, the maximum acoustic noise level is no longer only a nuisance, but may also represent potential hazard for humans if not appropriately taken care off. Without care in system design, the maximum noise level can exceed 140 dB peak, an internationally accepted legal barrier prohibiting the use of any technical equipment.

Another acoustic safety regulation, valid also for MRI systems rules that 99 dB(A) may not be exceeded without a hearing protection. One needs to be aware that the attenuation of conventional hearing

Table 1 Gradient induced energy deposition into the magnet at different field strength

Static magnetic field strength B_0 in T	Energy deposition at 50 K level in a.u.	Energy deposition at 4 K level in a.u.
0	40	0
0.5	40	0.1
1.0	40	2
1.5	50	20
3.0	150	200
5.5	300	3,500

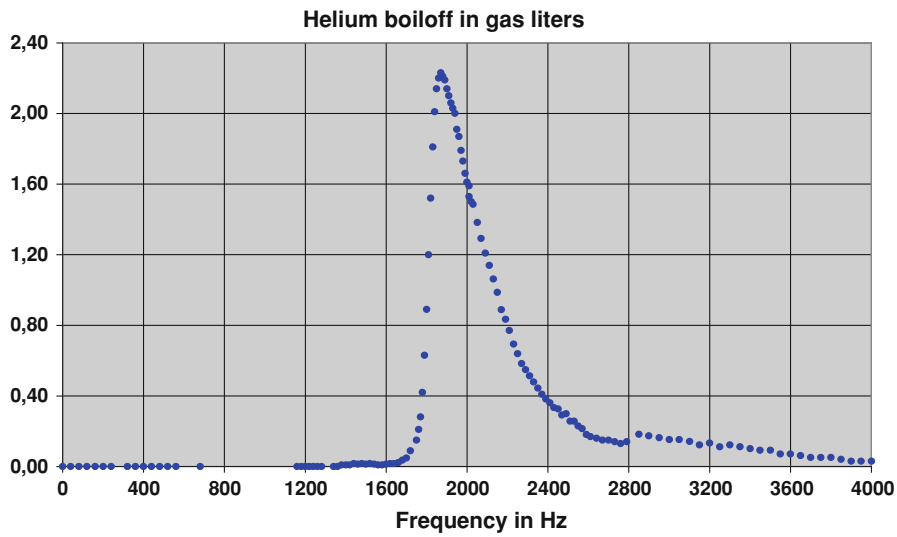

Fig. 5 Measurement results showing dependency of gradient induced helium boil-off on frequency using a sinusoidal gradient current with constant amplitude

protection is at best ~35 dB due to bone conduction of the skull.

The dominating noise at UHF systems will very likely be transmitted from the GC directly to the patient bore. So the mechanical characteristics of the innermost cylindrical barrier surrounding the volunteer are crucial for an acoustically acceptable system set up.

Care needs to be taken especially at mechanical interfaces to block the transmission of structure borne noise from the GC to the outer shell of the MRI system.

2.1.3 Helium Boil-Off

Maybe less visible, but even stronger influenced by the static magnetic field strength, are energy transmission phenomena such as gradient induced helium boil-off.

Without static magnetic field, all the conductive layers of a magnet will easily reflect and so shield incoming magnetic fields of any significant frequency. With static magnetic field present, complex nonlinear transmission phenomena start to appear. This energy transport depends largely on the choice of geometry and materials inside the magnet, but almost always rises dramatically with increasing static magnetic field. The main reason for this interaction is a coupled magneto-mechanic effect generated by Lorentz forces and induced eddy currents.

Calculations performed for a highly B_0-sensitive scenario show values of energy deposition maxima versus frequency—only gradient activity considered: Table 1.

For conventional systems with superconductors emerged in a liquid helium bath, all this energy at the 4 K level is finally dumped into the liquid helium, causing a helium phase transition from liquid to gas. Since only 2.6 J are necessary to evaporate 1 liter of liquid helium, considerable amounts of helium may be blown into the atmosphere by gradient activity. Losses up to half a liter of liquid helium per minute can be observed at UHF systems.

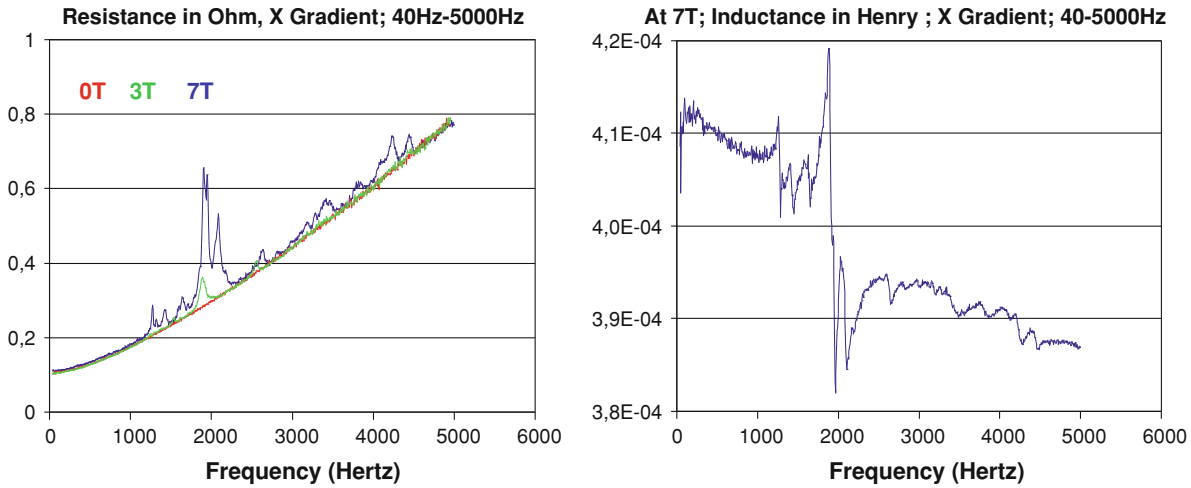

Fig. 6 Measurement results showing the frequency dependency of the impedance and the influence of the static magnetic field strength

Such extreme values can be avoided with a little knowledge of the system, since typical UHF boil-off spectra show a strongly resonant behavior (Fig. 5). The peaks observed can be explained by mechanical resonances of the conductive layers between the gradient coil and the helium bath. The vibration characteristics at the low temperatures and the high magnetic field of the cryoshields inside the magnet therefore define the Helium boil-off (Fig. 5).

Adapting sequences to avoid high signal contributions in the critical frequency range is a very effective means to reduce helium losses. For example, choosing a sinusoidal read-out gradient pulse scheme (Schmitt et al. 1998) for EPI pulse sequences has a significant effect, as the base frequency is typically not higher than 1 kHz. A sine pulse is monochromatic, the relevant boil-off frequency range is therefore entirely avoided and thus reduces boil-off significantly.

2.2 Higher Quality Requirements

UHF systems offer better signal to noise ratio, and therefore, offer improved image quality. Although the gradient system is not directly affected, new flaws or limitations of the gradient system may become noticeable.

2.2.1 Field Reliability

It is actually quite interesting to have a close look on the quality and reliability of the spatial and temporal gradient fields. Most of these effects are UHF independent but due to Lorentz forces they can become dominant.

2.2.1.1 Gradient Fields

Both, the nonlinearity of the gradient field and its correction, as well as the tiny ripples on the time signal of the gradient current due to the pulse width modulation in the gradient power amplifiers, GPA, are not specific to UHF, but need to be reevaluated for the specific quality demands at UHF.

Large vibration amplitudes of the GC are typical for UHF. The GC vibrates in a region exposed by ultra high static magnetic field causing changes to the impedance of the GC itself. Both, the resistance, the real part of the impedance, as well as the inductance, the imaginary part of the impedance, are affected. Figure 6 shows resistance over frequency for 0 T, 3 T, and 7 T of the same gradient coil and the inductance at 7 T (Fig. 6 right).

These frequency dependent impedance variations may make it hard for the GPA to work properly. If not considered properly the likelihood for imaging artifacts at the GC resonance frequencies may increase significantly with the static magnetic field strength. Introducing sinusoidal eddy current compensation may help remedy this effect and reduce N/2 ghosting in EPI imaging.

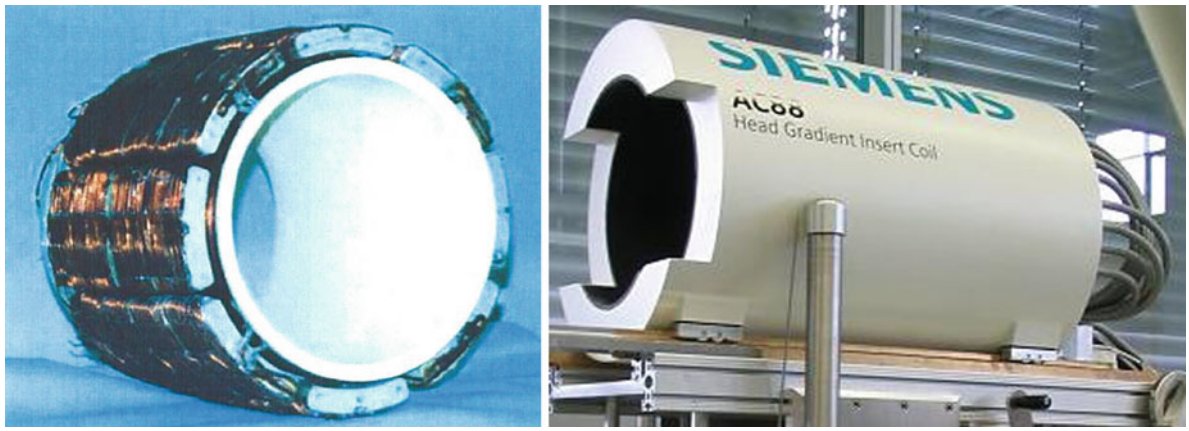

Fig. 7 Two examples for nonconventional head gradient coils: At *left*: Segment gradient coil (Stringer et al. 2005). At *right*: asymmetric gradient coil

2.2.1.2 Eddy Current Fields

An important feature of a gradient coil is the quality of the shielding. Gradient stray fields penetrating conductive layers of the magnet are turned into eddy currents that produce time varying fields themselves. These fields can have effects on image quality and need to be kept as small as possible. Long UHF magnets will catch the entire gradient stray field and so produce the maximum field disturbance.

As soon as there is movement of conductive parts relative to the magnetic field, eddy currents are produced which counteract the original movement (Lenz' law). With higher static magnetic fields, these vibration induced eddy currents will become larger and so will the induced eddy current fields.

The origins of vibrations are widespread from random building vibrations, with no time correlation to MR gradient pulsing, to GC movements highly correlated to the pulsing of gradient fields.

As a consequence of any type of these dynamic eddy current fields, the timing of the gradient fields becomes distorted, and therefore, spatial encoding is impaired. This may lead to image blurring and ghosting in the images. Maximum N/2-ghost intensities up to 90% of the signal intensity of the object have been observed at UHF systems at GC resonance frequencies. Any method reducing the vibration amplitudes of the GC itself or at least reducing the spread of these vibrations to other components will help improve image quality.

2.2.1.3 Higher Order Resistive Shim

The wish for better image quality also includes high quality requirements for magnet homogeneity. An effect already known from lower field strength is the influence of the susceptibility of the subject itself on field quality. At UHF systems this effect is more dominant compared to lower fields.

There exists now a growing list of publications stating that the usual first and second order resistive shims are not enough to counteract these patient induced susceptibility changes at UHF, suggesting that third order shims are required. In our newly developed gradient system for our UHF MRI scanners a selection (A30, A31, B31, A32) of the seven existing third order shims has been realized. The reason for this limited set of third order shims is the restricted space in the gradient coil body.

The use of resistive shim coils creating fields of third or even higher order spherical harmonics adds a new challenge to the design of the gradient system. Some of these higher order shim coils (e.g., of the types A30, A31, and B31) are able to couple inductively with a gradient. In such cases pulsing this gradient will lead to high dynamic currents flowing in the corresponding shim coil. Special emphasize has to be made on decoupling the higher order shims, as otherwise it even may destroy the shim power supply.

3 Dedicated Gradient Concepts

Peripheral nerve stimulation (PNS) is the hardest limitation for the performance of the gradient system (Budinger et al. 1991; Irnich and Schmitt 1995; Chronik and Rutt 2001; Schmitt et al. 1994; Mansfield and Harvey 1993; Nyenhuis et al. 1997). Rapid switching of strong gradients is the origin of induced electric fields inside the human body. These fields excite the peripheral nerve system and can cause the contraction of muscles.

The promise of stronger and faster gradients—a higher spatial resolution and better image quality—will match well with the UHF agenda, several dedicated gradient concepts have been developed to overcome the peripheral nerve stimulation limit and to best use the gradient fields available.

One way to overcome PNS issues is by going away from cylindrical gradient structures, as has been introduced by Martens et al. (1991), Cho and Yi (1991), and Vegh et al. (2005). Another possibility of fighting PNS is by changing the scale of cylindrical gradient coils and going more local, like head inserts as described in the following section.

3.1 Head Gradient Coils

The lowest trigger level for peripheral nerve stimulations appears to happen in the chest and abdomen of the body. Therefore, any gradient design, avoiding the induction of electric field loops in the body trunk, will allow higher gradient performance.

A comparably simple approach is to keep the conventional design of the MR components and adapt the MRI system in a way to only image parts of the human body less sensitive to PNS like the head or extremities.

Especially the transversal gradients offer an additional degree of freedom to reduce the stimulating fields, since the central wires alone—those close to the field of view—are able to produce the desired field characteristics. The return path loops which are outside the FOV can be positioned in a way to minimize the PNS phenomena (Crozier et al. 1994).

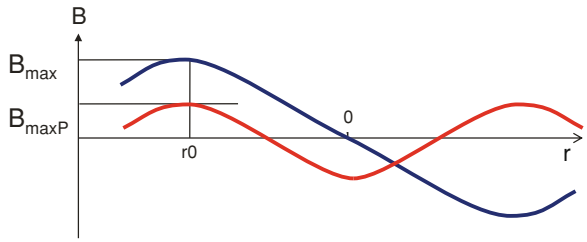

Fig. 8 Schematic plot of the field generated by a conventional gradient along the direction r(=x,y,z) compared to a multipolar gradient. At identical maximum gradient slope the field maximum B_{maxP} of a multipolar gradient is only a fraction of the maximum field of a conventional gradient

One possibility is to close the loops in radial direction, ending up with a segment coil design (Fig. 7). This concept has not been adopted to a wider use. The reason for not using these segment coils is that it takes too much space to realize a shielded coil (which is a must these days), when compared to conventional designs (Stringer et al. 2005).

Another approach is to close all loops on one end of the gradient coil cylinder, giving an asymmetric coil design, offering PNS reduction on the other end (Crozier et al. 1994). This design concept only shows its benefits when building head gradient coils. In our lab, we have designed and built dedicated head gradient sets with shoulder cut outs (Fig. 7) to allow centric placement of the head. These coils are successfully used at 3 T and UHF field strengths such as 7 T and 9.4 T and soon will be used at 11.7 T.

3.2 Gradient Array

3.2.1 New Concepts Using Nonlinear Gradients: Gradient Arrays, PatLoc etc

Entirely new gradient concepts are under evaluation today, which are aiming at a more efficient use of gradient fields (Hrovat et al. 1999; Patz et al. 1999). They are sometimes clustered under the phrase "gradient array". There are concepts using two gradients back-to-back in the axial direction (Parker and Hadley 2006), concepts adding a 4^{th} dynamic magnetic field (Hennig et al. 2008) and concepts using dynamic higher harmonic magnetic fields

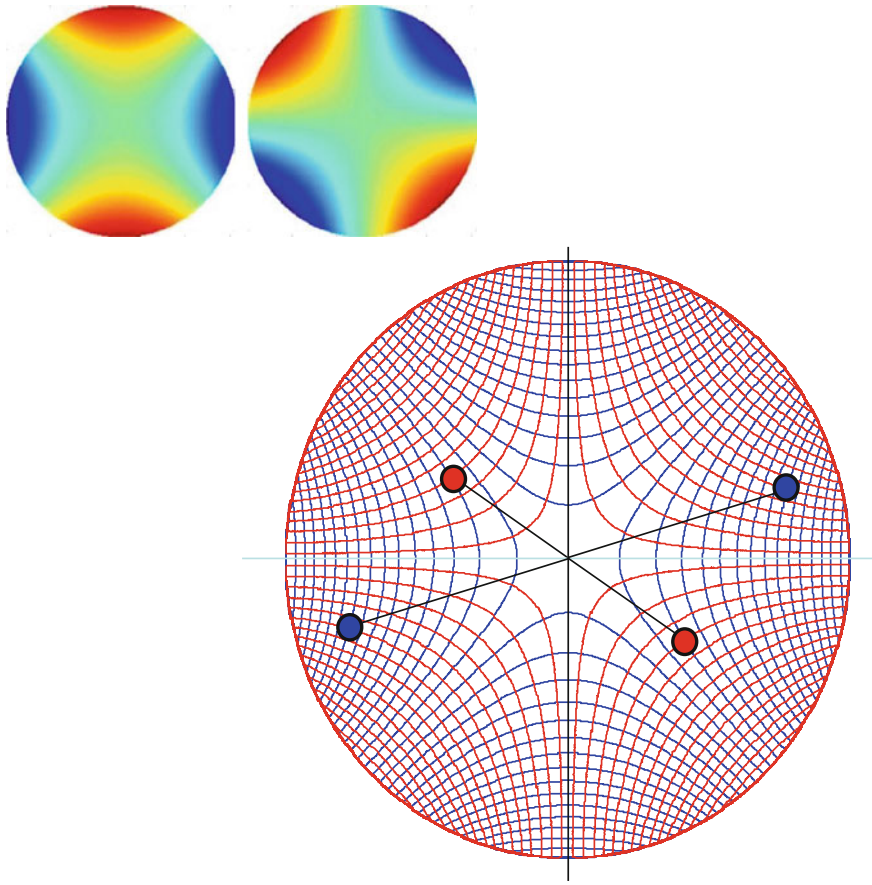

Fig. 9 (*insert top left*): Spatial encoding fields shaped as second order cylindrical harmonics. Two such identical fields rotated by 45° with respect to each other can be shown to be strictly orthogonal to each other at all points in the field. The contour plot (*large image*) illustrates the strong warping and the ambiguous encoding to be expected when such fields are used for image acquisition. The deformed squares formed by the intersection of the contour lines represent the pixel size of the encoded images

(Jason et al. 2010). Whatever concept may prove beneficial, UHF systems certainly will be the ones to push the boundaries the furthest.

One of the main driving forces to look beyond the use of conventional linear gradients has been their inherent limitation caused by peripheral nerve stimulation "Safety". The maximum field change occurs outside the linear region of the gradient (Fig. 8) which leads to the somewhat dissatisfactory situation that the performance is limited by a maximum field, which is not even useful in the performance of the gradient. A multipolar 'gradient' can deliver the same gradient strength (=slope of the magnetic field) at a fraction of the safety relevant field maximum (Fig. 8). Such a multipolar field has first been realized as a linear field along the z-axis by Parker (Parker and Hadley 2006). Meanwhile the concept has been extended to spatial harmonics of arbitrary geometry and order by Hennig (Hennig et al. 2008). The gradient (=first order spatial derivative) of the magnetic fields produced by such devices continuously varies in amplitude and direction. Therefore, it is more appropriate to call these 'spatial encoding magnetic' fields (SEM) rather than 'gradients'.

In order to encode a two-dimensional image, two orthogonal gradients have to be used. It is a nice feature of SEMs with cylindrical harmonic geometry that pairs of orthogonal gradients can be easily created by rotation. Using pairs of such SEMs (Fig. 9) as readout- and phase encoding-gradient, thus will nicely encode for a two-dimensional (but heavily distorted) image. An inherent challenge for multipolar SEMs is the fact that the resulting primary images are not only very heavily distorted but also inherently ambiguous. As shown in Fig. 10, points rotated by 360°/n—where n corresponds to the harmonic order—will be ambiguously encoded. The spatial encoding field is thus non-linear and non-bijective and can be decomposed into 2 bijective subfields.

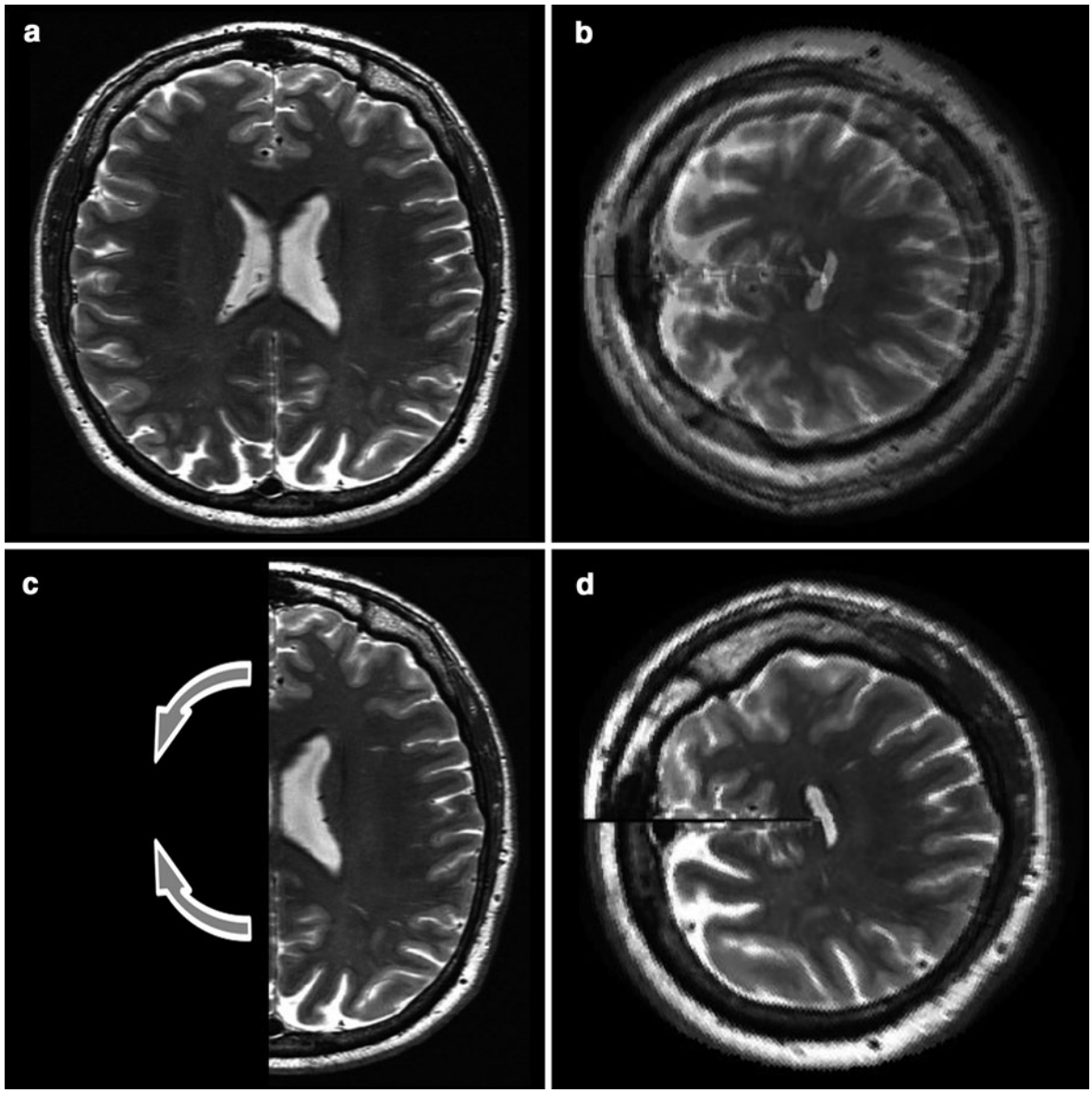

Fig. 10 Simulated results of a brain image (**a**) shows the strong warping and fold-over caused by the non-linear, non-bijective encoding. The imaging behavior becomes apparent by encoding a half-image (**c**), which is circularly warped to fill a full image in PatLoc coordinates

Parallel reception (see "What to do with All that Signal? Issues of High-resolution MRI"), therefore, is a necessity in SEM-imaging, which has consequently been called PatLoc (Parallel imaging Technique with local Gradient Fields). The number of independent RF-coils must be greater than or equal to the number of bijective subregions. Figure 11 illustrates the imaging behavior using simulations of a brain image. The warping becomes more intuitively understandable if SEM-transformation is applied to only one half of the image corresponding to one of the two bijective subregions. It becomes apparent that the circular warping leads to a 'zooming' effect on the peripheral parts of the image (like the cortex), whereas spatial resolution gets lower towards the center. With known field profiles, the PatLoc-images can be un-warped into Cartesian space to yield anatomically correct images.

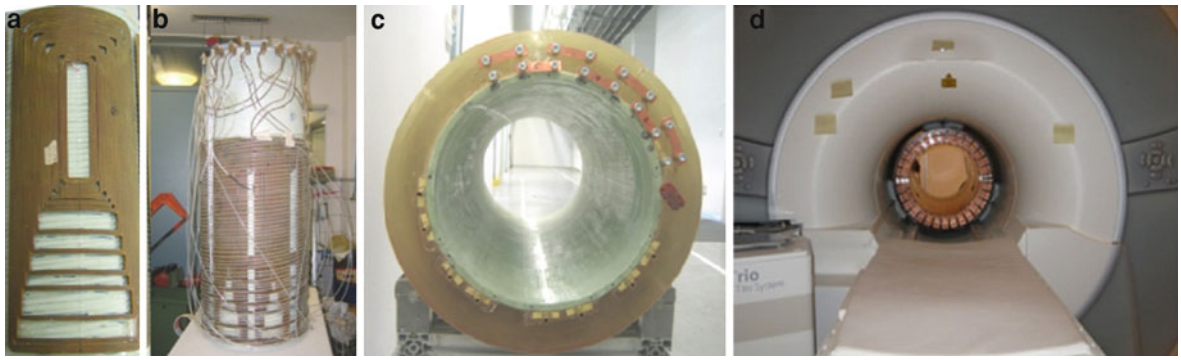

Fig. 11 Experimental PatLoc coil at different stages of assembly. (**a**) shows one of the eight individual coil windings, (**b**) shows one layer of the coil cooling four coil elements including lines for water cooling, final coil is shown outside (**c**) and inside (**d**) a 3 T experimental system (courtesy UKL Freiburg, Bruker Biospin (Ettlingen, DE), Siemens Healthcare (Erlangen, DE)

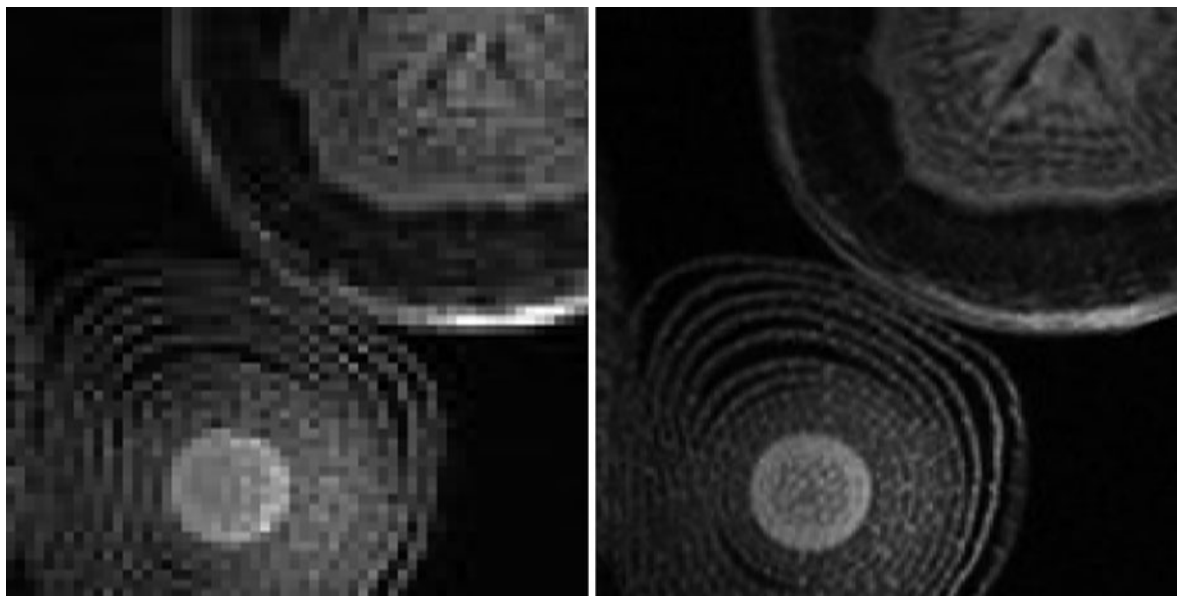

Fig. 12 Experimental PatLoc images acquired with conventional gradients (*left*) and PatLoc encoding (*right*) at identical field of view and matrix size

Figure 12 shows a PatLoc-coil built from 2 layers with 4 individual coil elements each at different stages of assembly. First images (Fig. 12) illustrate the improvement in spatial resolution at the peripheral part of the encoding region compared to a conventionally encoded image with equal field of view and matrix size. The range of possible applications for imaging using nonlinear SEMs only, is rather narrow. Current developments are based on combinations of PatLoc SEMs with conventional gradients to add more flexibility to image formation.

In addition to the examples shown, other imaging concepts based on non-linear gradients like T. Constables O-space imaging (Jason et al. 2010) are currently under development. None of this has so far been used at very high fields. It is too early to make predictions about possible areas of applications (if any), but it seems to be clear that this will not necessarily replace conventional gradients but rather lead to new applications not accessible to conventional imaging. One driving force for the development of PatLoc has been the combination with ultrafast

imaging techniques like MREG or Inverse Imaging. These are based on the use of very high integrated multi-coil arrays, where the small sensitive volumes of each coil element serves as primary source of spatial information. Such techniques inherently show much better spatial discrimination at the periphery and are thus a 'natural match' for combination with PatLoc.

References

Gradients General

Chapman BLW (2006) Gradients: the heart of the MRI machine. Curr Med Imag Rev 2:131–138
Schmitt F, Stehling MK, Turner R (1998) Echo-planar imaging: theory, technique and application. 141–178

GPAs

Mueller OM, Roemer P, Park JN, Souza SP (1991) A general purpose non-resonant gradient power system. Proceedings of the 10th Annual Scientific Meeting of the SMRM, San Francisco, p 130
Ideler KH, Nowak S, Borth G, Hagen U, Hausmann R, Schmitt F (1992) A resonant multi purpose gradient power switch for high performance imaging. Proceedings of the 11th Annual Scientific Meeting of the SMRM, Berlin, p 4044
Schmitt F, Arz W, Eberlein E, et al. (1998) An ultra-high performance gradient system for cardiac and neuro MR Imaging. Proceedings of the ISMRM, p 470

GC Design

FEM design: Pilsbury RD, Punchard WFB (1985) A finite element Fourier expansion technique for the design of a pulsed radial gradient system for magnetic resonance imaging (MRI), IEEE transactions on magnetics, vol. Mag-21, no. 6, november
Turner R (1986a) A target field approach to optimal coil design. J Phys D Appl Phys 19:147–151
Turner R (1988) Minimum inductance coils. J Phys E Sci Instrum 21:948–952
Turner R (1993a) Gradient coil design: a review of methods. Magn Reson Imag 11:903–920
Turner R (1986b) A target field approach to optimal coil design. J Phys D, Appl Phys 19:L147–L151
Turner R (1993b) Gradient coil design: a review of methods. Magn Resonance Imag 11(7):903–920
Roemer P, Edelstein WA, Hickey J (1986) Self shielded gradient coils. Proceedings of the 5th Annual Meeting of the SMRM, Montreal, p 1067
Mansfield P, Chapman B, Turner R, Bowley R (1985) Magnetic field screens. UK Patent 2 180 943 B, US Patent 4978920
Crozier S, Forbes LK, Doddrell DM (1994)The design of transverse gradient coil of restricted length by simulated annealing. J Magn Reson, Vol A107, 126–128

PNS

Budinger TF, Fischer H, Hentschel D, Reinfelder HE, Schmitt F (1991) Physiological effects of fast oscillating magnetic field gradients. J Comput Assist Tomogr 15:909–914
Irnich W, Schmitt F (1995) Magnetostimulation in MRI. Magn Reson Med 33:619–623
Chronik BA, Rutt BK (2001) A comparison between human magnetostimulation thresholds in whole-body and head/neck gradient coils. Magn Reson Med 46:386–394
Schmitt F, Wielopolski P, Fischer H, Edelman RR (1994) Peripheral Stimulation and their Relation to Gradient Pulse. Proceedings of the Society of Magnetic Resonance, p 102
Mansfield P, Harvey PR (1993) Limits to neural stimulation in echo-planar imaging. Magn Reson Med 29:746–758
Nyenhuis JA, Bourland JD, Schaefer DJ (1997) Analysis from a stimulation perspective of magnetic field patterns of MR gradient coils. J Appl Phys 81:4314–4316

Lorentz Forces-Mechanics-Vibratio-Noise

Haiying L, Junxiao L (1996) Gradient coil mechanical vibration and image quality degradation. Proceedings of the Society of Magnetic Resonance, pg 1393
Chapman BLW, Mansfield P (1995) Quiet gradient coils: Active acoustically and magnetically screened distribuited transverse gradient designs. Meas Sci Technol 6:349–354
Hedeen RA, Edelstein W (1996) Characterization and prediction of gradient acoustic noise in MR imagers. Proceedings of the Society of Magnetic Resonance, pg 1389
Stringer M, Doty GN, Shevgoor S, Xiao C, Laws N, Staab JP, Wald L, Ackerman JL, Doty FD (2005) "Progress in the development of a quiet, high-performance, head gradient coil Proceedings of the Society of Magnetic Resonance 13th Annual. Meeting ISMRM, Miami, FL

Non Conventional Gradients

Martens MA, Petropoulos LS, Brown RW, Andrews JH (1991) Insertable biplanar gradient coils for magnetic resonance imaging. Rev Sci Instrum 62(11):2639–2645
Cho ZH, Yi JH (1991) A novel type of surface gradient coil. J Magn Reson 94:471–495
Vegh V, Zhao H, Galloway GJ, Doddrell DM, Brereton IM (2005) The design of planar gradient coils. Part I: A winding path correction method. Concepts Magn Reson B Magn Reson Eng 27(1):17–24
Parker DL, Hadley JR (2006) Multiple-region gradient arrays for extended field of view, increased performance, and reduced nerve stimulation in magnetic resonance imaging. Magn Reson Med 56(6):1251–1260
Stockmann JP, Ciris PA, Galiana G, Tam L, RT Constable. O-Space Imaging: Highly Efficient Parallel Imaging Using

Second-Order Nonlinear Fields as Encoding Gradients With No Phase Encoding, Magnetic Resonance in Medicine 64(2): 447–456

Hennig Juergen, Welz AnnaMasako, Schultz Gerrit, Korvink Jan, Liu Zhenyu, Speck Oliver, Zaitsev Maxim (2008) Parallel imaging in non-bijective, curvilinear magnetic field gradients: a concept study. Magn Reson Mater Phy 21:5–14

Hrovat MI, Pulyer YM, Rybicki FY, Patz S (1999) Reconstruction algorithm for novel ultrafast MRI. Int J Imaging Syst Technol 10:209–215

Patz S, Hrovat MI, Pulyer YM, Rybicki FY (1999) Novel encoding technology for ultrafast MRI in a limited spatial region. Int J Imaging Syst Technol 10:216–224

Shimming/Homogeneity

Koch KM, Rothman DL, de Graaf RA (2009) Optimization of static magnetic field homogeneity in the human and animal brain in vivo. Progress in Nuclear Magnetic Resonance Spectroscopy 54: 69–96

Chen CN, Hoult DI (2005) Biomedical Magnetic Resonance Technology. Adam Hilger, New York (Iron shiming)

Neuberth G (2005) US Patent 6,897,750. (Iron shimming)

Hetherington HP, Chu W-J, Gonen O, Pan JW (2010) Robust fully automated shimming of the human brain for high-field 1 h spectroscopic imaging

Gruetter R, Boesch C (1992) Fast not iterative shimming of spatially localize signals. In vivo analysis of magnetic field long axis. J Magn Reson 96:323–334

Gruetter R (1993) Automatic localized in vivo adjustment of all first and second order shim coils. Magn Reson Med 29: 804–811

Shen J, Rothman DL, Hetherington HP, Pan JW (1999) Linear projection method for automatic slice shimming. Magn Reson Med 42:1082–1088

Radiofrequency Coils

Andrew G. Webb

Contents

Abstract

Producing a homogenous radiofrequency field within the patient at high field is challenging since the electromagnetic wavelength inside the body is significantly less than the body dimensions. An associated problem is the spatially inhomogeneous electric field that can produce localized thermal hot-spots. The use of transmit array coils, in which the magnitude and phase of the inputs to each element of the array are individually controlled, can significantly improve the RF field uniformity within a patient. Despite the challenges, there are also exciting new designs for RF coils and possibilities to control the RF fields which can only be put into practice at high fields. This chapter explains the basic principles of radiofrequency transmission and reception with specific focus on the challenges of UHF-MR and gives an overview of the state-of-the-art in this rapidly changing field.

1 Introduction

High field MR holds many promises in terms of improved image and spectral quality. For example, the increases in signal-to-noise (S/N) can be translated into higher spatial resolution or faster imaging times. In localized spectroscopy, the increased spectral resolution enables more accurate quantification of an increased number of metabolites compared to lower field strengths (Tkac et al. 2009). Differences in magnetic susceptibilities between tissues, whether intrinsic or pathological, result in substantially increased contrast at high fields (Duyn et al. 2007;

A. G. Webb (✉)
C.J. Gorter Center for High Field MRI,
Department of Radiology, C3-Q,
Leiden University Medical Center,
Albinusdreef 2, Leiden 2333 ZA, The Netherlands
e-mail: a.webb@lumc.nl

J. Hennig and O. Speck (eds.), *High-Field MR Imaging,* Medical Radiology. Diagnostic Imaging,
DOI: 10.1007/174_2010_131, © Springer-Verlag Berlin Heidelberg 2011

Li et al. 2006). Magnetic susceptibility differences and the increased intravascular contribution to the blood oxygen level dependent (BOLD) signal also enable higher resolution fMRI experiments to be performed (Yacoub et al. 2001). The intrinsically longer tissue and blood T_1 values can be used for improved contrast in MR angiography (Monninghoff et al. 2009; Maderwald et al. 2008; Kang et al. 2009; Zwanenburg et al. 2008) and perfusion imaging, respectively. Each of these subjects is treated in detail in different chapters in the book. However, in order to take full advantage of the improvements at high field, the radiofrequency (RF) coils must operate with maximum efficiency, and produce as homogeneous a field as possible throughout the patient. This becomes a major engineering challenge at fields of 7 Tesla and above. This chapter introduces the basic design concepts for both transmit and receive coils, which are broadly applicable to field strengths up to 3 Tesla. As the field increases to 7 Tesla and above, however, the interactions between the RF coil and the body itself start to influence, and ultimately dominate, the performance of the RF coil, particularly in terms of introducing severe non-uniformities in the RF field. In this case, a much different type of transmitter coil design is required. Although designing RF coils at very high fields is extremely challenging, there are also some intriguing possibilities for completely new types of design which only become possible at such high frequencies, and the final section in the chapter outlines these possibilities.

2 Basics of RF Coil Design

RF coils transmit electromagnetic energy into the body in order to produce the RF pulses used in every MR sequence. RF coils also detect the signal from the spatially encoded precessing magnetization. For most clinical studies at 1.5 and 3 Tesla a large "body coil", which is integrated into the cylindrical bore of the MR scanner is used to transmit the pulses of RF energy, and a separate array of smaller coils placed around the imaging volume of interest is used to receive the signal. Although RF coils are often described in introductory texts as being similar to antennas, in fact the aim of their design is diametrically opposite to that of an antenna (Hoult 2009) as illustrated in Fig. 1. An antenna, whether it be for radio, cell-phone, television or satellite transmission, is designed to radiate energy into the "far-field", in other words to transmit energy far away in all directions so that its coverage is as wide as possible. In contrast, an RF coil used for MRI is designed to concentrate the magnetic energy very close to the coil. In the case of the body coil, the aim is to reduce the amount of energy which is radiated away from the coil to a minimum, and to concentrate the energy as much as possible into the body.

In terms of designing the circuitry and geometry of an RF coil there are two major considerations. First, the coil must be made as efficient as possible. This means that, for the transmitting coil, the amount of energy required to produce the 90° and 180° pulses for the various imaging sequences is as small as possible, which in turn allows shorter pulses to be used. Second, the transmitted electromagnetic field within the patient should be as homogeneous as possible, so that subtle differences in image contrast can be unambiguously assigned to pathology rather than patient-specific non-uniformities in the RF field and subsequent shading in the image. Having a homogeneous RF field is also critical for efficient fat saturation over the entire imaging volume, and effective saturation bands to eliminate signal from moving organs, for example. The receiver coils should also be as efficient as possible in order to yield the maximum S/N of the image.

3 Design of Homogeneous Volume Transmit Coils

As outlined previously, the body coil in a 1.5 or 3 Tesla scanner is integrated into the magnet bore, and is cylindrical in shape. It can be shown using basic electromagnetic theory that a perfectly uniform spatial distribution of the RF transmit field transverse to the long axis of a cylinder is produced by a sinusoidal current distribution along the surface of a cylinder of infinite length: this is shown in Fig. 2a. Of course the coil must be of finite length, and a perfectly sinusoidal current distribution cannot be produced, but the basic design criterion for the volume coil is to approximate the sinusoidal surface current. The most common manifestation is termed the birdcage coil, first described in the mid-1980s (Hayes et al. 1985). It consists of a number of strips of metal (usually

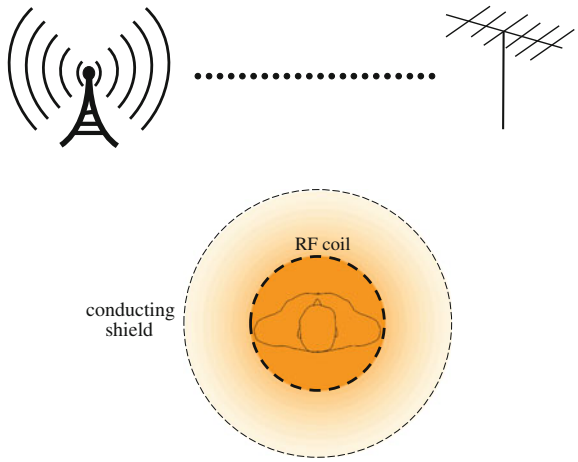

Fig. 1 An illustration of the differences between a radiofrequency antenna and a radiofrequency coil used for MRI. Shown at the *top*, a radiofrequency transmitting antenna is designed to radiate as much energy as possible away from the antenna. The antenna is said to be operating in the "far-field" regime. A large distance away, a receive antenna picks up the signal. In contrast, a radiofrequency coil used for MRI, shown below, is designed to concentrate as much of the RF energy as possible inside the structure itself. There is a small degree of radiation, but this is contained within a conducting shield which is placed around the RF coil. The aim of the design is to produce as strong and as homogeneous an RF field within the patient as possible. The RF coil is operating in a "near-field" regime

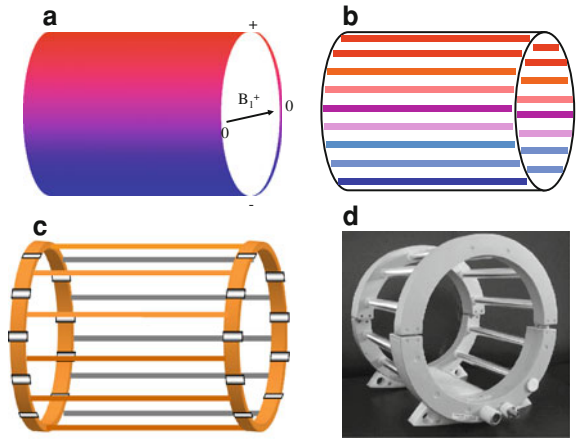

Fig. 2 **a** In order to produce a perfectly uniform RF transmit field in the transverse plane (shown by the *arrow*), the current distribution around the surface of a cylinder should have a sinusoidal distribution, with a maximum positive value (*deep red*) at the *top* of the cylinder, zero value at each side, and a maximum negative value (*deep blue*) at the *bottom*. **b** A discrete approximation to the continuous current distribution consists of a number of conducting "rungs", equally spaced around the periphery of a cylinder. **c** In order to produce the desired current distribution at the proton resonant frequency, a number of capacitors of equal value are distributed around the coil. The capacitors are usually placed in the end-rings, producing a "high-pass" birdcage design, but can alternatively be placed in the rungs which constitute a "low-pass" design. **d** Photograph of a commercial birdcage resonator

copper coated with silver to prevent oxidation) placed along the long axis of a cylinder, as shown in Fig. 2b: these are referred to as the rungs of the birdcage coil. Electrical connection between the rungs is provided by two endrings, as shown in Fig. 2c, which also shows the capacitors which are used to "tune" the coil to the relevant frequency (63.9 MHz for 1.5 Tesla or 127.8 MHz for 3 Tesla). These capacitors must be non-magnetic, and capable of operating with several thousand volts across their terminals when the RF pulses are delivered. The number of rungs in the birdcage is usually thirty-two: the larger the number the more homogeneous the field, but above thirty-two elements one encounters the law of diminishing returns in terms of the increase in design complexity.

Figure 2 shows that a sinusoidal current distribution produces a linear transmit, termed the B_1^+, field in a direction perpendicular to B_0, which is required to produce an MRI signal. However, intuitively one can see that a co-sinusoidal distribution would also produce a linear B_1 field, exactly orthogonal to the first B_1 field, and would also result in an MRI signal. Since the birdcage is a symmetric structure, providing that the number of rungs is a multiple-of-four, both sinusoidal and co-sinusoidal B_1 fields can be produced simultaneously by having two power inputs to the coil. This is known as operating the coil in quadrature mode (Glover et al. 1985), which produces a circularly polarized B_1 field. This reduces the power required for RF transmission by a factor-of-two, and also significantly improves the uniformity of the transmit field, compared to a single linear field.

When considering the design of a large body coil, one also has to take into account the finite wavelength of RF in the copper conductor itself. For example, the length of a body coil is typically ~65 cm, representing the length of one rung. The electromagnetic wavelength in a copper conductor at 3 Tesla is approximately 2.35 m, meaning that length of each rung is ~ one-quarter of a wavelength. This means that there will be a significant difference in the currents and voltages from one end of the rung to the other, and this will cause significant spatial inhomogeneities in the

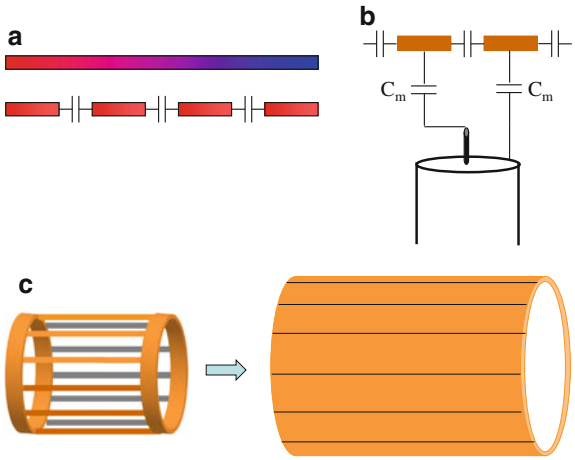

Fig. 3 **a** Illustration of the principle of capacitive segmentation of the conductive rungs in a birdcage. Without segmentation there is a phase shift along the rung which leads to a reduction in the efficiency and homogeneity of the RF coil. By segmenting, the effective length of each conductor within the coil is reduced, and one can assume that there is negligible phase change along each element. **b** A balanced impedance matching circuit used to impedance match the RF coil to 50 Ω to maximize coil efficiency. **c** The birdcage coil is surrounded by a conducting RF shield. In order to avoid inducing eddy currents, the shield is split lengthways. Large capacitors can be soldered across the gaps of the shield

transmitted field. It is also worth returning to the original discussion of an antenna: the most effective size for an antenna in terms of radiating energy into the far-field is one-half wavelength. As the dimensions of any structure within the RF coil approaches this value, the amount of energy radiated away will increase. Therefore, one needs a method by which to make the RF coil structure appear as if it were electrically shorter than it is physically. The simplest method is to break up each rung into several individual parts, each connected by a capacitor. This is shown in Fig. 3a. Now each segment is considerably smaller than one-quarter wavelength, the capacitors effectively "reset" the phase of the current and voltage for each segment, and radiation losses are reduced considerably.

In order to ensure maximum power transmission and efficient reception impedance matching of the coil must also be performed. Since amplifier outputs and transmission cables have an impedance of 50 Ω, this is the impedance to which the coil is matched at the proton resonance frequency (Traficante 1989). A balanced impedance-matching network should be used to reduce electric field losses in the sample, and the most common is a standard "pi-matching network", which is shown in Fig. 3b.

Finally, as indicated earlier, the aim of RF coil design is to concentrate the B_1 field inside the patient, and to minimize the amount of energy radiated outwards. An RF shield is placed around the birdcage coil to achieve this, as shown in Fig. 3c. This shield is constructed from thin copper (either solid or mesh) in order to avoid producing eddy currents from gradient switching.

As the field strength increases above 3 Tesla there are advantages to using a different geometry called a transverse electromagnetic mode (TEM) resonator as the body coil (Vaughan et al. 1994, 2004). Although the structures look quite similar, with each having a number of individual rungs and a shield, the two basic differences between a TEM and birdcage are: (1) the former uses distributed capacitance for the rungs, rather than a series of discrete capacitors, by forming each rung from a tubular structure with an inner and outer conductor separated by a dielectric material such as Teflon, and (2) the shield is connected to each individual rung thus forming a connected part of the structure, rather than "floating" as in the birdcage design. The pros and cons of each design provoke lively debate within the RF coil community, but both designs produce excellent efficiency and homogeneity of the transmit field at 1.5 and 3 Tesla, with the TEM also having been shown to be very effective at 7 Tesla (Vaughan et al. 2004).

4 Receive Arrays

Almost all clinical receive coils are arrays, i.e., structures containing a number of small separate coils to cover a larger field-of-view. These arrays can be cylindrical in shape, for example for brain or knee imaging as shown in Fig. 4a, or can consist of a large number of small loops which can be geometrically placed around the body for cardiac or extremity imaging, as shown in Fig. 4b, c. Currently, commercial arrays such as the total imaging matrix (TIM) from Siemens can support up to 74 separate receiver coils, and 128 element arrays (Schmitt et al. 2008) have been constructed in academic laboratories. There are two basic reasons for using an array of small coils,

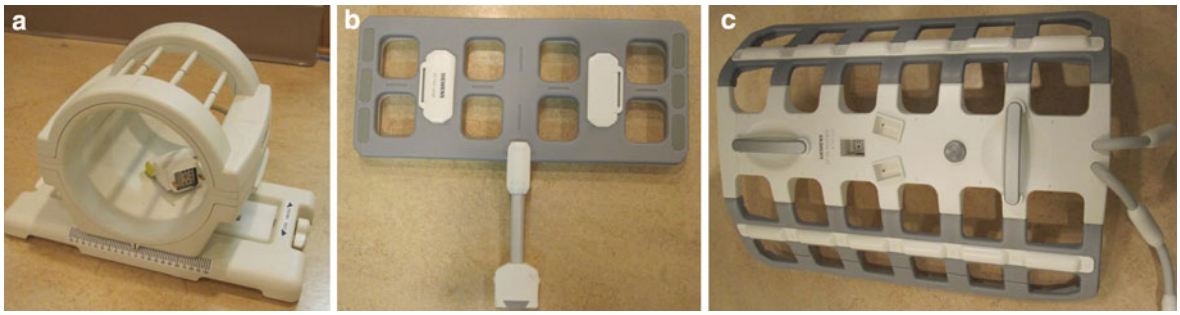

Fig. 4 **a** A twelve element receive array used to image the knee. **b** An eight element loop array, and **c** a twelve element receive array for imaging the spine

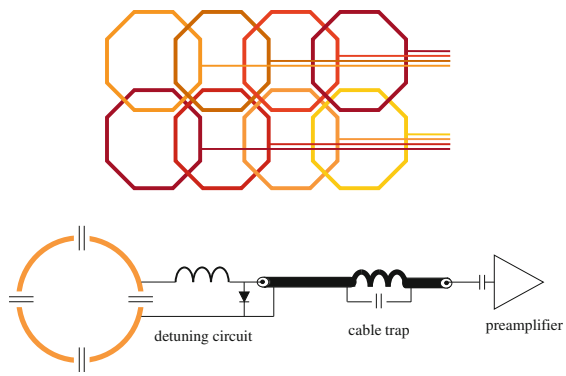

Fig. 5 (*Top*) Schematic of the physical layout of individual RF coils used to produce the arrays shown in Fig. 4b, c. The coils are overlapped to reduce the mutual inductance between individual elements. Each coil is connected to a separate cable. (*Bottom*) Each array element is capacitively split as described previously. A PIN-diode circuit is used to detune the element when the body coil is transmitting the RF pulses. A cable trap is used to reduce the current travelling on the outside of the cable connected to the coil for patient safety, robust performance and increased isolation between individual coils. Each element is connected to either a low- or high-impedance preamplifier. Signals from each channel are digitized separately and then combined in an optimal manner using signal processing to produce the final image

rather than one single large coil with an equivalent volumetric coverage. The first is that the sensitivity of each small coil is greater than that of the large coil and each small coil picks up noise only from a region of the body which is much smaller than the large coil. This means that the image S/N is increased compared to using a single larger coil, with the increase being greatest closest to the surface of the patient. The second reason is to use parallel imaging techniques to increase the imaging speed. The basic principle of parallel imaging (Sodickson and Manning 1997) is that the spatial distribution of signal at a given location from different receive coils can be used, in part, to determine the spatial origin of the signal, reducing the requirement for full k-space coverage in the phase-encoding direction (Sodickson and McKenzie 2001; Blaimer et al. 2004; Heidemann et al. 2003). A number of different methods have been implemented by different manufacturers, with different acronyms given to each, the most common being based on generalized autocalibrating partially parallel acquisitions (GRAPPA) (Griswold et al. 2002) and sensitivity encoding (SENSE) (Pruessmann et al. 1999).

In designing receive arrays, there are several important factors that must be considered. First, the individual receive elements must be electrically isolated from one another. All elements are tuned to the same frequency. If they were not isolated they would interact with one another, significantly reducing the efficiency of the array and also "mixing" the signal from different positions within the body to different coils. There are two basic methods by which this isolation can be achieved and typically both are used in an array. The first is geometrically overlapping the coils as shown in Fig. 5. Somewhat counter-intuitively, this actually reduces the electrical interaction between different coils to a much lower level than simply placing the coils next to one another. The second is termed preamplifier decoupling and is a method to reduce the current flowing in each separate coil, thus also reducing their effective interaction (Roemer et al. 1990; Wright et al. 1991).

Additionally, each element of the receive array must be decoupled from the transmit volume coil, and this is achieved using active PIN diode switching

circuits, as also shown in Fig. 5. Using similar arguments to before, the body transmit coil and receive array elements are tuned to the same frequency and so must be isolated from one another. PIN diode circuits in both the body coil and receive elements ensure that the body coil is tuned during pulse transmission and detuned during signal reception, and that the receive array elements are detuned during pulse transmission and tuned for signal reception.

5 Challenges of High Field RF Coil Design

In many texts on medical imaging modalities it is often stated that MRI "does not suffer from penetration effects" unlike, for example, ultrasound imaging. However, this is only true if the wavelength of the RF is much greater than the dimensions of the body. The wavelength in a given medium is dictated by a physical property known as the relative dielectric constant, also referred to as the relative permittivity (ε_r). To first order, the RF wavelength in tissue is given by:

$$\lambda_{\text{tissue}} \propto \frac{1}{f\sqrt{\varepsilon_r}} \tag{1}$$

where f is the frequency. Figure 6a shows that the relative dielectric constant of tissue, in this case muscle, decreases with frequency. Using Eq. 1 the corresponding electromagnetic wavelength is plotted as a function of frequency in Fig. 6b. The RF wavelengths at 1.5, 3, 7 and 9.4 Tesla are approximately 55, 30, 13 and 10 cm, respectively. Similar values are found for tissues such as white and gray matter in the brain.

The reason why a short wavelength causes problems can be understood by considering a simple example. As shown earlier, volume coils such as the birdcage coil have electrical currents with equal magnitude but opposite polarity flowing in the rungs on opposite sides of the coil. In a symmetric sample, this can create a "standing wave" pattern with constructive interference near the center of the sample and with regions of destructive interference at a distance of approximately one quarter-wavelength. As shown in Fig. 6b, at proton resonance frequencies for 1.5 and 3 Tesla the wavelength in tissue is large

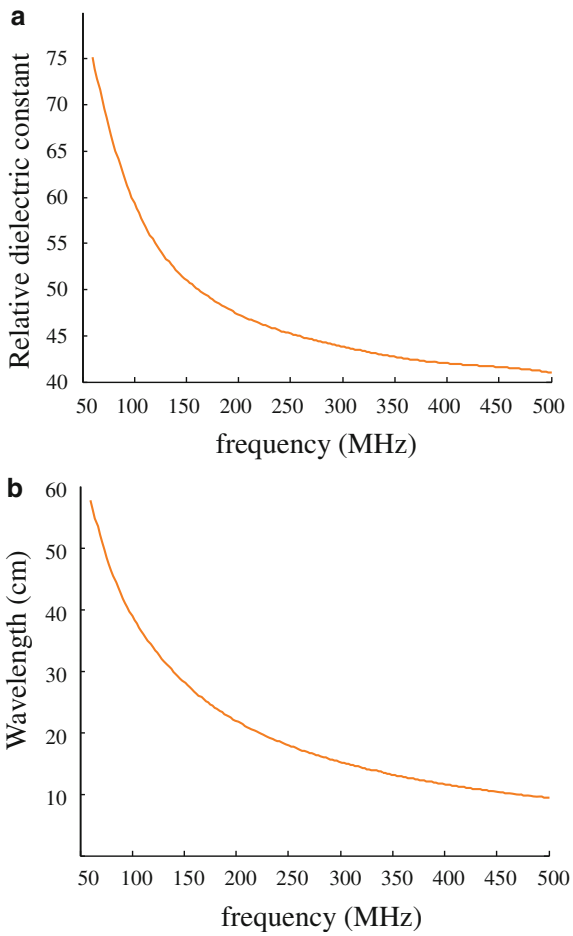

Fig. 6 **a** The relative dielectric constant of muscle decreases with frequency. **b** The corresponding wavelength of electromagnetic energy also decreases roughly exponentially as a function of frequency

compared to the dimensions of the body, and so these regions of destructive interference lie outside the imaging volume and are of little concern. At 300 MHz (7T), however, λ in brain is only $\sim$13 cm, and regions of constructive and destructive interference therefore occur.

The second factor which affects the distribution of the B_1^+ field is the tissue conductivity (σ). Whereas the sample's electric permittivity leads to a spatially dependant phase shift of the B_1^+-field, σ introduces an effective damping term which reduces the magnitude of the RF field as it penetrates through tissue. Compared to wavelength effects due to tissue

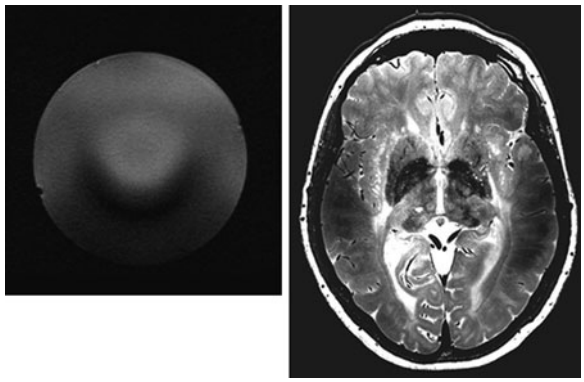

Fig. 7 (*Left*) A low-tip angle gradient echo image of a uniform sphere of water acquired at 7 Tesla. The transmit coil was a 16 element quadrature birdcage resonator. Severe sample-induced signal inhomogeneities are produced by constructive and destructive interference, as well as internal reflections and diffraction of the RF energy. (*Right*) Spin-echo image of the brain at 7 Tesla using the same transmit coil and a 16 element receiver array. There are significant signal voids in two particular areas of the brain. In addition, the lack of image contrast in the images is indicative of low tip-angle pulses, well below the nominal 90° and 180° values, being produced in these areas by the transmit coil

dielectric properties, the conductivity has a relatively minor effect on RF propagation, although it should be recognized that the conductivity of muscle does increase by ~25% from 1.5 to 7 Tesla. The main effects of tissue conductivity are in SAR and power deposition as covered later in this chapter.

Manifestations of complex wave effects can be seen in the two examples shown in Fig. 7. In Fig. 7 a gradient echo image at 7 Tesla is shown of a spherical sample of water, 15 cm in diameter, placed inside a birdcage coil. The amount of signal inhomogeneity is enormous, with almost complete signal cancellations in certain parts of the image. Water has a very high dielectric constant of ~80 at 7 Tesla, and therefore a very short wavelength compared to the sample dimensions. Figure 7 shows a spin-echo image of the brain, with again significant areas of very low signal.

The effect of the B_1^+ inhomogeneity as a function of field strength has been studied extensively (Collins and Smith 2001; Collins et al. 2002a, b; Wang et al. 2002). Figure 8 shows that, even using a low tip-angle gradient echo imaging sequence, there are significant image non-uniformities at fields higher than ~4T, with severe distortions at very high fields.

6 SAR and Temperature Considerations

In addition to the inhomogeneous RF magnetic field, the second major challenge in high field MRI is the heating produced by the RF electric field within the body (Collins et al. 2004; Wang et al. 2007). Basic electromagnetics shows that there must be an RF electric field associated with any RF magnetic field, and this electric field produces electrical currents in conductive tissues. The power deposited in the body can be calculated very simply in terms of the SAR given in Watts per kilogram of tissue (see also 'Neuroscientific Applications of High-Field MRI in Humans' and 'Safety').

$$\mathrm{SAR} = \frac{\sigma}{2\rho}|E|^2 \tag{2}$$

where σ is the tissue conductivity and ρ is the material density. There are strict regulatory guidelines on these values (IEC 2002) in terms of peak instantaneous and time-averaged values for both local and global regions-of-interest. European and Australasian regulations limit the whole body SAR to 1.5 W/kg averaged over 15 min (or 4 W/kg for what is termed the first control operational limit), the head SAR to 3 W/kg averaged over 10 min, and the local SAR for any 1 g of tissue to 8 W/kg for head/torso and 12 W/kg in the extremities, both averaged over 5 min (IEC 2002). The Food and Drug Administration (FDA) limits in the US are similar: instantaneous SAR should not exceed 4 W/kg averaged over the entire head, 8 W/kg for the trunk or 12 W/kg for extremities. Poorly perfused tissues are limited to a local SAR per 10 g of tissue of 10 W/kg averaged over 10 min. For pregnant women, infants and patients with vascular deficits the FDA recommends reducing the SAR limits by a factor-of-two.

Since it is very difficult to measure SAR in vivo, electromagnetic simulations play a very important role in determining where in the body heating is likely to occur, and especially where hot spots might be formed (Collins et al. 2004; Wang et al. 2007). A range of different body models have been developed, in which the body has been segmented into a wide variety of tissue types, each with an associated conductivity and

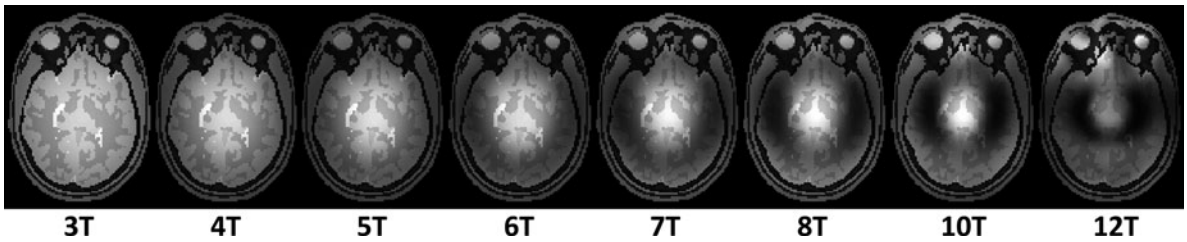

Fig. 8 Simulated gradient-echo images, assuming a low tip-angle excitation, as a function of field strength using a birdcage coil with ideal current distributions in the rungs

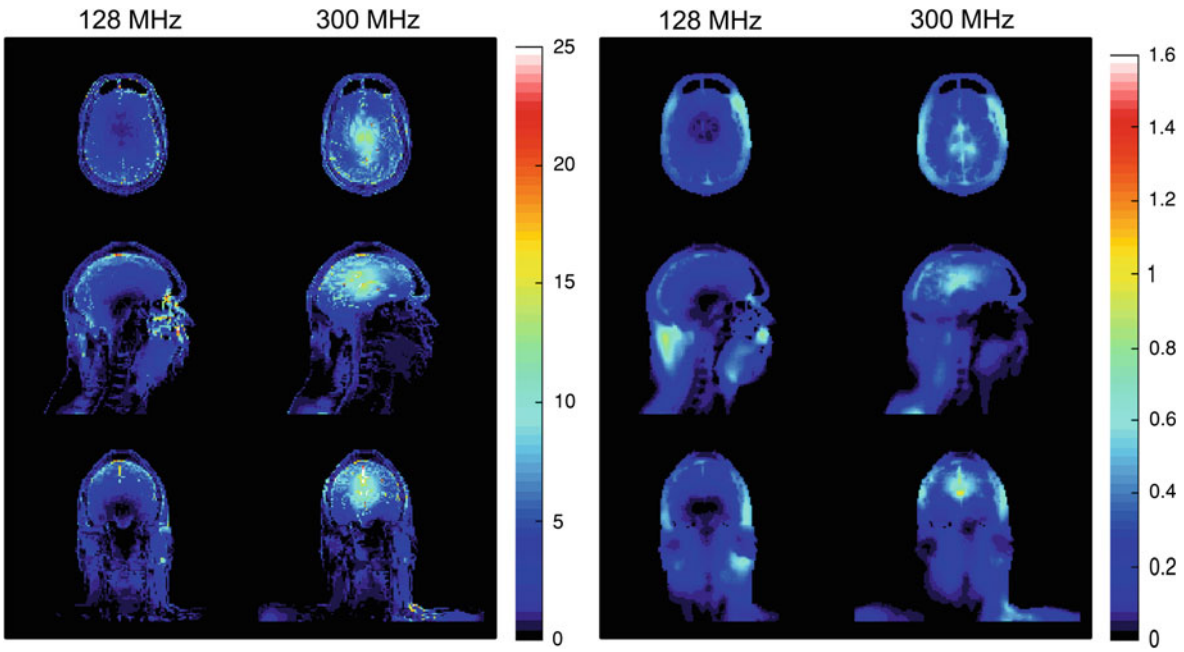

Fig. 9 Calculated distributions of (*left*) SAR (W/kg) and (*right*) corresponding temperature increase (°C) at 3 T (128 MHz) and 7 T (300 MHz) modeled during exposure to a head-average SAR of 3 W/kg. (*Top*) An axial plane passing through the center of the coil and brain, (*center*) corresponding sagittal and (*bottom*) coronal planes. The simulated RF coil was a sixteen-element TEM resonator

permeability value. A large number of vendors offer sophisticated electromagnetic modeling packages, each using a slightly different method for calculating the electric fields and SAR, although most are based on finite difference time domain (FDTD) algorithms.

In addition to the SAR, another important physiological measure is the temperature rise (ΔT) which is produced by the power deposited in the body. The temperature rise depends not only on the SAR, but also on the thermal conductivity of the tissue and the amount of blood perfusion which helps to reduce the temperature increase. For example, in the head a particular area of concern is the eyeballs which have a relatively high conductivity, producing high SAR, but very low perfusion which means that any heat build-up cannot easily be dissipated. Theoretical values of temperature maps can be derived using the Pennes bioheat equation (Pennes 1948). Figure 9 illustrates the SAR distribution in the brain at 3 and 7 Tesla, showing very different heating patterns at the two different frequencies (Collins et al. 2004).

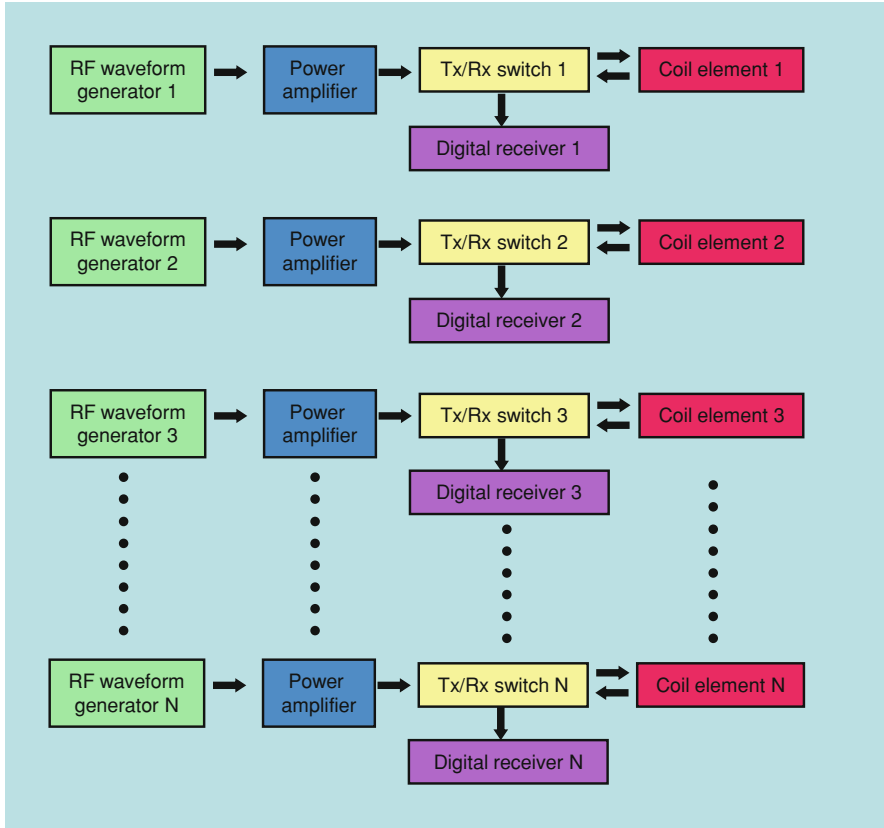

Fig. 10 Schematic of the hardware platform required to implement an N-element transmit array with variable magnitude and phase of the input signal to each element of the array

7 Transmit Arrays for High Field MRI

The fundamental problem with using a birdcage coil, for example, in high field MRI is that the spatial distribution of the magnetic and electric fields in the body are largely determined by the tissue dielectric and conductivity properties rather than those of the coil itself. In other words, using such a coil there are no RF parameters that can be controlled or altered to try to improve the situation. In the simple example considered previously, opposite currents run on opposite rungs of a birdcage and this must produce signal cancellation at certain spatial locations within the body. The potential solution to this problem has been well-known in electromagnetic hyperthermia for many years (Weihrauch et al. 2007; Wust et al. 1991; Behnia and Webb 2004; Behnia et al. 2002; Kowalski et al. 2002; Sullivan 1991), and consists of designing an RF coil in which the magnitude and phase of the current in the conductive elements can be controlled individually (either via open-loop or closed-loop control), thus providing a number of degrees of freedom. Based either on measurements or simulations, the signal input to each element of the RF coil can be optimized to maximize the uniformity of the transmit field within the patient, to minimize local and global tissue heating, or a combination of the two (Metzger et al. 2008).

Implementing such a design requires fundamental changes to both the system architecture (Van De Moortele et al. 2005) and the RF coil itself. In terms of hardware, each element of the transmit coil array essentially needs a copy of the driving system which is used for a single transmit coil at lower fields, as shown in Fig. 10. Individual waveform generators and RF amplifiers are used for each channel which allows different RF waveforms to be sent to each element of the transmit array.

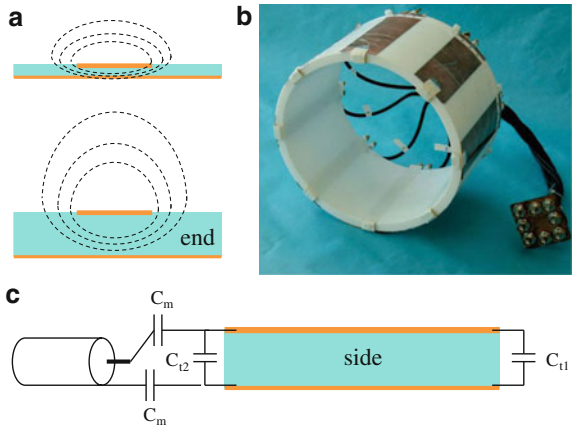

Fig. 11 Principles and application of stripline MRI coils. The stripline consists of a length of conductor, a dielectric, and a ground plane. **a** The effect of dielectric thickness on the penetration of the RF field (*dotted line*). If the dielectric (*blue slab*) is too thin, the field is compressed around the conductor and does not penetrate into the patient, as shown in the top configuration. If the thickness of the dielectric is increased, bottom configuration, then the penetration depth increases. The disadvantage of a thicker dielectric is that the coupling between array elements placed closely together increases compared to a thin dielectric. **b** An eight-element stripline head coil. Figure reproduced from (Adriany et al. 2005) with permission from John Wiley Ltd. **c** Two tuning capacitors (C_{t1} and C_{t2}) are used to tune each element to the proton resonance frequency, and the two matching capacitors, C_m, are used for impedance matching to 50 Ω

The most common building block for the transmit array coil itself is a stripline element, shown in Fig. 11 (Adriany et al. 2005, 2008; Van De Moortele et al. 2005). A stripline consists of a strip of conductor placed on top of a dielectric material such as Teflon, with a wide ground plane on the other side of the dielectric, as shown in Fig. 11a. This type of structure is widely used in the communications industry, and is extremely easy to construct. For a head coil shown in Fig. 11b typical dimensions of each stripline are ~12 mm width and 15 cm length, Teflon thickness ~5 mm, and 20 mm wide copper for the groundplane (Adriany et al. 2005). The stripline elements can either be decoupled by specific dimensions and geometry of substrate thickness, conductor width, and element separation (Lee et al. 2004; Lee et al. 2001), or by the addition of a capacitive decoupling network (Zhang and Webb 2004; Adriany et al. 2008). Finally, each element is fine-tuned to be impedance matched to exactly 50 Ω, as shown in Fig. 11c, and connected to a separate transmit/receive switch.

Figure 12 shows configurations of larger stripline elements which are used for imaging the torso at 7 Tesla. Using this type of configuration cardiac and abdominal imaging have both been performed successfully at 7 Tesla (Snyder et al. 2009; Vaughan et al. 2009) and appear to have a much more promising future than previously envisioned.

In vivo results, shown in Fig. 13, obtained at 9.4 Tesla using a similar stripline array illustrate the increase in signal homogeneity that is achievable simply by changing the phase of two elements of the array, in this case the two elements closest to the area in which the B_1 field is most inhomogeneous (Vaughan et al. 2006). In general, although most transmit arrays allow control of both magnitude and phase of the RF inputs to each channel, by far the most effective parameter appears to be the phase.

The system setup shown in Fig. 10 is quite complicated and expensive. There are a number of simplified schemes which, although currently only in development in academic laboratories, show considerable promise for commercial development in the future. One approach is, rather than to have large RF amplifiers mounted in an equipment rack, to move the RF amplifiers closer to the coil (thus avoiding significant power losses in the cables which may be 50% or more), or even to integrate them with each element of the array (Kurpad et al. 2006; Lee et al. 2009). This latter approach maintains the ability to provide independent control of the magnitude and phase of the driving voltage to each element of the array, and also has excellent isolation between separate array elements.

In addition to improving the RF field homogeneity, transmit arrays can also be used to improve localized imaging using the concept of Transmit-SENSE (Katscher et al. 2003, 2004), although this has yet to be developed as a clinical tool. The principal is to use the separate channels and elements to reduce the total duration of multi-dimensional RF pulses, which can be used for limited field-of-view zoom-imaging and imaging arbitrarily-shaped fields-of-view, as well as forming the basis for pencil-beam navigator pulses in cardiac imaging. In all of these applications, shorter RF pulses improve the performance considerably.

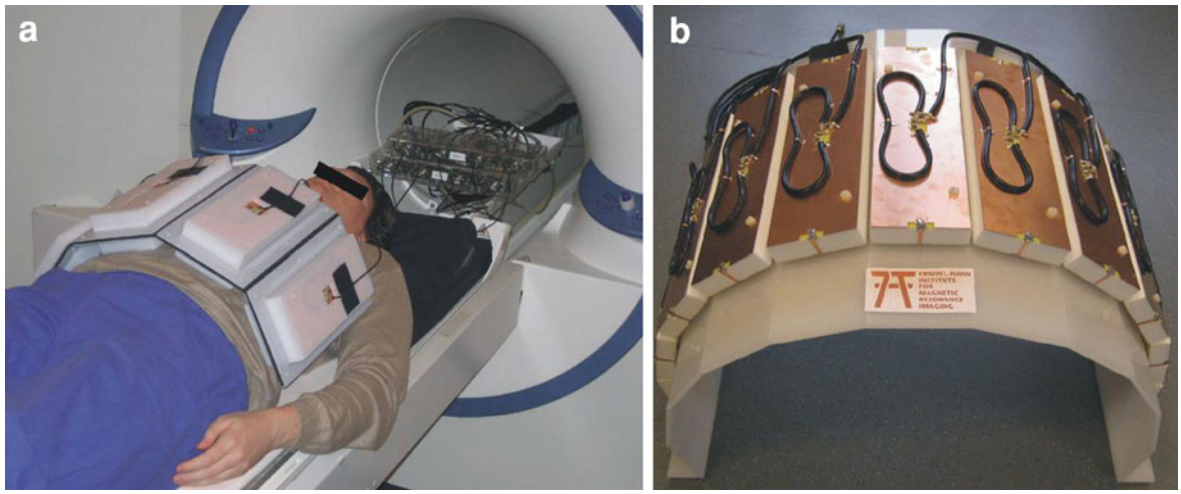

Fig. 12 **a** 8-channel transmit/receive torso array on a human volunteer. The four ventral centrally-fed stripline elements with meanders are enclosed in individual modules flexibly interconnected with neoprene; the four dorsal elements are situated in the patient table. The transmit/receive switches and pre-amplifiers are placed at the head of the table. Courtesy of Erwin L. Hahn Institute for MRI, Essen, Germany. **b** Upper part of a 16-channel transmit/receive array with 11 of 16 centrally fed stripline elements with meanders on a semicircular plastic frame. The remaining 5 elements are placed in the patient table. Courtesy of Erwin L. Hahn Institute for MRI, Essen, Germany

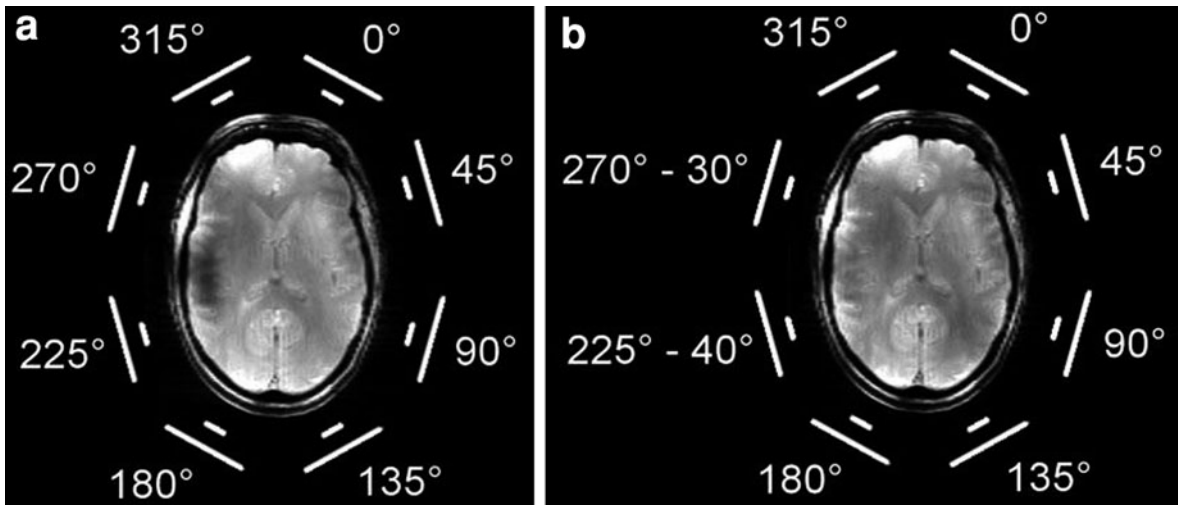

Fig. 13 Effect of the transmit phase on image homogeneity at 9.4 Tesla. **a** Scout FLASH image of a head inside a circularly polarized elliptical coil. The loss of signal near the left ear is the result of destructive interference reducing the net B_1^+. The relative transmit phase for each coil labeled near the two lines representing the conductor and ground planes of each coil is shown. **b** By adjusting only the relative transmit phase of the two coils closest to the area of low signal intensity, local destructive interference can be reduced. Figure reproduced from (Vaughan et al. 2006) with permission from John Wiley Ltd

From the receive point-of-view, the same receive arrays can be used as for lower field strengths. Minor modifications in terms of increased capacitive segmentation, and the use of stripline elements may be integrated, but essentially the performance of such arrays is not compromised by the high fields.

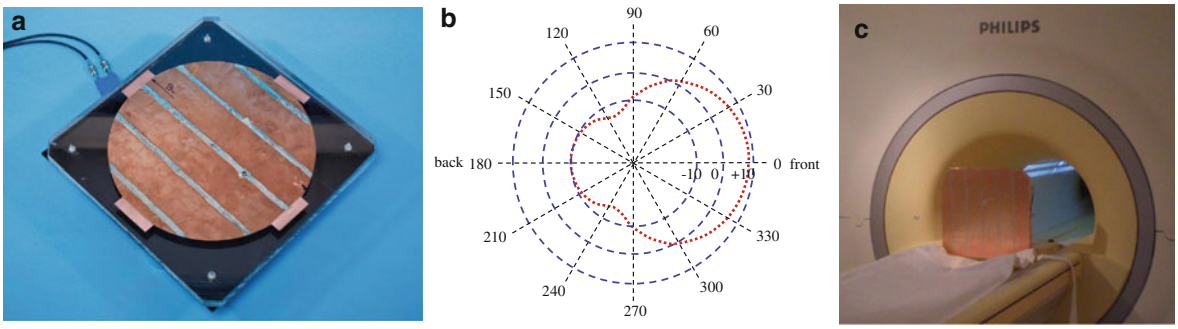

Fig. 14 **a** A patch antenna used to produce traveling waves within the magnet bore. The circle has diameter 35 cm, with a 3 cm thick acrylic spacer between it and a solid copper ground plane on the back. Fine tuning can be produced by varying the distance between the patch and the shield (Brunner et al. 2008). **b** Directivity plot for the patch antenna. The *red dotted circle* plots the energy distribution as a function of angle. Most of the energy is produced in the forward direction in a relatively wide direction. **c** Patch antenna placed at the bore of a 7 Tesla human magnet

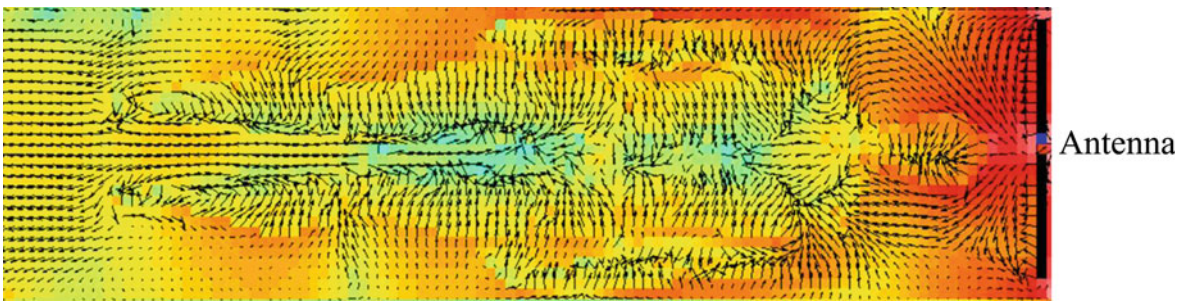

Fig. 15 Simulations showing the mode of operation of the patch antenna with a patient placed in the bore of the magnet. Plot of the energy flow (Poynting vector) with the patient's head placed closest to the patch antenna. The *arrows* show the direction of energy flow, with *red* representing the highest intensity and *blue* the lowest. As can be seen, the EM field refracts at the surface of the body and enters the body at an angle close to 90° to the direction of wave travel down the bore of the magnet. Limited penetration can be seen at the thickest parts of the body (abdomen, thorax)

8 Future Developments at High Field

Although there are considerable engineering challenging in designing coils at very high magnetic fields, there are also intriguing possibilities for new types of coils specifically for high fields. For example, the idea of using the magnet bore itself as a waveguide, coupled to an antenna placed well away from the patient, has recently been suggested as a promising method for obtaining large field-of-view images (Brunner et al. 2008). This approach has been dubbed "travelling wave MRI". Figure 14a shows a patch antenna which efficiently excites the fundamental mode for travelling through the magnet bore. It is particularly interesting, given the discussion in the first part of this chapter in which the difference between antennas and RF coils was stressed, that this device is a true antenna, albeit one with high directivity, i.e. the magnetic field is predominantly in the forward direction, as shown in Fig. 14b. The physical setup is shown in Fig. 14c in which the antenna is placed at the entrance of the magnet bore, with the patient placed inside the bore.

The reason why the traveling wave approach is specifically a high-field phenomenon is that the bore of the magnet acts like a high pass filter, and for a typical bore size of $\sim$60 cm the cut-off frequency for the high pass filter is almost exactly 298 MHz, corresponding to 7 Tesla. This means that this approach will only work at high field.

Figure 15 shows electromagnetic simulations which demonstrate some of the principles of how traveling wave MRI works. Figure 15 plots the Poynting vectors,

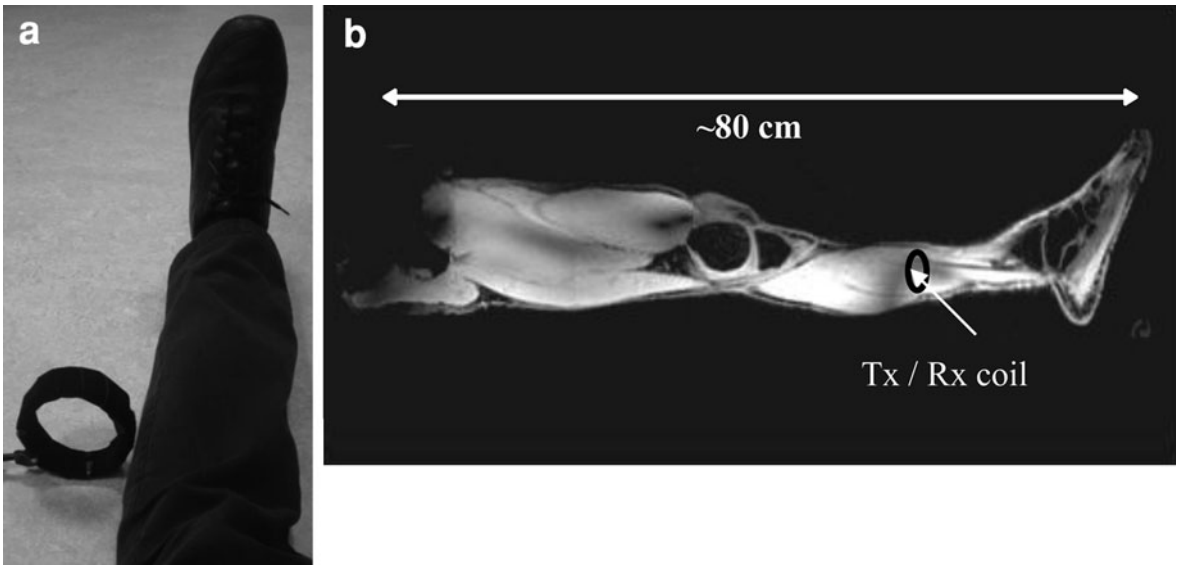

Fig. 16 **a** RF coil oriented along the B_0 axis and placed ~ 5 cm from the calf muscle. **b** A composite image formed from several 3D data sets which must be obtained separately due to the limited gradient linearity in the head-foot direction. The table position within the magnet changes, but the RF coil is not moved. The volume excited is several hundred times the dimensions of the coil. The coil is used in both transmit and receive mode

which can be thought of as an indication of energy flow. If there were no patient inside the magnet bore then the wave would essentially travel in a straight line down the bore of the magnet. However with a patient in place, due to the high dielectric constant of the body the RF energy effectively diffracts at the surface of the body and the energy flows into the body, as indicated by the change in direction of the arrows from straight along the bore to a perpendicular direction. As the wave travels down the bore of the magnet the intensity decreases due to attenuation in the body, but essentially the entire bore of the magnet acts like a very long RF coil. Of course, the effects of constructive and destructive interference within the body still occur, and RF penetration is also limited by tissue conductivity.

Placing a large patch antenna at one end of the magnet bore may not be clinically practical, therefore alternative coil configurations to take advantage of the traveling wave concept have been explored. For example, a small loop dipole can be placed close to the patient within the magnet bore (Webb et al. 2010). Figure 16 shows this basic setup which was used to acquire large field-of-view images of the entire leg and also to acquire localized MR lipid spectra from a voxel with volume 20 mL far away from the transmit

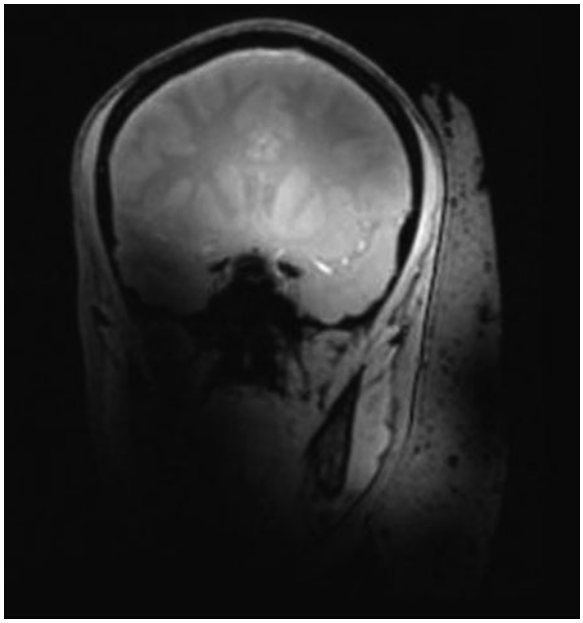

Fig. 17 A low-resolution coronal slice of the brain acquired with a gradient echo sequence at 7 Tesla. A high-dielectric material is placed on the right hand side of the patient. The increase in RF homogeneity can be seen compared to the contralateral side, which shows the typical loss in signal intensity in the lower lobes of the brain. A quadrature birdcage coil was used for transmission

coil in a clinically acceptable time of ~4 min. Although the antenna can be used also to receive the signal as in the original description (Brunner et al. 2008), it is relatively inefficient since it picks up noise not only from the entire body but also the surroundings of the magnet. Much more efficient is to use local receive arrays for signal reception, as described previously (Webb et al. 2010).

In addition to new RF coil designs there are interesting possibilities to shape the RF transmit field by using highly dielectric materials (Yang et al. 2006). These add yet another degree-of-freedom, in addition to those afforded by a transmit array, to improve the field characteristics. In particular these can be placed close to areas which experience a very low RF transmit field, in which case they make significant improvements to the RF homogeneity. Although water-bags can be used, they suffer from a number of disadvantages including high background signal. New high-dielectric materials which have much more desirable properties are just beginning to be introduced into the field (Haines et al. 2010). Figure 17 shows examples of 7 Tesla images acquired with these type of materials.

9 Conclusion

In the past 3 years, 7 Tesla MRI systems have increased significantly in number worldwide, and the number of clinical research papers and studies has increased exponentially. The early groundwork from academic groups in the late 1990s, primarily from the University of Minnesota, has quickly translated into neurological, cardiological and musculoskeletal studies at 7 Tesla in a number of hospitals. The major challenge has been the design of RF coils which are safe in terms of SAR and produce homogeneous RF fields similar to those at lower field strengths. Simple RF designs such as quadrature surface coils can easily be adapted for use at high fields and can provide clinically useful results (Versluis et al. 2009; Van Elderen et al. 2009). However, for large body coils the fundamental designs at 3 Tesla must be adapted into multi-element transmit arrays. Using hardware designs adapted from electromagnetic hyperthermia, and based upon successful demonstrations by a number of academic research groups, the commercial production of multi-element transmit arrays is just around the corner. Indeed such an approach has now been implemented at lower field strengths, where all commercial vendors now offer at least a two-coil transmit array for 3 Tesla, aimed primarily at body imaging. Perhaps most excitingly, whole body magnets at 7 and 9.4 Tesla offer the possibility to design entirely new types of RF coils/antennas which have only just begun to be explored.

Acknowledgments The MATLAB code used to generate values of dielectric constant versus frequency (http://pennstatehershey.org/web/nmrlab/resources/software/rftools) were provided by Chris Collins and Sukhoon Oh from the Penn State Center for NMR Research. Coil photographs were generously provided by Mark Ladd from the Erwin L. Hahn Institute, University of Essen-Duisberg and Chris Collins. Figures were also provided by Figures were kindly provided by Thomas Vaughan, Pierre-Francois van der Moortele, and Gregor Adriany from the Center for Magnetic Resonance Research, University of Minnesota.

References

Adriany G, van de Moortele PF, Wiesinger F, Moeller S, Strupp JP, Andersen P, Snyder C, Zhang X, Chen W, Pruessmann KP, Boesiger P, Vaughan T, Ugurbil K (2005) Transmit and receive transmission line arrays for 7 Tesla parallel imaging. Magn Reson Med 53:434–445

Adriany G, van de Moortele PF, Ritter J, Moeller S, Auerbach EJ, Akgun C, Snyder CJ, Vaughan T, Ugurbil K (2008) A geometrically adjustable 16-channel transmit/receive transmission line array for improved RF efficiency and parallel imaging performance at 7 Tesla. Magn Reson Med 59:590–597

Behnia B, Webb AG (2004) MRI-monitored electromagnetic heating using iterative feedback control and phase interference mapping. Concepts Magn Reson B 23B:1–15

Behnia B, Suthar M, Webb AG (2002) Closed-loop feedback control of phased-array microwave heating using thermal measurements from magnetic resonance imaging. Concepts Magn Reson B 15:101–110

Blaimer M, Breuer F, Mueller M, Heidemann RM, Griswold MA, Jakob PM (2004) SMASH, SENSE, PILS, GRAPPA: how to choose the optimal method. Top Magn Reson Imaging 15:223–236

Brunner DO, De Zanche N, Paska J, Froehlich J, Pruessmann KP (2008) Traveling wave MR on a whole-body system. International Society for Magnetic Resonance in Medicine, Toronto

Collins CM, Smith MB (2001) Calculations of B_1 distribution, SNR, and SAR for a surface coil adjacent to an anatomically-accurate human body model. Magn Reson Med 45:692–699

Collins CM, Yang B, Yang QX, Smith MB (2002a) Numerical calculations of the static magnetic field in three-dimensional

multi-tissue models of the human head. Magn Reson Imaging 20:413–424

Collins CM, Yang QX, Wang JH, Zhang X, Liu H, Michaeli S, Zhu XH, Adriany G, Vaughan JT, Anderson P, Merkle H, Ugurbil K, Smith MB, Chen W (2002b) Different excitation and reception distributions with a single-loop transmit-receive surface coil near a head-sized spherical phantom at 300 MHz. Magn Reson Med 47:1026–1028

Collins CM, Liu W, Wang J, Gruetter R, Vaughan JT, Ugurbil K, Smith MB (2004) Temperature and SAR calculations for a human head within volume and surface coils at 64 and 300 MHz. J Magn Reson Imaging 19:650–656

Duyn JH, van GP, Li TQ, de Zwart JA, Koretsky AP, Fukunaga M (2007) High-field MRI of brain cortical substructure based on signal phase. Proc Natl Acad Sci USA 104:11796–11801

Glover GH, Hayes CE, Pelc NJ, Edelstein WA, Mueller OM, Hart HR, Hardy CJ, Odonnell M, Barber WD (1985) Comparison of linear and circular-polarization for magnetic-resonance imaging. J Magn Reson 64:255–270

Griswold MA, Jakob PM, Heidemann RM, Nittka M, Jellus V, Wang J, Kiefer B, Haase A (2002) Generalized autocalibrating partially parallel acquisitions (GRAPPA). Magn Reson Med 47:1202–1210

Haines K, Smith NB, Webb AG (2010) New high dielectric constant materials for tailoring the B_1 + distribution at high magnetic fields. J Magn Reson 203:323–327

Hayes CE, Edelstein WA, Schenck JF, Mueller OM, Eash M (1985) An efficient, highly homogeneous radiofrequency coil for whole-body NMR imaging at 1.5-T. J Magn Reson 63:622–628

Heidemann RM, Ozsarlak O, Parizel PM, Michiels J, Kiefer B, Jellus V, Muller M, Breuer F, Blaimer M, Griswold MA, Jakob PM (2003) A brief review of parallel magnetic resonance imaging. Eur Radiol 13:2323–2337

Hoult DI (2009) The origins and present status of the radio wave controversy in NMR. Concepts Magn Reson A 34:193–216

IEC (2002) International standard, medical equipment—part 2: particular requirements for the safetyof magnetic resonance equipment for medical diagnosis, 2nd revision. International electrotechnical commission 601-2-33

Kang CK, Park CW, Han JY, Kim SH, Park CA, Kim KN, Hong SM, Kim YB, Lee KH, Cho ZH (2009) Imaging and analysis of lenticulostriate arteries using 7.0-Tesla magnetic resonance angiography. Magn Reson Med 61:136–144

Katscher U, Bornert P, Leussler C, van den Brink JS (2003) Transmit SENSE. Magn Reson Med 49:144–150

Katscher U, Bornert P, van den Brink JS (2004) Theoretical and numerical aspects of transmit SENSE. IEEE Trans Med Imaging 23:520–525

Kowalski ME, Behnia B, Webb AG, Jin HM (2002) Optimization of electromagnetic phased-arrays for hyperthermia via magnetic resonance temperature estimation. IEEE Trans Microw Theory Tech 49:1229–1241

Kurpad KN, Wright SM, Boskamp EB (2006) RF current element design for independent control of current amplitude and phase in transmit phased arrays. Concepts Magn Reson B 29B:75–83

Lee RF, Westgate CR, Weiss RG, Newman DC, Bottomley PA (2001) Planar strip array (PSA) for MRI. Magn Reson Med 45:673–683

Lee RF, Hardy CJ, Sodickson DK, Bottomley PA (2004) Lumped-element planar strip array (LPSA) for parallel MRI. Magn Reson Med 51:172–183

Lee W, Boskamp E, Grist T, Kurpad K (2009) Radiofrequency current source (RFCS) drive and decoupling technique for parallel transmit arrays using a high-power metal oxide semiconductor field-effect transistor (MOSFET). Magn Reson Med 62:218–228

Li TQ, van GP, Merkle H, Talagala L, Koretsky AP, Duyn J (2006) Extensive heterogeneity in white matter intensity in high-resolution T_2*-weighted MRI of the human brain at 7.0 T. Neuroimage 32:1032–1040

Maderwald S, Ladd SC, Gizewski ER, Kraff O, Theysohn JM, Wicklow K, Moenninghoff C, Wanke I, Ladd ME, Quick HH (2008) To TOF or not to TOF: strategies for non-contrast-enhanced intracranial MRA at 7 T. MAGMA 21:159–167

Metzger GJ, Snyder C, Akgun C, Vaughan T, Ugurbil K, van de Moortele PF (2008) Local B_1 + shimming for prostate imaging with transceiver arrays at 7T based on subject-dependent transmit phase measurements. Magn Reson Med 59:396–409

Monninghoff C, Maderwald S, Theysohn JM, Kraff O, Ladd SC, Ladd ME, Forsting M, Quick HH, Wanke I (2009) Evaluation of intracranial aneurysms with 7 T versus 1.5 T time-of-flight MR angiography—initial experience. Rofo 181:16–23

Pennes HH (1948) Analysis of skin, muscle and brachial arterial blood temperatures in the resting normal human forearm. Am J Physiol 155:459

Pruessmann KP, Weiger M, Scheidegger MB, Boesiger P (1999) SENSE: sensitivity encoding for fast MRI. Magn Reson Med 42:952–962

Roemer PB, Edelstein WA, Hayes CE, Souza SP, Mueller OM (1990) The NMR phased array. Magn Reson Med 16:192–225

Schmitt M, Potthast A, Sosnovik DE, Polimeni JR, Wiggins GC, Triantafyllou C, Wald LL (2008) A 128-channel receive-only cardiac coil for highly accelerated cardiac MRI at 3 Tesla. Magn Reson Med 59:1431–1439

Snyder CJ, DelaBarre L, Metzger GJ, van de Moortele PF, Akgun C, Ugurbil K, Vaughan JT (2009) Initial results of cardiac imaging at 7 Tesla. Magn Reson Med 61:517–524

Sodickson DK, Manning WJ (1997) Simultaneous acquisition of spatial harmonics (SMASH): fast imaging with radio-frequency coil arrays. Magn Reson Med 38:591–603

Sodickson DK, McKenzie CA (2001) A generalized approach to parallel magnetic resonance imaging. Med Phys 28:1629–1643

Sullivan D (1991) Mathematical-methods for treatment planning in deep regional hyperthermia. IEEE Trans Microw Theory Tech 39:864–872

Tkac I, Oz G, Adriany G, Ugurbil K, Gruetter R (2009) In vivo 1H NMR spectroscopy of the human brain at high magnetic fields: metabolite quantification at 4T vs. 7T. Magn Reson Med 62:868–879

Traficante DD (1989) Impedance: what it is and why it must be matched. Concepts Magn Reson 1:73–92

van de Moortele PF, Akgun C, Adriany G, Moeller S, Ritter J, Collins CM, Smith MB, Vaughan JT, Ugurbil K (2005) B_1

destructive interferences and spatial phase patterns at 7 T with a head transceiver array coil. Magn Reson Med 54:1503–1518

van Elderen SG, Versluis MJ, Webb AG, Westenberg JJ, Doornbos J, Smith NB, de RA, Stuber M (2009) Initial results on in vivo human coronary MR angiography at 7 T. Magn Reson Med 62:1379–1384

Vaughan JT, Hetherington HP, Otu JO, Pan JW, Pohost GM (1994) High frequency volume coils for clinical NMR imaging and spectroscopy. Magn Reson Med 32:206–218

Vaughan JT, Adriany G, Snyder CJ, Tian J, Thiel T, Bolinger L, Liu H, DelaBarre L, Ugurbil K (2004) Efficient high-frequency body coil for high-field MRI. Magn Reson Med 52:851–859

Vaughan T, DelaBarre L, Snyder C, Tian J, Akgun C, Shrivastava D, Liu W, Olson C, Adriany G, Strupp J, Andersen P, Gopinath A, van de Moortele PF, Garwood M, Ugurbil K (2006) 9.4T human MRI: preliminary results. Magn Reson Med 56:1274–1282

Vaughan JT, Snyder CJ, DelaBarre LJ, Bolan PJ, Tian J, Bolinger L, Adriany G, Andersen P, Strupp J, Ugurbil K (2009) Whole-body imaging at 7T: preliminary results. Magn Reson Med 61:244–248

Versluis MJ, Tsekos N, Smith NB, Webb AG (2009) Simple RF design for human functional and morphological cardiac imaging at 7tesla. J Magn Reson 200:161–166

Wang J, Yang QX, Zhang X, Collins CM, Smith MB, Zhu XH, Adriany G, Ugurbil K, Chen W (2002) Polarization of the RF field in a human head at high field: a study with a quadrature surface coil at 7.0 T. Magn Reson Med 48:362–369

Wang Z, Lin JC, Mao W, Liu W, Smith MB, Collins CM (2007) SAR and temperature: simulations and comparison to regulatory limits for MRI. J Magn Reson Imaging 26:437–441

Webb AG, Collins CM, Kan HE, Versluis M, Smith NB (2010) MRI and localized spectroscopy in human leg muscle at 7 tesla using longitudinal traveling waves. Magn Reson Med 63:297–302

Weihrauch M, Wust P, Weiser M, Nadobny J, Eisenhardt S, Budach V, Gellermann J (2007) Adaptation of antenna profiles for control of MR guided hyperthermia (HT) in a hybrid MR-HT system. Med Phys 34:4717–4725

Wright SM, Magin RL, Kelton JR (1991) Arrays of mutually coupled receiver coils: theory and application. Magn Reson Med 17:252–268

Wust P, Nadobny J, Felix R, Deuflhard P, Louis A, John W (1991) Strategies for optimized application of annular-phased-array systems in clinical hyperthermia. Int J Hyperthermia 7:157–173

Yacoub E, Shmuel A, Pfeuffer J, van de Moortele PF, Adriany G, Andersen P, Vaughan JT, Merkle H, Ugurbil K, Hu X (2001) Imaging brain function in humans at 7 Tesla. Magn Reson Med 45:588–594

Yang QX, Mao W, Wang J, Smith MB, Lei H, Zhang X, Ugurbil K, Chen W (2006) Manipulation of image intensity distribution at 7.0 T: passive RF shimming and focusing with dielectric materials. J Magn Reson Imaging 24:197–202

Zhang XZ, Webb A (2004) Design of a capacitively decoupled transmit/receive NMR phased array for high field microscopy at 14.1 T. J Magn Reson 170:149–155

Zwanenburg JJ, Hendrikse J, Takahara T, Visser F, Luijten PR (2008) MR angiography of the cerebral perforating arteries with magnetization prepared anatomical reference at 7 T: comparison with time-of-flight. J Magn Reson Imaging 28:1519–1526

Safety

Jürgen Hennig

Contents

Abstract

MR is accompanied to exposure to three different mechanisms of interaction: the main magnetic field, switched gradient fields used for spatial encoding, and the radiofrequency fields used for signal transmission. The physical mechanisms are identical to those at conventional MR. Exposure levels in UHF-MR nevertheless reach values of concern necessitating appropriate measures to ensure safety of patients, volunteers, and operating and technical personnel. This especially applies to energy deposition by radiofrequency fields. Specific absorption rate increases with frequency, at UHF-MR the problem is exacerbated by the necessity to use parallel transmission to generate homogeneous excitation. Gradient-induced peripheral nerve stimulation depends on local changes of the magnetic field, and not on the main field strength. Secondary effects like induced currents when moving in the field do become appreciable at UHF-MR and lead to sensory effects like vertigo and nausea. For both of these exposure categories the physical mechanisms are basically known, serious disagreement arises about safety margins when defining exposure levels for safe application especially with respect to induced currents. The most contentious issue relates to safety of the main field itself. There are numerous reports about interactions of magnetic fields with living tissues, but so far no known biological effects have been identified as a definite health risk at currently achievable field strengths. From a scientific point of view this seems to be good news for the safe applications of UHF-MR, but translating this lack

J. Hennig (✉)
Universität Freiburg, Abt. Roentgendiagnostik,
Breisacherstr. 60a, Freiburg 79106, Germany
e-mail: juergen.hennig@uniklinik-freiburg.de

J. Hennig and O. Speck (eds.), *High-Field MR Imaging,* Medical Radiology. Diagnostic Imaging,
DOI: 10.1007/174_2010_133, © Springer-Verlag Berlin Heidelberg 2011

of evidence into regulatory guidelines is a tricky and contentious issue with potential serious consequences for the field.

An ultrahigh-field MR system represents a very expensive, large, heavy, intimidating piece of equipment suggesting by its mere presence the question 'Is it safe to go in there?'. This question reflects a very valid concern based on the fact that in several respects ultrahigh-field MR comes with exposure to a scale of electromagnetic interactions, which was unknown to mankind prior to the arrival of MR technology. The magnetic field of a 7 T magnet is more than 100.000–200.000 times stronger than the earth magnetic field, which ranges between 30 microtesla in South America and Southern Africa and 60 microtesla around the poles. On the one hand, it is quite astounding that exposure to some interaction which exceeds the natural level by such a large factor is compatible at all with biological life. Just imagine what would happen, if we were exposed to a similarly exaggerated level of some other actuating variable (temperature, air pressure, gravity, light, UV-exposure….). On the other hand, a 1.5 T magnet, exceeding the earth field already by a factor of 25.000–50.000, is not even felt by humans and—as far as we know—has not caused any detrimental effects in the $>>100$ millions of patients which have so far been examined at this standard field strength. This large factor illustrates a key challenge regarding safety assessment of magnetic fields: The interaction of magnetic fields is extremely weak (but non-zero); therefore, biological effects are weak and risk assessment is not immediately apparent. The challenge becomes clear when comparing with electrical safety: The effect of touching a live wire is strong and immediate, so it is rather straightforward to establish and agree on safety limits regarding exposure to electrical current. For magnetic fields, risk assessment is a bit less straightforward, which doesn't mean that it can't be done using well-established scientific procedures.

Simple extrapolation from known experience is of course inadequate. A statement like 'we have gone so far without any problem, so we might as well go further on' is only acceptable, if one is sure that one doesn't stand at the brink of a precipice. On the other hand, the opposite statement 'we have to stop immediately otherwise we might fall into a precipice' is equally irrational as long as there is no indication that a precipice lies ahead and would automatically preclude all further progress.

Before discussing risks of exposure, in the following an overview of relevant exposure interactions related to UHF-MR is given. Apart from the main magnetic field additional sources of exposure and their risks have to be considered, namely, the exposure to the spatially and temporally varying electromagnetic fields caused by the switched gradients used for imaging and the exposure to the 300+ MHz radiofrequency field used for signal generation. All of these exposure categories constitute electromagnetic fields, so in a strict sense, the three types of exposure belong to the same physically category distinguished only gradually by frequency and amplitude. This gradual difference leads to different modes of interaction with biological tissues; therefore, there is some rationale to discuss them separately in addition to the practical fact that magnet, gradient, and radiofrequency fields are generated by different components, which need to operate under specific and pertinent guidelines. At the same time one needs to take care that conclusions and regulations drawn from different modes of interaction are consistent with each other. This especially applies to exposure to main magnetic fields and temporally variable fields generated by switched gradients. A static magnetic field is a time variable field with frequency zero, so exposure data for time variable fields extrapolated to zero frequency have to be consistent with data regarding static magnetic fields. Basically there is a similar overlap at the high frequency range, where time variable magnetic fields smoothly merge into the radiofrequency range, but this intermediate zone is at least currently not relevant for UHF-MR and is, therefore, largely disregarded.

Electricity and magnetism are inevitably linked although apparently separate in their physical manifestation. Several key factors for exposure to magnetic fields (static or time variant) are not primarily related to direct magnetic interactions but to interactions caused by electrical currents generated by magnetic fields. Therefore, and in order to give some intuition, the following chapter includes some basic discussion about the intricate relationship between magnetism and electricity.

1 Some Basic Facts About Electromagnetism

A magnetic moment is together with the electric charge and mass one of the fundamental properties of elementary particles. A natural macroscopic manifestation of this elementary property is found in lodestones, a type of mineral magnetite which is magnetic as a consequence of the alignment of specific electrons in the solid state configuration of magnetite. Magnetite is an iron oxide with a gross composition Fe_3O_4. It is the natural form of iron and as such abundant, lodestone as its magnetized form is relatively rare. From a historical perspective, a first account of magnetism in the west can be tracked to Petrus Peregrinus in 1289, who clearly described all relevant magnetic properties. The use of magnetite needles as navigational aid was already introduced in the early thirteenth century in medieval Europe and dates back to the Qin dynasty (221–206 BC) in China. The fact that the earth itself is a magnet was postulated in 1600 by William Gilbert, an English physicist and physician in his treatise 'De Magnete, Magnetisque Corporibus, et de Magno Magnete Tellure'.

The fact that magnetism and electricity are loosely correlated has been known (or hypothesized) from the early days of the physical exploration of electricity. Compelling evidence for such an interrelation was the observation that a flash striking a boat led to malfunction of its compass ("in 1681, a ship bound for Boston was struck by lightning. Observation of the stars showed that 'the compasses were changed'; 'the north point was turn'd clear south.'" "from F. Cajori, A History of Physics, Dover, New York, 1962, p. 102"). The relationship between electricity and magnetism pervades the work of eminent early scientists in the field such as Benjamin Franklin (1706–1790) and Charles Augustin Coulomb (1736–1806). Conclusive scientific evidence for this interaction was demonstrated in 1820 by the Danish physicist Oersted, who in his famous experiment showed that a magnetic needle is directly influenced by a current flowing through a wire. This was the starting point of intense research on the theory of electromagnetism which culminated in the seminal papers by Maxwell published between 1864 and 1873. The rest is history. Nowadays, the presence of electromagnetic fields is an all-embracing hallmark of modern civilization.

This glimpse on the historical development illustrates the still persisting intellectual struggle we have in getting an intuitive understanding of the intricate relationship between electricity and magnetism. The rather heterogeneous development of the field with several developments occurring in parallel and seemingly unrelated at first has led to several parallel schools of thinking. Engineering and physics have developed different and not always easy to reconcile terminology and nomenclature. The problem is emphasized by the still parallel usage of 'old' cgs- versus 'new' SI units. This diversity is historically grown but indicates a deeper lack of intuitive familiarity we have with electricity and magnetism. Both are invariably and intricately linked, one doesn't exist without the other. In our common perception we feel a (sometimes somewhat uncomfortable) familiarity with electricity, which is ever present in power lines, electrical sockets, and household appliances, whereas magnets are perceived as somewhat exotic devices found in compasses, novelty stores—and MR equipment (HiFi buffs might be aware of the use of small but strong magnets in loudspeakers).

In reality, however, most of the pertinent 'heavy duty'-work like electromotors, electrical trains, and elevators is performed by making use of the magnetic force generated by electrical current. Examples of practical use of the electrical aspect of electromagnetism are electrical heaters, mobile phones, TV, and radio. Even in air conditioners the bulk of the energy is invested in generating the magnetic force driving the pump driving the refrigerant circuit.

The message is—and this especially pertains to safety assessment—that it is not sufficient to look at the direct effects of the exposure entities (magnet, gradients, RF). One also has to consider derived effects like currents induced by magnetic fields and vice versa.

In the following the physical basis of the various modes of interactions will be introduced and discussed followed by a more exemplary than exhaustive overview of real and potential consequences of these effects related to human health and safety. From a scientific point of view it is always preferred to start with a known physical interaction and then to look at possible biomedical ramifications of the expected effects. Given our dire lack of insight into biological mechanisms such a mechanistic view will not be enough for safety assessment, but has to be supplemented by empirical and ultimately epidemiological studies.

Table 1 Physical and biomedical effects of magnetic fields

Physical mechanism	Physical effect	Biomedical effect
(homogeneous) Magnetic field B	Dia-, para-, ferromagnetic interactions	
	Torque on magnetic dipoles	Orientation of hemoglobin, membrane orientation
Spatially variable magnetic field dB/dx	Attractive force on magnetic materials	Danger from 'flying objects' dislocation of implants
Time variable magnetic field dB/dt	Induction of electrical currents	Nerve stimulation: peripheral, cardiac
Motion in magnetic fields B dx/dt	Induction of electrical currents, Hall-effect (for charged particles)	Phosphenes, vertigo, 'salty' tongue
	Magnet-hydrodynamic effect	Inductance of currents in moving blood, eddy current brake effect on blood

Safety is of course a highly relevant issue with potential impact far beyond the world of science. Therefore, the various aspects of exposure to electromagnetic fields in MR have been studied extremely thoroughly and rigorously by numerous groups. For detailed information the reader is urged to look up the references; the text is meant to merely illustrate key aspects.

2 Main Magnetic Field B_0

The main and most obvious (really the only obvious) effect of a static magnetic field is its strong attractive force on magnetic materials like iron. It is important to note that physically this attractive effect is not strictly related to the field itself, but to its spatial derivative, i.e., the gradient of the magnetic field. Natural magnets always generate strongly inhomogeneous fields; therefore, the attractive force is perceived to be invariably linked with the magnetic field itself. This is different for the homogeneous volume inside an MR magnet. Once a ferromagnetic object is in the magnet, it can be moved around force free, but to get it there one has to deal with the strong attractive forces generated by the strong gradients surrounding the homogeneous volume.

For a systematic overview of the interactions of the main magnetic field and its possible biomedical effects it is useful to categorize the various sources of interaction according to the underlying physical mechanism. Table 1 gives an overview of the physical mechanisms, their physical effects and potential biomedical effects. It should be noted that the last two mechanisms involve time as a variable and therefore are covered in the chapter on time variable fields, although these invariably have ramifications in the safe use of UHF-magnets even without gradients, as long as people are moved in and out of the magnet or move around in the fringe field.

2.1 Static Homogeneous Magnetic Field

A 'pure', constant, homogeneous magnetic field shows very few physical interactions: Primarily the magnetic properties of materials will interfere and modify the external magnetic field. In addition, a torque will be exerted on all magnetic dipoles, which will become aligned with the magnetic fields. This effect is responsible for the use of a magnetic compass in navigation (Fig. 1).

Magnetic properties of materials are determined by the electrons circling the atomic nucleus. In classical physics this will generate a ring current and, therefore, a magnetic field. According to the Lenz' rule this induced magnetic field will be opposed to the inducing field. Electrons in molecules are arranged in molecular orbitals described by quantum mechanics, so the classical description cannot be applied as such, but the basic principles still apply: Interaction of molecular electrons with an external magnetic field will induce a counterfield such that the external field is decreased. This property is called diamagnetism and applies to all matter.

In addition to this ubiquitous diamagnetism some materials contain free electrons which generate a magnetic moment by themselves. The resulting magnetic moment is—whenever it occurs—larger

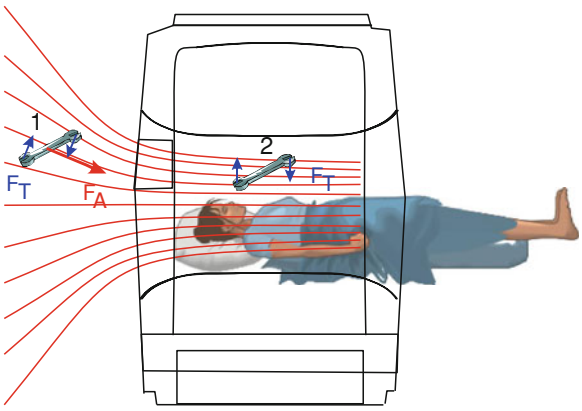

Fig. 1 Mechanical forces of a magnetic field. Outside the magnet, where the field (indicated by *red* field lines) is inhomogeneous (1), any magnetic material will experience an attractive force F_A in the direction of the field as well as a torque F_T, which acts to align the object with the field lines. In the homogeneous volume inside the magnet (2), F_A is zero and the object experiences torque F_T only

than the underlying diamagnetism from inner shell electrons. It will align in parallel to an external field and, therefore, lead to an increase in magnetic field strength. Dia- and paramagnetism are measured by the susceptibility χ. Materials in biological tissues and thus all human tissues are diamagnetic and have susceptibilities close to the susceptibility of water ($-9.04 \times$ 10-6 in SI units). In other words the magnetic field inside the body of a patient lying in a 7 T magnet is 'only' 6.99993672 T.

It should be noted that susceptibility values in the literature may be listed in SI units as well as in cgs units related by a factor of 4π. Unfortunately some confusion exists caused by erroneous usage even in some standard textbooks, which proliferates abundantly by the wonders of copy and paste in our connected digital world. Therefore, it appears to be prudent to allow for a factor of 4π to and fro in any values of uncertain origin.

Dia- and paramagnetism are very weak interactions. The effects of dia- and paramagnetic interactions will be superimposed by thermal motion. At room temperature the thermal energy kT is much higher than dia- and paramagnetic interactions. This changes significantly and dramatically, when the electron–electron interactions become stronger than the disturbing thermal forces. This is the case for elements with unpaired electrons in outer shells (in particular the d-shell) like Fe, Ni, and Co, but also Gadolinium, Dysprosium, and Erbium and some ferromagnetic alloys. In ferromagnetic materials coherent alignment of atomic magnetic moments occurs over extended regions called Weiss domains. Typical size of each such region is 10^{-5} to 10^{-3} m. Magnetic moments within each domain are aligned, but randomized between different domains, so the overall magnetic moment is zero. In an external magnetic field the magnetic moments within each domain align and generate a very large macroscopic magnetization. The characteristics of ferromagnetic materials are determined by interactions at the Bloch boundaries of the Weiss domains and are fundamentally different from those of dia- and paramagnetic substances. Very small particles contain only one Weiss domain with no Bloch boundary and, therefore, do not show typical ferromagnetic behavior. Consequently they are labeled as superparamagnetic.

Compared to diamagnetic water ($\chi \sim 10^{-5}$), the susceptibility of ferromagnetic materials is in the range 500–100.000 depending on the composition and conditions and can be as high as 1.000.000 for supermagnetic alloys.

The whole purpose of this excursion into the basics of magnetism in the chapter on MR Safety is to arrive at this staggering difference of magnetic properties between non-magnetic materials and ferromagnets, which spans 8–12 orders of magnitude. This seemingly paradoxical behavior of magnets to exert extremely strong forces on magnetic materials but apparently none whatsoever on anything else has certainly made a major contribution to the more esoteric uses of magnets in medicine and paramedical applications (Andrä 2007) (Fig. 2).

2.2 Inhomogeneous Magnetic Fields

First it should be noted that a spatially varying field is the norm; pure homogeneous fields as discussed in the previous chapter are the exception. The dominant interaction in a spatially varying field is the mechanical force F between the field gradient ∇B and the magnetic moment M of an object within this field:

$$F = M\nabla B \tag{1}$$

For dia- and paramagnetic substances M is given by

Fig. 2 Some magnetic devices claimed to be good for health found on the internet

$$M = \left(\chi/\mu_0\right) VB \tag{2}$$

where χ represents the susceptibility, $\mu 0$ is the permeability of vacuum, and V is the volume of the object (Fig. 3). The magnetic force

$$F = \left(\chi/\mu_0\right) VB\nabla B \tag{3}$$

is, therefore, proportional to the field-gradient product $B\ \nabla B$. For practical considerations, it is useful to compare magnetic attraction with gravitational force. Weight and attractive force are equal at:

$$\left(\chi/\mu_0\right) VB\nabla B = \rho Vg \tag{4}$$

where ρ represents the material density and g is the gravitational acceleration factor. For typical diamagnetic materials like water with χ in the order of 10^{-5} and $\rho \sim 1$ g/cm^3 weight and attractive force are about equal for $B\ \nabla B \sim 1400\text{T}^2/\text{m}$. As a rule of thumb the field of a magnet of length l drops of roughly quadratically as $B^2/\text{l} \sim \nabla B^2$. In practice, the fringe field is dependent on the magnet design. The highest field-gradient product is close to the opening of the magnet and it is higher for shielded versus unshielded magnets (Fig. 4).

At the maximum field strength of the currently available magnets the diamagnetic force is less than 5% of the gravitational force. For smaller vertical high field magnets the equilibrium condition can be reached and diamagnetic materials (including nuts, strawberries, insects, even small frogs) have been shown to levitate (Simon and Geim 2000). For ferromagnetic materials Eq. 4 has to be used with caution, since the magnetic moment is not linearly dependant on field strength and is limited by saturation of magnetization in iron. Still for ferromagnetic materials the fringe field of a low field magnet (>0.1 T) is sufficient to overcome the weight. The attractive force of a piece of iron in a fringe field of a 7 T magnet is $\gg 10^4$ times higher than its weight, which emphasizes the presence of even small amounts of magnetic materials as by far the most serious safety concern in UHF-MR and MR in general.

Due to the non-zero diamagnetic moment of living tissues, interactions of static magnetic fields with biological tissues exist and can be measured under appropriate conditions. Under in vivo conditions such effects are, however, small compared to thermal motion. Even for deoxygenated hemoglobin with a comparably strong paramagnetic susceptibility due to the unpaired free d-electron of iron, the magnetic

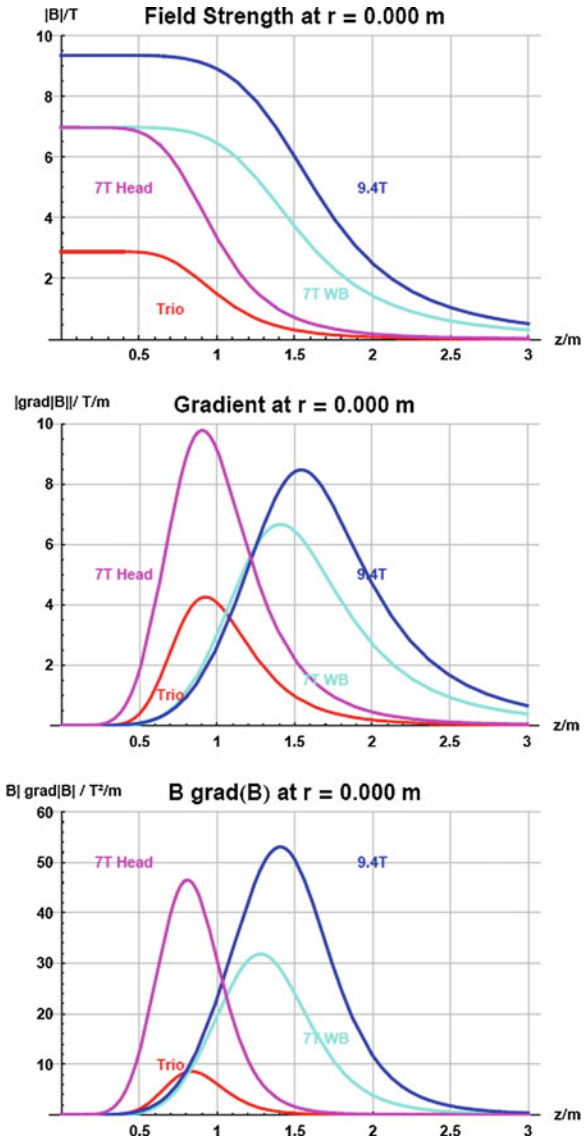

Fig. 3 Field strength (*top*), gradient (*middle*), and field strength-gradient product (*bottom*) along the z-axis of current high field human MR scanners. The origin of the z-axis is at the center of the magnet (courtesy F.Schmitt, Siemens, Erlangen)

forces are much too small to compete with thermal motion. For a detailed account of interaction mechanisms please refer to (Schenck 2005).

There is evidence that sensing of magnetic fields is involved in navigation of a variety of animals (fish, birds, bees…), so there may be biological systems capable to react to static magnetic fields (Kirschwink 1997). There is experimental evidence for several potential mechanisms involved in the sensing system. Among other more indirect measures, small magnetite particles may be involved. Strong and time variant magnetic fields may interfere with navigation of birds but only in a transient manner. Storks submitted to multiple MR scans have been reported to be perfectly able to migrate to Africa thereafter.

Human tissues also contain iron-containing proteins like ferritin. Just like for hemoglobin, the resultant forces are very low in comparison to thermal effects.

As a further hypothetical mechanism of interaction, magnetic fields have been shown to be able to interact with chemical reactions in particular in radical reactions, where unbound electrons are involved. Even under optimized conditions, tailored to maximize the effect, the resultant change is very low. Free radicals are known to be involved in some biochemical pathways (like in mitochondria). In spite of the immense progress in molecular biology our scientific understanding of the biochemical machinery in living organisms is still too particulate and limited to arrive at a conclusive risk assessment based on mechanistic evidence.

3 Time Variable Magnetic Fields and Motion in Magnetic Fields

In risk assessment of UHF-MR time variable magnetic fields are normally discussed in the context of exposure to magnetic field gradients and not to static fields With respect to static field exposure it needs to be considered, however, that motion in an inhomogeneous magnetic field will lead to a temporal change in field dB/dt, which will induce an electrical current in accordance with Faraday's law of induction. A current will also be induced by motion of conductive materials in a static magnetic field. Finally, moving electrically charged particles will be subject to a Lorentz force, which in turn will give rise to induced electrical fields and currents. The human body is electrically conductive and also contains free mobile ions. Therefore, all mechanisms are valid and need to be considered. Biologically it can be indeed difficult (and irrelevant) to separate the exact origin of an observed effect. Indeed all of these mechanisms are a consequence of one and the same principle which can be expressed by the Lorentz force law for the electromagnetic force F generated by a charge q moving in an electromagnetic field with electrical field strength E and magnetic induction B at velocity v:

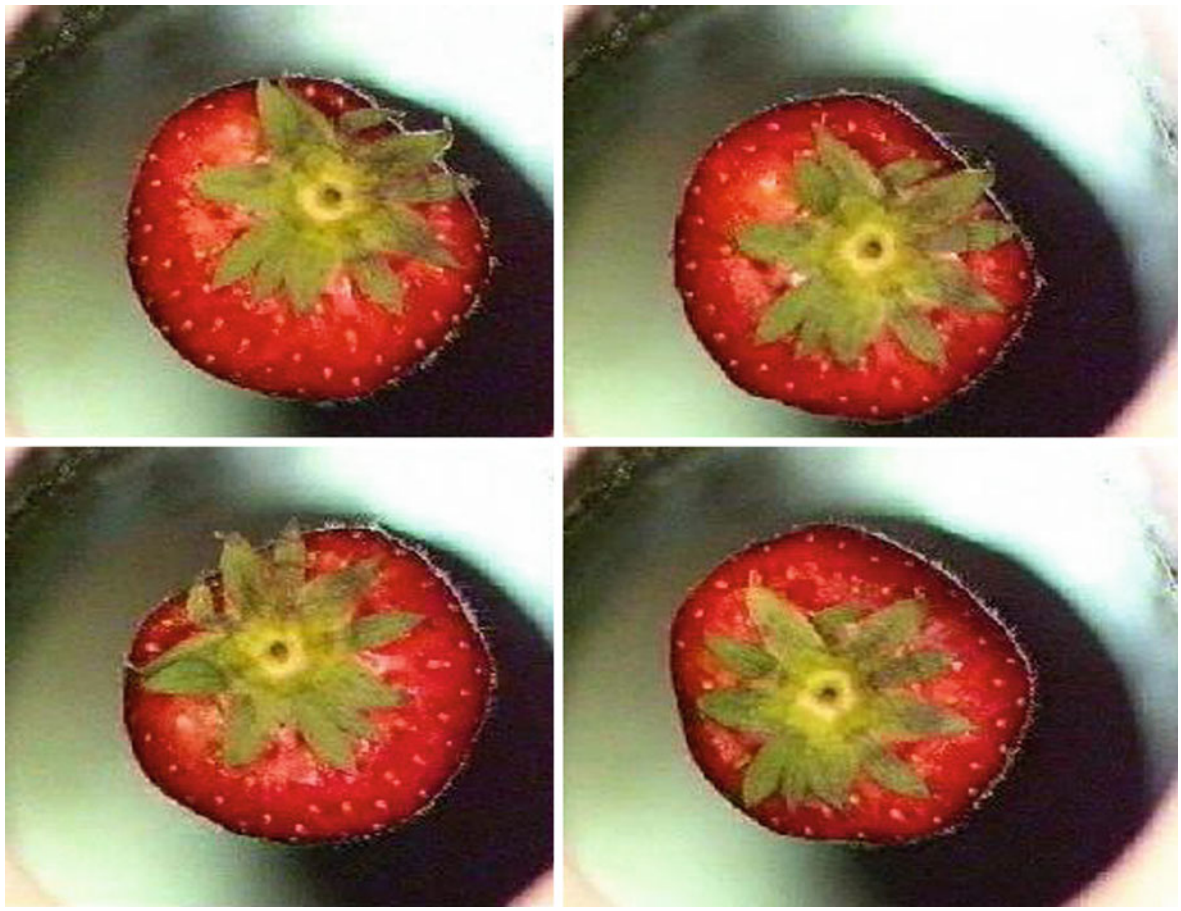

Fig. 4 Strawberry hovering in the opening of a 16 T magnet with 3.2 cm bore size. The diamagnetic force generated by the very high field combined with the strong gradient at the opening of the magnet is sufficient to overcome the gravitational force (courtesy of Jan Kees, High Field Magnet Laboratory, University Nijmegen)

$$\vec{F} = q\vec{E} + q\vec{v} \times \vec{B} \tag{5}$$

Depending on the context and the boundary conditions, the electromagnetic force is converted and can be expressed as an electrical potential or electrical field which in turn creates a voltage leading to a current by Ohm's law.

According to Faraday's law the induced voltage *emf* is given by:

$$emf = \left| \frac{d\Phi_B}{dt} \right| \tag{6}$$

where Φ_B represents the magnetic flux defined as the integral of the magnetic field B over the area of the surface S.

The main biologically relevant effects are:

- induced currents in conductive materials and in particular induced electrical fields/currents may interfere with neuronal conductance.
- magnetohydrodynamic effects by induced currents in pulsatile blood will generate hemodynamic effects.
- at high frequencies the deposited energy of alternating electromagnetic fields will cause tissue heating.

3.1 Neuronal Stimulation

The most obvious effects occurring in an MR scanner are related to the use of switched gradients. It should

be emphasized that according to Eqs. (5) and (6) the determining factor is the change in the magnetic field at a given location, not the gradient amplitude. For constant gradients with a linear change of field the maximum B_{max} lies outside the sensitive volume.

The main concern of time-varying fields in a temporally relevant domain is interference of induced fields/currents with nerve stimulation. The threshold field E_{TH} for nerve stimulation has been originally approximated by Reilly (Reilly 1989) to:

$$E_{TH} = {}^{E_{\min}}/_{(1-\exp(-ts/t_c))} \tag{7}$$

where E_{min} is the threshold field reached at long stimulus duration ts, which for non-linear ramps is defined as the ratio of the peak-to-peak field variation and the maximum slope of the gradient. For trapezoidal ramps ts is identical to the switching time. The time constant tc reflects the fact that nerves have a limited response time to follow an external stimulus. As an alternative and a better fit to experimental data E_{TH} is expressed by a hyperbolic dependence on ts given by:

$$E_{TH} = b(1 + c/ts) = \text{rheobase}\left(1 + {}^{\text{chronaxie}}/_{ts}\right) \tag{8}$$

Here the rheobase b describes the threshold limit at low frequency (equivalent to E_{min} in Eq. (7)) and the chronaxie c reflects the characteristic reaction time of nerves.

The electrical fields necessary for stimulation of peripheral nerves as well as for cardiac stimulation have been investigated by Reilly in extensive detail (Fig. 5).

The electrical fields are caused by a change in the local field dB/dt. For a constant gradient, which generates a linear change in field along the encoding direction, the maximum field B_{max} lies outside the imaging region.

The main emphasis in the assessment of gradient safety has been in the determination of the relation between dB/dt and the induced electrical field. According to Eq. (6) this largely depends on the area of the surface over which inductance occurs. Due to the anisotropic shape of the human body this is expected to be largest in the y-direction (coronal plane). Exact calculations require finite element modeling based on the conductance of individual

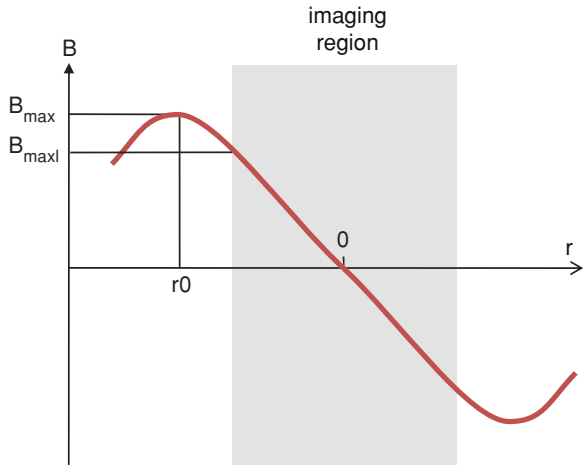

Fig. 5 Schematic plot of the field generated by a gradient along the direction r(= x, y, z). The region useful for imaging lies in the linear part of the field. The maximum field lies outside the imaging region

organs. Using typical values for the geometric boundary conditions and assuming a homogeneous conductor, the results from Reilly's spatially extended neural network (SENN) numerical stimulation model can be approximated by a hyperbolic fit (Eq. 8) with a rheobase value of 54 T/s and c = 0.138 ms for peripheral nerve stimulation (IEC 2008). A number of groups have performed experimental studies to investigate the correlation of observed stimulation thresholds with the Reilly fit. Results show very good agreement within the time window used (0.05–1 ms).

Calculations for cardiac stimulation show considerably higher stimulation thresholds. Reilly predicted for the most sensitive percentile of the population a rheobase value of b = 60 T/s and c = 3 ms.

Apart from ethical considerations hardware constraints set severe limits on the available range for experimental data even for animal experiments. The mean cardiac stimulation limit for dogs at 0.53 ms ramp time agrees well with Reilly's estimates and is 80 times higher than the peripheral nerve stimulation threshold.

Figure 6a shows the Reilly fit for PNS and the 1% cardiac stimulation fit as well as commonly used default values for human safety (IEC 2008). In Fig. 6b these values are translated into values for the maximum field change as a function of the switching time. Fig. 6c displays the maximum gradient amplitude for a very small head gradient coil with dBmax at position r = 15 cm from the center, Fig. 6d

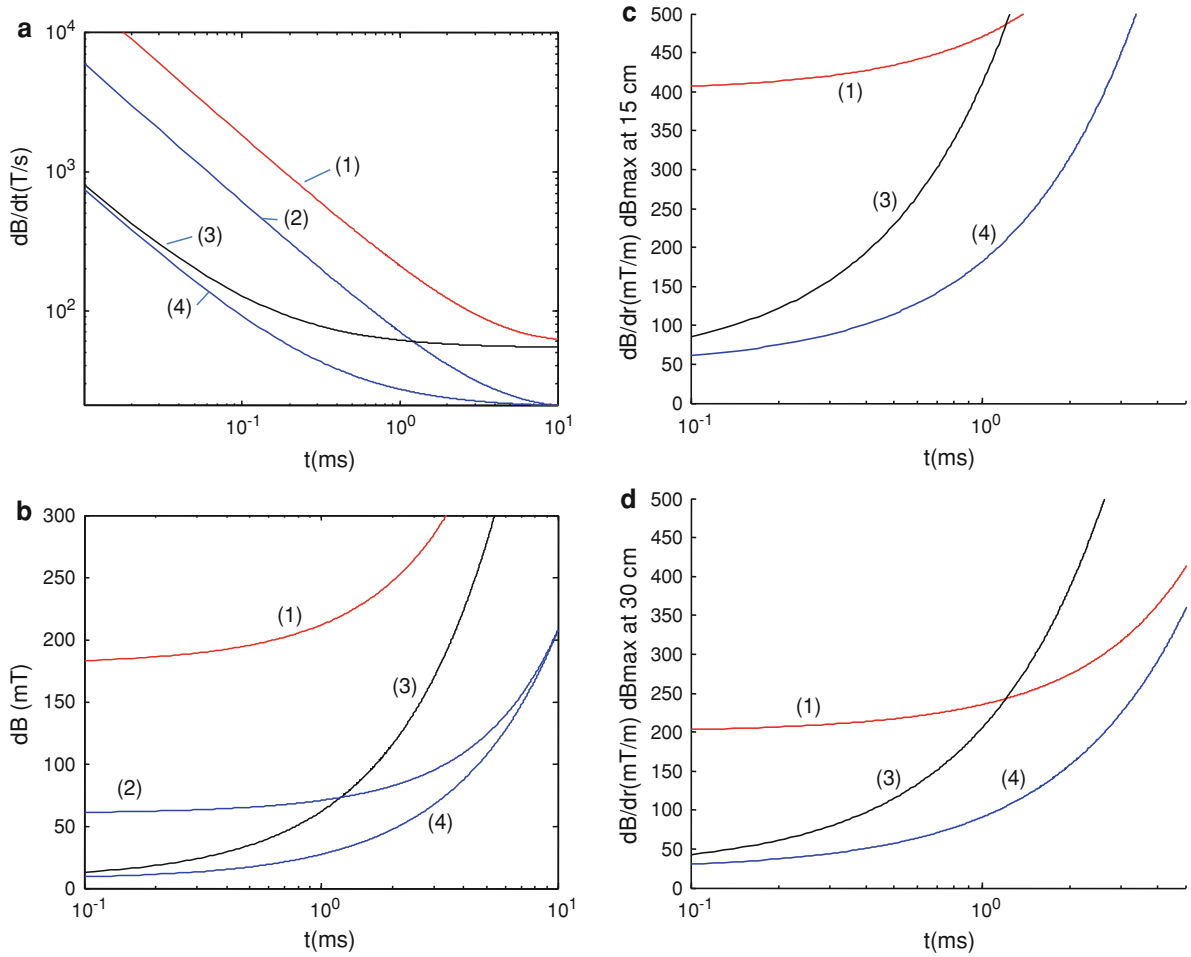

Fig. 6 Estimated limits for cardiac stimulation (most sensitive 1% percentile of population) (1), IEC-cardiac stimulation limit (2), Reilly nerve stimulation estimate (3), and default IEC limit L12 (4) as a function of the switching time t. (**a**) represents the corresponding rate of field change dB/dt, (**b**) shows the maximum field change dB for trapezoidal gradients, (**c**) and (**d**) show the maximum gradient dB/dr for a gradient head insert (**c**) and whole body gradient (**d**), respectively

corresponds to a whole body gradient with dBmax at r = 30 cm.

There is a convergence of the model fits for cardiac stimulation and peripheral nerve stimulation at longer switching times. At 10 ms switching time the ratio for cardiac stimulation to PNS is already close to the rheobase value of 60/54 = 1.1. It is not quite clear whether this is due to a breakdown of the hyperbolic approximation or a true concern. Calculations based on the energy required for stimulation indicate that even in the slow regime there still is a considerable safety factor of $>>10$ between PNS and cardiac stimulation.

The corresponding maximum field change is in the order of 0.6 T. Switching a 0.6 T magnet in 10 ms is clearly outside the regime encountered in MR (or anywhere else). For field-cycling MR, which is not an option to UHF-MR, the field strength to be switched in 1 s to approach this limit, would be 60 T (or 20 T, if the recommended safety factor of 3 is used). So this is no practical consideration in the foreseeable future, even during a magnet quench the resulting dB/dt will be far below these values due to the high inductance of the magnet windings.

Large change in magnetic field over several seconds is experienced when moving into the magnet.

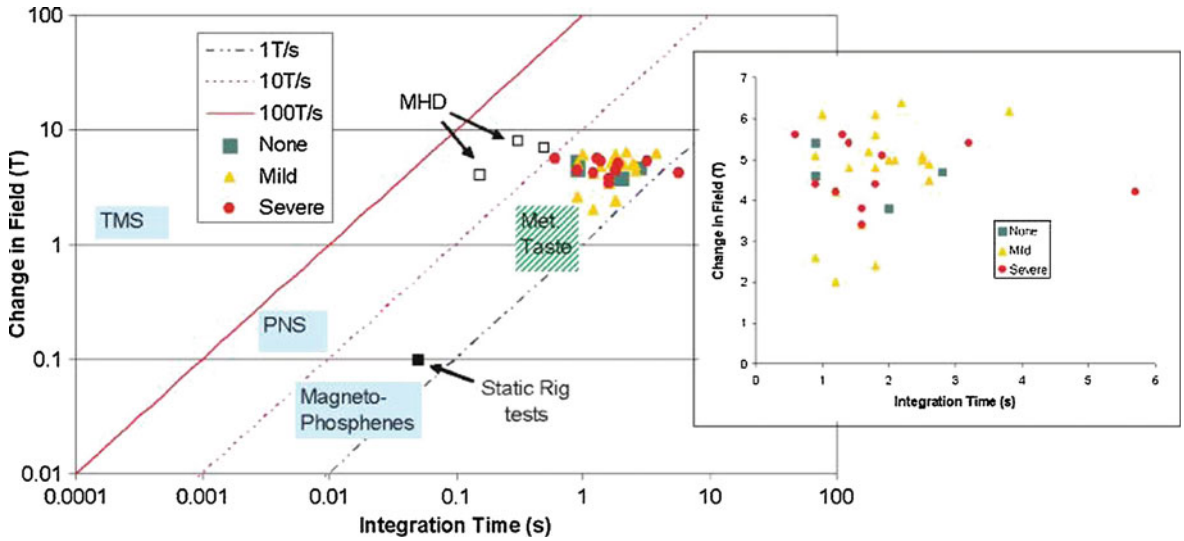

Fig. 7 Summary of effects of exposure to excursions of magnetic field over particular integration times for static-field moving-subject experiment. The inset graph shows measured values of field change for integration times taken from the recordings of dB/dt during movement of the subject at the iso-center of the 7 T magnet. The subject response grades are shown separately as None (*squares*), Mild (*triangles*), and Severe (*circles*).Note that linear scales have been used and error bars have been omitted for clarity. Uncertainty in any one measurement is typically of the order of 10%. In the main graph, iso-contours for various values of dB/dt are shown. Approximate operating regions of particular phenomena are given as a guide. The expected location of any possible minimum MHD effect is shown for calculations based on a 4- and 7 T magnetic field. (from Glover 2007, copyright Wiley)

According to Eq. (5) motion will induce an electromagnetic force and thus an E-field even when moving inside a homogeneous magnet as long as there is a motional component perpendicular to the field. This applies to patients and volunteers entering the magnet as well as to technicians moving in the proximity of the magnet. At commonly used field strength, this has not been regarded as a noticeable effect. At UHF-MR sensations like vertigo, nausea, phosphenes and metallic taste are consistently recorded (Glover and Bowtell 2007; Glover et al. 2007a; Glover et al. 2007b; Glover 2009). Metallic taste is caused by currents induced on the tongue just like licking a low-voltage battery. Vertigo and nausea have been shown to be related to effects in the vestibular system. Induced currents acting on the vestibular hair cells and/or magnetic susceptibility differences between vestibular organs and surrounding fluid will both lead to conflicting and confusing stimuli leading to the described symptoms. Both mechanisms are consistent with theoretical predictions (Glover et al. 2007a).

Figure 7 shows a summary of effects of exposure to excursions of magnetic field over particular integration times for static-field moving-subject experiment.

Detailed calculation of the induced electrical fields requires numerical simulations on realistic data (Virtual Human or similar) with sufficiently high spatial resolution. Such calculations have been recently performed (Crozier et al. 2007). The results show that the induced current density in brain, spine, and CSF by walking around in the fringe field of a 4 T magnet can be considerably higher than 100 mAm^{-2}, which is significantly higher than the 10–100 mAm^{-2}-range assumed previously. There are no reports so far that moving in the fringe field of a magnet leads to any appreciable perceptions known to be associated with UHF-MR (vertigo, nausea,…)—and much less health relevant effects—so as long as people avoid running around a UHF-MR system, this is not a real concern. It does become a severe legal problem in the conversion of experimental data into regulatory values (see Sect. 5).

3.2 Magnetohydrodynamic Effects

According to Eq. (5) motion in a magnetic field will create a force, which will deflect charged particles moving in a conductor (Hall-effect). This is the case for moving blood. The force is orthogonal to the magnetic field and to the direction of flow and proportional to the flow velocity. The effect is therefore largest for the ejective pulsatile flow in the aortic arch. According to Lenz' rule the induced current will in itself create a magnetic field such that its induced Lorentz force is opposed to the direction of motion. This is the well-known eddy current break effect which can be nicely illustrated with a non-magnetic but conductive piece of aluminum, which falls down in slow motion when dropped into the opening of a magnet. If you try this on your MR scanner at home, please make sure that the specimen is really non-magnetic!

The induced electrical field is superimposed with the field caused by the electrocardiogram. Therefore, ECG measured in the MR scanner will show an artificially high T-wave. This is a mere superposition of fields created by two totally different physical mechanisms and has nothing to do with any direct interference of the magnetic field with electrophysiological cardiac activity. According to model calculations the leakage current at the sinoatrial node is 115, 220, and 305 mAm^{-2} at 5, 10, and 15 T, respectively, which is well below the endogenous level of about 1,000 mAm^{-2} (Tenforde 2005). The effect increases linearly with field strength at lower fields, at higher fields the effect becomes sublinear due to the eddy current induced retardation of flow.

The percentage reduction in aortic flow rate of 1.29, 4.93, and 10.4% at 5, 10, 15 T, respectively, agrees well with data by Kinouchi of a 3% flow decrease at 8 T (Kinouchi et al. 1996). This may explain the observed increase in systolic blood pressure at 8 T as a compensatory physiological response. Within the currently achievable field strength the effect remains well within the physiological variations under normal environmental conditions (i.e., standing up vs. lying down). Since the effect increases quadratically with field strength this may ultimately limit the maximum field exposure in humans (see Fig. 8).

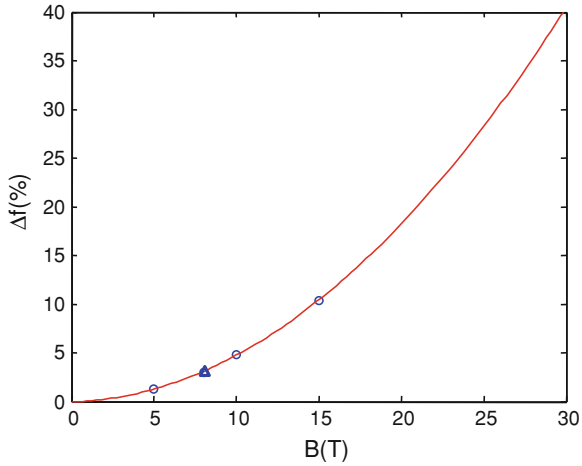

Fig. 8 Simulated percentage change in aortic flow Δf versus field strength. Values in *circles* are from (Tenforde 2005), *triangle* is from (Kinouchi et al. 1996)

3.3 Biological Effects: From Cellular and Molecular Scale to Animals to Humans

There have been numerous studies on the effect of static magnetic fields on specific biological interactions likely to be affected by magnetic fields (sensitive metabolisms involving free radicals, membrane orientation, orientation of blood cells …) as well as exposure studies on cell cultures (Miyakoshi 2005). A review of the literature can be found at (Schenck 2005) and (WHO 2006). Under in vitro conditions a wide variety of tissues and structures like bull sperm, paramecium cilium, collagen, foreskin fibroblasts, osteoblasts and different kinds of cells in cell cultures have shown some degree of orientation in strong magnetic fields. Under in vivo conditions these effects from the static field are superimposed by much stronger influence of thermal motion and gravity. None of the observed effects indicate any health or safety risk in organisms.

There have also been quite a number of studies on gene expression, mutagenesis, cell proliferation and cell damage. A number of effects as well as non-effects have been observed. A full account of the various studies would be beyond the scope of this book, any selection may appear eclectic. Therefore the reader is referred to the WHO-report (WHO 2006), which lists the known literature and also

comments on the experimental conditions. As a bottom line: None of the studies published so far raises any 'red flag' regarding molecular/cellular interactions indicating health risks, but the results are rather heterogeneous and non-conclusive, so more studies are required.

Similar conclusions apply to animal studies (Saunders 2005): There have been quite a number of studies which confirm observed effects in humans with respect to peripheral nerve stimulation and interference with the vestibular system. The data available so far do not indicate any immediate health risk. The studies performed so far are still rated to be too scarce to be conclusive.

With respect to exposure of humans it is estimated that more than 500 Million MR examinations have been performed so far without any reports about immediate effects beyond the known and expected (flying objects, implanted metal, sensory effects…). This doesn't rule out any long-term effects, which require well-controlled epidemiological studies to be detected. There have been some studies on exposure to magnetic fields in general, mostly on workers in pertinent industries like aluminum fabrication. A recent report concludes, that 'the available evidence from epidemiological studies is not sufficient to draw any conclusions about potential health effects of static magnetic field exposure' (Feychting 2005). A major methodological problem for such studies is the definition of a pertinent control group. For industrial workers, the magnetic field is just one (and most probably not even the main) exposure factor and it is hard to establish a control group exposed to exactly the same overall exposure except for the magnetic field.

This also applies to personnel operating clinical MR scanners: Hospitals are not exactly known as a health risk-free environment. The most obvious control group for MR technicians would be technicians working in the same department but not on MR equipment. This leaves techs working on x-ray, CT, DSA, and other equipment—not exactly the ideal control group. In addition any incidental contagion by some patient exposure will easily corrupt the statistics and may lead to highly misleading results one way or the other.

Scientific procedure requires a hypothesis, which is proven by rejecting the null hypothesis. Collecting data which confirm a hypothesis does not constitute scientific evidence. As an example consider the hypothesis that all birds are black. Collecting all black birds one may find will produce a huge pile of 'evidence' to support the hypothesis, which by its mere bulk may be very suggestive that the hypothesis is correct. This doesn't alter the fact that a single colored bird flying into the barn is sufficient to reject the hypothesis. So looking for confirming instances does not constitute scientific evidence. An unspecific hypothesis ('…is no health risk') cannot be confirmed or rejected by scientific procedure, since there is no concrete null hypothesis to be tested against.

Without any hypothesis about possible mechanisms leading to health risks the only feasible (but unsatisfactory) approach is to collect and accumulate data waiting for some incidental finding to show up, which may then be used to be evaluated and tested in more rigorous epidemiological studies. In order to be of any statistical relevance such a study will require testing for all imaginable health risks and include a huge number of subjects.

It is not even clear what would be the variable to be tested for. None of the known or observed interactions is accumulative, so what should the risk be measured against? Maximum field exposure? Duration of exposure to certain field levels?

Given this unclear status, it is not surprising that epidemiologists are not exactly keen to embark on such a huge and uncertain task.

Likewise none of the animal experiments or cell studies indicates that any relevant effects are to be expected, so it is fair to request additional studies. Given the low level of expectation that such studies will produce significant results it is kind of understandable that the enthusiasm of researchers to embark on such studies is somewhat limited. Scientists prefer to perform experiments where they expect some interesting result rather than another study which is inconclusive. As an additional practical consideration funding agencies for scientific research will be reluctant to support such studies as long as a clear and scientifically promising hypothesis is missing.

4 Radiofrequency Fields

RF-fields are time variable magnetic fields distinguished from gradients only by the different frequency range. The transition from the kHz-range of gradients to the 300+ MHz range of UHF-MR is nevertheless a

very fundamental one since it marks the transition from the near-field regime to the far-field regime. In the near-field regime, magnetic and electric fields appear as separate entities. The generation of electric fields by magnets and vice versa appears to be a secondary effect governed by the various laws as described above. At a frequency range where the wavelength approaches the dimensions of the body, this illusion breaks down and the fundamental identity of magnetic and electric fields as two aspects of one and the same entity becomes apparent and unavoidable. The wavelength λ is given by

$$\lambda = c/v = \frac{c_0}{\sqrt{\varepsilon\varepsilon_0\mu\mu_0}} \tag{9}$$

where ε, ε_0 represent the dielectric constant and and μ, μ_0 the magnetic permeability in matter and vacuum, respectively. The permeability of body tissues is close to one (s. above). The dielectrical constant depends on the frequency. For water and up to around 10 GHz the dielectric constant is 81, therefore the wavelength is shortened by a factor of 9 compared to vacuum or air. At 300 MHz the wavelength in air is 1 m, and $\sim$ 0.11 m in the body. According to Maxwell's equations the electrical component and the magnetic component are orthogonal to each other or in other words phase shifted by 90°. Therefore the maxima of the absolute electrical and magnetic fields are a quarter wavelength or $\sim$ 2.8 cm apart in homogeneous media. Figure 9 shows a diagram to indicate where typical applications for MR are located on a relative frequency-field scale. Human brain imaging at 7 T is shown to be somewhat more difficult compared to abdominal imaging at 3 T. Although for animal research magnets with much higher field strength exist, it is clear that human MR dives much closer into the awkward intermediate regime between near-field and far-field conditions.

The body consists mainly of water, but it is far from homogeneous. At interfaces of media with different dielectric constant, reflection and refraction occurs. The index of refraction n is proportional to the square root of the dielectric constant and therefore is $\sim$ 9 for water in that frequency range. Total reflection when going from media with high refraction index n_2 (= body) to low refraction index n_1 (= air) occurs at an angle α given by $\sin\alpha = n_2/n_1$or roughly 6° to the perpendicular of the surface. (As a fun exercise: try to imagine how a lake would look like if the refraction index of water at optical wavelength would still be 9). In other words and in a classical optical consideration, RF can enter the body, but has only a very small range of incidence angle to leave it again, and will thus be reflected multiple times before leaving again. This consideration indicates that the absorption coefficient for RF depends not only on the material properties but also on the size and shape. In the range of frequencies relevant to MR, the size/shape dependant effects dominate the material effects. The absorption coefficient of water rises monotonously with frequency. Due to size/shape dependant effects, the specific absorbed energy shows a maximum in the range between 20 and 200 MHz. For smaller objects the maximum is shifted to higher frequencies.

For realistic conditions, the respective contributions of the magnetic and electrical fields have to be calculated by numerical methods based on actual values of conductivity, permeability and dielectric constants for the different tissues types.

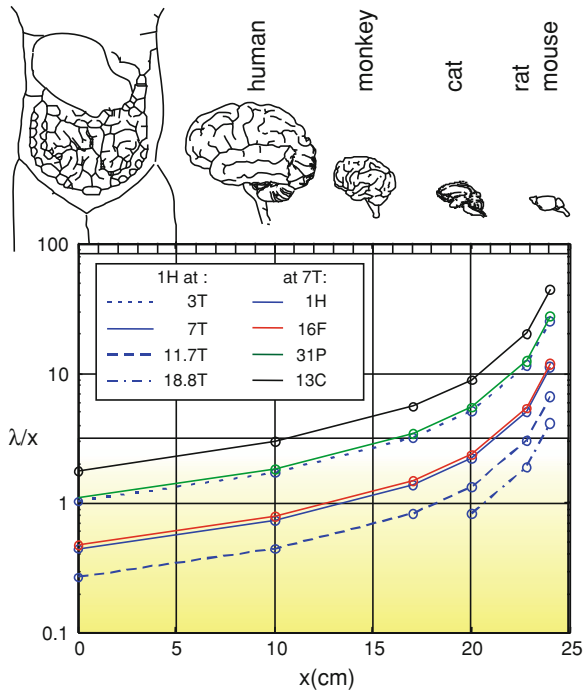

Fig. 9 Ratio of wavelength λ over linear scale x for different field strength and different nuclei and typical areas of application. *Yellow* background color indicates transition from near-field to optical regime

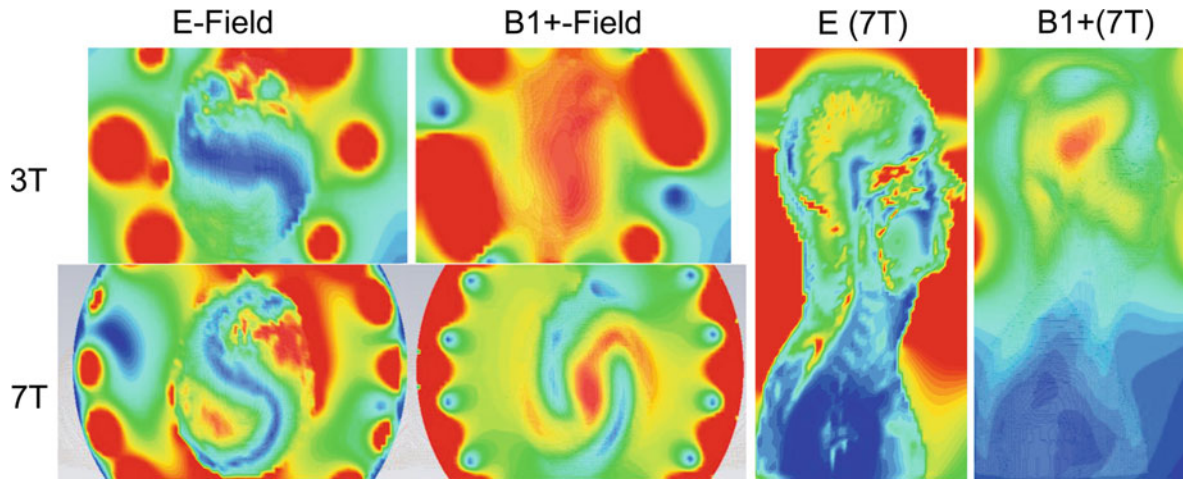

Fig. 10 Numerically simulated maps of E-field and B_1 + -field distribution at 3 T and 7 T calculated using numerical human data. The four images at *left* and *center* show the field distribution in a transverse plane, the two images on the *right* represent sagittal views from the same data set (courtesy O. Speck, OvGU Magdeburg)

An important factor to note is the fact, that the specific absorption rate, which measures the biologically relevant deposition of energy in the body, mainly depends on the electrical component of the field, whereas the excitation profile relevant to generate MR signal is proportional to the B_1^+-field, which is the component of the B_1-field pertinent to MR.

At low fields and frequencies it is rather straightforward to build a quadrature coil, which produces predominantly B_1^+ and low E-field. At higher frequencies used in UHF the counterrotating B_1^- - component, which is totally useless for MR - is less easy to suppress and will have a corresponding E-field component leading to increased SAR.

Even for one specific volunteer and ignoring direct conductive electrical coupling a given B_1^+-distribution (and thus a given flip angle distribution) may be accompanied by a range of B_1^--field profiles. Consequently the E-field (and thus the SAR) can be rather variable and there is no simple relationship between the B_1^+-field distribution and the electric fields and vice versa. Of course B_1^+, B_1^- and E-fields are not independent variables, but closely linked with each other by the Maxwell equations.

Figure 10 show results of numerical simulations of the E- and B_1^+-fields of a digitized human dataset. The field maps illustrate the inhomogeneity of the E-field distribution, which is mainly responsible for the specific absorption rate SAR. It shows that even for human brain applications 'hot spots' are expected to exist. It is also clear that the B_1^+-fields, which are responsible for the B_1-inhomogeneity, are not simply correlated to the E-fields. The 'hot spots' around the head at 7 T represent the rungs of the resonator. In order to protect subjects, appropriate measures need to be taken to make sure that no pathological heating of tissue occurs. It is clear that it is not sufficient to limit the overall absorbed RF-energy. Local 'hot spots' are to be avoided as well, so safety values need to consider both global as well as local limits.

The primary determining factor for safety considerations is the temperature increase achieved by the absorbed RF. This depends on the RF power applied and the tissue absorption but also on thermoregulation. Thermoregulation is a rather slow process therefore safety regulation limits use different time windows to allow for integration of thermal energy.

In the field of MR it is in general be considered safe if the temperature increase does not exceed 1°C. Whole body exposure to 4 W/kg has been calculated to lead to a temperature increase by about 0.6°C in good agreement to experimental data for 20–30 min exposure duration, so this value has been extensively used as guidance for regulatory exposure limits.

5 Safety and Regulations

It may be somewhat unusual to include a chapter about regulations into a scientific textbook, but in view of the fact that exposure in UHF-MR enters hitherto largely unchartered territory, it seems to be appropriate to discuss the issues of converting scientific insight into regulations as a kind of 'reality check'. At the time of preparing this book there are also unresolved pending issues relating to the ongoing legislation in the European Community which may have quite severe consequences on the further development of the field. It should be emphasized that the following reflects the author's personal and fully subjective view and assessment.

Just like in any other field, translation of the insight and knowledge about biomedical interactions of the various types of exposure (static field, gradients, RF) into regulations requires an assessment of the risk (if existent) versus benefit (if existent). The biological effects of exposure are determined by biology and therefore independent of the context during exposure (occupational, research, clinical, …). The risk can be influenced and minimized by special precautions including special training and instructions or monitoring devices. With respect to the benefit a sliding scale exists.

For patient examinations there is an expected immediate and relevant benefit to the patient. Guidelines are set to define the operating conditions under which an examination may be performed without additional considerations. If justified by the expected diagnostic benefit, guidelines may be exceeded (i.e., in examinations during pregnancy). So far there are no clear clinical indications to use UHF-MR in clinical diagnosis, so this issue is not pertinent for the time being, but may become so in the near future.

For exposure of the general population, the benefit is indirect and 'soft' (economic impact), so a rather stringent evaluation needs to be made to minimize risks.

Most pertinent for UHF-MR are two exposure categories, which lie somewhere in between:

For research applications there is no immediate benefit for the subjects, but a scientific benefit either with respect to new insight in basic research or new insight about the pathophysiology of disease leading to (potentially) better diagnosis and treatment. This is the most pertinent case for UHF-MR. All such studies have to be approved by the pertinent ethical body (IRB or else), any risk for the subject needs to be minimized.

Finally occupational exposure poses in some respects the most sensitive issue. Regulations regarding occupational exposure once issued are legally binding and it is the responsibility of the employer to make sure that these are maintained. So it is of utmost importance that these values are set in a way to maximize the benefit for research, clinical application and the society in general while minimizing the risk for the individual. In a controlled working environment means can be taken to minimize potential risks of exposure compared to an uncontrolled public environment. It is therefore generally accepted that especially for applications with a potential and significant benefit occupational exposure may be somewhat elevated compared to exposure of the general public. The various 'ingredients' going into risk assessment (clinical/scientific benefit, economic impact, freedom of choice, potential damage, …) are incommensurable, so there are and will always be political, ideological, and personal preferences going into the various weighing factors leading to regulatory decision making. The death toll deemed to be acceptable for roaming the motorways at neck breaking speed is quite astounding (and quite variable between cultures and countries). Unhealthy food habits as the number one 'killer' in the US and Europe is treated rather leniently, whereas smokers have become close to being criminalized over the past few decades, to name just a few examples for the vagaries of the regulatory process—and of public perception.

There are a number of independent international bodies involved in providing the necessary information, documentation and guidance. The most prominent are the IEC and ICNIRP. IEC comprises electrical engineers from all fields. It follows a very open and transparent procedure in the preparation of its guidelines. A first draft of the current paper has been published over the internet open for comment and discussion to the community at large. After several iterations a paper was finalized which comprises the state of the art at the time of creating the document and which is heavily used by industry in the design and specifications of MR systems (IEC 2008).

Regulatory agencies have acknowledged ICNIRP as the basic reference in defining regulatory legislation. The EU-Directive 2004/40/EC, which regulates the

occupational exposure limits for workers in industry at large from power stations to trains to electrical compliances was based on existing ICNIRP guidelines (ICNIRP 1994, 1998). After protests against the dire consequence of the limitations the directive may have specifically on the development of MR, ratification of the directive has been postponed until 2012. An EU-directive does not in itself constitute legislature, but once ratified, all member states are bound to convert the ruling into national law.

ICNIRP is according to its statutes '… established as an independent and neutral scientific commission, which writes its guidance and recommendations on the basis of established scientific principles only'. ICNIRP has also published a policy paper ('General Approach to Protection against Non Ionizing Radiation' (ICNIRP, R Int Commission NonIonizing 2002)) in which the purely scientific scope and rationale of its mission is acknowledged:

'ICNIRP recognizes that the acceptability and adoption of a complete system of protection also requires data and evaluations based on social, economic, and political considerations. It is ICNIRP's view that these matters are more appropriate to the functions of national governments and their designated authorities.' Regarding the qualification of effects as health relevant it is also stated that 'Biological effects without any identified adverse health consequences do not form a basis for limiting of exposure to NIR. However, ICNIRP recognizes that concern about other unsubstantiated health effects may in itself adversely affect the health of a person, and that this may be best addressed by providing appropriate information.' In the formulation of guidelines a two-tier system is being used, where risk levels are first defined according to the direct biologically effective quantity. Since this often cannot be measured in practice (like the induced electrical field potential leading to neuronal stimulation), these primary values are translated into action values based on some directly measurable external exposure (like the local change in magnetic field).

In order to review the field and to prepare the basis for the decisions of the main committee, typically working groups are implemented consisting of experts in the respective field under discussion.

This approach of implementing ICNIRP as an association of independent scientists has the big advantage that it is (as far as humanly possible) independent of external influence and pressure. One inherent price to pay is a certain slowness of pace in adapting existing guidelines to new developments. With one regular meeting per year it is tough to stay 'on the ball'. Several iterations in the decision formation always means several years to pass before a decision is reached. In spite of the intense discussion and concerns following the EU-directive published in April 2004 it took a full 5 years until revised guidelines were issued.

Additional meetings may be called for as needs arise and in fact the new 'Guidelines on Limits of Exposure to Static Magnetic Fields' (ICNIRP, P Int Comm Non-Ionizing Radiation 2009) have been followed by an Amendment to the ICNIRP "Statement on Medical Magnetic Resonance (MR) Procedures: Protection of Patients shortly thereafter" (ICNIRP, R Int Commission Nonionizing 2009). This amendment is specifically addressed at the use of UHF-MR beyond 8 T and states:

> For the experimental operating mode above 8 T, a progressively cautious approach is suggested for increasingly high magnetic flux densities due to uncertainties regarding possible effects of flow potentials on heart function. In the light of these possible effects, it is concluded that patients should be exposed to such fields only with appropriate clinical monitoring.

Unfortunately this amendment applies only to patients and does not clarify the situation with respect to workers and normal volunteers. For the latter the amendment may serve as a sufficient basis for an IRB application, but workers are at the current state still out in the open.

The main concern relates to the effects related to motion in the magnetic field. Technicians and doctors invariably move around in the fringe field of the magnet, service engineers may need to enter the magnet during maintenance or setup of new devices. Motion in the opening of an UHF-MR magnet may induce the known sensory phenomena like salty taste, phosphenes, and nausea. In the guidelines for static magnetic fields it is stated, that 'exposure up to 8 T can be permitted if the environment is controlled and appropriate work practices are implemented to control movement-induced effects. Sensory effects due to the movement in the field can be avoided by complying with basic restrictions set in the ELF guidelines', which reads harmless enough. The ELF guidelines set limits for exposure in the frequency range from 0 to 300 GHz. For slowly occurring changes up to 1 Hz the induced current density is limited to 40 mAm^{-2},

which is a factor of 10 lower than the expected thresholds for visually evoked potentials or such. Recent simulations (Crozier et al. 2007) have shown that this limits are easily exceed locally even while walking around in the fringe field of a 1.5 or 3 T magnet, a regime where not even harmless sensory effects have been observed let alone any harmful adverse effects. If enforced, standard procedures like positioning of the patient, injection of contrast agent during examination, or direct patient supervision during even standard scans at routine field strengths will be severely hindered, interventional MR will become seriously endangered.

With respect to the maximum static fields exposure, the ICNIRP guidelines state: 'It is recommended that occupational exposure of the head and trunk should not exceed a spatial peak magnetic flux density of 2 T except for the following circumstance: for work applications for which exposures above 2 T are deemed necessary, exposure up to 8 T can be permitted if the environment is controlled and appropriate work practices are implemented to control movement-induced effects. Sensory effects due to the movement in the field can be avoided by complying with basic restrictions set in the ELF guidelines.'

What about higher fields? There are already 9.4 T scanners around and 11.7 T will become available soon. It is quite clear that it would be irresponsible to declare this regime as safe. We just don't have enough data yet. It is equally clear that it would be irresponsible to declare this range 'off limits' just because there is not enough information to declare it safe. This is only a dilemma at superficial glance. History of science is replete with examples of entering new territory with—at the time of discovery—often unclear safety risks. Any new technology ever introduced has an unconfirmed and incomplete safety profile at the time of implementation—this applies to the various uses of electricity as well as to cars, trains, electronic communications, any new materials and technologies … There are well-established procedures to deal with the unknown as expressed by ICNIRP:

> The ICNIRP approach to providing advice on limiting exposure to NIR (non-ionizing radiation) necessarily requires well-based scientific data related to established health effects. When, in the absence of sufficient scientific evidence for the existence of a suspected adverse health effect, there are calls for protective measures, a number of approaches to risk management have been applied. These approaches generally center on reducing needless exposure to the suspected agent. However, ICNIRP emphasizes the need to ensure that the practical manner in which such approaches are applied should not undermine or be to the detriment of science-based exposure guidelines. ICNIRP notes the clarification afforded by the European Commission (CEC 2000; Foster et al. 2000) on the practical application of one such approach, the Precautionary Principle. For example, this includes the degree to which the Principle is based on the science (requiring an evaluation of risk research), and the provisional nature of measures pending further acquisition of scientific data.

In other words: as long as scientific evidence for adverse health effects is missing, one should proceed with caution, any restrictions should be provisional pending further data. How has this philosophy been translated into the ICNIRP guidelines?:

> ICNIRP considers that the exposures permitted under the guidelines should be based on levels for which there is appreciable evidence, and should not go higher than this merely because of lack of evidence of adverse effects.

This is in flat disagreement to ICNIRP's own statutes: Rather than proceeding with caution, exposure beyond 8 T is effectively downright forbidden. Translated to other fields of science and technology this would mean that any innovation should be forbidden: The best one can say about any new technology before submitting it to humans (with due concern and precaution) is that there is lack of evidence of adverse effects.

For research the guidelines contain a loophole: "Note: It is recognized that, for research purposes, there might be a wish to investigate the effects of these higher levels; such experimental exposures, however, are a matter for ethics committees (institutional review boards)."

This is nice for scientists who use such a system. It is less useful for service engineers who are under these guidelines unable to work on such magnets.

Looking at the long history of defining appropriate guidelines for the use of MR, one cannot help but feel that the mysterious forces attributed to magnetism seem to prevail the judgment of regulatory decision makers.

European regulations allow research on highly toxic chemicals and contagious disease, radioactive materials and other fields with an extremely high risk profile. For none of the gadgets of modern life (with more or less questionable benefits), television, radio, computers, mobile phones and epidemiological

studies about its safe use have been required or performed prior to large-scale introduction.

The further development of UHF-MR, however, seems to be endangered not because it is unsafe, but, to the contrary, because no serious health-related effects are known, and therefore, its safety is unproven and unprovable.

References

Andrä W (2007) Magnetism in medicine. Wiley-VCH, Weinheim

CEC (Commission of the European Communities) (2000) Communication from the commission on the precautionary principle. CEC, Brussels, 02.02.2000, COM(2000) 1

Crozier S, Trakic A et al (2007) Numerical study of currents in workers induced by body-motion around high-ultrahigh field MRI magnets. J Magn Reson Imaging 26:1261–1277

Directive 2004/40/EC of the European Parliament and of the Council of 29 April 2004

Feychting M (2005) Health effects of static magnetic fields—a review of the epidemiological evidence. Prog Biophys Mol Biol 87(2–3):241–246

Foster KR, Vecchia P, Repacholi MH (2000) Risk management. Science and the precautionary principle. Science 288(5468):979–981

Glover PM (2009) Interaction of MRI field gradients with the human body. Phys Med Biol 54(21):R99–R115

Glover PM, Bowtell R (2007) Measurement of electric fields due to time-varying magnetic field gradients using dipole probes. Phys Med Biol 52(17):5119–5130

Glover PM, Cavin I et al (2007a) Magnetic-field-induced vertigo: a theoretical and experimental investigation. Bioelectromagnetics 28(5):349–361

Glover PM, Eldeghaidy S et al (2007b) Measurement of visual evoked potential during and after periods of pulsed magnetic field exposure. J Magn Reson Imaging 26:1353–1356

ICNIRP (1994) Guidelines on limits of exposure to static magnetic-fields. Health Phys 66(1):100–106

ICNIRP (1998) Guidelines for limiting exposure to time-varying electric, magnetic, electromagnetic fields (up to 300 GHz) (vol 74, p 494, 1998). Health Phys 75(4):442–442

ICNIRP, P Int Comm Non-Ionizing Radiation (2009) Guidelines on limits of exposure to static magnetic fields. Health Phys 96(4):504–514

ICNIRP, R Int Commission NonIonizing (2002) General approach to protection against non-ionizing radiation. Health Phys 82(4):540–548

ICNIRP, R Int Commission Nonionizing (2009) ICNIRP statement on the guidelines for limiting exposure to time-varying electric, magnetic, and electromagnetic fields (up to 300 GHz). Health Phys 97(3):257–258

IEC (2008) Standard IEC 60601-2-33: Medical electrical equipment, International Electrotechnical Commission

Kinouchi Y, Yamaguchi H et al (1996) Theoretical analysis of magnetic field interactions with aortic blood flow. Bioelectromagnetics 17(1):21–32

Kirschwink JL (1997) Magnetoreception—homing in on vertebrates. Nature 390(6658):339–340

Miyakoshi J (2005) Effects of static magnetic fields at the cellular level. Prog Biophys Mol Biol 87(2–3):213–223

Reilly JP (1989) Peripheral-nerve stimulation by induced electric currents—exposure to time-varying magnetic-fields. Med Biol Eng Comput 27(2):101–110

Saunders R (2005) Static magnetic fields: animal studies. Prog Biophys Mol Biol 87(2–3):225–239

Schenck JF (2005) Physical interactions of static magnetic fields with living tissues. Prog Biophys Mol Biol 87(2–3):185–204

Simon MD, Geim AK (2000) Diamagnetic levitation: flying frogs and floating magnets (invited). J Appl Phys 87(9):6200–6204

Tenforde TS (2005) Magnetically induced electric fields and currents in the circulatory system. Prog Biophys Mol Biol 87(2–3):279–288

WHO (2006) Environmental health criteria 232: static fields. Geneva, Switzerland, ISBN 92-4-157232-9

Contrasts, Mechanisms and Sequences

Oliver Speck, Matthias Weigel, and Klaus Scheffler

Contents

Abstract

Since its beginnings, the main magnetic field strength of MR-systems has constantly been increased for high resolution spectrometers, small animal imaging systems and clinical MRI. The obvious motivation is the higher signal-to-noise ratio achievable. However, other effects that result from changes in the relaxation times, the ratio of the object extensions with respect to the RF wave length, or the deposited energy have to be considered. The basic physical effects and their consequences for the most common measurement methods, such as fast gradient echo, turbo spin echo and echo planar imaging are presented and discussed in this chapter.

O. Speck (✉)
Department of Biomedical Magnetic Resonance,
Otto-von-Guericke University,
Leipziger Str. 44, 39120 Magdeburg, Germany
e-mail: oliver.speck@ovgu.de

M. Weigel
Medical Physics, Department of Radiology,
University Medical Center,
Breisacher Str. 60a, 79106 Freiburg, Germany

K. Scheffler
Department of Neuroimaging/MRZ Department,
University of Tübingen/MPI for Biological Cybernetics,
Spemannstr. 41, 72076 Tübingen, Germany

1 Basic Considerations

On a first naïve look, increasing the magnetic field strength B_0 from commonly used 1.5 T to 7 T may seem to raise issues related to raising the financial funds needed or siting the heavy magnet and dealing with the large fringe field. Although these are certainly points that need to be addressed during the planning phase of a high field installation, a number of considerations related to the physical properties of radio-frequency waves, the tissue under observation, and the interaction of the human body with the main

J. Hennig and O. Speck (eds.), *High-Field MR Imaging,* Medical Radiology. Diagnostic Imaging,
DOI: 10.1007/174_2010_101, © Springer-Verlag Berlin Heidelberg 2011

magnetic field or the radio-frequency field are more fundamental and require attention.

Safety aspects related to the exposure of the human body to the static magnetic and radio-frequency fields are addressed in chapter "Safety". In this chapter, the consequences of the increased static magnetic field strength are described and discussed.

1.1 B_0 and Signal-to-Noise Ratio

The most apparent consequence of the increased static magnetic field strength B_0 is the correspondingly increased Larmor frequency ω (in radian per second) that is directly proportional to B:

$$\omega = \gamma B, \tag{1}$$

where γ is the gyromagnetic ratio ($\gamma = 2\pi 42.577$ MHz/T). This change of the Larmor or resonance frequency has impact on a number of aspects because the MR signal is a direct consequence of the interaction between the magnetization precessing at the Larmor frequency and the magnetic fields created by the main magnet, the gradient system, the radio-frequency coils, and the tissue present in the magnet. If these frequency-related aspects are not considered, and a user was simply using a standard method, the resulting image would be rather unsatisfactory as shown in Fig. 1. This example demonstrates many of the challenges arising at high magnetic field strength:

- Inhomogeneous signal intensity throughout the image;
- Inhomogeneous contrast across the image;
- Contrast variation compared to clinical images;
- Large fat–water shift;
- Limited volume coverage due to high specific absorption rate (SAR).

All these challenges are results of the higher Larmor frequency and need to be addressed in order to take full advantage of the higher magnetic field. What is this main advantage that drives the development of high-field MR? It is the high signal-to-noise ratio (SNR) that can be achieved. MR is a notoriously insensitive method. Magnetic resonance imaging is mainly based on the proton nuclear spin resonance signal. Although there is a large abundance of protons in tissue, the proton magnetization generated even in strong magnetic fields is very low. This is a result of two counteracting processes that determine

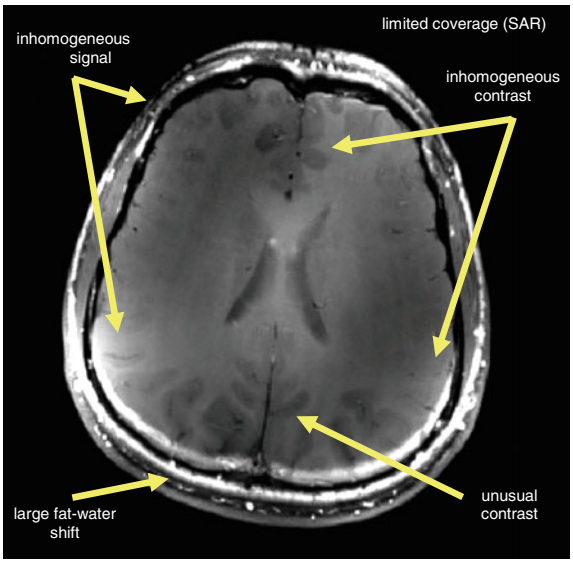

Fig. 1 Nominally T_1-weighted spin-echo image acquired at 7 T with the methods known from 1.5 T (TE = 12 ms, TR = 600 ms, 4-mm slice thickness, matrix 256 × 256)

the tissue magnetization. On the one hand, proton spins aligned along the magnetic field are in a lower energy state and therefore, this is the preferred orientation. If no other effect was present, the magnetization in a magnetic field would be 100%. However, on the other hand, thermal energy destroys such alignment and randomly orients the proton spins. Both effects simultaneously act on the spins, and an equilibrium between the two energy-state populations N_{up} and N_{down} is established according to the Boltzmann statistics:

$$\frac{N_{\text{up}}}{N_{\text{down}}} = e^{-\frac{\Delta E}{kT}} = e^{-\frac{\hbar\gamma B_0}{kT}} \approx 1 - \frac{\hbar\gamma B_0}{kT}. \tag{2}$$

In this equation, $\hbar$ is the reduced Planck constant ($\hbar = 1.055 \times 10^{-34}$Js), k is the Boltzmann constant ($k = 1.381 \times 10^{-23}$ J/K), and T the absolute temperature (in K). For a field strength of 3 T and at body temperature, only 1 out of 100,000 spins is net aligned with the magnetic field. This small excess of down (aligned) versus up spins results in the net magnetization that is exploited to generate the MR signal. The temperature cannot be reduced in living objects. Therefore, higher signal can be generated by the use of higher field strength. Because the exponent in Eq. 2 is extremely small for all achievable magnetic field strengths and temperatures in living tissue, the

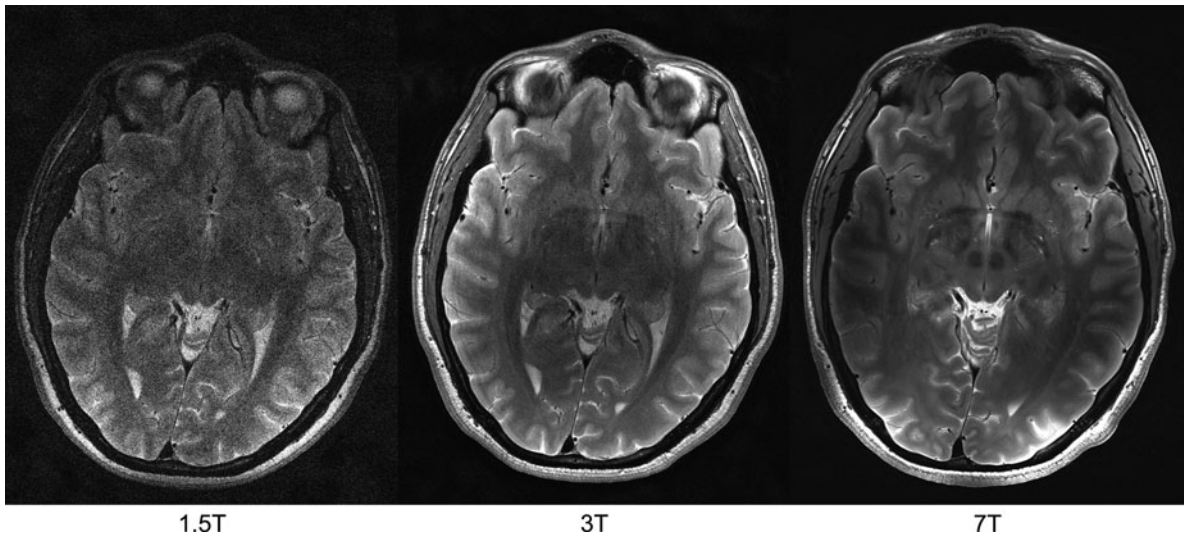

Fig. 2 SNR comparison at field strengths 1.5, 3, and 7 T. T_2 weighted high resolution TSE images with similar acquisition protocols were acquired on the same volunteer: TE = 55 ms, TR = 7000 ms, flip angle = 138°, matrix = 1024 × 648, voxel size 0.23 × 0.23 × 2 mm^3. 7 T leads to a significant SNR gain over 3 and 1.5 T. RF power deposition ratios, quantified in terms of the maximum permissible specific absorption rate (SAR), were 0.08/0.3/0.9 for 1.5 T/3 T/7 T, respectively

formula can be very well approximated by the linear expansion given on the right-hand side of Equation 2. Thus, it becomes clear that the magnetization increases linearly with the magnetic field strength, and for 7 T, only about 2.4 spins out of 100,000 are net aligned. In order to achieve a net magnetization of 10% at body temperature, a magnetic field strength of 30,000 T is necessary. This puts the notion of "ultra high magnetic field" as we currently use it for 7 T or even 11.7 T into a whole new perspective.

Apart from hardware-related effects (RF-coils, etc.) and considering that the noise is dominated by the object and not by electronic noise (as for human in vivo examinations), the SNR of an MR experiment is given by the available magnetization M_0 and a number of sequence-dependent parameters. The most important parameters are the voxel volume V, the number of phase encoding steps nPE and signal averages nA, and the acquisition bandwidth BW.

$$\mathrm{SNR} \sim M_0 V \sqrt{\frac{nPE\, nA}{BW}} \tag{3}$$

In addition, the type of sequence and sequence parameters such as the echo time TE and the repetition time TR can have a more complex influence on SNR.

Let us assume that the magnetization is two times higher at 7 T compared to 3 T (for ease of arguments, we use 2 — the true value is slightly larger). If everything else was identical (we will see later that further effects have to be taken into account), the corresponding gain in SNR of a factor of two could be used to reduce the number of averages, or in general, the scan time, by four. If this argument is turned around, four averages are necessary to achieve identical SNR at 3 T compared to a single average 7 T scan. Thus, high field strength could be used very effectively to shorten scan time. Alternatively, the image resolution could be improved. The higher SNR allows a reduction of the voxel volume by a factor of two in the same scan time. Because space is three-dimensional, this corresponds to a linear reduction of the voxel length by a factor of 0.79 only (cube root 0.5). It is obvious that high resolution is expensive in terms of SNR, and a 1-mm isotropic resolution scan at 3 T can be expected to be of similar image quality at 0.8-mm resolution at 7 T. With this resolution increase, all the SNR benefits from 7 T have been exploited. If additional effects reduce the efficiency at high field, this improvement will turn out to be even less.

The comparison of morphological T_2 weighted TSE imaging at different field strength is shown in Fig. 2. The SNR gain at higher field strength is evident and allows for higher resolution acquisition opening new possibilities in many applications. However, additional

effects such as changes in image contrast, homogeneity and RF-power deposition also occur.

1.2 Specific Absorption Rate

The specific absorption rate (SAR) is the amount of energy absorbed by the tissue when it is exposed to an electromagnetic field, given as power per tissue mass (W/kg). It can be calculated globally over the whole body or locally for small tissue volumes (typically 1 g or 10 g). It is important to note that the magnetic component of the transmit RF-field interacts with the spin system and causes the corresponding flip angle. However, this magnetic component does not contribute to the energy deposited. The SAR is determined by the electric component of the RF-field. The electric field can displace charges in the tissue with density ρ and thus create electric currents that depend on the strength of the electric field E and the electric conductivity σ of the tissue.

$$\mathrm{SAR} = \frac{\sigma E^2}{\rho}. \tag{4}$$

The result of this energy deposition is heating of the tissue due to resistive losses. The maximum SAR exposure for humans is limited by regulatory authorities. For example, within the European Union, currently, a maximum SAR of 3.2 W/kg for the exposure of the head has been defined. This value refers to the average over 6 min. Additionally, the local SAR limit over each 10 g of tissue is 10 W/kg, and over any 10-s period, SAR must not exceed three times these values.

Unfortunately, SAR in human subjects is very difficult to detect because the electric field cannot be directly assessed. The induced temperature increase is usually very small and its spatial distribution is also difficult to measure. Among others, the local SAR depends on the RF-frequency (and thus the magnetic field strength), the RF-coil used, the measurement sequence (TR, number and flip angle of pulses), and the configuration of the tissue exposed in the coil. Therefore, SAR predictions are largely based on numerical simulations that calculate the electromagnetic fields on the basis of tissue models and coil configurations in so-called FDTD (finite difference time domain) simulations. However, very few numeric human tissue models are available and the variability between subjects cannot be explored exhaustively. Depending on the uncertainty of the simulations, higher safety margins are needed in order to guarantee safe operation.

In general, SAR increases with field strength. For field strengths up to 3 T, SAR increases approximately quadratically. Thus, the SAR increases fourfold from 1.5 to 3 T. Because the gyromagnetic constant γ is independent of the field strength, an RF-pulse of 90° flip angle and 1-ms duration requires identical magnetic RF-field amplitude B_1 at any field strength. The electric field E is related to the temporal derivative of the B_1 field (as given by Faraday's law of induction). For higher frequencies, the rate of change of B_1 increases and so does E. For high field strength, the RF-wavelength is short (see next chapter) and the situation becomes more complex. Depending on the tissue type and distribution within the coil, the distribution of E and thus the SAR becomes more inhomogeneous (Collins et al. 1998). Thus, the extrapolation of the SAR to higher field strength is non-trivial and may deviate from quadratic behavior. It has been predicted that the increase of SAR will show an increase less than quadratic (Hoult and Phil 2000). In general, the E-field distribution becomes more localized and so-called hot spots occur that can have largely higher local SAR than the surrounding tissue. As a consequence, the local-to-global SAR ratio can increase and require a reduction of the permissible RF-power. From Fig. 3, it is obvious that the symmetry of the SAR distribution with respect to the object is largely lost at very high field strength. This is surprising at first glance because no obvious reason for breaking the symmetry is present in the object, and this asymmetry is also present in perfectly spherical objects. The asymmetry is induced due to the fact that the excitation coil has to be driven in one (linear polarization) or two (quadrature drive, circular polarization) positions at the coil structure breaking the otherwise cylindrical symmetry of most coils. In this example, the global SAR is increasing by a factor 4.7 from 3 to 7 T. At the same time, the strongest local hot spot increases by a factor of 6.7 leading to an increase in the local-to-global SAR ratio.

In conclusion, the SAR increases dramatically with field strength. Within the given SAR limitations, many standard sequences are severely crippled at high field strength. A number of remedies exist for particular sequences (see specific chapters below).

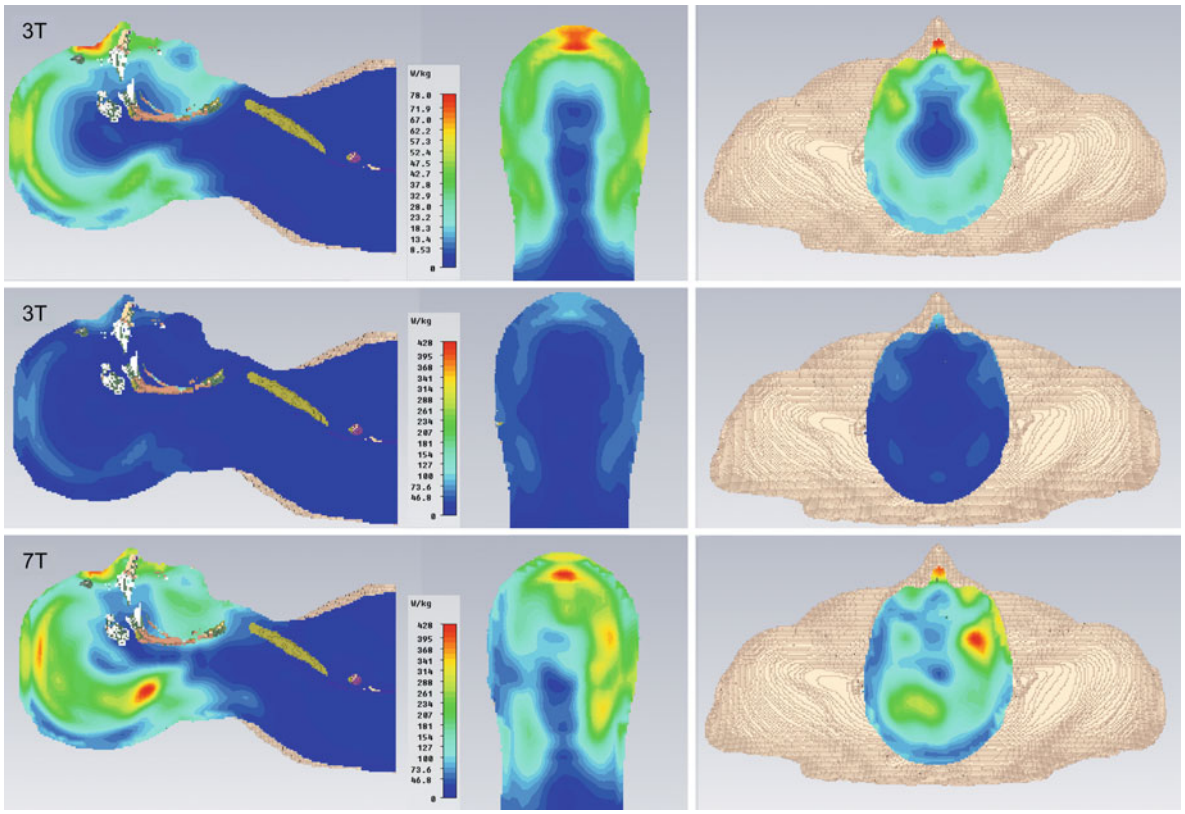

Fig. 3 The SAR distribution in the same human head at 3 (*top* and *center*) and 7 T (*bottom*) for continuous irradiation (therefore the high SAR values). The 3 T data are displayed with two different scales. In the top row, the SAR is individually scaled to demonstrate the distribution differences compared to 7 T. In the center row, the 3 T data are scaled identically to the 7 T data demonstrating the dramatic increase in power absorption. The SAR increases strongly at higher field strength, and in addition, the distribution becomes more localized showing numerous hot spots throughout the head, and the symmetry of the SAR distribution with respect to the tissue distribution is lost

In general, spin echo-based methods are more SAR-critical than gradient-echo sequences. Magnetization preparation, e.g., inversion, and spatial or spectral saturation, can be prohibited by the given SAR limitations. If a sequence exceeds SAR limits, longer TR, longer RF-pulse length, or fewer slices may allow performing the examination, albeit reducing the efficiency in terms of SNR per unit time and thus, in part, the advantage of high field.

1.3 B_1-Inhomogeneity

At low main magnetic field strength, the wavelength of the RF-field B_1 is large compared to the human body. Therefore, although B_1 varies with the Larmor frequency, it can be considered as constant in space for a given time point. This field can be treated a quasi-static. The results of this situation are relatively homogeneous B_1 amplitude and flip angles throughout the object. At higher magnetic field strength, this assumption is no longer valid and we have to consider properties of the RF-field, the tissue, and their interaction.

In this context, an important property of tissue is its relative dielectric permittivity ε_r, which describes the ability of a material to be polarized by an external electric field. The dielectric permittivity of water at low frequencies (frequencies below 2 GHz are low in this case) is very high with a value of approximately 80 depending on the exact frequency and temperature. The value of ε_r is reduced if salt is dissolved. The relative magnetic permeability μ_r is the ratio between the magnetic field in a material or tissue, and free space. Water is diamagnetic and thus μ_r is slightly smaller but very close to 1. Due to these tissue

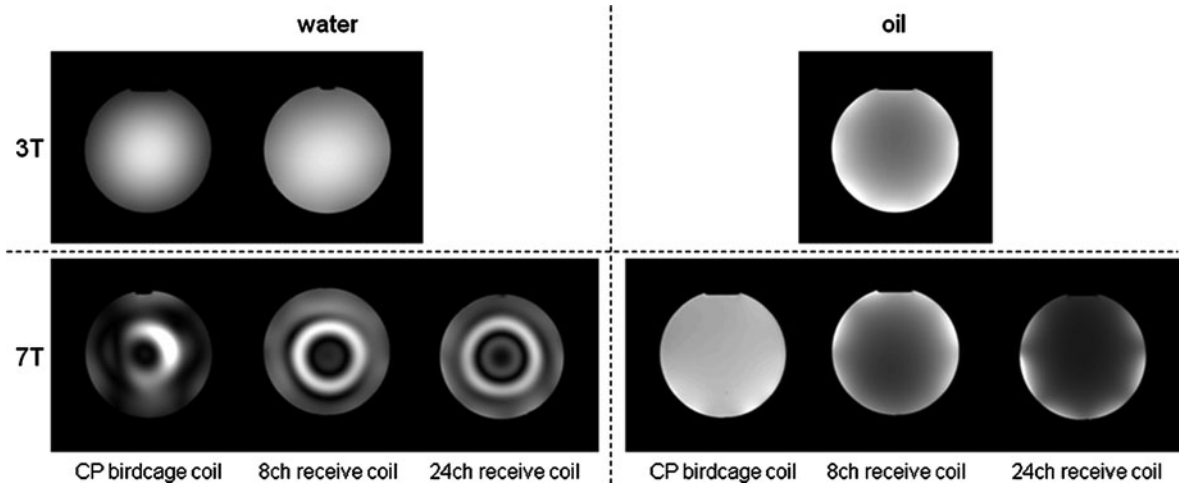

Fig. 4 Images of a spherical phantom filled with water or oil at 3 and 7 T (all images are gradient-echo images with a TR of 500 ms and a TE of 5 ms; the nominal flip angle was 60 degrees as adjusted by the scanner). Whereas water has a high permittivity of about 80, the permittivity of oil is much lower, and thus, no effects of short wave length are seen. Images have been acquired with a volume coil for transmission and reception, and with a multi-channel receive-coil array that compensates, in part, the transmission field inhomogeneity (the images are differently scaled to visualize the inhomogeneity)

properties, the RF-wavelength λ in tissue is reduced relative to the wavelength in vacuum and can be calculated as follows:

$$\lambda = \frac{2\pi c}{\omega\sqrt{\varepsilon_r \mu_r}}. \tag{5}$$

Here c is the speed of light (approximately 300,000 km/s). For 7 T, the RF-wavelength in vacuum or air is about 1 m and can become much smaller than the body extensions in human tissue with a wavelength of about 15 cm. Thus, wave effects become relevant in most parts of the body and interference patterns in the object develop. They result in spatially varying amplitude and phase of the magnetic excitation RF-field B_1. Although the absolute phase of the RF-pulses and thus the magnetization is not of high importance for most MR methods, because magnitude images are reconstructed, the amplitude is. For standard RF-pulses, the RF-amplitude is directly proportional to the local flip angle that thereby becomes spatially variable. This results in spatial variation of the excited magnetization and thus the MR signal. Due to the so-called principle of reciprocity, the coil sensitivity for signal reception has the same spatial distribution as the RF-field generated by the coil. Therefore, the resulting image intensity distribution is determined by the sequence sensitivity to flip angle variations (transmit field inhomogeneity) and the receive-coil sensitivity distribution. If the same coil is used for transmission and reception, the effects are enhanced. If the excitation flip angle distribution and the receive sensitivity of two different coils used for transmission and detection compensate, a higher uniformity can be achieved. This effect can be observed in Fig. 4. At 3 T, the excitation flip angle in the water phantom is somewhat inhomogeneous with higher flip angles in the object center. This effect is amplified if the same coil is used for signal reception because the coil sensitivity is higher in the object center. If a surface coil array is used, the receive-coil sensitivity is higher in the periphery of the object as can be seen from the 3 T oil image and partly compensates the inhomogeneity in the water phantom. At 7 T, the oil phantom is still excited with homogeneous flip angle distribution, and the signal in the oil phantom is mainly determined by the receive-coil sensitivity. With more and smaller receive coils, the signal in the periphery is enhanced. However, the short RF-wavelength in the water phantom at 7 T leads to very significant flip angle variations throughout this phantom. Even with receive-coil arrays, the signal variations across this 17-cm object are pronounced.

The signal intensity distribution does not only depend on the RF-field inhomogeneity and the receive-coil sensitivity, but also on the sequence used and the flip angles applied. For most sequences, the

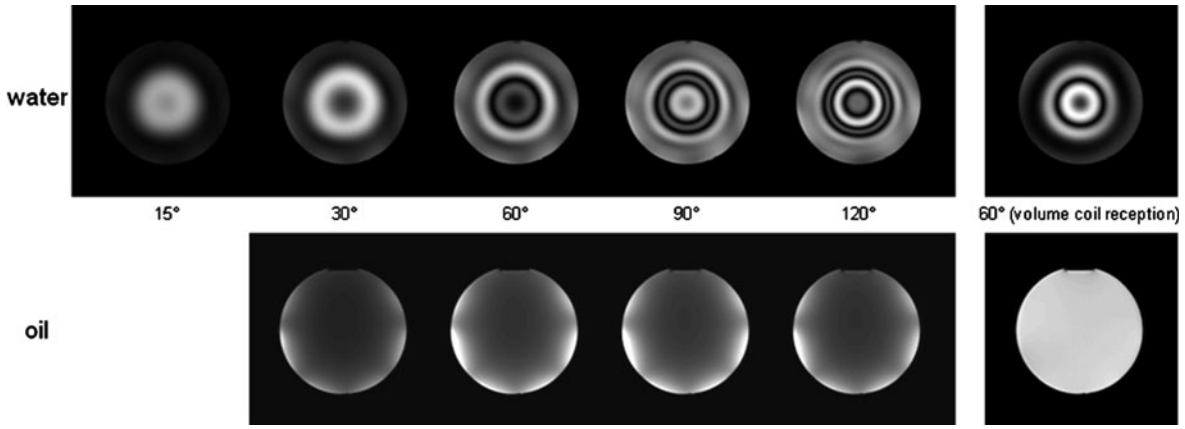

Fig. 5 The flip-angle distribution and homogeneity at 7 T depend strongly on the RF-amplitude and object properties (gradient-echo images with TR of 500 ms and TE of 4 ms are displayed with different nominal excitation flip angles). The images have been acquired with a CP excitation and a 24-channel receive coil. Only the two images on the right were acquired with the CP coil used for excitation and reception. Again, for oil, the excitation is homogeneous. The signal intensity for this gradient-echo acquisition is given by the sine of the excitation flip angle, and the intensity distribution is given by the receive-coil sensitivity. In water, the signal distribution strongly varies with the nominal excitation flip angle due to the sine relation. The strong enhancement of the periphery with the array coil reception relative to the volume coil reception is also obvious in this case

signal intensity is a complex function of the RF flip angle. For a simple gradient echo, the signal depends on the sine of the excitation flip angle. Correspondingly, the intensity distribution can change dramatically with different settings of the nominal flip angle (see Fig. 5).

The effect of signal intensity inhomogeneity may be distracting but is not much different from the experience with local receiver coils at lower field strength. These intensity variations lead to local differences in the SNR. The full benefit of the increased SNR at high field is only realized in the brightest regions. In addition to the image intensity effects caused by inhomogeneous flip angle distributions across the object, a second more troublesome effect has to be considered. The contrast of most MR sequences depends on the flip angle, and thus, locally different image contrast can be generated due to the varying RF-pulse flip angles across the object (Fig. 6).

One remedy for the B_1-dependent local contrast variations is the contrast generation by means of so-called adiabatic pulses that exhibit low or no dependence of the flip angle on the B_1 amplitude. Alternatively, methods with low sensitivity of the contrast on the flip angle can be applied (see subsection on sequences). Besides these classical sequence-related solutions for the challenge of inhomogeneous

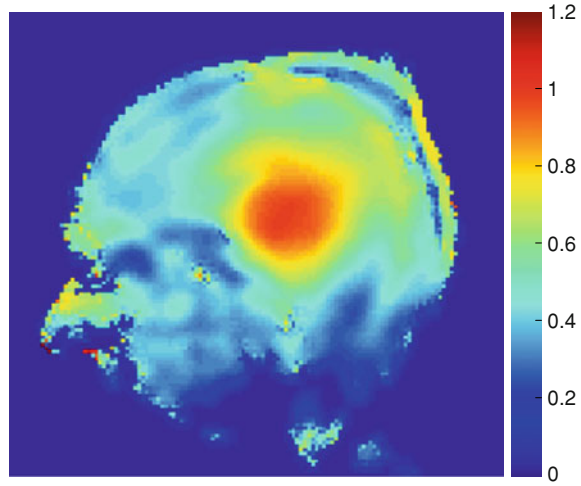

Fig. 6 B_1 field measured in a human head at 7 T. The flip angle is given relative to the nominal value. Therefore, a value of 1 corresponds to the adjusted flip angle. The B_1-field is highest in the center of the brain. In comparison to the phantom data, it becomes obvious that the flip angle distribution in the human brain at 7 T is less problematic than in a water phantom of similar size. However, significant variation of more than a factor 2 is present

RF-excitation, novel approaches have been proposed: RF-shimming (Mao et al. 2006) and parallel transmission (Katscher et al. 2003). Very first implementations of RF-shimming are available. However, these

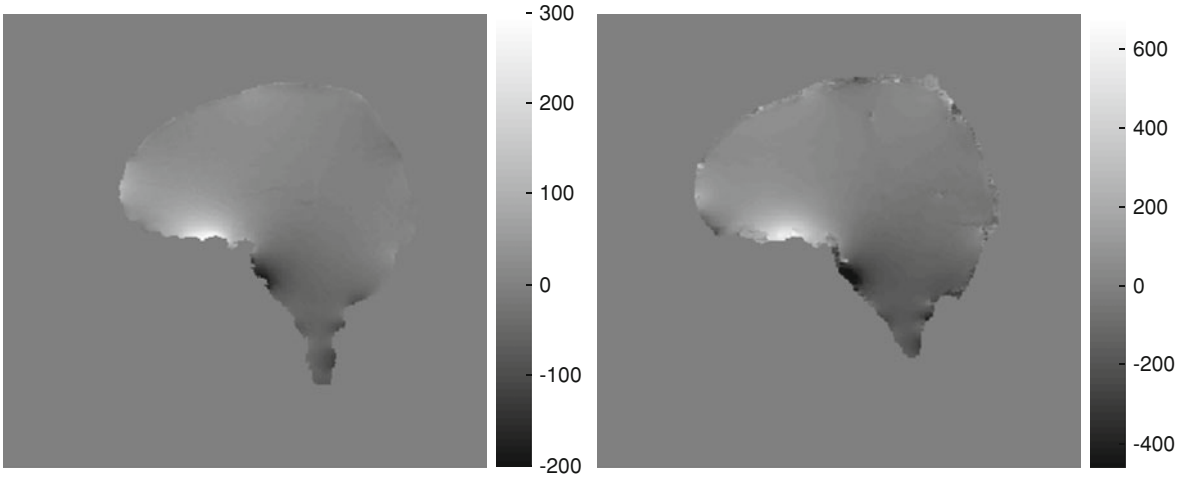

Fig. 7 Magnetic field maps of the human brain at 3 (*left*) and 7 T (*right*). Although the pattern is largely identical and caused by the head's magnetic properties, the scale (in Hz) is increased by a factor 2.3 for the 7 T data corresponding to the field strength difference

approaches are largely experimental and not widely available yet. The basic principle is related to parallel imaging. Different RF-pulses are transmitted by more than one transmission coil simultaneously either without (RF-shim) or with (parallel transmission) the application of time varying gradients.

1.4 B_0-Inhomogeneity

B_0-inhomogeneities arise from two sources: imperfections of the hardware, mainly the magnet, and object-induced variations of the magnetic field. Although the hardware imperfections are usually very well controlled by means of cryo-, iron-, or room-temperature shims, the magnetic properties of the object under study are of concern. The magnetic field variation induced by an object depends on the type and distribution of materials in the magnet (Fig. 7). The magnetic susceptibility describes the magnetization of an object exposed to an external magnetic field. The magnetization of tissue is usually not saturated even at high magnetic field strength, and thus, the susceptibility is field-strength independent. Therefore, the relative magnetic field inhomogeneity is independent from the main magnetic field strength. However, for most practical applications, the absolute field variation given in μT or Hz is relevant and this increases proportional to the field strength.

Whereas this increased shift is exploited as an advantage in spectroscopy, the larger variation of resonance frequencies has significant effects on many imaging methods. If identical gradient strength is applied, a higher spatial error occurs in all sequences that employ a readout gradient and most prominently in methods with very long readout times, such as echo-planar imaging (EPI) where the effective bandwidth in phase encoding direction is very low resulting in strong geometric distortions (see subchapter on EPI). These increased distortions at 7 T could be reduced to the level of 3 T if 2.3 times higher acquisition bandwidth was used. Although this could in principle speed up acquisition, it will also reduce part of the SNR advantage. A less considered effect is the displacement in the slice selection direction in 2D-imaging. Field inhomogeneities can lead to significant bending of the selected slice. The deformation of the slice selection plane is proportional to the (absolute) field inhomogeneity divided by the bandwidth of the RF-pulse. In order to reduce SAR, pulses are frequently prolonged resulting in even lower RF-pulse bandwidth compared to lower field strength. This further amplifies this effect and can lead to "potato-chip slice selection". Similarly, the selection plane for water and fat can be significantly shifted against each other due to the high frequency difference of approximately 1,000 Hz at 7 T (Bernstein et al. 2006).

The larger absolute local off-resonance frequencies are equivalent to larger local frequency differences over a predefined volume. Therefore, in addition to the geometric displacement in the reconstructed images, the resonance frequencies across one imaging voxel exhibit a wider spread. In non-refocused (gradient-echo based) imaging, this frequency spread leads to dephasing of the transversal magnetization during the echo time and a corresponding signal loss. The signal loss depends on the frequency variation across a voxel and thus the B_0-inhomogeneity (gradient) relative to the voxel extension. It can be reduced by a reduction of the voxel size. Depending on the range of the field inhomogeneities, these inhomogeneities lead to different effects and can also carry different information. Long-range (macroscopic) inhomogeneities are caused, e.g., by tissue interfaces such as air-tissue or bone-tissue, and lead to the distortion and signal loss described above. Smaller field disturbing structures (mesoscopic), such as, e.g., vessels, result in signal loss in T_2*-weighted sequences, but the dephasing is refocused in T_2-weighted spin echo sequences if the frequency distribution can be considered constant during the echo time and single protons do not move far enough to exhibit different frequencies. These effects are exploited in susceptibility weighted imaging (SWI). If the scale of the inhomogeneities is even smaller (microscopic), such that the diffusion length of water molecules is large compared to the scale of the inhomogeneity, signal is also reduced in refocused sequences resulting in reduced T_2 relaxation times.

1.5 Relaxation Times

The main parameters that determine the signal intensity and contrast in most MR sequences are the longitudinal and transversal relaxation times T_1 and T_2. Although T_1 and T_2 are material or tissue constants, they depend on the Larmor frequency and therefore on the magnetic field strength.

In the frequency range for MR (up to GHz), the spontaneous inversion of an isolated proton is highly unlikely. During longitudinal relaxation, the spin system exchanges energy with the surrounding. Longitudinal relaxation is thus driven by stimulated emission. Because the tissue spectral density decreases with increasing frequency, the longitudinal relaxation time generally increases with magnetic field strength. Extrapolations from earlier measurement at lower field strength led to believe that T_1 relaxation times converge for high field strength and thus T_1 contrast is difficult to achieve (Koenig et al. 1984; Fischer et al. 1990). Careful measurements of T_1 over a wide range of field strengths showed that T_1 for all brain tissue types follows a power law with an exponent of 0.34–0.38 (Rooney et al. 2007). T_1 times in tissue increase by approximately a factor 2 at 7 T compared to 1 T (Fig. 8). Therefore, contrast between tissue types can even be increased at high field, albeit the gain is less than linear. It is to be noted that the longitudinal relaxation time of CSF does not change significantly over this range of field strengths due to the low interaction in such a homogeneous liquid.

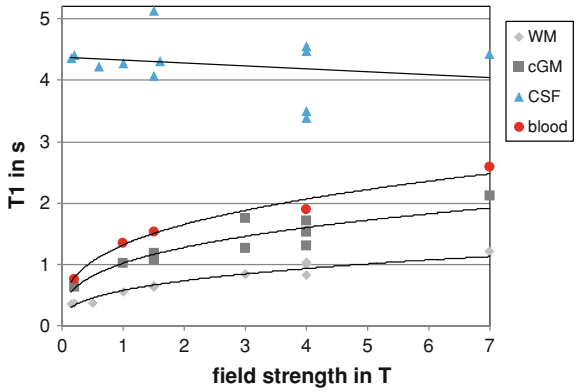

Fig. 8 The longitudinal relaxation time T_1 as a function of field strength (adapted from (Rooney et al. 2007) and references therein; data from 11 studies). T_1 is prolonged with increasing field strength for white matter (WM), cortical gray matter (cGM), cerebrospinal fluid (CSF), and blood, following a power law with exponent 0.34–0.38. Only the T_1 of CSF remains largely unchanged

A discussion of the influence of the magnetic field strength on the transversal relaxation time T_2 is more complicated. It had been predicted that T_2 does not change strongly with field strength (Fischer et al. 1990). However, T_2 as measured in any experiment does not only reflect the intrinsic transversal relaxation (mainly due to homonuclear spin–spin interactions and hyperfine interactions with paramagnetic centers), but also the effects of spin diffusion and exchange. The latter two effects depend on the type of experiment performed. If a single spin echo is formed, spins can diffuse to larger distances and have a higher probability for exchange between RF-pulses. They

can experience different effective field strengths in inhomogeneous media leading to phase accumulation that cannot be refocused in a spin echo. If multiple refocusing pulses with short spacing are used to form a spin echo at the same echo time, the spins can only accumulate smaller phase differences between RF-pulses and thus, the effective transversal relaxation time appears larger (Michaeli et al. 2002). In general, the transverse relaxation time T_2 significantly decreases with increasing magnetic field strength (Jezzard et al. 1996). However, the exact T_2 values for different tissue types and measurement techniques vary considerably between reports.

T_2* is the apparent transversal relaxation time and determines the signal and contrast in gradient echo sequences. All the effects mentioned with respect to T_2 also contribute to T_2* signal decay. In addition, longer range stationary inhomogeneities causing signal dephasing within a voxel further accelerate this decay. Because these inhomogeneities scale with the field strength (see previous subchapter), T_2* decreases even faster than T_2 with field strength. Although the quantification of T_2* is less confounded by methodological aspects compared to T_2, the experimental conditions (i.e., the location and the local shim) largely influence the results.

These changes of the relaxation times have to be considered in the sequence design and parameter selection. The increased T_1 leads to longer lasting saturation of longitudinal magnetization. Therefore, the repetition time *TR* of a sequence has to be increased in order to achieve T_1-contrast comparable to lower field strength. Even in measurements with short echo time *TE*, reduced T_2 and T_2* leads to T_2-contaminations. If T_2- or T_2*-weighting is desired, the optimum echo time depends on the transversal relaxation time. It is easy to show that the best sensitivity for the detection of local differences or temporal changes of T_2 or T_2* is obtained if the echo time equals the transversal relaxation time. In addition, the signal amplitude changes during the acquisition of a single echo or throughout the acquisition of an echo train after a single excitation due to transversal relaxation. If this acquisition time is long compared to the transverse relaxation time, considerable blurring of the resulting image is to be expected. Consequently, more time is required to re-establish longitudinal magnetization after an excitation and less time is available to read out the signal. In common MR methods, this requires a prolongation of the repetition time and a reduction of the echo time in order to achieve contrasts and artifact behavior comparable to lower field strength. Although this is reducing the efficiency of many standard imaging methods at high field, a number of methods have been adapted to these requirements or different measurement methods are being established as new standards for high field imaging.

For certain applications, these apparent disadvantages of altered relaxation times turn into an advantage. A few examples are as follows:

- Time-of-flight (TOF)-angiography: in TOF-angiography, the differentiation between vessels and static tissue is given by the flow of blood into the imaging volume. Inflowing blood carries unsaturated longitudinal magnetization and therefore contributes a higher signal than saturated stationary tissue. The information content is higher for long T_1 times because the displacement history is stored for longer time periods. Thus, the contrast between inflowing blood and static tissue can be improved at high field strength.
- Arterial spin labeling (ASL): similar to TOF-angiography, ASL exploits the use of blood as an endogenous contrast agent. The longitudinal magnetization of blood is labeled proximal to the imaging volume. After a transit time, where this magnetization enters the capillary system, the magnetization is detected. The difference of measurements with and without such proximally labeled blood allows for the determination of tissue perfusion. With longer longitudinal relaxation times, the blood label persists longer, and thus, the effect is not only larger but also more distal portions of the vascular system can be studied.
- Susceptibility weighted imaging (SWI): the visualization of magnetic properties of tissue has been termed susceptibility weighted imaging. Because the heterogeneity of the magnetic field in tissue increases with field strength, the effect on the signal magnitude and contrast (T_2*) and on the tissue phase strongly increases. Structures that contain paramagnetic substances such as deoxyhemoglobin, iron, or ferritin exhibit high negative contrast in T_2* weighted sequences at high field. This has been exploited to visualize venous structures (venography) or to increase tissue contrast (phase imaging).

- Blood oxygen level–dependent effect (BOLD): whereas SWI aims at the depiction of anatomical structures, functional imaging by means of the BOLD effect detects brain areas with altered blood oxygenation upon neuronal activation. Similarly to SWI, the BOLD effect also increases with field strength due to stronger local susceptibility effects during oxygenation changes (see Neuroscientific Applications of High-Field MRT in Humans).

In all the applications listed above, the contrast (relative signal change) increases at higher field strength due to the effects of altered relaxation times or stronger susceptibility effects. In addition, the SNR increases as described. Therefore, these applications benefit twice and the resulting contrast-to-noise ratio increases more than linearly with field strength. These applications can thus be regarded as the "high field winners" as opposed to other applications, where the SNR gain is partially reduced due to the adverse effects mentioned in this chapter.

1.6 Magnetization Transfer Effects

In many biological tissues, at least two pools of magnetization can be distinguished based on their relaxation behavior. Free bulk water in interstitial space or cytosol can move with little restriction. Therefore, microscopic field inhomogeneities and interactions with other spins average out leading to reduced dephasing and thus long transversal relaxation times T_2. Protons in macromolecules and in water bound to large molecules move much slower due to the larger size of the structure and correspondingly, the relaxation time T_2 is much shorter. In this case, T_2 is typically shorter than 1 ms, and therefore, these signals do not contribute in standard MR imaging sequences. The line width or frequency spectrum of each pool is inversely proportional to the transverse relaxation time T_2. Bulk water has a narrow line width and the macromolecule pool spreads over a larger frequency region (Fig. 9).

Only RF-excitation within the spectrum of each pool can affect the corresponding protons. An RF-pulse with a frequency a few kHz away from the bulk water resonance will saturate the bound fraction but not the bulk water. These water molecules of the bound pool are in exchange with bulk water. During this process, the protons maintain their magnetization

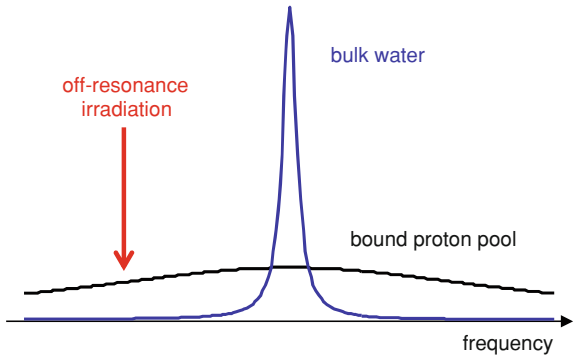

Fig. 9 The frequency distribution of bulk water and bound protons. Off-resonance RF-pulses will only excite and saturate the pool with the broad frequency spectrum. This magnetization can be exchanged with the bulk water pool by means of the magnetization transfer effect reducing the bulk water signal

state. In addition, magnetization can be transferred from one proton in the bound pool to a bulk water proton via spin–spin interaction. This transfer of magnetization or saturation from bound protons to protons in bulk water is called magnetization transfer (MT). This effect reduces the magnetization available in bulk water depending on the irradiation of the bound proton fraction by RF-pulses with frequencies away from the bulk water resonance line. The MT-effect can carry information about the amount of large molecules and their interaction with free water. It is mainly applied in the brain (where the MT-effect is stronger in white than in gray matter) and in joint imaging. In order to measure the MT-effect, two measurements with and without additional off-resonance RF-pulses are performed and divided. Areas with high MT-effect will show lower signal in the scan with additional irradiation, whereas free water will show no difference. The additional RF-irradiation commonly employs multiple high amplitude RF-pulses.

Quantification of the MT effect in tissue is commonly achieved by a comparison of two acquisitions with and without the addition of a series of off-resonance RF-pulses that saturate the bound proton pool. The relative signal decrease (MT ratio) between the two acquisitions is a measure for the presence of these large molecules and their interaction with the free water pool. MT measurements are difficult to perform at high field strength because SAR is frequently very high and additional MT-pulses are prohibited. Thus, high field is currently not the preferred ground for MT

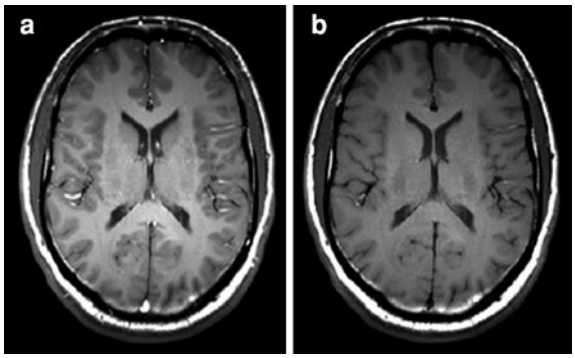

Fig. 10 T_1-weighted spin-echo image acquired at 3 T **a** as single slice and **b** multi slice acquisition. MT-effects due to the excitation of the other slices are stronger in white matter and thus reduce the otherwise high white matter signal in (**b**). As a result, the contrast in the multi slice acquisition is significantly reduced

measurements. However, another aspect of MT has to be considered. MT is present in most sequences and thus has an impact on the contrast. In multi-slice acquisitions, all RF-pulses used to interact with the magnetization of all but one slice will add to the MT-effect of this particular slice (Fig. 10). Therefore, the signal in structures that exhibit a high MT-effect will be reduced compared to single slice measurements. This effect can either increase or decrease the contrast in the image depending on the native sequence weighting. It has to be considered in the sequence design and image reading.

1.7 Acoustic Noise

The source of acoustic noise in MRI is Lorentz forces acting on the gradients when strong currents are flowing, similar to a speaker where current is flowing though a coil positioned inside a magnet. These forces lead to deformation of the gradient set and are thus audible. Because the Lorentz forces are proportional to the currents and the magnetic field strength, they increase linearly with field strength. The gradient coils and amplifiers employed at high field are similar to those used at lower field strength. Therefore, the acoustic noise also increases linearly with field strength. Compared to a 3 T system, the forces are roughly doubled at 7 T. This corresponds to a sound pressure increase of 6 dB, whereas the human ear perceives an increase between 6 and 10 dB (depending on the frequency range) as twice the noise level. Thus, 7 T MRI can be expected to be noisier compared to a 3 T system if similar hardware is employed. However, it will likely be less than twice as loud. On many high field systems, extensive noise reduction measures are introduced allowing imaging of human subjects with similar noise protection as used at 3 T.

2 Phase, Susceptibility, Exchange

The absolute phase of the MR signal or an MR image is determined by a large number of effects including hardware aspects that carry little information about the object. Therefore, the phase information is discarded in many methods and only the signal magnitude of a complex-valued image is displayed. However, a number of properties can be encoded in the image phase if proper imaging methods are applied. In order to remove the above-mentioned phase effects of no interest, most of these methods acquire at least two data sets with modification of one aspect that leads to a phase change of the signal. The phase difference between the acquisitions can be related to this encoded property. A prominent example is flow encoding in phase contrast angiography, where the phase difference between two acquisitions with different flow encoding gradients is proportional to the flow velocity within each voxel. The determination of the magnetic field strength from the phase difference of two gradient-echo images with different echo time is another example. At higher magnetic field, the frequency differences between tissues with varying magnetic susceptibility increases linearly (see subchapter on B_0). Therefore, field-related effects, such as the phase differences in field mapping, increase, whereas the flow-related phase effects do not depend on the magnetic field strength.

The detection of a net phase shift or difference requires the phase variation to be on a spatial scale that is larger than the image resolution. Only then the phase-shifted signals add coherently and form a strong signal with altered phase. If the effects that lead to a phase shift are on a smaller spatial scale, the phases of signals within one voxel will differ. The net amplitude and phase in this situation will depend on the distribution of the phase variation inside each voxel and lead to a corresponding signal reduction that is characterized by T_2^* (see subchapter on relaxation times). As mentioned already, both effects, the phase shift and the signal reduction caused by signal dephasing, increase with magnetic field strength.

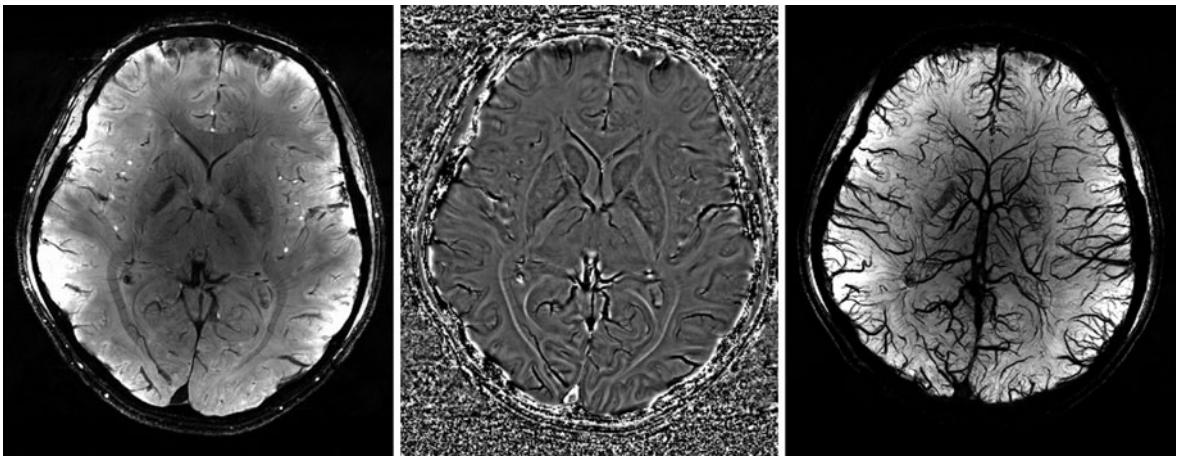

Fig. 11 Susceptibility weighted images: The T_2*-weighted magnitude image (*left*) is filtered by a mask calculated from the phase information (*middle*) in order to enhance the contrast between tissue and structures with increased microscopic field inhomogeneity. Venograms are calculated from these data as minimum intensity projections over a small volume (*right*)

Although the phase shift increases linearly, the T_2*-reduction due to signal dephasing increases linearly to quadratically with field strength depending on the motion of spins relative to the spatial scale of the field variation. A number of applications, which are based on differences in susceptibility, benefit not only from the increased SNR, but also from this strongly increased contrast. The increase in field strength leads to an immediate gain that is much stronger than linear, and therefore, susceptibility-based methods are the true winners at high field. This was first realized for BOLD-based functional MRI (fMRI), the application that drove the development of high field magnets (see chapter on Neuroscience). Other methods, such as SWI or direct phase imaging, also benefit strongly and are described in the following. In addition to the increase in the effect strength, a further advantage is the decrease of the required echo time leading to shorter scan times. In order to optimally detect changes in T_2* or the signal phase, the echo time should equal the T_2* relaxation time of the tissue.

Although for many tissue types T_2* is reduced mildly for higher field strength, T_2 and T_2* of venous blood are dramatically affected. T_2 of venous blood is over 100 ms at 1.5 T and therefore close to tissue T_2 resulting in low vessel contrast. The transversal relaxation time of blood is decreasing strongly with increasing main magnetic field strength. At 7 T, T_2 and T_2* are below 10 ms and much shorter than tissue relaxation times. This is mainly caused by the strong magnetic moment of deoxygenated hemoglobin and the fast exchange between blood plasma and erythrocytes. A strong increase in contrast between tissue and venous blood vessels is therefore observed. In addition, to the increased dephasing of signals in blood and around deoxygenated blood vessels, the signal phase is altered due to the net field difference in and around these vessels. In SWI, the information contained in T_2* and in the signal phase are combined in order to generate strong contrast between brain tissue and structures with increased microscopic susceptibility heterogeneity (Haacke et al. 2004). The phase information is used to generate an image filter to enhance the T_2*-weighted data. One main application is the visualization of venous blood vessels in so-called venography (Reichenbach et al. 1997). In order to visualize veins, projections are calculated similarly to angiographic data, which are often displayed as maximum intensity projections. Because the venous blood is of low intensity, venograms are calculated from minimum intensity projections (Fig. 11).

T_2*-weighted imaging at high field strength can identify structures such as fiber bundles in anatomical images based on their orientation-dependent relaxation times (Li et al. 2006). In SWI, the phase information is used to enhance the contrast in T_2*-weighted data. In 2007, it has been demonstrated that the phase information at 7 T alone carries information about the tissue microstructure and provides strong tissue contrast otherwise not seen in conventional imaging (Duyn et al. 2007). At high field, the phase contrast can exceed the magnitude image contrast by up to a factor

of 10, and structures become apparent that have previously not been identified by regular imaging. A strong contrast between gray and white matter is apparent in the phase data. In addition, structures within white matter can be identified that correlate with tissue microstructure such as fiber bundle density and orientation. A challenge in these phase images arises from the signal phase related to coil sensitivities and magnetic field inhomogeneities as described above. The small phase differences of interest have to be separated from these effects. The most common approach is to assign long-range phase variations to these inhomogeneities and filter the image to contain only local phase variations (Chen et al. 2010). The basis for the phase difference between these structures is topic of an ongoing debate. Proposed mechanisms include the variation of the concentration of substances with different magnetic properties (susceptibility), such as venous blood, tissue iron, or myelin. An additional source of phase (frequency) variation is the presence of macromolecules that can shift the frequency of free water protons due to fast positional exchange between free water and water associated with the macromolecules as well as due to susceptibility effect of the macromolecules (Zhong et al. 2008; He and Yablonskiy 2009; Luo et al. 2010). Although the presence of all these effects has been confirmed, their relative contributions are not yet fully understood and verified.

The acquisition parameters for high-field T_2*-weighted imaging and phase imaging are similar across many publications and laboratories. The main difference lies is the application of 2D multi-slice vs. 3D acquisitions. Although 3D acquisitions are preferred in order to result in isotropic data sets that can be reformatted to arbitrary orientations, most groups chose a 2D acquisition scheme. The intrinsic SNR advantage of 3D acquisitions is largely compensated by the significantly longer repetition time and higher flip angle in 2D multi-slice protocols. In most studies, very high in-plane resolution is preferred at the cost of larger slice thickness. Up to 200 μm in-plane resolution with 2-mm slice thickness is used. Echo times TE of 15–20 ms are common with repetition times TR of about 750 ms. Flow-compensated gradients are preferable in order to avoid flow- or pulsation-related artifacts in these otherwise very flow-sensitive acquisitions. The highest possible SNR in the high-resolution acquisitions can be achieved with a low receiver bandwidth (as low as 50 Hz/px) (Fig. 12).

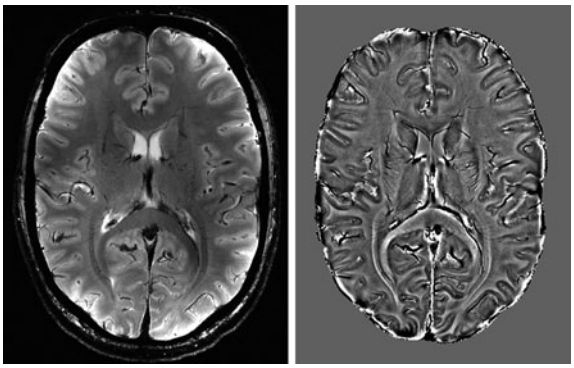

Fig. 12 Magnitude (*left*) and phase image (*right*) acquired with high-resolution gradient-echo imaging at 7 T (0.2 × 0.2 × 2 mm, TE 17 ms, TR 750 ms). Strong contrast between gray and white matter as well as within these structures is visible predominantly in the phase image. It is to be noticed that the phase data contain complementary information and not just a different representation of the magnitude information. This can, for example, be seen in the optic radiation where additional structures can be identified in the phase images

If corrected for global shim inhomogeneities (Baudrexel et al. 2009), a reduced T_2* relaxation time is frequently associated with increased iron concentration in the brain (Ordidge et al. 1994). Therefore, quantitative T_2* mapping is developing into a useful tool for imaging patients with disorders that are related to brain iron deposits such as in Parkinson disease (Martin et al. 2008) (Fig. 13).

The strongly increased sensitivity of high magnetic field MRI to microscopic distortion of the magnetic field, e.g., by iron deposits, promises improvements in the detection of small concentrations of contrast agents that are based on small iron particles [SPIO (small particles of iron oxide), USPIO (ultra-small particles of iron oxide)] (Bulte and Kraitchman 2004; Himmelreich and Dresselaers 2009).

3 How to Deal with Motion?

For some specific applications, such as cardiac MRI, TOF angiography, or MR elastography, motion is the primary target of the MRI examination, and this useful information is encoded in the MR signal. However, for very most MR measurements, subject motion is the arch-enemy causing image artifacts in anatomical imaging or signal fluctuations and reduced sensitivity in fMRI. Especially at very high magnetic field strength where the increased SNR allows for high

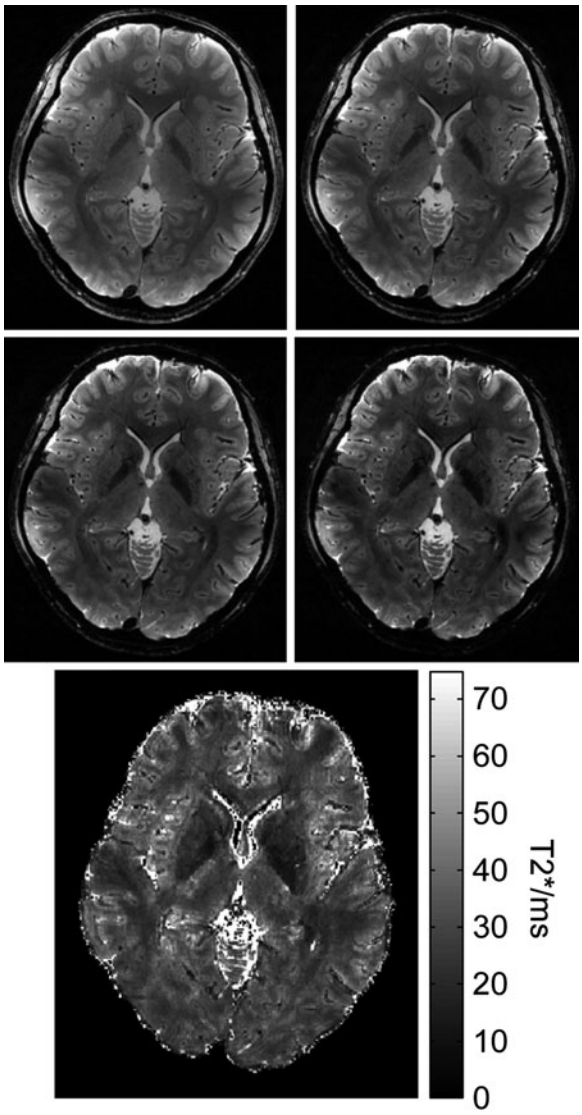

Fig. 13 T_2* can be quantified from multi-echo gradient-echo acquisitions. In these 2D acquisitions with echo times of 8, 13, 18, and 23 ms (*top row*), the shim-related signal loss is dominated by through-slice dephasing (resolution 0.8 × 0.8 × 1.5 mm). Correction for linear inhomogeneities in slice direction results in largely shim-independent T_2*-quantification. In this healthy subject, the higher iron content in the putamen with lower T_2* values is evident

spatial resolution, even small subject motion can degrade image quality. The sensitivity of different MR imaging methods against motion varies significantly. The obvious effect originates from the physical displacement of the object during the acquisition time. This can be compared to the shutter time of a photographic picture. If during the exposure time the positional displacement is significant relative to the voxel size, image blurring can be observed. In MR imaging, data are not directly acquired in image space but in spatial frequencies (k-space). Thus, in addition to the amount of motion during the acquisition time, the timing becomes relevant. Motion during the acquisition of the center of k-space results in more pronounced artifacts compared to motion during the acquisition of outer k-space. A further aspect in MR imaging is the accrual of signal phase between the excitation of transverse magnetization and the readout. If motion occurs along the direction of an imaging gradient, the signal phase is altered. Thus, even for small amounts of displacement, varying motion between k-space lines can cause significant artifacts (e.g., pulsating vessels). The motion sensitivity of MR sequences thus does not only depend on the acquisition duration but also on the sequence type. The latter effect of phase errors is not particularly field strength–dependent because the type and amount of subject motion can be expected to be independent of the main magnetic field strength, and the encoding gradients are limited mainly by peripheral nerve stimulation and also similar across field strengths. However, whereas for clinical field strength, frequently, the SNR is limiting the acquisition of high-resolution data, at very high field strength, high resolution can be achieved in tolerable scan times. Therefore, the requirements for the patient to remain motionless are higher. It has been shown that as a rule of thumb for artifact-free images, the object has to maintain position with an accuracy 10 times higher than the resolution (Maclaren et al. 2010). Even for a highly motivated and cooperative subject, it is certainly very difficult to remain within 20 μm throughout a scan of several minutes' duration for 200 μm resolution. Therefore, motion correction becomes of high importance for high-resolution structural imaging at high field, i.e., if potentially less cooperative patients are to be examined.

Three categories of motion correction strategies can be distinguished as follows:

1. Fast imaging to "freeze" the motion is efficient but limited in its applications for high-resolution imaging. The most prominent example of fast imaging is EPI (Mansfield and Maudsley 1977). It is very fast and virtually free from motion artifacts. However, only limited resolution can be achieved.

2. Retrospective motion correction is based on either data self-consistency or on motion information detected by MRI methods (navigator techniques) or external sensors (Friston et al. 1995; Thesen et al. 2000; Kim et al. 1999; Welch et al. 2002a, b; Atkinson et al. 1999). These methods try to reverse the aversive effects of motion on the raw data during the reconstruction process using either known or estimated motion information.
3. Prospective methods also use information about the object pose. However, these methods adapt the measurement method itself during the scan, such that the acquisition volume follows the object motion (Zaitsev et al. 2006; Derbyshire et al. 1998).

In order to acquire high-resolution data with large volume coverage and sufficient SNR, even fast imaging methods such as FLASH, TrueFisp, or TSE require several minutes of scan time. With a fast repetition time of only 4 ms, a 3D acquisition with a moderate matrix size of 512 × 256 × 256 takes about 4 min and 22 s. If other than low flip angles are used, this is likely to be longer due to SAR limitations. The amount of acceleration, e.g., by means of parallel imaging is limited due to the corresponding SNR loss. It thus becomes obvious that motion sensitivity can hardly be avoided in very high-resolution imaging.

If scan time is long and motion during the acquisition cannot be avoided, retrospective correction of the raw data by appropriate steps in the image reconstruction can reduce image artifacts. It is commonly exploited that rotation of a rigid body leads to a corresponding rotation of the data in k-space and that translation in image space corresponds to a linear phase evolution in the raw data. A number of methods have been proposed to correct for such motion-related modulations of the raw data. All these methods require the interpolation of raw data onto different grid points, a process that can be numerically expensive and may lead to data quality losses. The main difference between the various methods is the technique that is used to determine the object motion. One group of methods is using additionally acquired signals, so-called navigators, in order to determine the object position for each acquisition step (Welch et al. 2002a, b; Ehman and Felmlee 1989). This adds to the scan time and cannot be generalized to arbitrary sequences. A second group of methods uses repeated and thus redundant acquisition of the k-space center to estimate and correct motion during the reconstruction. These self-navigated sequences commonly correct for 2D in-plane motion, although 3D variants have been proposed. Projection acquisition methods repeatedly traverse k-space in different directions, crossing the center with each acquisition (Glover and Noll 1993), segmented spiral acquisitions (Glover and Lee 1995; Liu et al. 2004) start at the k-space center and move outward in a spiral trajectory. The center portion can be acquired with higher density, resulting in repeated acquisition of this portion. Periodically rotated overlapping parallel lines (PROPELLER) (Pipe 1999) is a sequence that acquires blocks of k-space, that rotate about the k-space center. Again, this results in repeated overlapping measurements of the center portion. From the redundantly sampled center part of k-space, motion information can be estimated. This is subsequently used to correct the corresponding segment of the raw data, which are subsequently combined.

Prospective motion correction methods offer intrinsic advantages over the other approaches. However, certain limitations remain. If motion information is determined by means of MR navigator signals (Ehman and Felmlee 1989) or active markers (small local RF-coils attached to the object (Ooi et al. 2009; Dumoulin et al. 1993), sufficient time in the measurement sequence has to be available to accommodate the acquisition and minimize the effects on the spin system steady state. Alternatively, external motion sensors, e.g., optical devices can be applied to measure object motion during the acquisition without interference with the magnetization. Whereas MR-based methods naturally deliver motion information in the coordinate system of the gradient set, external sensors have to be accurately cross-calibrated to allow coordinate transformation from the motion detection system into the MR scanner coordinate system.

The main advantage of prospective approaches is the reduction of spin history effects together with the fact that the desired imaging volume is fully covered throughout the scan. Especially for small imaging volumes or 2D acquisitions, retrospective methods are limited because parts of the object may leave the imaging volume or plane in case of larger motion and thus unrecoverable information loss may occur. This is avoided in prospective methods where the imaging orientation and position are updated throughout the scan by recalculation of the gradient rotation matrix and the RF-frequencies according to the object motion.

It has been shown that prospective motion correction methods can significantly improve anatomical image quality in case of subject motion at 7 T (Qin et al. 2009). Similarly, the detection sensitivity for functional activation can be increased relative to retrospective image–based correction if the volume prospectively follows the subject's head motion (Speck et al. 2006). However, these first implementations also show some limitations of prospective correction. These are frequently related to delays in the detection and application (including sequence recalculation) of motion during the scan. Therefore, a combination with retrospective approaches that correct for residual errors during the reconstruction seems attractive.

Other limitations and challenges of prospective motion correction are shared with retrospective correction methods. In general, the image quality largely depends on the accuracy of motion detection relative to the image resolution. The residual error has to be below the level of motion acceptable for this scan (about 1/10 of the resolution) (Maclaren et al. 2010). In addition, the methods are limited to the correction of translation and rotation, allowing only rigid body motion to be corrected. In case of large motion or large objects, the non-linear nature of the magnetic gradient fields can cause severe artifacts because the assumption of a rigidly moving body is invalid if the object shape changes with position or orientation. In addition, all effects that are not stationary with respect to the object coordinate system can lead to image quality degradation even if positional errors are perfectly corrected. These effects include local receiver coil sensitivities (Bammer et al. 2007) and motion-related changes in the magnetic field distribution, i.e., in case of rotation vs. the z-axis. In these cases, the imaged object changes phase and/or intensity even in the object coordinate system leading to residual artifacts that have to be accounted for if the origin is known or can be estimated.

Prospective motion correction methods offer the potential to be generally applicable to scenarios where motion can be approximated as rigid body motion. Thus, they are best suited for head imaging. Whereas clinical imaging is regularly impacted by patient motion in uncooperative subjects such as small children or elderly subjects, very high-resolution imaging even in cooperative subjects frequently shows residual motion artifacts. These high-resolution acquisitions, which are one of the driving forces behind high-field MRI, can benefit from correction for small motion during prolonged scans. In case of uncooperative patients, otherwise non-diagnostic results may be salvageable using such methods. However, commercial implementations are scarce. Most of the methods described are currently developed and applied in research studies only.

4 Turbo Spin Echo Sequences

4.1 Why Turbo Spin Echo Sequences?

The fundamental spin echo (SE) sequence has been a workhorse of MRI since the early days of MR (Hahn 1950). Among its benefits are the insensitivity to susceptibility and inhomogeneity effects, a well-defined contrast behavior such as pure T_2 contrast and the sensitivity for a broad variety of pathologic conditions, which make it an indispensable tool for clinical diagnosis. Thus, spin echo sequences are also highly valuable for high field imaging. However, one disadvantage is the considerable acquisition time necessary. For 2D imaging, the acquisition time is as follows:

$$TA_{SE-2D} = N_p \cdot TR, \tag{6}$$

where N_p is the number of (measured) phase encoding steps and TR the repetition time. N_p is equal to the matrix size in the phase encoding direction if no acceleration method is used.

Particularly for T_2 weighted images with diagnostically suitable resolution, TA can become prohibitively long. An example: At 7 T field strength, T_1 relaxation times are considerably longer than at 1.5 T. For "pure" T_2 weighted images, i.e. images acquired with negligible T_1 weighting, a TR of 7000 ms is used. Such a spin echo sequence would already necessitate 25 min to acquire a moderate matrix size of 256×214. Hence, a vital point was to reduce these very long acquisition times whilst maintaining the benefits of spin echo sequences originally suggested by Hahn.

4.2 Standard Turbo Spin Echo Sequences

The repetition time TR of T_2 weighted spin echo sequences is dominated by the magnitude of T_1 to

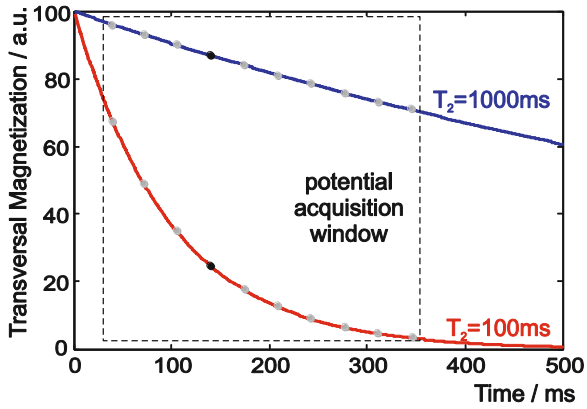

Fig. 14 Sampling of transversal magnetization in a TSE sequence during the potential acquisition window, which is directly related to the tissue specific T_2. After initial excitation at $t = 0$, transversal magnetization is created, which then decays exponentially with the transversal relaxation time T_2. Besides "the echo" defined by the user via the protocol TE (*black dot*), a TSE sequence measures additional (*spin*) echoes before and after this echo time as long as signal is present (*gray dots*)

avoid significant T_1 weighting, which directly sets limits to the minimal acquisition time TA (Eq. 6). A neat solution to this problem is the widely known turbo spin echo (TSE) or fast spin echo (FSE) sequence.

TSE sequences exploit the fact that transversal magnetization after excitation is present for a much longer time than needed for the measurement of a single spin echo. Figure 14 illustrates this observation in terms of a signal decay curve with a *potential acquisition window* (dashed box). The basic acquisition concept of TSE sequences, i.e. acquiring multiple echoes after one excitation, is therefore equivalent to other basic types of multi echo sequences such as EPI.

Figure 15 displays the general sequence diagram of a 2D-TSE imaging sequence, which was originally suggested as the *rapid acquisition with relaxation enhancement* (RARE) sequence by Hennig et al. (1986). It is based on the conditions of a Carr–Purcell–Meiboom–Gill (CPMG) sequence (Carr and Purcell 1954; Meiboom and Gill 1958). These fundamental *CPMG conditions* "guarantee" optimal signal intensity and signal response in multi spin echo sequences (Fig. 15): (1) A sequence timing with constant echo spacing ESP and a time distance of ESP/2 between the excitation pulse and the first refocusing pulse. (2) Identical gradient areas in each refocusing interval on each axis, half of the gradient area in the first refocusing interval. (3) A 90° phase shift for the excitation pulse relative to all refocusing pulses.

One main aspect of the TSE sequence is the different phase encoding for each echo (Fig. 15). Remembering that each echo represents a measured line in (Cartesian) *k*-space, this acquisition mode is actually responsible for the acceleration of acquisition time.

All major manufacturers define the speedup of the TSE either by the term *echo train length* (ETL) or *turbo-factor*. The acquisition time of a TSE sequence is therefore determined by the following relation:

$$\mathrm{TA}_{\mathrm{TSE-2D}} = \frac{N_\mathrm{p} \cdot \mathrm{TR}}{\mathrm{ETL}}. \tag{7}$$

The extreme cases are ETL = 1 (SE) and ETL = N_p. The latter means that all phase encoding steps are measured after a single excitation (*single-shot sequence*). Single-shot TSE imaging is often combined with a Half-Fourier reconstruction scheme (Feinberg et al. 1986) to form a *Half Fourier Acquired Single-Shot Turbo Spin Echo* (HASTE) sequence (Kiefer et al. 1994; Patel et al. 1997).

The primary advantage of TSE is the reduced scan time compared to spin echo sequences, particularly T_2 weighted imaging with long TR becomes economical. TSE based acquisition schemes belong to the most common sequences used for MR imaging today. In the following, further TSE basics are discussed with noteworthy differences for high field TSE imaging.

4.2.1 Basic Properties and Important Parameters

Echo Train Length

ETL directly determines the scan time reduction factor in Eq. 7. If time is the only concern, a single-shot TSE should be favorable compared to a TSE with lower ETL. However, the maximal ETL is restricted by the potential acquisition window as defined in Fig. 14. Its boundaries are given by the beginning and "end" of transversal magnetization decay. Thus, the maximal time available for sampling is directly related to T_2. The echo train duration (ETD) is

$$\mathrm{ETD} = \mathrm{ETL} \cdot \mathrm{ESP}. \tag{8}$$

As a rule of thumb, ETD should not exceed approximately twice the relaxation time T_2. Since T_2

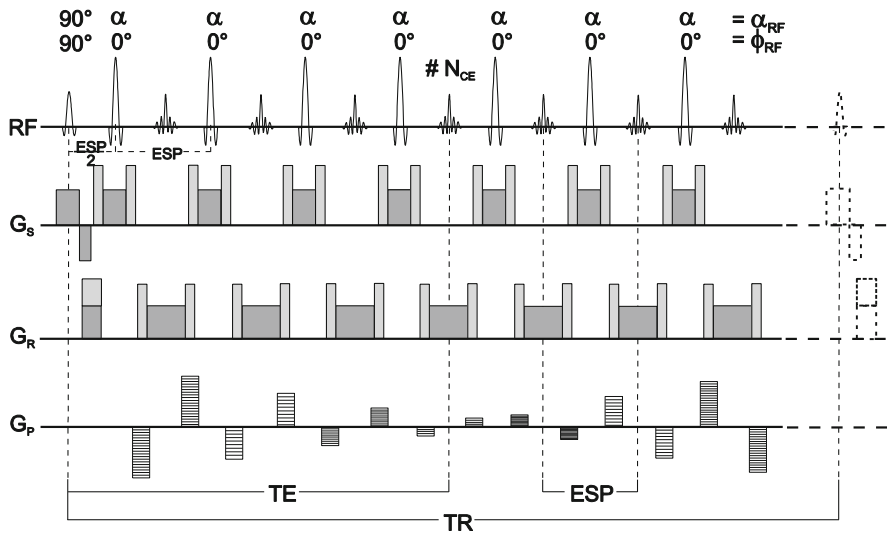

Fig. 15 Diagram of a typical 2D-TSE sequence. All imaging gradients (*dark gray*) and crusher gradients (*light gray*) are in accordance with the CPMG conditions. For the original standard TSE $\alpha = 180°$

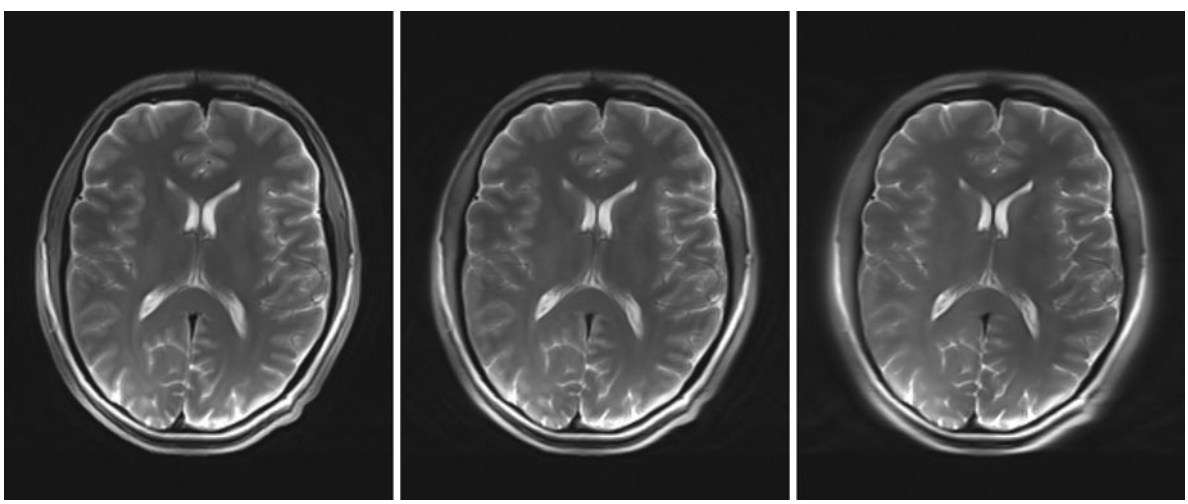

Fig. 16 Tissue dependent T_2 blurring along the phase encoding direction in TSE imaging at 7 T. Increased blurring can be observed for longer ETL from left (ETL = 13) via the center (ETL = 26) to the right (ETL = 52) image. Whilst the cerebral and fatty tissues show a considerable blurring, the CSF in the ventricles does not due to different T_2 magnitudes

is tissue-specific, the upper limit of ETD, and thus ETL, is usually set by the lowest T_2 present in the image (see also Fig. 14).

The Fourier transformation used for image reconstruction presumes that all echoes have the same intensity. This assumption is violated due to the T_2 decay of successive echoes, which results in a broadening of the point spread function (PSF). Since T_2 is tissue-specific, a tissue-specific signal blurring along the phase encoding direction in the reconstructed image occurs.

The general decrease of T_2 relaxation times at high fields shortens the T_2 dependent potential acquisition window for TSE imaging and, therefore, intensifies this blurring effect. Figure 16 demonstrates this effect in practice at 7 T.

Two additional — more indirect — effects also restrict the maximal ETL. First, ETD defines the time needed to measure one slice per excitation. Since all slices are measured successively within the same TR in multi-slice acquisition mode, the maximal ETL is reached if ETD times the given number of slices

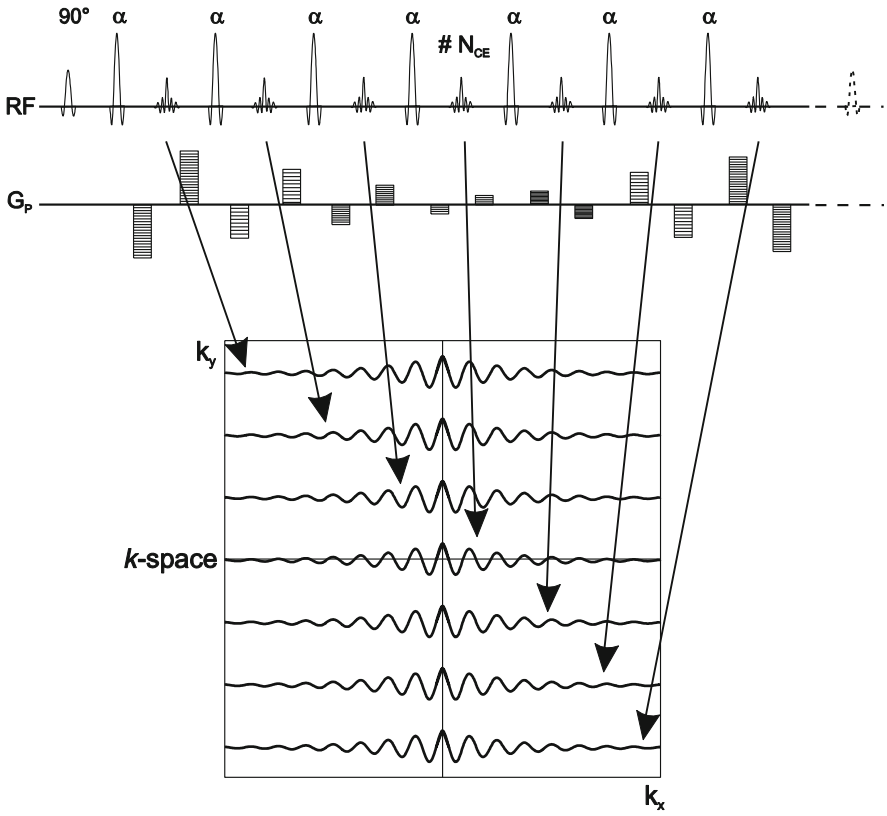

Fig. 17 Example for a linear phase encoding scheme for TSE imaging. Here, the fourth echo resides in central k-space and is denoted with N_{CE} (center echo). It determines the resulting image contrast

exceeds TR. Similarly, the number of slices is limited for given ETD and TR. Secondly, SAR often sets stricter upper limits to ETL and the number of slices, particularly at high fields. SAR limitation and remedies are of major importance for TSE imaging, and will be discussed in the following paragraphs in further detail.

View Ordering and the Definition of TE

A spin echo sequence acquires all echoes at identical echo times $TE_{protocol}$, hence, produces images with a T_2 weighting corresponding to $TE_{protocol}$. A TSE sequence generates ETL echoes with different echo times $TE_N = N*ESP$ in one echo train, N being the echo index 1…ETL (see also Fig. 15). These echoes with non-uniform T_2 weighting contribute to the same *k*-space. Besides introducing signal blurring effects as described above, the assembly of the acquired echoes in *k*-space is one of the key aspects in TSE imaging, since it directly defines the effective T_2 weighting of the reconstructed image. Generally, the sorting scheme is called *view ordering*, *reordering or phase encoding scheme* (Melki et al. 1991; Mulkern et al. 1990, 1991).

A basic property of Fourier based *k*-space is that image contrast is predominantly determined by its low spatial frequency components. Therefore the definition: *The TE of a TSE sequence is defined as the TE_N when the central k-space line is acquired*. This corresponds to the echo that obtains the smallest phase-encoding gradient area in a TSE train. It is frequently called the center echo and its contrast will mainly define the TSE image contrast (Constable et al. 1992; Mulkern et al. 1991).

Figure 17 clarifies view ordering for TSE imaging. A reordering of the echoes will change the resulting center echo and, thus, alter image contrast (Constable et al. 1992; Melki et al. 1991; Mulkern et al. 1990, 1991). In practice, the scanner software usually chooses the appropriate phase encoding scheme to realize the desired TE selected by the operator.

Generally, the first echo in the echo train has a minor T_2 weighting and is, hence, used as the center echo for the acquisition of proton density weighted or T_1 weighted images. The intermediate echoes and late echoes are employed as center echoes for images of different strength of T_2 weighting. Figure 18

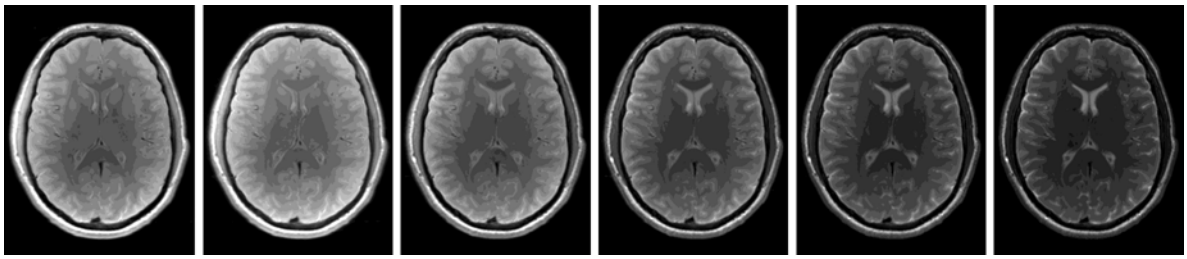

Fig. 18 Generation of different T_2 contrasts due to different phase encoding schemes in standard TSE imaging at 3 T. The six examples from left to right have TEs of 10, 20, 40, 60, 80 and 100 ms. Thus, TSE images with a corresponding T_2 weighting result. TR is 5000 ms. The images were acquired in single-slice acquisition mode. For multi-slice imaging, the perceived T_2 contrasts tend to increase due to additional MT effects

demonstrates the effect of different view ordering schemes on image contrast in practice.

For high field imaging, the fundamental concept of reordering does not require any modifications or adaptations. However, the considerably reduced T_2 relaxation times lead to pronounced T_2 contrasts even at echo times that were considered to produce low T_2 weightings at common field strengths of 1.5 or 3 T. Figure 19 illustrates this salient field strength effect for TSE imaging.

Dynamical susceptibility effects contribute to the decrease of apparent T_2 observed (Carr and Purcell 1954; Hahn 1950; Ordidge et al. 1994). These diffusion-dependent signal attenuations occur in regions with strong susceptibilities, e.g. high iron depositions in the putamen, and are denoted as $T_2^{\dagger}$ -effects. Due to the repeated refocusing of magnetization, TSE sequences are inherently less susceptible to $T_2^{\dagger}$-effects than spin echo sequences (Carr and Purcell 1954; Hahn 1950; Ordidge et al. 1994). However, since susceptibility effects considerably increase towards ultra high fields, these dynamical susceptibility effects also increase and are partially responsible for the strong and concise T_2 contrast perceived in 7 T TSE images as shown in Fig. 19, for instance.

Common Imaging Properties and Artifacts

Generally, TSE sequences produce contrast-equivalent images to spin echo sequences, at least for refocusing flip angles of 180°. Thus, the signal intensity weighting I for a tissue with given PD, T_1, and T_2 in a standard TSE sequence with 180° refocusing pulses can be quantified identically to a spin echo sequence as:

$$I_{\mathrm{TSE}180^\circ} \propto \mathrm{PD} \cdot \exp\left(-\frac{\mathrm{TE}}{T_2}\right) \cdot \left(1 - \exp\left(-\frac{\mathrm{TR}}{T_1}\right)\right), \tag{9}$$

given the approximation that ETD is short compared to TR.

Equation 9 underlines the observation that, basically, TSE sequences are capable to generate all three contrasts PD, T_1, T_2 similar to the spin echo sequence. In practice, longer echo trains introduce a noticeable T_2 weighting in the image, which reduces the quality for T_1 weighted imaging in particular. Additional MT effects due to multi-slice imaging further decrease the quality of T_1 weighted TSE images especially at high fields (Speck 2005), hence, TSE sequences are frequently used for T_2 weighted imaging only.

TSE images are well-known for their *bright lipid* or *bright fat phenomenon*, the effect intensifying with strong T_2 weightings. It is caused by a modification of the spin-spin interaction (J-coupling) in lipid tissues (Henkelman et al. 1992; Melki et al. 1992; Williamson et al. 1996). J-coupling itself does not depend on the field strength; however, the more intense T_2 contrast may also enhance the visual effect of "bright fat".

B_1 inhomogeneities cause an alteration of the excitation and refocusing flip angle in TSE images. Generally, this leads to signal variations and contrast changes within the images in the same way as for other MRI sequences. A close look at Fig. 19 also reveals B_1 inhomogeneities that intensify towards higher field strengths. But, the resulting signal and contrast variations may be lower than expected for TSE images compared to other sequences, because stimulated echo contributions to the measured signal will partially compensate for the lower (refocusing)

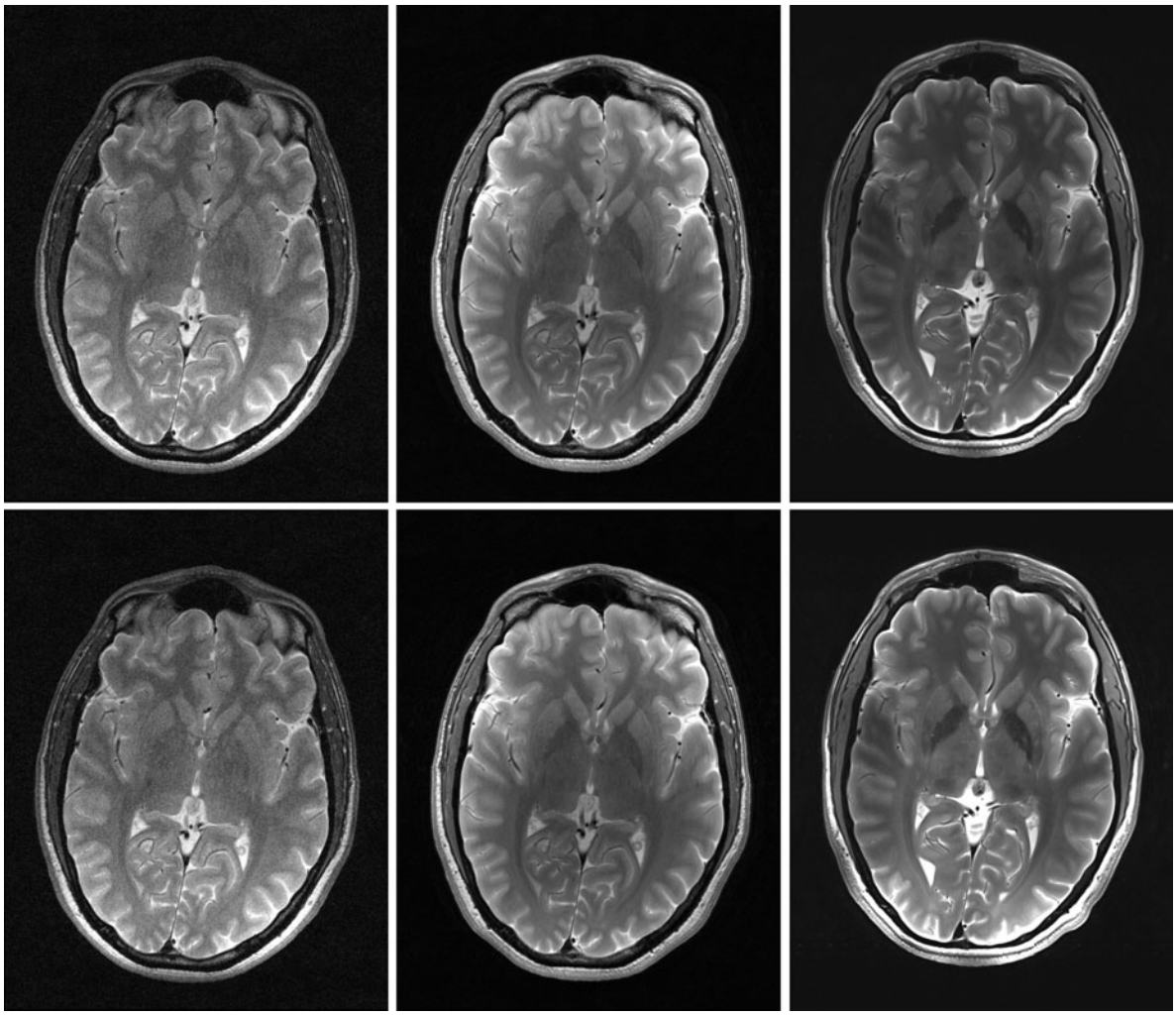

Fig. 19 Effect of different field strengths in T_2 weighted high resolution TSE imaging demonstrated for 1.5 (*left*), 3 (*center*) and 7 T (*right*). Identical TSE protocols with similar slice location and orientation were acquired in the human head on the same volunteer: TE = 58 ms, TR = 7000 ms, $\alpha_{const} = 180°$, voxel size = $0.46 \times 0.46 \times 2.5$ mm^3. The different T_2 contrasts due to the decrease of (apparent) T_2 relaxation times with increasing field strength are salient. For the upper row software chose the "optimal" window-leveling for each image individually, whereas in the lower row an identical window-leveling was applied for better direct visual comparison

flip angles. This effect of low flip angle refocusing will be discussed in further detail below.

Specific Absorption Rate

The repeated use of refocusing RF pulses in TSE sequences represents a challenge especially at high fields, thus SAR mitigation is both a serious and major issue. Besides general concepts such as modified RF pulses, larger TR and less slices, SAR relevant parameters for TSE sequences are ETL and, particularly, the flip angle α:

$$SAR_{TSE} \propto ETL \cdot \alpha^2. \quad (10)$$

Reducing ETL would reduce the speed of TSE, if no additional *k*-space concepts such as partially parallel acquisition techniques or partial Fourier reconstruction methods are applied. Hence, the focus often lies on the reduction of the flip angle, which represents an effective means due to the quadratic behavior in Eq. 10. To be more precise, a reduction of the refocusing flip angle is considered. The SAR contribution of the excitation pulse to the total SAR is only

minor, and its reduction would result in a direct loss of signal intensity.

The implications of low refocusing flip angle imaging for signal response and image contrast are discussed in the next chapter.

4.3 Turbo Spin Echo Sequences with Low Refocusing Flip Angles

For imaging purposes at high fields, lower than 180° refocusing pulses (standard TSE) are applied frequently due to SAR limitations. The possibility to lower the refocusing flip angle in TSE and therefore efficiently reduce SAR has been the focus of many studies (Busse 2004; Hennig 1988, 1991; Hennig and Scheffler 2001; Hennig et al. 2003; Mugler et al. 2001; Weigel and Hennig 2008; Woessner 1961). For a reduction of the refocusing flip angle to 150°, SAR is lowered by 30% while the signal intensity is only marginally reduced. The diagrams in Figs. 15 and 17 already considered the possibility of a reduced (constant) flip angle. Changing the flip angle represents a great potential in saving SAR but also means a change in signal response and intensity.

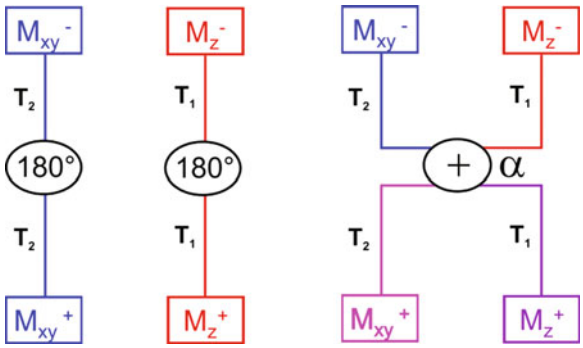

Fig. 20 Different magnetization response to refocusing flip angles of 180° (and multiples thereof, *left*) and arbitrary refocusing flip angles α (*right*). As long as the refocusing flip angles are solely α = 180°, no exchange between M_Z and M_{XY} magnetization components occurs. Transversal M_{XY} magnetization is fully refocused. But, RF pulses with α ≠ 180° mediate a mixing of M_{XY} and M_Z magnetization components. M_{XY} is only partially refocused; another part of M_{XY} is converted into M_Z magnetization. Furthermore, a part of former M_Z magnetization is converted into M_{XY}. The degree of refocusing and the way of mixing depends on the applied flip angle α. Colors underline the whole effect: "Blue" and "red" magnetization remains separated for 180° refocusing, but mixes to "shades of magenta and violet" for generic flip angles. It should be noted that M_{XY} magnetization suffers T_2 decay, whereas M_Z magnetization experiences T_1 relaxation

4.3.1 General MR Physics of Low Refocusing Flip Angles

An important aspect to understand about modern TSE sequences favored for high field imaging is the effect of low refocusing flip angles. Figure 20 presents a pictorial description of the magnetization response to different flip angles.

The scheme of Fig. 20 also defines the two fundamental ways of echo generation: (1) *spin echoes* and (2) *stimulated echoes*. It should be noted that M_{XY} is the measured transversal magnetization, i.e. it corresponds to the echoes:

(1) Transversal magnetization M_{XY}^- before the RF pulse is refocused to M_{XY}^+ after the RF pulse. This is the common spin echo. Its echo intensity depends on α, thus, the refocusing is imperfect in general.
(2) Transversal magnetization M_{XY}^- before the RF pulse is converted into longitudinal magnetization M_Z^+ after the RF pulse. Another RF pulse can convert it back to transversal magnetization M_{XY}^{++} after this second RF pulse. This "detour" via M_Z corresponds to the generation of a *stimulated echo*.

Why are stimulated echoes so important and frequently mentioned in current TSE literature? Generally, all echoes but for the first generated by a TSE are a superposition of both spin echoes and stimulated echoes. The quest for higher SAR savings represents a considerable motivation to further lower the flip angles, which increases the amount of stimulated echo contributions and decreases the fraction of refocused spin echoes. This effect has important consequences for the signal intensity and its relaxation and the resulting image contrast.

4.3.2 TSE Sequences with Low Constant Refocusing Flip Angles

Conventional TSE sequences, i.e. TSE with constant flip angles, display a signal response depending on the refocusing flip angle as depicted in Fig. 21. The echo intensity drops gradually from 100% to 0% for refocusing flip angles between 180° and 0°, however, in very different ways for TSE compared to spin echo sequences. Additional stimulated echo contributions for TSE imaging generate notably high signal

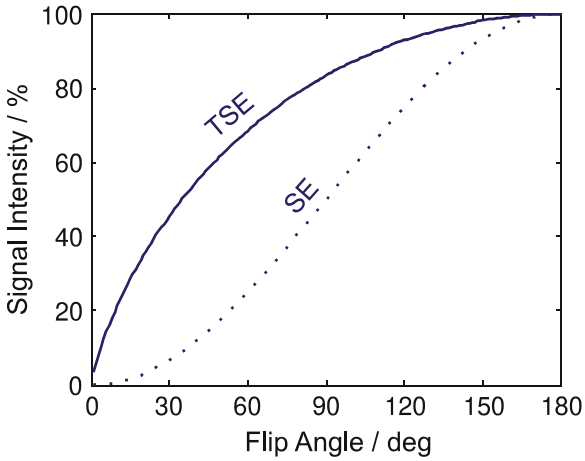

Fig. 21 Maximum signal intensity of spin echo and TSE sequences depending on the constant refocusing flip angle. A TSE with 150° flip angles, for example, provides still 97% signal intensity compared to a standard TSE. Note that the TSE signal intensity drops slowly even for pronounced flip angle reductions. The additional stimulated echo contributions, which tend to get larger for lower α, maintain high signal levels for the TSE compared to the spin echo sequence. The already non-linear response for the spin echo is caused by the non-linearity of the Bloch equation. Please note that the displayed effect is solely based on the refocusing by the RF-pulses, any relaxation effects are omitted

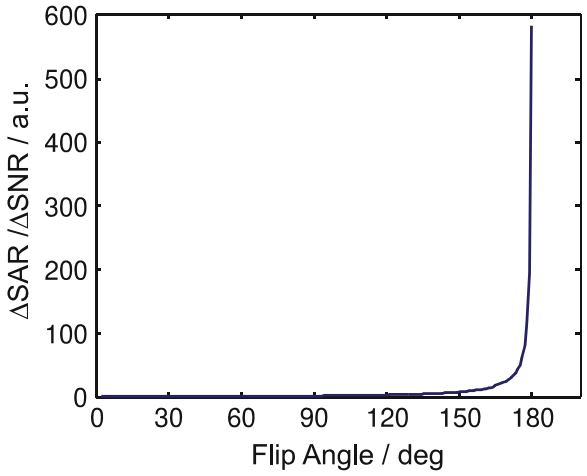

Fig. 22 Quantitation of SAR increase per SNR increase for a given constant refocusing flip angle in TSE imaging. Note the steep increase of the function above flip angles of approximately 150°, meaning that large amounts of SAR have to be invested for the residual few percents of SNR gain. Thus, one may define the upper boundary for economical TSE imaging at flip angles of about 150° from such a point of view. The lower flip angle boundary would be defined by minimal SNR requirements

intensities for low α (Alsop 1997; Hennig 1988, 1991) as compared to spin echo.

The dramatic increase of SAR for high flip angles as depicted by Eq. 10. How much additional RF-Power has to be invested to reach a certain signal increase? For conventional TSE sequences the answer is depicted in Fig. 22. A good compromise between SAR and SNR for constant refocusing flip angle TSE is reached between 130° and 150°.

Figure 23 presents a comparison of conventional TSE imaging with different flip angles at 7 T.

The above investigation is, basically, independent of the field strength applied. However, especially for ultra high field imaging it only tells half of the truth: So far, relaxation effects were not considered! Figure 20 already noted that spin echoes purely consist of transversal magnetization and are therefore purely T_2 weighted, whereas stimulated echoes derive from longitudinal magnetization components that experience T_1 weighting. Yet, for most biological tissues $T_1 \gg T_2$. Thus, magnetization decay is prolonged for all stimulated echo contributions which experience longitudinal magnetization pathways (Busse et al. 2006; Hennig 1988; Mugler et al. 2000a, b; Weigel and Hennig 2006). TSE sequences for high field imaging directly exploit this possibility, since low flip angles improve both SAR mitigation and signal level persistence for sampling. Since T_1 increases and T_2 decreases even more at ultra high fields, this advantageous effect further cultivates low flip angle TSE imaging at high fields in practice.

The significantly different relaxation rate for M_Z compared to M_{XY} magnetization in conjunction with the fact that only M_{XY} magnetization can be directly measured in MRI experiments, formed the almost obvious term to *store magnetization in the z-direction* for the conversion of M_{XY} to M_Z magnetization: A part of magnetization seems to disappear — but can be recalled with a later RF pulse.

4.3.3 TSE Sequences with Varying Refocusing Flip Angles

Nowadays, TSE with reduced constant flip angles represent the conventional and established type of TSE sequences. Particularly motivated by high field imaging, improved variants of TSE apply varying refocusing flip angles that, generally, allow for higher SAR savings and a larger flexibility in shaping echo amplitudes (Busse 2004; Lebel and Wilman 2007; Hennig et al. 2003, 2004; Weigel and Hennig 2008),

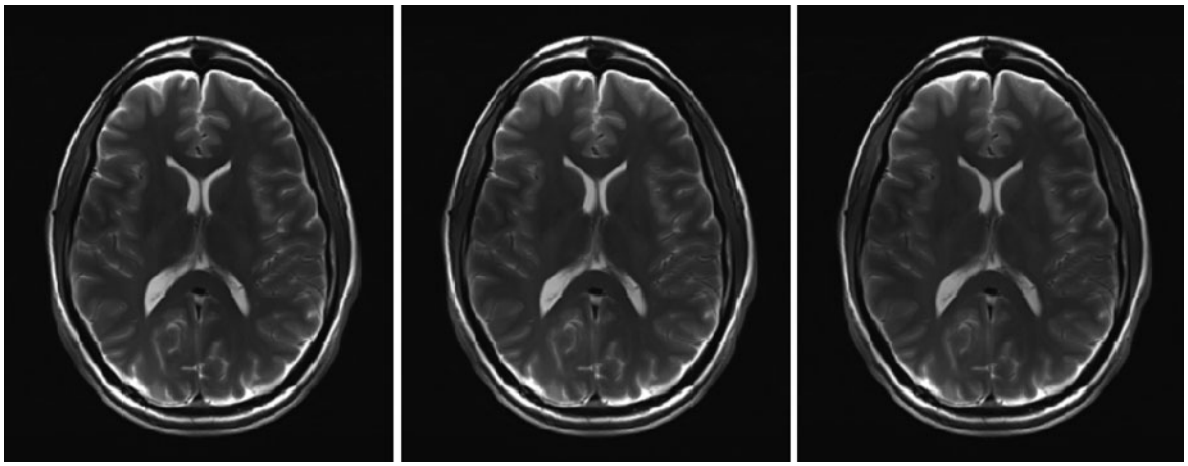

Fig. 23 Comparison of TSE images acquired with different constant refocusing flip angles 180° (*left*), 150° (*center*) and 120° (*right*). Other contrast parameters were: TR = 7200 ms, TE = 60 ms

controlling image contrast (Busse et al. 2006; Hennig et al. 2003; Weigel and Hennig 2006; Weigel et al. 2007) and prolonging the potential acquisition window without further image blurring (Busse et al. 2008; Hennig et al. 2004; Lebel and Wilman 2009; Mugler et al. 2000a, b).

The foundation for using varying flip angles is the *transition between pseudo steady states* (TRAPS) method suggested by Hennig et al. (2003). It was shown that the flip angle of the refocusing pulses can be varied freely along an RF pulse train if a few conditions are fulfilled. The most important condition is a preparation of the spin system close to the *static pseudo steady state* (SPSS) (Alsop 1997; Hennig and Scheffler 2000; Le Roux and Hinks 1993). This SPSS can be regarded as the optimal arrangement of spins for a given flip angle α, thus, leading to maximal SNR and best image quality achievable (Alsop 1997; Hennig and Scheffler 2000; Le Roux and Hinks 1993). And it also allows for flexible flip angle variations (Hennig et al. 2003). Varying the refocusing flip angle in TSE means to tune the spin system along the signal response curve shown in Fig. 21, if relaxation effects are neglected. Additional cornerstones for the TRAPS method are discussed in Refs. (Busse 2004; Lebel and Wilman 2007; Weigel and Hennig 2008) in further detail.

In the following, TSE sequences making use of varying refocusing flip angles via the TRAPS principle are generally referred to as *hyperTSE sequences* (Weigel and Hennig 2008), regardless of a 2D or 3D acquisition mode and irrespective of a possible vendor. Familiar names for types of hyperTSE sequences of different vendors include Hyperecho, FAS (flip angle sweep) and MART (modulated angle refocusing train) as established 2D implementations (Busse 2004; Gieseke et al. 2004); SPACE, VISTA and CUBE as established 3D implementations (Busse et al. 2006; Busse et al. 2008; Mugler et al. 2000a, b). These vendor-specific methods represent TSE sequences with different flip angle envelopes based on the TRAPS concept; and often include other mechanisms such as parallel imaging.

The design goals for many hyperTSE sequences are: (1) The quest for even higher SAR savings while maintaining high SNR levels. (2) Optimized TSE sampling efficiency during the potential acquisition window.

The basic idea is to apply high flip angles generating echoes with high signal intensity for central *k*-space, which will produce images with high SNR (Hennig and Scheffler 2001; Hennig et al. 2003). For sampling of peripheral *k*-space, reduced flip angles generating echoes with moderately lower signal intensity are employed. Another focus is to use very low flip angles in the beginning of the RF pulse train in order to store greater portions of magnetization in the z-direction; then to successively "recall" this magnetization with higher flip angles to the end of the RF pulse train, which helps to prolong signal decay along the echo train and, thus, sustains signal intensity for a longer time (larger acquisition window, see last section). The effective imaging properties such as PSF, SNR and contrast of hyperTSE sequences depend on

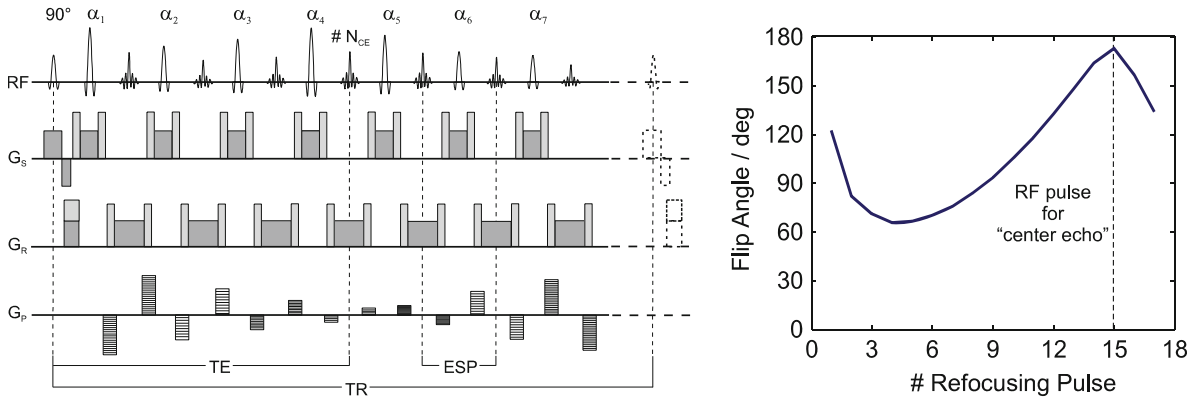

Fig. 24 *Left*: Exemplary sequence diagram for a hyperTSE sequence. A closer look quickly reveals that it only differs in one important aspect compared to conventional TSE sequences: Each refocusing pulse has an individual flip angle, which varies along the RF pulse train. The first flip angle is higher to catalyze for the mandatory SPSS conditions. *Right*: Flip angle schedule for a 2D-hyperTSE sequence with medium long ETL and a late center echo, which uses a refocusing flip angle range of $60° < \alpha < 170°$ (Weigel and Hennig 2008). High flip angles are applied around the center echo $N_{CE} = 15$ and lower flip angles for the rest. This ensures high SAR savings and maintains full SNR. With 170° the peak flip angle is still high, particularly for ultra high field imaging

the specific flip angle variation. Even resolution improvements compared to standard TSE imaging are possible, since another degree of freedom in shaping the echo intensities and therefore the PSF is available (Hennig et al. 2004). Figure 24 sketches the sequence diagram of an exemplary hyperTSE. Together with an exemplary flip angle schedule frequently employed for 2D-hyperTSE sequences with high TE, i.e. a late center echo in the echo train. Practical application of such a 2D-hyperTSE sequence for very high resolution imaging at 7 T is shown in Fig. 25.

Prolonged acquisition windows have been accomplished by "very long echo trains" or "extended echo trains", i.e. high turbo factors of 100–400 echoes, while applying flip angles as low as approximately 20°. This concept was first introduced by Mugler *et al.* for single-slab 3D-TSE imaging (Mugler et al. 2000a, b). Conventional 3D-TSE sequences tend to have prohibitively long acquisition times close to 1 h or even more due to their large TR compared to gradient echo sequences. Clinically acceptable scan times of a few minutes can be realized for full volume coverage, e.g. of the brain, exploiting the above mentioned increasing flip angle scheme. Extended echo trains have also been introduced for 2D hyperTSE applications (Lebel and Wilman 2009). Current challenges for this approach at ultra high fields are to establish reliable SPSS conditions due to B_1 inhomogeneity issues and to keep SAR at a minimum.

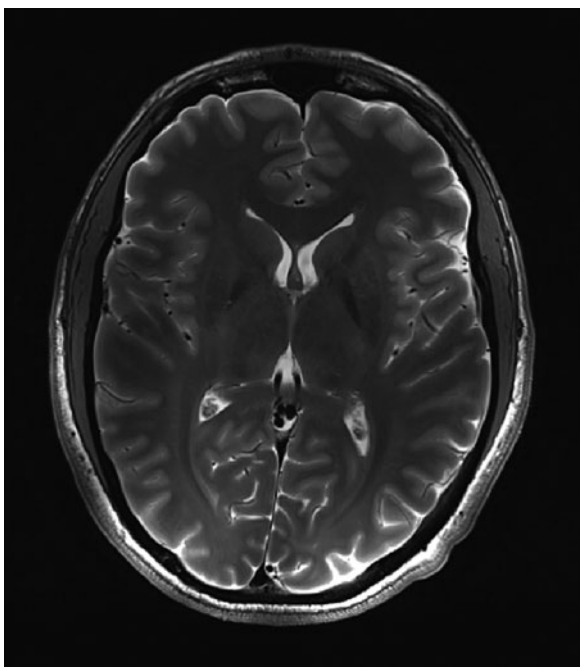

Fig. 25 Very high resolution hyperTSE imaging at 7 T. Important protocol parameters are: TR = 7000 ms, TE = 59 ms, resolution = 0.38 × 0.38 × 2.0 mm^3, TA = 4 min, 36 s

4.3.4 Characterization of Contrast

The use of low refocusing flip angles alters the signal response of TSE sequences. Contrast changes will therefore result, since different signal pathways are

the source of image contrast. To be more precise, low refocusing flip angles introduce additional T_1 weighting into the signal intensities and, hence, into the image (Hennig et al. 2003; Weigel and Hennig 2006, 2008). To avoid any confusion: This is not the same effect as caused by a finite repetition time TR, where T_1 weighting results if the condition $TR \gg T_1$ is poorly fulfilled. For arbitrary flip angles a mixing of T_1 weighted longitudinal and T_2 weighted transversal magnetization within the generated echo train itself occurs, directly following the pictorial rationale demonstrated in Fig. 20. For the same reason, the basic contrast definition of Eq. 9 is only correct for standard TSE sequences with (ideal) 180° refocusing flip angles: Eq. 9 neglects the additional T_1 contributions that depend on the flip angle(s) and TE.

The essential idea is to define a parameter ft that represents the net fraction of time [0 … 100%] during which magnetization has been present as transverse magnetization and therefore experiences T_2 decay (Hennig et al. 2003). During the residual fraction of time 100%-ft the magnetization is present in the longitudinal state and, hence, experiences T_1 weighting. Thus, the relaxation term fm can be depicted as (Hennig et al. 2003; Weigel and Hennig 2006)

$$\mathrm{fm} = \exp\left(-\frac{\mathrm{ft}(\alpha_i)\cdot \mathrm{TE}}{T_2}\right) \cdot \exp\left(-\frac{(100\% - \mathrm{ft}(\alpha_i))\cdot \mathrm{TE}}{T_1}\right). \quad (11)$$

ft arises from the mixing of magnetization and, thus, depends on the applied refocusing flip angles α_i. It also characterizes directly the T_2 contributions to the image contrast. For standard TSE ft = 100%, i.e. Eq. 11 collapses to the pure standard T_2 weighting term exp(-TE/T_2) as one would expect. Otherwise, contrast is a quantifiable mixture of T_1 and T_2 dependent on both TE and α_i (Hennig et al. 2003; Weigel and Hennig 2006; Weigel and Hennig 2008). For high flip angles close to 180°, ft will be close to 1 and, hence, image contrast will be dominated by T_2. The more α decreases, the stronger additional T_1 contributions will become.

For most biological tissues T_1 is much larger than T_2, even more so at high field. In this case, the T_1-dependent term in Eq. 11 can be neglected and the signal intensity I measured with a conventional TSE or hyperTSE is proportional to

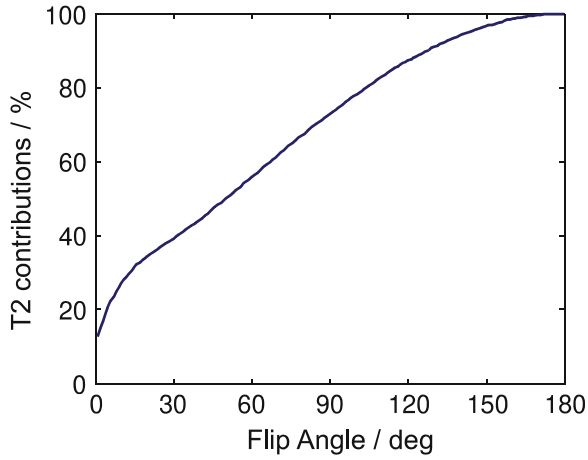

Fig. 26 Direct T_2 contributions ft in % in conventional TSE sequences in dependence of the refocusing flip angle α. TSE sequences with flip angles of 120° exhibit 87% of T_2 contrast contribution, indicating 13% contribution of T_1 contrast. Such low constant flip angle TSE sequences are often employed to mitigate SAR issues at ultra high fields. Yet, the resulting contrast changes are frequently ignored. On the contrary, sometimes these additional T_1 contributions are even perceived as "enhanced T_2 contrast at high fields'. The data was calculated from the theory published in Weigel and Hennig (2006)

$$I_{\text{generic TSE}}(\alpha_i) \propto \mathrm{PD}\cdot \exp\left(-\frac{\mathrm{ft}(\alpha_i)\cdot \mathrm{TE}}{T_2}\right) \cdot \left(1 - \exp\left(-\frac{\mathrm{TR}}{T_1}\right)\right). \quad (12)$$

Equation 12 differs from the contrast description of a standard TSE (Eq. 9) in one aspect only: ft. Although T_1 weighting was neglected, reduction of T_2 contrast results, which is depicted by ft. Thus, the T_2 contrast of a given low flip angle TSE is identical to that of a standard TSE sequence with the corrected TE

$$\mathrm{TE}_{\text{corrected}} = \mathrm{TE}_{\text{eff}} = \mathrm{ft}\cdot \mathrm{TE}_{\text{protocol}}. \quad (13)$$

$\mathrm{TE}_{\text{corrected}}$ is usually referred to as the effective TE (TE_{eff}) or contrast-equivalent TE ($\mathrm{TE}_{\text{equiv}}$) (Busse et al. 2006; Hennig et al. 2003; Weigel and Hennig 2006). Since ft < 1 for TSE with low refocusing flip angles, such sequences provide a defined but reduced T_2 contrast that corresponds to standard TSE with a reduced echo time TE_{eff} for a given $\mathrm{TE}_{\text{protocol}}$ (Hennig et al. 2003; Weigel and Hennig 2006; Weigel and Hennig 2008). To get a notion of ft, depicting the true T_2 contributions to the image, Fig. 26 demonstrates its magnitude for constant flip angle (conventional) TSE sequences.

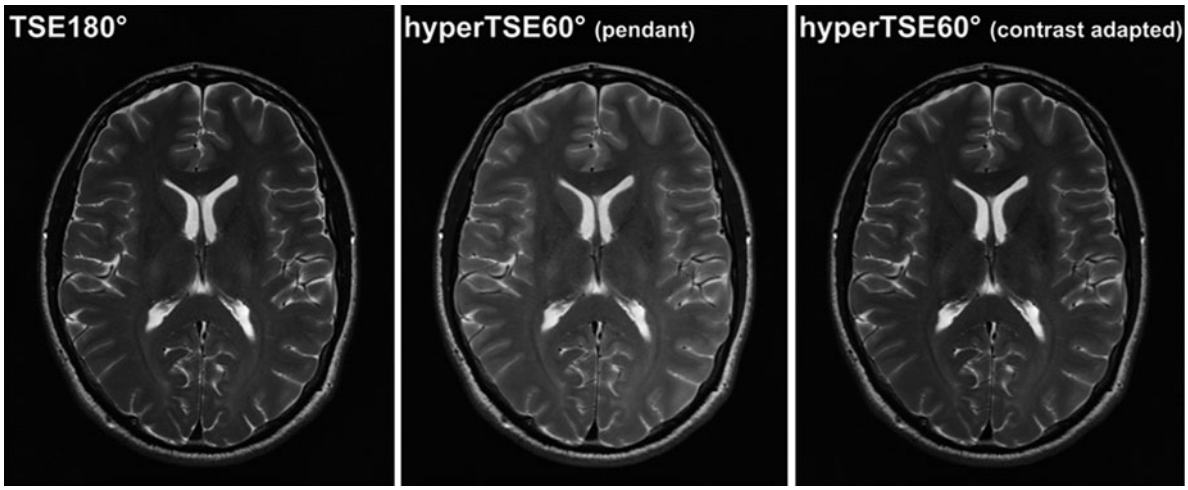

Fig. 27 Representative example at 3 T for TE_{eff} reduction and matching between a standard TSE and a hyperTSE with a minimum flip angle of 60°. The standard TSE (*left*) and hyperTSE60° (*center*) have identical protocols except for the different course of refocusing flip angles. The T_2 contrast in the center image is clearly reduced although both have the same $TE_{protocol}$ = 112 ms. However, their TE_{eff} are quite different: $TE_{eff\text{-}TSE180°}$ = 112 ms, $TE_{eff\text{-}hyperTSE60°}$ = 86 ms. A contrast adaptation to TE_{eff} = 112 ms reinstates full T_2 contrast again by increasing TE to 140 ms for the hyperTSE60° (*right*). The SAR savings for both hyperTSE sequences were approximately 70%. Identical window leveling was used in the figure

Compared to conventional TSE, hyperTSE sequences apply even lower flip angles during the RF pulse train. Since ft significantly depends on the exact type of flip angle modulation, it is difficult to give exact values for orientation in this case. ft can be as low as ∼ 70% for 2D-hyperTSE sequences of medium ETL with flip angle schedules as demonstrated in Fig. 24 (Weigel and Hennig 2006; Weigel and Hennig 2008). However, some vendors begin to display values for TE_{eff} (Eq. 13) as additional information during the protocol setup.

Patient studies underline the usefulness and clinical relevance of the contrast characterization framework (Tetzlaff et al. 2008), which is valid for a large class of generic TSE sequences. It was also successfully applied to inversion recovery prepared hyperTSE sequences (Weigel et al. 2007). However, for extended echo train imaging ft seems to develop a significant dependence on the relaxation times T_1 and T_2 (Mugler 2007). Thus, a loss of concise tissue contrast will result, since the T_2 contrast contributions ft in the image depend on the tissue under observation. Additionally, with such long ETL T_1 relaxation along the echo train is not negligible anymore (Busse et al. 2006; Mugler 2007; Weigel and Hennig 2008). The increasing T_1 relaxation times may partially counterbalance this effect at ultra high fields. As a rule of thumb, TSE sequences with TE higher than approximately 200 ms will most probably use so many RF pulses that the uniformity of ft for all tissues is not guaranteed anymore. Yet, it is important to note that the essential conclusion of the T_2 contrast framework via ft remains the same: Low flip angle TSE sequences produce a considerably reduced T_2 contrast that can be quantitated.

Adaptation of Contrast

So far, the contrast framework was only used to depict the reduced T_2 contrast. With low refocusing flip angles, the effective TE is reduced. However, increasing $TE_{protocol}$ allows for a reinstatement of T_2 contrast (Busse et al. 2006; Weigel and Hennig 2006, 2008; Weigel et al. 2007). In particular, a matching of the corresponding TE_{eff} from a given TSE or hyperTSE with a standard TSE sequence leads to equivalent T_2 contrasts. Thus, T_2 contrast can be fully reinstated or adapted to clinical requirements:

Matching of T_2-contrast:

$$TE_{eff-any\ TSE} = TE_{eff-TSE180°}. \tag{14}$$

Figure 27 demonstrates T_2-contrast reinstatement and matching in practice.

5 EPI

Echo-planar imaging (EPI) has been proposed by Sir Peter Mansfield in 1977 (Mansfield and Maudsley 1977). This can be regarded as the dawn of fast MR imaging. Until then spatial encoding of information required multiple excitations and acquisitions. One-dimensional spatial information was encoded by means of a linear magnetic field gradient applied during the data acquisition. In order to encode a full object or slice, the excitation and acquisition had to be repeated either with variation of the readout gradient orientation [zeugmatography or projection imaging introduced by Paul Lauterbur (Lauterbur 1973; Lauterbur 1974)] or with varying additional phase encoding gradients of different length [2D FT Zeugmatography as introduced by (Kumar et al. 1975)] or later of different amplitude [spin-warp imaging as proposed by Edelstein et al. (1980)]. The basic concept of EPI is to use not only a constant gradient during the acquisition but to vary the gradient during the acquisition. The encoding of more than one dimension during a single readout thus becomes feasible. In its basic variant, EPI utilizes an alternating readout gradient that traverses k-space repeatedly in alternating directions. In addition, a perpendicular small phase-encoding gradient is applied to propagate along the phase-encoding direction covering a two-dimensional area of k-space after a single excitation (Fig. 28). This concept of the acquisition of multiple echoes after a single excitation has later been extended in many ways leading to segmented acquisitions, to a spin echo variant [turbo-spin echo (TSE) (Hennig et al. 1986)], or to combinations thereof [gradient- and spin-echo imaging GRASE (Oshio and Feinberg 1991)]. Further extensions include other two-dimensional trajectories, such as spiral (Ahn et al. 1986) or rosette (Noll 1997) acquisitions.

The beauty of EPI lies in its speed and the fact that only a single excitation is required for an image. EPI is therefore robust against motion artifacts that otherwise result in image blurring and phase inconsistencies between excitations. This speed and robustness has opened numerous applications. The detection of brain activation based on the BOLD effect (Ogawa et al. 1990), the measurement of the directional dependence of tissue water diffusion in diffusion-weighted or diffusion tensor imaging (DWI, DTI) (Wesbey et al. 1984a, b), or fast measurements of perfusion exploiting signal changes during the passage of a contrast agent bolus (pMRI) (Rosen et al. 1990) are the most prominent examples.

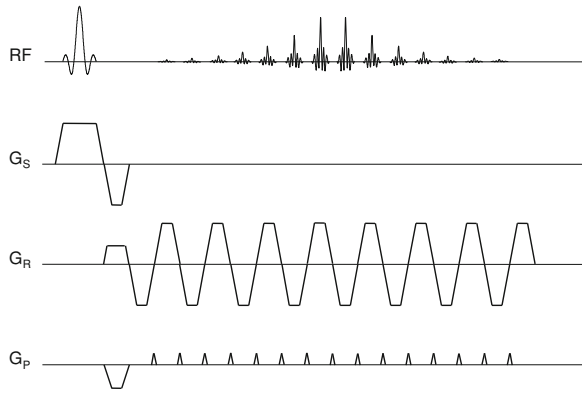

Fig. 28 The basic sequence diagram of an EPI sequence. The prominent features are the repeated readout in alternating directions (G_R) and the small phase encoding gradients that advance the k-space trajectory in phase direction (G_P). Thereby, a two-dimensional plane can be sampled after a single excitation of the spin system

However, this speed comes at a price. For imaging with a standard acquisition bandwidth of 50 kHz and a matrix size of 256 × 256, the data acquisition duration without any of the required overhead (excitation, encoding, magnetization recovery) lasts 1.3 s. EPI employs gradient echo refocusing of the signal. Thus, the signal has to be sampled before the transversal magnetization is lost due to T_2* decay. In order to avoid excessive image blurring, the acquisition time is limited by T_2* that usually is on the order of 100 ms or less. EPI is made possible by the use of very high receiver bandwidths and limitation of the acquisition matrix to lower resolution (typically 64 or 128). The high bandwidths cause an SNR loss proportional to the square root of the bandwidth, whereas the lower resolution results in an SNR gain proportional to the voxel volume (third power of voxel edge length). Thus, we can say that resolution is traded for speed.

Even for such lower resolution, the demands on the gradient system in terms of slew rate and gradient amplitude are high due to the very high bandwidth, and early realizations of EPI were rather limited due to gradient performance. The development of strong and actively shielded gradients in the mid 80s allowed the first applications of EPI (Mansfield 1984).

Interestingly, the routine application of EPI started only about 10 years later, whereas other applications, such as angiography, benefitted much earlier from the improved gradient performance. At this time, the image quality of EPI was not considered to be adequate for clinical imaging. With the advent of functional imaging after the discovery of the BOLD effect, the situation changed rapidly (Kwong et al. 1992). For this application, speed was more important than resolution, and the possibility to scan large parts of the brain with temporal resolution of only a few seconds and sensitivity to neuronal activity opened whole new research fields in fMRI and functional neuroscience.

Despite the introduction of other acquisition methods for fMRI over the last decade, such as spiral imaging, balanced free precession (Scheffler et al. 2001), or turbo-spin-echo, EPI remains to be the workhorse for the detection of brain activation and is the standard method at 1.5 and 3 T. One of the main motivations for the introduction of even higher magnetic field strength is the growing BOLD sensitivity. Therefore, EPI is required to be applied at high field. Although EPI is fast and sensitive to T_2* (in the gradient-echo variant) or T_2 (in the spin-echo variant), it remains to be a somewhat troublesome acquisition method. The image quality can be influenced by a number of factors that can cause a loss of resolution, signal, sensitivity, or geometric fidelity. In part, these problems can be corrected by proper reconstruction or selection of acquisition parameters. However, many of the EPI challenges are related to the frequency offset within the imaging volume and therefore increase with magnetic field strength.

An understanding for the unusual sensitivity of EPI to off-resonance effects can be gained from an analysis of the signal evolution in k-space. For regular spin-warp imaging, the signal phase evolves along the read-encoding direction according to the local off-resonance condition. Along the phase-encoding direction, the phase is constant if the off-resonance conditions are unchanged. Consequently, off-resonance effects manifest themselves in read direction. Prominent effects are the fat–water shift or geometric distortions in read encoding direction. The strength of this effect is directly related to the readout gradient strength and given by the off-resonance frequency relative to the acquisition bandwidth. Because EPI is commonly performed with very large acquisition bandwidths of 1,500–3,000 Hz/px, such distortions in readout direction are negligible even at high magnetic field strength. However, another effect has to be considered because all echo-signals are acquired consecutively without RF-refocusing. Along the EPI echo train, signal amplitude changes due to T_2*-decay lead to an amplitude modulation along the phase encoding direction and local off-resonance leads to a phase modulation. The amplitude modulation leads to blurring of the image along the phase encoding direction. With faster signal decay relative to the total acquisition duration, the image gets more blurred. For a constant off-resonance, such as for the fat–water shift or magnetic field inhomogeneities, a linear phase evolution of the signal occurs in phase encoding direction (Fig. 29). The time between the acquisitions of neighboring k-space lines is given by the echo spacing and is usually on the order of 0.5–2 ms. Consequently, the total effective bandwidth in phase encoding direction in EPI is between 500 and 2,000 Hz or about 10–30 Hz/px and thus extremely low. Because the gradient performance is similar for different field strength and frequently limited by physiological constraints such as peripheral nerve stimulation, these numbers are similar for all field strengths. However, the off-resonance effects increase linearly with field strength, and so does the corresponding shift in phase encoding direction.

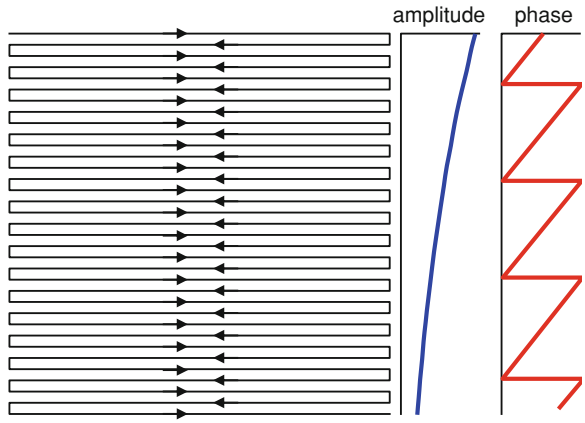

Fig. 29 The evolution of the signal amplitude and phase along the phase encoding direction for an EPI acquisition. The amplitude modulation due to T_2*-decay results in blurring, and the phase evolution (in this case linear due to constant local off-resonance condition) leads to spatial shift of the voxels in image space

One of the prominent aspects and challenges of EPI, the so-called Nyquist- or N/2-ghost, is a consequence of the inverse acquisition direction of every

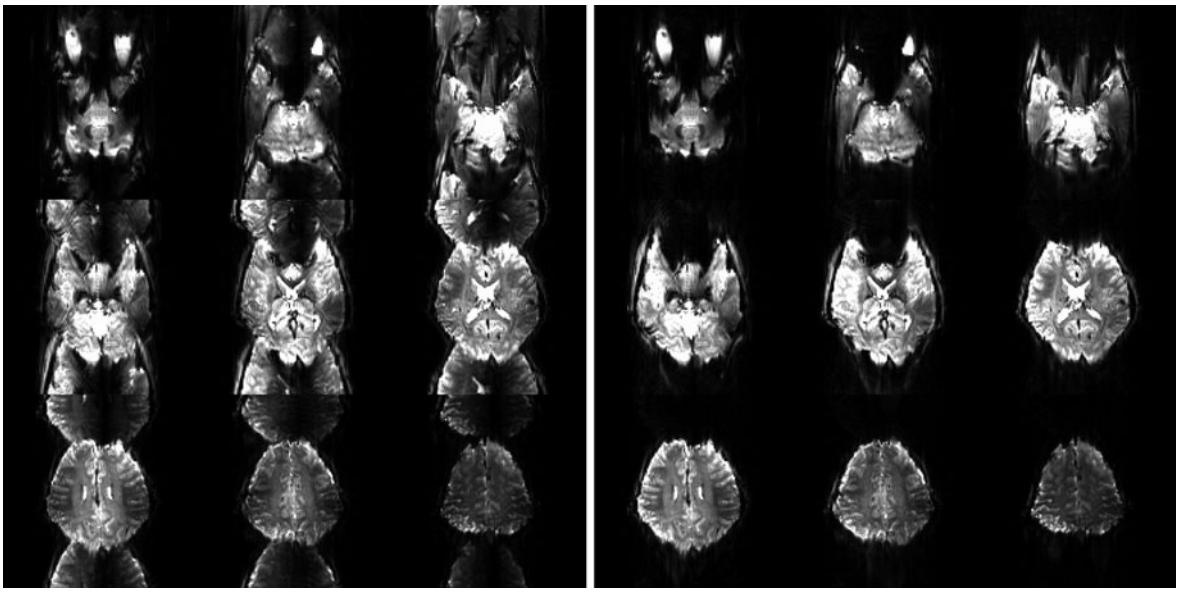

Fig. 30 7 T EPI data reconstructed without any correction for the Nyquist ghost (left) and after correction (right). The image lookup table has been scaled to highlight the Nyquist artifact. The artifact is corrected by a small (subsample) shift of the k-space data in readout direction. In the corrected data, the strong distortions are striking within the brain and even stronger in the skull that is smeared dramatically across very many voxels in some regions

other read encoding line. Every signal aspect that is not symmetric in time will lead to an oscillatory modulation with a period of 2 k-space lines. Causes for such a modulation can be small timing differences between the readout gradient and the data acquisition or eddy current–related gradient deviations. As a consequence, the object is represented twice in the field of view (FoV), the real object and the Nyquist ghost shifted by half a FoV (Fig. 30). Remedies for this artifact are commonly based on reference data either from within the EPI echo train or from a separate acquisition. The strength and correction is largely independent of the field strength and therefore not further discussed in this chapter.

To summarize, the EPI-specific challenges that increase with high field strength are as follows:

- The geometric distortions due to local magnetic field inhomogeneities (B_0-shim) increase linearly with field strength (Fig. 31).
- T_2* is decreasing at high field, and therefore, the signal amplitude reduction during the echo train is increased leading to increased blurring of the images in phase encoding direction effectively reducing the spatial resolution in this dimension.
- During the long readout train, dephasing of magnetization that leads to signal loss is more pronounced due to the increased macroscopic magnetic field inhomogeneity. Certain brain regions become difficult to assess.
- The frequency difference between the fat and water signal increases linearly with field strength (approximately 1,000 Hz at 7 T) and leads to very pronounced spatial displacement of fat versus water in phase encoding direction. This can easily be as much as half a FoV or even more.
- Due to the fast switching of strong gradients that is required for fast EPI acquisition, the sequence is among the loudest methods on many scanners. At high field strength, the acoustic noise can become very high.
- The high SAR at high field can be limiting for very fast acquisitions, although EPI is intrinsically not very demanding on SAR if applied in its gradient-echo version.

The first five of these detrimental effects increase not only with field strength but also with image resolution. Higher resolution leads to longer echo spacing resulting in even lower effective bandwidth in phase encoding direction. In addition, the total ETL increases quadratically with the EPI image resolution and stronger gradient amplitudes are required. One of the main motivations for high field, however, is to

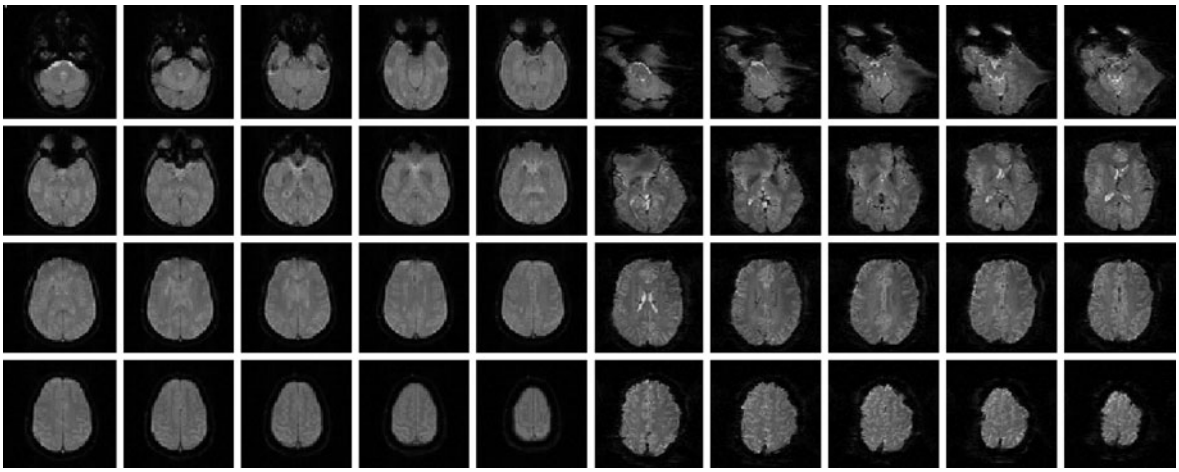

Fig. 31 Echo planar imaging (EPI) at 1.5 T (left) and 7 T (right). The increased SNR has been exploited to increase the resolution at 7 T. Without specific measures to counteract the increased sensitivity of off-resonance effects, the images are severely distorted in the phase encoding direction (in this case in the left–right direction as opposed to Fig. 21 where the phase encoding direction is anterior-posterior)

exploit the increased sensitivity and SNR for higher spatial resolution acquisitions. It thus becomes obvious that high-field, high-resolution EPI is challenging and requires increased efforts to result in adequate image quality for fMRI applications. Some of the solutions for high-resolution EPI at high field are described and discussed in the following.

Perhaps the single most important and efficient method that reduces the disadvantages of the large off-resonance effects in EPI at high magnetic field is parallel imaging (Sodickson and Manning 1997; Pruessmann et al. 1999). With parallel imaging, only a subset of the read encoding lines in k-space is acquired. The remaining lines are reconstructed from these reduced data with the knowledge of the spatial sensitivity of multiple receiver coils used. It is therefore that spatial information is not only encoded by means of magnetic field gradients but also in the distribution of signals via the sensitivities of the receiver coils. In the reconstructed images, the SNR is reduced depending on the acceleration factor R and the so-called g-factor that depends mainly on R and the coil configuration:

$$\mathrm{SNR}_{\mathrm{PI}} = \frac{\mathrm{SNR}}{g\sqrt{R}}. \tag{15}$$

The g-factor varies spatially and is always larger than or equal to one. It specifies the amplification of noise in the reconstruction process. In general, g is lower for coil arrays with more and smaller receiver coils and larger for higher acceleration factors. As for most fast imaging methods, parallel imaging thus reduces the image SNR. However, the drastically reduced readout duration has very beneficial effects on the challenges described above. In EPI, reduction factors up to four have been shown to be feasible, thereby reducing the amplitude modulation and the phase accrual during the echo train by the same factor (see Fig. 32). Correspondingly, geometric distortions, fat–water shift, and blurring in phase encoding direction are also reduced by the reduction factor. In addition, the minimum echo time is reduced significantly leading to higher signal amplitudes that can compensate for part or even all of the SNR loss caused by the acceleration. For many applications, this reduction in echo time allows to achieve the optimum echo time, e.g., in BOLD-based functional imaging where the echo time should equal the T_2^* of the tissue. The application of parallel imaging in EPI can therefore reduce many of the detrimental effects to a level that is comparable to EPI without acceleration at significantly lower field strength (Fig. 33). For further reduction of the minimum achievable echo time, an asymmetric readout in the phase encoding direction is frequently applied. The Hermitian symmetry of k-space can be exploited to reconstruct images from such reduced data by means of partial Fourier algorithms (Feinberg et al. 1986). Similar to

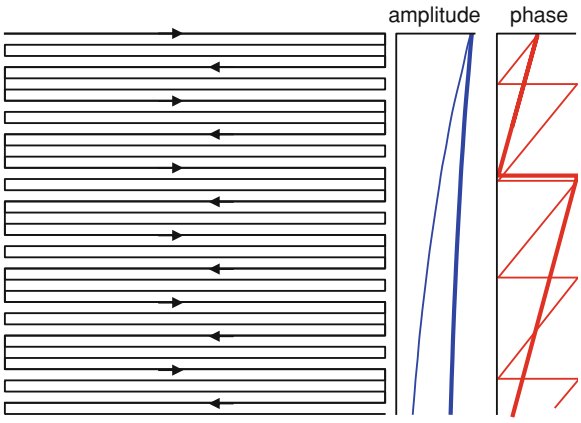

Fig. 32 The application of parallel imaging to EPI has significant impact on many aspects related to shortening the echo train. In this example, effects of an acceleration factor of 3 are displayed. Because only one out of three k-space lines are to be acquired, the full extent of the phase encoding direction is traversed in one-third of the time compared to full sampling. As a result, the signal decay as well as the phase evolution due to off-resonance effects are reduced by a factor of three (thick lines)

parallel imaging, the number of acquired phase encoding lines is reduced and a corresponding reduction in the SNR proportional to the square root of the reduction is expected. However, asymmetric sampling allows for shorter echo times, recovering part of this loss. Other than for parallel imaging, no noise amplification is introduced.

Despite the reduction of geometric distortions through the application of parallel imaging, significant deviations between EPI data and geometrically correct spin-warp acquisitions are remaining. They can be especially problematic, if results based on the EPI data are displayed as overlay onto anatomical data as it is common practice for fMRI, diffusion weighted MRI, or perfusion-weighted MRI. Additional methods for the determination and correction of geometric distortions have been introduced and are crucial for high-field EPI. All methods have in common that the local shift of the signal in phase encoding direction is estimated from additional measurements and that the images are corrected by reformation of the images according to the inverse of the distortion field. One of the earliest methods is based on the measurement of a magnetic field map as calculated from the phase different between two gradient-echo acquisitions with different echo times (Jezzard and Balaban 1995). In order to resolve the two-Pi ambiguities in the phase data, the data have to be "unwrapped" to remove the phase discontinuities. Another method applied the phase encoding gradient with opposite polarities in two scans, resulting in distortions in opposing directions (Andersson and Skare 2002; Morgan et al. 2004). An extension of these two shot methods is the so-called PSF mapping method that samples not only two points to estimate the local phase accumulation but more points with varying offset in phase encoding direction (Fig. 34), thereby, the shift of each voxel is determined directly without ambiguities and can be corrected (Robson et al. 1997; Zeng and Constable 2002; Zaitsev et al. 2004). These methods have found widespread application in the neuroscience community and are implemented in software packages used for processing of functional MR data. However, even the best of these methods cannot recover information that has been lost during the imaging process, i.e., when areas in the object have been compressed strongly. If multiple voxels collapse into one, the signal can be distributed to the location in the undistorted space. However, a separation of these signals is not possible.

Although most of the high field–related problems of EPI can be reduced by the methods described so far, a remaining major aspect is dephasing of the magnetization within one voxel due to macroscopic magnetic field inhomogeneities that can lead to severe signal reductions. This signal loss is directly related to the frequency distribution within each voxel. A number of methods have been proposed to reduce this signal loss including z-shimming (Glover 1999; Constable and Spencer 1999), specifically tailored RF-pulses with phase modulation across the slice (Cho et al. 1996; Stenger et al. 2000), or simply reducing the voxel size (Frahm et al. 1993; Speck et al. 2007). Whereas the first two methods aim at a compensation of the linear terms of the magnetic field inhomogeneity and require additional measurement time either for preparation or repeated scans with different compensation settings, the last method is very generally applicable and simple. The spread of frequencies within each voxel is reduced by decreasing the extent of the voxel. The susceptibility-related signal loss can thereby be reduced significantly (Fig. 35). An alternative description of the reduced dephasing effect can be given in view of the k-space sampling scheme. For higher resolution, k-space coverage is extended to include higher spatial frequencies. Inhomogeneities shift the k-space signal

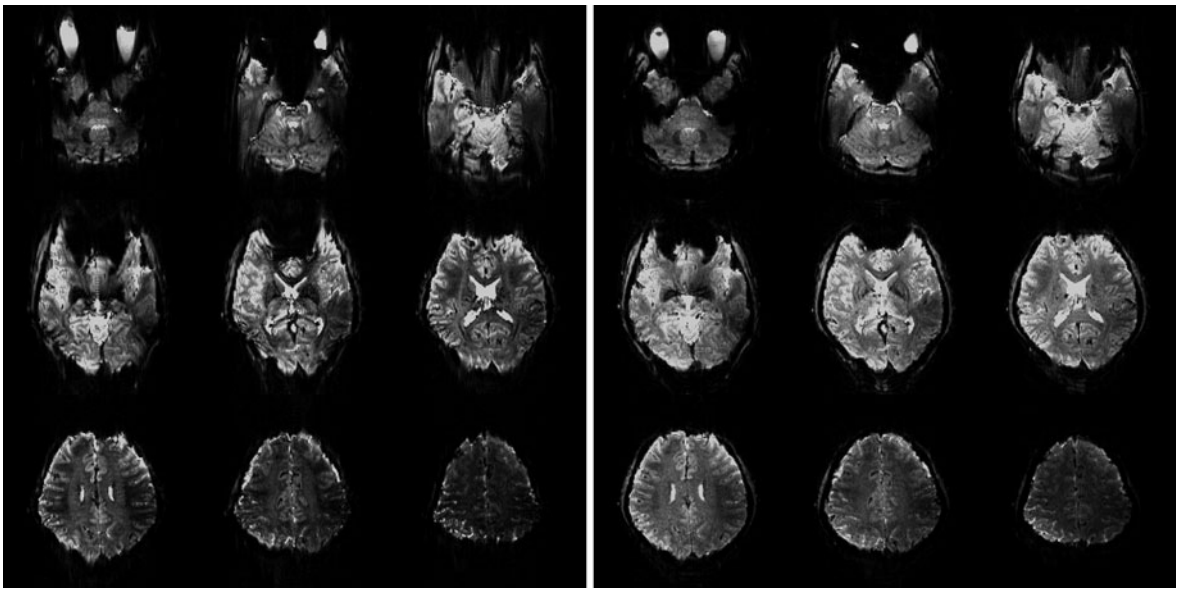

Fig. 33 7 T EPI data without (left) and with two parallel imaging acceleration factor of two (right). In this acquisition with a matrix size of 160, the geometric distortions are reduced by a factor of two. In addition, the echo time could be reduced from 39 to 22 ms. This echo time is approximately equal to T_2* and therefore optimal for susceptibility weighted imaging such as fMRI on the basis of the BOLD effect. However, distortions are still significant

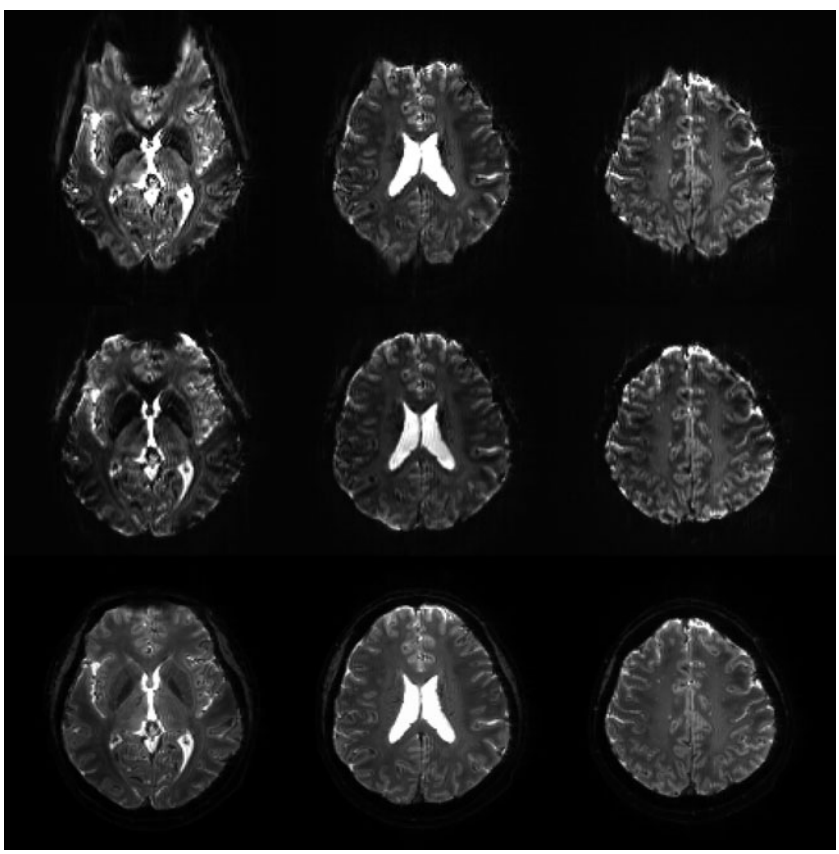

Fig. 34 EPI slices acquired at 7 T with an acquisition matrix of 160 × 160 (top row). In this example, no parallel imaging has been applied, and the geometric distortions are dramatic. The EPI data corrected by remapping the data according to the PSF measurement (middle row) are much improved and are geometrically a perfect match to the undistorted gradient-echo images (bottom row). A few areas of low signal remain due to strong local susceptibility gradients (that were originally also the reason for the strong distortions)

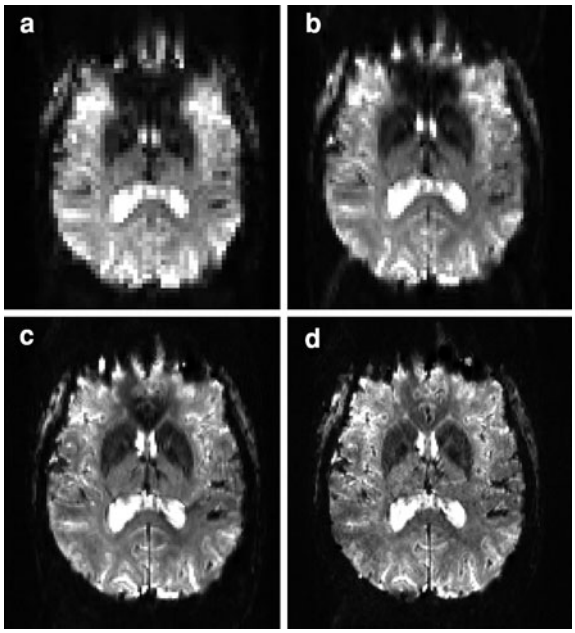

Fig. 35 The signal dropouts in EPI at 7 T can be severe. They are mainly caused by signal dephasing across the voxel. In this example, the voxel edge lengths are **a** 3 mm, **b** 2 mm, **c** 1.4 mm, and **d** 1.1 mm isotropic. With higher spatial resolution, the frequency variation across the voxel is reduced and the signal improves in many areas, such as the inferior frontal lobe. However, certain regions such as the putamen remain low in their signal due to microscopic inhomogeneities caused by iron deposition [figure modified from Speck et al. (2007)]

away from the center. Once the low spatial frequency signals "escape" the covered k-space region, the signal drops quickly. With larger coverage, this high-energy part of the data is still acquired even in case of a large shift due to local magnetic field gradients. With smaller k-space extend (corresponding to lower resolution) the signal from such inhomogeneous regions can be shifted outside the k-space area sampled and the signal is lost.

As mentioned above, fat signal is strongly shifted relative to the water signal in EPI acquisitions. This fat signal can therefore overlap with the structures of interest and obscure effects of interest. The common approach is to apply fat saturation pulses to selectively reduce the longitudinal fat magnetization prior to the excitation of each slice. This fat saturation, however, does not only require about 10–15 ms time per slice, it also increases the SAR due to its frequent application and high flip angle. Alternatively, spatial-spectral excitation pulses are used at lower field strength that only excite water signal in a given slice.

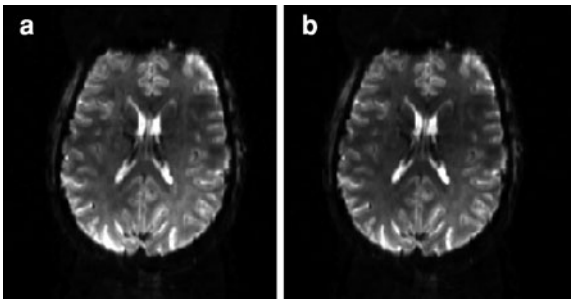

Fig. 36 At high field strength, the subcutaneous fat signal in gradient-echo EPI is strongly reduced due to short T_2* of the fat. In this example of an EPI slice at 7 T, the acquisition was performed **a** without and **b** with fat suppression. The images are virtually indistinguishable, and even the unsuppressed image does not display significant amounts of fat

These binomial pulses require pulse spacing inversely proportional to the fat–water shift. For 7 T, this spacing is only 500 μs resulting again in very high SAR if the available RF-power is sufficient to deliver high flip angle pulses in such a short time. For gradient-echo EPI of the human brain, it was noticed that the fat signal is strongly reduced due to very short subcutaneous fat T_2*. Therefore, no or only reduce fat saturation is required, resulting in reduced SAR levels and faster scanning (Fig. 36).

Methods for acoustic noise reduction have been described above and include passive noise dampening built into the system. In addition, the gradient waveform has a significant impact on the loudness of a sequence. The oscillating readout gradient in EPI produces a significant portion of the sound energy. Commonly, this gradient is switched in trapezoidal form, leading to sharp edges in the temporal current profile. Modification of the readout gradient to a smoother sinusoidal waveform can limit the acoustic frequencies that are mechanically excited if the base frequency does not fall into an acoustic resonance of the gradient system.

All the details given above can be summarized into current recommendations for high-field EPI that also represents commonalities between the developments and approaches of multiple high-field laboratories. For gradient-echo EPI, such as for fMRI, high resolution of 1–1.5 mm isotropic voxel size offers significant sensitivity advantages over lower field strength and minimizes signal loss. High parallel imaging acceleration factors of 3 or 4 allow keeping the echo time close to T_2*. A TE of 20–25 ms should

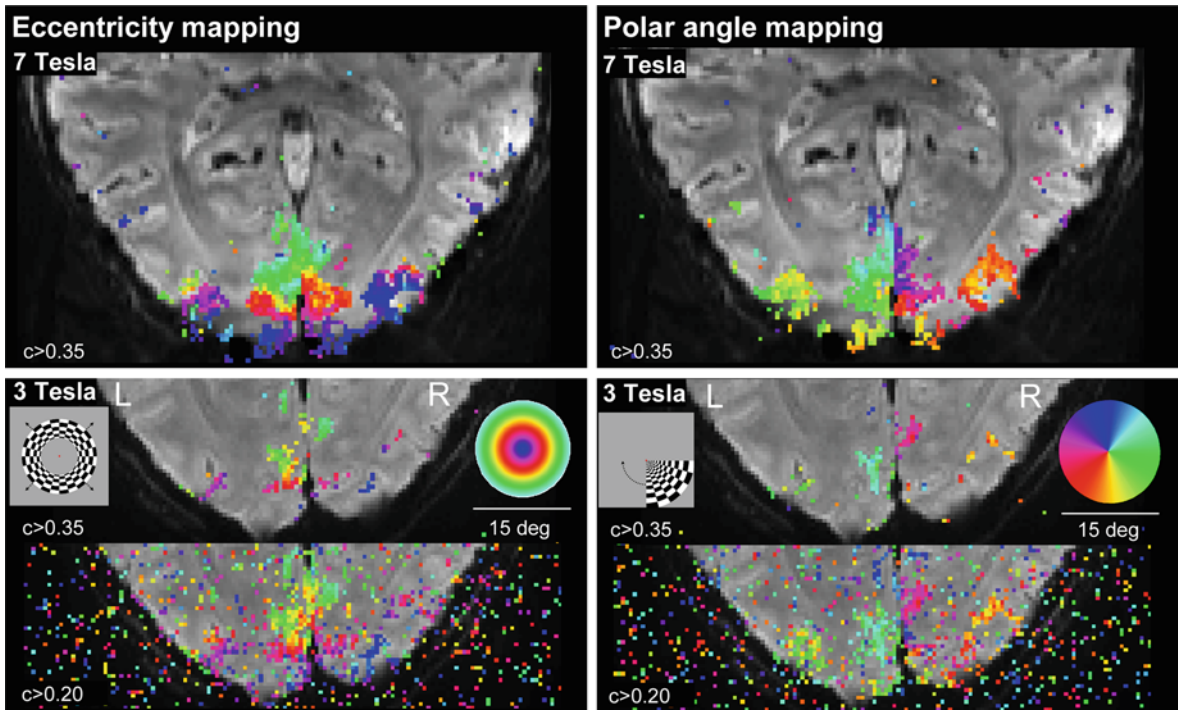

Fig. 37 One example of high resolution (1.1 mm isotropic) fMRI at 7 T and 3 T. The cortical representation of the visual field is mapped. The stimulus consists of expanding (eccentricity) or rotating (polar angle) luminance changes. At 7 T, a single 4-min experiment is sufficient to map the retinotopy reliably. At 3 T with identical experimental design and conditions, the effect is "hidden" in the noise floor [adapted from (Hoffmann et al. 2009)]

be used. Such high acceleration factors require receive-coil arrays with many elements to limit the noise amplification. Partial Fourier encoding or echo shifting in the phase encoding direction is also beneficial in order to reduce the echo time. High bandwidth and short echo spacing limit the geometric distortions and blurring. Fat saturation can be removed for gradient-echo EPI or the flip angle reduced. The image orientation has to be chosen based on the available coverage (with high resolution, only smaller volumes can be scanned in a given time) and to minimize signal loss (Deichmann et al. 2003). Remaining geometric distortions should be corrected by means of field-map based or PSF-based methods.

It is obvious that most of the methods described in this chapter can be applied to improve EPI at lower field strength, and many of them have actually been developed and applied at 1.5 and 3 T. However, the application of high-resolution EPI at lower field strength is limited by the available SNR. For example, very high-resolution retinotopic mapping yields much higher sensitivity at 7 T compared to 3 T (Hoffmann et al. 2009). In this example, with short scan durations of only 4 min, the sensitivity gain of high field at high resolution is striking. At lower field strength, comparable quality and sensitivity can only be reached with much longer scan time (Fig. 37).

6 Steady-state Sequences (FLASH, trueFISP)

6.1 Basic Principles of SSFP Sequences

Steady-state free precession (SSFP) sequences are characterized by a fast train of excitation and gradient pulses. Between excitation RF-pulses or within TR, the magnetization is not able to return to its thermal equilibrium. As a consequence, RF-pulses will influence both the remaining transversal and the remaining longitudinal magnetization. The steady-state magnetization of an SSFP experiment is thus a superposition of different transversal and longitudinal states, and the acquired image amplitude becomes a complex function of the investigated tissue's relaxation properties. The steady state is characterized by a certain

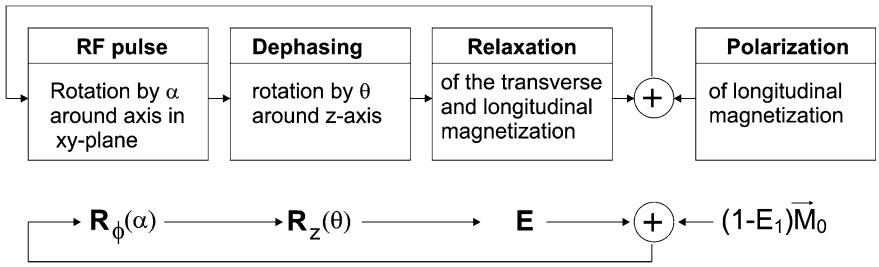

Fig. 38 Flow and recycling of magnetization during an SSFP sequence

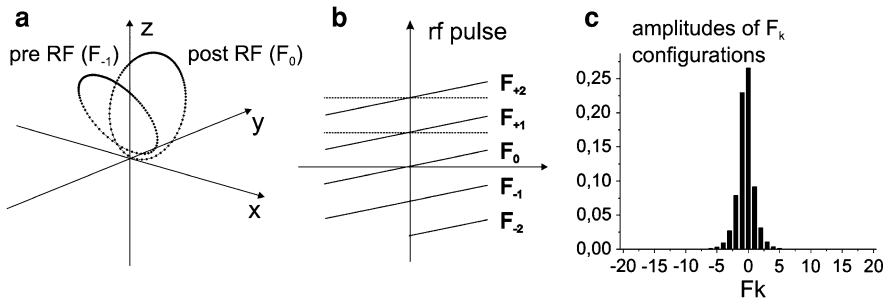

Fig. 39 **a** The dots on the two ellipses correspond to the tips of magnetization vectors in the steady state dephased between $\pm\pi$ within TR. **b** is the corresponding phase-graph description or Fourier transformation of the spatial distribution shown in **a**, and **c** are the corresponding amplitudes of the phases shown in **b**

distribution of magnetization vectors. If a steady state has been established, this distribution will be exactly the same for each TR. The steady-state distribution can also be described by a certain distribution of different configurations in k-space. The populations or amplitudes of these configurations are given by the Fourier components in k-space of the corresponding spatial distribution [see Fig. 14 (Kaiser et al. 1974; Hennig 1991; Scheffler 1999)]. A steady state can only be reached for sequences with (1) fixed TR (in order to have identical T_1 and T_2 relaxation within each TR period), (2) constant flip angle (the phase of the excitation pulse may vary linearly or quadratically from pulse to pulse), and (3) constant dephasing within TR (the dephasing induced by switched gradients and susceptibility effects at a certain spatial position must be the same within each TR) (Sobol and Gauntt 1996; Zur et al. 1991). From (3), it can be deduced that the phase encoding gradient, which changes from excitation to excitation, has to be refocused (compensated by a second gradient pulse with opposite gradient area).

The analytical description of the steady state in the spatial domain can be achieved by solving the eigenvector equation that describes the three processes of excitation (rotation by α around an axis in the x–y plane), dephasing (rotation by θ around z-axis), and T_1 and T_2 relaxation. This process is illustrated in Fig. 38 and mathematically corresponds to the following:

$$\vec{M}^+ = R_x(\alpha)\left(R_z(\phi)E\vec{M}^+ + M_0(1-E_1)\hat{z}\right) \qquad (16)$$

with $E = \mathrm{diag}(E_2, E_2, E_1)$ and $E_{1,2} = \exp(-TR/T_{1,2})$.

The (unique) solution in the spatial domain and in k-space is shown in Fig. 39 for fixed parameters of TR, α, T_1, and T_2.

The corresponding analytical solution of Eq. 16 is given by (Zur et al. 1988)

$$\vec{M}^+ = (1 - R_x(\alpha)R_z(\phi)E)^{-1}(M_0(1-E_1)\hat{z}) \qquad (17)$$

The steady-state magnetization does not depend on the chosen gradient waveform that is switched between the excitation pulses. The steady-state magnetization generated just after and before the excitation pulse (sometimes called F_0 or S+ and F_{-1} or S−, respectively) is thus identical for all types of gradient-echo sequences. The signal intensity and the phase of the steady-state magnetization as a function

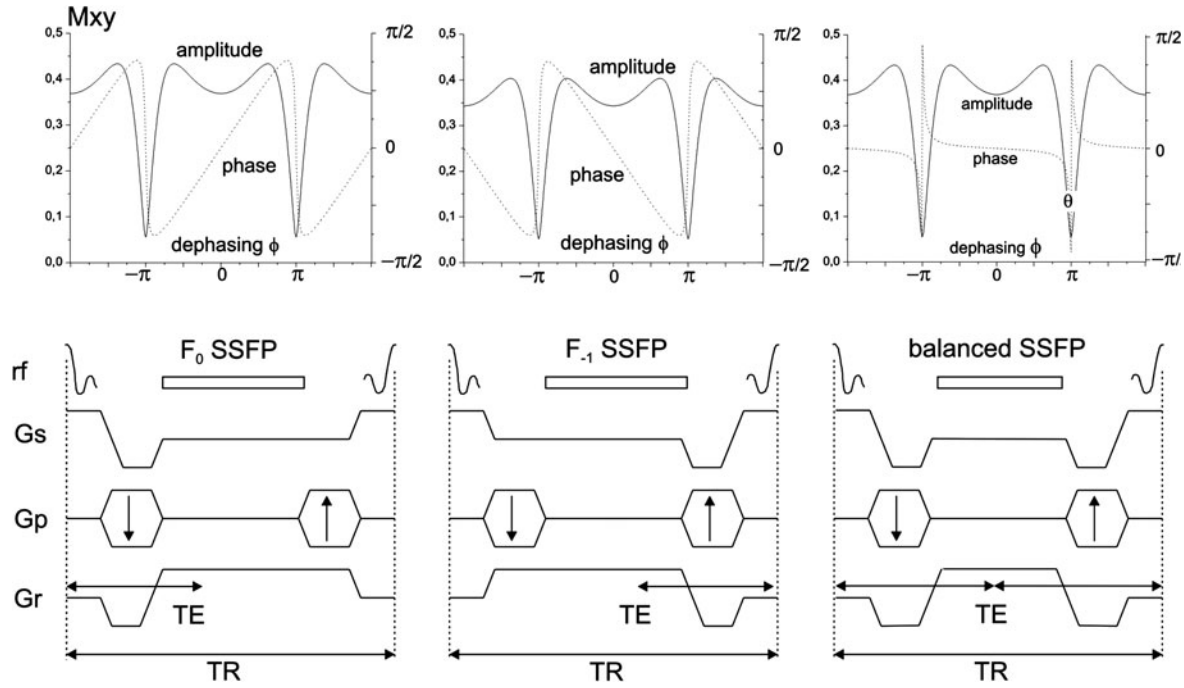

Fig. 40 Signal amplitude and phase of SSFP magnetization and corresponding sequence diagram

of the dephasing between excitation pulses as well as the corresponding sequence timing are shown in Fig. 40 (left, middle).

The type of the readout gradient selects whether the F_0 or the F_{-1} magnetization (or both) is used for imaging. A conventional bipolar readout gradient selects the F_0 signal (refocused FLASH, GRASS, FAST, FISP, FFE, …), whereas the time-reversed gradient waveform selects the F_{-1} signal (PSIF, CE-FAST, T_2-FFE, …). The resulting signal intensity of these sequences can be calculated by summing up the magnetization given in Eq. 17 over a full 2π period (if the gradient-induced dephasing between excitation pulses is adjusted in such a way that the phase difference within one imaging voxel is $\pm\,\pi$) (Zur et al. 1988; Gyngell 1989).

The eigenvector Eq. 16 can also be used to describe SSFP sequences for which the gradient-induced dephasing between excitation pulses is zero, see Fig. 40, right. The amplitude and phase profile as a function of the dephasing between excitation pulses is calculated for the time point TE = TR/2. In the ideal case of a perfect shim dephasing within TR is zero. The resulting signal intensity of balanced SSFP (bSSFP) is thus not a sum of isochromats dephased between $\pm\,\pi$ (as for non-balanced SSFP), but can be described as a single magnetization vector. The length or amplitude of this vector is given by the frequency profile in Fig. 40, right. The signal intensity of bSSFP strongly depends on the residual dephasing of the magnetization within TR. A very high signal can be observed if the magnetization rotates by an angle of $\phi = \pi$ within TR. The steady-state signal is almost suppressed if the magnetization does not precess within TR ($\phi = 0$). In most cases, bSSFP is used with alternating excitation pulses, or equivalently, with excitation pulses showing a linearly increasing phase of π from pulse to pulse. As a result, the amplitude-frequency profile of bSSFP as shown in Fig. 40 is shifted by π, and the highest signal will be obtained for on-resonance spins (zero dephasing within TR). Using alternating excitation pulses, the magnetization flips continuously between two positions that are located on an $\alpha/2$ cone. Because magnetization is not spoiled as for the F_0 and F_{-1} SSFP sequence, bSSFP is very sensitive to field inhomogeneities, and thus often shows banding artifacts, especially at very high field strength.

Besides non-balanced SSFP (F_0- and F_{-1}-SSFP) and bSSFP, a forth type of SSFP sequence, the so-called RF-spoiled non-balanced SSFP or FLASH sequence, is frequently used in clinical applications. The sequence timing is identical to the F_0-SSFP

sequence, Fig. 40, left, but the phase of the RF-pulse is varied quadratically from excitation to excitation (Zur et al. 1991). This RF-phase scheme suppresses coherent superposition of configurations with negative index (refocused or spin-echo configurations) and therefore introduces a strong T_1-weighting of the steady-state signal with negligible T_2 dependence.

6.2 Contrast and Artifacts of SSFP Sequences at High Field

Except for the RF-spoiled non-balanced SSFP (FLASH) sequence, all other SSFP sequences show a mixed T_1- and T_2-dependent contrast because of superposition of different echo paths during the steady state. The signal intensity of FLASH is almost purely T_1-weighted, i.e., corresponds to a sequence where no transverse magnetization is recycled via RF-pulses (which is basically not possible except for $T_2 \ll TR$). The resulting signal intensity can be described by the Ernst formula, which is a very good approximation for RF-spoiled non-balanced SSFP using 50° or 117° as quadratic RF-phase increment:

$$S_{\mathrm{FLASH}} = M_0 \frac{1 - E_1}{1 - E_1 \cos\alpha} \sin\alpha \qquad (18)$$

excluding a certain T_2* decay during TE. The optimal flip angle to produce the highest signal for a given TR and T_1 is given by $\cos(\alpha) = E_1$. In general, due to increased T_1 at high fields, the optimal flip angle is lower compared to lower fields.

bSSFP exhibits a relatively complicated contrast that is composed (it is not just a product) of T_1 and T_2 contributions. On-resonance, the resulting signal intensity is a function of T_1, T_2, TR, and flip angle α, and is given by (Zur et al. 1988; Freeman and Hill 1971)

$$S_{\mathrm{bSSFP}} = M_0 \frac{\sqrt{E_2}(1 - E_1)\sin\alpha}{1 - (E_1 - E_2)\cos\alpha - E_1 E_2}, \qquad (19)$$

This formula can be simplified if $TR \ll T_1, T_2$ (Haake et al. 1999):

$$S_{\mathrm{bSSFP}} = M_0 \frac{\sin\alpha}{1 + \cos\alpha + (1 - \cos\alpha)(T_1/T_2)}. \qquad (20)$$

The optimal flip angle depends on T_1 and T_2 and is given by

$$\cos\alpha = \frac{T_1/T_2 - 1}{T_1/T_2 + 1}, \qquad (21)$$

which results in a signal amplitude of $S_{\mathrm{bSSFP}} = \frac{1}{2} M_0 \sqrt{T_2/T_1}$ (Haake et al. 1999).

If T_1 and T_2 are similar (i.e., for CSF or fat), the optimal flip angle is around α = 70–90°, and the maximum possible signal approaches 50% of M_0. This is a very remarkable feature of bSSFP, and there exists no other type of sequence that is able to continuously acquire 50% of the total available spin polarization M_0. However, the contrast of bSSFP is given by the ratio of T_2 and T_1, which is certainly not optimal for diagnostic purposes. A typical feature of the bSSFP contrast is the very high signal intensity of liquids and fat (both have different T_1 and T_2 values, but a similar ratio of T_2 and T_1). Furthermore, because T_1 increases and T_2 decreases at high fields, the resulting ratio T_2/T_1 becomes smaller and thus the resulting signal. At the same time, however, the optimal flip angle is also reduced that is beneficial in terms of SAR.

The two non-balanced SSFP variants F_0-SSFP and F_{-1}-SSFP exhibit an even more complicated contrast than bSSFP. F_0-SSFP is more T_1-weighted than F_{-1}-SSFP, which is stronger T_2-weighted, and their signal intensities are given by

$$S_{S0-\mathrm{SSFP}} = M_0 \frac{1 - e(\alpha)(E_1 - \cos\alpha)}{1 + \cos\alpha} \sin\alpha \qquad (22)$$

and

$$S_{S-1-\mathrm{SSFP}} = M_0 \frac{1 - e(\alpha)(1 - E_1\cos\alpha)}{1 + \cos\alpha} \sin\alpha \qquad (23)$$

with

$$e(\alpha) = \left(1 - E_2^2\right)^{\frac{1}{2}} \left(1 - E_1^2 E_2^2 - 2E_1\left(1 - E_2^2\right)\cos(\alpha) + \left(E_1^2 - E_2^2\right)\cos^2(\alpha)\right)^{-\frac{1}{2}} \qquad (24)$$

(Zur et al. 1988). These equations are only valid if all pathways sum up correctly. In case of disturbed phase relation between consecutive pathways, for example, produced by motion or flow, reduced signal intensities and artifacts occur. Because for both SSFP variants transverse magnetization is recycled via refocusing RF-pulses, the resulting signal benefits from long T_2. Again, shorter T_2 at very high fields will therefore

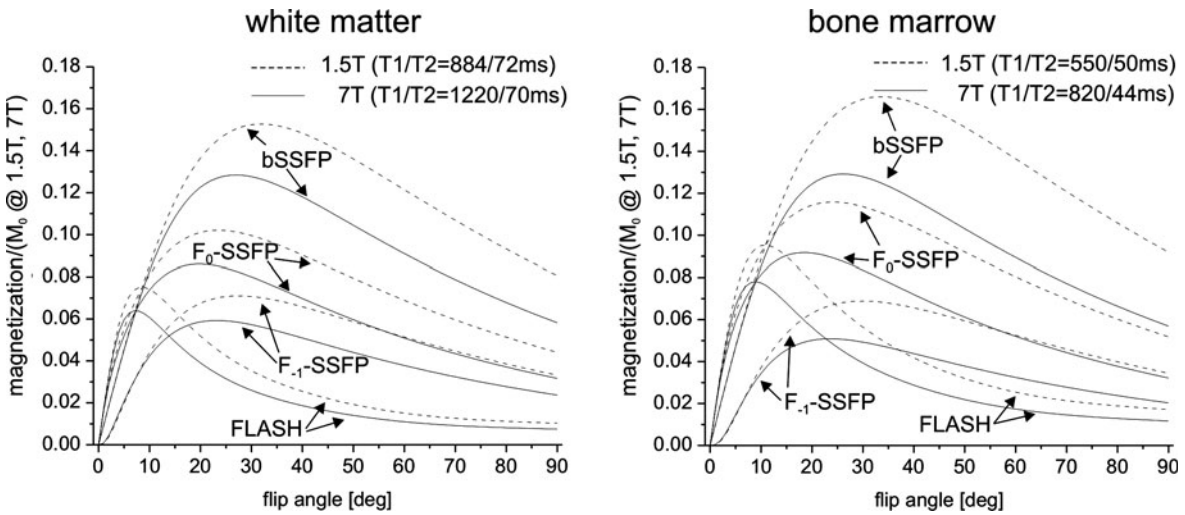

Fig. 41 SSFP signal amplitudes for white matter and bone marrow at 1.5 and 7 T. Relaxation times are taken from (Rooney et al. 2007; Michaeli et al. 2002). TR was set to 10 ms for all sequences

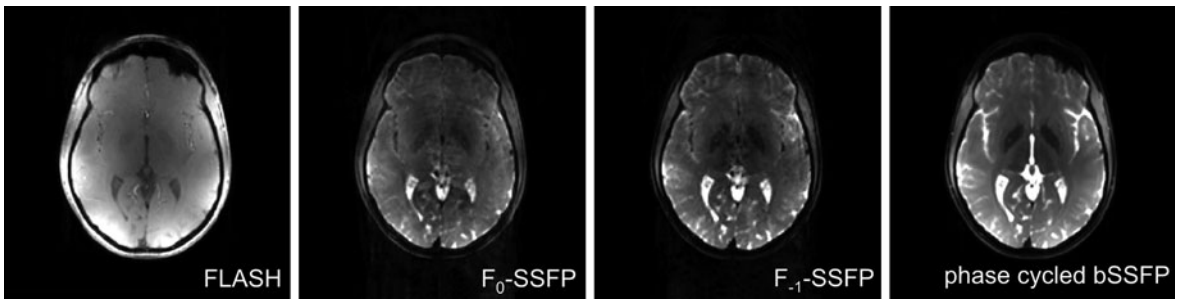

Fig. 42 Single slice out of a 3D data set acquired with isotropic 1.3-mm resolution using a non-selective excitation pulse. Sequence parameters were as follows: FLASH TR/TE/FA = 10/3.2 ms/10°, F_0-SSFP 3.8/1.7 ms/25°, F_{-1}-SSBP 3.8/1.7 ms/25°, bSSFP 7.4/3.5 ms/25°, and four phase cycles

reduce the signal. Figure 41 shows two examples of signal intensities of the four SSFP variants as a function of the flip angle for white matter and bone marrow, for 1.5 and 7 T.

In general, the steady-state amplitudes are always higher for 1.5 T compared to 7 T. This is based on the fact that T_1 is significantly shorter at 1.5 T than for 7 T, whereas T_2 is only slightly longer at 1.5 T compared to 7 T. At 1.5 T, this results in a higher signal for the T_1-weighted FLASH sequences, and also for the non-RF-spoiled SSFP sequences that are mainly T_2/T_1-weighted. The signal loss due to change in relaxation times at 7 T is in the order of 20–30%. However, the equilibrium magnetization M_0 is roughly four times higher at 7 T resulting in a signal gain of about 300% compared to 1.5 T. The contrast, i.e., the relative signal difference between different tissues is roughly comparable between 1.5 and 7 T, assuming short echo times below 5 ms. However, the signal and contrast of SSFP sequences strongly depend on the applied flip angle. Especially at low flip angles in the range of 5–20°, signal intensities may vary by a factor of 5, as can be seen in Fig. 41. B_1 inhomogeneities at 7 T therefore lead to very strong contrast and signal variations at low flip angles. This is especially true for the FLASH sequence that shows a sharp signal peak around the optimal Ernst angle. Balanced SSFP and non-balanced SSFP exhibit a much smoother signal variation as a function of the flip angle and less rapid signal decay at high flip angles. Here, signal variations are only about 30% for flip angles between 20 and 40°. Figure 42 shows a

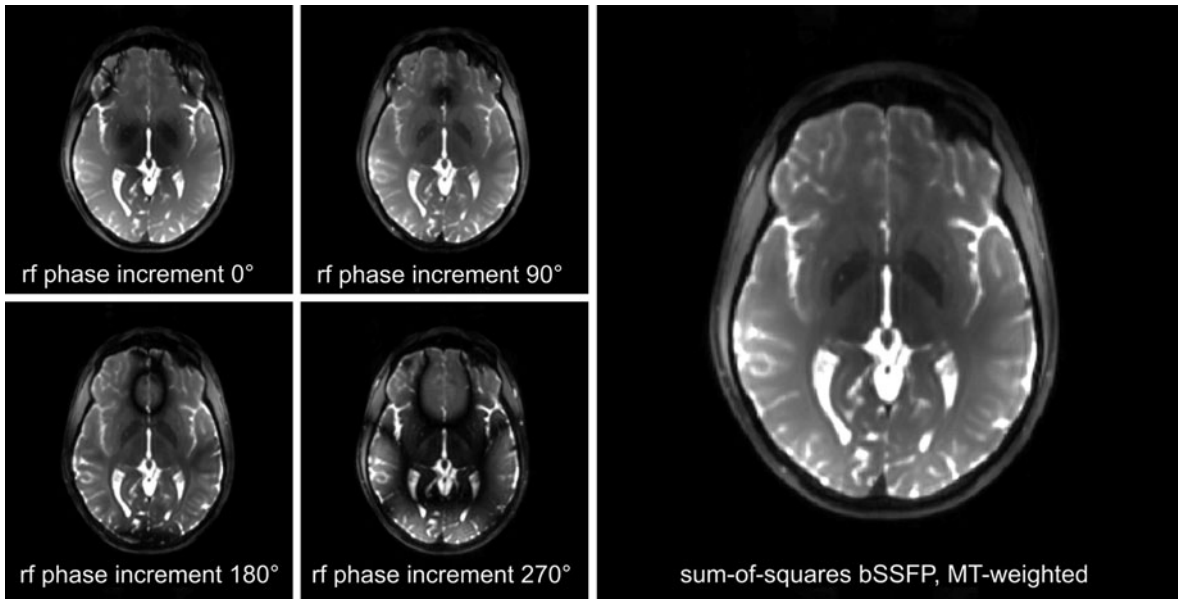

Fig. 43 Right images show the root sum of squares reconstruction of four-phase cycled bSSFP acquisitions shown on the left. With TR/TE/FA = 3.8/1.7 ms/25° and RF-pulse duration of 1.2 ms, bSSFP shows magnetization transfer (MT) effects due to partial saturation of bound protons (Bieri and Scheffler 2006) leading to a slightly increased gray–white matter contrast compared to the non-MT-weighted bSSFP measurement shown in Fig. 17 right (4.8 ms RF-pulse duration)

comparison of the four SSFP variants acquired at 7 T with an eight channel transmit and receive coil. FLASH was acquired with a flip angle of 10° and TR of 10 ms and thus shows strong signal variations due to B_1 inhomogeneities. Less signal variations are visible for the non-RF-spoiled SSFP sequences acquired at 25°, which roughly gives the highest signal for white matter. As for 1.5 T, there is almost no contrast between gray and white matter and very high signal for CSF.

6.3 Potential Artifacts of SSFP Sequences at High Fields

A well-known potential artifact in bSSFP imaging is banding, i.e., dark bands that occur if the local frequency is 1/(2TR) or −1/(2TR) away from on-resonance. Local frequency offsets are mainly produced by tissue susceptibility differences and the resulting B_0 inhomogeneity scales linearly with the main magnetic field. With a typical TR of 5 ms, banding-free bSSFP can only be achieved in confined regions at 7 T where local frequency variations are below 200 Hz, for example, in the cerebrum or knee. If longer TR has to be used (in order to reduce SAR) or in regions with larger susceptibility variations, phase-cycled bSSFP has to be applied. Phase cycling is composed of a set of bSSFP acquisitions that are repeated with different linear phase increments of the RF-pulse. As a result, the frequency profile shown in Fig. 40, right, is shifted to different locations, see Fig. 43, left, and subsequent combination of image sets will cancel banding artifacts. In the simplest case, two bSSFP images are acquired with and without alternating RF-pulses (0 and 180° RF-phase advance), and the final images are calculated as a maximum intensity projection of both data sets (constructive interference in steady state (CISS) method (Casselman et al. 1993). Depending on the applied flip angle and tissue relaxation times, residual signal variations might still be visible. This can be further improved with more phase cycling steps (for example, 0, 90, 180, and 270°) and dedicated data combination such as root sum of squares (Bangerter et al. 2004) or non-linear averaging (Elliott et al. 2007), as shown in Fig. 43. The signal of non-balanced SSFP sequences does not depend on the local frequency, and thus, no banding is visible, and application at 7 T is unproblematic.

6.4 SAR Issues for SSFP at High Fields

Transmitted RF-power is proportional to B_1^2 times B_0^2. An easy way to reduce power deposition without contrast modification is an increase of the RF-pulse duration that quadratically reduces RF-power. With constant repetition time, the resulting mean RF-power deposition and thus SAR is reduced linearly with RF-pulse duration. At 1.5 T, a rectangular 30° RF-pulse with a duration of 100 μs and a repetition time of 3 ms is feasible. Assuming similar SAR models for 1.5 and 7 T, the same sequence can be applied at 7 T by increasing the RF-pulse duration to about 1,000 μs and TR to 5 ms. For the MT-weighted bSSFP image shown in Fig. 43, a flip angle of 25° using a RF-pulse duration of 1,200 μs and TR of 3.8 ms was possible, due to a slightly more conservative SAR model applied at this scanner at 7 T. Similar considerations are valid for shaped pulses. Increased RF-pulse length will also lead to an increased repetition time. For a spatial resolution of 1 mm and using a standard gradient system with 40 mT/m and 200 T/(sm), repetition times of 8–10 ms are feasible at 7 T. FLASH and non-balanced SSFP can thus be applied at 7 T without significant constraints. For bSSFP, banding becomes critical at 8–10 ms repetition time and phase cycling is thus mandatory.

References

Ahn CB, Kim JH, Cho ZH (1986) High-speed spiral-scan echo planar NMR imaging-I. IEEE Trans Med Imaging 5:2–7

Alsop DC (1997) The sensitivity of low flip angle RARE imaging. Magn Reson Med 37:176–184

Andersson JL, Skare S (2002) A model-based method for retrospective correction of geometric distortions in diffusion-weighted EPI. Neuroimage 16:177–199

Atkinson D, Hill DL, Stoyle PN et al (1999) Automatic compensation of motion artifacts in MRI. Magn Reson Med 41:163–170

Bammer R, Aksoy M, Liu C (2007) Augmented generalized SENSE reconstruction to correct for rigid body motion. Magn Reson Med 57:90–102

Bangerter NK, Hargreaves BA, Vasanawala SS et al (2004) Analysis of multiple-acquisition SSFP. Magn Reson Med 51:1038–1047

Baudrexel S, Volz S, Preibisch C et al (2009) Rapid single-scan T_2*-mapping using exponential excitation pulses and image-based correction for linear background gradients. Magn Reson Med 62:263–268

Bernstein MA, Huston J 3rd, Ward HA (2006) Imaging artifacts at 3.0 T. J Magn Reson Imaging 24:735–746

Bieri O, Scheffler K (2006) On the origin of apparent low tissue signals in balanced SSFP. Magn Reson Med 56:1067–1074

Bulte JW, Kraitchman DL (2004) Iron oxide MR contrast agents for molecular and cellular imaging. NMR Biomed 17:484–499

Busse RF (2004) Reduced RF power without blurring: correcting for modulation of refocusing flip angle in FSE sequences. Magn Reson Med 51:1031–1037

Busse RF, Hariharan H, Vu A et al (2006) Fast spin echo sequences with very long echo trains: design of variable refocusing flip angle schedules and generation of clinical T_2 contrast. Magn Reson Med 55:1030–1037

Busse RF, Brau AC, Vu A et al (2008) Effects of refocusing flip angle modulation and view ordering in 3D fast spin echo. Magn Reson Med 60:640–649

Carr HY, Purcell EM (1954) Effects of diffusion on free precession in nuclear magnetic resonance experiments. Phys Rev 94:630–638

Casselman JW, Kuhweide R, Deimling M et al (1993) Constructive interference in steady state-3DFT MR imaging of the inner ear and cerebellopontine angle. AJNR 14:47–57

Chen Z, Johnston LA, Kwon DH et al (2010) An optimised framework for reconstructing and processing MR phase images. Neuroimage 49:1289–1300

Cho ZH, Ro YM, Park ST et al (1996) NMR functional imaging using a tailored RF gradient echo sequence: a true susceptibility measurement technique. Magn Reson Med 35:1–5

Collins CM, Li S, Smith MB (1998) SAR and B_1 field distributions in a heterogeneous human head model within a birdcage coil. Specific energy absorption rate. Magn Reson Med 40:847–856

Constable RT, Spencer DD (1999) Composite image formation in z-shimmed functional MR imaging. Magn Reson Med 42:110–117

Constable RT, Anderson AW, Zhong J et al (1992) Factors influencing contrast in fast spin-echo MR imaging. Magn Reson Imaging 10:497–511

Deichmann R, Gottfried JA, Hutton C et al (2003) Optimized EPI for fMRI studies of the orbitofrontal cortex. Neuroimage 19:430–441

Derbyshire JA, Wright GA, Henkelman RM et al (1998) Dynamic scan-plane tracking using MR position monitoring. J Magn Reson Imaging 8:924–932

Dumoulin CL, Souza SP, Darrow RD (1993) Real-time position monitoring of invasive devices using magnetic resonance. Magn Reson Med 29:411–415

Duyn JH, van Gelderen P, Li TQ et al (2007) High-field MRI of brain cortical substructure based on signal phase. Proc Natl Acad Sci USA 104:11796–11801

Edelstein WA, Hutchison JM, Johnson G et al (1980) Spin warp NMR imaging and applications to human whole-body imaging. Phys Med Biol 25:751–756

Ehman RL, Felmlee JP (1989) Adaptive technique for high-definition MR imaging of moving structures. Radiology 173:255–263

Elliott AM, Bernstein MA, Ward HA et al (2007) Nonlinear averaging reconstruction method for phase-cycle SSFP. Magnetic resonance imaging 25:359–364

Feinberg DA, Hale JD, Watts JC et al (1986) Halving MR imaging time by conjugation: demonstration at 3.5 kG. Radiology 161:527–531

Fischer HW, Rinck PA, Van Haverbeke Y et al (1990) Nuclear relaxation of human brain gray and white matter: analysis of field dependence and implications for MRI. Magn Reson Med 16:317–334

Frahm J, Merboldt KD, Hanicke W (1993) Functional MRI of human brain activation at high spatial resolution. Magn Reson Med 29:139–144

Freeman R, Hill H (1971) Phase and intensity anomalities in Fourier transform NMR. J Magn Reson 4:366–383

Friston KJ, Ashburner J, Poline JB et al (1995) Spatial realignment and normalization of images. Hum Brain Mapp 2:165–189

Gieseke J, Wattjes M, Lutterbey G et al (2004) Ultra fast T_2-weighted TSE sequences using flip angle sweep with half-fourier and SENSE at 3 T. Neuroradiology 46(Suppl 1):122

Glover GH (1999) 3D z-shim method for reduction of susceptibility effects in BOLD fMRI. Magn Reson Med 42:290–299

Glover GH, Lee AT (1995) Motion artifacts in fMRI: comparison of 2DFT with PR and spiral scan methods. Magn Reson Med 33:624–635

Glover GH, Noll DC (1993) Consistent projection reconstruction (CPR) techniques for MRI. Magn Reson Med 29:345–351

Gyngell M (1989) The steady-state signals in short-repetition-time sequences. J Magn Reson 81:474–483

Haacke EM, Xu Y, Cheng YC et al (2004) Susceptibility weighted imaging (SWI). Magn Reson Med 52:612–618

Haake E, Brown R, Thompson M et al (1999) Fast imaging in the steady state. In: Haacke E, Brown R, Thompson M, Venkatesan R (eds) Magnetic resonance imaging: physical principles and sequence design, Wiley, New York, pp 451–512

Hahn EL (1950) Spin echoes. Phys Rev 80:580–594

He X, Yablonskiy DA (2009) Biophysical mechanisms of phase contrast in gradient echo MRI. Proc Natl Acad Sci USA 106:13558–13563

Henkelman RM, Hardy PA, Bishop JE et al (1992) Why fat is bright in RARE and fast spin-echo imaging. J Magn Reson Imaging 2:533–540

Hennig J (1988) Multiecho imaging sequences with low refocusing flip angles. J Magn Reson 78:397–407

Hennig J (1991) Echoes—How to generate, recognize, use or avoid them in MR-imaging sequences. Part I + II. Concepts Magn Reson 3:125–143, 179–192

Hennig J, Scheffler K (2000) Easy improvement of signal-to-noise in RARE-sequences with low refocusing flip angles. Magn Reson Med 44:983–985

Hennig J, Scheffler K (2001) Hyperechoes. Magn Reson Med 46:6–12

Hennig J, Nauerth A, Friedburg H (1986) RARE imaging: a fast imaging method for clinical MR. Magn Reson Med 3:823–833

Hennig J, Weigel M, Scheffler K (2003) Multiecho sequences with variable refocusing flip angles: optimization of signal behavior using smooth transitions between pseudo steady states (TRAPS). Magn Reson Med 49:527–535

Hennig J, Weigel M, Scheffler K (2004) Calculation of flip angles for echo trains with predefined amplitudes with the extended phase graph (EPG)-algorithm: principles and applications to hyperecho and TRAPS sequences. Magn Reson Med 51:68–80

Himmelreich U, Dresselaers T (2009) Cell labeling and tracking for experimental models using magnetic resonance imaging. Methods 48:112–124

Hoffmann MB, Stadler J, Kanowski M et al (2009) Retinotopic mapping of the human visual cortex at a magnetic field strength of 7 T. Clin Neurophysiol 120:108–116

Hoult DI, Phil D (2000) Sensitivity and power deposition in a high-field imaging experiment. J Magn Reson Imaging 12:46–67

Jezzard P, Balaban RS (1995) Correction for geometric distortion in echo planar images from B_0 field variations. Magn Reson Med 34:65–73

Jezzard P, Duewell S, Balaban RS (1996) MR relaxation times in human brain: measurement at 4 T. Radiology 199:773–779

Kaiser R, Bartholdi E, Ernst R (1974) Diffusion and field-gradient effects in NMR Fourier spectroscopy. J Chem Phys 60:2057–2061

Katscher U, Bornert P, Leussler C et al (2003) Transmit SENSE. Magn Reson Med 49:144–150

Kiefer B, Grässner J, Hausmann R (1994) Image acquisition in a second with half-Fourier-acquisition single-shot turbo spin echo. J Magn Reson Imaging 4:86

Kim B, Boes JL, Bland PH et al (1999) Motion correction in fMRI via registration of individual slices into an anatomical volume. Magn Reson Med 41:964–972

Koenig SH, Brown RD 3rd, Adams D et al (1984) Magnetic field dependence of $1/T_1$ of protons in tissue. Invest Radiol 19:76–81

Kumar A, Welti I, Ernst RR (1975) NMR Fourier zeugmatography. J Magn Reson 18:69–83

Kwong KK, Belliveau JW, Chesler DA et al (1992) Dynamic magnetic resonance imaging of human brain activity during primary sensory stimulation. Proc Natl Acad Sci USA 89:5675–5679

Lauterbur PC (1973) Image formation by induced local interactions: examples employing nuclear magnetic resonance. Nature 242:190–191

Lauterbur PC (1974) Magnetic resonance zeugmatography. Pure Appl Chem 40:149–157

Le Roux P, Hinks RS (1993) Stabilization of echo amplitudes in FSE sequences. Magn Reson Med 30:183–190

Lebel RM, Wilman AH (2007) Intuitive design guidelines for fast spin echo imaging with variable flip angle echo trains. Magn Reson Med 57:972–975

Lebel RM, Wilman AH (2009) Time-efficient fast spin echo imaging at 4.7 T with low refocusing angles. Magn Reson Med 62:96–105

Li TQ, van Gelderen P, Merkle H et al (2006) Extensive heterogeneity in white matter intensity in high-resolution T_2*-weighted MRI of the human brain at 7.0 T. Neuroimage 32:1032–1040

Liu C, Bammer R, Kim DH et al (2004) Self-navigated interleaved spiral (SNAILS): application to high-resolution diffusion tensor imaging. Magn Reson Med 52:1388–1396

Luo J, He X, d'Avignon DA et al (2010) Protein-induced water 1H MR frequency shifts: contributions from magnetic susceptibility and exchange effects. J Magn Reson 202:102–108

Maclaren J, Speck O, Stucht D et al (2010) Navigator accuracy requirements for prospective motion correction. Magn Reson Med 63:162–170

Mansfield P (1984) Real-time echo-planar imaging by NMR. Br Med Bull 40:187–190

Mansfield P, Maudsley AA (1977) Planar spin imaging by NMR. J Magn Reson 27:101–119

Mao W, Smith MB, Collins CM (2006) Exploring the limits of RF shimming for high-field MRI of the human head. Magn Reson Med 56:918–922

Martin WR, Wieler M, Gee M (2008) Midbrain iron content in early Parkinson disease: a potential biomarker of disease status. Neurology 70:1411–1417

Meiboom S, Gill D (1958) Modified spin-echo method for measuring nuclear relaxation times. Rev Sci Instrum 29:688–691

Melki PS, Mulkern RV, Panych LP et al (1991) Comparing the FAISE method with conventional dual-echo sequences. J Magn Reson Imaging 1:319–326

Melki PS, Jolesz FA, Mulkern RV (1992) Partial RF echo-planar imaging with the FAISE method. II. Contrast equivalence with spin-echo sequences. Magn Reson Med 26:342–354

Michaeli S, Garwood M, Zhu XH et al (2002) Proton T_2 relaxation study of water, *N*-acetylaspartate, and creatine in human brain using Hahn and Carr–Purcell spin echoes at 4 T and 7 T. Magn Reson Med 47:629–633

Morgan PS, Bowtell RW, McIntyre DJ et al (2004) Correction of spatial distortion in EPI due to inhomogeneous static magnetic fields using the reversed gradient method. J Magn Reson Imaging 19:499–507

Mugler JP (2007) Signal and contrast properties of very-long spin-echo trains for 3D T_2-weighted turbo-spin-echo imaging; Berlin, Germany, p 1716

Mugler JP, Bao S, Mulkern RV et al (2000a) Optimized single-slab three-dimensional spin-echo MR imaging of the brain. Radiology 216:891–899

Mugler JP, Kiefer B, Brookeman JR (2000b) Three-dimensional T_2-weighted imaging of the brain using very long spin-echo trains, Denver, USA, p 687

Mugler JP, Wald LL, Brookeman JR (2001) T_2-weighted 3D spin-echo train imaging of the brain at 3 Tesla: reduced power deposition using low flip-angle refocusing RF pulses. 2001; Glasgow, United Kingdom, p 438

Mulkern RV, Wong ST, Winalski C et al (1990) Contrast manipulation and artifact assessment of 2D and 3D RARE sequences. Magn Reson Imaging 8:557–566

Mulkern RV, Melki PS, Jakab P et al (1991) Phase-encode order and its effect on contrast and artifact in single-shot RARE sequences. Med Phys 18:1032–1037

Noll DC (1997) Multishot rosette trajectories for spectrally selective MR imaging. IEEE Trans Med Imaging 16:372–377

Ogawa S, Lee TM, Kay AR et al (1990) Brain magnetic resonance imaging with contrast dependent on blood oxygenation. Proc Natl Acad Sci USA 87:9868–9872

Ooi MB, Krueger S, Thomas WJ et al (2009) Prospective real-time correction for arbitrary head motion using active markers. Magn Reson Med 62:943–954

Ordidge RJ, Gorell JM, Deniau JC et al (1994) Assessment of relative brain iron concentrations using T_2-weighted and T_2*-weighted MRI at 3 Tesla. Magn Reson Med 32:335–341

Oshio K, Feinberg DA (1991) GRASE (Gradient- and spin-echo) imaging: a novel fast MRI technique. Magn Reson Med 20:344–349

Patel MR, Klufas RA, Alberico RA et al (1997) Half-fourier acquisition single-shot turbo spin-echo (HASTE) MR: comparison with fast spin-echo MR in diseases of the brain. AJNR Am J Neuroradiol 18:1635–1640

Pipe JG (1999) Motion correction with PROPELLER MRI: application to head motion and free-breathing cardiac imaging. Magn Reson Med 42:963–969

Pruessmann KP, Weiger M, Scheidegger MB et al (1999) SENSE: sensitivity encoding for fast MRI. Magn Reson Med 42:952–962

Qin L, van Gelderen P, Derbyshire JA et al (2009) Prospective head-movement correction for high-resolution MRI using an in-bore optical tracking system. Magn Reson Med 62:924–934

Reichenbach JR, Venkatesan R, Schillinger DJ et al (1997) Small vessels in the human brain: MR venography with deoxyhemoglobin as an intrinsic contrast agent. Radiology 204:272–277

Robson MD, Gore JC, Constable RT (1997) Measurement of the point spread function in MRI using constant time imaging. Magn Reson Med 38:733–740

Rooney WD, Johnson G, Li X et al (2007) Magnetic field and tissue dependencies of human brain longitudinal 1H2O relaxation in vivo. Magn Reson Med 57:308–318

Rosen BR, Belliveau JW, Vevea JM et al (1990) Perfusion imaging with NMR contrast agents. Magn Reson Med 14:249–265

Scheffler K (1999) A pictorial description of steady-states in rapid magnetic resonance imaging. Concepts Magn Reson 11:291–304

Scheffler K, Seifritz E, Bilecen D et al (2001) Detection of BOLD changes by means of a frequency-sensitive trueFISP technique: preliminary results. NMR Biomed 14:490–496

Sobol WT, Gauntt DM (1996) On the stationary states in gradient echo imaging. J Magn Reson Imaging 6:384–398

Sodickson DK, Manning WJ (1997) Simultaneous acquisition of spatial harmonics (SMASH): fast imaging with radiofrequency coil arrays. Magn Reson Med 38:591–603

Speck O (2005) Spin-echo based T_1-contrast at 3 T: the problem and a simple solution. Proceedings of the 13th Annual Meeting of the ISMRM, Miami Beach, USA, p 2197

Speck O, Hennig J, Zaitsev M (2006) Prospective real-time slice-by-slice motion correction for fMRI in freely moving subjects. MAGMA 19:55–61

Speck O, Stadler J, Zaitsev M (2008) High resolution single-shot EPI at 7 T. MAGMA 21:73–86

Stenger VA, Boada FE, Noll DC (2000) Three-dimensional tailored RF pulses for the reduction of susceptibility artifacts in T(*)(2)-weighted functional MRI. Magn Reson Med 44:525–531

Tetzlaff RH, Mader I, Kuker W et al (2008) Hyperecho-turbo spin-echo sequences at 3 T: clinical application in neuroradiology. AJNR Am J Neuroradiol 29:956–961

Thesen S, Heid O, Mueller E et al (2000) Prospective acquisition correction for head motion with image-based tracking for real-time fMRI. Magn Reson Med 44:457–465

Weigel M, Hennig J (2006) Contrast behavior and relaxation effects of conventional and hyperecho-turbo spin echo sequences at 1.5 and 3 T. Magn Reson Med 55:826–835

Weigel M, Hennig J (2008) Development and optimization of T_2 weighted methods with reduced RF power deposition (Hyperecho-TSE) for magnetic resonance imaging. Zeitschrift fur medizinische Physik 18:151–161

Weigel M, Zaitsev M, Hennig J (2007) Inversion recovery prepared turbo spin echo sequences with reduced SAR using smooth transitions between pseudo steady states. Magn Reson Med 57:631–637

Welch EB, Felmlee JP, Ehman RL et al (2002a) Motion correction using the k-space phase difference of orthogonal acquisitions. Magn Reson Med 48:147–156

Welch EB, Manduca A, Grimm RC et al (2002b) Spherical navigator echoes for full 3D rigid body motion measurement in MRI. Magn Reson Med 47:32–41

Wesbey GE, Moseley ME, Ehman RL (1984a) Translational molecular self-diffusion in magnetic resonance imaging. I. Effects on observed spin-spin relaxation. Invest Radiol 19:484–490

Wesbey GE, Moseley ME, Ehman RL (1984b) Translational molecular self-diffusion in magnetic resonance imaging. II. Measurement of the self-diffusion coefficient. Invest Radiol 19:491–498

Williamson DS, Mulkern RV, Jakab PD et al (1996) Coherence transfer by isotropic mixing in Carr–Purcell–Meiboom–Gill imaging: implications for the bright fat phenomenon in fast spin-echo imaging. Magn Reson Med 35:506–513

Woessner DE (1961) Effects of diffusion in nuclear magnetic resonance spin-echo experiments. J Chem Phys 34:2057–2061

Zaitsev M, Hennig J, Speck O (2004) Point spread function mapping with parallel imaging techniques and high acceleration factors: fast, robust, and flexible method for echo-planar imaging distortion correction. Magn Reson Med 52:1156–1166

Zaitsev M, Dold C, Sakas G et al (2006) Magnetic resonance imaging of freely moving objects: prospective real-time motion correction using an external optical motion tracking system. Neuroimage 31:1038–1050

Zeng H, Constable RT (2002) Image distortion correction in EPI: comparison of field mapping with point spread function mapping. Magn Reson Med 48:137–146

Zhong K, Leupold J, von Elverfeldt D et al (2008) The molecular basis for gray and white matter contrast in phase imaging. Neuroimage 40:1561–1566

Zur Y, Wood ML, Neuringer LJ (1991) Spoiling of transverse magnetization in steady-state sequences. Magn Reson Med 21:251–263

Zur Y, Stokar S, Bendel P (1988) An analysis of fast imaging sequences with steady-state transverse magnetization refocusing. Magn Reson Med 6:175–193

What to do with All that Signal? Issues of High-resolution MRI

Oliver Speck

Contents

Abstract

The basic description of field strength–related changes, i.e., in magnetization and relaxation times, as well as challenges, such as B_1 or B_0 inhomogeneity and SAR, has been given in Contrasts, Mechanisms, and Sequences, together with some of the consequences and remedies for major MR imaging methods. In this chapter, a few general aspects and possible exploitations of the increased SNR at high field are described. In addition, limitations of improvements at high field strength and currently remaining challenges are discussed and set the stage for the following chapters on particular applications of high-field MR.

1 Signal to Noise and Related Parameters

As described earlier, the magnetization increases linearly with magnetic field strength and could lead to a corresponding linear increase in SNR if other properties and parameters were constant. The changes in relaxation times (T_1 generally longer, T_2/T_2^* generally shorter at higher field strength) result in a more complex situation. For many common methods, the efficiency (SNR per unit time) is reduced because longer repetition times are required due to increased T_1. The reduced transversal relaxation times T_2 and T_2^* require shorter echo times demanding higher acquisition bandwidth leading to SNR reduction. On the other hand, more slices can be acquired in the same TR or higher contrast can be achieved such as particularly in susceptibility weighted acquisition methods.

O. Speck (✉)
Department of Biomedical Magnetic Resonance, Otto-von-Guericke University, Leipziger Strasse 44, Haus 65, 39120 Magdeburg, Germany
e-mail: oliver.speck@ovgu.de

J. Hennig and O. Speck (eds.), *High-Field MR Imaging,* Medical Radiology. Diagnostic Imaging,
DOI: 10.1007/174_2010_102, © Springer-Verlag Berlin Heidelberg 2011

Therefore, the changes in relaxation times can be either advantageous or detrimental depending on the particular situation and measurement method. For most imaging methods, significant SNR increase remains.

An additional concern rises from the inhomogeneous RF-excitation that leads to spatially varying flip angles. Therefore, the optimal conditions for a particular imaging sequence can only be maintained over a small volume. For large imaging volumes, the SNR and contrast can vary significantly compromising the gain of higher magnetic field strength. As long as no generally applicable solution for the safe generation of homogeneous RF flip angles has been implemented, focusing on small volumes of interest by means of optimized local adjustments is the preferred strategy for many applications.

If the image quality (by such measures as SNR or contrast) for a particular sequence and application is sufficient at lower field strength, the added SNR at high field can be invested in either increased speed or resolution. The potential gain in speed is proportional to the square of the SNR gain. This can be very high given that an acceleration method is available to exploit the SNR. If the acceleration by means of parallel imaging is too high, noise amplification will compromise the performance. The amount of acceleration with tolerable noise amplification is determined by the receiver coil configuration and the RF wave length (Wiesinger et al. 2004). It has been demonstrated that higher field strength offers potential benefits in parallel imaging if optimal receive coil arrays are used. Although many applications at high field strength employ parallel imaging, reduced scan times have not been the primary purpose of many studies. This may primarily be due to the fact that very few clinical studies have been performed at 7T. Clinical research has so far been performed in the brain where scan time reduction is not a major driving force. Also, costs per patient are not as important in these research settings that currently do not generate income from reimbursements. Therefore, the full potential of accelerated acquisitions may be exploited in future applications.

The gain in SNR or CNR can also be invested in higher resolution. Without a reduction of slice thickness in 2D imaging, a linear gain translates into a reduction of the voxel edge length by a factor 1.5 compared to 3T. In 3D imaging, a linear SNR increase can be invested into a reduction by approximately 1.3 compared to 3T. These numbers do not account for any of the additional effects previously described. For many methods, the gain will be somewhat lower. Only methods that benefit from contrast improvements in addition to the SNR gain can be expected to perform even better at very high resolution than this simple estimation suggests. The best known examples are susceptibility contrast–based methods, namely gradient echo applications with echo times in the range of T_2* as applied for functional imaging as well as for anatomical magnitude and phase imaging. These have been described in the previous chapter, and applications are shown in the following chapters.

2 High-resolution Structural Brain Imaging

Due to the absence of gross physiological motion, the scan time for brain imaging is less limited than for many other parts of the body. Therefore, many users accept comparably long scan times in brain imaging studies to achieve high-resolution depiction of cranial anatomy. However, the scan time in normal volunteers and more so in patients is limited by the ability of the subjects to hold still. For very high-resolution acquisitions even in the absence of head motion, the motion of the brain inside the scull due to blood and CSF pulsation may further limit the imaging resolution. With the high SNR and contrast at 7 Tesla, very high-resolution data can be acquired in acceptable imaging times of less than 20 min. A few examples are given in the following. The application to neuroscience and clinical research will be described in chapters Neuroscientific Applications of High-Field MRI in Humans, Clinical Neuro and Beyond, and Oncology.

In Fig. 1, high-resolution phase data from a normal subject acquired at 3T and 7T are displayed. The data are acquired with identical resolution of 0.2 × 0.2 × 2 mm. All imaging parameters are identical with the echo time adjusted to be in the range of the average T_2* relaxation time for each field strength (30 ms for 3T and 18 ms for 7T). The overall appearance is similar between the two field strengths. However, at this high resolution, the SNR at 3T is too low to appreciate fine details such as the boundaries between gray and white matter, the laminar structure of the cortex, or the fine venous vessels that are nicely

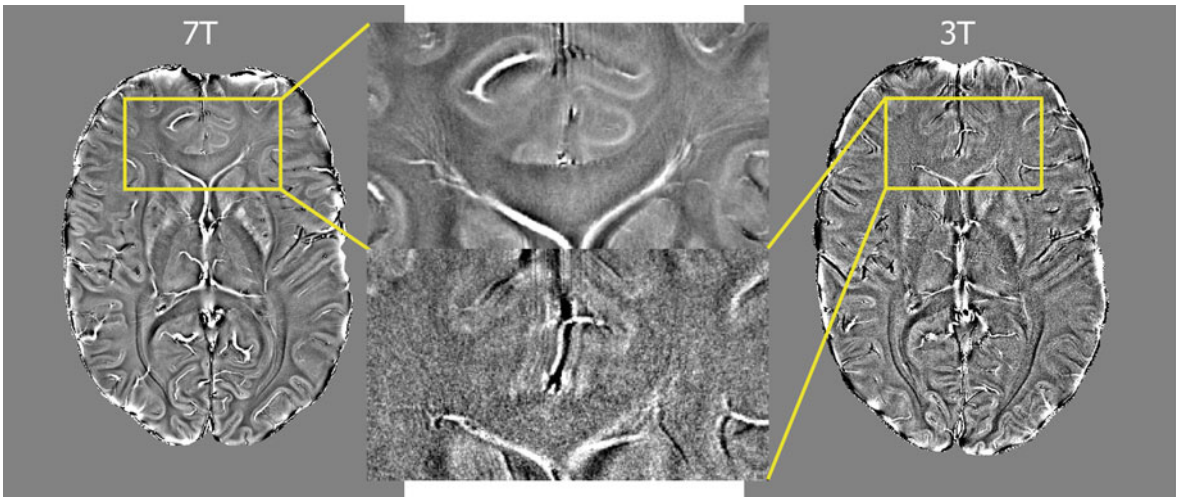

Fig. 1 Very high-resolution phase images reconstructed from a 2D gradient echo acquisition at 3T and 7T. The imaging parameters are identical with the echo time adjusted to the average T_2* time of each field strength (TR 750 ms, TE at 3T 30 ms, TE at 7T 18 ms, flip angle 45°, resolution 0.2 × 0.2 × 2 mm, both acquired with an eight-channel head coil). During the processing of the phase images, low spatial frequency background variations due to macroscopic field inhomogeneities have been removed to highlight the structure-related image phase

depicted at 7T. In addition, due to the longer echo time that is required to achieve this contrast at 3T, the number of slices per TR is lower, and therefore, the spatial coverage is even larger at 7T within the same scan time of about 10 min. Such T_2* or phase-based gradient echo acquisitions are likely the methods that benefit most from high field strength: higher SNR, stronger contrast, shorter echo time needed and thus larger coverage. These advantages have been exploited to generate the first brain anatomy atlas from 7T images that is based on high-resolution 2D gradient echo data (Cho 2010).

It has been pointed out in the previous chapter that T_1 contrast is difficult to obtain at high field strength with standard spin echo methods. For high-resolution T_1-weighted imaging, magnetization prepared methods with gradient echo–based fast acquisitions, such as MPRAGE, have become the standard for anatomical imaging at lower field strength. The application of such methods at 7T is mainly compromised by the inhomogeneous RF excitation field that leads to spatially varying signal and—more problematic—contrast. A number of methods have been proposed to correct for these effects. They are similar in that they acquire a reference image without inversion of the longitudinal magnetization. A simple combination of the two data sets can be performed through division of the inverted by the non-inverted acquisition. Because spatially varying effects of the flip angle and T_2* weighting are equal in both acquisitions, only T_1 weighting remains (Fig. 2). The methods differ in that they acquire a low- or high-resolution reference data set either in a separate or combined measurement (Marques et al. 2010; Van de Moortele 2009). This correction assumes a perfect and homogeneous inversion by the use of an adiabatic inversion pulse. However, in areas of very low RF-amplitude, the adiabatic conditions may not be met, and residual artifacts can be seen. Improvements in the design of the inversion pulse can further reduce such difficulties (Hurley et al. 2010).

With these modifications, the SNR gain of higher field strength can be exploited for higher resolution. Because no "extra gain" contributes, such as for gradient echo imaging, the possible reduction in voxel volume for 3D acquisitions is given by the SNR and/or scan time increase.

T_2-weighted imaging by the use of turbo spin echo methods has always been regarded to be a method with high RF power absorption due to the large number of high flip angle refocusing pulses. Therefore, its use at 3T was already compromised by SAR limitations. The main remedy has been the reduction of the refocusing flip angle leading to a quadratic reduction in SAR with only moderate losses in signal and modifications in the image contrast (Norris 1991).

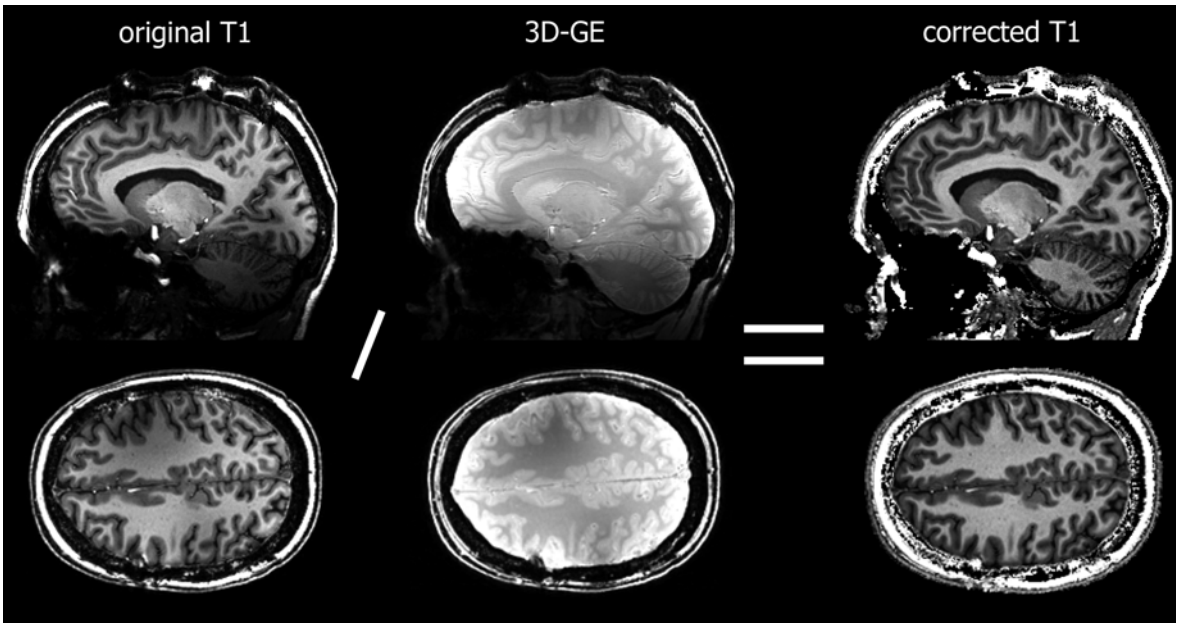

Fig. 2 T_1-weighted 3D-MPRAGE acquisition and GE reference scan for RF-inhomogeneity correction through division at 7T. The corrected data show very good homogeneity in signal and contrast, which is even improved compared to the original data due to the inverted contrast in the GE scan. The scan covers the complete patient brain with an isotropic resolution of 0.6 mm. The voxel volume is therefore only 21% of a 1-mm isotropic acquisition. High field strength, long scan time, and an optimized 24-channel receive head coil allow for very high image quality with excellent SNR, contrast, and homogeneity. The patient had prior biopsies (see scull artifacts) and tolerated the 20-min scan well without obvious motion artifacts

The introduction of variable refocusing flip angles throughout the echo train allowed routine application of (hyper-) TSE at higher field strength (Hennig and Scheffler 2001; Hennig et al. 2003; Weigel and Hennig 2008). At 7T, further reduction of SAR is achieved through the lengthening of the refocusing pulses and modification of the pulse profile by means of the VERSE (variable rate selective excitation) principle (Hargreaves et al. 2004).

An example of T_2-weighted hyper-TSE imaging at 7T is given in Fig. 3. The method has been optimized for high-field imaging by the modifications mentioned above. As a result, up to 20 slices with a resolution of $0.2 \times 0.2 \times 2$ mm can be acquired within only 4 min. The images are displayed without any further processing such as intensity correction. This demonstrates the high robustness of CPMG-based multi-spin echo methods against flip angle variations across the object.

Even more problematic than T_2-weighted TSE acquisitions at high field are T_2-weighted fluid attenuated inversion recovery acquisitions (FLAIR). Due to the required high fidelity inversion that can only be achieved with adiabatic pulses, the SAR level quickly exceeds given limits. A recently proposed remedy is the use of 3D methods where the inversion is only needed once per volume rather than once per slice (Zwanenburg et al. 2010). In order to stay within reasonable acquisition times, the combination with very long echo trains of varying low refocusing flip angle is advantageous.

The combination of high-field strength with optimized 3D imaging yields high SNR values that can be exploited for high-resolution acquisitions. In the example below, a nominal isotropic resolution of 0.8 mm with full brain coverage was achieved in 12 min (Fig. 4). However, an evaluation of the applicability of these modified methods with fluid-suppressed T_2 contrast for clinical purposes has not yet been performed.

3 Diffusion-weighted Imaging at 7T

Almost all contrast generation processes in MRI destroy signal selectively and thereby introduce signal intensity differences. Some of the most extreme

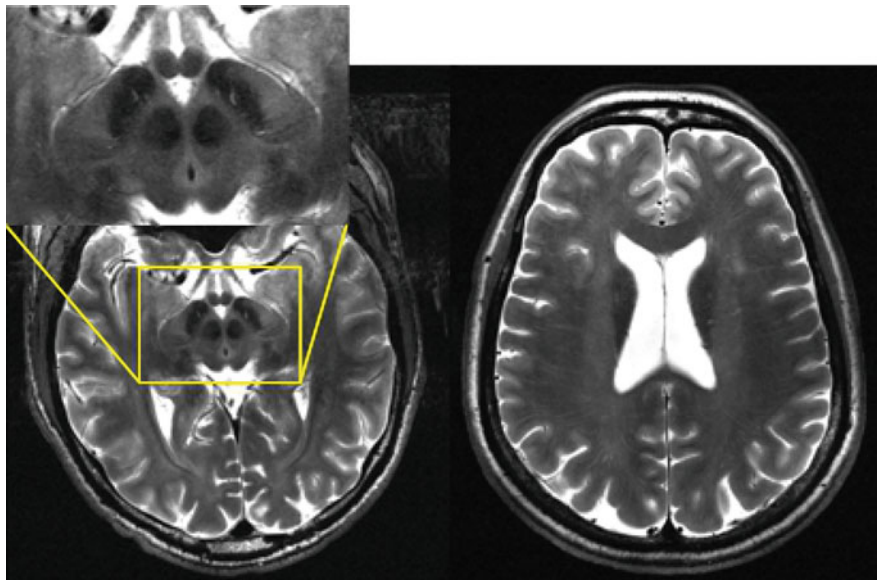

Fig. 3 Hyper-TSE images acquired at 7T. In order to stay within the safe SAR limits, the flip angle variation along the echo train has been optimized, the refocusing pulse length has been increased to 6 ms, and the pulse profile has been modified according to the VERSE principle. In this acquisition, 18 slices with a very high resolution of 0.2 × 0.2 × 2 mm were covered within only 4 min. The images show exquisite detail demonstrating contrast within the white matter suggestive of orientational dependence on the fiber structure. Also, high contrast in the deep nuclei can be seen. The image intensity is only 10% lower than a reference single slice acquisition without the SAR reduction methods

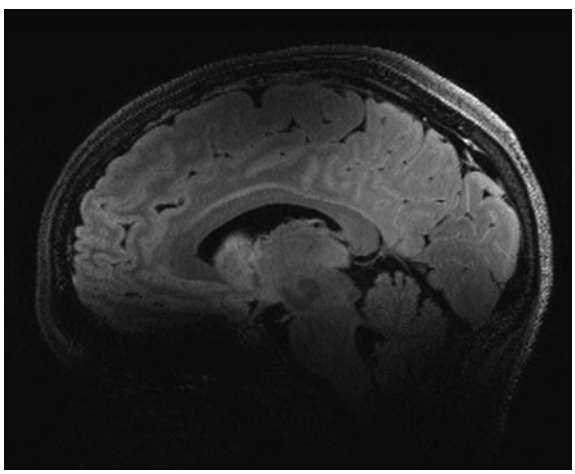

Fig. 4 T_2-weighted 3D fluid attenuated inversion recovery scan at 7T with a nominal isotropic resolution of 0.8 m. The midsagittal slice demonstrates good suppression of CSF. The effective T_2 contrast for the nominal echo time of 320 ms is significantly lower due to the use of very low refocusing flip angles and similar to a 2D acquisition with an echo time of 70 ms

methods with respect to signal destruction are diffusion-weighted imaging (DWI) or diffusion tensor imaging (DTI). In order to encode directional information of the underlying anatomical structures, strong and long gradient pulses have to be applied that reduce the signal according to the microscopic noncoherent motion of magnetization. In order to generate sufficient contrast, i.e., between motion parallel and perpendicular to fiber structures, the tissue signal is attenuated by an order of magnitude or more. In addition, many acquisitions with different diffusion gradient encoding directions are needed. Sufficient volume coverage can only be achieved with very fast imaging methods that further reduce the SNR. As a consequence, diffusion-weighted methods are notoriously SNR hungry. It is therefore tempting to move such measurements to higher field strength. Diffusion-weighted applications could benefit significantly from higher SNR in order to improve otherwise limited resolution. A closer look at current diffusion measurement methods reveals a number of challenges in this transition to higher field strength. Diffusion encoding gradients are long and thus lead to long echo times. Many vendors use double instead of single spin echo signal generation in order to allow eddy current–compensated gradient schemes. This further prolongs the minimum echo time and introduces strong signal

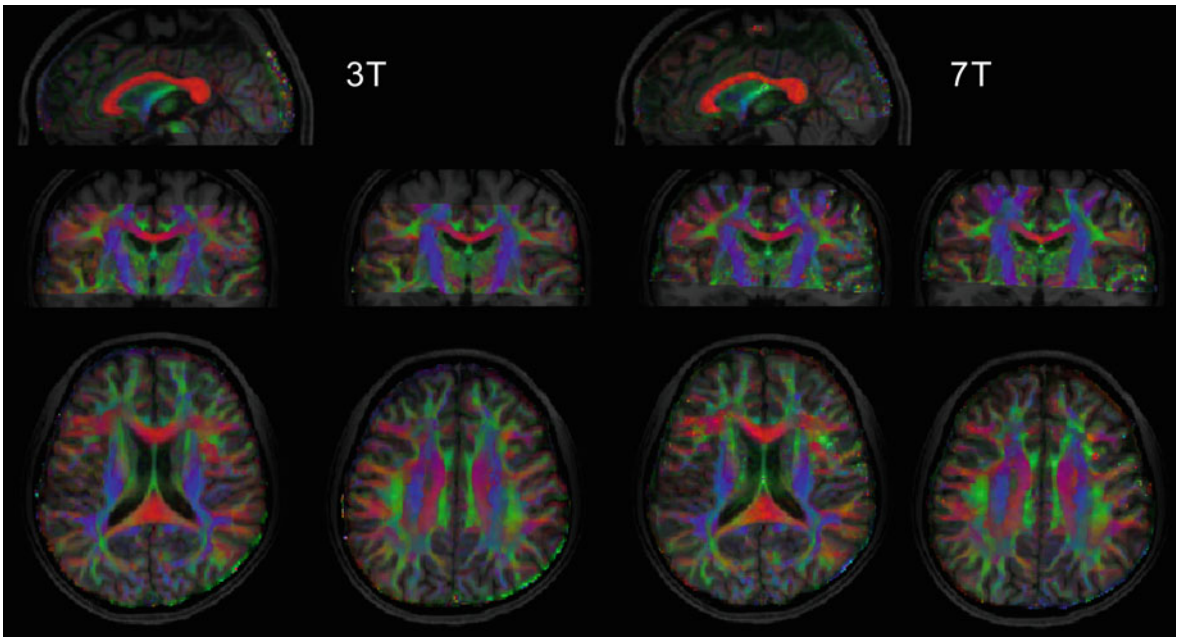

Fig. 5 DTI images acquired in the same subject at 3T and 7T with double spin echo EPI. The images have an isotropic resolution of 1.9 mm covering 35 slices. The b-factor is 800 s/mm^2 and 12 directions with four averages were measured. The images appear very similar. However, the SNR of the 7T data is about 15% lower than of the 3T data

inhomogeneities due to flip angle variations. The diffusion encoding strength is given by the so-called b-factor. For a commonly used b-factor of 1,000 s/mm^2, the minimum echo time on commercially available whole body–gradient hardware is about 80 ms. As described in the previous chapter, the T_2 relaxation time decreases with higher field strength. Therefore, the higher available magnetization is decaying faster during the diffusion encoding time. If the average T_2 of brain tissue is reduced from 75 ms at 3T to 50 ms at 7T, as suggested in first studies, the increased magnetization at 7T will almost decay to the 3T value at the echo time of 80 ms. This suggests that diffusion-weighted methods with the commonly used measurement methods (double spin echo EPI) cannot be expected to improve much from higher field strength. Due to all these factors and the general challenges at high field strength, diffusion had been regarded to be very difficult at 7T.

A comparison of diffusion tensor data in the same subject at 3T and 7T with very similar acquisition parameters is shown in Fig. 5. In this example with an echo time of 80 ms and a b-factor of 800 s/mm^2, the SNR of the 7T data is approximately 15% lower than that of the 3T data reflecting the reduction due to imperfect refocusing pulses. However, this can be regarded a small success because DTI measurements at 7T are possible, and therefore, subjects do not necessarily require a second examination at lower field strength.

The comparison may change to the benefit of 7T with future developments exploiting other diffusion encoding strategies or using stronger gradient systems that allow a reduction of the echo time. Although such developments will also improve the image quality and SNR at lower field strength, high-field DTI measurements are likely to benefit more due to the shorter T_2 relaxation time.

4 Non-contrast Angiography

The use of contrast agent in the acquisition of arterial first-pass bolus angiograms has allowed for fast and robust measurements of the arterial vasculature in most parts of the body including the abdomen and extremities. However, the fast bolus passage limits the acquisition time to a few seconds and thus the achievable resolution. For depiction of the intricate anatomy of the neurovascular system, very high

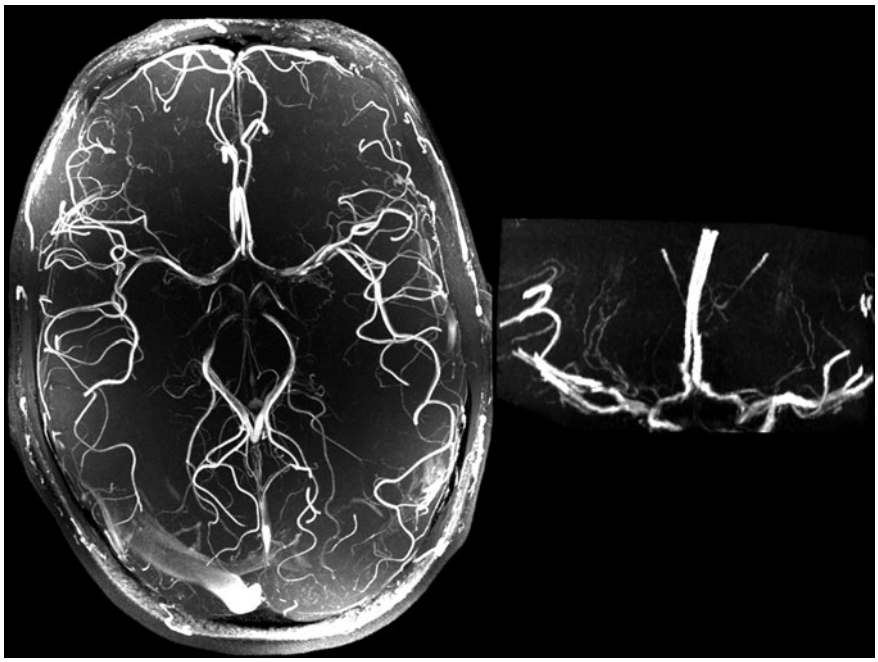

Fig. 6 Maximum intensity projections through a 3D ToF angiogram of a healthy volunteer in axial direction (left) and a targeted MIP of the lenticulostriate arteries branching of the middle cerebral arteries. Although the SNR in this high-resolution acquisition (0.3 × 0.3 × 0.4 mm) is very high and the arteries are well depicted even into the periphery of the vascular system, the background suppression is less efficient compared to lower field acquisitions. The venous suppression is also reduced (see superior sagittal sinus) because no spatial saturation has been added due to SAR constraints

resolution is desirable. Therefore, non-contrast enhanced time-of-flight (ToF) methods are frequently applied despite their significantly longer acquisition times.

ToF methods exploit the fact that unsaturated blood is entering the imaging volume during the repetition time and therefore yields much higher signal intensity than stationary tissue that is repeatedly saturated due to the short TR excitation pulses. At high field strength, ToF benefits not only from the higher SNR but also from the increase in longitudinal relaxation times. The increased tissue T_1 results in stronger background suppression. In addition, the longer blood T_1 increases the lifetime of the unsaturated magnetization that enters the imaging volume. Together, an increase in vessel-to-background contrast can be expected in addition to the linear SNR increase. However, other factors can compromise this gain. Mainly, the SAR limitation is of importance. In order to achieve high vessel signal and strong background suppression, a high flip angle with short TR is desired. This may not be achievable in all situations. In addition, the background signal can be further suppressed through the application of magnetization transfer pulses that saturate only brain tissue signal with its macromolecule contribution, whereas blood signal is not reduced. Such MT-pulses have to be omitted at very high field strength (Ladd 2007).

Altogether, ToF angiography is one of the "more-than-linear" winners of high magnetic field strength, and very high-resolution ToF angiography of the neurovascular system has shown unprecedented detail such as the lenticulostriate arteries that deliver blood from the middle cerebral artery to the basal ganglia (Kang et al. 2009). The high signal and contrast of this method allows very high-resolution 3D acquisitions with high acceleration factors due to the sparse nature of the vascular anatomy. Figure 6 shows a 3D ToF angiogram with very high resolution of 0.3 × 0.3 × 0.4 mm acquired in only 10 min. More details on angiographic methods and their clinical applications are presented in Clinical Neuro and Beyond.

References

Cho Z-H (2010) 7.0 Tesla MRI: brain atlas: in vivo atlas with cryomacrotome correlation. Springer, Heidelberg

Hargreaves BA et al. (2004) Variable-rate selective excitation for rapid MRI sequences. Magn Reson Med 52(3):590–597

Hennig J, Scheffler K (2001) Hyperechoes. Magn Reson Med 46(1):6–12

Hennig J, Weigel M, Scheffler K (2003) Multiecho sequences with variable refocusing flip angles: optimization of signal behavior using smooth transitions between pseudo steady states (TRAPS). Magn Reson Med 49(3):527–535

Hurley AC et al. (2010) Tailored RF pulse for magnetization inversion at ultrahigh field. Magn Reson Med 63(1):51–58

Kang CK et al. (2009) Imaging and analysis of lenticulostriate arteries using 7.0-Tesla magnetic resonance angiography. Magn Reson Med 61(1):136–144

Ladd ME (2007) High-field-strength magnetic resonance: potential and limits. Top Magn Reson Imaging 18(2): 139–152

Marques JP et al. (2010) MP2RAGE, a self bias-field corrected sequence for improved segmentation and T_1-mapping at high field. Neuroimage 49(2):1271–1281

Norris DG (1991) Ultrafast low-angle RARE: U-FLARE. Magn Reson Med 17(2):539–542

Van de Moortele PF et al. (2009) T_1 weighted brain images at 7 Tesla unbiased for proton density, T_2* contrast and RF coil receive B_1 sensitivity with simultaneous vessel visualization. Neuroimage 46(2):432–446

Weigel M, Hennig J (2008) Development and optimization of T_2 weighted methods with reduced RF power deposition (Hyperecho-TSE) for magnetic resonance imaging. Z Med Phys 18(3):151–161

Wiesinger F, Boesiger P, Pruessmann KP (2004) Electrodynamics and ultimate SNR in parallel MR imaging. Magn Reson Med 52(2):376–390

Zwanenburg JJ et al (2010) Fluid attenuated inversion recovery (FLAIR) MRI at 7.0 Tesla: comparison with 1.5 and 3.0 Tesla. Eur Radiol 20(4):915–922

Neuroscientific Applications of High-Field MRI in Humans

Robert Turner

Contents

Abstract

The chief advantages of using high-field MRI for neuroscientific research are the improvements in spatial resolution and contrast that become available. Neuroscientists are interested in the spatial organisation of brain grey matter, in cortex and deep brain structures, and in the connectivity of white matter neuronal fibres. At lower field, it is very hard to distinguish cortical areas purely by their anatomical differences, or to discriminate subcomponents of basal ganglia and thalamus. This has led to a widely accepted method of functional image analysis involving warping of individual brains to a standardised template, together with significant image smoothing, which eliminates the possibility of detailed MRI-based mapping of human brain, and severely handicaps the exploration of individual differences and monitoring of brain changes over time. Even at a field of 3 T, the spatial resolution of MR tractography is limited to about 1.5 mm isotropic, hindering discrimination of crossing fibres. However, at fields of 7 T and above, the available high isotropic resolution of 0.4 mm and the varying myelin content of grey matter allow several cortical areas to be quite easily distinguished, and the varying iron content of deeper brain structures reveals their internal features. Higher spatial isotropic resolution in tractography can also be achieved, of 1 mm or better. Because blood oxygenation-dependent contrast (BOLD) also improves at high field, functional maps with submillimetre resolution can be acquired, showing

R. Turner (✉)
Max-Planck-Institute for Human Cognitive and Brain Sciences, Leipzig, Germany
e-mail: turner@cbs.mpg.de

J. Hennig and O. Speck (eds.), *High-Field MR Imaging,* Medical Radiology. Diagnostic Imaging,
DOI: 10.1007/174_2010_103, © Springer-Verlag Berlin Heidelberg 2011

columnar structures such as ocular dominance and orientation columns. These results will enable a much more precise correlation of brain functions with the neural tissue that supports them, and is likely to bring about major conceptual changes in systems neuroscience, especially in analysis methodology.

1 Introduction: Current Uses of MRI in Human Neuroscience

When MRI was developed in the 1970s, the major professional interest in applications came from radiology, but since about 1985 neuroscientists have become progressively more interested in MR brain imaging. At first this interest focused on the possibility of correlating low-resolution PET images of brain activity with higher resolution anatomical images, but with the invention by Ogawa et al. (1990), Turner et al. (1991) and Kwong et al. (1992) of blood oxygenation-dependent (BOLD) functional MRI in the early 1990s this picture changed dramatically. In 1995, dedicated MRI scanners had already been installed in several neuroscience laboratories, such as the Functional Imaging Laboratory in Queen Square, London.

Parallel to these developments in functional MRI, there have been many excellent studies of neurophysiology, almost all at high magnetic field. Typical of these are the studies by Goense and Logothetis (2008), Mangia et al. (2007) using MR spectroscopy to investigate neurometabolism and Kim et al.'s (1999) development of $CMRO_2$ imaging methods (Zhu et al. 2008). Other powerful approaches include the study of neuroanatomy using tractography and manganese fibre tracking (Lin et al. 2001; Simmons et al. 2008), and function using BOLD contrast and, more recently, blood pool contrast agents (e.g. Leite et al. 2002; Jin and Kim 2008).

In 2009, MRI was seen as the most important means of understanding the spatial organisation of human brain function. Functional MRI, using some form of echo-planar imaging (Mansfield 1977), has been routinely used at field strengths up to 3 T, to track over time local changes in cerebral blood oxygenation induced by experimental conditions experienced by the human subject, with durations from milliseconds to tens of seconds. Such conditions range from active tasks to passive experiencing of stimuli, and even to the low-level task of lying still within the scanner. The dominant methods of analysis (SPM, FSL, AFNI, etc.) used the General Linear Model to create parametric maps of areas of cortex with condition-correlated activation. In order to simplify statistical inference, and to allow easy comparison across subject groups, data were almost always smoothed from a raw acquired isotropic resolution of about 3–6 mm or more. From such maps, it must be said, a great deal has been learned regarding the functional specialisations of particular brain areas.

Anatomical (or 'structural') MRI is used to provide images of higher resolution and better grey/white matter contrast, in order to give better identification of the location of activated areas, and also to enable comparisons over time and across subject of the morphometry of grey and white matter. For this latter purpose the technique of voxel-based morphometry (VBM) was devised, which used a statistical construct, 'grey matter density' as a practical variable with easily manageable statistical characteristics (Ashburner and Friston 2000). This allows fast and relatively accurate comparison of brain morphometry across subjects or time. Smoothing of image data is again required, up to 10 mm.

A further neuroscientific use of anatomical brain images has been found in the area of electrophysiology. Both EEG and MEG suffer from similar problems of source localisation, due to the ill-conditioned nature of the electromagnetic inverse problem. However, considerable progress has been made in correlating the spatial and temporal behaviour of neural activity using the constraint that the sources lie somewhere in the cortical sheet, which can be quite precisely located using MRI data (Lin et al. 2006).

The fact that MR images can be sensitised to the movement of water molecules in any desired direction, using 'diffusion gradients' inserted between spin excitation and data acquisition has opened up another very important area of neuroscience research. This concept was first developed by Le Bihan in 1986 but only became practicable when Turner et al. (1990a, b) recognised that the use of snapshot diffusion-weighted EPI would avoid the severe motion artefacts

normally associated with more conventional MRI acquisition in living subjects. Because water movements in nerve fibres are highly anisotropic, with water molecules crossing membranes only with difficulty, DW-EPI turned out to have great power in assessing the orientation of axonal bundles forming brain white matter (Moseley et al. 1990). Out of this has arisen the concept of 'fractional anisotropy' (FA), a quantitative scalar measure of the anisotropy of diffusive water movement in brain tissue, usually white matter (Basser et al. 1994). Since FA is a scalar, FA maps can be analysed and compared across subjects and across time, using established GLM methods. From the same diffusion-weighted imaging data the structure of the larger fibre tracts can also be inferred (Basser et al. 2000), giving rise to the expanding research area of MR tractography, which provides for the first time a reasonably accurate in vivo picture of brain connections on a scale of millimetres.

The observation made by Biswal et al. (1995), as a student, that low-frequency fluctuations of BOLD signal in human brain showed non-random spatial correlations between coupled areas considered to have structural connections, has led to a very large field of enquiry loosely described as 'resting state fMRI', even though such spontaneous fluctuations are now known to persist during imposed tasks, and to depend on preceding and awaited task conditions even when no task is present. The resting state connectome, as it is called, appears to correlate quite well with the structural connectome (Honey et al. 2009).

In all of these fields of enquiry, except tractography, two implicit or explicit assumptions have been made. The first is that MRI cannot discriminate between anatomically distinct adjacent areas of cortex, because it has inadequate spatial resolution and there is insufficient contrast within grey matter. The second assumption, a corollary to the first, is that it is enough for neurocognitive purposes to identify brain areas of activation or altered grey matter density by citing only the co-ordinates in MNI space that characterise the peak in a heavily smoothed parametric map of the relevant variable.

The advent of very high-field MRI brings the first of these assumptions into question, and opens a debate regarding the desirability of maintaining the second. In order to clarify this point, it is important to appraise the potential neuroanatomical capabilities of MRI, given higher SNR. What characteristics of tissue affect anatomical MRI signal?

2 Myelin and Myeloarchitecture in the Brain

2.1 Myelin

Brain tissue comprises about 70–80% water, about 12% lipids and about 8% protein, the proportions depending on whether the tissue is white or grey matter (O'Brien and Sampson 1965). As the major structural element, lipids mostly form the membranes constituting cell walls, myelin axonal sheaths and the walls of intracellular organelles such as mitochondria. Membranes characteristically have low water permeability, and thus strongly constrain water diffusion. Since lipid protons have a typically short T_2, they can be detected spectroscopically only with a very short echo time, but membranes have a powerful effect on the relaxation of nearby water protons, reducing both their T_1 and T_2. Furthermore, myelin has a powerful magnetisation transfer effect on water, due to exchange of water protons with lipid OH and NH endgroups, and the presence of cholesterol, which comprises about 35% of the total lipid content of brain tissue and is embedded inside the membrane (Koenig 1991). In addition, it is possible that iron-containing proteins found in the oligodendrocytes that generate the myelin sheaths may also play a direct role in T_2* and MR phase contrast (Li et al. 2009). Brain tissue with high lipid content, such as white matter, has a resulting reduced water content, and thus a smaller water proton density.

Thus, it can be stated that the major source of contrast in MR images of brain tissue is myelin, for any MRI modality—whether T_1 contrast, T_2 contrast, T_2* contrast, proton density contrast, magnetisation transfer contrast, or diffusion-weighted contrast. Quantitative T_1 maps of human brain strikingly resemble cadaver brain sections stained for myelin (Fig. 1). Another important source of contrast, iron sequestered in the form of ferretin, dominates only in the relatively small subcortical structures of the putamen, caudate nucleus, red nucleus, subthalamic

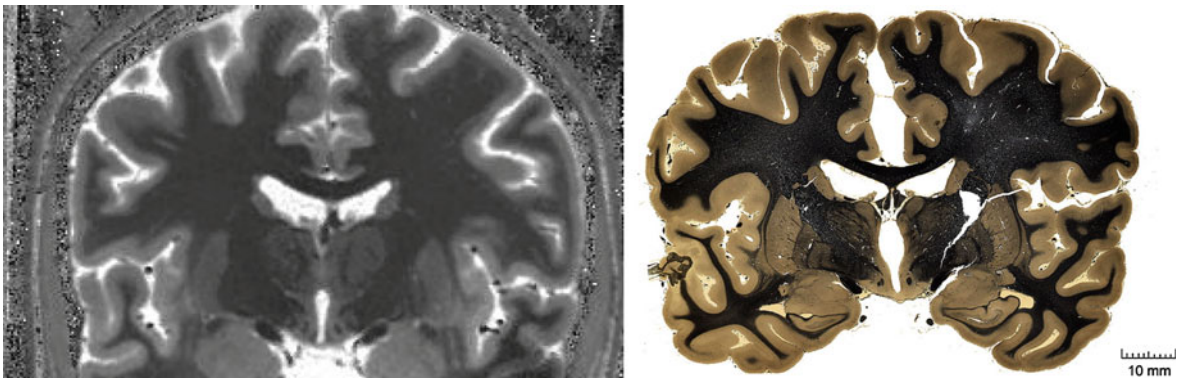

Fig. 1 Comparison between a T_1 map (*left*) obtained at 7 T in vivo using inversion recovery MP-RAGE MRI (0.5-mm isotropic resolution, nine inversion times) and a similar section of cadaver brain (*right*) stained for myelin (courtesy of JI Johnson, Michigan State University)

nucleus and substantia nigra. This enables exquisite depiction of these brain organelles (Fig. 2).

2.2 Myeloarchitecture

Brain cortical myeloarchitecture has been sadly neglected for almost a century. In the early 1900s, Oscar and Cecile Vogt made impressive analyses of cortical myeloarchitecture, but their magnum opus, published in 1919, has never been translated into English. Neither has the important work of Paul Flechsig (1920). Much greater attention has been paid, on the other hand, to cytoarchitectonic parcellations of human grey matter, typified by the classic work of Brodmann (1909). At the time of writing, the majority of imaging neuroscientists use this classification scheme to indicate the location of cortical areas specific to particular tasks.

MRI has been an important clinical modality nearly 30 years. However, MRI is insensitive to cytoarchitectonic differences across cortical areas. The neuronal cell bodies, visualised by the Nissl stain and forming the basis of Brodmann area classification, have similar water content and similar size distributions in each area, and thus show similar MRI contrast. Nevertheless, MR scientists have shown very little interest in myeloarchitectonic studies. However, any random section of human cadaver brain tissue shows a great deal of myelin structures within the cortex, with clearly defined territories that are highly likely to correspond closely with the much more familiar Brodmann areas (see Fig. 3).

3 Benefits of High-Field MRI

Numerous studies (e.g. Otazo et al. 2006) have demonstrated that spectroscopic signal-to-noise ratio (SNR) increases approximately linearly with field strength, given a long TR time and 90° flip angle. Different imaging strategies benefit from this increase in different ways, due to the field dependences of T_1 (which increases) and T_2 (which decreases).

Structural imaging techniques using low flip angles, such as FLASH and MP-RAGE, do not gain the full linear increment in SNR, because the increased T_1 implies a reduced Ernst angle (at which the steady-state magnetisation for a train of pulses is maximised), and thus a smaller fraction of the available spin magnetisation. On the other hand, techniques such as Turbo-Spin-Echo (TSE) (De Vita et al. 2003) and Gradient Echo and Spin Echo (GRASE) gain SNR super-linearly, because the longer T_1 means that the echo train decays more slowly, and thus the acquisition window for each excitation can be longer. One of the major technical problems at ultra-high field is the roughly quadratic increase in RF power deposition (i.e. higher specific absorption rate, SAR), which makes TSE problematic already at 7 T. While the Hyperecho technique (Weigel and Hennig 2006) reduces this problem, much more freedom from SAR difficulties can be achieved using GRASE (Oshio and Feinberg 1991), with substantially the same advantages as TSE in image SNR and contrast.

For gradient-echo EPI, used in most fMRI studies, the gain of SNR with field strength is in principle

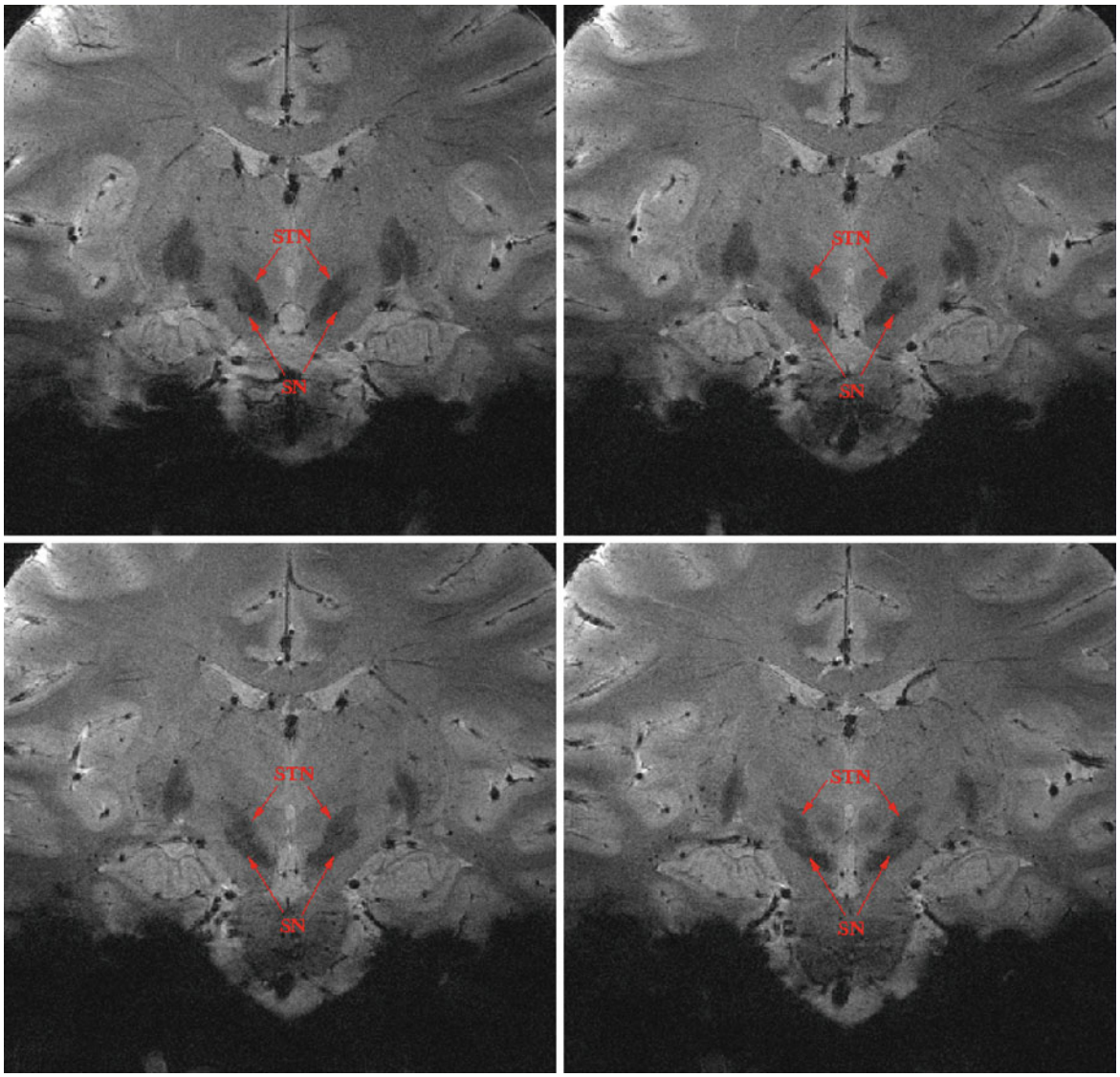

Fig. 2 Four adjacent slices of normal human brain at 7 T, using a 24-channel Nova RF coil and a 2D FLASH sequence with in-plane resolution of 230 × 230 μm^2, slice thickness 1 mm. Subthalamic nucleus and substantia nigra (indicated by *arrows*) can be clearly discriminated

approximately linear, even though T_2* of grey matter is only about 25 ms at 7 T, because a shorter echo time can still obtain good BOLD contrast. Acceptable image quality can only be achieved at 7 T, however, by employing parallel imaging with an acceleration factor of 3 or 4, which can reduce SNR. Figure 4 shows the complete set of 100 slices using gradient echo EPI to cover most of the brain at 1-mm isotropic resolution. The TR time was only 5.4 s. FMRI contrast-to-noise (CNR) is a more complicated story because the signal from spontaneous fluctuations of blood oxygenation must be considered, which also scales with field strength.

The SNR of an increasingly important sequence, diffusion-weighted EPI (Turner et al. 1990a, b), is more difficult to maintain at high-field strength. Accurate determination of diffusion parameters requires application of diffusion gradients giving a

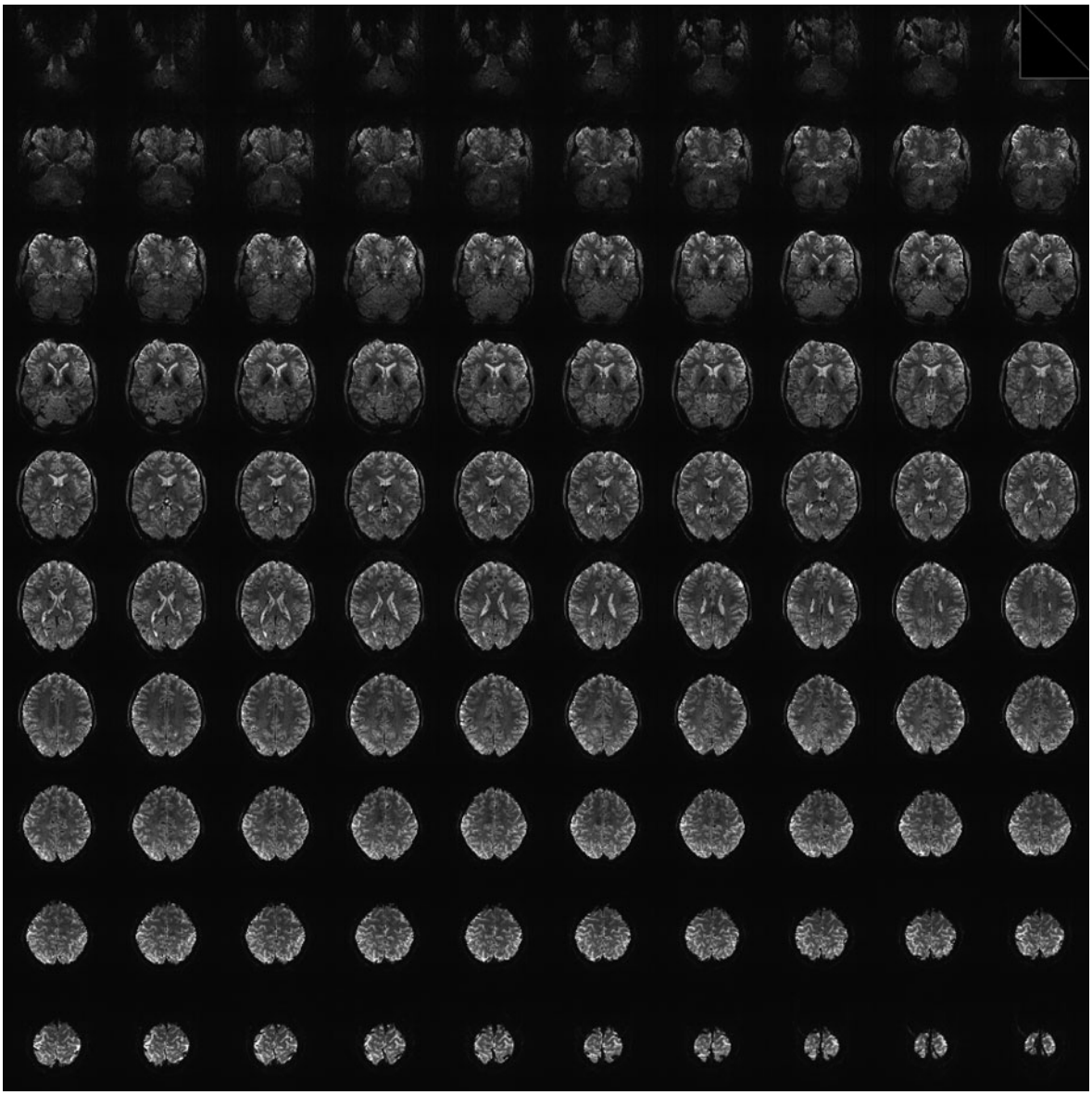

Fig. 3 Gradient-echo EPI images at 7 T of normal human in vivo, with 1-mm isotropic resolution. GRAPPA acceleration factor = 4

high b-factor, which generally means a relatively long duration of more than 20 ms per lobe. This makes the eventual echo time TE quite long, above 70 ms even when a high-acceleration factor is used, by which time the shorter T_2 at 7 T has caused much of the signal to disappear. Only by means of very powerful gradients (best provided by a head-only set of gradient coils) can a shorter TE be achieved, and thus higher image intensity.

4 In Vivo Neuroanatomy at High Field

As pointed out by Pierre Robitaille as early as 1999 (Abduljalil et al. 1999), ultra-high-field MRI opens a new window into the anatomy of the human brain. It provides high contrast and high resolution. Good quality images of the entire brain with 0.5-mm

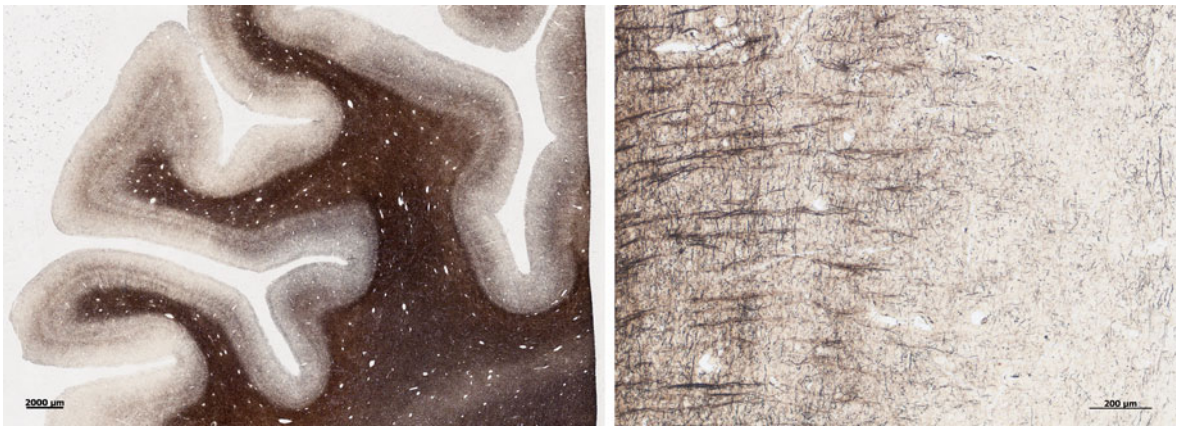

Fig. 4 Micrographs of myelin-stained sections of human cadaver brain (prepared by Reimann and Geyer). *Left* General view showing spatial variation of myeloarchitecture and bands of Baillarger; *right* close-up showing intersecting fibre orientations

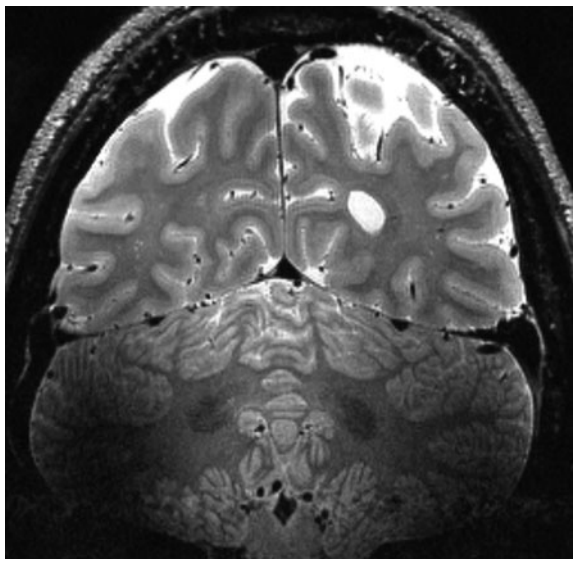

Fig. 5 Coronal MRI scan of human occipital lobes at 7 T, in vivo, showing the Stria of Gennari in the calcarine sulci. Turbo-spin-echo (TSE) image, single average, with 24-channel array coil (Nova Medical), TR/TE = 4,330/27 ms, voxel size 0.5 × 0.5 × 0.5 mm^3, scan time 11:40 min for 30 slices

isotropic resolution can be obtained in about 10 min. Significant volumes of brain tissue can indeed be acquired in acceptable scan times with 0.05 mm^3 voxel volume.

Tissue contrast results from differences in T_1, T_2, T_2*, MTC, MRI phase and diffusion characteristics caused by the presence of myelin, and differences in T_2, T_2* and phase caused by the presence of iron. As a result of myelin contrast, at least one of the bands of Baillarger is distinguishable in several cortical areas with many types of MRI sequence. These are layers of myelinated fibres, found in some cortical areas but not others, which run parallel to the cortical surface (Fig. 3). Their thickness is typically 0.3 mm or less. Figures 5 and 6 show the appearance of these myelinated layers in identified cortical areas. For comparison, Fig. 7 shows the appearance in a 3-T MR image (Turner et al. 2008) of the most visible such layer, the Stria of Gennari that defines primary visual cortex.

A further example of the capability of 7-T MRI to identify cortical areas via their myeloarchitecture is shown in Fig. 8. The primary auditory cortex, A1, is known to lie on Heschl's Gyrus, a distinctive feature of the superior temporal lobe (although this is sometimes found doubled or even tripled). A1 has characteristically somewhat denser myelination than adjacent cortical areas (Hackett et al. 2001; Bock et al. 2009). T_1-weighted images show a decreased T_1 on the crown of Heschl's Gyrus, which has been used to parcellate A1 using 3-T MRI (Sigalovsky et al. 2006). When quantitative maps of T_1 are created at 7 T using inversion recovery images this appears clearly (Fig. 8a) because image intensity variations due to inhomogeneous RF fields are thus removed. Such maps may be segmented to produce an estimate of the extent of A1 in each hemisphere (Fig. 8b).

It is anticipated that many more cortical areas will be identifiable by similar means. Automated image analysis techniques are under development that can cluster data, without supervision, into spatially

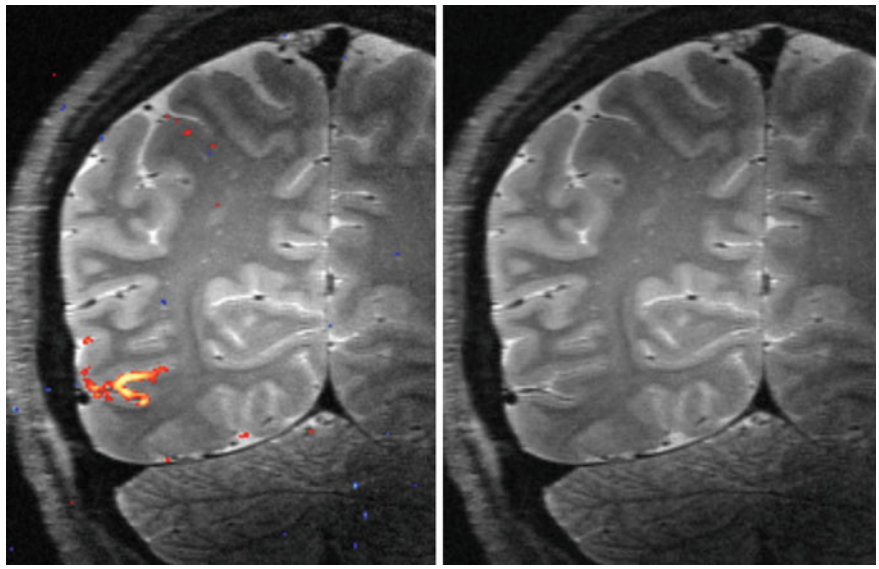

Fig. 6 Coronal TSE image at 7 T of human occipital lobes, showing cortical area V5/MT. *Right* fMRI activation map with isotropic resolution of 1.2 mm, highlighting V5 activated with an expanding star-field visual stimulus, superimposed on a 0.5-mm isotropic resolution TSE image. *Left* TSE image only, showing underlying layer structure in this region

compact areas with similar cortical structure. The implications of this work for imaging neuroscience are highly significant.

The most popular current strategies in imaging neuroscience, as mentioned earlier, involve localisation with reference to poorly defined 'Brodmann Areas' identified by matching a smoothed, averaged activation map with Talairach's approximate indication (Talairach and Tournoux 1993) of these cortical subdivisions on a single quite atypical cadaver brain, or by comparing the individual data with the Jülich probabilistic atlas (Eickhoff et al. 2005) which synthesises results from ten cadaver brains. However, where specific cortical areas can be identified by their MRI characteristics, activations can be localised in a far more meaningful way, by reference to areas with precise boundaries defined by myeloarchitecture and hence cytoarchitecture (Bridge et al. 2005; Walters et al. 2007; Hinds et al. 2009), rather than as at present, to a single point in MNI space. Researchers are starting to associate structure and function much more directly, which will enable them thus to address questions at the heart of neuroscience relating neuronal organisation with neural computational processes.

Beyond this lies the possibility of a radical rethink of how task-related and spontaneous activation patterns are analysed, and how human brains are compared across subject and time. If a sufficient number of corresponding cortical areas can be identified and their borders mapped using high quality in vivo anatomical MRI, there should be no need for the current practice of warping to a template brain and smoothing. Instead, the averaging necessary to provide summary statistics could be performed on an area-by-area basis, comparing like with like, and thus avoiding an enormous amount of what is now guesswork and hope that the normalisation procedure has in fact aligned corresponding areas in the different subjects' brains. Furthermore, the statistical power in functional and morphometric studies is likely to increase dramatically, since a major spatial source of variance would thus be removed.

5 fMRI at High Field, Columnar Structure and Precise Localisation

Since the earliest days of fMRI, when the Ugurbil group at Minnesota (Ogawa et al. 1992) and the Turner group at NIH (1993) first demonstrated at 4 T that BOLD contrast increased with field strength, there has been growing interest in the ultimate limits of fMRI spatial and temporal resolution. Given the known neural architecture of human primary visual cortex, organised as ocular dominance columns, roughly parallel bands about 1 mm across and alternately receptive to each eye, it was natural that resolving these columns should be one of the first challenges addressed by fMRI researchers. In 1992, at

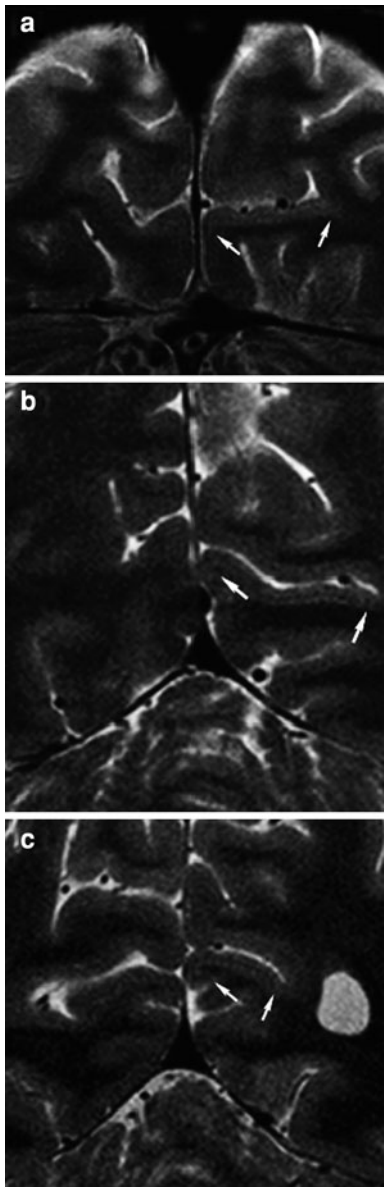

Fig. 7 Coronal TSE sections of occipital lobes of three volunteer subjects at 3 T. Resolution 0.4 × 0.4 × 0.5 mm^2, acquisition time 40 min for ten slices

the usual field strength of 1.5 T, it was generally necessary to use voxels of 3 mm or more to obtain adequate SNR, though there were sporadic efforts (e.g. Frahm et al. 1993) to use smaller voxels. Clearly higher sensitivity would be needed to resolve ocular dominance columns, and in 1997 this was achieved by Menon, working at 4 T (Menon et al. 1997). He used a segmented FLASH sequence to achieve an in-plane resolution of 0.55 mm, with 4-mm slice thickness, and studied a volunteer subject with a flat calcarine sulcus, so that the five image slices obtained could be aligned parallel with the grey matter surface. At the time this result was controversial, but it has since been adequately replicated (Cheng et al. 2001; Yacoub et al. 2007).

It is interesting to note how little impact this demonstrated competence of BOLD fMRI has had on mainstream neuroscience. The most highly cited of Menon's papers (1997) on the topic received only 124 citations by 2009, and the great majority of these were by other MRI scientists, not by neuroscientists. It may be the case that this refinement of fMRI is providing answers to questions regarding neuronal organisation that have not yet become important to those hoping better to understand how the brain works.

Nonetheless, further evidence of the value of high-field fMRI in distinguishing local patterns of neural specialisation continues to appear. Retinotopic maps of visual cortex with the unprecedentedly high spatial resolution of 1.1 mm isotropic have been produced at 7 T (Hoffmann et al. 2009). Recently, Yacoub et al. (2008) showed that visual orientation columns in human primary visual cortex could also be detected at 7 T (Fig. 9), confirming previous work on cats (Fukuda et al. 2006). Cortical layer-dependent activity has been noted in animal studies (Zhao et al. 2006; Goense and Logothetis 2006). The highest spatial resolution appears to be obtained using spin-echo BOLD, which detects changes of oxygenation only in the smallest cerebral vessels (Boxerman et al. 1995), or cerebral blood volume-dependent techniques that for best sensitivity entail injection of a blood pool contrast agent (e.g. Leite et al. 2002), used for this purpose so far only in animal models. If layer-specific activity could be reliably detected in humans, the layer-dependent efferent and afferent organisation of all cerebral cortex could be demonstrated and further explored.

The importance of performing fMRI at ultra-high field has been demonstrated by several groups. It was Hyde et al. (2001) who first pointed out that the effect on fMRI signal of spontaneous fluctuations (Biswal et al. 1995) in blood oxygenation scales with field in the same way as task-correlated changes, thus determining an optimal voxel size dependent on field strength. This important insight was followed up by Krüger and Glover (2001) and explored fully by Triantafyllou et al. (2005). To

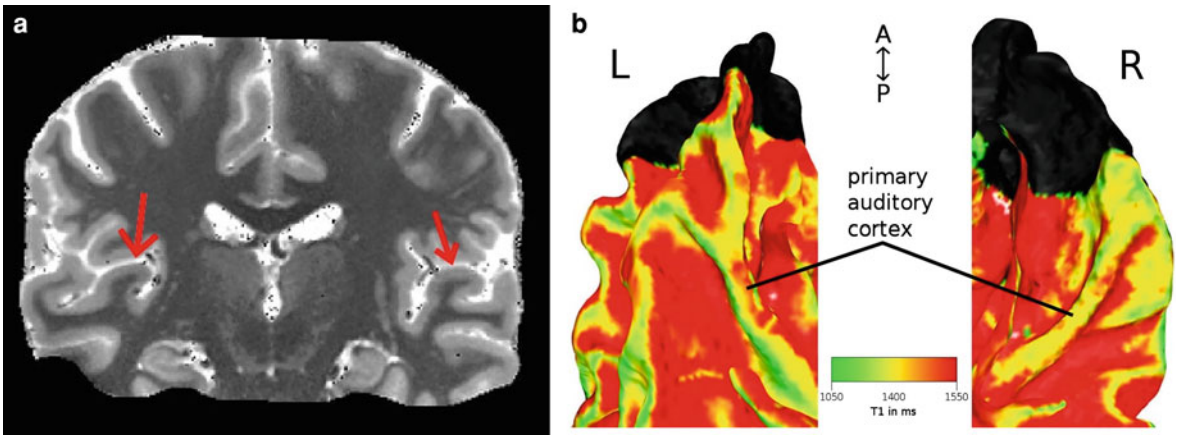

Fig. 8 *Left* Coronal T_1 map at 7 T, 0.5-mm isotropic resolution, passing through Heschl's Gyrus bilaterally. Crown of Heschl's Gyrus has a shorter T_1. *Right* Volume rendered cluster analysis of cortical intensity data, obtained using mean values of central 50% of cortical profiles. Primary auditory cortex appears as a separate cluster on the crown of Heschl's Gyrus

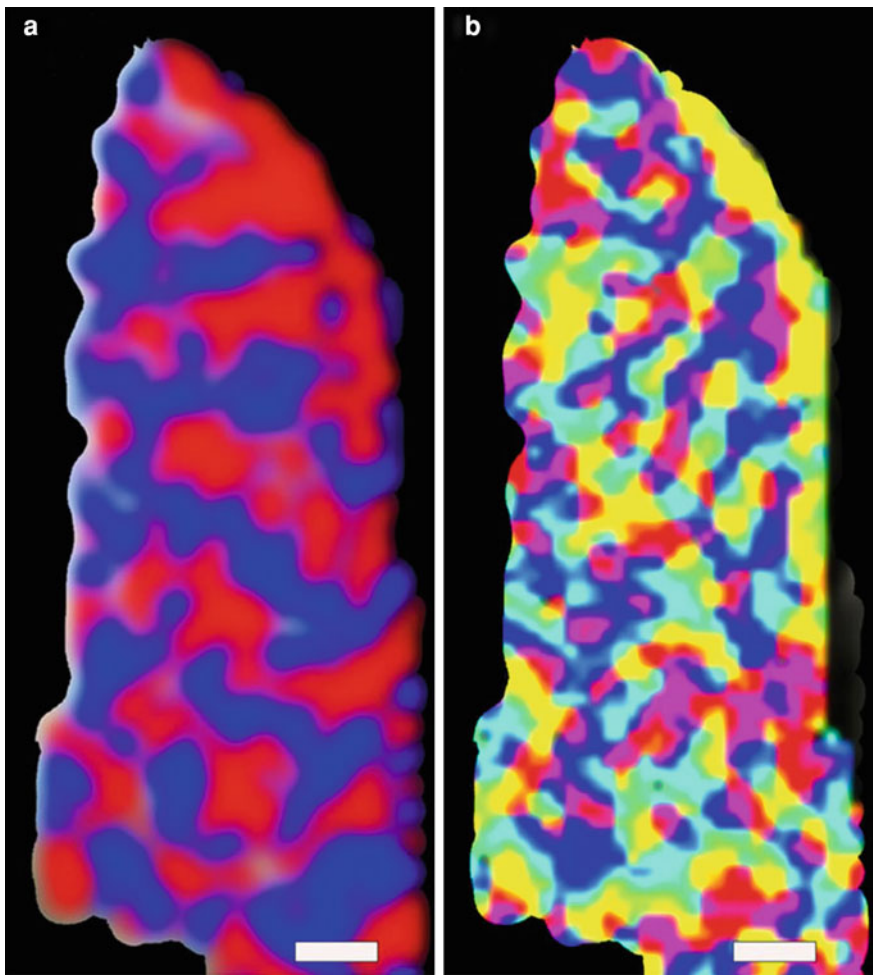

Fig. 9 BOLD fMRI data from primary visual cortex of a single volunteer subject. Spatial resolution $0.5 \times 0.5 \times 3.0$ mm^2. *Left* Ocular dominance columns; *right* orientation columns [reprinted from Yacoub (2009). Thanks to Yacoub, University of Minnesota]

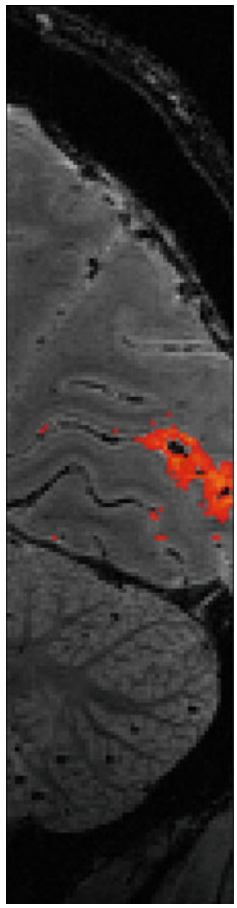

Fig. 10 BOLD fMRI data using zoomed EPI with 0.65-mm isotropic resolution at 7 T. Reversing checkerboard visual stimulation was used to activate primary visual cortex V1. The fMRI data is superimposed on a FLASH reference scan with 0.6-mm isotropic spatial resolution, where the Stria of Gennari can clearly be seen in more anterior parts of the calcarine fissure, where it is not overlaid by the activation results

summarise this argument and its supporting observations, the most effective use of high-field strength in fMRI is obtained when the voxel size is chosen such that the thermal noise of the scanner and spontaneous neurophysiological fluctuations make roughly equal contributions to the signal variance (Triantafyllou et al. 2005). Of course, this depends on the RF coil efficiency, but even with relatively simple RF coils this point is reached at 7 T for a voxel resolution smaller than 1 mm isotropic. How large the voxel should be depends on several factors, such as the field strength, the receiver coil diameter, the filling factor and the acceleration factor. Generally speaking, smaller voxels (especially thinner slices) reduce EPI drop-out caused by variations in magnetic susceptibility at tissue boundaries (Deichmann et al. 2002; Weiskopf et al. 2007), at the cost of SNR. Such a resolution can be achieved in various ways, besides the FLASH technique used by Menon as already mentioned, which is vulnerable to motion artefacts, zoomed EPI with outer volume suppression (Pfeuffer et al. 2002; Heidemann et al. 2008) (Fig. 10) or inner volume selection (Turner et al. 1990a, b), and 3D single shot GRASE (Ramanna and Feinberg 2008). It is vital to keep the echo train as short as possible at 7 T, so parallel imaging is required. Typically an acceleration factor of 4 is adequate to achieve the desired resolution while still maintaining good image quality.

6 Animal Neuroscience Studies at High Field

It is beyond the scope of this chapter to list in more detail the numerous MRI and MRS studies of animal brain that have been performed at field strengths of 4.7 T and greater. Much of this work has been devoted to clarifying the origins of the BOLD signal seen in human brain, in any case, and comparatively little basic neuroscience work has been conducted. The main exception to this has been that of Logothetis and his team (1999), who have explored many aspects of macaque monkey brain that would have been inaccessible by other means. They have used impressive MRI techniques combined powerfully with implanted intra-cortical electrodes to obtain simultaneously the high temporal resolution of electrophysiology, the precise localisation available with electrode methods, and the systematic network insights of fMRI. A recent study by Canals et al. (2009), for instance, uses fMRI to explore the spatially distributed brain changes due to long-term potentiation in monkey hippocampus.

7 Conclusions

High-field MRI is beginning to make a dramatic impact on human neuroanatomy. With an isotropic resolution of 0.4 mm and better, many structures can be distinguished in vivo that could previously be observed only in cadaver brain sections. As regards functional MRI, perhaps its most important applications in human neuroscience will lie in two areas—first, providing accurate localisation of function to complement the major gain in anatomical grey matter specificity and the ensuing opportunities for in vivo cortical parcellation, and second, in assisting

multivariate approaches to studying brain function, such as voxel classification.

References

Abduljalil AM, Kangarlu A, Zhang X, Burgess RE, Robitaille PM (1999) Acquisition of human multislice MR images at 8 Tesla. J Comput Assist Tomogr 23(3):335–340

Ashburner J, Friston KJ (2000) Voxel-based morphometry—the methods. Neuroimage 11(6 pt 1):805–821

Basser PJ, Mattiello J, Le Bihan D (1994) Estimation of the effective self-diffusion tensor from the NMR spin echo. J Magn Reson B 103(3):247–254

Basser PJ, Pajevic S, Pierpaoli C, Duda J, Aldroubi A (2000) In vivo fiber tractography using DT-MRI data. Magn Reson Med 44(4):625–632

Biswal B, Yetkin FZ, Haughton VM, Hyde JS (1995) Functional connectivity in the motor cortex of resting human brain using echo-planar MRI. Magn Reson Med 34(4):537–541

Bock NA, Kocharyan A, Liu JV, Silva AC (2009) Visualizing the entire cortical myelination pattern in marmosets with magnetic resonance imaging. J Neurosci Methods 185(1):15–22

Boxerman JL, Bandettini PA, Kwong KK, Baker JR, Davis TL, Rosen BR, Weisskoff RM (1995) The intravascular contribution to fMRI signal change: Monte Carlo modeling and diffusion-weighted studies in vivo. Magn Reson Med 34(1):4–10

Bridge H, Clare S, Jenkinson M, Jezzard P, Parker AJ, Matthews PM (2005) Independent anatomical and functional measures of the V1/V2 boundary in human visual cortex. J Vis 5(2):93–102

Brodmann K (1909) Vergleichende Lokalisationslehre der Grosshirnrinde in ihren Prinzipien dargestellt auf Grund des Zellenbaues. Johann Ambrosius Barth Verlag, Leipzig

Canals S, Beyerlein M, Merkle H, Logothetis NK (2009) Functional MRI evidence for LTP-induced neural network reorganization. Curr Biol 19(5):398–403

Cheng K, Waggoner RA, Tanaka K (2001) Human ocular dominance columns as revealed by high-field functional magnetic resonance imaging. Neuron 32(2):359–374

Deichmann R, Josephs O, Hutton C, Corfield DR, Turner R (2002) Compensation of susceptibility-induced BOLD sensitivity losses in echo-planar fMRI imaging. Neuroimage 15(1):120–135

De Vita E, Thomas DL, Roberts S, Parkes HG, Turner R, Kinchesh P, Shmueli K, Yousry TA, Ordidge RJ (2003) High resolution MRI of the brain at 4.7 Tesla using fast spin echo imaging. Br J Radiol 76(909):631–637

Eickhoff SB, Stephan KE, Mohlberg H, Grefkes C, Fink GR, Amunts K, Zilles K (2005) A new SPM toolbox for combining probabilistic cytoarchitectonic maps and functional imaging data. Neuroimage 25(4):1325–1335

Flechsig P (1920) Anatomie des menschlichen Gehirns und Rückenmarks auf myelogenetischer Grundlage. Thieme, Leipzig

Frahm J, Merboldt KD, Hänicke W (1993) Functional MRI of human brain activation at high spatial resolution. Magn Reson Med 29(1):139–144

Fukuda M, Moon CH, Wang P, Kim SG (2006) Mapping iso-orientation columns by contrast agent-enhanced functional magnetic resonance imaging: reproducibility, specificity, and evaluation by optical imaging of intrinsic signal. J Neurosci 26(46):11821–11832

Goense JB, Logothetis NK (2006) Laminar specificity in monkey V1 using high-resolution SE-fMRI. Magn Reson Imaging 24(4):381–392

Goense JB, Logothetis NK (2008) Neurophysiology of the BOLD fMRI signal in awake monkeys. Curr Biol 18(9):631–640

Hackett TA, Preuss TM, Kaas JH (2001) Architectonic identification of the core region in auditory cortex of macaques, chimpanzees, and humans. J Comp Neurol 441(3):197–222

Heidemann RM, Fasano F, Vogler M, Leuze C, Pfeuffer J, Turner R (2008) Improving image quality by combining outer volume suppression and parallel imaging: zoomed EPI with GRAPPA at 7T. Proc Int Soc Magn Reson Med 16:1284

Hinds O, Polimeni JR, Rajendran N, Balasubramanian M, Amunts K, Zilles K, Schwartz EL, Fischl B, Triantafyllou C (2009) Locating the functional and anatomical boundaries of human primary visual cortex. Neuroimage 46(4):915–922

Hoffmann MB, Stadler J, Kanowski M, Speck O (2009) Retinotopic mapping of the human visual cortex at a magnetic field strength of 7T. Clin Neurophysiol 120(1):108–116

Honey CJ, Sporns O, Cammoun L, Gigandet X, Thiran JP, Meuli R, Hagmann P (2009) Predicting human resting-state functional connectivity from structural connectivity. Proc Natl Acad Sci USA 106(6):2035–2040

Hyde JS, Biswal BB, Jesmanowicz A (2001) High-resolution fMRI using multislice partial k-space GR-EPI with cubic voxels. Magn Reson Med 46(1):114–125

Jin T, Kim SG (2008) Cortical layer-dependent dynamic blood oxygenation, cerebral blood flow and cerebral blood volume responses during visual stimulation. Neuroimage 43(1):1–9

Kim SG, Rostrup E, Larsson HB, Ogawa S, Paulson OB (1999) Determination of relative $CMRO_2$ from CBF and BOLD changes: significant increase of oxygen consumption rate during visual stimulation. Magn Reson Med 41(6):1152–1161

Koenig SH (1991) Cholesterol of myelin is the determinant of gray-white contrast in MRI of brain. Magn Reson Med 20(2):285–291

Krüger G, Glover GH (2001) Physiological noise in oxygenation-sensitive magnetic resonance imaging. Magn Reson Med 46(4):631–637

Kwong KK, Belliveau JW, Chesler DA, Goldberg IE, Weisskoff RM, Poncelet BP, Kennedy DN, Hoppel BE, Cohen MS, Turner R, Cheng HM, Brady TJ, Rosen BR (1992) Dynamic magnetic resonance imaging of human brain activity during primary sensory stimulation. Proc Natl Acad Sci USA 89:5675–5679

Leite FP, Tsao D, Vanduffel W, Fize D, Sasaki Y, Wald LL, Dale AM, Kwong KK, Orban GA, Rosen BR, Tootell RB, Mandeville JB (2002) Repeated fMRI using iron oxide contrast agent in awake, behaving macaques at 3 Tesla. Neuroimage 16(2):283–294

Logothetis NK, Guggenberger H, Peled S, Pauls J (1999) Functional imaging of the monkey brain. Nat Neurosci 2:555–562

Le Bihan D, Breton E, Lallemand D, Grenier P, Cabanis E, Laval-Jeantet M (1986) MR imaging of intravoxel incoherent motions: application to diffusion and perfusion in neurologic disorders. Radiology 161(2):401–407

Li TQ, Yao B, van Gelderen P, Merkle H, Dodd S, Talagala L, Koretsky AP, Duyn J (2009) Characterization of T(2)* heterogeneity in human brain white matter. Magn Reson Med 62(6):1652–1657

Lin CP, Tseng WY, Cheng HC, Chen JH (2001) Validation of diffusion tensor magnetic resonance axonal fiber imaging with registered manganese-enhanced optic tracts. Neuroimage 14(5):1035–1047

Lin FH, Belliveau JW, Dale AM, Hämäläinen MS (2006) Distributed current estimates using cortical orientation constraints. Hum Brain Mapp 27(1):1–13

Mangia S, Tkác I, Gruetter R, Van de Moortele PF, Maraviglia B, Uğurbil K (2007) Sustained neuronal activation raises oxidative metabolism to a new steady-state level: evidence from 1H NMR spectroscopy in the human visual cortex. J Cereb Blood Flow Metab 27(5):1055–1063

Mansfield P (1977) Multi-planar image formation using NMR spin echoes. J Phys C 19:L55

Menon RS, Ogawa S, Strupp JP, Uğurbil K (1997) Ocular dominance in human V1 demonstrated by functional magnetic resonance imaging. J Neurophysiol 77(5): 2780–2787

Moseley ME, Cohen Y, Kucharczyk J, Mintorovitch J, Asgari HS, Wendland MF, Tsuruda J, Norman D (1990) Diffusion-weighted MR imaging of anisotropic water diffusion in cat central nervous system. Radiology 176(2):439–445

O'Brien JS, Sampson EL (1965) Lipid composition of the normal human brain: gray matter, white matter, and myelin. J Lipid Res 6(4):537–544

Ogawa S, Tank DW, Menon R, Ellermann JM, Kim SG, Merkle H, Ugurbil K (1992) Intrinsic signal changes accompanying sensory stimulation: functional brain mapping with magnetic resonance imaging. Proc Natl Acad Sci USA 89(13):5951–5955

Ogawa S, Lee TM, Kay AR, Tank DW (1990) Brain magnetic resonance imaging with contrast dependent on blood oxygenation. Proc Natl Acad Sci USA 87:9868–9872

Oshio K, Feinberg DA (1991) GRASE (Gradient- and spin-echo) imaging: a novel fast MRI technique. Magn Reson Med 20(2):344–349

Otazo R, Mueller B, Ugurbil K, Wald L, Posse S (2006) Magn Reson Med 56:1200–1210

Pfeuffer J, van de Moortele PF, Yacoub E, Shmuel A, Adriany G, Andersen P, Merkle H, Garwood M, Ugurbil K, Hu X (2002) Zoomed functional imaging in the human brain at 7 Tesla with simultaneous high spatial and high temporal resolution. Neuroimage 17(1):272–286

Ramanna S, Feinberg DA (2008) Single-shot 3D GRASE with cylindrical k-space trajectories. Magn Reson Med 60(4): 976–980

Sigalovsky IS, Fischl B, Melcher JR (2006) Mapping an intrinsic MR property of gray matter in auditory cortex of living humans: a possible marker for primary cortex and hemispheric differences. NeuroImage 32:1524–1537

Simmons JM, Saad ZS, Lizak MJ, Ortiz M, Koretsky AP, Richmond BJ (2008) Mapping prefrontal circuits in vivo with manganese-enhanced magnetic resonance imaging in monkeys. J Neurosci 28(30):7637–7647

Talairach J, Tournoux P (1993) Referentially oriented cerebral MRI anatomy: an atlas of stereotaxic anatomical correlations for gray and white matter. Thieme Medical Publishers, New York

Triantafyllou C, Hoge RD, Krueger G, Wiggins CJ, Potthast A, Wiggins GC, Wald LL (2005) Comparison of physiological noise at 1.5 T, 3 T and 7 T and optimization of fMRI acquisition parameters. Neuroimage 26(1):243–250

Turner R, Le Bihan D, Maier J, Vavrek R, Hedges LK, Pekar J (1990a) Echo-planar imaging of intravoxel incoherent motion. Radiology 177(2):407–414

Turner R, von Kienlin M, Moonen CT, van Zijl PC (1990b) Single-shot localized echo-planar imaging (STEAM-EPI) at 4.7 tesla. Magn Reson Med 14(2):401–408

Turner R, Le Bihan D, Moonen CTW, Despres D, Frank J (1991) Echo-planar time course MRI of cat brain deoxygenation changes. Magn Reson Med 22:159–166

Turner R, Jezzard P, Wen H, Kwong KK, Le Bihan D, Zeffiro T, Balaban RS (1993) Functional mapping of the human visual cortex at 4 and 1.5 tesla using deoxygenation contrast EPI. Magn Reson Med 29(2):277–279

Turner R, Oros-Peusquens AM, Romanzetti S, Zilles K, Shah NJ (2008) Optimised in vivo visualisation of cortical structures in the human brain at 3 T using IR-TSE. Magn Reson Imaging 26(7):935–942

Vogt C, Vogt O (1919) Allgemeinere Ergebnisse unserer Hirnforschung. J Psychol Neurol 25:279–461

Walters NB, Eickhoff SB, Schleicher A, Zilles K, Amunts K, Egan GF, Watson JD (2007) Observer-independent analysis of high-resolution MR images of the human cerebral cortex: in vivo delineation of cortical areas. Hum Brain Mapp 28(1):1–8

Weigel M, Hennig J (2006) Contrast behavior and relaxation effects of conventional and hyperecho-turbo spin echo sequences at 1.5 and 3 T. Magn Reson Med 55(4):826–835

Weiskopf N, Hutton C, Josephs O, Turner R, Deichmann R (2007) Optimized EPI for fMRI studies of the orbitofrontal cortex: compensation of susceptibility-induced gradients in the readout direction. MAGMA 20(1):39–49

Yacoub E, Shmuel A, Logothetis N, Uğurbil K (2007) Robust detection of ocular dominance columns in humans using Hahn Spin Echo BOLD functional MRI at 7 Tesla. Neuroimage 37(4):1161–1177

Yacoub E, Harel N, Ugurbil K (2008) High-field fMRI unveils orientation columns in humans. Proc Natl Acad Sci USA 105(30):10607–10612

Zhao F, Wang P, Hendrich K, Ugurbil K, Kim SG (2006) Cortical layer-dependent BOLD and CBV responses measured by spin-echo and gradient-echo fMRI: insights into hemodynamic regulation. Neuroimage 30(4):1149–1160

Zhu XH, Zhang N, Zhang Y, Uğurbil K, Chen W (2008) New insights into central roles of cerebral oxygen metabolism in the resting and stimulus-evoked brain. J Cereb Blood Flow Metab. Sep 10

Clinical Neuro and Beyond

Mark E. Ladd, Elke R. Gizewski, and Dagmar Timmann

Contents

M. E. Ladd (✉)
Erwin L. Hahn Institute for Magnetic Resonance Imaging,
University Duisburg-Essen, Arendahls Wiese 199,
45141 Essen, Germany
e-mail: mark.ladd@uni-duisburg-essen.de

E. R. Gizewski
Department of Neuroradiology,
University Hospital Giessen,
Klinikstrasse 29, 35385 Giessen, Germany

D. Timmann
Experimental Neurology, Department of Neurology,
University Hospital Essen, Hufelandstrasse 55,
45122 Essen, Germany

Abstract

Magnetic resonance imaging (MRI) is one of the most important methods for the diagnosis and therapy monitoring of disease, and in particular neurological disease. Today, magnets up to 3 T are in use in clinical routine. An important trend in clinical care for the coming years could be the introduction of MRI systems with even higher static magnetic fields, particularly 7 T. These imagers offer the potential to significantly enhance not only spatial resolution, but also certain tissue contrasts. In this chapter, initial research results are presented which already demonstrate potential advantages of the ultra-high magnetic field for neurological diagnostics. Although the technical challenges for examining organs in the abdomen and thorax are much higher than in the brain, very preliminary work is also being pursued targeted toward clinical application of 7 T in these body regions. Further investigations are required, however, to evaluate the clinical relevance of these techniques. It can be expected that 7 T MRI scanners could find their way from the research environment into clinical practice in the next few years, with initial applications very likely in the brain; thus, the significance of MRI for neurology will once again be extended.

1 Introduction

Since the introduction of magnetic resonance imaging (MRI) in the early 1980s, this examination technique has developed into a widespread imaging method for

J. Hennig and O. Speck (eds.), *High-Field MR Imaging,* Medical Radiology. Diagnostic Imaging,
DOI: 10.1007/174_2010_104, © Springer-Verlag Berlin Heidelberg 2011

non-invasively depicting various anatomical regions. Particularly in the field of neurology, MRI has established itself as an indispensable tool (European Federation of Neurological Societies Task Force 2001). Through technological innovations such as diffusion and perfusion imaging, the scope of MRI has been continuously expanded. Also functional MRI (fMRI), with its ability to non-invasively depict the activation level of various brain regions, has significantly improved pre-operative evaluation and planning in, for example, brain tumor patients, as well as opened up new possibilities for monitoring post-operative progress (Weiller et al. 2006).

Despite many technical advances in recent years, the development potential of the MR method is not nearly exhausted. A major trend of the past and the coming years is the introduction of magnets with much more powerful static magnetic fields. 3 T magnets have now established themselves in routine clinical practice (Schild 2005), and this field strength has proven to be particularly beneficial for neurological diagnosis (Moseley et al. 2009). In essence, the available signal from the body tissue is determined by the static magnetic field because the higher this field, the larger the surplus of hydrogen protons, which are oriented parallel to the magnetic field. It is accordingly possible to achieve images with higher spatial resolution using the enhanced signal strength. Also very important at higher field strengths are new, unique tissue contrasts, some of which may be hidden in the phase of the measured signal rather than in the magnitude. Therefore, the question arises whether magnets with even higher field strength than 3 T can provide objective benefits for answering clinical questions.

Currently, there are about 35 MRI systems with a field strength of 7–9.4 T in operation for performing human research. Many of these systems are dedicated to pursuing fundamental neuroscience questions, but several research groups have now initiated projects to investigate whether these field strengths are suitable for clinical use. The expectation is that for certain dedicated questions, a much more accurate diagnosis is possible than in the past (Ladd 2007). It is now likely that the next standard field strength for clinical use beyond 3 T will be 7 T. In this chapter, some preliminary study results are described to demonstrate the potential of ultra-high field imaging at 7 T for use in neurology and the depiction of various pathologies. In addition, a brief look is taken at early efforts to extend these advantages to applications in the torso.

2 Promising Characteristics of Ultra-high Field

What potential advantages for clinical diagnostics can be expected at higher magnetic fields? MRI is not particularly sensitive when it comes to the extraction of signal from the body tissues. In many cases it is limited by the available signal-to-noise ratio (SNR). The most significant and obvious impetus for the use of stronger magnets lies in the fact that the SNR increases approximately linearly with the magnetic field strength (Hoult and Phil 2000; Vaughan et al. 2001). SNR is proportional to the voxel size, so that the enhanced SNR can be invested into higher spatial resolution, i.e., smaller voxels. Alternatively, the required measurement time can be shortened, although at a practical level almost all studies at 7 T have invested the SNR currency into finer structural depictions, and likely clinical benefits are expected to be achieved by following this strategy.

Not only imaging but also the non-invasive detection of metabolic products by use of MR spectroscopy (MRS) should, theoretically, be significantly improved by the enhanced signal at ultra-high field. The distinction between different metabolites is problematical at lower field strengths for another reason as well: The signals may partially overlap one another and not be separable. Spectral separation increases linearly with magnetic field strength, so that hereby the quantitative determination of additional metabolites should be made feasible (Srinivasan et al 2009). A very homogeneous magnetic field is required, however, and the spectral widths of the individual metabolic resonances play an important role in the success of MRS (Otazo et al. 2006). Particularly in neurological diseases, in vivo MRS studies may play an important role, since the measurement of metabolite levels can supply valuable information about pathological processes such as ischemia, demyelination, or neurodegeneration (Cecil 2006).

As a further possible diagnostic benefit, altered tissue contrasts emerge at high field. Novel contrasts are frequently produced by the augmented sensitivity to differences in magnetic susceptibility. The magnetic susceptibility of a tissue is influenced by the iron

and myelin content, among other factors. 7 T is a powerful tool for the detection of minute differences in these tissue components. Initial work with T_2*-weighted images and phase imaging has revealed a distinct laminar contrast in the grey matter and fiber bundles in the white matter at 7 T (Lee et al. 2010; Li et al. 2006). There is also a great interest to quantify tissue iron content in various neurological diseases, e.g., Alzheimer's disease, Parkinson's disease and multiple sclerosis, since a disturbed iron metabolism is suspected to be linked with these pathologies (Brass et al. 2006).

The magnetic susceptibility of blood is largely determined by the oxygen content. This effect is the basis for the blood oxygenation level dependent (BOLD) contrast, which is used to capture brain activation in fMRI studies. This contrast also opens new perspectives in the structural representation of the venous system (Koopmans et al. 2008) or in the detection of microhemorrhages. Venules with a diameter of 100 μm can be well depicted (Dashner et al. 2004) based on susceptibility effects.

3 Obstacles to Clinical Use

The desired weighting (T_1, T_2, etc.) is determined by, among other parameters, the excitation flip angle achieved. Due to the shorter radiofrequency (RF) wavelength at high field strength, it is extremely challenging to obtain a uniform flip angle distribution during RF excitation (Vaughan et al. 2001). Hence, there is now an unpredictable spatial distribution of different flip angles, and the tissue contrast varies across the imaging field-of-view. This problem cannot be compensated by image post-processing, and new strategies and technologies must be developed to achieve high quality and reliable coverage of the body from head to foot with suitably homogeneous excitation; such techniques are currently the subject of significant research efforts. Particularly, spin-echo sequences or sequences with inversion pulses, such as FLAIR, suffer from inhomogeneous excitation. Gradient-echo sequences are markedly less sensitive to flip angle inhomogeneities (Wang et al. 2004).

Another challenge in ultra-high field imaging is also associated with the RF excitation: Far more RF energy is deposited in the tissue, so that potential tissue warming may place significant constraints on the allowable imaging parameters. Practically, this limitation leads to prolonged measurement times, since, for example, fewer sections can be acquired concurrently. The maximum allowable excitation flip angle is also constrained by these limits, which can hamper any technique relying on high flip angles such as turbo-spin-echo or steady-state sequences. The deposited energy rises approximately with the square of the static magnetic field (Hoult and Phil 2000); a 3 T imager thus generates four times more warming than a 1.5 T scanner under similar conditions. Several strategies have been introduced in recent years, however, to overcome this obstacle.

Another much-discussed aspect of ultra-high field imaging that has been put forward as a possible obstacle to clinical use are physiological side-effects of the magnetic field. Such effects are observed even at 1.5 T, but they increase in frequency and intensity with rising field strength. These effects include dizziness, nausea, phosphenes (light flashes), and a metallic taste in the mouth. These are transient effects that generally disappear quickly when one distances oneself from the magnetic field or remains stationary within the magnetic field. Our own observations at 7 T have shown that these effects occur with only moderate severity in the vast majority of volunteers and only in isolated cases do they present a practical obstacle to clinical application (Theysohn et al. 2008). In that study, a 7 T examination was terminated prematurely in less than 5% of subjects. With increasing experience with patient handling and how subjects are positioned within the magnetic field, including the speed of the patient table through the field, most significant reactions can be avoided. The number of 7 T examinations that are terminated prematurely has now dropped to less than 2% at our institution. Negative aspects related to the magnetic field are in general rated less severe than several other aspects of an MRI examination which are commonly encountered and well-tolerated at lower field strength, such as exam duration or the need to lie still (Fig. 1).

4 Arterial System

With increasing field strength the relaxation times T_1 and T_2* of the tissue to be examined are changed. T_1 will be longer, for example, which is anticipated to

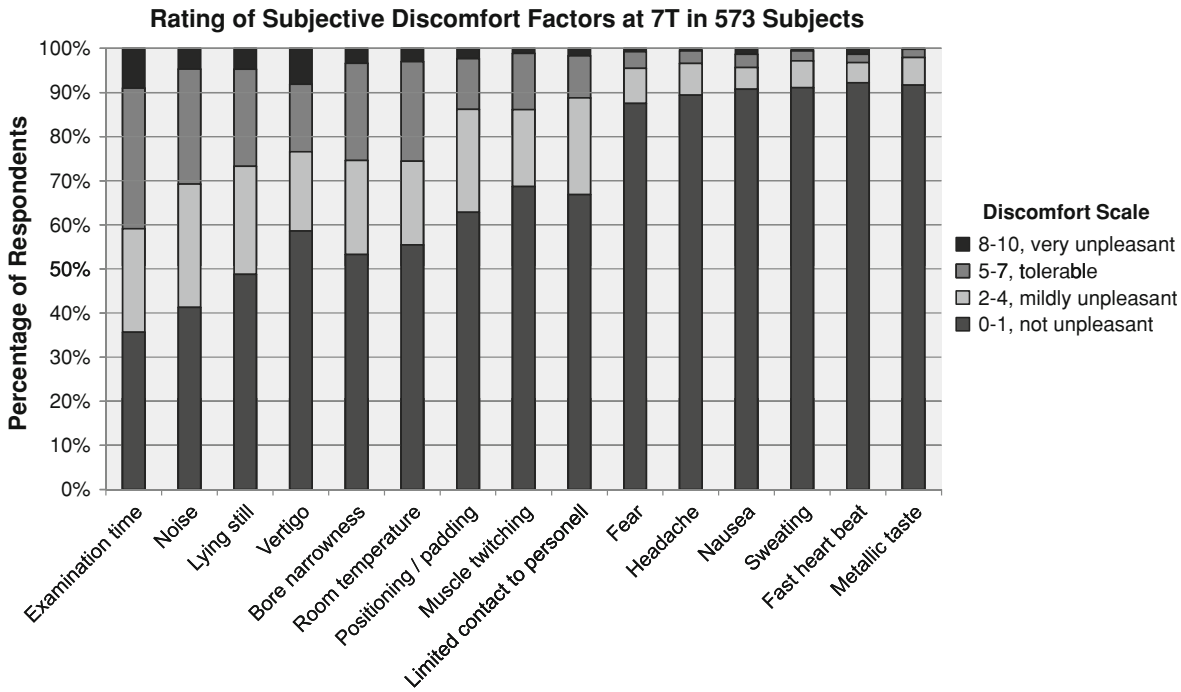

Fig. 1 Subjective rating of various discomfort factors at 7 T in 573 subjects. The factors are ordered according to their mean value, with the factor having the highest mean (most discomfort) on the left and the factor having the lowest mean (least discomfort) on the right. Of the factors that can be directly attributed to the high static magnetic field strength, vertigo produced the most discomfort but was considered less unpleasant than examination duration, acoustic noise, or lying still

benefit time-of-flight (TOF) angiography. Combined with the much higher spatial resolution which can be implemented due to enhanced sensitivity, the depiction of much finer vessel branches is achievable (Heverhagen et al. 2008; Kang et al. 2008). With this technique it is now possible to depict very small blood vessels in vivo such as the lenticulostriate arteries (Cho et al. 2008; Kang et al. 2009). Established investigation protocols that are optimized for field strengths of 1.5 or 3 T, however, cannot be transferred directly to MRI at 7 T; SAR limitations, the altered tissue T_1 and T_2 times at 7 T, and new image artifacts, such as encountered through increased susceptibility, necessitate optimization of existing sequences.

Thus far it has been shown that a reliable depiction of all diagnostically relevant intracranial vessels is possible. Various gradient-echo sequences can be used [TOF, interpolated 3D fast low-angle shot (3D FLASH), and magnetization-prepared rapid gradient-echo (MPRAGE)] (Maderwald et al. 2008; Zwanenburg et al. 2008). Due to the increased resolution (approximately $0.5 \times 0.5 \times 0.5$ mm^3), the intracranial vessels can be traced far into the periphery (Fig. 2). The use of MPRAGE to depict the intracranial vessels is only possible with ultra-high field strength. This option opens up new possibilities in the diagnosis of intracranial vascular changes: In addition to the vessels themselves, which appear hyperintense without contrast medium as in TOF MR angiography (MRA), the perivascular structures are depicted with good resolution and can be assessed in the source images (Fig. 3). Here, further evaluations are needed to show, for example, how this can be helpful in the workup of vascular stenosis. It is possible that this approach can make the additional acquisition of a CT scan to visualize wall calcifications superfluous. Such calcifications are important to depict when considering an endovascular therapy.

Another possible clinical application is the depiction of aneurysms. It is known that small aneurysms may pose a risk of bleeding, so that even these small

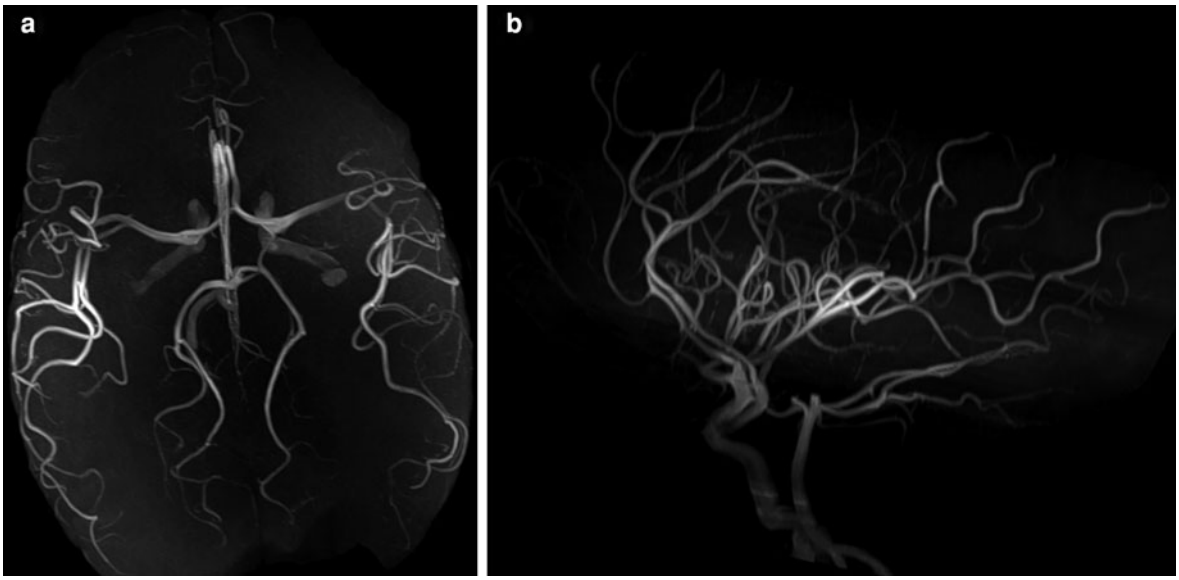

Fig. 2 Owing to the high spatial resolution (approximately $0.5 \times 0.5 \times 0.5$ mm^3), the intracranial vessels in this TOF MRA at 7 T can be traced far into the periphery. **a** A 3D axial MIP reconstruction of the Circle of Willis is shown and **b** a sagittal MIP of the same dataset

structures should be reliably detectable with a non-invasive method. So far, however, TOF MRA at lower field strength is limited in that aneurysms smaller than 3 mm may not always be detected. A higher resolution and improved contrast would be very helpful. It must be remembered though, that TOF MRA at high field strength is subject to increased artifacts. Initial results have shown advantages of ultra-high field, but further investigations are needed to evaluate the clinical relevance of these benefits (Monninghoff et al. 2009a, b) (Fig. 4).

5 Cavernomas/Vascular Malformations

The detection of intra-axial cavernomas by MRI is based on the appearance of susceptibility artifacts in gradient echo sequences. The precise anatomy, particularly of small lesions, often remains obscured at field strengths of up to 3 T. The more central such a lesion is located, the more imperative it is to estimate the risk of bleeding vs. the risk of surgical removal. In a recent study it was verified that intracranial cavernous hemangiomas, which had already been detected at 1.5 T, could be depicted at 7 T after the optimization of T_2*-weighted gradient-echo sequences (Schlamann et al. 2010). A significant increase in spatial resolution, however, could be achieved with susceptibility-weighted sequences [susceptibility weighed imaging (SWI)]. Such sequences already result in a more sensitive detection of hemosiderin deposits at 1.5 and 3 T and hence of cavernous hemangiomas; at 7 T the influence of susceptibility is even further enhanced (Fig. 5). Thus, two factors, spatial resolution and susceptibility sensitivity, come together to significantly improve the depiction of cavernomas, and in particular enhance the sensitivity for their detection. In the assessment of clinical relevance, it will be important to determine whether additional cavernomas can be found in eloquent regions, or to reliably assess whether there is an associated cavernous hemangioma in the presence of a DVA (developmental venous anomaly).

6 Microangiopathy/Congophilic Angiopathy

The radiological workup of patients with dementia can lead to the recognition of certain causes of dementia. One main cause of vascular dementia is

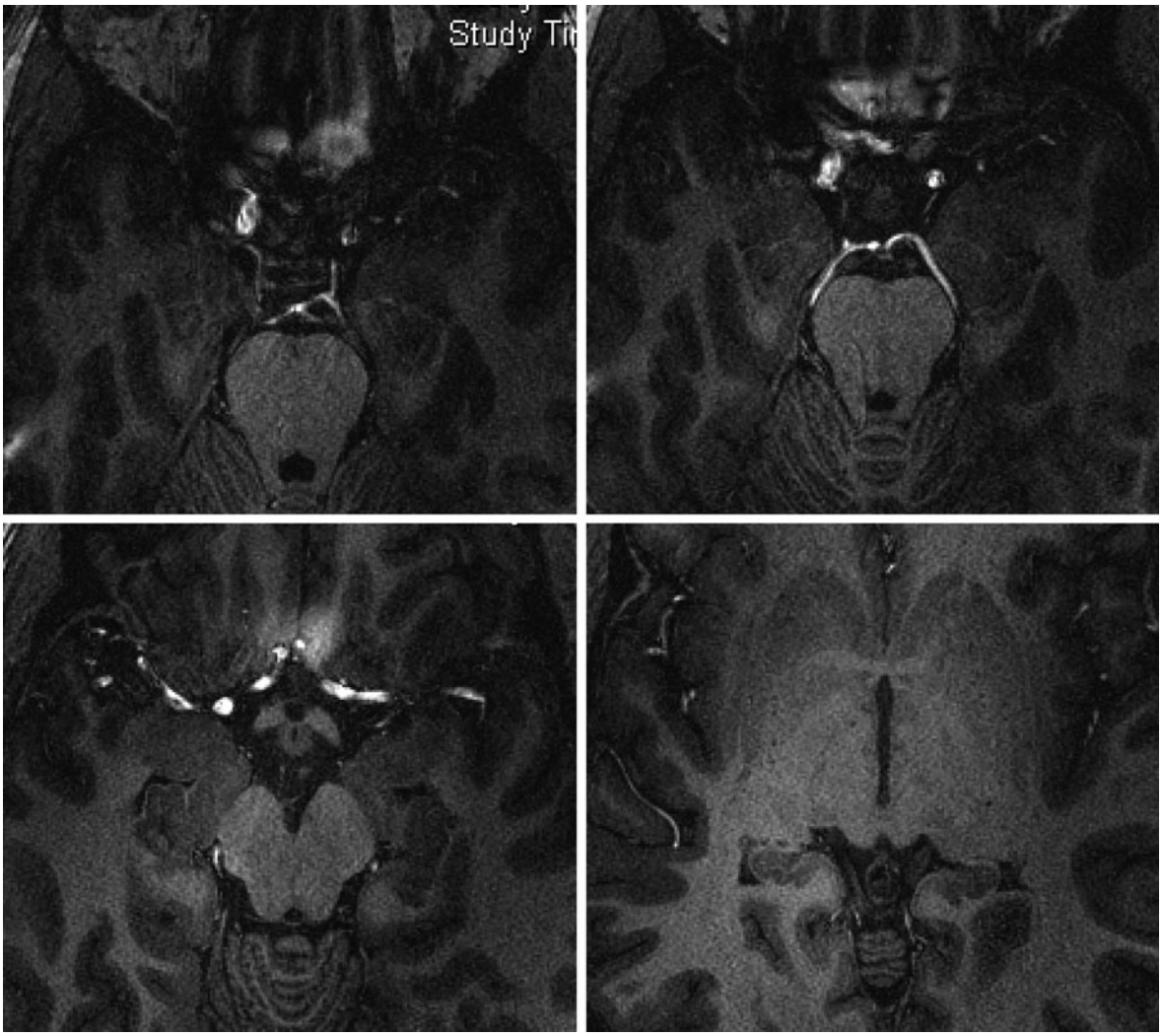

Fig. 3 The MPRAGE sequence at 7 T opens up new possibilities for non-contrast-enhanced vascular imaging in the diagnosis of intracranial vascular lesions: In addition to the vessels themselves, which are hyperintense without application of contrast agent as in the TOF MRA, the perivascular structures are depicted in the source images with good resolution and can be evaluated with perfect registration to the vasculature

cerebral microangiopathy, which can be established both in CT as well as in clinical MRI (Meyer et al. 2005). In the pathogenesis of these white matter changes, arterial hypertension is considered to be the main cause, so that such changes are found not only in dementia patients but also in many patients with cardiovascular disease. Hypertension is in principle amenable to treatment; the compliance of these patients is, however, often low. Visualization of the changes in an individual's brain, which are well represented in a FLAIR sequence, could perhaps improve compliance by demonstrating them to the patient.

Ultra-high field is certainly not necessary for this, even though a FLAIR sequence is now also possible at 7 T after several adaptations (Fig. 6a). In the case of such microangiopathic white matter changes, a gradient-echo sequence should definitely be supplemented (T_2*-weighted or SWI). What has already been observed in the earlier section on cavernomas is valid here: These sequences are particularly sensitive to susceptibility artifacts as may originate from

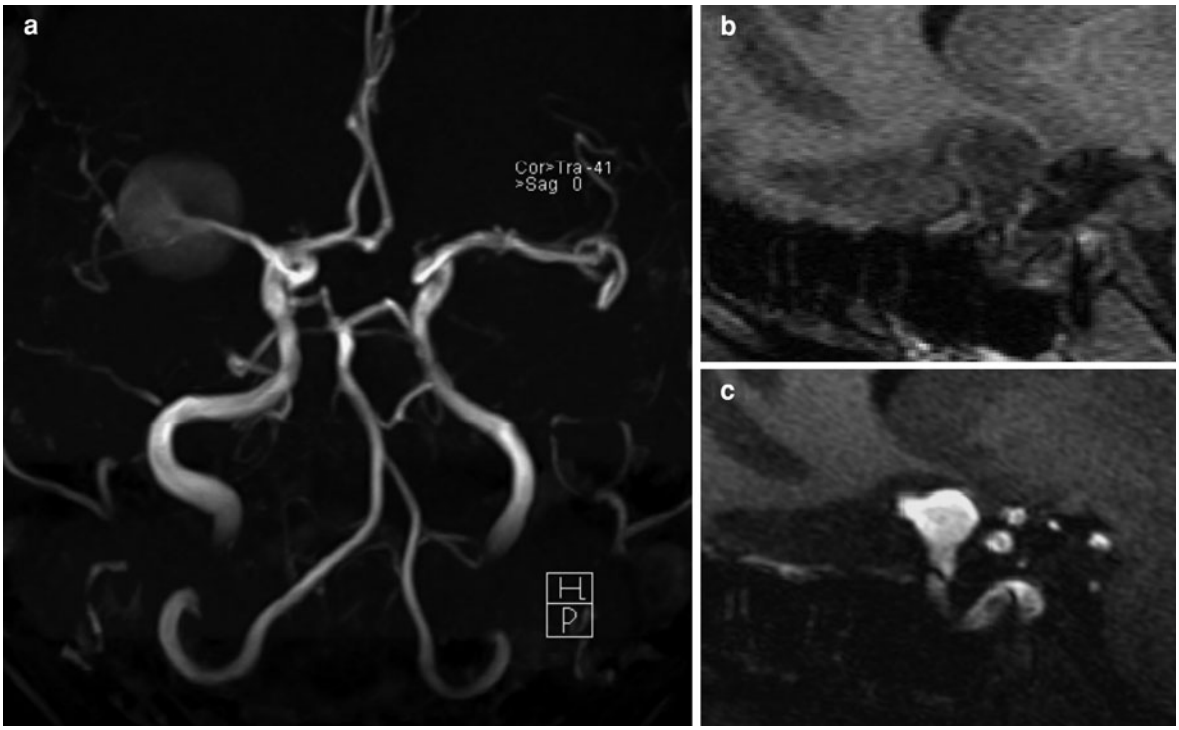

Fig. 4 **a** TOF MRA at 7 T with good depiction of a medial cerebral artery aneurysm. However, a limitation of the TOF MRA technique is also revealed: This aneurysm has very limited flow and is thus contrasted rather poorly. **b**, **c** An aneurysm depicted with an MPRAGE sequence. At 1.5 T (**b**), this is not possible; at 7 T (**c**) the aneurysm is depicted quite well. Further studies are needed to demonstrate whether the flow-associated problems of TOF MRA can be reliably overcome with the MPRAGE technique

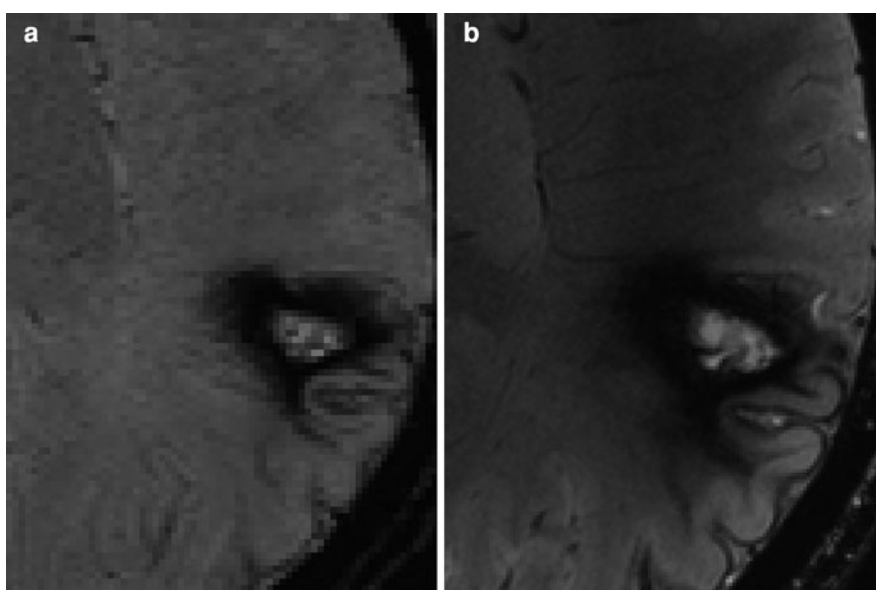

Fig. 5 Higher field strengths lead to more sensitive detection of hemosiderin deposits and hence of cavernous hemangiomas. A large, superficial cavernoma is shown at 1.5 T (**a**) compared to 7 T (**b**). Especially the internal structure is revealed with higher resolution at 7 T

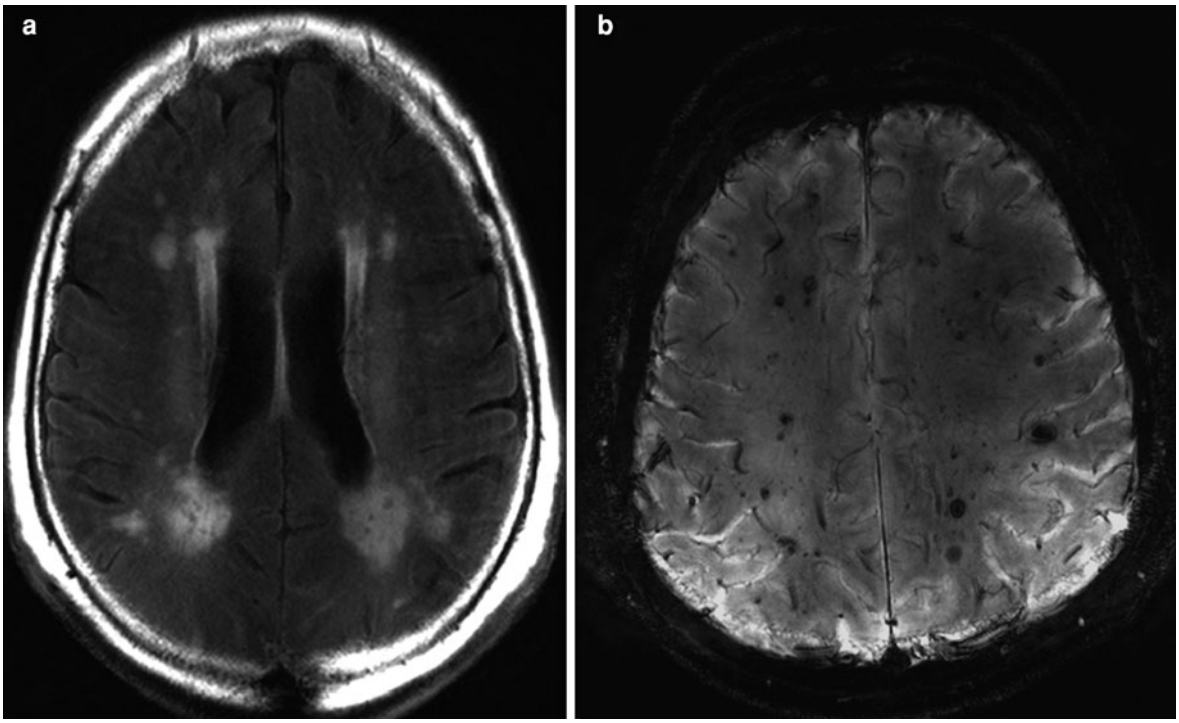

Fig. 6 **a** Example of a 2D FLAIR sequence, which is feasible at 7 T after several parameter adaptations. The contrast is, however, somewhat unusual and lower between grey and white matter compared to 1.5 and 3 T studies. **b** Small microbleeds, which can occur in patients with microangiopathy, can be more sensitively detected at ultra-high field in T_2*-weighted sequences

hemosiderin deposits in brain tissue. This allows the identification of small microbleeds that can occur in patients with microangiopathy, even if the microangiopathic changes themselves are not yet very pronounced (Fig. 6b). Previous investigations have shown a correlation between the number of microbleeds and the extent of cognitive deficits (Werring et al. 2004). Furthermore, it was put forward that in patients with microbleeds, secondary prevention measures with anticoagulants should be reconsidered (Derex et al. 2004; Lee et al. 2004). Currently, there is already evidence that microbleeds are an important criterion with regard to microangiopathies and can be evaluated with clinical MRI today. With the help of higher field strengths such as 7 T, the detection limit for microbleeding is improved significantly (Fig. 7). If many microbleeds have already been established at 1.5 or 3 T, the patient does not need to undergo a 7 T MRI, but if an anticoagulant therapy is planned in a patient with known microangiopathy and often coexisting cardiovascular pathologies, one should be as certain as possible that no microbleeding exists, so that the prophylactic therapy can be individually adapted and large intracerebral bleedings prevented. In such cases, the more sensitive detection method could be important and helpful.

7 Metastases and Primary Brain Tumors

As in the previous two sections, the significantly increased susceptibility sensitivity of 7 T is not a disadvantage but rather an advantage for the diagnosis of this disease group. The improved depiction of lesions could be evaluated in a small group of melanoma patients, taking advantage of susceptibility effects. Here it could be shown that much smaller melanoma metastases could be detected at 7 T in the SWI than at lower field strength; about twice as many metastases smaller than 2 mm were discovered in the 7 T examination (unpublished data). However, more Tesla is not always better: in the contrast-enhanced MPRAGE, metastases were not detected more sensitively than at 1.5 T (Fig. 8). It can be concluded that a more sensitive staging for patients with certain

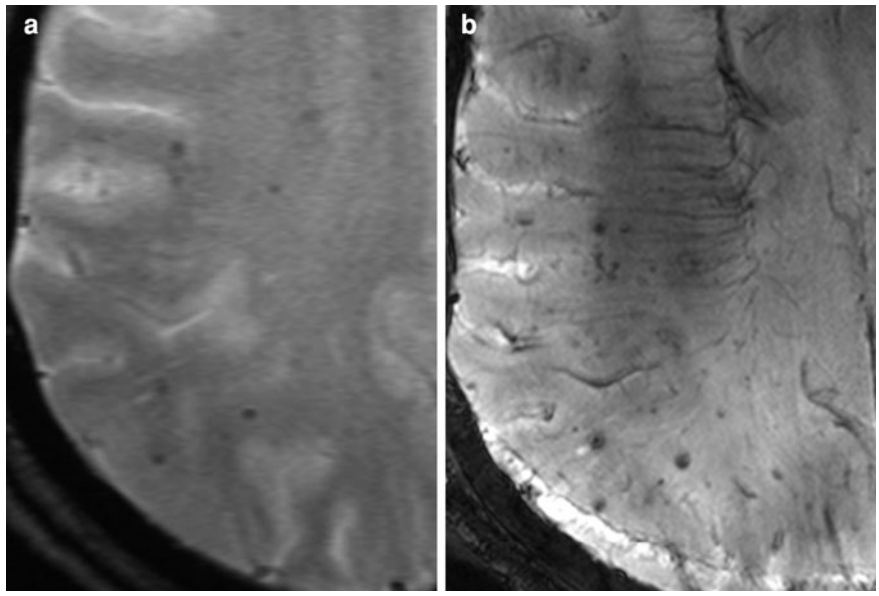

Fig. 7 The detection threshold for microbleeds is markedly lowered with the help of higher field strengths such as 7 T, as shown here in a direct comparison of 1.5 T (**a**) with 7 T (**b**). Small microbleeds less than 2 mm are clearly visible at 7 T; at 1.5 T, they are often not detectable

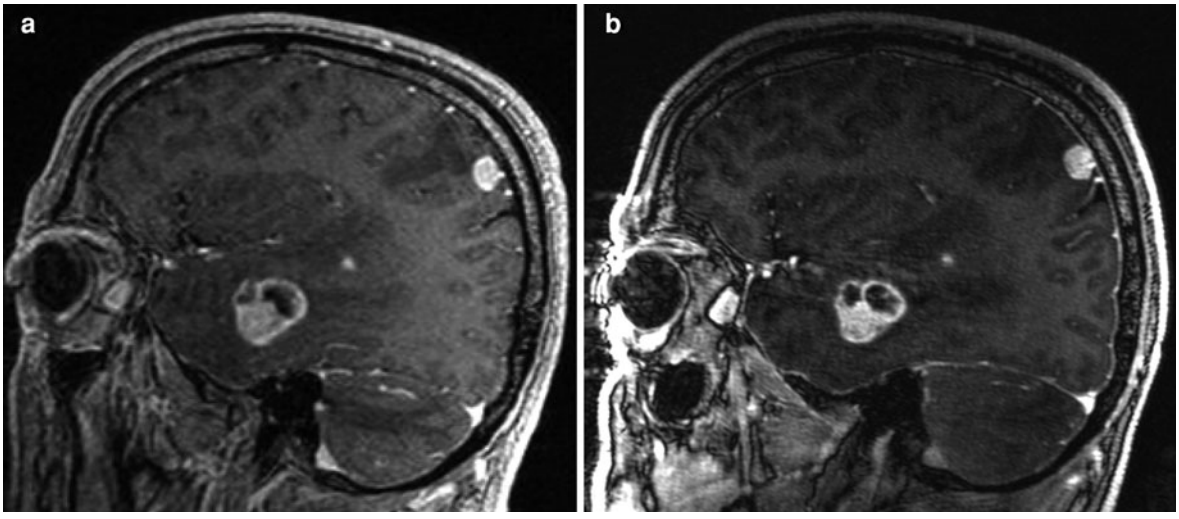

Fig. 8 More Tesla is not always better: In the contrast-enhanced MPRAGE, melanoma metastases could not be detected more sensitively at 7 T (**b**) compared to 1.5 T (**a**)

primaries (e.g. melanoma) is possible at 7 T, but with the SWI rather than with the T_1 sequence after administration of gadolinium contrast agent.

The increased sensitivity to susceptibility artifacts can be used not only to make hemosiderin visible. The appearance of venous vessels is also markedly increased by the enhanced artifact extent. This can be helpful to reveal the vascular distribution and possible neovascularization in primary brain tumors (Moenninghoff et al. 2009). Gliomas can be already well depicted with conventional field strengths. A marked improvement in spatial resolution in the T_2 or T_1-weighted sequences, even though visually appealing, will have rather little influence on the therapy and thus be of minor clinical relevance. The improved representation of vessel-rich areas, however, could be of relevance: These areas should be indicative of higher malignancy (Fig. 9). A more accurate target determination could thus be conducted before a stereotactic biopsy. In addition to other techniques such as MRS, the visualization of augmented vascular presence could be a further

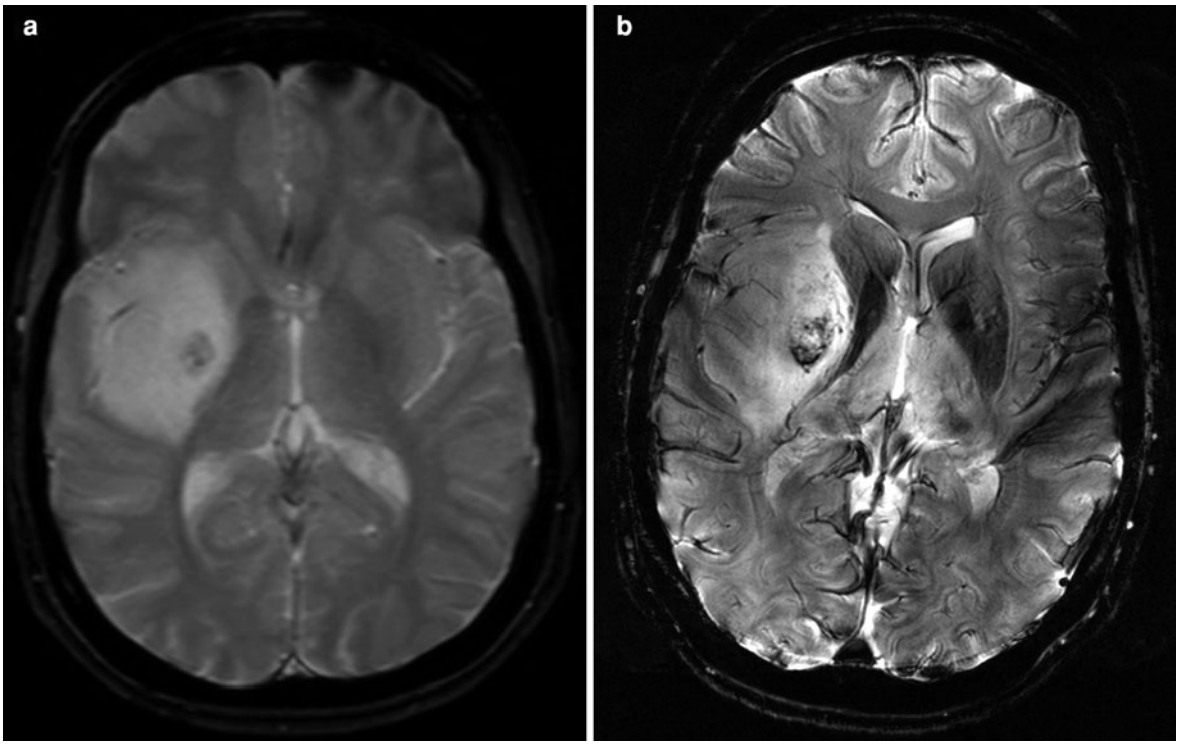

Fig. 9 An improved depiction of vessel-rich areas and also of microbleeds is possible in primary brain tumors at 7 T (**b**) vs 1.5 T (**a**). These areas are presumably associated with increased malignancy grade, so that such an examination might be suitable to optimize stereotactic biopsy planning

component in the assessment of primary brain tumor malignancy.

8 Hippocampus

Also for this brain region near the skull base, imaging sequences need to be optimized due to SAR limitations, different tissue T_1 and T_2 times, and increased susceptibility effects. As at 3 T, proton density (PD), T_2, and T_2*-weighted sequences are well suited to achieve a reliable depiction of the hippocampus at 7 T. In addition, the resolution should be as high as possible with regard to both the slice thickness and the in-plane resolution.

The high-resolution depiction of the hippocampi is possible at 7 T without significant artifacts with PD, T_2, and T_2* sequences, but also with the T_1 MPRAGE with an isotropic 0.5 mm resolution (Theysohn et al. 2009). The internal anatomy of the hippocampus can be visualized with very good resolution and thus motivates the search for clinical applications (Fig. 10a). Cryptogenic epilepsy, for instance, remains an unresolved problem; in these patients, no structural abnormality can be diagnosed at MRI up to 3 T (Zijlmans et al. 2009). The higher resolution of 7 T MRI would appear to be beneficial and is currently being evaluated; initial investigations have been conducted in patients with known mesial sclerosis (Breyer et al. 2009) (Fig. 10b). Subsequently, patients with a known temporal focus in EEG but occult lower field imaging results will be examined with ultra-high field. In such cases, a detectable structural change would clearly have therapeutic relevance.

9 Multiple Sclerosis

For Multiple Sclerosis (MS), MRI has long been the crucial imaging modality and is also of major importance for the clinical assessment. Here, standard

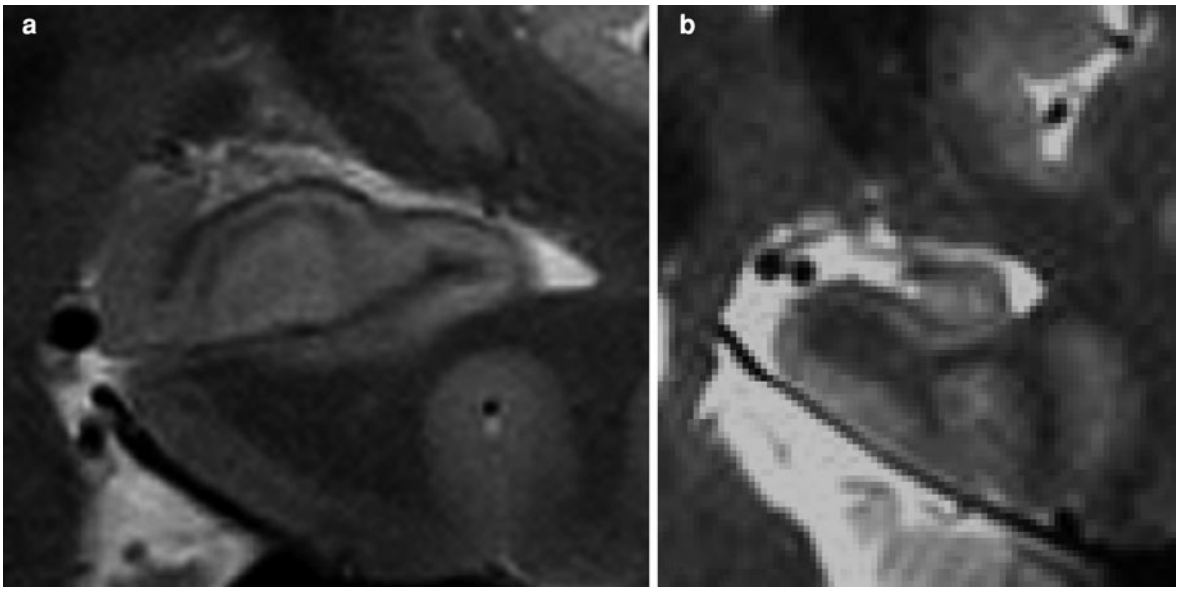

Fig. 10 **a** The normal anatomy of the hippocampus can be captured at 7 T with very good resolution. **b** The hippocampus of a patient with a history of mesial sclerosis depicted in the higher resolution which reveals not only the reduced volume and possibly a signal change, but also direct evidence of the changed configuration and structure of the hippocampal cortex

examination protocols are performed with a slice thickness up to 5 mm and a matrix not lower than 256 × 256. Essential sequences include a PD + T_2 turbo-spin-echo (TSE), a FLAIR, and a sagittal T_2-weighted TSE through the corpus callosum with a thinner section thickness (2 mm, 512 matrix). Also important is a T_1-weighted sequence after contrast administration. A diffusion-weighted sequence is also frequently performed to potentially detect active foci.

Nevertheless, a definitive statement about the progression and the severity of the disease is not really possible, even when using multiple radiological parameters. Where might higher resolution be helpful? In the context of the first appearance of clinical symptoms, MRI can often diagnostically confirm MS. Some lesions, however, cannot be depicted, or are only very poorly depicted at 1.5 or 3 T. This is important if, for example, this is the only lesion of the patient. In particular, cortical lesions are often difficult to depict; 7 T, with increased resolution, can be more successful in this regard (Kollia et al. 2009; Metcalf et al. 2009; Mainero et al. 2009) (Fig. 11a). Moreover, it is possible to reveal the anatomical features of the plaques almost microscopically: the typical localization of the plaques around small venules can, for example, be clearly shown (Tallantyre et al. 2008; Ge et al. 2008) (Fig. 11b).

10 Cerebellum/Cerebellar Nuclei

More and more is known about the pathogenesis of many hereditary ataxias, and many promising new therapeutic approaches can be derived from this knowledge. Worldwide, a series of studies on the drug treatment of Friedreich's ataxia are already being conducted (Schulz et al. 2009). It can be expected that in the foreseeable future the effectiveness of potential drugs for the most common autosomal dominant spinocerebellar ataxias (SCA1, 2, 3, and 6) will be tested in multicenter trials. Because of the slowly progressive nature of these degenerative diseases, the establishment of biomarkers is of particular interest. In the search for suitable MRI parameters for disease progression, ultra-high field MRI provides a number of potential advantages compared with conventional field strengths.

With conventional and voxel-based morphometry, the degree of atrophy of the cerebellum and its subsections can be detected. The degree of cerebellar atrophy has been found to correlate with clinical ataxia scores (Brandauer et al. 2008; Schulz et al. 2010). An open question remains how long the minimum appropriate time intervals must be in order to capture, for example, the natural disease progression

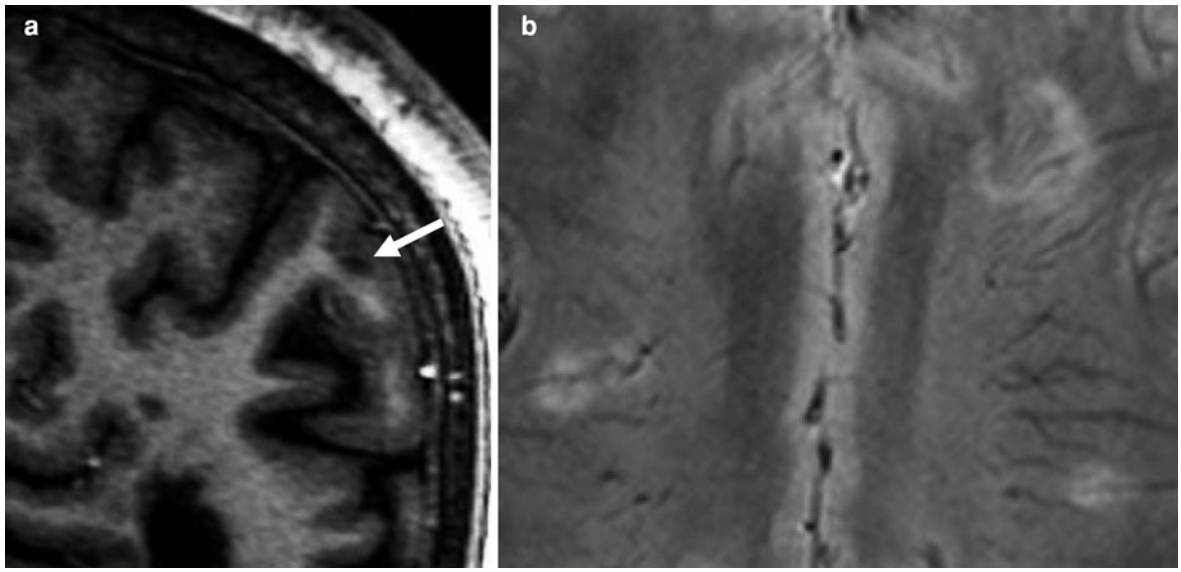

Fig. 11 **a** With the increased resolution at 7 T, a cortical MS lesion can be depicted as shown here in the MPRAGE. **b** In addition, it is possible to show the anatomical features of MS plaques in more detail, almost microscopically: The typical localization of the plaques around small venules can be well visualized in this thin-section T_2-weighted sequence

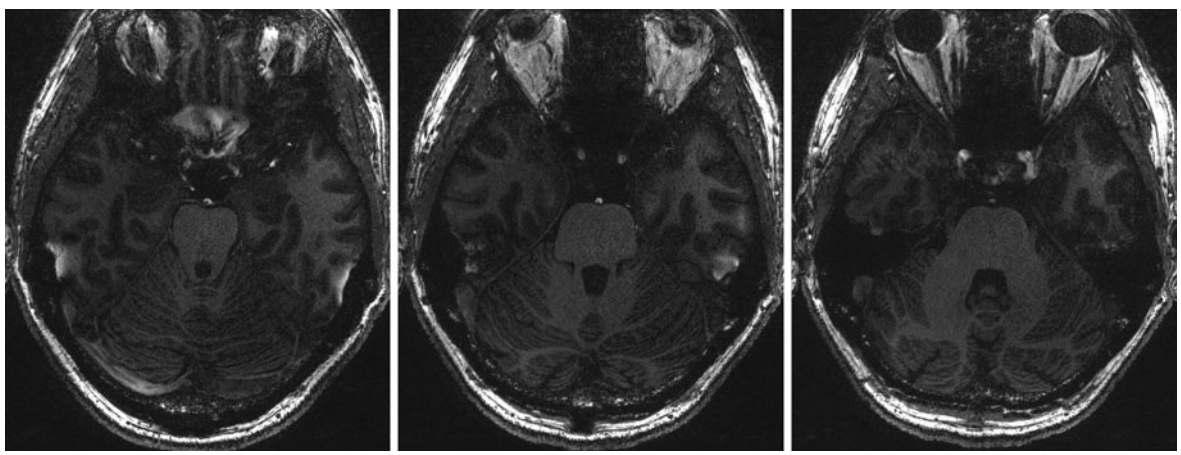

Fig. 12 Axial 7 T MPRAGE image of the cerebellum in a healthy volunteer acquired with a resolution in the submillimeter range (0.5 mm × 0.5 mm × 0.5 mm)

MR-volumetrically. It is likely that the sensitivity increases with higher spatial resolution. Ultra-high field MRI offers the capability of submillimeter resolution (Fig. 12). However, the use of semi-automatic evaluation routines is further complicated by the increased inhomogeneity in the grey levels.

Furthermore, ultra-high field MRI offers the opportunity to more accurately depict the fine structure of the cerebellum. Hereditary ataxias affect the cerebellar cortex and nuclei to varying degrees. In Friedreich's ataxia and SCA3, degeneration of the cerebellar nuclei is dominant, particularly of the dentate nucleus. In the case of SCA1, SCA2, and SCA6, however, the cerebellar cortex is particularly affected. The dentate nucleus and also the other cerebellar nuclei can be depicted at very high resolution using 7 T MRI (Maderwald et al. 2009a) (Fig. 13).

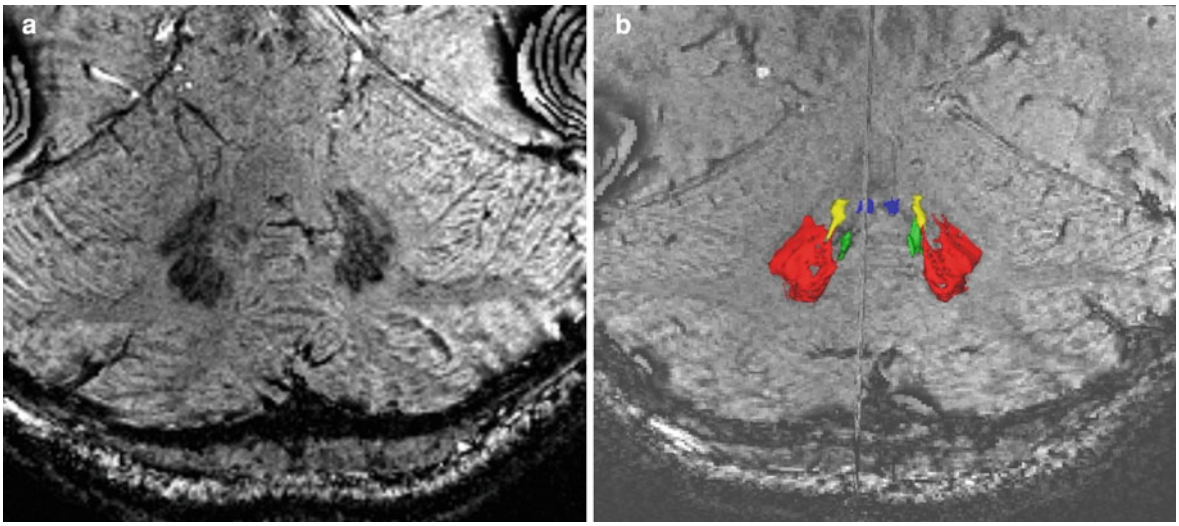

Fig. 13 The dentate nucleus in a healthy subject. **a** Axial 7 T SWI (resolution 0.5 mm × 0.5 mm × 0.5 mm). **b** 3D reconstruction of the cerebellar nuclei: *red* dentate nucleus, *yellow* emboliform nucleus, *green* globose nucleus, *blue* fastigial nucleus

In addition to determining the nuclear volume, the assessment of possible changes in the iron content of the dentate nucleus is of interest. For an increasing number of neurodegenerative diseases it has been proposed that an altered iron metabolism plays a role in the pathogenesis (Berg and Youdim 2006). In Friedreich's ataxia, a frataxin deficiency leads to impairment of cellular iron metabolism, and the dentate nucleus is particularly vulnerable because of its high iron content. The iron content in the brain can be examined by MRI (Chavhan et al. 2009); these techniques are based on the effect that iron leads to a shortening of the T_2 and T_2* relaxation times. This effect increases with increasing field strength, which has been shown for 3 T compared to 1.5 T, and it is likely that 7 T will bring further advantages.

Two studies conducted at 1.5 T could show that the relaxation times in the dentate nucleus were slightly reduced in subjects with Friedreich's ataxia compared with controls (Waldvogel et al. 1999; Boddaert et al. 2007). This could not be confirmed in an initial study by our group at 7 T. In a group of 15 subjects with Friedreich's ataxia, no significant decrease in relaxation times was found either at 7 T or in comparative measurements at 1.5 T. On the other hand, the volume of the dentate nucleus was significantly smaller compared to healthy individuals (Rabe et al. 2009). These results are consistent with histological findings showing a decrease in the number of neurons in the dentate nucleus but no reduction of the iron content (Koeppen et al. 2007). In our patient population, the disease was quite advanced. It could be that the detectable iron content at the onset of disease (when only a few cells in the dentate nucleus have perished) is elevated. Future studies must clarify whether relaxation measurements in the dentate nucleus are suitable as biomarkers in Friedreich's ataxia in dependence on disease stage.

Unlike in Friedreich's ataxia and SCA3, the cerebellar cortex is particularly affected in SCA1, SCA2, and SCA6. In animal studies using ultra-high field MRI, the molecular layer could be rendered distinct from the granular layer (Marques et al. 2009). In the aforementioned forms of SCA, changes in the granular layer and the molecular layer have been described in addition to degeneration of the Purkinje cells (Koeppen 2005). Ultra-high field MRI examinations with corresponding spatial resolution would be one potential way to better understand the pathophysiology of the disease over its progression.

11 Clinical Functional MRI

With the ever increasing field strength of available magnets, fMRI will continue to gain in importance in the future. The BOLD signal rises appreciably

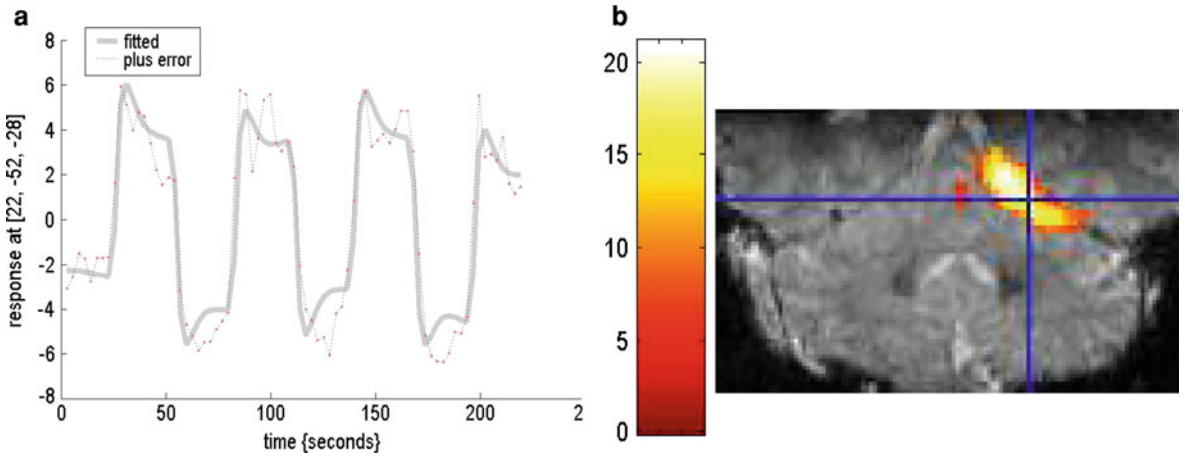

Fig. 14 **a** The measured hemodynamic response function (HRF) of a subject at 7 T performing a simple finger movement shows good agreement with the assumed HRF. **b** After optimization of the sequence, a stable and good quality activation could be achieved even for the very artifact-prone cerebellar brain regions. The issue of susceptibility is especially problematic for fast EPI sequences at ultra-high field. With optimized sequences, good activation is obtainable even for regions with strong artifact potential as shown here in the posterior fossa

with increasing field strength, as it benefits doubly from both the higher SNR and the increased susceptibility sensitivity. This makes it possible, among other prospects, to examine individual events using fMRI without the necessity for repetitions of the active stimuli in contrast to the rest condition, which can be suboptimal for some investigations. Furthermore, a significantly improved spatial resolution is possible, so that activations can be represented in millimeter resolution (Yacoub et al. 2001).

However, fMRI at ultra-high field strengths is not straightforward: Part of the benefits which enable an increased BOLD contrast can also lead to major problems. The increased sensitivity to susceptibility artifacts often leads to significant disturbances in BOLD imaging; in particular, echo planar sequences (echo planar imaging, EPI) are very susceptible to these artifacts, so the sequences must be suitably optimized for fMRI at 7 T (Poser and Norris 2009).

11.1 Cerebrum

Initial fMRI studies in the cerebrum have therefore often focused on the high-resolution but focused display of, for example, the visual cortex (Pfeuffer et al. 2002). In these studies, the artifact problems are minimized by the fact that as few tissue transitions as possible with associated dephasing problems are near the area of interest. Often, surface coils were used with a rather small field-of-view. Meanwhile, whole-brain investigations using fMRI have been carried out at least for some well-established paradigms (Gizewski et al. 2007; Speck et al. 2008; Walter et al. 2008). In one of these studies, a simple finger movement paradigm was performed (Gizewski et al. 2007). With this robust paradigm, a stable activation of the sensorimotor areas could be achieved. This was verified in each subject by considering the hemodynamic response curve in addition to the activation image (Fig. 14a). After optimization of the sequence, a stable and good quality activation was achieved even for the very artifact-prone portions of the cerebellar brain regions (Fig. 14b). Even complex issues have now been investigated at 7 T, for example the emotional processing of erotic stimuli (Walter et al. 2008). The ultra-high field is of great interest for such experimental questions, especially since the activation of the deep brain structures can be performed reliably and with more signal. Many additional interesting questions will be pursued in the future.

As at lower filed strengths, the following question applies to fMRI at ultra-high field: What is the possible clinical benefit? The most common clinical application of fMRI is usually the representation of

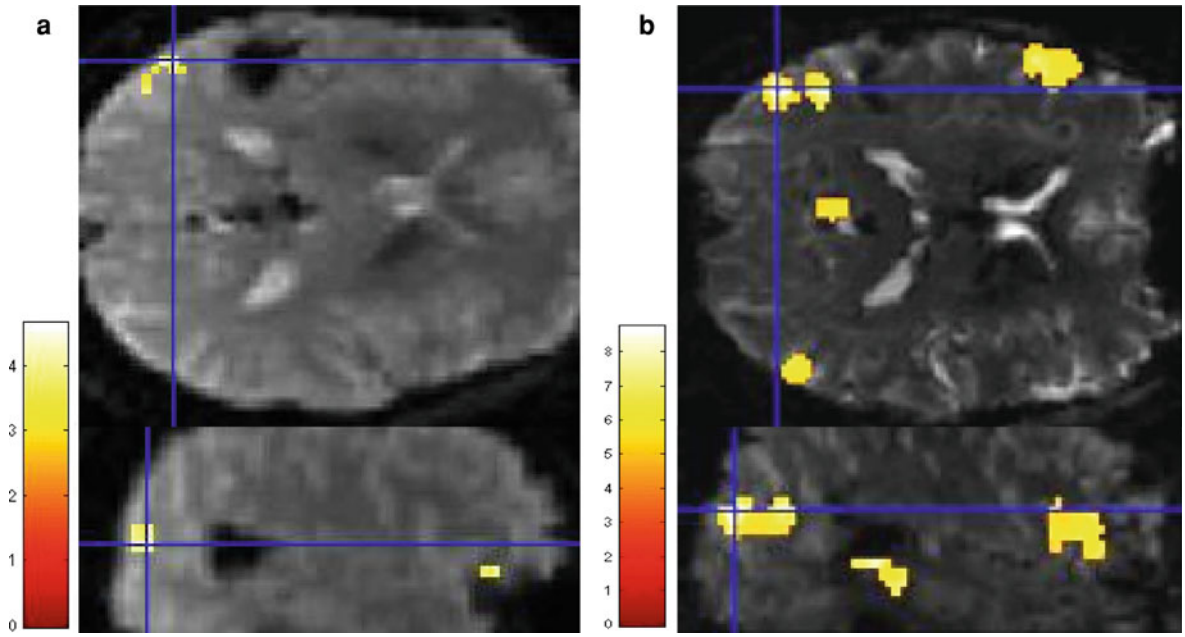

Fig. 15 Results of a speech paradigm applied in a patient with a cavernoma in the left parietal lobe. This example clearly demonstrates the signal gain of 7 T (**b**) vs 1.5 T (**a**) and the much larger cluster size. On the other hand, the increased vulnerability to susceptibility artifacts at 7 T can be recognized: The EPI sequence on which these activations are superimposed exhibits greater distortion at 7 T than at 1.5 T. The use of parallel imaging, however, leads to a significant reduction in artifact problems

eloquent areas before tumor removal. Typically, this involves motor or linguistic paradigms, which can also be well applied even at 7 T. However, tumors located close to the motor centers are often near the brain surface and thus the skull. This again leads to problems with susceptibility. A further optimization of the sequences and suppression of artifacts can be achieved by the application of multi-channel coils. With these coils it is possible to apply parallel imaging, which especially benefits from the ultra-high field (Wiesinger et al. 2006). Figure 15 shows a first result with an optimized sequence used in conjunction with a speech paradigm in a patient with a cavernous hemangioma in the left parietal lobe. With parallel imaging, distortions are significantly reduced, which in turn is important to allow a precise overlay on high-resolution structural images in patients. The success of fMRI especially in cancer patients can be significantly higher at 7 T, as here the increased signal facilitates good activations even with limited subject compliance. To what extent this advantage is relevant to clinical practice is the subject of a current study.

11.2 Cerebellum

A large number of studies at conventional field strengths show activations of the cerebellar cortex, the main input structure of the cerebrum, and these studies have contributed significantly to a better understanding of the physiology of the cerebellum. For example, for some time the cerebellum has been assigned not only motor but also non-motor functions (Timmann and Daum 2007; Strick et al. 2009). On the other hand, there are currently very few studies that have been able to demonstrate activation of the cerebellar nuclei, the main output structure of the cerebellum (Dimitrova et al. 2006; Habas 2009). The increased sensitivity and improved spatial resolution of ultra-high field MRI could change this in the future.

There are several reasons why activation of the cerebellar nuclei can be detected less reliably than the cerebellar cortex. Firstly, the iron content of the nuclei is high, which on the one hand facilitates the structural depiction of the nuclei via susceptibility artifacts, but on the other hand reduces the available

BOLD contrast through signal voids. Another reason is due to the small size and geometry of the nuclei, which leads to a relatively large preponderance of partial volume effects. Even with voxel sizes of a few cubic millimeters, almost all voxels contain both white matter and nuclear constituents, and the former contribute little or nothing to the activation (Logothetis and Wandell 2004). In fact, a good portion of the improved sensitivity of ultra-high magnetic field MRI probably derives from the reduced voxel size and consequently the reduced partial volume effects (Logothetis et al. 2002). A third reason is the physiology of the BOLD effect in the cerebellar nuclei. The BOLD signal may be due primarily to the glutamatergic collaterals of the mossy and climbing fibers to the nuclei. Since the climbing fibers have a lower discharge frequency and do not have strong contacts as to the Purkinje cells in the cerebellar cortex (no "complex spikes" in the cerebellar nuclei) (Sultan et al. 2000), the mossy fiber input might predominate. Although the exact ratio is unknown, the mossy fiber and parallel fiber synapses in the cortex are much more numerous than in the nuclei; consequently, the BOLD effect may be lower in the cerebellar nuclei than in the cortex.

Since the position of the cerebellar nuclei is variable, normalization quality is crucial for group analysis. The normalization of the cerebellar nuclei has been greatly improved in our group in cooperation with Jörn Diedrichsen (Institute of Cognitive Neuroscience, University College London, UK). Initial 7 T fMRI studies show that activation of the dentate nucleus can be reliably achieved by finger movements (Kueper et al. 2009) (Fig. 16).

The improved SNR of ultra-high field MRI increases the probability of detecting an activation of the cerebellar nuclei. However, the above-mentioned problems, many of which are particularly marked in the posterior cranial fossa, counteract part of the improved SNR. Tissue/bone and air interfaces near the cerebellum, other susceptibility effects, and pulsation of cerebrospinal fluid and large blood vessels lead to signal dropouts, distortions, and other artifacts. Head coils, imaging techniques, and pulse sequences need to be further optimized for application at ultra-high field. ECG, pulse, and respiratory triggering are possibilities to minimize the effects of physiological motion in the posterior fossa.

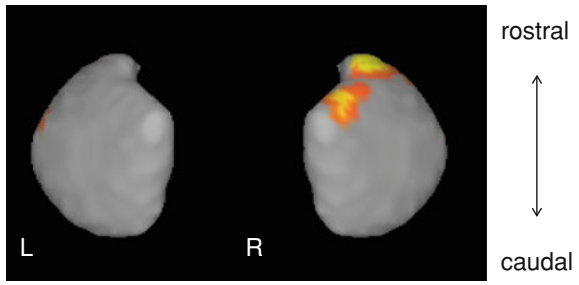

Fig. 16 7 T fMRI of the cerebellar nuclei. Activation of the dorso-ventral portion of the ipsilateral dentate nucleus elicited by tapping of the right index finger. Activation is shown on the surface of a dentate nucleus template used for normalization (Jörn Diedrichsen, Institute of Cognitive Neuroscience, University College London, UK)

Technical problems remain to be resolved, but ultra-high field MRI promises reliable detection of cerebellar nuclei activation in addition to an improved spatial resolution of the cerebellar cortex. Since it is likely that the quality of fMRI of the brain stem will improve in parallel in a similar way, activations of the red nucleus and the inferior olivary nucleus should be more readily detectable (Habas et al. 2009). It would then become feasible to investigate cerebellar control circuits in humans.

12 Beyond Clinical Neuro

The most prominent technical hindrance to clinical application of 7 T is the uneven RF penetration and excitation of the body tissue, particularly in anatomical regions with large cross-sections (Fig. 17). Due to this technical difficulty, the most promising initial clinical application of 7 T MR imaging is in the head or extremities, and later chapters in this book focus in particular on musculoskeletal imaging at ultra-high field.

From a neurological point of view, the application of 7 T or other ultra-high fields for studies of the spine would be very limited without an extended field-of-view. At the moment, new technologies for RF excitation at ultra-high field are being investigated to enable high-quality and reliable coverage of the body from head to foot as is already the case at 1.5 and 3 T. Figure 18a shows a prototype of a multichannel transmit coil for the spinal region (Kraff et al. 2009). With this coil, the 8 elements can be controlled

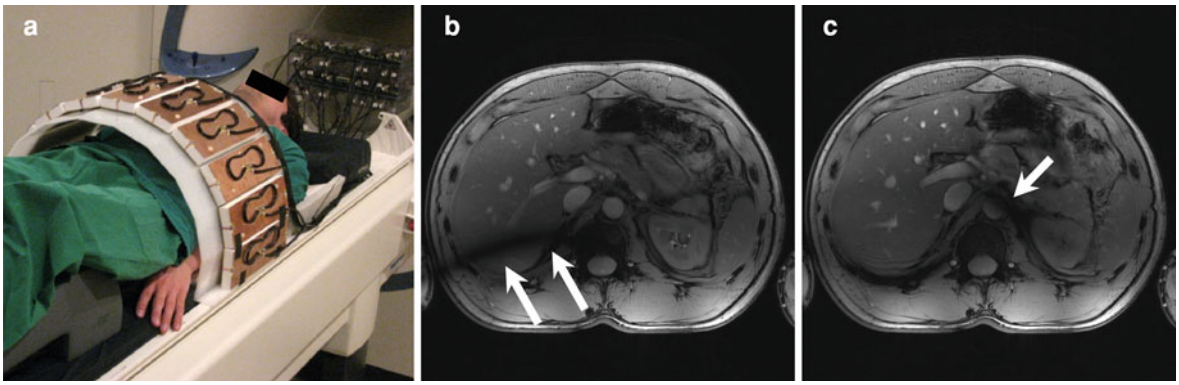

Fig. 17 **a** A 16-channel body array composed of 11 anterior stripline elements and 5 posterior stripline elements. **b** Axial section (T_1-weighted 2D FLASH) through the liver and kidney exposing a substantial inhomogeneity in the B_1 transmit field on the right side (*arrows*) when exciting with the standard circularly polarized mode. **c** The same section acquired with the second-order circularly polarized mode (45° phase progression between elements rather than 22.5°) revealing a smaller B_1 inhomogeneity limited to a periaortal focus (*arrow*)

independently of each other during tissue excitation. Thus, a significant improvement in excitation uniformity and coverage is reached (Fig. 18b, c). Such advances suggest that in the future 7 T magnets could be used for the diagnostic workup of the entire central nervous system.

Is general, large field-of-view imaging within the thorax and abdomen feasible at high field, and what improvements in clinical diagnosis can be expected? Although the answer to the latter question remains open, one can expect that advantages will be pursued utilizing similar strategies to those used in brain imaging: higher spatial resolution; improved spectroscopy and spectroscopic imaging, both for hydrogen and other nuclei; extraction of additional information from the image phase; and new or improved tissue contrasts, particularly those related to magnetic susceptibility.

Initial research within the thorax and abdomen has centered around the pursuit of technical solutions to help alleviate RF inhomogeneities and demonstrate basic imaging feasibility (Snyder et al. 2009; Vaughan et al. 2009). This work generally involves multi-channel transmit coils and the use of either static or dynamic RF shimming of the B_1^+ transmit field (van den Bergen et al. 2007; Katscher and Bornert 2006). The feasibility of basic abdominal and cardiac imaging have both been demonstrated.

Figure 17a depicts a multi-channel coil that is based on stripline elements (Orzada et al. 2009; Orzada et al. 2010), and Fig. 19 depicts several standard imaging sequences obtained in the liver at 7 T with a similar coil but only 8 elements. This work was conducted in healthy volunteers, and patient investigations are still outstanding. However, even these early imaging results demonstrate the successful transformation of the increased SNR into a high spatiotemporal resolution, yielding highly defined anatomical depiction and confirming the expected improved performance of parallel imaging (Umutlu et al. 2010). Nevertheless, the impact of enhanced structural resolution on disease diagnosis still remains to be determined.

Especially non-enhanced angiographic applications in the abdomen appear promising (Fig. 20), as the high signal intensity of the hepatic or renal vasculature provides excellent conspicuity of the vessels. The potential for robust vascular imaging without contrast agent is attractive because of the lower cost and because of data linking nephrogenic systemic fibrosis to gadolinium contrast agent exposure (Darwish and Wood 2009). This inherently positive vessel-to-background contrast at 7 T in various gradient-echo sequences regardless of image orientation has also been observed in other anatomical regions (Maderwald et al. 2008; Monninghoff et al. 2009a). The etiology of the high vascular signal intensity at 7 T remains partially unresolved, as inflow as well as steady-state effects seem to be accountable. Also, due to the utilization of local transmit/receive RF coils at 7 T, flowing spins are not pre-saturated by RF pulses before they enter the

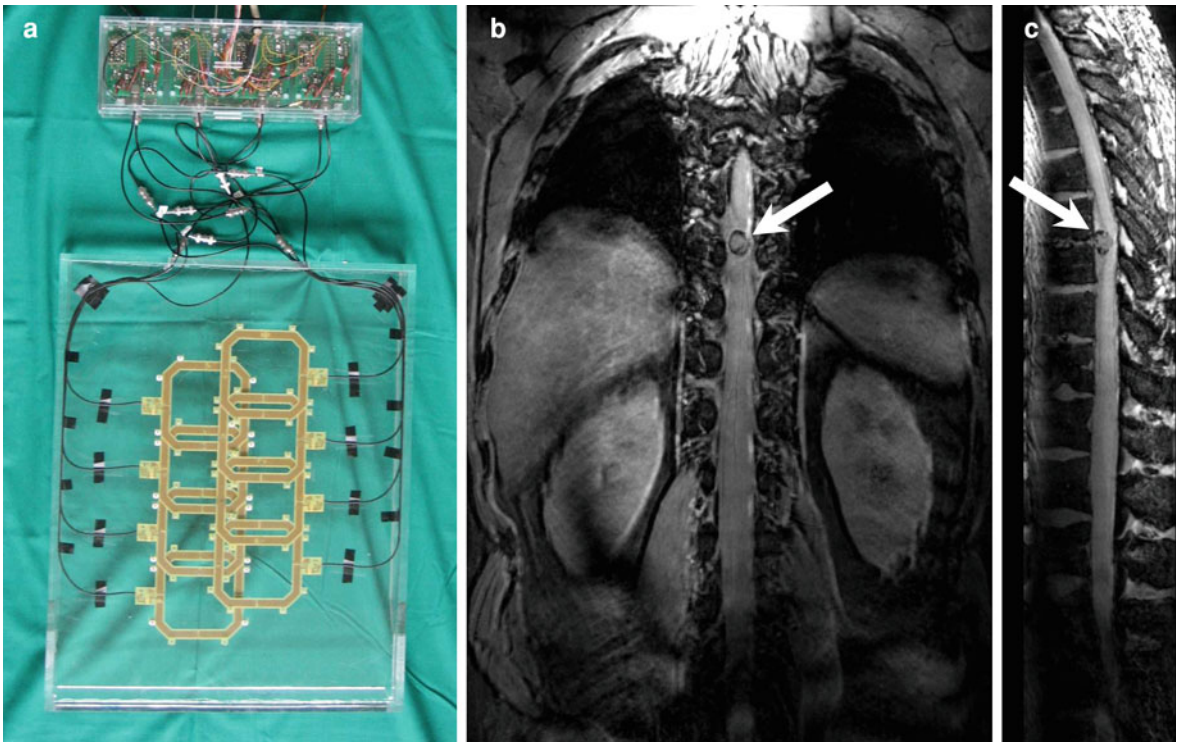

Fig. 18 **a** 7 T spine coil consisting of 8 loop elements that can all be individually driven during RF transmission. The preamplifiers and T/R-switch electronics are visible at the top of the image. **b** Coronal and **c** sagittal 3D FLASH images (0.69 mm isotropic resolution; parallel imaging with reduction factor 2; acquisition time 9 min.) in a patient with a herniated disc (*arrows*) showing displacement of the posterior longitudinal ligament

imaging region. Hence, the impact of inflowing "fresh" spins to the hyperintense blood signal may be greater than with an extended body transmit coil.

The hyperintense blood pool in spoiled gradient-echo sequences is also particularly advantageous for wall function studies of the heart (Maderwald et al. 2009b). Although balanced steady-state free precession (bSSFP) sequences (e.g. TrueFISP, FIESTA, or balanced FFE) represent the state-of-the-art for wall-motion studies at lower field strengths and demonstrate outstanding performance at 1.5 T, such bSSFP sequences are severely compromised at 7 T by contrast loss (myocardium-to-blood), dark banding artifacts due to off-resonance effects, and generally severe signal inhomogeneities. In addition, SAR restrictions inhibit the utilization of a suitably high excitation flip angle. Cine spoiled gradient-echo sequences (e.g. FLASH, SPGR, or FFE), on the other hand, provide suitable imaging quality with good signal homogeneity over almost the entire cardiac volume and good myocardium-to-blood contrast (Fig. 21).

A clear weakness of cardiac imaging at 1.5 T and even at 3 T is the unreliable depiction of the coronary arteries. At 7 T, it should be theoretically possible to further improve spatial resolution and thus resolve fine details of these very small structures. Initial coronary imaging at 7 T has been demonstrated, but there are still many technical challenges to be addressed before image quality is competitive with either 1.5 or 3 T (van Elderen et al. 2009). In addition to other challenges, respiratory and cardiac triggering are vital to compensate for physiologic motion during any type of cardiac study. At 7 T, ECG triggering functions quite poorly due to the elevated T wave and other interferences (Abi-Abdallah et al. 2007). An alternative which has been pursued to sidestep this issue is to use acoustic rather than electrical-based triggering (Frauenrath et al. 2009).

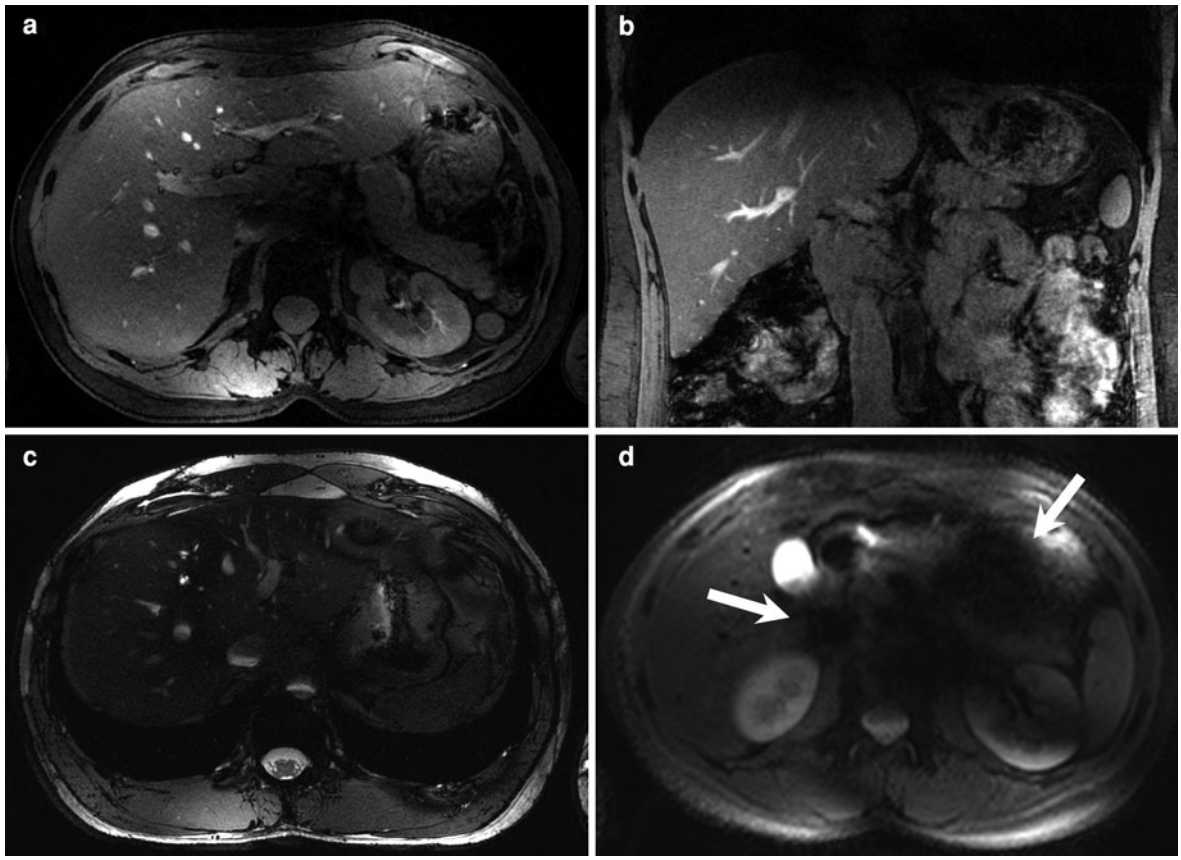

Fig. 19 Various image contrasts in the liver acquired axially with an 8-channel stripline body array. The elevated SNR at 7 T enables imaging at higher spatial resolution. **a**, **b** Axial and coronal 2D FLASH with fat saturation acquired at 0.8 × 0.8 × 2.0 mm^3 (non-interpolated). **c** TrueFISP (1.3 × 1.6 × 4.0 mm^3) demonstrating excellent homogeneity of the static magnetic field through absence of significant banding artifacts. **d** T_2-weighted turbo-spin-echo (TSE) (1.4 × 1.4 × 5.5 mm^3) with poor image quality because of flip angle limitations and the inhomogeneous B_1 transmit field (*arrows*)

One organ that has been targeted very early at 7 T is the prostate (Metzger et al. 2008; Klomp et al. 2009). It is very challenging to grade the aggressiveness of prostate carcinoma, even at 3 T. With the broad application of blood screening tests based on the serum level of prostate-specific antigen (PSA), the early detection of prostate cancer has been significantly improved. However, specificity of the PSA test is very low, as benign prostate inflammation leads to many false positive results, and many of the detected cancers are not aggressive and could be left untreated to avoid the risks and side-effects of treatment. It is hoped that MRI and MRS or MR spectroscopic imaging (MRSI) at 7 T could improve characterization and staging of prostate cancers. Initial work has demonstrated proton MRSI with voxel sizes down to 3.5 mm^3, significantly reducing partial volume effects (Klomp et al. 2009).

13 Outlook

Because of the very positive experience with imaging at 7 T thus far, it seems possible that this field strength will be introduced in the foreseeable future as the next clinical alternative beyond 3 T, although the role of ultra-high field strength in the clinic remains to be determined. It is likely that such systems will be utilized for dedicated problem solving in cases where

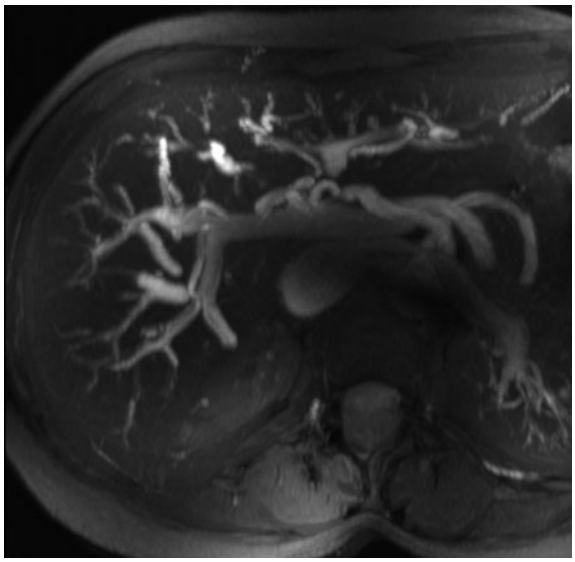

Fig. 20 Axial MIP of a TOF MRA (TR/TE 17/4.7 ms, flip angle 60°, 1.6 × 0.8 × 2.5 mm^3, slab thickness 3.33 cm) in the liver. At 7 T, the vasculature is depicted with high contrast to the parenchyma even without intravenous contrast agent, in contrast to lower field strengths

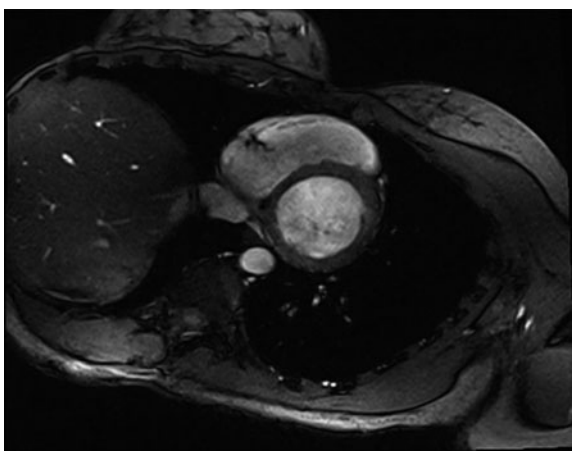

Fig. 21 Short-axis CINE spoiled gradient-echo (FLASH) acquired with a flexible body array with four posterior and four anterior stripline elements (flip angle 60°, 1.4 × 1.4 × 4.0 mm^3, 20 phases per RR interval, acquisition time 11 s). The myocardium-to-blood contrast at 7 T is superior vs lower field strengths, making spoiled gradient-echo an alternative to balanced steady-state free precession for cardiac functional studies

lower field strengths fail to deliver a conclusive answer rather than for general clinical routine. Currently, new 7 T magnets with active, superconducting shielding are being introduced by the manufacturers; this significantly reduces the need for passive steel shielding and makes it thus much easier to set up a system in hospitals and clinics with manageable construction and siting effort. As previously mentioned, particularly problematic at 7 T at the present time is still the uneven illumination of the body anatomy during high-frequency excitation of large anatomical cross-sections (Fig. 17). Thus, it is likely that the first clinical devices will have a limited approval to conduct examinations of the head and extremities.

For research purposes, human MRI systems especially at 7 and 9.4 T are in operation. MRI systems are already being planned with even higher field strength: 10.5, 11.7, or even 14 T. Where is the upper limit in the magnetic field strength? Is it likely that with further technical advances ever larger magnets will find their way into clinical routine? On the one hand, there are technical and economic obstacles. Conventional superconducting magnets are usually constructed from niobium–titanium wire, and a 7 T MRI system already costs several million dollars/Euros. Above 10 T the use of this material becomes very difficult, and more expensive alternatives such as niobium-tin are often necessary, at least for part of the magnet windings. Nevertheless, past experience has taught that such obstacles can be overcome.

Most probably the ceiling in the magnetic field strength will be determined by physiological side effects. Other aspects of MR imaging such as the switching of the gradient magnetic field or the excitation with RF energy are already constrained by physiological limits. In the U.S., the legal limits for clinical diagnostic use of MRI magnets are regulated by the Food and Drug Administration (FDA). Here, the ceiling currently lies at 8 T (United States Food and Drug Administration 2003). In Europe the limit is lower at 4 T (International Electrotechnical Commission 2008), and all examinations at 7 T are therefore performed as part of studies which are approved by the local ethics committee. An increase in the European limit is expected in the coming years, as more and more experience with studies at higher field strengths is gathered. Experience at 7 T is very positive up till now, and the method is well tolerated by most subjects (Theysohn et al. 2008).

The key to the clinical justification of such a technology lies in the identification of applications where the higher magnetic field and related properties

such as increased signal lead to a better diagnosis and ultimately to a better outcome for patients. The first step is to demonstrate that the improved image quality can lead to a change in therapy and treatment of particular patient groups. This evaluation has already begun for 7 T. Initial experience confirms that 7 T MRI represents an extremely promising technology to optimize existing diagnostic possibilities in many neurological diseases, and this potential is likely to be expanded to various pathologies throughout the body as the technology progresses.

Acknowledgments Parts of this work were supported by the German Research Foundation (Deutsche Forschungsgemeinschaft, DFG Ti 239/9-1), the Dr. Werner Jackstädt Foundation, and the German Federal Ministry of Education and Research (Bundesministerium für Bildung und Forschung, BMBF 01EZ0716).

References

Abi-Abdallah D, Robin V, Drochon A, Fokapu O (2007) Alterations in human ECG due to the MagnetoHydroDynamic effect: a method for accurate R peak detection in the presence of high MHD artifacts. Conf Proc IEEE Eng Med Biol Soc 2007, 1842–1845

Berg D, Youdim MB (2006) Role of iron in neurodegenerative disorders. Top Magn Reson Imaging 17:5–17

Boddaert N, Le Quan Sang KH, Rotig A et al (2007) Selective iron chelation in Friedreich ataxia: biologic and clinical implications. Blood 110:401–408

Brandauer B, Hermsdorfer J, Beck A et al (2008) Impairments of prehension kinematics and grasping forces in patients with cerebellar degeneration and the relationship to cerebellar atrophy. Clin Neurophysiol 119:2528–2537

Brass SD, Chen NK, Mulkern RV, Bakshi R (2006) Magnetic resonance imaging of iron deposition in neurological disorders. Top Magn Reson Imaging 17:31–40

Breyer T, Wanke I, Maderwald S et al (2009) Imaging of patients with hippocampal sclerosis at 7 Tesla: initial results. Acad Radiol 17:421–426

Cecil KM (2006) MR Spectroscopy of metabolic disorders. Neuroimaging Clin N Am 16:87–116, viii

Chavhan GB, Babyn PS, Thomas B, Shroff MM, Haacke EM (2009) Principles, techniques, and applications of T_2*-based MR imaging and its special applications. Radiographics 29:1433–1449

Cho ZH, Kang CK, Han JY et al (2008) Observation of the lenticulostriate arteries in the human brain in vivo using 7.0T MR angiography. Stroke 39:1604–1606

Darwish T, Wood B (2009) Nephrogenic systemic fibrosis: what internists need to know. Mo Med 106:373–376

Dashner RA, Kangarlu A, Clark DL, RayChaudhury A, Chakeres DW (2004) Limits of 8-Tesla magnetic resonance imaging spatial resolution of the deoxygenated cerebral microvasculature. J Magn Reson Imaging 19:303–307

Derex L, Nighoghossian N, Hermier M et al (2004) Thrombolysis for ischemic stroke in patients with old microbleeds on pretreatment MRI. Cerebrovasc Dis 17:238–241

Dimitrova A, de Greiff A, Schoch B et al (2006) Activation of cerebellar nuclei comparing finger, foot and tongue movements as revealed by fMRI. Brain Res Bull 71:233–241

European Federation of Neurological Societies Task Force (2001) The future of magnetic resonance-based techniques in neurology. Eur J Neurol 8:17–25

Frauenrath T, Hezel F, Heinrichs U et al (2009) Feasibility of cardiac gating free of interference with electro-magnetic fields at 1.5 Tesla, 3.0 Tesla and 7.0 Tesla using an MR-stethoscope. Invest Radiol 44:539–547

Ge Y, Zohrabian VM, Grossman RI (2008) Seven-Tesla magnetic resonance imaging: new vision of microvascular abnormalities in multiple sclerosis. Arch Neurol 65: 812–816

Gizewski ER, de Greiff A, Maderwald S et al (2007) fMRI at 7 T: whole-brain coverage and signal advantages even infratentorially? Neuroimage 37:761–768

Habas C (2009) Functional imaging of the deep cerebellar nuclei: a review. Cerebellum 9:22–28

Habas C, Guillevin R, Abanou A (2009) In vivo structural and functional imaging of the human rubral and inferior olivary nuclei: a mini-review. Cerebellum 9:167–173

Heverhagen JT, Bourekas E, Sammet S, Knopp MV, Schmalbrock P (2008) Time-of-flight magnetic resonance angiography at 7 Tesla. Invest Radiol 43:568–573

Hoult DI, Phil D (2000) Sensitivity and power deposition in a high-field imaging experiment. J Magn Reson Imaging 12:46–67

International Electrotechnical Commission (2008) Medical electrical equipment – Part 2–33: Particular requirements for the safety of magnetic resonance equipment for medical diagnosis. IEC 60601-2-33. 2.2 edn.

Kang CK, Hong SM, Han JY et al (2008) Evaluation of MR angiography at 7.0 Tesla MRI using birdcage radio frequency coils with end caps. Magn Reson Med 60: 330–338

Kang CK, Park CW, Han JY et al (2009) Imaging and analysis of lenticulostriate arteries using 7.0-Tesla magnetic resonance angiography. Magn Reson Med 61:136–144

Katscher U, Bornert P (2006) Parallel RF transmission in MRI. NMR Biomed 19:393–400

Klomp DW, Bitz AK, Heerschap A, Scheenen TW (2009) Proton spectroscopic imaging of the human prostate at 7 T. NMR Biomed 22:495–501

Koeppen AH (2005) The pathogenesis of spinocerebellar ataxia. Cerebellum 4:62–73

Koeppen AH, Michael SC, Knutson MD et al (2007) The dentate nucleus in Friedreich's ataxia: the role of iron-responsive proteins. Acta Neuropathol 114:163–173

Kollia K, Maderwald S, Putzki N et al (2009) First clinical study on ultra-high-field MR imaging in patients with multiple sclerosis: comparison of 1.5T and 7T. AJNR Am J Neuroradiol 30:699–702

Koopmans PJ, Manniesing R, Niessen WJ, Viergever MA, Barth M (2008) MR venography of the human brain using

susceptibility weighted imaging at very high field strength. MAGMA 21:149–158
Kraff O, Bitz AK, Kruszona S et al (2009) An eight-channel phased array RF coil for spine MR imaging at 7 T. Invest Radiol 44:734–740
Kueper M, Diedrichsen J, Thuerling M et al (2009) Functional imaging of the deep cerebellar nuclei using 7 T MRI. In: Neuroscience, Society for Neuroscience. Chicago :BB32 460.8
Ladd ME (2007) High-field-strength magnetic resonance:potential and limits. Top Magn Reson Imaging 18:139–152
Lee SH, Bae HJ, Kwon SJ et al (2004) Cerebral microbleeds are regionally associated with intracerebral hemorrhage. Neurology 62:72–76
Lee J, Hirano Y, Fukunaga M, Silva AC, Duyn JH (2010) On the contribution of deoxy-hemoglobin to MRI gray-white matter phase contrast at high field. Neuroimage 49:193–198
Li TQ, van Gelderen P, Merkle H et al (2006) Extensive heterogeneity in white matter intensity in high-resolution T_2*-weighted MRI of the human brain at 7.0 T Neuroimage 32:1032–1040
Logothetis NK, Wandell BA (2004) Interpreting the BOLD signal. Annu Rev Physiol 66:735–769
Logothetis N, Merkle H, Augath M, Trinath T, Ugurbil K (2002) Ultra high-resolution fMRI in monkeys with implanted RF coils. Neuron 35:227–242
Maderwald S, Ladd SC, Gizewski ER et al (2008) To TOF or not to TOF: strategies for non-contrast-enhanced intracranial MRA at 7 T. MAGMA 21:159–167
Maderwald S, Küper M, Thürling M et al (2009a) 3D visualization of deep cerebellar nuclei using 7T MRI. In: Proceedings of the 17th scientific meeting. International Society for Magnetic Resonance in Medicine, Honolulu, p 963
Maderwald S, Orzada S, Schäfer L et al (2009b) 7T Human in vivo cardiac imaging with an 8-Channel transmit/receive array. In: Proceedings 17th Scientific Meeting, International Society for Magnetic Resonance in Medicine. Honolulu, p 821
Mainero C, Benner T, Radding A et al (2009) In vivo imaging of cortical pathology in multiple sclerosis using ultra-high field MRI. Neurology 73:941–948
Marques JP, Maddage R, Mlynarik V, Gruetter R (2009) On the origin of the MR image phase contrast: an in vivo MR microscopy study of the rat brain at 14.1 T. Neuroimage 46:345–352
Metcalf M, Xu D, Okuda DT et al (2009) High-resolution phased-array MRI of the human brain at 7 Tesla: initial experience in multiple sclerosis patients. J Neuroimaging 20:141–147
Metzger GJ, Snyder C, Akgun C et al (2008) Local B_1+ shimming for prostate imaging with transceiver arrays at 7T based on subject-dependent transmit phase measurements. Magn Reson Med 59:396–409
Meyer JS, Quach M, Thornby J, Chowdhury M, Huang J (2005) MRI identifies MCI subtypes: vascular versus neurodegenerative. J Neurol Sci 229–230:121–129
Moenninghoff C, Maderwald S, Theysohn JM et al (2009) Imaging of adult astrocytic brain tumours with 7 T MRI: preliminary results. Eur Radiol 20:704–713
Monninghoff C, Maderwald S, Theysohn JM et al (2009a) Evaluation of intracranial aneurysms with 7 T versus 1.5 T time-of-flight MR angiography—initial experience. Rofo 181:16–23
Monninghoff C, Maderwald S, Wanke I (2009b) Pre-interventional assessment of a vertebrobasilar aneurysm with 7 Tesla time-of-flight MR angiography. Rofo 181:266–268
Moseley ME, Liu C, Rodriguez S, Brosnan T (2009) Advances in magnetic resonance neuroimaging. Neurol Clin 27:1–19, xiii
Orzada S, Quick H, Ladd M et al (2009) A flexible 8-channel transmit/receive body coil for 7 T human imaging. In: Proceedings of the 17th scientific meeting, International Society for Magnetic Resonance in Medicine, Honolulu, p 2999
Orzada S, Maderwald S, Kraff O et al (2010) 16-channel Tx/Rx body coil for RF shimming with selected Cp modes at 7T. In: Proceedings 18th Scientific Meeting, International Society for Magnetic Resonance in Medicine. Stockholm, p 50
Otazo R, Mueller B, Ugurbil K, Wald L, Posse S (2006) Signal-to-noise ratio and spectral linewidth improvements between 1.5 and 7 Tesla in proton echo-planar spectroscopic imaging. Magn Reson Med 56:1200–1210
Pfeuffer J, van de Moortele PF, Yacoub E et al (2002) Zoomed functional imaging in the human brain at 7 Tesla with simultaneous high spatial and high temporal resolution. Neuroimage 17:272–286
Poser BA, Norris DG (2009) Investigating the benefits of multi-echo EPI for fMRI at 7 T. Neuroimage 45:1162–1172
Rabe K, Kraff O, Orzada S et al (2009) Volumetrische und relaxometrische Vermessung des Nucleus dentatus im 7T Magnetfeld bei Patienten mit einer Friedreich Ataxie. Akt Neurol 36:S54
Schild H (2005) Clinical highfield MR. Rofo 177:621–631
Schlamann M, Maderwald S, Becker W et al (2010) Cerebral cavernous hemangiomas at 7 Tesla: initial experience. Acad Radiol 17:3–6
Schulz JB, Boesch S, Burk K et al (2009) Diagnosis and treatment of Friedreich ataxia: a European perspective. Nat Rev Neurol 5:222–234
Schulz JB, Borkert J, Wolf S et al (2010) Visualization, quantification and correlation of brain atrophy with clinical symptoms in spinocerebellar ataxia types 1, 3 and 6. Neuroimage 49:158–168
Snyder CJ, DelaBarre L, Metzger GJ et al (2009) Initial results of cardiac imaging at 7 Tesla. Magn Reson Med 61:517–524
Speck O, Stadler J, Zaitsev M (2008) High resolution single-shot EPI at 7T. MAGMA 21:73–86
Srinivasan R, Ratiney H, Hammond-Rosenbluth KE, Pelletier D, Nelson SJ (2009) MR spectroscopic imaging of glutathione in the white and gray matter at 7 T with an application to multiple sclerosis. Magn Reson Imaging (in press)
Strick PL, Dum RP, Fiez JA (2009) Cerebellum and nonmotor function. Annu Rev Neurosci 32:413–434
Sultan F, Möck M, Thier P (2000) Functional architecture of the cerebellar system. In: Klockgether T (ed) Neurological Ataxia, Marcel Dekker, New York, pp 1–52
Tallantyre EC, Brookes MJ, Dixon JE et al (2008) Demonstrating the perivascular distribution of MS lesions in vivo with 7-Tesla MRI. Neurology 70:2076–2078

Theysohn JM, Maderwald S, Kraff O et al (2008) Subjective acceptance of 7 Tesla MRI for human imaging. MAGMA 21:63–72

Theysohn JM, Kraff O, Maderwald S et al (2009) The human hippocampus at 7 T–in vivo MRI. Hippocampus 19:1–7

Timmann D, Daum I (2007) Cerebellar contributions to cognitive functions: a progress report after two decades of research. Cerebellum 6:159–162

Umutlu L, Bitz AK, Maderwald S et al (2010) 7T liver MRI in humans: initial results. In: Proceedings of the 18th scientific meeting, International Society for Magnetic Resonance in Medicine, Stockholm, p 2624

United States Food and Drug Administration. Guidance for industry and FDA staff: criteria for significant risk investigations of magnetic resonance diagnostic devices, 2003

van den Bergen B, Van den Berg CA, Bartels LW, Lagendijk JJ (2007) 7 T body MRI: B_1 shimming with simultaneous SAR reduction. Phys Med Biol 52:5429–5441

van Elderen SG, Versluis MJ, Webb AG et al (2009) Initial results on in vivo human coronary MR angiography at 7 T. Magn Reson Med 62:1379–1384

Vaughan JT, Garwood M, Collins CM et al (2001) 7T vs. 4T: RF power, homogeneity, and signal-to-noise comparison in head images. Magn Reson Med 46:24–30

Vaughan JT, Snyder CJ, DelaBarre LJ et al (2009) Whole-body imaging at 7T: preliminary results. Magn Reson Med 61:244–248

Waldvogel D, van Gelderen P, Hallett M (1999) Increased iron in the dentate nucleus of patients with Friedrich's ataxia. Ann Neurol 46:123–125

Walter M, Stadler J, Tempelmann C, Speck O, Northoff G (2008) High resolution fMRI of subcortical regions during visual erotic stimulation at 7 T. MAGMA 21:103–111

Wang D, Heberlein K, LaConte S, Hu X (2004) Inherent insensitivity to RF inhomogeneity in FLASH imaging. Magn Reson Med 52:927–931

Weiller C, May A, Sach M, Buhmann C, Rijntjes M (2006) Role of functional imaging in neurological disorders. J Magn Reson Imaging 23:840–850

Werring DJ, Frazer DW, Coward LJ et al (2004) Cognitive dysfunction in patients with cerebral microbleeds on T2*-weighted gradient-echo MRI. Brain 127:2265–2275

Wiesinger F, Van de Moortele PF, Adriany G et al (2006) Potential and feasibility of parallel MRI at high field. NMR Biomed 19:368–378

Yacoub E, Shmuel A, Pfeuffer J et al (2001) Imaging brain function in humans at 7 Tesla. Magn Reson Med 45:588–594

Zijlmans M, de Kort GA, Witkamp TD et al (2009) 3T versus 1.5T phased-array MRI in the presurgical work-up of patients with partial epilepsy of uncertain focus. J Magn Reson Imaging 30:256–262

Zwanenburg JJ, Hendrikse J, Takahara T, Visser F, Luijten PR (2008) MR angiography of the cerebral perforating arteries with magnetization prepared anatomical reference at 7 T: comparison with time-of-flight. J Magn Reson Imaging 28:1519–1526

Oncology

Michael Bock, Stefan Delorme, and Lars Gerigk

Contents

Abstract

Magnetic resonance imaging is used in oncology in particular for tumor staging, planning of surgery and radiation therapy, and monitoring of tumor response and early detection of recurrence. For all applications high field MRI can be advantageous, because the spatail resolution of the MR images is increasing with field strength, and thus smaller lesions become detectable. Furthermore, functional imaging techniques benefit from the higher field strength, which are used as early indicators for therapy response or tumor reccurence before morphological changes are visible. Several technical limitations such as the increased specific absorption rates (SAR), the limited B_1 homogeneity of the transmit coils or the increased image distortion due to susceptibility differences make high field MRI of tumors challenging. Nevertheless, high resolution morphological and functional images of brain tumors have been acquired showing the internal tumor structure, the presence of neo-angiogenic vessels, and the functional changes of the tumor tissue.

1 Introduction

After cardio-vascular disease, cancer is the second-most frequent cause of death in the developed countries. Early detection of cancer is challenging as cancerous lesions develop gradually from a small cell agglomeration to a larger lesion, which is only detectable if it has exceeded an imaging modality dependent size. Thus, high-resolution imaging might

M. Bock · S. Delorme (✉) · L. Gerigk
Department of Medical Physics in Radiology,
Department of Radiology,
German Cancer Research Center (DKFZ),
Im Neuenheimer Feld 280, 69120 Heidelberg, Germany
e-mail: s.delorme@dkfz-heidelberg.de

J. Hennig and O. Speck (eds.), *High-Field MR Imaging,* Medical Radiology. Diagnostic Imaging,
DOI: 10.1007/174_2010_105, © Springer-Verlag Berlin Heidelberg 2011

help to detect cancer at an earlier stage, which in turn could open new therapeutic options.

During cancer therapy imaging might also be very helpful, in particular for an early detection of therapy response. For this, both morphological and functional information are required. In particular, functional imaging often serves as an early indicator for tumor response before morphological changes are visible. The detection of non-responders is very important to offer the patient treatment alternatives and to reduce the side effects of a potentially useless therapy.

High-field MRI can offer various advantages in this context, as for example: high-resolution MRI for the detection of small cancerous lesions and metastases, functional imaging using perfusion, diffusion, and oxygenation sensitive imaging techniques, blood oxygen level-dependent (BOLD) MRI to assess neuro-functionally active areas in the brain close to a tumor, or MR spectroscopy for tumor differentiation.

In this chapter, we first describe in general the challenges that diagnostic imaging aims to solve in the context of oncology. Then, the MR imaging technologies for tumor detection are presented, which especially benefit from the higher field strengths. Finally, image examples are presented for selected tumor entities.

2 Challenges and Limitations of Imaging Methods in Oncology

From the onset of a tumor disease, diagnostic imaging modalities are accompanying the patient, and under certain circumstances they lead to a diagnosis even before symptoms are detectable. X-ray, ultrasound, computed tomography (CT), and MR imaging as well as scintigraphy and positron emission tomography (PET) are used to

- detect a tumor disease at an asymptomatic stage to improve the chances of healing;
- ascertain a tumor in the presence of clinical symptoms or at pathologic findings;
- differentiate a malignant tumor from a benign lesion;
- assess the degree of local infiltration and to detect lymph node involvement or metastatic spread;
- evaluate tumor response to radiation therapy or chemotherapy;
- find a recurrent tumor early enough to initiate an effective treatment.

In addition, nearly every modern radiation therapy technique requires images for treatment planning to define the tumor volume. For high-precision and stereotactic radiation treatment, the patients are imaged in a fixed coordinate frame, and the radiation dose is calculated using the information of the different imaging modalities.

The requirements of modern imaging systems in oncology have grown with their capabilities. For lung, skeleton, and breast conventional X-ray imaging is still important; however, the majority of oncologic imaging techniques utilize cross-sectional methods to visualize the morphology in three dimensions without projection artifacts. In addition, new functional imaging techniques allow assessing, for example, organ motion, blood supply, metabolism, microstructure, or even the expression of cellular receptors. At present, no imaging modality alone can provide all this information simultaneously, even though MR imaging has the potential to acquire most of this information in one setting.

2.1 Tumor Staging

In the so-called TNM tumor staging, medical imaging is used to assess three fundamental oncologic questions:

1. What are the size and the extent of the primary tumor (T staging)?
2. Are adjacent lymph nodes already involved in the tumor disease (N staging)?
3. Are distal metastases present (M staging)?

The exact definition of the extent of the *primary tumor* requires an adequate spatial resolution of the diagnostic images and a sufficient contrast between normal and tumor tissue. Tumors in hollow organs with a smooth or blurred boundary against the neighboring tissue can be regarded as infiltrating lesions. However, inflammatory side reactions can lead to tissue changes that are difficult to differentiate from a tumor invasion. The infiltration of blood vessels, which would open a pathway for the generation of metastases, is also difficult to diagnose—at present, the contact area/length between tumor and blood vessel or the angular sector size of the tumor around the vessel cross section are used as very coarse criteria. At current clinical MR field strengths the spatial

resolution is typically not sufficient to evaluate the vessel wall directly.

The staging of the *lymph nodes* is another unsolved clinical problem. Lymph nodes are pre-formed structures, and a reactive enlargement of the nodes due to inflammation is often seen near tumors, even though the lymph node itself is not infiltrated. In locations, where lymph nodes are accessible with high-frequency ultrasound (e.g., in the neck and thigh), or where endoscopes can be brought close to the nodal structures, the shape, the internal structure, and the vascular architecture partially allow differentiating between reactive enlargement and tumor infiltration. In the thorax and the abdomen, CT and MRI are used for lymph node assessment, and the nodal size is the only suboptimal criterion. In this context, MR contrast agent uptake or MR signal intensity provide no additional information.

The limitations in the *metastasis* detection are related to the detection sensitivity, which is dependent on the size and the image contrast of the metastasis. For example, metastasis contrast is very high in the lung, but can be very low in the liver. The specificity of metastasis imaging, i.e., the differentiation of a metastasis from a benign lesion, is a further complication. In most epithelial tumors, the hematogeneous metastazation follows well-described patterns with preferred infiltration of the liver, lung, bone, or the brain, which is not found in other tumors. Metastases in unexpected localizations are often not detected, in particular, if they have a low contrast against the normal tissue as, e.g., in muscle, or if they are surrounded by many irregularly shaped structures as in the mesentery close to the small bowel.

2.2 Radiation Therapy Planning

The definition of the target volume in radiation therapy is associated with even higher requirements to diagnostic imaging for staging. Modern radiation treatment concepts provide dose gradients with millimeter-scale dimensions, and this precision has to be matched by the imaging technology that is used for treatment planning. Even with high-resolution images, the desired precision is hard to achieve, as the definition of a precise tumor boundary remains challenging. In brain gliomas, for example, micro-invasion and inflammatory processes make it difficult to delineate the gross tumor volume (GTV) with a millimeter precision. Therefore, an (often very subjective) safety margin is added by the clinician to define the clinical target volume (CTV). Current research in radiation therapy aims to find methods to visualize occult tumor in the margin to match GTV and CTV.

When morphologic imaging alone is insufficient, functional techniques such as perfusion and diffusion measurements, metabolic imaging techniques or imaging of receptor expression are tested for radiation therapy planning. Besides MRI, nuclear medicine techniques such as PET are utilized, and the use of combined hybrid imaging systems such as PET/CT and, more recently, PET/MR allow assessing this information with a higher spatial precision and in a shorter scan time.

Another problem of radiation therapy planning is the organ motion, which is caused by breathing, blood pulsation, peristalsis, and patient restlessness, and which can only partially be compensated by fixation devices. This further imprecision is taken into account be defining a so-called planning target volume (PTV), the size of which is often based on empirical data about and statistical assumptions of the motion patterns. Currently, new imaging methods are investigated to detect the individual 3D organ motion in real time; however, the generation and the use of these motion data during radiation therapy still pose fundamental problems.

2.3 Tumor Response to Therapy

In order to assess the response of a tumor to therapy, the change in tumor size is currently the only clinically accepted parameter. This size criterion must be regarded with caution due to the problems associated with the tumor shape and due to the often limited differentiation against the normal surrounding tissue as in peritoneal carcinosis or in tumors at the perimeter of hollow organs. Another limitation of size measurements is the fact, that in bone metastases the sclerosis persists even if the metastasis responds to therapy. Furthermore, tumor size can change very slowly, so that, for example, all cycles of a chemotherapy need to be applied before a detectable size change can be expected.

Biologically inactive tumor rests have been described, for example, in malignant lymphomas or in metastases of stem cell tumors, which change in size under treatment and can thus imitate a tumor progression. Therapies with signal transduction inhibitors might in the future lead to negligible changes in tumor size, even though the constant tumor size has to be regarded as a success of this new tumor therapy. Thus, size measurements of tumors in follow-up studies need a very careful interpretation by an experienced radiologist.

As in therapy planning, one possible new approach to tumor response assessment is the use of functional imaging techniques. Tissue perfusion measurements with contrast agents, cell density measurements with diffusion MRI, neuronal fiber tracking with diffusion tensor imaging (DTI) as well as metabolic measurements with MR spectroscopy to assess proliferation and tumor necrosis are currently studied to improve the early diagnosis of response to tumor therapy. Even though MRI offers this wide range of different technologies, the very sensitive techniques of nuclear medicine with their highly specific novel markers should be regarded as strong competitors in the measurement of therapy response.

3 High Field MR Imaging Techniques in Oncology

As described in previous chapters, the use of established MRI imaging techniques at higher field strengths is challenging due to conflicting technical and physiologic requirements: technically, high-field MRI requires an increased RF power and stronger gradient amplitudes, whereas the physiology puts upper limits to both the amount of RF energy deposited in the human body (SAR limits), and to the strength and rate of gradient-induced field strength tolerated by the nervous system (peripheral nerve stimulation).

In the following an incomplete list of MR imaging techniques is given that have been utilized for high-field MRI of the brain. Even though applications in other anatomical regions have been realized such as the spine (Kraff et al. 2009) or the knee (Kraff et al. 2007), at present the main application of high-field MRI is in the investigation of intracranial lesions—this focus on the brain is due to the absence of RF technology that can reliably and safely overcome the standing wave limitations in larger anatomical areas such as the abdomen. Owing to its small size, the prostate has also been investigated at high fields, because here dedicated transmit-receive endorectal coils can be utilized.

Even though in principle, a nearly arbitrary spatial resolution can be achieved with MRI (neglecting relaxation and diffusion limits), the required SNR in oncologic routine would demand very long acquisition times. As a general rule, individual image acquisitions should not be longer than 10 min, because the patients typically do not remain still for a longer time span. Therefore, the following list of imaging techniques has been chosen to fulfill this clinical requirement, even though more optimal imaging options with longer acquisition times exist.

3.1 High-Resolution Morphological Imaging

Both during staging and during treatment follow-up, high-resolution MRI of the morphology of a tumor lesion is very important. Lesion shape, internal lesion structure, and lesion infiltration into neighboring or surrounding tissue need to be assessed and their temporal behavior during therapy must be evaluated. For this purpose, the following pulse sequence techniques have been chosen.

3.1.1 Three-Dimensional Gradient Echo

Two- and three-dimensional spoiled gradient echo pulse sequences such as fast low angle shot (FLASH) have been used to create spin density or T_1w images of the brain. FLASH imaging has several advantages over other steady state imaging techniques. When used with short repetition times and low-flip angles, it can provide spin density weighted data sets of the whole human brain with isotropic sub-millimeter resolution. Variations of the flip angle due to B_1 inhomogeneities (which can be as large as a factor of 2) do not lead to contrast changes that render the 3D data sets uninterpretable. Three-dimensional FLASH MRI can be combined with parallel image acquisition techniques accelerating the image acquisition in both phase encoding and partition encoding direction. Thus, even for large 3D data sets, acquisition times of less than 10 min become feasible. Figure 1 shows 3D FLASH datasets from a patient with glioblastoma

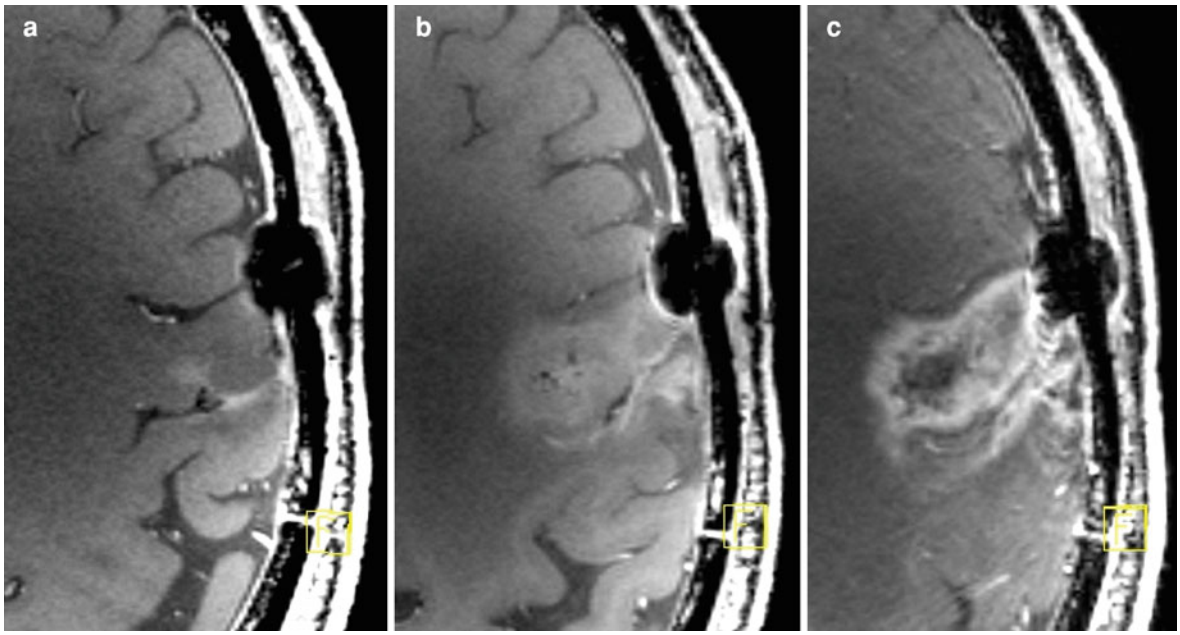

Fig. 1 Axial reconstructions of 3D-FLASH datasets (7 T, TR 6.6, TE 2.4 ms, matrix 448 × 448, FoV 230 × 230 mm, reconstruction with 3 mm slice thickness) show the time course of a recurrent glioblastoma multiforme. Contrast enhancement at the posterior rim of the former resection cavity could be demonstrated first at 7 T MRI (**a**). The follow-up examinations after 5 (**b**) and 8.5 months (**c**) show an increase in size and central necrosis (**c**). The susceptibility artifact is caused by a cranial fixation system for the bone flap (Craniofix)

multiforme over a time course of 8.5 months. They show the heterogeneous interior of the tumor as well as normal brain tissue.

To create a T_1 contrast with 3D FLASH MRI is challenging at higher fields, as higher flip angles are required which often lead to an excessive energy deposition. Furthermore, both the longer T_1 values at higher fields (Wright et al. 2008) and the local flip angle variations make highly T_1w FLASH MRI difficult. Nevertheless, even with moderate flip angles ($\alpha = 10°–13°$) 3D data sets with a good T_1 contrast can be created that allow for differentiating between gray and white brain matter.

Magnetization prepared pulse sequences have been proposed as, e.g., magnetization prepared rapid acquisition GRE (MPRAGE) to further increase the T_1 contrast. Here, the T_1 contrast is established by an (often non-selective) pre-pulse, for example, a 90° or 180° pulse. Image data are then acquired after a contrast-determining delay time TI. Owing to the loss of contrast during image data readout, this process needs to be repeated until the full k-space for the 3D data set has been acquired. With magnetization prepared techniques, a very good T_1 contrast can be created, because preparation pulses can be used which are largely immune to B_1 inhomogeneities (e.g., adiabatic pulses or B_1-insensitive rotation pulses). Unfortunately, the longer tissue T_1 at higher field strength requires longer TI values of 1,000 ms and more to establish the contrast, which can become a considerable dead time in the pulse sequences leading to suboptimal acquisition times of 20 min and more.

Recently, MPRAGE has been combined with FLASH by acquiring two data sets after the non-selective preparation in quick succession. Here, the first data set is T_1 weighted, and the second data set has a spin density contrast, as the low-flip angle readout pulses of the first acquisition drive the longitudinal magnetization into the FLASH steady state. This approach has been implemented to normalize the image data which helps reducing the signal inhomogeneities often seen near the skull. These inhomogeneities are caused by the inhomogeneous receive sensitivities of the multiple receive coil elements which are necessary for highly parallel imaging applications.

At sub-millimeter spatial resolution, FLASH and MPRAGE data sets acquired in 10 min or less show a

limited SNR which is mainly due to two reasons: the increase in field strength increases the SNR only linearly, whereas an isotropic increase in spatial resolution in all three dimensions would require a cubed increase in SNR. Second, the longer T_1 values require lower flip angles to avoid signal saturation, which reduces SNR further. Thus, though robust, FLASH techniques are suboptimal with regard to SNR.

3.1.2 Two- and Three-Dimensional Spin Echo MRI

Spin echo (SE) pulse sequences utilize SAR-intensive RF pulses, they require long repetition times due to the saturation of the magnetization, and they are less time-efficient because additional refocusing pulses are necessary. Nevertheless, for many imaging applications, SE imaging is still considered the gold standard because susceptibility-induced field distortions at tissue interfaces are significantly less pronounced.

Conventional SE techniques encode one k-space line per repetition. Thus, they are intrinsically slow—in particular, if high-resolution data sets with matrix sizes of up to 2,048 are acquired. This time-inefficiency is even more pronounced at higher fields, because longer TRs are needed to establish for T_1-weighted as well as for T_2-weighted image acquisitions. In order to accelerate SE techniques, so-called fast or turbo SEs (TSE) are used, where the SE is refocused N_{TSE} times after one excitation with different k-space encoding. In clinical imaging, therefore, TSE techniques are preferred, as they allow reducing the acquisition time by a factor of N_{TSE} over conventional SE imaging. For a 1,024 matrix with a TR of 1,000 ms, the imaging time for a conventional SE technique would amount to 17 min, which is reduced to less than 2 min in TSE with $N_{TSE} = 9$.

In oncology, it is essential to detect lesions when they are very small: a brain metastasis from a melanoma is often only detectable with conventional MRI when its diameter is 2 mm and more (Fig. 2). For this reason, not only a high in-plane resolution but also thin slices are essential in high-field oncologic MRI. In particular, in TSE pulse sequences the slice thickness of both the 2D excitation pulse (90° pulse) and the SE refocusing pulse (180° pulse) need to be well-defined, since it is the combined effect of these pulses in the echo train that leads to the echo formation. RF pulses exciting thin slices are difficult to realize as they require long and well-defined pulse shapes with many side-lobes. Nevertheless, very good TSE images with slice thicknesses of 2 mm have been realized, and in-plane spatial resolutions of 300 μm and less have been achieved (Fig. 3).

In order to further reduce the slice thickness, truly three-dimensional image acquisition techniques are required. In TSE imaging, 3D acquisitions are more difficult to realize because at the end of the echo train the magnetization is predominantly oriented in the transverse plane. Thus, the time of at least one average T_1 needs to be waited until the next excitation (90°) pulse can be applied. These long-waiting times make 3D TSE MRI at high fields impracticable in clinical imaging.

In general, the high-RF power transmitted during both the excitation and the refocusing pulses is a limiting factor for TSE imaging at high fields. In order to reduce the SAR, often refocusing flip angles down to 120° and less are used. A further reduction can be achieved using so-called hyperechoes. In addition, the power of each RF pulse can be further minimized with the VERSE technique that reduces the slice selection gradient during those sections of the RF pulse which contribute most to the overall RF power of the pulse (Conolly et al. 1988). As a reduction in gradient amplitude is associated with a prolongation of these sections, the RF pulse amplitude decreases which leads to a lower RF power deposition. In general, all of these techniques are used together to create TSE protocols for oncologic imaging. Unfortunately, even then the RF power exceeds the regulatory limits, and only a reduced (and thus suboptimal) number of imaging slices can be acquired.

3.1.3 Time-of-Flight MR Angiography

Time-of-flight MR angiography (TOF-MRA) has been shown to profit especially from the higher field strengths (Kang et al. 2008). Despite the increase in intravascular signal also the suppression of signals from static tissue is improved, as the longer T_1 values of the tissue at higher field strength lead to significantly lower background signal and thus to a better vessel-to-background signal ratio (von Morze et al. 2007).

At higher field strengths dedicated background suppression techniques such as magnetization transfer contrast (MTC) are not needed, which is beneficial as the MTC pulses with their high-RF power deposition would not be applicable. Owing to the omission of

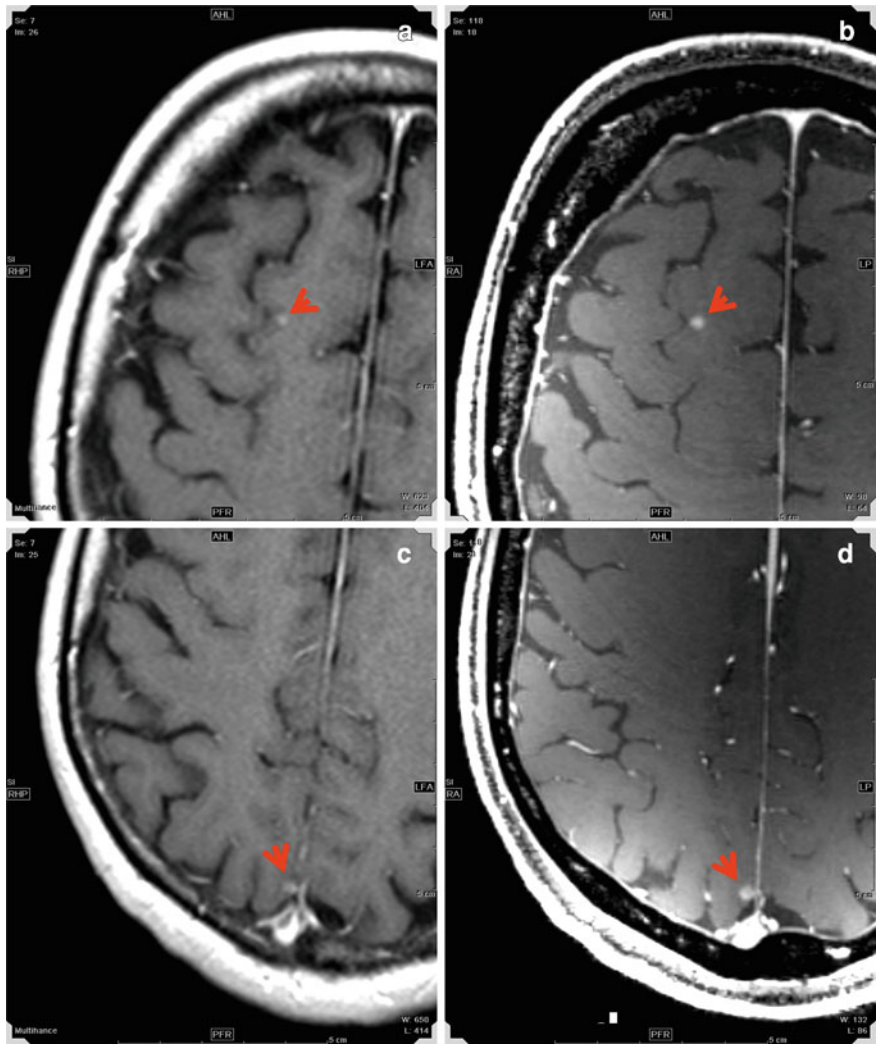

Fig. 2 In this 66-year-old female patient with a malignant melanoma, an enhancing structure was found in the right frontal lobe (*arrow*), which at 1.5 T (**a**, TR 588 ms, TE 7,7 ms, matrix 256 × 192, slice thickness 4 mm) could not definitely be differentiated between a vessel and a metastasis. At 7 T (**b**, TR 6,6, TE 2,4 ms, matrix 448 × 448, 0,5 mm slice thickness), this lesion could be identified as metastasis due to its spherical character. Another metastasis was found in the right parietal lobe (**d**, *arrow*), which was overlooked at 1.5 T (**c**) because of its proximity to the falx

these pulses and due to the higher spatial resolution of the TOF-MRA data acquisition, typically shorter TR values are used to maintain image acquisition times of less than 10 min. Nevertheless, a twofold increase in spatial resolution increases the acquisition time by a factor of 4 (2 in PE direction, 2 in SL direction), and thus often parallel imaging techniques are applied to shorten the duration of the image acquisition (Maderwald et al. 2008).

Since many variables of the image acquisition need to be optimized for clinical TOF-MRA protocols, a direct comparison of low- and high-field TOF-MRA is difficult. For example, the inhomogeneous RF excitation, which affects the local signal intensities of the traveling spins in the blood stream, needs to be taken into account at higher fields. These inhomogeneities are caused by the transmit coils in combination with the standing wave phenomena at higher field strengths, whereas at lower fields the homogeneous body coil is used for RF excitation resulting in a much higher RF homogeneity.

In oncology, TOF-MRA offers the possibility to visualize the tumor vasculature (Fig. 4a). At lower field strengths the spatial resolution of a millimeter or more is often insufficient to detect the delicate microvasculature of highly malignant tumors, but at higher field strengths spatial resolutions of 600 µm and better have been realized. With this resolution, detection of the irregular vascular networks formed by neo-angiogenesis becomes feasible, so that TOF-MRA might become a valuable tool for the direct delineation of the vascular supply of the tumor.

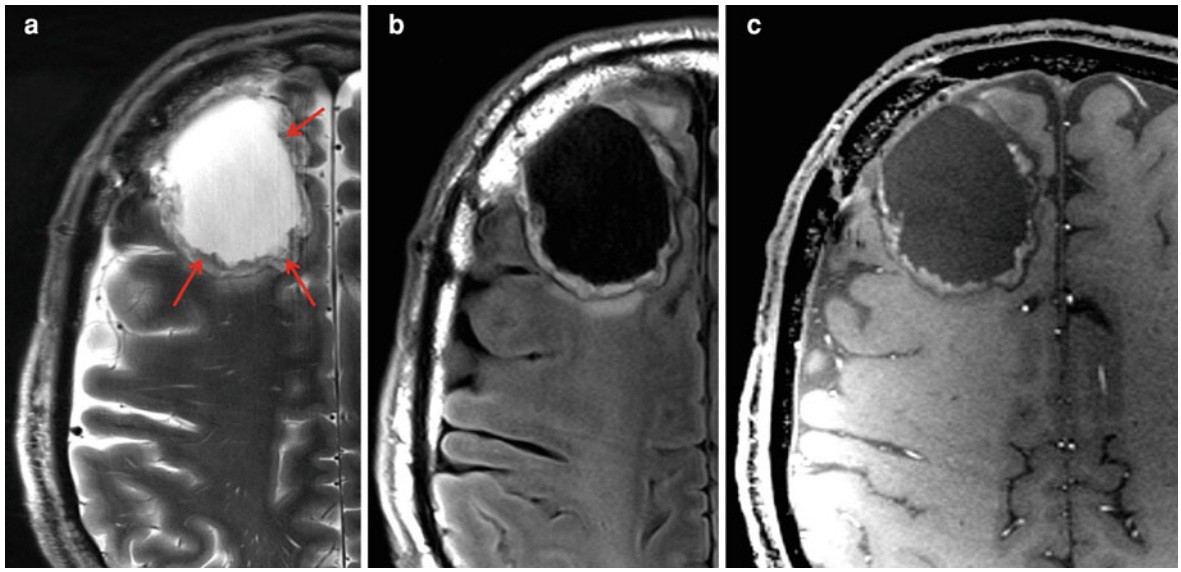

Fig. 3 High-resolution morphological imaging at 7 T in T_2 (**a**, T_2-TSE, TR 12,000, TE 57 ms, matrix 768 × 624, FoV 220 × 179 mm, slice thickness 2 mm), FLAIR (**b**, TR 12,000, TE 83, TI 2,760 ms, matrix 512 × 298, FoV 230 × 179 mm, slice thickness 2 mm), and T_1 after i.v. Gadolinium (**c**, T_1-FLASH 3D, TR 6.6, TE 2.4 ms, matrix 448 × 448, FoV 230 × 230 mm, reconstructed with 3 mm slice thickness) in a patient with oligodendroglioma. Around the central necrosis, the rim of tumor tissue (*arrows*) is surrounded by T_2-hyper-, T_1-hypointense edema

Changes of these vascular networks induced, for example, by an anti-angiogenic therapy could thus be detected on a morphologic scale.

3.2 MRI for Stereotactic Therapy Planning

In order to correctly calculate the radiation dose applied to the target volume in radiation therapy, CT data are required from which the attenuation of the radiation beam in bone (e.g., the skull) can be estimated. As CT images do not show the tumor lesion with sufficient image contrast, MRI data sets are often used for the definition of the PTV because of their superior soft tissue contrast. Thus, during radiation therapy planning CT and MR imaging data need to be combined to correctly apply the radiation dose to the tumor.

For image combination, all image distortions in the data sets need to be corrected to guarantee that the same anatomical information is seen in the geometrically matched data sets. Even though global matching of MR and CT data in the brain is relatively simple due to the rigidity of the skull bone, local matching is complicated by the local MR image distortions caused by both the inhomogeneities of MR system's fields (B_0 and gradients) and the tissue susceptibilities. The system inhomogeneities are typically known and do not vary significantly over time, so that a correction is possible even a long time after the images have been acquired. Susceptibility differences at the tissue boundaries, however, cause patient-specific local field gradients that lead to image distortions near these tissue interfaces.

Two strategies can be employed to minimize susceptibility-induced image distortions: high-gradient amplitudes to overpower the field distortions, and field distortion measurements to retrospectively correct the geometric signal intensity variations. With stronger gradient amplitudes, the field inhomogeneities of the image-encoding gradients are higher than the local field gradients caused by the susceptibility changes $\Delta B = \Delta\chi\ B_0$; however, with increasing field strength this requires that the gradient amplitudes are linearly increased with B_0. Even though technically feasible, these high-gradient amplitudes lead to increased dB/dt, which causes painful peripheral nerve stimulation. In addition, the higher readout gradient amplitudes result in higher readout bandwidths so that the SNR is reduced accordingly. During RF excitation, these higher gradient amplitudes

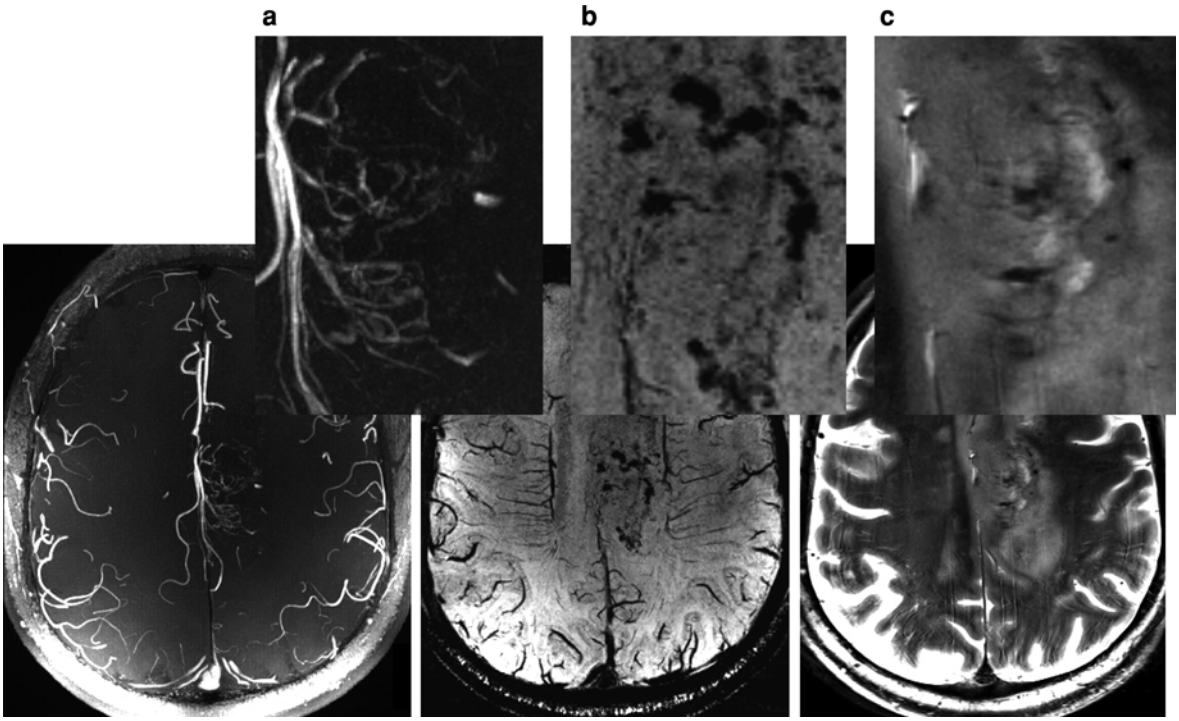

Fig. 4 In this patient with a left parasagittal glioblastoma multiforme, TOF angiography at 7 T (**a**, TR 15, TE 4,8 ms, matrix 704 × 490, FoV 200 × 147 mm, slice thickness 0.4 mm) is able to visualize the intratumoral vessels. SWI (**b**, TR 25, TE 18 ms, matrix 512 × 389, FoV 200 × 169 mm, minIP-reconstruction, 9.6 mm slice thickness) shows intratumoral hemorrhage as well as venous vessels. T_2 TSE (**c**, TR 12,000, TE 57 ms, matrix 768 × 624, FoV 220 × 179 mm, slice thickness 2 mm) shows the detailed internal morphology of the tumor

also lead to shorter RF pulses which in turn result in higher B_1 amplitudes and increased SAR values.

An alternative is the use of a retrospective image unwarping which requires the measurement of the local image distortion. In order to measure the local field inhomogeneity, one can use a field-mapping pulse sequence which acquires 3D data sets with multiple echo times. The local magnetic field deviation is calculated from the phase difference using the known inter-echo spacing ΔTE. The field map is then used to unwarp the images taking into account the readout gradient amplitude. Successful image unwarping requires a fully three-dimensional data set, as image distortions also occur in slice selection direction.

3.3 Functional MRI for Lesion Characterization

Biological parameters such as blood flow velocity, organ perfusion, cellular integrity, or tissue elasticity can be assessed with functional MR imaging techniques such as phase contrast MRI, arterial spin labeling (ASL), diffusion measurements, or elasticity measurements. In oncology, functional information is needed to complement the structural (morphological) information about a tumor lesion, for example, to differentiate low from high-grade tumors, to assess recurrent tumor at an early stage and to describe the functional heterogeneity of a lesion for an optimized therapeutic approach. Several of the functional imaging techniques benefit especially from an increased field strength due to the increase in signal, the prolongation of the relaxation times or the increased absolute field inhomogeneity.

3.3.1 Susceptibility-Weighted MRI

Differences in magnetic susceptibility are found at tissue interfaces and between oxygenated and deoxygenated blood. Susceptibility-weighted MRI (SWI) is using conventional 3D spoiled gradient echo

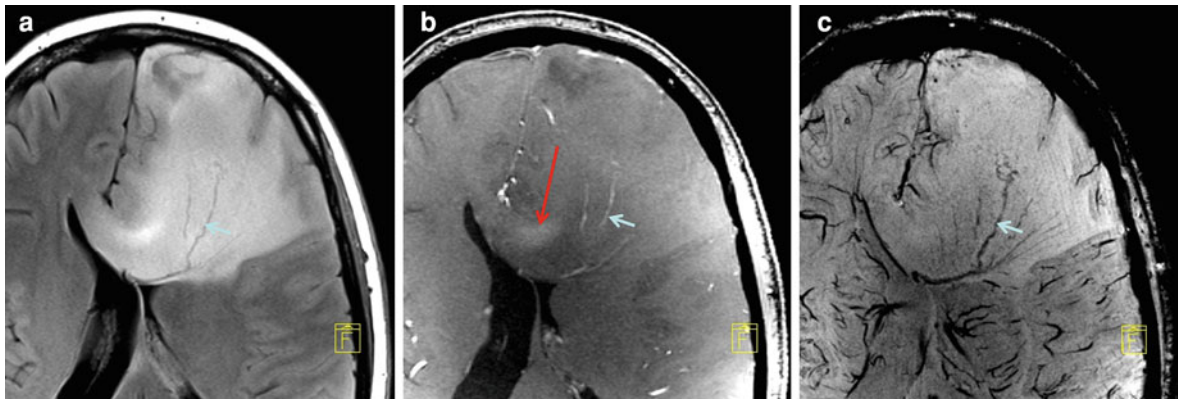

Fig. 5 In another case of left frontal Oligodendroglioma, FLAIR shows the hyperintense infiltration of the corpus callosum (**a**, TR 12,000, TE 83, TI 2760 ms, matrix 512 × 298, FoV 230 × 179 mm, slice thickness 2 mm), and T_1 after i.v. Gadolinium (**b**, T1-FLASH 3D, TR 6.6, TE 2.4 ms, matrix 448 × 448, FoV 230 × 230 mm) shows a contrast enhancement (*large arrow*). Whereas larger intratumoral vessels can be seen in all morphological datasets, the smaller venous vessels can only be detected with SWI (**c**, TR 25, TE 18 ms, matrix 512 × 389, FoV 200 × 169 mm, minIP-reconstruction, 9.6 mm slice thickness)

(FLASH) acquisitions to create a susceptibility contrast in the 3D data. Therefore, 3D data sets are post-processed using the phase information to specifically reduce the signal in those areas where a change in magnetic susceptibility is found. In SWI images of the brain, the veins are shown dark due to the paramagnetic venous blood against the bright background signal of the surrounding diamagnetic brain tissue (MR venography). In order to create an overview over the venous vasculature, so-called minimum intensity projections (minIP) are calculated over a limited range of images.

With increasing B_0, the *absolute* difference in magnetic field between the tissues is increasing linearly. Thus, susceptibility-induced signal changes are more pronounced at higher field strengths, if comparable imaging parameters (most importantly, the echo time) are used as in low-field MRI. In particular, the signal dephasing at the tissue interfaces in the presence of a static field gradient causes a signal loss, which is stronger at higher field strengths, if the same TE is used as in low-field MRI.

In oncology, SWI is used to differentiate various internal tumor structures, and to map the venous vasculature of the tumor (Fig. 5) (Christoforidis et al. 2002). Furthermore, blood products of various iron content are highlighted allowing the identification of for example microbleeds (Fig. 4b).

3.3.2 Diffusion

The self-diffusion of water molecules can be used to create a diffusion contrast in the MR images. This contrast originates from the Brownian motion of the water molecules in the presence of diffusion weighting gradients, which lead to a signal attenuation that is more pronounced for higher diffusion constants *D*. From a series of two or more diffusion-weighted images (DWI) with different diffusion sensitizing gradients the apparent diffusion constant can be calculated. In general, the diffusion in tissue is not isotropic, and the diffusion in anisotropic tissues can be represented by a tensor. DTI is, for example, used to map the direction of fiber structures in the brain.

Diffusion-weighted images at higher field strengths profits from the increased SNR, however, there are two signal loss mechanisms that can partly or totally compensate this signal gain:

1. At higher field strengths, the transverse relaxation time T_2 is decreasing, so that the signal acquired at TE is smaller due to T_2 signal decay. Since the diffusion-weighting gradients are of the same strength as at lower fields (often, similar gradient hardware is used), TE cannot be reduced without compromising the diffusion weighting.
2. Diffusion-weighted images often uses EPI readouts, which are prone to image distortion from susceptibility gradients. At higher field strengths,

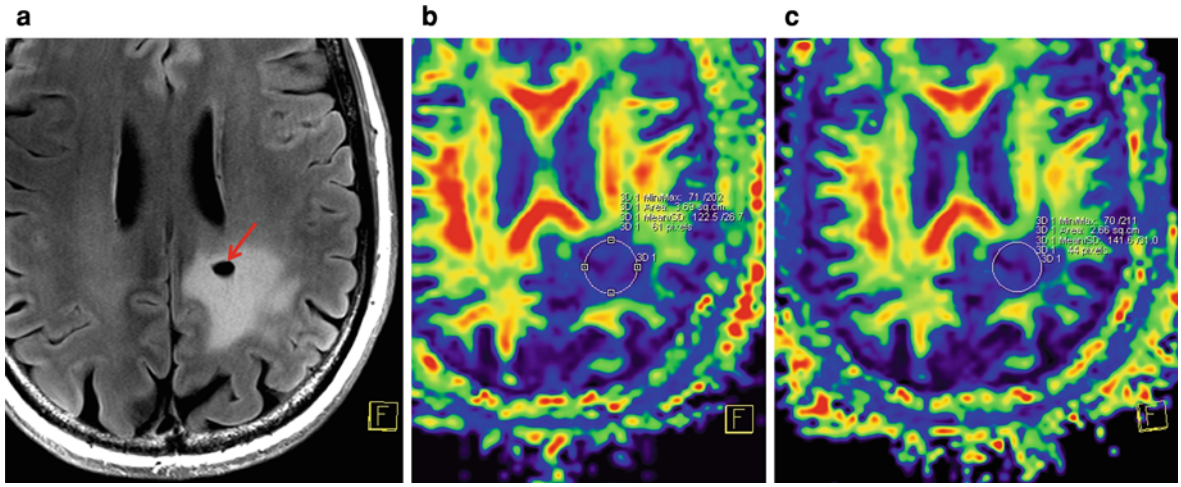

Fig. 6 The FLAIR sequence (**a**, 7 T, TR 12,000, TE 83, TI 2,760 ms, matrix 512 × 298, FoV 230 × 179 mm, slice thickness 2 mm) shows the extent of a low-grade astrocytoma with a defect from biopsy (*arrow*). DWI at both 3 T (**b**, TR 6,400, TE 91 ms, matrix 96 × 96, FoV 240 × 240 mm, slice thickness 2.5 mm) and 7 T (**c**, TR 3,800, TE 51 ms, matrix 100 × 70, FoV 230 × 161, slice thickness 2 mm) show a comparable area of reduced fractional anisotropy, which is typical for low-grade astrocytoma

this image distortion is counteracted by the use of parallel imaging, which increases the gradient amplitudes in phase encoding direction. Unfortunately, the reduced number of data acquisitions in parallel also reduces the available SNR. In summary, DWI at higher field strengths often yields results comparable to MRI at 1.5 or 3 T at comparable imaging times (Fig. 6).

Tumor tissue is often showing more restricted water diffusion compared to normal tissue. DWI is therefore often used in combination with whole body imaging methods to create survey images for tumor staging. DTI on the other hand can be used to identify destruction or infiltration of fiber structures by tumor tissue, and it can help to map vital fiber connections near tumors in surgical therapy planning.

3.3.3 Perfusion

Several MRI techniques for the measurement of perfusion are currently in clinical use. Contrast agent-based methods utilize the shortening of the relaxation times T_1 and T_2 which create a transient contrast during the first passage of a bolus of the agent (dynamic contrast-enhanced MRI, DCE). With T_1 techniques, the signal increases with contrast agent concentration, whereas it is reduced using T_2- or T_2*-weighted imaging. ASL on the other hand imprints a change of the longitudinal magnetization on the arterial blood proximal to the tissue of interest, and then monitors the passage of this magnetization at a later stage.

At higher field strengths, lower contrast agent concentrations can be used to create the same T_2* contrast because of the higher phase differences caused by the contrast agent. In T_2* perfusion methods great care has to be taken not to increase the concentration beyond a pulse sequence-dependent threshold value. With increasing concentration, ever smaller signals are detected, and if the signal becomes too small to be differentiated from noise, a meaningful measurement of perfusion is impossible. This T_2* effect can also influence T_1-weighted perfusion measurements because even at very low TE the contrast agent-induced T_2 reduction can be detected.

Arterial spin labeling in general profits both from the increased SNR and the longer T_1 value of blood (Gardener et al. 2009): the longer the T_1 of blood, the more persistent is the imprinted ASL contrast. A long-lasting arterial contrast is required to delineate the passage of the arterial bolus through the micro-vasculature—to reach the capillary bed this observation period should be longer than 2 s, which is difficult to achieve at lower field strengths as the relaxation time of blood at 1.5 T is about 1.2 s. On the other hand, it

can be difficult to achieve an efficient inversion of an arterial bolus in the feeding arteries at very high fields due to the strong inhomogeneities of the B1 field, which stem from the limited coverage of the transmit RF coils and the standing wave phenomena observed at higher fields. These effects can be partly compensated by the use of adiabatic inversion pulses; however, these pulses significantly increase the local SAR.

In oncology, perfusion MRI is used to differentiate active tumor areas from surrounding normal tissue and from necrotic tumor areas. Furthermore, perfusion information can be utilized in tumor staging, or during therapy follow-up for an early assessment of tumor response. One particular application in oncology is the visualization of the active induction of vessel growth in tumors (neo-angiogenesis). At lower field strengths, neo-angiogenesis can be only indirectly seen via an increased tumor perfusion. At very high-field strengths, alternatively it can be directly visualized with high-resolution MRA which depicts the irregular neo-angiogenic vascular network.

3.3.4 Blood Oxygen Level-Dependent

The BOLD contrast as first published by Ogawa et al. (1990) describes the change of the susceptibility contrast in the brain under different oxygenation states of the blood. Activated neuro-functional areas have an increased arterial blood supply which is not matched by the local oxygen consumption. Thus, an excess of oxygen is present in the draining veins, and an increased concentration of the diamagnetic oxyhemoglobin is found. Thus, under activation the T_2* decay due to signal dephasing is reduced in the vicinity of the vein, and an increased signal is observed. This signal increase is very small at lower field strengths, but scales approximately linearly with B_0 (van der Zwaag et al. 2009). In neuro-functional MRI (fMRI) this signal increase is used to map areas of the brain that are activated while performing a neuro-functional test. Thus, at higher field strengths the image acquisition of an fMRI experiment can be shortened due to the increase in image contrast.

In oncology, fMRI is used to localize functional areas in the vicinity of a tumor to provide additional information about possible risk structures during therapy. This functional mapping is often needed, because the growing tumor has shifted the functional areas so that a morphological identification of their locations is not possible.

Another application of the BOLD contrast is the measurement of the oxygen extraction fraction (OEF). Here, a model of the signal decay is compared with multi-echo SE and gradient echo data. By fitting the signal curves, the OEF can be determined from the measurement data.

3.3.5 Non-proton MRI

MRI with other nuclei than protons is challenging at clinical field strengths, because the SNR is significantly lower than that of ^{1}H-MRI. The reduced signal intensity is mainly due to the lower biological concentration of the rare nuclei, and additionally, due to the lower gyromagnetic ratio.

Thus, only very few nuclei are suitable for in vivo imaging studies. In particular, the nucleus ^{23}Na has been extensively used for MR imaging because ^{23}Na-MRI has the potential to provide a sensitive marker for cell vitality (Ouwerkerk 2007). With a sensitivity that is 22,000-fold smaller than with ^{1}H-MRI, ^{23}Na-MRI requires linear voxel dimensions that are about 30 times larger to acquire images with comparable SNR. Thus, even at higher magnetic fields typically the spatial resolution in ^{23}Na-MRI is of the order of 4–6 mm.

In oncology, ^{23}Na-MRI could provide information about the cellular integrity, and thus would be a sensitive marker for tumor lesions. With high-field MRI, the required imaging times for a whole-brain ^{23}Na MR image acquisition can be reduced to less than 10 min, and are thus in a clinically acceptable range.

Another interesting nucleus in oncology is ^{17}O, a stable isotope of the oxygen nucleus ^{16}O. The natural abundance of ^{17}O is about 0.038%, and thus, this nucleus has to be enriched to provide sufficient MR signal. When enriched ^{17}O gas is inhaled, the oxygen is bound to hemoglobin and is then transported to the cells, where it is metabolized into water ($H_2{}^{17}O$). Only in this form is the ^{17}O nucleus detectable by MRI, and thus ^{17}O MRI could provide a very sensitive measure of oxygen metabolism (Atkinson and Thulborn 2010).

3.4 Applications in Oncology

So far, high-field MRI in oncology has almost exclusively been applied to brain studies, because transmit and receive coils were first available for this body

Fig. 7 Incidental finding of a benign enchondroma at 7 T. T_2 TSE, TR 12,000, TE 55 ms, matrix 1,024 × 512, FoV 350 × 175, slice thickness 2 mm). Dedicated 15 ch knee coil (Rapid)

region, the need for high-resolution morphological and functional imaging is most pronounced and several causes of deteriorated image quality like motion and air are less present in the brain than in the body. Since head coils for 7 T have to be designed in a different way than for lower field strengths, since they are transmit and receive coils, and have to be closer to the skull surface, the coverage of the skull base can be limited especially in subjects with a large head.

Besides the brain, another proven application for imaging at 7 T is extremity joints like the knee, where RF coils of the birdcage type can be employed (Fig. 7). With the development of clinically usable parallel transmit coils (together with an appropriate SAR calculation), this situation will change in the nearer future, and advanced whole body imaging protocols will become available.

In the brain, the advantages of high-field strengths like 7 T can be clearly seen in imaging studies which profit from a very high spatial resolution ($\Delta x < 500$ μm), for example, the detection of small metastatic lesions (Fig. 2) or early diagnosis (Mönninghoff et al. 2010) of recurrent tumor after surgical resection (Fig. 1). In MRI examinations performed for the exclusion of "tumor," either in the form of a tumor recurrence or metastatic disease, often uncertainties arise from small areas of contrast enhancement which cannot be differentiated between tumor tissue and vascular enhancement with sufficient certainty. The result will usually be a recommendation for a short-term follow-up. This approach leads to increased cost, a possibly delayed detection of tumor tissue and subsequent therapy and not at least to uncertainty in the patient. The high resolution which can be achieved with 7 T MRI can help to secure the diagnosis of a tumor recurrence, allowing a timely change of the therapy. This is also true for the detection of metastases, e.g., in patients with higher-level melanoma. Aside from the differentiation between tumor and vessel, the higher resolution also eases the detection of metastases in the vicinity of other enhancing structures like meninges, falx, and veins (Fig. 2).

The higher quality of TOF-MRA data at 7 T can be used to visualize the arterial vasculature in tumors, which might provide additional information about neo-angiogenic vessels (Fig. 4a). The increased susceptibility effects at higher fields strengths can further improve SWI, where the visualization of the venous intratumoral vessels is already striking at 3 T, but is further improved at 7 T (Fig. 5).

3.4.1 Gliomas

In glioma patients, the extent of the contrast-enhancing tumor core can usually be measured with sufficient precision on 3 T or even 1.5 T images. However, for novel therapeutic agents like anti-angiogenetic substances, the sole measurement of the tumor size is no longer considered to be valid. These substances stabilize the blood–brain-barrier, leading to a reduction in the extravasation of contrast agent. The disappearance of the contrast enhancement in T_1-weighted imaging leads to the misconception of a therapy response, which is actually only a pseudoresponse of the imaging correlate. With TOF angiography at 7 T, due to the increased resolution and sensitivity for flow, it is possible to image tumor vessels directly, which was not possible at 3 T in a clinically acceptable acquisition time. This allows the assessment and possibly quantification of neovascularization.

Another advantage of 7 T MRI for glioma patients is the increased sensitivity for contrast enhancement due to the shortening of T_1. This leads to an increased sensitivity for subtle alterations of the blood–brain-

barrier with minimal contrast uptake, which will significantly influence the GTV for radiotherapy planning or the management of possible recurrences. Owing to the increased signal intensity of the contrast enhancement and due to the higher resolution, which allows for a better differentiation between enhancing tissue and vessels or other physiologic structures like meninges or falx, tumor recurrence can be detected at an earlier time point with higher confidence, allowing an earlier adaption of the therapy, which can influence survival and quality of life.

3.4.2 Metastases

Like with primary brain tumors, the detection of small metastases profits from the increased sensitivity for contrast enhancement as well as from the high-spatial resolution (Mönninghoff et al. 2010). These advantages improve the differentiation from normal structures and increase the conspicuity of the lesions, leading to earlier and more complete lesion detection. This is especially important in metastases where the difference between a solitary metastasis and multiple metastases will lead to a different therapy (Fig. 2).

4 Summary

For applications in oncology, the increased signal strength at 7 T can be transformed into higher resolution at an acceptable acquisition time. In combination with the higher conspicuity of contrast enhancing lesions, detection rates of small lesions and the diagnostic confidence can be improved. High-resolution vascular imaging can be used for direct imaging of neoangiogenesis. In future, the capabilities of multimodal brain tumor imaging will be further enhanced by advanced physiologic imaging like diffusion and perfusion. Also, the imaging of other nuclei like sodium or oxygen will allow for metabolic imaging as in PET.

References

Atkinson IC, Thulborn KR (2010) Feasibility of mapping the tissue mass corrected bioscale of cerebral metabolic rate of oxygen consumption using 17-oxygen and 23-sodium MR imaging in a human brain at 9.4 T. Neuroimage. 51(2): 723–733

Christoforidis GA, Grecula JC, Newton HB, Kangarlu A, Abduljalil AM, Schmalbrock P, Chakeres DW (2002) Visualization of microvascularity in glioblastoma multiforme with 8-T high-spatial-resolution MR imaging. AJNR Am J Neuroradiol 23(9):1553–1556

Conolly S, Nishimura DG, Macovski A, Glover G (1988) Variable-rate selective excitation. J Magn Reson 78:440–458

Gardener AG, Gowland PA, Francis ST (2009) Implementation of quantitative perfusion imaging using pulsed arterial spin labeling at ultra-high field. Magn Reson Med 61(4): 874–882

Kang CK, Hong SM, Han JY, Kim KN, Kim SH, Kim YB, Cho ZH (2008) Evaluation of MR angiography at 7.0 Tesla MRI using birdcage radio frequency coils with end caps. Magn Reson Med 60(2):330–338

Kraff O, Theysohn JM, Maderwald S, Saylor C, Ladd SC, Ladd ME, Barkhausen J (2007) MRI of the knee at 7.0 Tesla. Rofo 179(12):1231–1235

Kraff O, Bitz AK, Kruszona S, Orzada S, Schaefer LC, Theysohn JM, Maderwald S, Ladd ME, Quick HH (2009) An eight-channel phased array RF coil for spine MR imaging at 7 T. Invest Radiol 44(11):734–740

Maderwald S, Ladd SC, Gizewski ER, Kraff O, Theysohn JM, Wicklow K, Moenninghoff C, Wanke I, Ladd ME, Quick HH (2008) To TOF or not to TOF: strategies for non-contrast-enhanced intracranial MRA at 7 T. MAGMA 21(1–2):159–167

Mönninghoff C, Maderwald S, Theysohn JM, Schütt P, Gauler T, Kraff O, Ladd ME, Ladd SC, Wanke I (2010) Imaging of brain metastases of bronchial carcinomas with 7 T MRI—initial results. Rofo 182(9):764–772

Ogawa S, Lee TM, Kay AR, Tank DW (1990) Brain magnetic resonance imaging with contrast dependent on blood oxygenation. Proc Natl Acad Sci USA 87:9868–9872

Ouwerkerk R (2007) Sodium magnetic resonance imaging: from research to clinical use. J Am Coll Radiol 4(10): 739–741

van der Zwaag W, Francis S, Head K, Peters A, Gowland P, Morris P, Bowtell R (2009) fMRI at 1.5, 3 and 7 T: characterising BOLD signal changes. Neuroimage 47(4): 1425–1434

von Morze C, Xu D, Purcell DD, Hess CP, Mukherjee P, Saloner D, Kelley DA, Vigneron DB (2007) Intracranial time-of-flight MR angiography at 7T with comparison to 3T. J Magn Reson Imaging 26(4):900–904

Wright PJ, Mougin OE, Totman JJ, Peters AM, Brookes MJ, Coxon R, Morris PE, Clemence M, Francis ST, Bowtell RW, Gowland PA (2008) Water proton T_1 measurements in brain tissue at 7, 3, and 1.5 T using IR-EPI, IR-TSE, and MPRAGE: results and optimization. MAGMA 21(1–2): 121–130

Advanced Musculoskeletal Magnetic Resonance Imaging at Ultra-high Field (7 T)

Siegfried Trattnig, Klaus Friedrich, Wolfgang Bogner, Klaus Scheffler, Oliver Bieri, and Goetz H. Welsch

Contents

S. Trattnig (✉) · K. Friedrich · W. Bogner · G. H. Welsch
Department of Radiology,
High-Field MR Imaging Centre,
Medical University of Vienna,
Währinger Gürtel 18-20, 1090 Vienna, Austria
e-mail: siegfried.trattnig@meduniwien.ac.at

K. Scheffler · O. Bieri
Division of Radiological Physics,
Department of Medical Radiology,
University of Basel Hospital, Petersgraben 4,
4031 Basel, Switzerland

G. H. Welsch
Department of Trauma Surgery,
University Hospital of Erlangen,
Krankenhaustrasse 12, 91054 Erlangen, Germany

Abstract

The major advantage of high-field and ultra-high field MR is the shift from morphological to biochemical and metabolic imaging techniques which normally suffer from low sensitivity at standard field strength (1.5 T). The high signal-to-noise ratio of the higher field systems provides biochemical and metabolic imaging in reasonable scan times, which promotes their widespread clinical application. This development enables the diagnosis of diseases such as osteoarthritis, degenerative disc disease, and muscle disease at their earliest stages, before morphological changes occur. Thus, the imaging pre-requisites are available for the evaluation and follow-up of new disease-modifying drugs and the trend toward more personalized medicine.

Abbreviations

MR	Magnetic resonance
SNR	Signal-to-noise ratio
SAR	Specific absorption rate
TSE	Turbo Spin Echo
HASTE	Half-Fourier acquisition single-shot turbo spin echo
TrueFISP	True Fast Imaging with Steady-state Free Precession

J. Hennig and O. Speck (eds.), *High-Field MR Imaging,* Medical Radiology. Diagnostic Imaging,
DOI: 10.1007/174_2010_99, © Springer-Verlag Berlin Heidelberg 2011

RF	Radiofrequency
MRI	Magnetic resonance imaging
μMRI	Microscopy magnetic resonance imaging
OA	Osteoarthiritis
UTE	Ultrashort echo time
NYUMC	New York University Langone Medical Center
TFCC	Triangular fibrocartilage complex
PG	Proteoglycan
GAG	Glycosaminoglycans
FCD	Fixed charge density
TQF	Triple-quantum filtered
TPI	Twisted projection imaging
SQ	Single-quantum
dGEMRIC	Delayed gadolinium enhanced MRI of cartilage
MACT	Matrix-associated autologous transplantation
3D GRE	Three dimensional gradient echo
IR	Inversion recovery
IVD	Intervertebral discs
AF	Annulus fibrosus
NP	Nucleus pulposus
B_0	Main magnetic field
TR	Repetition time
SE T_2	Spin-echo T_2 relaxation time constant
^{31}P-MRS	Phosporus MR spectroscopy
^{1}H-MRS	Hydrogen MR spectroscopy
CSA	Chemical shift anisotropy
ATP	Adenosine triphosphate
PME	Phosphomonoesters
PDE	Phosphodiester
CSDE	Chemical shift displacement error
3D-CSI	Three dimensional Chemical Shift Imaging
PCr	Phosphocreatine
ADP	Adenosine diphosphate
PC	Phosphocholine
PE	Phosphoethanolamine
Pi	Inorganic phosphate
GPC	Glycophosphocholine
Spsp	Spectral-spatial
FATSAT	Fat saturation
MTC	Magnetization transfer contrast
CW	Continuous wave
SSFP	Steady-state free precession
DESS	Double-echo steady state

1 Applications: Musculoskeletal

1.1 Advanced Morphological Imaging

The most striking advantage of high- (3 T) and ultra high-field (above 3 T) MR imaging systems, compared to 1.5 T units and below is the increased feasibility to perform functional (biochemical) imaging. However, the importance of morphological imaging, which should be fundamental to every functional imaging study, should not be neglected.

At 1.5 T menisci, cortical bone, tendons, ligaments, and most other musculoskeletal tissues feature a low signal-to-noise ratio (SNR). SNR can be increased significantly using high- and ultra-high field systems; this gain in SNR can be translated into either higher temporal or spatial resolution for better morphological imaging.

1.1.1 Limiting Factors

The actual improvement in SNR is also tissue and pulse sequence-dependent, and thus, for most practical purposes, is less than the theoretically expected factor of 2.3 when advancing from 3 to 7 T. The field-strength-dependent SNR gain is outweighed by the frequency dependency of relaxation times, and the need to adjust sequence parameters (e.g., bandwidth and pulse parameters), to reduce artefacts, and not exceed the limits for the specific absorption rate (SAR). At 3 T, the SAR already limits the available slice coverage and, at 7 T, it is even worse. SAR issues and the resulting limited slice coverage are especially pronounced for sequence types such as turbo spin echo (TSE), half-Fourier acquisition single-shot turbo spin echo (HASTE), and True fast imaging with steady-state free precession (TrueFISP), which employ a chain of radiofrequency (RF) pulses (Hinton et al. 2003). Strategies to overcome that limitation include the concatenation of slices (which will prolong the acquisition time), an increase in the RF pulse length, a reduction of the flip angle (which will both decrease SNR and/or image contrast), the use of parallel imaging techniques (which will also decrease SNR), or the application of the hyper-echo technique introduced by Hennig and Scheffler (2001).

Another problem is dielectric effects, which are related to the electric and dielectric properties of the

bone and muscle interface, especially when imaging slim, muscular patients. However, this problem was manageable at 3 T, for example, by using saline bags and/or oscillating RF coils (Schmitt et al. 2005). New coil and shimming concepts might be necessary to overcome this drawback for diagnostic imaging at ultra-high fields.

T_1-weighted imaging is challenging due to B_1 field inhomogeneities. The change in the transmitted B_1 field throughout the image plane results in a variation of the flip angle that may result in different T_1 weighting, and thus, varying image contrast (Vaughan et al. 2002). Two-dimensional (2D) T_1-weighted spin-echo imaging becomes more difficult with increasing magnetic field strength. The prolongation of T_1 relaxation times typically results in lower T_1 contrast in 2D spin-echo imaging (Bottomley et al. 1984).

For T_2-weighted imaging, TSE sequences are used as the standard in clinical routine. However, these sequences include consecutive 180° RF pulses to reduce acquisition time. Thus, SAR becomes an issue when using TSE at 7 T. One can manage this by minimizing the number of slices or prolonging RF pulse duration. The existing B_1 profile can be compensated by using normalization techniques that are well-accepted, result in good clinical image quality, and are mostly also available on ultra-high field units (Wald et al. 1995).

Overall, for 3 T systems, problems have been sufficiently solved but for ultra-high field systems, problems are even worse and have been only partly resolved up to now. For example, more dedicated ultra-high field, multi-channel, multi-element coils need to be developed to allow the use of parallel imaging techniques, thus helping to overcome SAR restrictions. Another limiting factor is the strength and the slew rate of the gradient pulses used in the ultra-high field MR scanners, which, as yet cannot be increased proportionally to B_0. This limits the improvement of the in-plane resolution at ultra-high field compared to 3 T.

1.1.2 Microscopic Imaging

The improvement in spatial resolution of MRI for better visualization of more delicate anatomic structures has a long tradition derived from microscopy in conventional anatomy.

The basic MRI technique is capable of studying structural organization from whole-body levels down to micrometers, but the design of the imaging technology dictates that the size of the instrument is scaled to the investigated structure. Thus, biological MR imaging equipment and studies might be subdivided into three classes: microimaging of small biological samples, small animal microimaging, and human imaging.

Small-sample and animal imaging systems take advantage of the small magnet bore diameters that create extremely uniform magnetic fields, small receiver coils that result in an increased sensitivity per spin, efficient small-diameter gradient coils, and ultra high magnetic field strengths 14 T and higher. The combination of these factors can increase imaging sensitivity more than three orders of magnitude, compared to regular 1.5 T clinical MR scanners. The elegant images obtained with these microimaging systems probe down to the cellular level. Alhadlaq et al. performed a sample study using a 7 T/89 mm magnet and found that μMRI could quantitatively detect changes in collagen fiber architecture in early OA and resolve topographical variations in the cartilage microstructure of the canine tibia. Disease-induced changes in tissue were examined across the depth of the cartilage at a μMRI resolution of 13.7–23.1 μm (Alhadlaq et al. 2004). Another group reported an in vivo animal model study that achieved a voxel size of $44 \times 44 \times 176\ \mu m^3$ using a 7 T/210 mm magnet. These authors had measured the medial tibial cartilage thickness in the normal rabbit and in the anterior cruciate ligament transection rabbit model of osteoarthritis, and thus, were able to quantify the progression of cartilage thinning (Boulocher et al. 2007).

Recently, high-field and ultra-high field MR scanners have become capable of whole-body human studies that match the field strength previously applied to small-sample and animal microimagers. In addition, the sensitivity advantages of small receive coils, as employed in traditional microimaging, have been partially translated to human imaging by the development of multiple small receiver channels on clinical systems. By recording from multiple small receive coils, the size of those coils can be reduced similar to the size of those used in small-animal imaging, while simultaneously maintaining coverage suitable for human imaging. Technology is developing rapidly in this field, progressively shifting the boundaries of MR microimaging, and allowing

human imaging to more directly incorporate the methodology from animal and small biologic sample studies.

1.1.3 Beneficial Applications

Cartilage imaging, trabecular bone imaging, and ultra-short echo time (UTE) imaging are among those fields in musculoskeletal radiology that benefit the most from high field-strength imaging.

Cartilage Imaging

Cartilage imaging at higher field strengths is expected to improve the visualization of cartilage pathology and the segmentation of cartilage. With decreasing voxel size, partial-volume effects can be reduced, which enables us to measure cartilage volume and thickness even more reliably than with 1.5 T systems. Most of the experience reported in the literature is found in cartilage imaging of the knee joint. Krug et al. (2009) used a voxel size of 312 × 312 × 1000 μm^3 in their 7 T images used for cartilage segmentation, and Regatte and Schweitzer (2007) even went on to a 254 × 254 × 1000 μm^3 voxel size.

High-resolution images of the cartilage can be acquired not only in the knee, but also in smaller joints (e.g., in the wrist), thus improving the visualization of cartilage interfaces (Friedrich et al. 2009).

Fat suppression is important for accurate cartilage imaging. Due to the larger chemical shift between water and fat resonances, fat suppression is easier to achieve at 7 T than at 3 T (Regatte and Schweitzer 2007).

Trabecular Bone Imaging

It has been shown that dual X-ray measurement of bone density is not sufficient to characterize bone quality, because the trabecular bone architecture, apart from the bone density, contributes significantly to mechanical strength, and thus, fracture risk (Goldstein et al. 1993; Kleerekoper et al. 1985). Such bone structure is ideally characterized by microscopic computed tomography (CT) (Borah et al. 2002; Ding et al. 2002). However, CT cannot be used routinely in vivo due to the high radiation dose. In vivo trabecular bone imaging is one of the emerging applications for high-resolution morphological MRI. High spatial resolution is critical to visualize and quantitatively assess the morphology of trabecular bone with the average diameter of the individual trabeculae being in the order of 100–150 μm. Regatte and Schweitzer (2007) for example, were able to perform such high resolution trabecular bone imaging in the distal tibia using a voxel size of 156 × 156 × 1,000 μm^3.

Compared to 3 T, 7 T increases SNR by a factor of two, and thus, improves the visualization of trabecular bone structure (Krug et al. 2007). Susceptibility artifacts, due to differences in magnetic susceptibility between trabecular bone and bone marrow, result in an artificial broadening of the trabeculae signal void, especially in gradient-echo sequences (Hopkins and Wehrli 1997). This effect scales with field strength and has been shown to have the advantage that it enhances small trabeculae, which would otherwise disappear because of the partial volume effect (Krug et al. 2009).

Krug et al. (2008) were able to demonstrate high correlations between 3 and 7 T MRI, as well as between MRI and high-resolution CT with regard to the apparent trabecular bone number. For most of the other structural bone parameters, including bone fraction, trabecular spacing, and the number of trabeculae, high correlations were also found between 3 and 7 T MRI.

UTE Imaging

UTE pulse sequences have echo times about 10–20 times shorter than the shortest times generally available for the clinical routine. Thus, tissues with a majority of short T_2 components (e.g., cortical bone, menisci, tendons, ligaments, labri, and periosteum) can be visualized as the highest signal tissue on an image despite the very short T_2 of 0.42–0.50 ms (Robson et al. 2003).

UTE imaging has great potential, especially in musculoskeletal imaging, and has recently become a major research focus in this field (Robson et al. 2003; Du et al. 2009; Rahmer et al. 2009). High-field MR scanners have substantially improved the image quality of UTE imaging, compared to 1.5 T, due to increased SNR, stronger gradient systems, and the increased chemical shift difference between water and fat (Gold et al. 1998).

There are many possible applications for this technique in musculoskeletal imaging. One recent article, for example, describes the use of UTE for the morphological evaluation of anterior cruciate ligament grafts (Rahmer et al. 2009). Some authors have already applied UTE sequences for musculoskeletal imaging at

7 T (Regatte and Schweitzer 2007), but, future studies will have to evaluate the expected benefits of in vivo UTE imaging at ultra-high field MRI in detail.

1.1.4 Clinical Applications

It should also be noted that, for many indications, it is not clear whether advanced image quality improves diagnostic accuracy. Ultra-high field MR images might further improve our diagnostic confidence, but, based on our current experience, it is unlikely that the diagnostic accuracy for these conditions, including morphologic imaging alone (without additional functional imaging), will be improved substantially with the transition from 3 to 7 T. For these and other common indications, where diagnostic accuracy is already high at 1.5 T, the relative advantage of 3 T or above might be to shorten acquisition time, while maintaining an equivalent level of contrast and resolution, or, to combine information from morphological and functional imaging.

However, there are indications in which accurate diagnosis was limited by the available SNR at 1.5 T, which now are likely to benefit from 3 T or even 7 T scanners.

The reports about morphological imaging of the joints at 7 T in the literature are limited and mainly focus on the knee, ankle, and wrist.

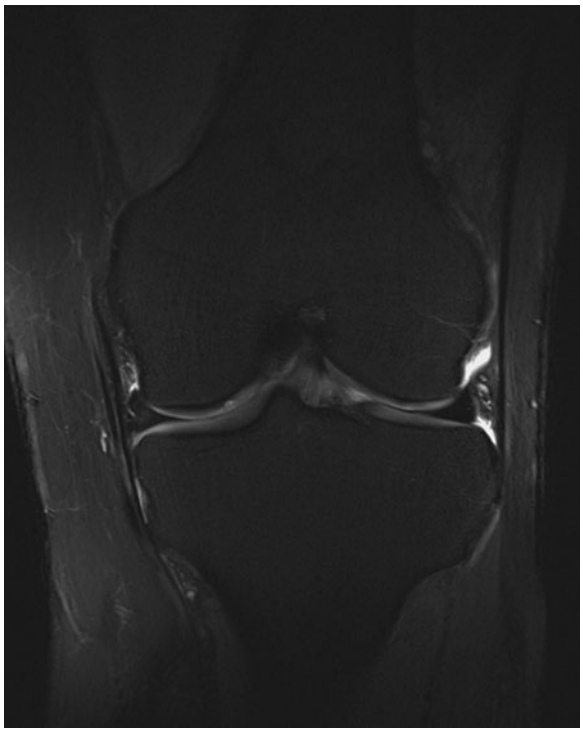

Fig. 1 Coronal image of the knee of a 36-year-old female volunteer, acquired using a proton density-weighted, TSE sequence (repetition time, 2,400 ms; echo time, 40 ms). Incidentally, a small cartilage lesion (*arrow*) was found in this asymptomatic healthy subject on the medial femoral condyle

Knee Imaging

Chang et al. (2009) performed the first in vivo 7 T MRI study of the knee. These authors investigated trabecular bone microarchitecture and detected activity-related changes in Olympic fencers, compared to healthy controls.

Other authors have used 7 T for the morphological assessment of articular cartilage and reported up to a 2.4-fold increase in SNR compared to 3 T (Krug et al. 2008). One study detected an increase in SNR from 3 to 7 T that was significant only for the gradient-echo sequences, but not for the TSE sequences (Stahl et al. 2009). Due to SAR limitations, scan parameters for the TSE sequence had to be modified, which resulted in an incomplete coverage of the knee joint, extensive artifacts, and worse fat saturation. Contrast-to-noise ratio and image quality were increased for the gradient-echo sequences, but decreased for the TSE sequences. Comparing 3 and 7 T, the level of confidence for diagnosing cartilage lesions was higher in the gradient-echo and lower in the TSE sequences; however, overall, the TSE sequences at 3 T had the highest confidence score. Evaluation of bone marrow edema was decreased at 7 T due to the limited performance of the TSE sequence.

Kraff et al. (2007) performed a comparison between knee imaging at 1.5 and 7 T, and also reported that, due to the SAR limitations with the fast spin-echo sequences, several measurements were needed for complete coverage of the knee joint. They also confirmed that bone marrow edema was better visualized at 1.5 T than at 7 T.

Using an in-house-built RF eight-channel receive and four-channel transmit coil from the New York University Langone Medical Center (NYUMC) (Friedrich et al. 2009) in a collaborative project, we were able to perform morphological imaging of the knee joint at 7 T with excellent image quality. The images were acquired with a proton density-weighted, TSE sequence with fat saturation and a voxel size of $137 \times 137 \times 2500\ \mu m^3$. With 25 slices and a spacing of 3.1 mm between the slices, the whole knee was scanned within 2 min and 35 s (Fig. 1).

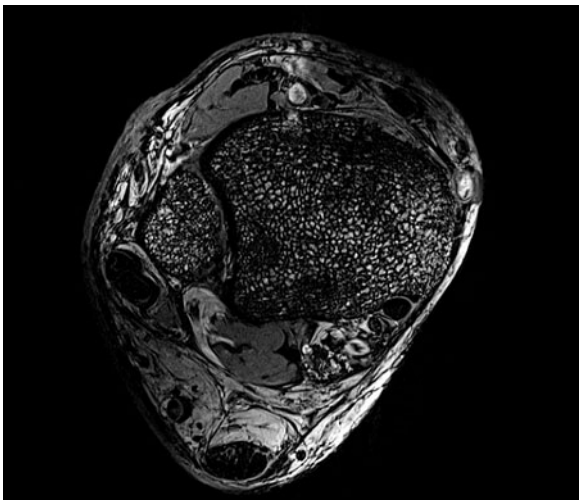

Fig. 2 Axial image of the ankle (distal tibia and fibula) of a 41-year-old male volunteer, acquired using a volumetric, interpolated, breath-hold examination (VIBE) sequence (repetition time, 13.9 ms; echo time, 7.1 ms; flip angle, 12°; bandwidth, 130). The trabecular bone microstructure of the distal tibia and fibula can be appreciated

Fig. 3 Coronal image of the ankle of a 22-year-old male patient with a cartilage transplant in the trochlea tali, acquired using a proton density-weighted, TSE sequence with fat saturation (repetition time, 2,880 ms; echo time, 40 ms). The transplant (*arrow*) can be clearly differentiated from the original cartilage on the medial aspect of the trochlea tali

However, as yet, there is no study that verifies a statistically significant increase in diagnostic accuracy for the detection of common pathologies in the knee when moving to MR scanners with field strengths above 3 T.

Ankle Imaging

Imaging the ankle at 7 T is mainly limited by the lack of commercially available dedicated ankle coils. Thus, one group used an eight-channel head array coil to perform trabecular bone imaging at 7 T, and found that the relative noise enhancement factor was lower at 7 T than at 3 T for parallel imaging acceleration factors higher than three (Banerjee et al. 2006, 2008). Using the same multipurpose extremity coil as in Fig. 1, we performed high-resolution trabecular bone imaging at 7 T, with a voxel size of 234 × 234 × 1000 μm^3 (Fig. 2), and high-resolution cartilage imaging with a voxel size of 137 × 137 × 2000 μm^3 (Fig. 3).

Wrist and Hand Imaging

The wrist is an especially challenging region because of the small size of the relevant anatomical structures, such as the intrinsic and extrinsic ligaments, the articular cartilage, and the triangular fibrocartilage complex (TFCC). Sensitivity, specificity, and accuracy for imaging the TFCC pathology are higher at 3 T than at 1.5 T (Anderson et al. 2008). Trabecular bone imaging has also already been performed on the wrist using 3 T MR scanners, which resulted in a 16-fold increase in SNR, compared to 1.5 T, and a maximum spatial resolution of 200 × 200 × 2000 μm^3 (Lenk et al. 2004).

Farooki et al. (2002) were the first to image the wrist at field strengths above 3 T; they qualitatively compared 1.5 T with 8 T, and concluded that 8 T was superior in the visualization of the infrastructure of the median nerve and in the definition of the boundaries of the carpal tunnel. Other authors went on to quantify the difference between 1.5 and 7 T MRI of the wrist, and found that SNR was about five times higher in tendon, bone, muscle, and nerve (Behr et al. 2009). These authors achieved a maximum spatial resolution of 160 × 160 × 1500 μm^3.

The NYUMC research group also uses their in-house-built RF eight-channel receive and four-channel transmit coil mentioned earlier for wrist imaging, enabling the possibility of performing parallel imaging.

The maximum spatial resolution they achieved was $80 \times 80 \times 2000\ \mu m^3$ (Friedrich et al. 2009).

2 Advanced Functional (Biochemical) Imaging of Articular Cartilage

2.1 Proteoglycan-Specific Techniques

2.1.1 Sodium Imaging

Background and Basic Findings

Articular cartilage consists mainly of an extracellular matrix made of type II collagen, proteoglycan, chondrocytes, and water (Mankin 1971). Proteoglycan (PG) contains a linear protein core to which many glycoproteins known as glycosaminoglycans (GAG) (Roughley and Lee 1994) are attached. PG serves to cross-link the collagen fibrils in the extracellular matrix to provide both compressive and tensile strength to the matrix. The sulfate and carboxyl groups of the GAG impart a negative fixed charge density (FCD) to the matrix. These negative ions attract positive counter-ions (sodium) and water molecules and provide a strong electrostatic repulsive force between the proteoglycans. These osmotic and electrostatic forces are responsible for the swelling pressure of cartilage. The configuration of the PG macromolecules also contributes to the resistance of the matrix to the passage of water molecules, and thus, affects the mechanics of the cartilage in this fashion. In summary, PG and GAG are the most important macromolecules for the biomechanical properties of articluar cartilage.

The onset of osteoarthritis (OA) is well understood to be associated with primarily biochemical phenomena. The ability to quantify these molecular changes will provide a tool for the early diagnosis of osteoarthritis and treatment monitoring. The loss of proteoglycan from the extracellular matrix has been reported to be the event that initiates the onset of OA (Lohmander 1994; Grushko et al. 1989).

The loss of PG with the onset of OA results in a reduction of FCD in cartilage. Maroudas et al. (1969) have shown that the FCD of cartilage is correlated to the GAG content of cartilage. Since the FCD is counter-balanced by sodium ions, the loss of PG (and hence, GAG and FCD) due to cartilage degeneration results in the loss of sodium ions from the tissue. The loss of the negatively charged PG lowers the FCD in the tissue, thereby releasing positively charged sodium ions. A method has been proposed to quantify FCD both in vitro and in vivo using sodium magnetic resonance (MR) imaging and the Donnan equilibrium equation:

$$FCD = \frac{\left(Na_S^+\right)^2}{Na_t^+} - Na_t^+ \qquad (1)$$

where Na_s is the sodium concentration in the surrounding synovial fluid and Na_t is the sodium concentration in the tissue (Lesperance et al. 1992).

Sodium MR imaging has been validated as a quantitative method of computing FCD and, hence, PG content, in healthy humans (Borthakur et al. 2000, 2002; Shapiro et al. 2002).

Simultaneous imaging of phantoms that consist of known sodium concentrations and relaxation times enables the creation of a sodium concentration map of articular cartilage. The corresponding FCD map can be calculated on the basis of the sodium map findings using Eq. (1).

Healthy human cartilage FCD ranges from a concentration of 50–250 mM, depending on age and location in the tissue (Lesperance et al. 1992). As demonstrated in controlled cartilage degradation experiments (Borthakur et al. 2000; Shapiro et al. 2000), the sensitivity of sodium MR imaging is adequate for detecting changes in PG content as small as 5%.

Due to the sparse cellular content (2% by volume) and highly ordered nature of the articular cartilage, most of the sodium in the extracellular matrix of cartilage is in a slow motion regime and exhibits multiple quantum coherences. It should be noted here that 40% of total sodium is observed directly through the central transition, which decays with a longer relaxation time constant (T_2 slow), compared with the 60% of sodium that contributes to the satellite transitions, which decays with a faster relaxation time constant (T_2 fast). Therefore, in order to acquire the maximum sodium signal, one has to use ultra-short RF pulses and fast acquisition schemes. Otherwise, a significant amount of the fast-decaying signal will be lost before detection and this will lead to a low SNR.

Normally, the signals from free sodium and the cartilage-bound ordered sodium overlap each other,

and several methods have been developed for their separation. A number of techniques are based on the evolution under residual quadrupolar interactions.

For example, in the double-quantum filter experiment (Navon et al. 2001; Kemp-Harper et al. 1997) the transverse magnetization operators, $T^{1}_{1+/-1}$, evolve into second-rank tensors under the action of the quadrupolar interaction. These second-rank tensors can then be converted into double-quantum coherences ($T^{2}_{1+/-2}$), which can be filtered out using phase cycling). Alternatively, in the Jeener–Broeckaert experiment, the rotational properties of different rank tensors (Kemp-Harper et al. 1997) are exploited to perform this selection. Both techniques were adapted to detect the filtered signal through the central transition to maximize SNR and resolution (Kemp-Harper et al. 1997). However, these techniques require a large phase cycle and are difficult to implement on MRI scanners since they use a large number of pulses. More recently, methods based on frequency-sweep pulses (Ling and Jerschow 2005, 2006) and quadrupolar nutation (Choy et al. 2006) were demonstrated, which exploit coherence transfer properties that depend on the quadrupolar interaction. The quadrupolar coupling itself was shown to correlate with the onset of cartilage degeneration (Shinar and Navon 2006; Ling et al. 2006).

Another form of signal separation is performed by the triple-quantum-filtered (TQF) experiments, in which the selected signal arises from quadrupolar nuclei in slow motion (Jaccard et al. 1986). Slow-motion gives rise to third-rank tensors, which, upon conversion to triple-quantum coherences, can be filtered out by phase cycling.

The feasibility of performing TQF sodium imaging of articular cartilage was first demonstrated on bovine cartilage samples (Reddy et al. 1997). Then, TQF imaging of the human knee was performed in vivo (Borthakur et al. 1999). In the in vivo study, a twisted projection imaging (TPI) sequence, with an ultrashort 400 μs time delay between signal excitation and detection was employed. Images were acquired with a voxel size of 0.5 cm^3. The total imaging time for a three dimensional (3D) data set of 16 slices was 20 min, and provided images with an SNR of 8:1. Single-quantum (SQ) images were also acquired with a voxel size of 0.06 cm^3. Total SQ imaging time for a 3D data set with an SNR of 16:1 was 10 min. The calculated transverse relaxation times, T_{2slow} and $T_{2fast,}$ were 0.84 and 9.6 ms. These studies clearly demonstrate the importance of a short-echo imaging sequence like TPI in imaging SQ, as well as TQF signal, from sodium. These studies also show that it requires almost three times the total imaging time to acquire TQF images with the same SNR (but 10 times larger voxels) than SQ images, i.e., the TQF signal is an order of magnitude weaker than the SQ signal.

Since $1/T_{2fast}$ is sensitive to slow molecular motions, it is determined by fast exchange of the bulk sodium ions with those ions interacting with macromolecules. It has been shown that, in all cases where the decay of the SQ coherences is bi-exponential, higher order coherences can be formed and the separation of the two SQ relaxation times can be preferentially achieved by TQF (Shinar and Navon 2006; Shinar et al. 1992).

Clinical Application of Sodium Imaging

Sodium MRI experiments were performed on the knee cartilage of healthy as well as early stage OA patients at 4 T and demonstrated the feasibility of sodium MRI in computing PG loss in early stage OA. The sodium 3D image data set, using a surface coil, was acquired with a voxel size of 59 μm × 59 μm × 3.8 mm after interpolation with an SNR of 12:1 in about 20 min. In comparison, it took 30 min to obtain a 3D data set using a volume coil with the same SNR but an increased voxel size of 74 μm × 74 μm × 5.7 mm (Wheaton et al. 2004a). With the effects of B_1 inhomogeneity and voxel size accounted for, the surface coil provides an improvement in SNR by a factor of 2. Alternately, an image can be obtained with a surface coil in 25% of the time that it takes to acquire one with a volume coil image with an identical SNR and voxel size (Shapiro et al. 2002). The utility in measuring FCD changes in an animal model of OA with sodium MRI has been described (Wheaton et al. 2004b).

The major advantage of sodium MRI, especially of cartilage, is that it is highly specific for PG content and since the sodium from surrounding structures in the joint is low (< 50 mM), cartilage can be visualized with very high contrast without the requirement for any exogenous contrast agent such as that in delayed Gadolinium Enhanced MRI of Cartilage (dGEMRIC) (Burstein et al. 2001). It can be used to quantify early molecular changes in osteoarthritis.

The disadvantages of sodium MRI are that it requires field strengths of > 3 T to obtain quality sodium images that enable accurate quantification of cartilage FCD. Furthermore, due to the limitations of gradient strengths and other hardware requirements, most of the sodium imaging experiments reviewed here employed echo times of more than 2 ms. Since the fast T_2 decay of cartilage lies in the range 1–2 ms, substantial signal is lost before the acquisition. This is one of the major contributors to the low SNR of sodium compared to conventional proton MRI. In addition, the sodium gyromagnetic ratio (γ) is one-quarter that of protons; thus, sodium MRI requires four times stronger gradients to obtain images with a resolution identical to that of proton MRI. Nevertheless, the resolution is not only a function of the gyromagnetic ratio, but also of the receiver bandwidth. The MR sensitivity for ^{23}Na is only 9.2% of the ^{1}H MR sensitivity, and the in vivo concentration is $\sim$360 times lower than the in vivo water proton concentration. The combination of these factors results in a ^{23}Na signal that is approximately 4000 times smaller than the ^{1}H signal.

However, recent advances in magnet technology, improved gradient performance, and multi-coil RF technology (parallel receive as well as transmit) may enable one to achieve an ultra short TE (< 200 μs) that could significantly improve resolution and SNR. Radiofrequency coil technology (multiple channel capability) and parallel imaging approaches and tuned pre-amplifiers would further contribute to high SNR. These advances may potentially make clinical sodium MRI feasible on 3T scanners. Further, the recent proliferation of 7 T whole-body MRI scanners in clinical research centers could have a significant impact on sodium MRI and its potential for clinical use. Since SNR scales as $B_0^{7/2}$ (Hoult et al. 1986; Chen et al. 1986; Ugurbil et al. 2003), and the lack of B_1 penetration and B_0 susceptibility are issues that pose problems with proton imaging, sodium MRI can be particularly advantageous at higher fields. Further, unlike proton T_2, which increases with field, as the T_1 of sodium is predominantly due to quadrupolar interaction, it may not change appreciably at higher fields. This would retain the rapid averaging capability of sodium MRI, even at high fields. The low γ of sodium will also mean significantly lower power deposition compared to proton imaging. It is, therefore, very likely that, with the improved SNR, sodium MRI at 7 T and higher fields would emerge as a robust tool for quantitative imaging of cartilage. Although sodium MRI has high specificity and does not require any exogenous contrast agent, it does require special hardware capabilities (multinuclear), specialized RF coils (transmit/receive) and likely 3D-ultra-short TE sequences. These challenges currently limit the clinical use of sodium MRI on standard clinical scanners. Nevertheless, sodium MRI has been successfully demonstrated in vivo on pigs, in human wrists, and in a human knee (Borthakur et al. 2002, 2006; Reddy et al. 1998).

We have recently applied sodium imaging in patients after matrix-associated autologous transplantation (MACT). Our sodium measurements were performed using a ^{23}Na-only (78.61 MHz) circularly polarized transmit/receive knee coil with an inner diameter of 19 cm (Stark Contrast, Erlangen, Germany). A reference sample containing 308 mM of NaCl was fixed to the inner surface of the sodium coil to normalize the inter-scan signal variability. Using a 7 T whole body system and a modified three dimensional gradient echo (3D GRE) sequence, we achieved a sufficiently high SNR of 24 (range: 17–30) in native cartilage, which allowed us to visualize even the femoral condyle cartilage layer, which is thinner than the patellar cartilage, but is the preferred location for cartilage transplantation. The reports about sodium imaging of the knee joint have, to date, focused on the patellar cartilage layer. The resolution we achieved was high enough to visualize even the thin cartilage layer of the adjacent proximal tibiofibular joint. In our patient group, sodium imaging allowed to distinguish different concentrations of sodium, which correlates to GAG content in transplants, compared to native, healthy cartilage (Fig. 4). The mean normalized sodium values were 125 (range: 72–244) for the repair tissue within the cartilage transplant and 192 (range: 98–259) for healthy cartilage.

We found a good correlation between sodium imaging and dGEMRIC for the quantification of GAG concentration in patients after MACT.

In summary, these findings indicate that sodium imaging at 7 T can be clinically useful. Indeed, this technique could establish a new standard in biochemical imaging of articular cartilage, with its direct correlation to GAG concentration, the component of the ultrastructure of cartilage that is lost in the earliest

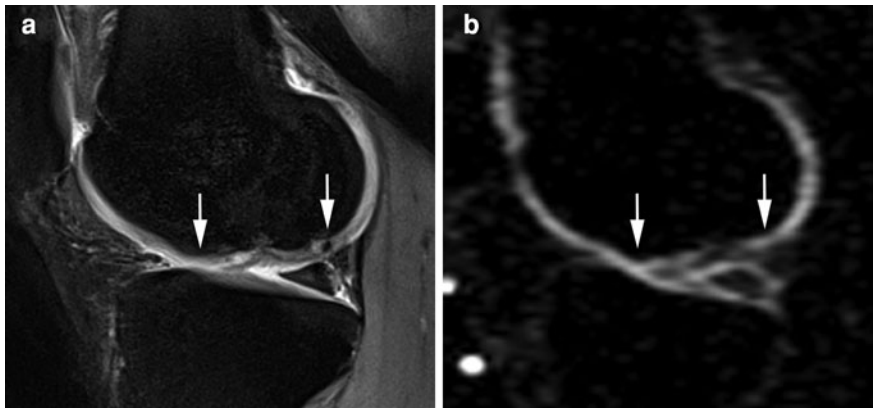

Fig. 4 Conventional proton density weighted FSE image with fat suppression of a 23-year-old male, 70 months after MACT, acquired at 7 T (**a**). Corresponding sodium image was measured with a 3D-GRE sequence at 7 T (**b**). *Arrows* delineate the borders of the transplant

stages of OA and plays the most important role in the biomechanical properties of cartilage.

2.1.2 dGEMRIC at 7 T

Background and Basic Findings

For the visualization of GAG, in addition to sodium imaging, dGEMRIC (McKenzie et al. 2006; Burstein et al. 2001) has gained significant importance.

The dGEMRIC technique is based on the fact that proteoglycans contain negatively charged side chains that lead to an inverse proportionality in the distribution of the negatively charged contrast agent molecules with the concentration of proteoglycans. Consequently, T_1(Gd), which depends on the Gd-DTPA^{2-} concentration, becomes a specific measure of tissue proteoglycan concentration. The value of this technique and the possible clinical applications has been repeatedly reported (Kim et al. 2003; Tiderius et al. 2003; Burstein and Gray 2006).

In the majority of these studies only T_1 after penetration of Gd-DTPA^{2-} (T_1(Gd)), has been used. However, from studies on cartilage implants and from studies at higher field strength (3 T), it has been reported that the delta relaxation rate R1, calculated as $1/T_1$(Gd) − $1/T_1$pre-contrast, would be more representative of Gd-DTPA^{2-} concentration, where T_1pre-contrast = T_1 before contrast administration (Watanabe et al. 2006; Williams et al. 2007).

Recently, whole-body scanners operating at 7 T are increasingly being used for clinical studies on patients (Regatte and Schweitzer 2007; Michaeli et al. 2002; Christoforidis et al. 2002). To date, no studies are known that describe contrast agent behavior at this field strength. From earlier studies, it is known that the relaxivity of contrast agents decreases with increasing field strength (Rohrer et al. 2005), which may significantly influence the efficacy of the dGEMRIC technique. The ultra-high magnetic field at 7 T, with the higher SNR, offers high resolution protocols for articular cartilage imaging, which have not been possible, to date, in vivo. Recently, at 3 T, the application of a dual-flip angle excitation pulse GRE technique was shown to be comparable to standard inversion recovery (IR) sequences in the evaluation of cartilage implants, but provided a significant reduction in scan time (Trattnig et al. 2007a).

A comparison of a standard T_1 mapping IR sequence, with a dual flip angle excitation pulse 3D GRE technique in a phantom study at 7 T, showed a lower correlation in the longer range of T_1 values from 800 ms and higher. In addition, only half the central slices demonstrated a significant correlation between IR and GRE. The T_1 values pre- and post-contrast differed significantly between the IR and the GRE techniques and the difference between T_1 values pre- and post-contrast was lower with the GRE T_1 mapping technique. The post-contrast drop in T_1 values was more pronounced with IR compared to the GRE technique. In the evaluation of the feasibility of the dGEMRIC technique at 7 T in volunteers Fig. 5 shows an example of pre- and post-contrast T_1 maps calculated from IR dGEMRIC measurement.

A similar separation between $1/T_1$(R1) pre-contrast and $1/T_1$(R1)(Gd) was observed at ultra-high field 7 T, compared to reported values at 3 T, although a lower contrast agent relaxivity was expected at 7 T, which would lead to less separation. The effect on the behavior of contrast agents at different field strengths depends on two basic mechanisms: the nuclear magnetic relaxation dispersion and

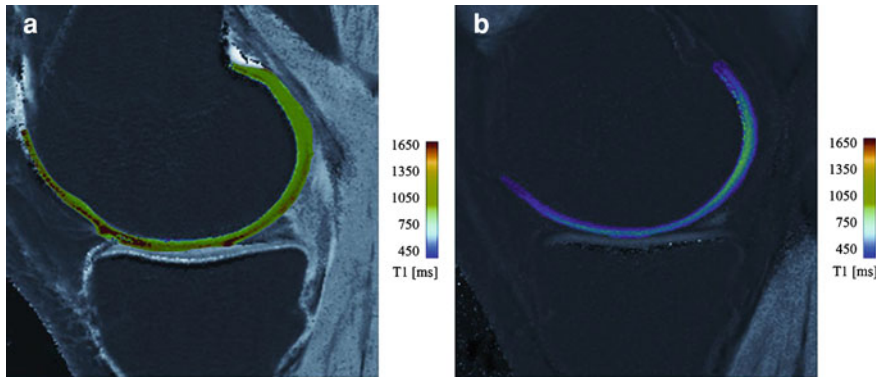

Fig. 5 Pre- and post-contrast images of T_1 maps, measured using dGEMRIC. The IR technique was applied. Figure **a** shows pre-contrast color-coded cartilage, figure **b** shows post-contrast cartilage

the field-dependent relaxation of tissue (Rinck et al. 1988). The nuclear magnetic relaxation dispersion or relaxivity of a paramagnetic ion to water protons, described by Solomon–Bloembergen–Morgan equation, is higher at lower magnetic field strengths and decreases at higher magnetic fields (Wood and Hardy 1993). In a recent report, it was already described that, at a field strength of 3 T, the use of T_1(Gd) as a measure of Gd-DTPA2- distribution may be less suitable at 3 T than at 1.5 T, but may be still useful if pre-contrast T_1 values are calculated, as well (Williams et al. 2007). From the calculated T_1 values of an IR sequence at 7 T, this statement is true for 7 T, as well, and the use of T_1(Gd) seems to be similarly appropriate at 7 T as an index of Gd-DTPA2-concentration in cartilage than at 3 T.

The dual flip angle excitation pulse GRE technique provided unreliable results at 7 T, which may be caused by several factors: first, the optimal flip angle for the GRE method is tissue T_1-dependent, which means that different sets of flip angles for the pre- and post-contrast T_1 measurement should be used for 7 T compared to 3 T. However, homogenous excitation is an issue at 7 T and makes this technique problematic. Second, gradient echo sequences are more prone to static magnetic field inhomogeneities.

In summary, it could be demonstrated, for the first time, that dGEMRIC is feasible at 7 T (Welsch et al. 2008b). The difference between pre- and post-contrast T_1 values is high enough to be useful for quantification with the dGEMRIC technique and the combination of 7 T ultra-high resolution, together with functional MR, seems to be possible and may be an important step into molecular imaging of articular cartilage in the near future.

3 Collagen Fiber- and Water-specific Techniques

To visualize the ultra-structure of articular cartilage and other soft tissues in the musculoskeletal system at high and ultra-high fields is a promising approach in molecular imaging (Burstein and Gray 2006). Depending on anatomic localization and considering the available coil configurations, within the different large and small joints, biochemical MR imaging can be achieved to assess the constitution of the specific tissues. T_2 relaxation time mapping is the most widely used technique, and was first used to describe the composition of hyaline articular cartilage in the knee joint based on its collagen structure and hydration.

At 3 T, in addition to the knee joint, the imaging of the cartilage of the hip joint as well as the ankle, the shoulder, the elbow, and the wrist are also goals of biochemical T_2 MR studies. Nevertheless, at 7 T, the applicability is very much linked to the available coil technology. As large patient groups suffer from osteoarthritis (OA) of different joints, the ability to describe articular cartilage at high und ultra-high fields is becoming increasingly important. In addition to idiopathic OA, cartilage defects in younger patients can lead to the development of OA in later years. Thus, surgical and non-surgical treatment options require sophisticated follow-up to show their potential benefit in the prevention of degenerative cartilage disease. Basically, articular cartilage is complex, dense, connective tissue that relies on the diffusion of solutes for its nutrition (Buckwalter and Mankin 1998). Responsible for the biomechanical properties

of articular cartilage is the extracellular matrix, mainly composed of water (~75%), collagen (~20%), and proteoglycan aggregates (~5%) (Buckwalter and Mankin 1998; Poole et al. 2001). Water either moves freely throughout the matrix or is bound to macromolecules. Collagen in hyaline cartilage is largely type II, which creates a stable network throughout the cartilage. The negatively charged PG are composed of a central core protein to which GAG are bound. Articular cartilage is stratified primarily according to the orientation of collagen within a 3D network (Poole et al. 2001; Goodwin et al. 2000). To visualize this zonal structure is one basic requirement for high-quality, high-resolution T_2 mapping, and, with the increased signal, ultra-high fields might open new possibilities for an anatomical zonal evaluation of articular cartilage.

In addition to the transverse relaxation time (T_2) of articular cartilage (Mosher and Dardzinski 2004), recently, T_2* relaxation is being discussed for the depiction of the collagen matrix (Welsch et al. 2008b). As mentioned above, for both methodologies, based on the stratification of cartilage from the subchondral bone to the cartilage surface, the zonal evaluation of articular cartilage is crucial.

In addition to articular cartilage, in the knee joint, the meniscus, in particular, is more and more the focus of T_2 relaxation time mapping. However, problems due to lower echo times within the meniscal tissue occur and will currently limit its application at ultra-high fields. Normal human meniscal tissue has been found to be composed of ~70% water, ~25% collagen, and ~1% GAGs, with a regional variation based on the location in the knee joint. The predominantly dense framework is based on type I collagen fibers in a mainly circumferential orientation (Messner and Gao 1998).

One other large group of patients with musculoskeletal problems, besides OA, are people who suffer from back pain. Degenerative disc disease is regarded as the most prevalent cause of back pain, and can be visualized using biochemical MRI. In intervertebral discs (IVD), the annulus fibrosus (AF) consists of fibro-cartilage and its function as a rigid containment for the nucleus pulposus (NP) accounts for its fibrous structure and low water content. The gelatinous structure of the NP, however, consists mostly of water, bearing a low yield of collagenous material. Degeneration of IVDs is initiated by the incapacity of disc cells to maintain a highly hydrated proteoglycan-rich matrix for the NP, as well as a loss of the collagen structure that affects the mechanical integrity of the IVD. Due to the high reliance of IVDs on their biochemical composition, functional MR techniques are becoming increasingly important in the diagnosis and treatment follow-up of patients with back pain. Although it will take some time until the spine can be assessed at ultra-high fields due to existing problems with body coils, the value of biochemical MRI in this field is very high.

3.1 T_2 Relaxation Time Mapping of Articular Cartilage at Ultra-high Fields

The transverse relaxation time constant (T_2) of cartilage is a sensitive parameter for the evaluation of changes in water and collagen content and tissue anisotropy (Mosher and Dardzinski 2004). Cartilage T_2 reflects the interaction of water and the extracellular matrix on a molecular level. The collagen fiber orientation defines the layers of articular cartilage. Thus, the 3D organization and curvature of the collagen network, influenced by water mobility, the proteoglycan orientation, and the resulting magic angle at 55° (with respect to the main magnetic field (B_0)), influence the appearance of T_2 (Goodwin et al. 1998, 2000). In healthy articular cartilage, an increase in T_2 values from the deep to superficial cartilage layers can be observed, based on the anisotropy of collagen fibers running perpendicular to cortical bone in the deep layer of cartilage (Smith et al. 2001). Histologically validated animal studies have shown this zonal increase in T_2 values as a marker of hyaline or hyaline-like cartilage structure after cartilage repair procedures in the knee (Watrin-Pinzano et al. 2004; White et al. 2006). To visualize this zonal variation in vivo, high spatial resolution is essential, which can already be achieved with high-field MR, together with dedicated multi-channel coils in clinical approaches. Nevertheless, with ultra-high field MR, the prospects of T_2 mapping increase, and, with higher spatial resolution, the goal of cartilage molecular imaging might be reached. Thus, for musculoskeletal MRI at ultra-high fields, the utilization of biochemical sequences and, for example, the use of T_2 mapping techniques should increase.

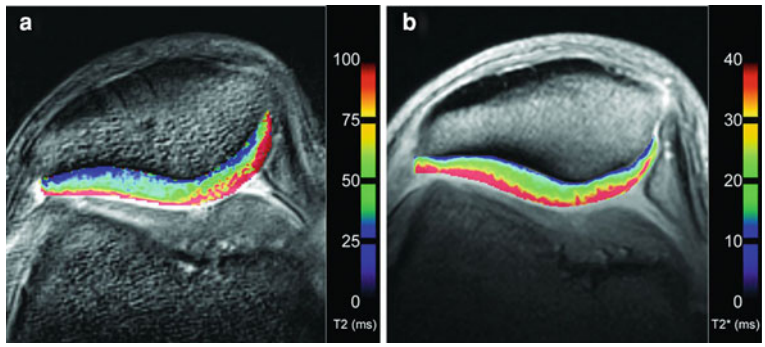

Fig. 6 Axial multi-echo spin-echo T_2 sequence (*left*) and gradient-echo T_2* sequence (*right*), with high in-plane resolution, depicting the patellar cartilage of a healthy volunteer. The zonal variation as an increase in T_2 or T_2* values from the subchondral border to the joint surface becomes visible

Analyses of T_2 relaxation times in the knee have previously been performed at 1.5 T or more recently at 3 T (David-Vaudey et al. 2004; Mosher et al. 2005; Trattnig et al. 2007b). These studies have demonstrated the feasibility, as well as the benefit of a functional evaluation of articular cartilage to demonstrate pre-morphologic abnormalities. Studies comparing T_2 relaxation at 1.5 and 3 T reported a less-pronounced dependence on the magnetic field strength compared to longitudinal T_1 relaxation. However, a shortening of T_2 values at 3 T by approximately 10%, and by 10–20% at 4 T compared to 1.5 T, have been published (Gold et al. 2004; Stanisz et al. 2005; Bolog et al. 2006). But, T_2 values reported in the literature depend, to a great extent, on the sequence evaluated. Stanisz et al. (Stanisz et al. 2005) found T_2 values at both 1.5 and 3 T, in their study, to be similar to those of Smith et al. (2001), but higher compared to the evaluation by Gold et al. (2004). All three study groups used different sequences in their quantitative evaluation of T_2 with different echo times. Our own group uses a traditional multi-echo spin echo technique for standard T_2 mapping, showing slightly lower T_2 relaxation time values for articular cartilage of the knee at 7 T (Fig. 6a) than studies using a similar T_2 technique at 3 T (Trattnig et al. 2007b). Although an available comparison of T_2 relaxation times at 3 and 7 T also did not find a shortening of T_2 values (Pakin et al. 2006), an ongoing study by our group shows a significant decrease of T_2 relaxation times from 3 to 7 T.

The different cartilage locations (patella, femur, and tibia) were evaluated in one study by our group at 7 T using SE T_2 mapping (Welsch et al. 2008b) and showed results comparable to those of Pakin et al. (2006), with a significant decrease in T_2 values between femoral and tibial weight-bearing cartilage. Furthermore, the patella showed lower T_2 values than the femoral condyle. In a study by Mosher et al. (2004), T_2 values of the femoral condyle were assessed, as well as the tibia and the patella, and all three anatomic regions showed roughly equivalent results. However, in a later study by the same group, studying T_2 relaxation after exercise, a different behavior for the femoral and tibial cartilage were observed (Mosher et al. 2005). Reported differences in T_2 relaxation times based on their anatomic location might be explained by different biomechanical properties, and thus, a different ultra-structure of the respective articular cartilage. However, especially at ultra-high fields, the orientation of the cartilage, with regard to the main magnetic field, might play another very important role. In the field of OA, there are no available studies about the use of T_2 mapping at ultra-high fields. Nevertheless, at high-fields, one problem with quantitative T_2 is the fact that an increase as well as a decrease of T_2 values can be interpreted as a sign of ongoing cartilage degeneration (Burstein and Gray 2006).

In cartilage repair tissue, global (bulk; full-thickness) T_2 and especially zonal T_2 evaluations have shown very promising results. Thus, in the follow-up after matrix-associated autologous chondrocyte transplantation (MACT), the visualization of cartilage repair tissue maturation was possible at high-fields and a differentiation between cartilage repair tissue at the patella and the medial femoral condyle could be achieved (Trattnig et al. 2007b; Welsch et al. 2008a, 2009a). Comparable to the results at 3 T, 7 T multi-echo spin-echo T_2 mapping could also be used for the assessment of patients after cartilage repair (Welsch et al. 2008b). Furthermore, using T_2 mapping, cartilage repair tissues after different repair procedures could be distinguished (Welsch et al. 2008c).

Although cartilage repair tissue after microfracture technique (MFX), histologically seen as fibrocartilage, shows no zonal increase from deep to superficial cartilage aspects, repair tissue after MACT, histologically reported as hyaline-like, shows a significant stratification.

Using ultra-high-field MRI, T_2 mapping techniques might offer new insights into the characterization of cartilage repair tissue after surgical repair techniques. In addition, T_2 mapping of non-surgical cartilage repair procedures (e.g., approaches based on growth factors) and therapy concepts in early OA might also benefit from ultra-high fields. Particularly for the evaluation and the validation of T_2 relaxation time mapping in OA, ultra-high field scanners may provide a clearer insight into early changes of the collagen matrix, resolving existing limitations (Burstein and Gray 2006; David-Vaudey et al. 2004; Dunn et al. 2004).

3.2 T_2* Relaxation Time Mapping of Articular Cartilage at Ultra-high Fields

In addition to standard SE T_2 mapping, T_2* weighted 3D gradient-echo articular cartilage mapping has shown reliable results in the evaluation of OA cartilage changes of the knee (Murphy 2001). In recent studies, T_2* mapping, with short scan times, was correlated to standard SE T_2, and provided information comparable to that obtained for articular cartilage using SE T_2, but with overall lower T_2* values (Hughes et al. 2007; Wietek et al. 2007). Furthermore, also for T_2*, a clear zonal variation between the deep and the superficial cartilage layers was described for healthy cartilage.

In cartilage repair, T_2* mapping provides promising results, and, in patients after cartilage transplantation techniques, a zonal stratification was visible, but, in patients after MFX, this stratification could not be found (Hughes et al. 2007). Thus, for standard T_2, as well as for T_2*, zonal assessment of healthy and altered articular cartilage is crucial.

For T_2*, the zonal variation between the subchondral border and the cartilage surface might have another explanation, due to the influence of local susceptibility fields on T_2* and this must be further studied. These local fields can operate at a macroscopic level, i.e., at the bone/cartilage interface or at the microscopic level, i.e., associated with the underlying microstructure of the cartilage. If these processes produce local changes in the macroscopic static field gradients, this might be more distinct in the deep cartilage zone.

When comparing high fields (3 T) and ultra-high fields (7 T), in an ongoing study, this zonal increase between the deep and the superficial cartilage layers was significantly more strongly pronounced at 3 T, for both T_2 and T_2* relaxation times ($p < 0.05$). Thus, the meaning of the zonal stratification must be further elucidated, especially in the evaluation of altered articular cartilage. In the zonal T_2 or T_2* assessment, ultra-high fields may offer the possibility to enclose a third cartilage layer (deep, middle,and superficial) that would adapt much more to the anatomical composition of articular cartilage. This possibility is still limited by insufficient resolution at high fields.

In ultra-high fields, T_2* could be used for the depiction of healthy hyaline cartilage and in patients after MACT (Welsch et al. 2008b). The T_2* relaxation times seem to be shorter at ultra-high fields (Fig. 6b) compared to high fields (comparable to standard SE T_2) (Welsch et al. 2009b). Again, however, histological validation must confirm the properties of articular cartilage depicted by T_2* at high and ultra-high fields.

4 Advanced Metabolic Imaging at 7 T

4.1 Musculoskeletal Phosphorus Spectroscopy

Phosphorus MR spectroscopy (^{31}P-MRS) has the potential to become increasingly important in future musculoskeletal ultra-high-field MR (≥7 T). ^{31}P-MRS has become a popular tool among muscle physiologists, even on lower magnetic field scanners, since it reveals the major factors of muscle metabolism non-invasively (Boesch 2007; Kemp et al. 2007; Phielix and Mensink 2008; Prompers et al. 2006). In particular, it allows the quantification of high-energy phosphates and intracellular pH (Kemp et al. 2007), which are important indicators for muscular metabolism, especially short-term bioenergetics. Consequently, after the first successful human applications,

^{31}P-MRS was expected to enter the clinical routine rather quickly. Currently, several groups use this method regularly for the investigation of muscle diseases (Ko et al. 2008; Lodi et al. 2001; Szendroedi et al. 2007, 2009), but its application for clinical research is not widespread (Boesch 2007; Taylor 2000). Quite the contrary, ^{31}P-MRS has remained, to some extent, a research tool for physiology and pathology. The reasons for this, on clinical scanners, include the special hardware requirements; the lower spatial resolution of ^{31}P-MRS compared to ^{1}H-MRS; and ^{31}P-MRS experiments can be very time consuming.

4.1.1 ^{31}P-MRS at Ultra-high-Field

Most MR techniques would benefit from an increase in static field strength (B_0) due to the increased SNR. MRS, in addition, would improve by an increase in spectral resolution. Practically, several ^{1}H-MRI/MRS methods face severe limitations at 7 T that partially diminish this advantage. The most important limitations are the increased SAR requirements and inhomogeneities in B_1 fields. Since the Larmor frequency of ^{31}P-MRS at 7 T (120 Hz) is comparable to that of ^{1}H-MRS at 3 T (123 Hz), these limitations are much less stringent for ^{31}P-MRS than for ^{1}H-MRS. SAR limits in ^{31}P-MRS are usually not reached at 7 T, unless ^{1}H decoupling and nuclear overhauser enhancement is applied, as shown in the brain (Lei et al. 2003). Water/fat suppression at higher fields becomes increasingly unreliable and requires additional SAR, but no such suppression is necessary in ^{31}P-MRS.

Rather, there are some physical properties of ^{31}P nuclei that facilitate the use of ^{31}P-MRS at higher field strengths. In ^{1}H-MRS, the T_1 relaxation times of metabolites decrease for higher B_0 (Krssak et al. 2004). This reduces the net increase in SNR per unit time. On low field scanners, ^{31}P-MRS, and muscle ^{31}P-MRS in particular, was handicapped by inherently long metabolite T_1 relaxation times (Meyerspeer et al. 2003), but, with increasing field strength, a significantly decreased T_1 was observed for most ^{31}P metabolites both in phantoms and in vivo (Bogner et al. 2009; Devre et al. 1990; Evelhoch et al. 1985). In high-field ^{31}P-MRS, relaxation is no longer dominated by dipole–dipole relaxation alone. Chemical shift anisotropy (CSA) plays an increasingly important role in relaxation pathways with increasing B_0. The effect of CSA is prominent, particularly for very anisotropic ^{31}P metabolites, such as ATP and phosphomonoesters (PME) (Bogner et al. 2009; Devre et al. 1990; Evelhoch et al. 1985). Recently, it was shown that T_1 decreases by 62–30% for ^{31}P metabolites between 3 and 7T in the human calf muscle (Bogner et al. 2009). Only the T_1 of the symmetric Pi molecule was found to be relatively constant with changing B_0. Decreasing T_1 relaxation times lead to additional SNR per unit time or reduced measurement times.

CSA affects also the T_2 relaxation of ^{31}P metabolites. Significantly stronger decreases in T_2 than could be explained by dipole–dipole relaxation alone were found between 3 and 7 T in the human calf muscle (24–53% decrease). Again, the reduction in T_2 correlated with molecular symmetry (Bogner et al. 2009).

Despite the strong decrease in T_2, the spectral resolution was enhanced. In non-localized ^{31}P-MRS, the linewidth of PCr (39% decrease in T_2) increased only from 7 ± 1 to 11 ± 2 Hz (+72%), while the additional frequency dispersion increased between 3 and 7 T was +133%. Better spectral resolution was reported for localized ^{31}P-MRS spectra of the human calf muscle at 7 T (6 ± 1 Hz linewidth for PCr) (Bogner et al. 2010). Even without relaxation effects, the SNR was doubled between 3 and 7 T in fully relaxed spectra (Bogner et al. 2009).

To illustrate the improved spectral quality, Fig. 7 shows two non-localized ^{31}P-MRS spectra in the human calf muscle at 3 and 7 T, along with an ISIS-localized spectrum at 7 T. Even without decoupling, the spectral resolution is sufficient to separate both the PME and phosphodiester (PDE) signals.

One technical problem in ^{31}P-MRS at ultra-high field that has to be mentioned is the chemical shift displacement error (CSDE). Due to a large frequency dispersion and a low gyromagnetic ratio in ^{31}P-MRS, the CSDE can be considerably larger than in ^{1}H-MRS, if selective pulses are applied. If 3D CSI-based localization or special broad-band localization pulses are used, this problem can be eliminated (Lei et al. 2003; Bogner et al. 2010).

4.1.2 Dynamic ^{31}P-MRS

Well-known metabolites that can be quantified by ^{31}P-MRS include the high energy phosphates phosphocreatine (PCr), adenosine triphosphate (ATP),

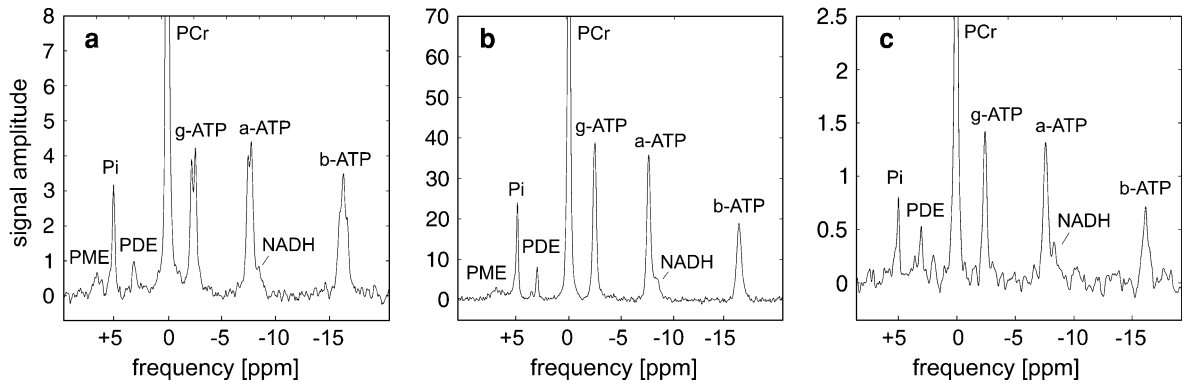

Fig. 7 Typical in vivo ^{31}P NMR spectra from the human calf muscle acquired by a surface coil: **a** non-localized spectrum at 3 T, **b** non-localized spectrum at 7 T, **c** ISIS localized spectrum of the soleus muscle with a 2.5 cm isotropic resolution in 2 min. Note the significant SNR improvement from (**a**) 3 T to (**b**) 7 T. The spectral quality for (**c**) localized spectra at 7 T is sufficient for reliable quantification, providing more specific information than non-localized spectra

adenosine diphosphate (ADP-indirect), and inorganic phosphate (Pi), which are all involved in the creatine kinase reaction. One of the most important features of ^{31}P-MRS is its ability to monitor time-dependent changes of metabolite concentrations. In so-called "dynamic" MRS studies, the muscle can be stressed with exercise inside the magnet while the biochemical response is monitored with a time resolution of several seconds (Prompers et al. 2006). At the same time, the spectral distance between Pi and PCr allows an accurate determination of the intracellular pH. Due to the decrease in T_1, this time resolution can even be improved at 7 T, compared to lower B_0. At lower B_0, the examined muscle tissue was typically dependent on the sensitive volume of a surface coil. At 7 T, it was shown that localized dynamic ^{31}P-MRS can be applied even on specific muscles of interest (Meyerspeer et al. 2009).

Different indices such as the rate of PCr decrease, the drop in pH, the initial rate of PCr recovery, and the recovery of ADP, were used to characterize muscle energetics in vivo. The initial PCr recovery was correlated with the maximum oxidative rate in tissue, while the recovery of ADP is considered the most sensitive and reliable non-invasive measure of mitochondrial dysfunction (Argov et al. 1996). Recently, the ability of dynamic ^{31}P-MRS to identify malfunctions in energy metabolism was demonstrated in patients with myasthenia gravis. (Ko et al. 2008).

A large clinical spectrum of mitochondrial disorders (Taylor et al. 1994; Kuhl et al. 1994; Matthews et al. 1991) and glycolytic defects (Duboc et al. 1987) can be studied with ^{31}P-MRS. Particularly during recovery, ^{31}P-MRS is the most sensitive and specific method for the assessment of the skeletal muscle mitochondrial rate of ATP production (Taylor et al. 1994). Prolonged rate of PCr recovery, faster pH recovery, and a delay in ADP recovery can be observed in mitochondrial dysfunctions.

^{31}P-MRS is also a suitable tool for physiopathologic studies. It has become an interesting tool in the study of systemic diseases that affect muscle metabolism, such as renal or heart failure, and peripheral vascular or thyroid disease (Taylor 2000).

^{31}P-MRS allows the investigation of gene function on metabolism (Lodi et al. 1999), diabetes research (Phielix and Mensink 2008; Szendroedi et al. 2007; Pedersen et al. 2009; Praet et al. 2006), and can be an excellent tool for therapeutic trials (Lodi et al. 2001; Taivassalo et al. 1996), since, unlike muscle biopsy, it can be easily applied repeatedly to assess treatment response over long periods (Cottin et al. 2000).

4.1.3 Oncologic ^{31}P-MRS

Other ^{31}P metabolites that can be of interest, especially for oncology, include phosphocholine (PC) and phosphoethanolamine (PE). The elevation of PC in ^{31}P-MRS and total choline in ^{1}H-MRS are two of the most widely established characteristics of cancer cells. Several studies have detected high levels of PC or PE compared to normal tissues (Negendank 1992; de Certaines et al. 1993). A glycophosphocoline (GPC) to PC switch appears to be an early phenotypic change during carcinogenesis, as observed in benzo(a)pyrene immortalized cells. In cancerous tissue, PC becomes the major choline phospholipid

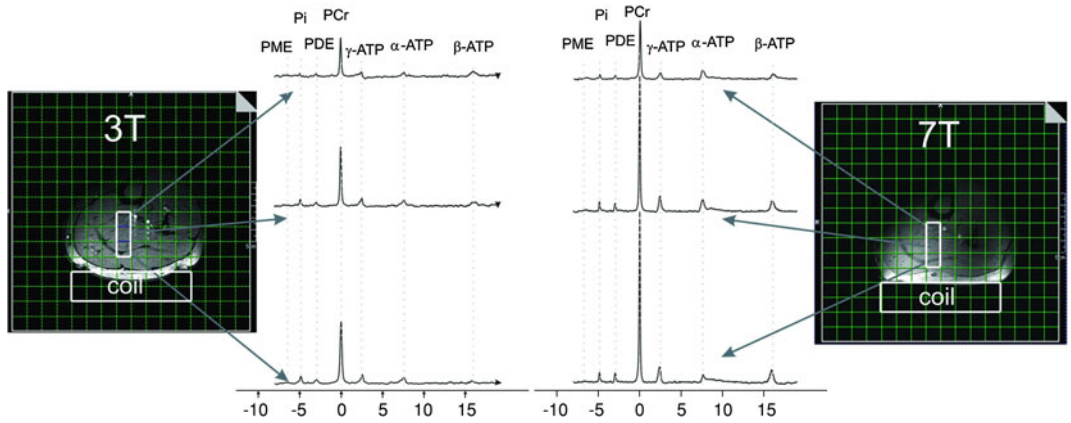

Fig. 8 The in vivo spectra of the human calf muscle acquired by ^{31}P-3D-MRSI, with optimized excitation flip angle at 3 (*left*) and 7 T (*right*) are shown. Spectra from corresponding locations are displayed after noise equalization and filtering by a matched filter in equal scale

metabolite. ^{31}P-MRS allows the separation of GPC and PC. This makes it a more specific method for the study of the metabolic characteristics of cancer than H-MRS.

At lower field strengths, ^{31}P-MRS was rarely used in vivo for cancer research, since good localization of relatively small volumes with sufficient SNR is required for definition of the tumor regions. At 7 T, single-voxel localized ^{31}P-spectra can be acquired in clinically acceptable measurement times of a few minutes (Bogner et al. 2010), and 3D metabolic mapping can be performed with a spatial resolution similar to that previously shown in ^{1}H-MRS on clinical scanners (Fig. 8) (Chmelik et al. 2010).

5 Musculoskeletal Morphology—Spectrally Selective Steady-State Free Precession (SSFP) Sequences

5.1 Chemical Shift Artifacts

Chemical shift artifacts may significantly degrade image quality, since fat is often found adjacent to or interspersed within the tissues of interest (Regatte and Schweitzer 2007). As a result, various clinical studies have demonstrated that fat suppression may enhance diagnostic information to enable the detection of musculoskeletal abnormalities with an accuracy equivalent to that of arthroscopy (Hardy et al. 1998). In addition, fat suppression (or water excitation) eliminates the need for high receiver bandwidths to suppress chemical shift artifacts, and thereby enables the detection of signal changes with increased SNR. This has led to increased clinical use of fat-suppressed sequences for musculoskeletal imaging (preferably in 3D for high SNR (Thomasson et al. 1996)) and several techniques have been presented to selectively excite or suppress water or fat with or without spectral-spatial (spsp) selection (Zur 2000; Meyer et al. 1990).

Conventional fat suppression techniques are often based on spectrally selective RF pulses (so-called FATSAT pulses) to pre-saturate the signal from the lipids (Rosen et al. 1984). A major disadvantage of such FATSAT pulses is the additional time required and their incompatibility with most steady-state free precession (SSFP) sequences, such as the double-echo steady state (DESS) sequence and many others that have gained increased popularity in musculoskeletal imaging (Hardy et al. 1996; Eckstein et al. 2006). This is in contrast to spsp water (or fat) excitation pulses that can be implemented into any kind of SSFP sequence in conjunction with slice- or volume-selective magnetic field gradients (Zur 2000).

In general, selective excitation (or suppression) of water or fat is based on the frequency shift of about 3.4 ppm of the methylene protons of fatty acids, which is below than that of water protons. With increasing field strength, the chemical fat–water shift ($\Delta\nu$) increases and amounts to $\Delta\nu = 1040$ Hz at 7.0 T (as compared to $\Delta\nu = 440$ Hz at 3 T and $\Delta\nu = 220$ Hz at 1.5 T), offering alternative spsp

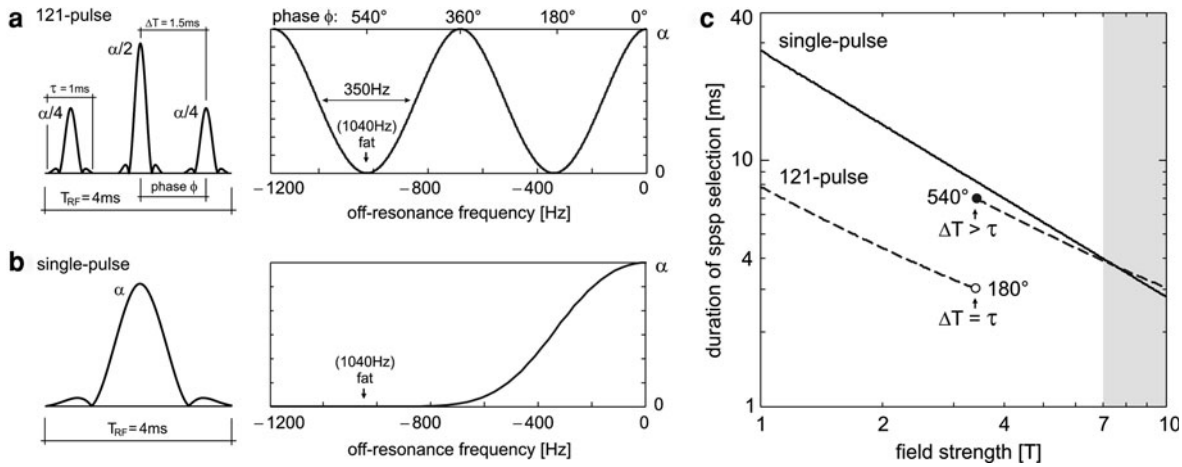

Fig. 9 **a** At 7.0 T, fat is shifted by about −1040 Hz from the water resonance, i.e., roughly one cycle/ms. Thus, due to subpulse limitations ($\tau \sim 1$ ms), the conventionally applied $\phi = 180°$ phase advance at 1.5–3.0 T must be increased to $\phi = 540°$ at 7.0 T or more. **b** The frequency selectivity, as achieved with a single RF pulse, is non-periodic and depends only on its duration (T_{RF}) and envelope. **c** At low-to-high field strengths (1.0 to about 3.4 T), spsp excitation from a single RF pulse seems impractical due to exceedingly long excitations ($T_{RF} \sim 20$ ms at 1.5 T, see *solid line*) that may hamper proper slice selection from relaxation effects or other system imperfections, such as field inhomogeneities. With increasing field strength, however, the time needed for the $\phi = 180°$ phase advance for binomial excitation (*dashed line*) falls below the subpulse spacing (at 3.4 T for the preparation displayed in Fig. 9a), forcing an increase in the phase advance to 540°. In combination with the decreasing preparation time for single RF frequency selectivity with increasing field strength, similar preparation times can be achieved at ultra-high fields (>7.0 T)

excitation schemes that are too time-consuming at low fields, i.e., the application of a single, frequency selective, RF pulse for either water or fat excitation (Bieri et al. 2008a).

Generally, spsp RF pulse design is based on a train of N subpulses with a (constant) duration τ and interpulse spacing, $\Delta T > \tau$ (the subpulse tip angles $\alpha_{i=1\ldots N}$ can be calculated, e.g., using binomial coefficients (Hore 1983)). Often, a good compromise between better fat suppression and moderately increased TR is offered by second-order binomials (e.g., 1–2–1), as displayed in Fig. 9a. The excitation spectrum of a binomial pulse is periodic to the inverse of the RF subpulse spacing (1/ΔT Hz), and selective excitation of water protons is granted for $1/\Delta T = 2 \cdot \Delta\nu/(2n - 1)$, where n is a natural number. At 7.0 T, this limits the subpulse duration to $\tau < 500$ µs (with $n = 1$), which seems impractical, considering the usual SAR limitations. As a result, the phase advance must be increased from 180° (i.e., one-half turn with $\Delta T = 0.5$ ms) to 540° (i.e., one and a half turns with $\Delta T = 1.5$ ms).

Figure 9b shows the frequency bandwidth for a single RF pulse with essentially the same duration (envelope) as the second-order binomial (subpulses) (Hamming-filtered sinc-pulse with one side maximum). In contrast to the spsp pulses, the spectrum of a single RF pulse is no longer periodic but confined to a single transition region. From this, excellent selectivity can be expected within the volume of interest and the spectral width of a single pulse (*fwhm*: full width at half maximum) depends only on its duration (T_{RF}) and its time bandwidth (*TBW*), i.e., $T_{RF} \times fwhm = TBW$. At low to high fields, spsp preparation is, thus, by far more time efficient (~5 times); however, the demand of a bigger phase advance from subpulse duration constraints cancels this advantage at high to ultra-high fields and spsp preparation becomes more time-consuming at field strengths of 7.0 T and above (Fig. 9c).

Spectral spatial imaging with single RF pulses (Fig. 9b) can be easily implemented with any kind of SSFP sequence and an example of this is shown for SSFP-ECHO in Fig. 10 as a function of RF pulse prolongation. Particularly with a large FOV (Fig. 11), spectral selection from single RF excitation is more effective as compared to the common spsp excitation scheme (Fig. 9a) and provides improved and more homogeneous fat suppression over the entire imaged volume. However, it might be noteworthy that single, e.g., water-selective, RF pulses inevitably excite fat in

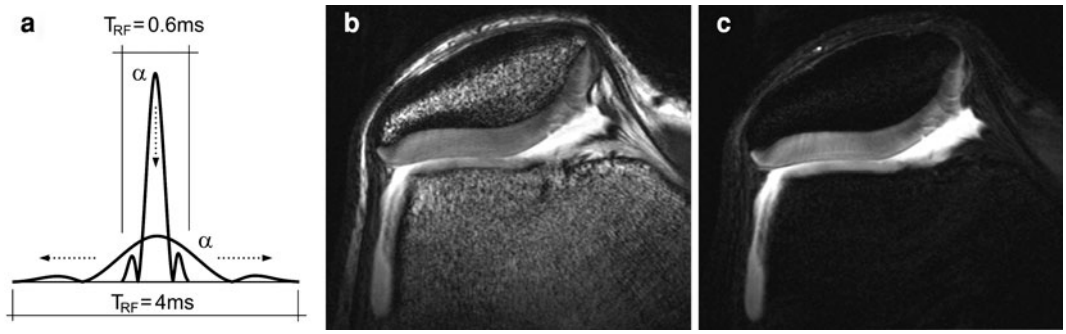

Fig. 10 Axial 3D SSFP-ECHO images (40 slices, 280 μm × 280 μm × 3000 μm resolution, $\alpha = 30°$, 320 Hz/pixel) of the patella of the knee joint at 7.0 T using a surface single-loop coil. **a** The spsp selectivity of a single RF pulse relates to its pulse duration, $fwhm = TBW/T_{RF}$. **b** With short RF pulses ($T_{RF} = 600$ μs), water–fat unselective images were acquired within 3.5 min (TE/TR = 3.0/6.9 ms). **c** With elongated RF pulses ($T_{RF} = 4000$ μs), fat-free images were acquired within 5 min (TE/TR = 4.7/10.3 ms). Early fissures through the cartilage layer are visualized on the high resolution scan at 7 T

a nearby volume (i.e., where the slice selection gradient shifts the local frequency by +1,040 Hz). For 3D volumes, this does not represent a critical issue since such unintended excitations can be easily shifted either outside the imaged object (as for the human knee) or outside the sensitivity area of the local transmit/receive coil. Spatial selectivity from single RF pulses can, thus, be rather seen, instead, as the result of a smart arrangement of the FOV or of the spatial sensitivity of the coils used.

At ultra-high fields, the application of single RF pulses leads to decreased power depositions, and thus, to an overall reduced specific absorption rate (SAR), which still represents a major restriction for many pulse sequences in vivo. Moreover, the ease of applicability and implementation of single spsp pulses might be of great benefit for a vast number of other applications where fat suppression is desirable or fat–water separation is required for quantification purposes.

6 Musculoskeletal Biochemical Mapping—Magnetization Transfer-Sensitized Steady State Free Precession (MT-sensitized SSFP)

Physically, MT refers to the magnetic coupling of spin states from macromolecular compartments (i.e., "rigid" protons) with those of bulk free water (i.e., "free" protons) through exchange processes (Wolff and Balaban 1989, 1994; Henkelman et al. 2001). Unfortunately, with conventional imaging techniques, rigid protons cannot be observed directly with MRI, since they are embedded in a relatively stable but heterogeneous magnetic environment, which causes a loss of phase coherence much too rapidly ($T_2 \sim 10$ μs) for imaging. However, magnetization is transferred from the macromolecular to the liquid phase and vice versa by intermolecular cross-relaxation and proton chemical exchange. This generates a unique form of image contrast in tissues, the so-called magnetization transfer contrast (MTC), as first demonstrated in rabbits by Wolff and Balaban (1989) using a continuous wave (CW) saturation technique. Practically, however, the majority of human MT imaging experiments are performed by repetitive off- or on-resonance binomial RF pulses, not only because RF transmitters are designed for pulsed and not for CW operation, but also to keep SAR and imaging times within reasonable limits (Henkelman et al. 2001; Sled and Pike 2001).

The musculoskeletal system and particularly, cartilage, features a large MT effect that provides an excellent contrast between muscle and fat, and between the cartilage and the synovial fluid (Wolff et al. 1991). As a result, MTC offers excellent delineation of the articular cartilage from the surrounding joint effusion (Wolff and Balaban 1994; Wolff et al. 1991); thus, cartilage MT may provide a valuable technique for the assessment of medical treatments because of the insights into the structure

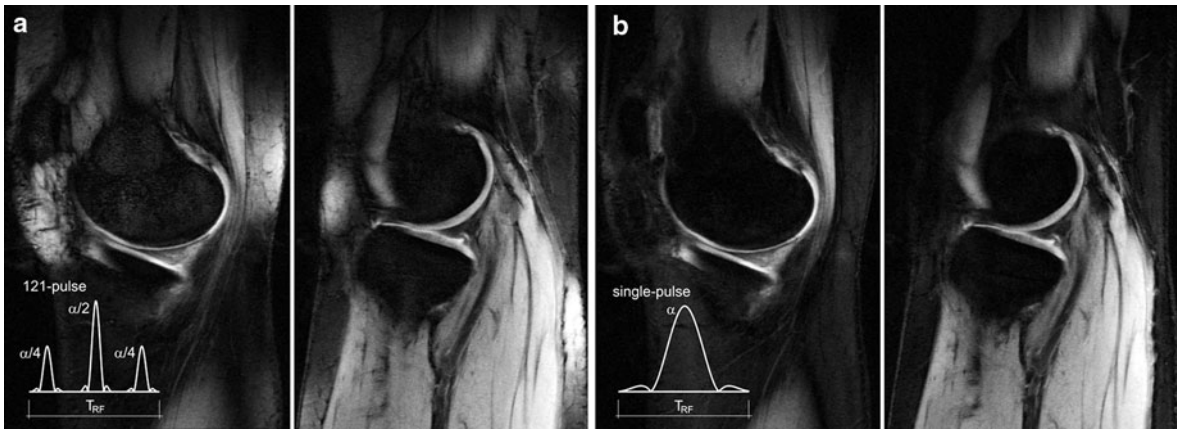

Fig. 11 Water-selective 3D DESS images of the human knee joint at 7.0 T using a CP volume coil (300 μm × 300 μm × 3000 μm resolution, α = 30°, 360 Hz/pixel, TE/TR = 5.7/14.3 ms). Sagittal images (72 slices) were acquired within 8 min. **a** For the spsp binomial preparation, incomplete fat suppression (trabecular bone marrow, fatty tissue) is observed and the results from the limited transition bandwidth (~350 Hz, see Fig. 9a). **b** Single pulse excitation benefits from its widespread suppression (see Fig. 9b) to deliver robust, high-quality, fat-free images. Likewise, the extended excitation bandwidth can improve the overall depiction of cartilage

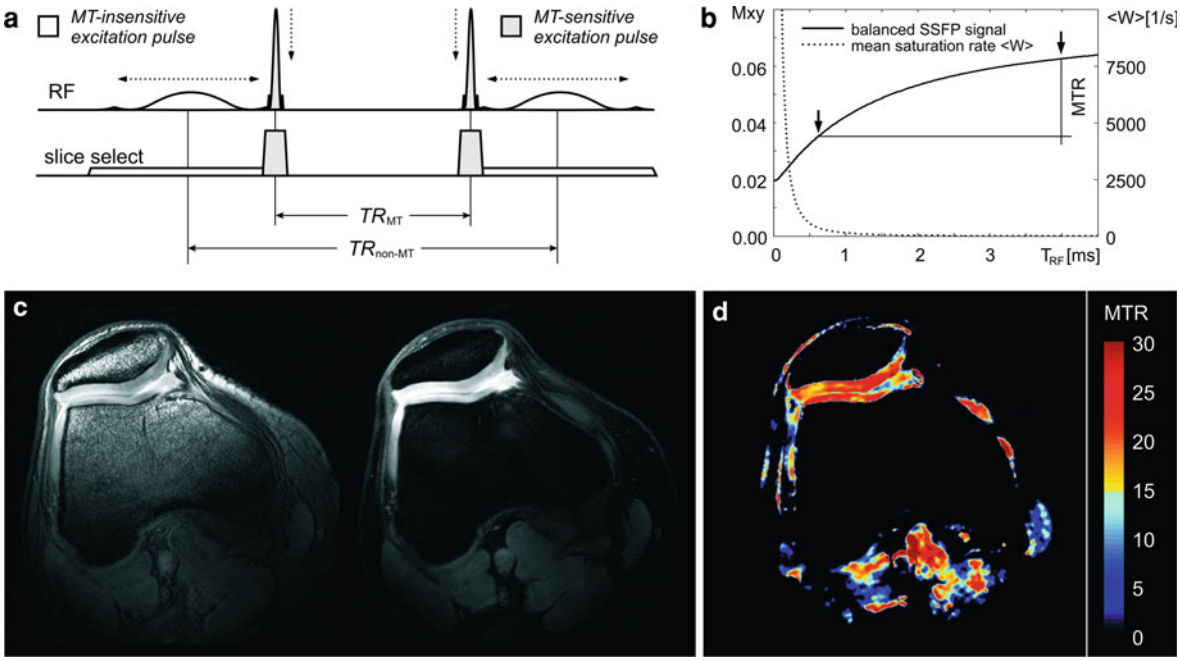

Fig. 12 Magnetization transfer (MT) imaging using steady-state free precession (SSFP) type of sequences. **a** The key to MT-sensitized SSFP imaging is RF pulse elongation: strong saturation of restricted pool protons is achieved with minimal RF pulse duration, whereas minimal saturation results in heavily prolonged RF pulses. **b** Simulation of the analytical solution to a binary spin-bath model for balanced SSFP showing the steady-state signal (Mxy) and the mean saturation rate (W) as a function of the RF pulse duration (T_{RF}) for human cartilage (binary spin-bath model parameters: F = 0.17; R = 60 s^{-1}; $T_{2,r}$ = 8.3 μs; $T_{2,f}$ = 27 ms; T_1 = 1170 ms). For bSSFP, MTR ~40 [pu] is found for cartilage with the sequence settings described in (**a**); however, lower MTR values are expected for non-balanced SSFP sequences such as SSFP-FID (Bieri et al.2008b). **c** Sample images (280 μm × 280 μm × 3000 μm) from an axial 3D SSFP-FID scan (40 slices) of the patella of the knee joint at 7 T using a surface single-loop coil. MT-weighted images (*left*) were acquired within 3.5 min (α = 30°, 320 Hz/pixel, TE/TR = 3.0/6.9 ms, using T_{RF} = 600 μs), whereas non-MT weighted images (*right*) were acquired within 5 min (α = 30°, 320 Hz/pixel, TE/TR = 4.7/10.3 ms, using T_{RF} = 4000 μs). **d** The feasibility of MT imaging at 7 T is demonstrated by the construction of an MTR image from the two scans shown in (**c**) with MTR values for the patellar cartilage of about 25–30 [pu], which was close to theoretical expectations

and biochemical composition of cartilage in vivo. Several studies have indicated that the collagen network is the most important contributor to the observed MT effect (Gray et al. 1995), but other matrix components (such as GAG side chains of proteoglycans) contribute as well (Gray et al. 1995; Lattanzio et al. 2000). As a result, MT was shown to be not only sensitive to changes of the collagen network, as for cartilage repair (Palmieri et al. 2006; Welsch et al. 2008d), but also to subtle early cartilage degradations (Wachsmuth et al. 1997), a still-inaccessible process in osteoarthritis.

Figure 12a shows a new concept for MT-sensitized imaging, with steady-state free precession (SSFP), that is quicker than previous methods. This framework does not demand the dedicated playout of additional MT-sensitizing RF pulses, since saturation of the macromolecular spins is a direct cause of the heavy duty cycle of conventional SSFP (Bieri and Scheffler 2006). It has been shown that decreasing saturation levels in the macromolecular pool can be achieved by simple RF pulse elongation (Bieri et al. 2008b), lowering the irradiation power of the RF pulse train. Since RF pulse elongation per se has only a very limited impact on the steady-state, as established by the liquid phase (as long as $TR << T_2$), transfer of saturation from the macromolecular pool leads to different apparent steady-state signals, as shown in Fig. 12b (using an analytical description of a binary spin bath model for balanced SSFP (Gloor et al. 2008) with parameters for cartilage taken from (Stanisz et al. 2005)).

In contrast to common MT sequences, MT-sensitized SSFP circumvents the requirement for dedicated off- or on-resonance preparation pulses, thus offering exceptionally short repetitions times and high sampling efficiencies. Furthermore, RF pulse elongation is a very generic concept that can be applied without limitation to all types of SSFP sequences, regardless of whether the protocols are balanced, unbalanced, or even RF-spoiled. This allows SSFP-based MT imaging of targets with high susceptibility variation at ultra-high magnetic fields, an example of which is shown for the musculoskeletal system with SSFP-FID (Fig. 12c), where balanced SSFP suffers from considerable off-resonance-related image degradations. The prominent signal variation in the trabecular bone with RF pulse prolongation, especially at ultra-high fields, is not related to MT, but to spectral spatial excitation of fat (Bieri et al. 2008a).

In its simplest form of quantification, MT contrast is mapped into so-called MT ratio (MTR) images (Dousset et al. 1992). MTR images from SSFP are generated from two image acquisitions: one with short and one with considerably elongated RF pulses (representing the MT weighted, i.e., attenuated, and non-MT weighted, i.e., unaffected, images, respectively). After pixel-wise subtraction of the MT from the non-MT weighted image, the resulting MT contrast is normalized against the non-MT weighted image to yield an MTR map with values expressed in percentage units [pu]. The corresponding MTR map of the two SSFP-FID images, as given in Fig. 12c, is shown in Fig. 12d, and demonstrates the possibility for the acquisition of high-resolution 3D MTR imaging of cartilage at high to ultra high- field strengths. Thus, offering a fast and intrinsic 3D imaging modality with high SNR, MT-sensitized SSFP might emerge as a valuable MR technique for the ultra-structural assessment of cartilage degeneration, repair, and function.

References

Alhadlaq HA et al (2004) Detecting structural changes in early experimental osteoarthritis of tibial cartilage by microscopic magnetic resonance imaging and polarised light microscopy. Ann Rheum Dis 63(6):709–717

Anderson ML et al (2008) Diagnostic comparison of 1.5 Tesla and 3.0 Tesla preoperative MRI of the wrist in patients with ulnar-sided wrist pain. J Hand Surg Am 33(7):1153–1159

Argov Z, DeStefano N, Arnold DL (1996) ADP recovery after a brief ischemic exercise in normal and diseased human muscle - A P-31 MRS study. NMR Biomed 9(4):165–172

Banerjee S et al (2006) Autocalibrating parallel imaging of in vivo trabecular bone microarchitecture at 3 Tesla. Magn Reson Med 56(5):1075–1084

Banerjee S et al (2008) Rapid in vivo musculoskeletal MR with parallel imaging at 7T. Magn Reson Med 59(3):655–660

Behr B et al (2009) MR imaging of the human hand and wrist at 7 T. Skeletal Radiol 38(9):911–917

Bieri O, Scheffler K (2006) On the origin of apparent low tissue signals in balanced SSFD. Magn Reson Med 56(5): 1067–1074

Bieri O et al (2008a) Optimized spectrally selective steady-state free precession sequences for cartilage imaging at ultra-high fields. Magn Reson Mater Phys Biol Med 21(1–2):87–94

Bieri O et al (2008b) Steady state free precession magnetization transfer imaging. Magn Reson Med 60(5):1261–1266

Boesch C (2007) Musculoskeletal spectroscopy. J Magn Reson Imaging 25(2):321–338

Bogner W et al (2009) Assessment of P-31 relaxation times in the human calf muscle: a comparison between 3 T and 7 T in vivo. Magn Reson Med 62(3):574–582

Bogner W et al (2010) In vivo 31P-MRS at 7T by single voxel E-ISIS with GOIA selection pulses. In: ISMRM, Stockholm

Bolog N, Nanz D, Weishaupt D (2006) Muskuloskeletal MR imaging at 3.0 T: current status and future perspectives. Eur Radiol 16(6):1298–1307

Borah B et al (2002) Risedronate preserves trabecular architecture and increases bone strength in vertebra of ovariectomized minipigs as measured by three-dimensional microcomputed tomography. J Bone Miner Res 17(7):1139–1147

Borthakur A et al (1999) In vivo triple quantum filtered twisted projection sodium MRI of human articular cartilage. J Magn Reson 141(2):286–290

Borthakur A et al (2000) Sensitivity of MRI to proteoglycan depletion in cartilage: comparison of sodium and proton MRI. Osteoarthritis and Cartilage 8(4):288–293

Borthakur A et al (2002) Quantifying sodium in the human wrist in vivo by using MR imaging. Radiology 224(2):598–602

Borthakur A et al (2006) Sodium and T_1rho MRI for molecular and diagnostic imaging of articular cartilage. NMR Biomed 19(7):781–821

Bottomley PA et al (1984) A review of normal tissue hydrogen NMR relaxation times and relaxation mechanisms from 1-100 MHz: dependence on tissue type, NMR frequency, temperature, species, excision, and age. Med Phys 11(4):425–448

Boulocher C et al (2007) Non-invasive in vivo quantification of the medial tibial cartilage thickness progression in an osteoarthritis rabbit model with quantitative 3D high resolution micro-MRI. Osteoarthritis Cartilage 15(12):1378–1387

Buckwalter JA, Mankin HJ (1998) Articular cartilage: degeneration and osteoarthritis, repair, regeneration, and transplantation. Instr Course Lect 47:487–504

Burstein D, Gray ML (2006) Is MRI fulfilling its promise for molecular imaging of cartilage in arthritis? Osteoarthritis and Cartilage 14(11):1087–1090

Burstein D et al (2001) Protocol issues for delayed Gd(DTPA)(2-)-enhanced MRI (dGEMRIC) for clinical evaluation of articular cartilage. Magn Reson Med 45(1):36–41

Chang G, Regatte RR, Schweitzer ME (2009) Olympic fencers: adaptations in cortical and trabecular bone determined by quantitative computed tomography. Osteoporos Int 20(5):779–785

Chmelik M et al (2010) Faster T_1 relaxation times allow additional SNR-per-unit-time optimization in 31P MRSI at 7T. In: ISMRM, Stockholm

Chen CN et al (1986) The field dependence of NMR imaging. I. Laboratory assessment of signal-to-noise ratio and power deposition. Magn Reson Med 3(5):722–729

Choy J, Ling W, Jerschow A (2006) Selective detection of ordered sodium signals via the central transition. J Magn Reson 180(1):105–109

Christoforidis GA et al (2002) Visualization of microvascularity in glioblastoma multiforme with 8-T high-spatial-resolution MR imaging. AJNR Am J Neuroradiol 23(9):1553–1556

Cottin Y et al (2000) Muscle metabolism assessed by phosphorus-31 nuclear magnetic resonance spectroscopy after myocardial infarction in rehabilitated patients: a 1-year follow-up. Plos Medicine 20(1):44-49

David-Vaudey E et al (2004) T_2 relaxation time measurements in osteoarthritis. Magn Reson Imaging 22(5):673–682

de Certaines JD et al (1993) In vivo 31P MRS of experimental tumours. NMR Biomed 6(6):345–365

Devre RM, Maerschalk C, Delporte C (1990) Spin-lattice relaxation-times and nuclear Overhauser enhancement effect for P-31 metabolites in model solutions at 2 frequencies - implications for in vivo spectroscopy. Magn Reson Imaging 8:691–698

Ding M et al (2002) Age-related variations in the microstructure of human tibial cancellous bone. J Orthop Res 20(3):615–621

Dousset V et al (1992) Experimental allergic encephalomyelitis and multiple-sclerosis - lesion characterization with magnetization transfer imaging. Radiology. 182(2):483-491

Du J, Takahashi AM, Chung CB (2009) Ultrashort TE spectroscopic imaging (UTESI): application to the imaging of short T_2 relaxation tissues in the musculoskeletal system. J Magn Reson Imaging 29(2):412–421

Duboc D et al (1987) Phosphorus NMR-spectroscopy study of muscular enzyme deficiencies involving glycogenolysis and glycolysis. Neurology 37(4):663–671

Dunn TC et al (2004) T_2 relaxation time of cartilage at MR imaging: comparison with severity of knee osteoarthritis. Radiology 232(2):592–598

Eckstein F et al (2006) Double echo steady state magnetic resonance imaging of knee articular cartilage at 3 Tesla: a pilot study for the osteoarthritis initiative. Ann Rheumatic Dis 65(4):433–441

Evelhoch JL et al (1985) 31P spin-lattice relaxation times and resonance linewidths of rat tissue in vivo: dependence upon the static magnetic field strength. Magn Reson Med 2(4):410–417

Farooki S et al (2002) In vivo high-resolution MR imaging of the carpal tunnel at 8.0 tesla. Skeletal Radiol 31(8): 445–450

Friedrich KM et al (2009) In vivo 7.0-tesla magnetic resonance imaging of the wrist and hand: technical aspects and applications. Semin Musculoskelet Radiol 13(1):74–84

Gloor M, Scheffler K, Bieri O (2008) Quantitative magnetization transfer imaging using balanced SSFP. Magn Reson Med 60(3):691–700

Gold GE et al (1998) MR imaging of articular cartilage of the knee: new methods using ultrashort TEs. AJR Am J Roentgenol 170(5):1223–1226

Gold GE et al (2004) Musculoskeletal MRI at 3.0 T: relaxation times and image contrast. AJR Am J Roentgenol 183(2):343–351

Goldstein SA, Goulet R, McCubbrey D (1993) Measurement and significance of three-dimensional architecture to the mechanical integrity of trabecular bone. Calcif Tissue Int 53 Suppl 1:S127–132; discussion S132–133

Goodwin DW, Wadghiri YZ, Dunn JF (1998) Micro-imaging of articular cartilage: T_2, proton density, and the magic angle effect. Acad Radiol 5(11):790–798

Goodwin DW, Zhu H, Dunn JF (2000) In vitro MR imaging of hyaline cartilage: correlation with scanning electron microscopy. AJR Am J Roentgenol 174(2):405–409

Gray ML et al (1995) Magnetization-transfer in cartilage and its constituent macromolecules. Magn Reson Med 34(3):319–325

Grushko G, Schneiderman R, Maroudas A (1989) Some biochemical and biophysical parameters for the study of the pathogenesis of osteoarthritis: a comparison between the processes of ageing and degeneration in human hip cartilage. Connect Tissue Res 19(2–4):149–176

Hardy PA et al (1996) Optimization of a dual echo in the steady state (DESS) free-precession sequence for imaging cartilage. JMRI-J Magn Reson Imaging 6(2):329–335

Hardy PA, Recht MP, Piraino DW (1998) Fat suppressed MRI of articular cartilage with a spatial-spectral excitation pulse. J Magn Reson Imaging 8(6):1279–1287

Henkelman RM, Stanisz GJ, Graham SJ (2001) Magnetization transfer in MRI: a review. NMR Biomed 14(2):57–64

Hennig J, Scheffler K (2001) Hyperechoes. Magn Reson Med 46(1):6–12

Hinton DP et al (2003) Comparison of cardiac MRI on 1.5 and 3.0 Tesla clinical whole body systems. Invest Radiol 38(7):436–442

Hopkins JA, Wehrli FW (1997) Magnetic susceptibility measurement of insoluble solids by NMR: magnetic susceptibility of bone. Magn Reson Med 37(4):494–500

Hore PJ (1983) Solvent suppression in Fourier-transform nuclear magnetic-resonance. J Magn Reson 55(2):283–300

Hoult DI, Chen CN, Sank VJ (1986) The field dependence of NMR imaging. II. Arguments concerning an optimal field strength. Magn Reson Med 3(5):730–746

Hughes T et al (2007) T_2-Star relaxation as a means to diffrentiatie cartilage repair tissue after microfracturing therapy. Intern Soc Magn Reson Med 15:183

Jaccard G, Wimperis S, Bodenhausen G (1986) Multiple-quantum NMR-spectroscopy of S = 3/2 spins in isotropic-phase - a new probe for multiexponential relaxation. J Chem Phys 85(11):6282–6293

Kemp-Harper R et al (1997) Na-23 NMR methods for selective observation of sodium ions in ordered environments vol. 30:157 Prog Nucl Magn Reson Spectrosc 31:287

Kemp GJ, Meyerspeer M, Moser E (2007) Absolute quantification of phosphorus metabolite concentrations in human muscle in vivo by P-31 MRS: a quantitative review. NMR Biomed 20(6):555–565

Kim YJ et al (2003) Assessment of early osteoarthritis in hip dysplasia with delayed gadolinium-enhanced magnetic resonance imaging of cartilage. J Bone Joint Surg-Am Vol 85A(10):1987–1992

Kleerekoper M et al (1985) The role of three-dimensional trabecular microstructure in the pathogenesis of vertebral compression fractures. Calcif Tissue Int 37(6):594–597

Ko SF et al (2008) 31P MR spectroscopic assessment of muscle in patients with myasthenia gravis before and after thymectomy: initial experience. Radiology 247(1):162–169

Kraff O et al (2007) MRI of the knee at 7.0 Tesla. Rofo 179(12):1231–1235

Krssak M et al (2004) H-1 NMR relaxation times of skeletal muscle metabolites at 3 T. Magn Reson Mater Phys Biol Med 16(4):155–159

Krug R et al (2007) In vivo bone and cartilage MRI using fully-balanced steady-state free-precession at 7 tesla. Magn Reson Med 58(6):1294–1298

Krug R et al (2008) In vivo ultra-high-field magnetic resonance imaging of trabecular bone microarchitecture at 7 T. J Magn Reson Imaging 27(4):854–859

Krug R et al (2009) Imaging of the musculoskeletal system in vivo using ultra-high field magnetic resonance at 7 T. Invest Radiol 44(9):613–618

Kuhl CK et al (1994) Mitochondrial encephalomyopathy - correlation of P-31 exercise MR spectroscopy with clinical findings. Radiology 192(1):223–230

Lattanzio PJ et al (2000) Macromolecule and water magnetization exchange modeling in articular cartilage. Magn Reson Med 44(6):840–851

Lei H et al (2003) In vivo P-31 magnetic resonance spectroscopy of human brain at 7 T: an initial experience. Magn Reson Med 49(2):199–205

Lenk S et al (2004) 3.0 T high-resolution MR imaging of carpal ligaments and TFCC. Rofo 176(5):664–667

Lesperance LM, Gray ML, Burstein D (1992) Determination of fixed charge density in cartilage using nuclear magnetic resonance. J Orthop Res 10(1):1–13

Ling W, Jerschow A (2005) Selecting ordered environments in NMR of spin 3/2 nuclei via frequency-sweep pulses. J Magn Reson 176(2):234–238

Ling W, Jerschow A (2006) Frequency-selective quadrupolar MRI contrast. Solid State Nucl Magn Reson 29(1–3):227–231

Ling W et al (2006) Behavior of ordered sodium in enzymatically depleted cartilage tissue. Magn Reson Med (5):1151–1155

Lodi R et al (1999) Deficit of in vivo mitochondrial ATP production in patients with Friedreich ataxia. Proc Natl Acad Sci 96(20):11492–11495

Lodi R et al (2001) Antioxidant treatment improves in vivo cardiac and skeletal muscle bioenergetics in patients with Friedreich's ataxia. Ann Neurol 49(5):590–596

Lohmander LS (1994) Articular cartilage and osteoarthrosis. The role of molecular markers to monitor breakdown, repair and disease. J Anat 184 (Pt 3):477–492

Mankin HJ (1971) Biochemical and metabolic aspects of osteoarthritis. Orthop Clin North Am 2(1):19–31

Maroudas A, Muir H, Wingham J (1969) The correlation of fixed negative charge with glycosaminoglycan content of human articular cartilage. Biochim Biophys Acta 177(3):492–500

Matthews PM et al (1991) In vivo muscle magnetic resonance spectroscopy in the clinical investigation of mitochondrial disease. Neurology 41(1):114–120

McKenzie CA et al (2006) Three-dimensional delayed gadolinium-enhanced MRI of cartilage (dGEMRIC) at 1.5T and 3.0T. J Magn Reson Imaging 24(4):928–933

Meyerspeer M et al (2009) Dynamic 31P MRS of exercising human muscle in a 7T whole body system, with STEAM and semi-LASER localisation. In: ISMRM, Honolulu

Messner K, Gao J (1998) The menisci of the knee joint. Anatomical and functional characteristics, and a rationale for clinical treatment. J Anat 193 (Pt 2):161–178

Meyer CH et al (1990) Simultaneous spatial and spectral selective excitation. Magn Reson Med 15(2):287–304

Meyerspeer M, Krssak M, Moser E (2003) Relaxation times of P-31-metabolites in human calf muscle at 3 T. Magn Reson Med 49(4):620–625

Michaeli S et al (2002) Proton T_2 relaxation study of water, N-acetylaspartate, and creatine in human brain using Hahn and Carr-Purcell spin echoes at 4T and 7T. Magn Reson Med 47(4):629–633

Mosher TJ, Dardzinski BJ (2004) Cartilage MRI T_2 relaxation time mapping: overview and applications. Semin Musculoskelet Radiol 8(4):355–368

Mosher TJ et al (2004) Effect of gender on in vivo cartilage magnetic resonance imaging T_2 mapping. J Magn Reson Imaging 19(3):323–328

Mosher TJ et al (2005) Change in knee cartilage T_2 at MR imaging after running: a feasibility study. Radiology 234(1):245–249

Murphy BJ (2001) Evaluation of grades 3 and 4 chondromalacia of the knee using T_2*-weighted 3D gradient-echo articular cartilage imaging. Skeletal Radiol 30(6):305–311

Navon G et al (2001) Multiquantum filters and order in tissues. NMR Biomed 14(2):112–132

Negendank W (1992) Studies of human tumors by MRS: a review. NMR Biomed 5(5):303–324

Pakin SK et al (2006) Ultra-high-field MRI of knee joint at 7.0T: preliminary experience. Acad Radiol 13(9):1135–1142

Palmieri F et al (2006) Magnetization transfer analysis of cartilage repair tissue: a preliminary study. Skelet Radiol 35(12):903–908

Pedersen BL, Baekgaard N, Quistorff B (2009) Muscle mitochondrial function in patients with Type 2 diabetes mellitus and peripheral arterial disease: implications in vascular surgery. Eur J Vasc Endovasc Surg 38(3):356–364

Phielix E, Mensink M (2008) Type 2 diabetes mellitus and skeletal muscle metabolic function. Physiology & Behavior 94(2):252–258

Poole AR et al (2001) Composition and structure of articular cartilage: a template for tissue repair. Clin Orthop Relat Res (391 Suppl):S26-33

Praet SFE et al (2006) P-31 MR spectroscopy and in vitro markers of oxidative capacity in type 2 diabetes patients. Magn Reson Mater Phys Biol Med 19(6):321–331

Prompers JJ et al (2006) Dynamic MRS and MRI of skeletal muscle function and biomechanics. NMR Biomed 19(7):927–953

Rahmer J, Bornert P, Dries SP (2009) Assessment of anterior cruciate ligament reconstruction using 3D ultrashort echo-time MR imaging. J Magn Reson Imaging 29(2):443–448

Reddy R, Insko EK, Leigh JS (1997). Triple quantum sodium imaging of articular cartilage. Magn Reson Med 38(2):279–284

Reddy R et al (1998) Sodium MRI of human articular cartilage in vivo. Magn Reson Med 39(5):697–701

Regatte RR, Schweitzer ME (2007) Ultra-high-field MRI of the musculoskeletal system at 7.0T. J Magn Reson Imaging 25(2):262–269

Rinck PA et al (1988) Field-cycling relaxometry: medical applications. Radiology 168(3):843–849

Robson MD et al (2003) Magnetic resonance: an introduction to ultrashort TE (UTE) imaging. J Comput Assist Tomogr 27(6):825–846

Rohrer M et al (2005) Comparison of magnetic properties of MRI contrast media solutions at different magnetic field strengths. Invest Radiol 40(11):715–724

Rosen BR, Wedeen VJ, Brady TJ (1984) Selective Saturation NMR imaging. J Comput Assist Tomogr 8(5):813–818

Roughley PJ, Lee ER (1994) Cartilage proteoglycans: structure and potential functions. Microsc Res Tech 28(5):385–397

Schmitt M et al (2005) B_1 homogenization in abdominal imaging at 3T. In: Proc Int Soc Magn Reson Med 331

Shapiro EM et al (2000) Sodium visibility and quantitation in intact bovine articular cartilage using high field (23)Na MRI and MRS. J Magn Reson 142(1):24–31

Shapiro EM et al (2002) 23Na MRI accurately measures fixed charge density in articular cartilage. Magn Reson Med 47(2):284–291

Shinar H, Navon G (2006) Multinuclear NMR and microscopic MRI studies of the articular cartilage nanostructure. NMR Biomed 19(7):877–893

Shinar H, Eliav U, Navon G (1992) Single and multiple quantum NMR relaxation-times of sodium and potassium in red-blood-cells. Israel J Chem 32(2–3):299–304

Sled JG, Pike GB (2001) Quantitative imaging of magnetization transfer exchange and relaxation properties in vivo using MRI. Magn Reson Med 46(5):923–931

Smith HE et al (2001) Spatial variation in cartilage T_2 of the knee. J Magn Reson Imaging 14(1):50–55

Stahl R et al (2009) Assessment of cartilage-dedicated sequences at ultra-high-field MRI: comparison of imaging performance and diagnostic confidence between 3.0 and 7.0 T with respect to osteoarthritis-induced changes at the knee joint. Skeletal Radiol 38(8):771–783

Stanisz GJ et al (2005) T_1, T_2 relaxation and magnetization transfer in tissue at 3T. Magn Reson Med 54(3):507–512

Szendroedi J et al (2007) Muscle mitochondrial ATP synthesis and glucose transport/phosphorylation in type 2 diabetes. Plos Medicine 4(5):858–867

Szendroedi J et al (2009) Impaired mitochondrial function and insulin resistance of skeletal muscle in mitochondrial diabetes. Diabetes Care 32(4):677–679

Taivassalo T et al (1996) Combined aerobic training and dichloroacetate improve exercise capacity and indices of aerobic metabolism in muscle cytochrome oxidase deficiency. Neurology 47(2):529–534

Taylor DJ (2000) Clinical utility of muscle MR spectroscopy. Semin Musculoskelet Radiol 4(4):481–502

Taylor DJ, Kemp GJ, Radda GK (1994) Bioenergetics of skeletal-muscle in mitochondrial myopathy. J Neurol Sci 127(2):198–206

Thomasson D, Purdy D, Finn JP (1996) Phase-modulated binomial RF pulses for fast spectrally-selective musculoskeletal imaging. Magn Reson Med 35(4):563–568

Tiderius CJ et al (2003) Delayed gadolinium-enhanced MRI of cartilage (dGEMRIC) in early knee osteoarthritis. Magn Reson Med 49(3):488–492

Trattnig S et al (2007a) Three-dimensional delayed gadolinium-enhanced MRI of cartilage (dGEMRIC) for in vivo evaluation of reparative cartilage after matrix-associated autologous chondrocyte transplantation at 3.0T: preliminary results. J Magn Reson 26(4):974–982

Trattnig S et al (2007b) Quantitative T_2 mapping of matrix-associated autologous chondrocyte transplantation at 3 Tesla - an in vivo cross-sectional study. Investig Radiol 42:442–448

Ugurbil K et al (2003) Ultrahigh field magnetic resonance imaging and spectroscopy. Magn Reson Imaging 21(10):1263–1281

Vaughan JT et al (2002) Detunable transverse electromagnetic (TEM) volume coil for high-field NMR. Magn Reson Med 47(5):990–1000

Wachsmuth L, Juretschke HP, Raiss RX (1997) Can magnetization transfer magnetic resonance imaging follow proteoglycan depletion in articular cartilage? Magn Reson Mater Phys Biol Med 5(1):71–78

Wald LL et al (1995) Phased array detectors and an automated intensity-correction algorithm for high-resolution MR imaging of the human brain. Magn Reson Med 34(3):433–439

Watanabe A et al (2006) Delayed gadolinium-enhanced MR to determine glycosaminoglycan concentration in reparative cartilage after autologous chondrocyte implantation: Preliminary results. Radiology 239(1):201–208

Watrin-Pinzano A et al (2004) Evaluation of cartilage repair tissue after biomaterial implantation in rat patella by using T_2 mapping. Magn Reson Mater Phy 17(3–6):219–228

Welsch GH et al (2008a) Evaluation and comparison of cartilage repair tissue of the patella and medial femoral condyle by using morphological MRI and biochemical zonal T_2 mapping. Eur Radiol 19(5):1253–1262

Welsch GH et al (2008b) In vivo biochemical 7.0 Tesla magnetic resonance: preliminary results of dGEMRIC, zonal T_2, and T_2* mapping of articular cartilage. Invest Radiol 43(9):619–626

Welsch GH et al (2008c) Cartilage T_2 assessment at 3-T MR imaging: in vivo differentiation of normal hyaline cartilage from reparative tissue after two cartilage repair procedures–initial experience. Radiology 247(1):154–161

Welsch GH et al (2008d) Magnetization transfer contrast and T_2 mapping in the evaluation of cartilage repair tissue with 3T MRI. J Magn Reson Imaging 28(4):979–986

Welsch GH et al (2009a) Quantitative T_2 mapping during follow-up after matrix-associated autologous chondrocyte transplantation (MACT): Full-thickness and zonal evaluation to visualize the maturation of cartilage repair tissue. J Orthop Res 27(7):957–963

Welsch GH et al (2009b) Biochemical (T_2, T_2* and magnetization transfer contrast) MRI of knee cartilage - feasibility at ultra-high-field (7.0T) and comparison to high-field (3.0T). Magma 22(Suppl. 1) p.124

Wheaton AJ et al (2004a) Proteoglycan loss in human knee cartilage: quantitation with sodium MR imaging–feasibility study. Radiology 231(3):900–905

Wheaton AJ et al (2004b) Sodium magnetic resonance imaging of proteoglycan depletion in an in vivo model of osteoarthritis. Acad Radiol 11(1):21–28

White LM et al (2006) Cartilage T_2 assessment: differentiation of normal hyaline cartilage and reparative tissue after arthroscopic cartilage repair in equine subjects. Radiology 241(2):407–414

Wietek B et al (2007) T_2 and T_2* mapping of the human femoral-tibial cartilage at 1.5 and 3 Tesla. Intern Soc Magn Reson Med 15:516

Williams A et al (2007) Suitability of T(1Gd) as the dGEMRIC index at 1.5T and 3.0T. Magn Reson Med 58(4): 830–834

Wolff SD, Balaban RS (1989) Magnetization transfer contrast (Mtc) and tissue water proton relaxation invivo. Magn Reson Med 10(1):135–144

Wolff SD, Balaban RS (1994) Magnetization-transfer imaging—practical aspects and clinical-applications. Radiology 192(3):593–599

Wolff SD et al (1991) Magnetization transfer contrast—Mr-imaging of the Knee. Radiology 179(3):623–628

Wood ML, Hardy PA (1993) Proton relaxation enhancement. J Magn Reson Imaging 3(1):149–156

Zur Y (2000) Design of improved spectral-spatial pulses for routine clinical use. Magn Reson Med 43(3):410–420

High Field MR Spectroscopy: Investigating Human Metabolite Levels at High Spectral and Spatial Resolution

Duan Xu and Daniel B. Vigneron

Contents

Abstract

Magnetic Resonance Spectroscopy (MRS) offers a unique window to cellular metabolism through its ability to detect the concentrations of small mobile biological compounds non-invasively. Nevertheless, MRS has failed to broadly enter the clinical routine despite its success in scientific studies. Limitations in sensitivity, spatial resolution, and spectral identification, which can be severe at lower fields, are reduced for ultra-high field MRS allowing unprecedented in vivo studies of cellular metabolite levels at 7 T. In this chapter, the challenges, methods, capabilities, and applications of ultra-high field magnetic resonance spectroscopy are presented. Also included are examples of the unique metabolic information obtained using 7 T MR systems for the study of human cellular metabolite levels in both normal volunteers and patients. High resolution MR spectroscopic imaging has provided improved detection of small brain lesions and enhanced assessment of brain tumor presence and extent. While the majority of MRS research has focused on neurological applications, the increased sensitivity and spectral resolution can improve the metabolic characterization of pathologies in other organs as well.

1 Introduction

While the main focus of ultra high field MR development has been on anatomic and functional imaging based on water protons, ultra-high magnetic fields can also greatly improve the detection of biochemical

D. Xu · D. B. Vigneron (✉)
Department of Radiology and Biomedical Imaging,
MC 2512, University of California,
1700 4th St. QB3 Building, Suite 102,
San Francisco, CA 94158, USA
e-mail: dan.vigneron@radiology.ucsf.edu

J. Hennig and O. Speck (eds.), *High-Field MR Imaging,* Medical Radiology. Diagnostic Imaging,
DOI: 10.1007/174_2011_201, © Springer-Verlag Berlin Heidelberg 2011

information based on protons and other nuclei such as ^{31}P and ^{13}C. The benefit of high magnetic field for Magnetic Resonance Spectroscopy (MRS) is manifested in several ways. The higher signal-to-noise ratio (SNR) with higher field strength allows the detection of smaller concentrations of metabolites and/or shorter scan times. In addition, the increased field causes the frequency separation between spectral resonances to increase and can simplify the characterization of multiplet signals from coupled spin systems. In this chapter, we present an overview of the challenges, methods, capabilities, and applications of ultra-high field magnetic resonance spectroscopy for the study of human cellular metabolite levels in both, normal volunteers and patients with a number of different pathologies.

2 Factors in High Field Spectroscopy Acquisition

2.1 Signal to Noise (B_0)

The single largest benefit of going towards ultra-high field MR (7 T) is the gain in the signal to noise ratio (SNR) as it has been described for imaging in many of the previous chapters. The linear gain in SNR with field strength can be exploited for increased spatial and/or temporal resolution, and allows detection of lower concentration metabolites compared to lower field strength. In addition, the chemical shift of spectral components increases linearly with field strength, leading to correspondingly wider separation of spectral lines. In contrast, the line splitting of multiplet peaks (caused by spin–spin J-coupling) depends only on the spin system involved and is thus independent of the magnetic field strength. If the chemical shifts of the contributing spins are large compared to the spin–spin J-coupling, cleaner multiplet signals evolve and are thus easier to detect and identify at higher field strength. In a recent paper by Snyder et al., simultaneous detection of the J-coupled signals of glutamate and glutamine was enabled by optimizing acquisition parameters using a standard PRESS sequence (Snyder and Wilman 2010) opposed to methods at lower field strength that require elaborate signal editing schemes. However, these advantages come at a price with the most common issues for high field MRS being similar to those faced in imaging and include B_0 and B_1 inhomogeneity, requirements of peak RF power, SAR limitations, and increased chemical shift misregistration.

2.2 B_0 and B_1 Field Effects

It is well studied that as the main magnetic field increases in strength, the homogeneity of the field in absolute units decreases. It is much harder to achieve a uniform field, as the strength of the magnet gets larger and the additionally induced field variations due to the distribution of tissues with varying magnetic susceptibility in the subject increase. However, in order to fully benefit from the increased frequency separation of different signals at higher fields, the line widths of the signal peak (again in absolute units) should be maintained. As the line width is given by the natural line width plus additional broadening caused by dephasing due to magnetic field inhomogeneities, the full high field benefit can only be achieved if the relative field homogeneity improves in parallel to the field strength increase. Passive and first order superconducting shims are no longer able to provide the required field uniformity for spectroscopic investigations. Higher order shims are needed to avoid broadening of the resonance lines and thus to produce high quality spectra with good line separation. This was already noted at low field (Spielman et al. 1998) and becomes even more important at high field (Tkac et al. 2001; Xu et al. 2008; Mekle et al. 2009). In all current generation 7 T scanners, second order shims are available. It is an ongoing discussion, whether higher spatial order shim coils are necessary and how much improvement they could provide. Due to the large magnetic susceptibility variations in the regions of the nasal sinuses and the skull base, these areas are generally avoided in the volume used for field homogeneity optimization. It is generally very difficult to obtain high field homogeneity and thus spectra with good peak separation over the entire brain. However, many regions can be adequately studied with regionally minimized line width particularly when spectra are acquired in small volumes. For this reason, locally optimized single voxel acquisitions generally produce spectra with superior quality compared to large volume 3D spectroscopic imaging methods (MRSI) that acquire multiple spatially encoded spectra from an extended region

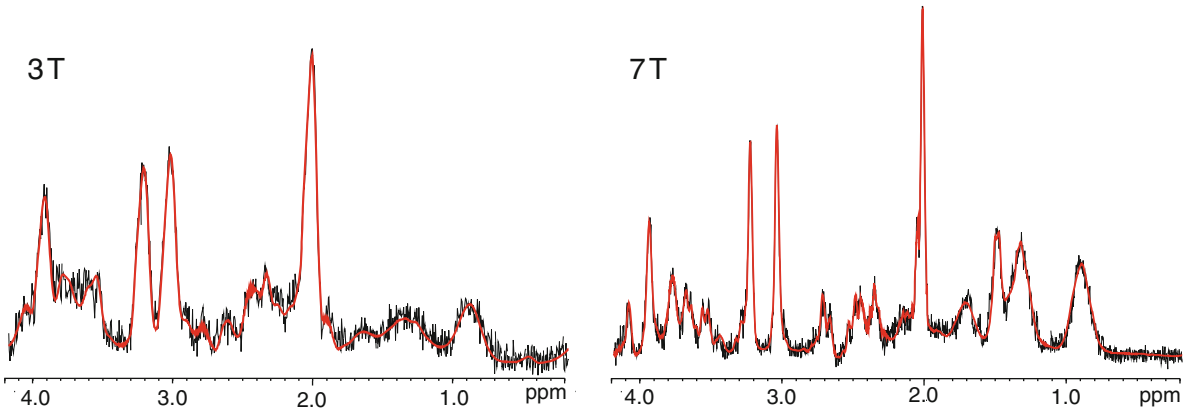

Fig. 1 Comparison of STEAM spectra acquired at 3 T (*left*) and 7 T (*right*). Spectra were acquired in a volume of 2 cm^3 in the anterior cingulated cortex with TE/TM = 20/15 ms, TR = 3,000 ms, and 128 averages. The improved SNR and increased spectral separation are clearly visible. Courtesy of Dr. Oliver Speck from the University of Magdeburg

simultaneously. Single voxel spectra acquired at 3 T and 7 T (see Fig. 1) demonstrate the improvement achieved at higher field strength. On the other hand, MRSI methods allow for the measurement of many small voxels and thus benefit strongly from the increased SNR at high field, albeit the full benefit can be limited by increased field inhomogeneity over these larger regions.

At 7 T, dielectric effects of tissue can result in large variations of the B_1 field strength and thus flip angle across the object and are particularly detrimental for large volume imaging applications. These effects also affect MRS studies, especially those with large spatial coverage. Whereas the RF-field homogeneity is generally very high over the volume of interest for a single voxel examination, the non-uniformity in excitation and refocusing is an important consideration when acquiring 2D or 3D spectroscopic data in larger volumes. This is especially problematic for PRESS methods as two spin echoes with high B_1 sensitivity are required for refocusing. For single voxel methods, a localized adjustment of the RF-amplitude can resolve the B_1 inhomogeneity locally. This is different for MRSI methods that cover larger regions. The B_1 difference through the human head can easily vary up to 40% (Xu et al. 2006) as has been noticed and demonstrated in the previous chapters. Various strategies have been introduced to combat this variability such as employing pulses with adiabatic characteristics (Tkac et al. 2001) and B_1 shimming (Metzger et al. 2008; Setsompop et al. 2008; Hetherington et al. 2010). Excitation with adiabatic pulses will be discussed later in this chapter. B_1 shimming has limited adoption at the current time due to the requirements of multiple excitation coils and specialized RF hardware that are not yet standard on commercial 7 T MR scanners. In addition, safety issues have to be resolved for such multi-channel excitation systems. Currently, the high field gain in spectroscopy over larger regions (in particular MRSI) is somewhat limited but, as described below, has been successfully applied for volunteer and patient studies.

2.3 Chemical Shift Effects

As frequency increases with field, metabolic resonances become increasingly separated, as measured in Hertz. This is a major advantage for high field MRS in particular for the detection and quantification of metabolites with overlapping signals. The increase in spectral separation requires a larger spectral acquisition bandwidth to acquire the range of metabolite signals. In contrast to imaging, this increased bandwidth does not directly lead to an SNR reduction because the signals are acquired without readout gradient and the noise is thus also frequency resolved. However, a second effect of this wider metabolite frequency separation is a stronger chemical shift misregistration. Similar to the fat–water shift in imaging, the excitation volumes of metabolites with different resonance frequencies are shifted relative to each other. To reduce its impact, excitation

considerations must be made. Specially designed high bandwidth RF pulses can be used to mitigate these errors (Xu et al. 2008; Balchandani et al. 2008), which will be discussed later in this chapter. Alternatively, different acquisition strategies can be considered such as Hadamard encoding noted by Goelman et al. 2007. However, these methods have not found widespread application despite their long time availability.

2.4 RF Excitation

The RF excitation pulses' spatial and frequency profiles are a major factor determining the quality of the acquired MR spectra. The main reason for this critical dependence is the large difference in concentration between water or fat and the metabolites to be examined by MRS. Typically, the metabolite concentrations are 4–6 orders of magnitude lower than those of water or fat. Whereas, in imaging a small out of slice excitation of 1% of the desired volume will lead to 1% unwanted signal contamination. Such a 1% excitation of unsuppressed water or fat outside of the target volume can result in signal contaminations that dominate the spectrum. At high field, RF excitation properties become even more important because of the larger frequency range of the metabolites and the B_1 variation across the region of interest. B_1 variation does not only impact the SNR of the spectra but alters the metabolite peak heights or areas. The effect is especially pronounced for acquisitions using large flip angles such as the most commonly used PRESS sequence (90°–180°–180°) in particular when larger volumes are acquired. Adiabatic pulses have long been used in RF excitation to combat B_1 inhomogeneity (Ross et al. 1992; Garwood and DelaBarre 2001; Scheenen et al. 2008). However, adiabatic full passage pulses at lower fields already require a significant amount of peak power while producing prohibitively high SAR. This is exacerbated at higher fields. Carefully designed phase modulated RF pulses with an adiabatic envelope can achieve uniform excitation over a range of B_1 at a much lower peak RF level (Xu et al. 2008; Balchandani et al. 2008). Due to the prolongation of T_1 at higher fields, to avoid saturation and thus T_1 weighting, the repetition time (TR) is extended. This reduces SAR although the potential scan time reduction of MRS at high field is somewhat reduced.

Whereas SAR limitations can typically be avoided in MRS, the above described high bandwidth RF-pulses can demand high RF peak power, but the problem can be alleviated by phase modulation (Le Roux et al. 1998; Schulte et al. 2004). Volume coils currently available for 7 T examinations of the head in combination with the standard 8 kW RF amplifier can typically deliver peak B_1 fields of 20 μT. Compromise has to be made between the spatial and spectral selectivity of the pulse.

Two methods that have been used at high field to achieve high selectivity or to reduce the contribution of unwanted out of volume signal contributions are spatial–spectral RF-excitation and very selective saturation.

2.4.1 Spectral–Spatial RF

The use of spectral–spatial RF (SSRF) pulses has distinct advantages. Due to their spectral selectivity, metabolites can be included and excluded by design. Water can be effectively removed by placing it in the stop-band of the pulse. Similarly, lipid can also be excluded, which is advantageous in acquiring large volume MRSI in the brain. The subcutaneous lipid otherwise can fold into the field of view and distort the spectra for excitations with limited spatial extent. In addition and perhaps the most important characteristic of the SSRF pulses is that they have high bandwidth. The high bandwidth helps to reduce the chemical shift artifact, allowing similar appearance of metabolites across voxels in a large FOV. Furthermore, SSRF pulses can be designed to have low levels of chemical shift misregistration by symmetrically sweeping the frequencies (Xu et al. 2008; Balchandani et al. 2008). Non-linear phase modulation can provide over 40% reduction in peak power for the 180° pulses in 7 T PRESS MRSI studies (Xu et al. 2008) including those in Figs. 2, 3, 4 and 5. This is again important for large volumetric MR spectroscopic imaging acquisitions. The main limitation for the application of SSRF pulses is their long duration which precludes short TE MRS, but improves long TE MRSI as demonstrated later in this chapter.

2.4.2 Very Selective Saturation

As mentioned above, even small out of volume excitation can result in significant unwanted signal contamination. Outer volume suppression is an efficient method to further reduce these unwanted signals.

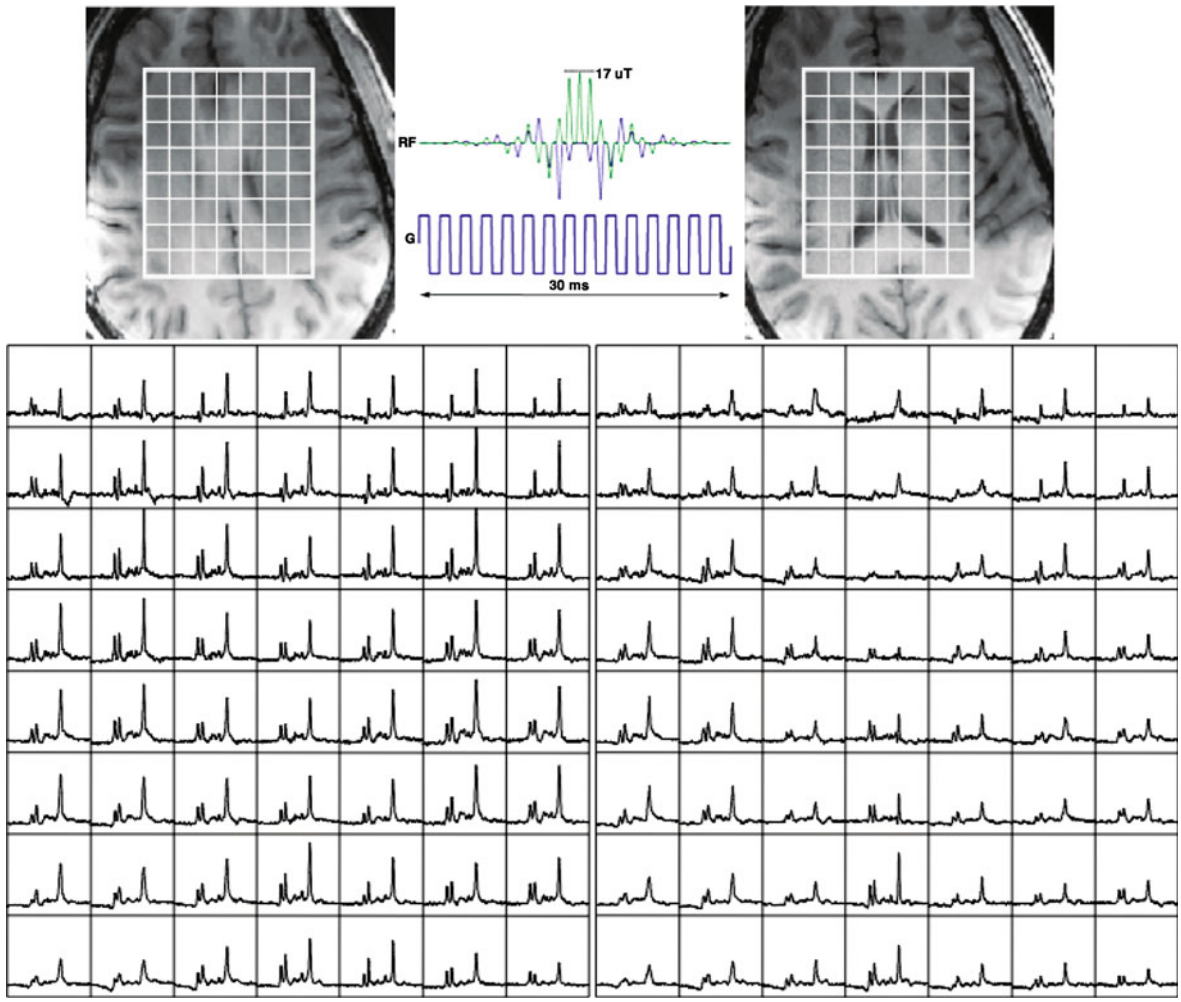

Fig. 2 3D MRSI covering over 200 cm^3 of the brain at a 1 cm^3 spatial resolution using 180° SSRF PRESS-MRSI (*top middle*) with VSS to negate chemical shift misregistration effects with phase-modulation to reduce peak power. This demonstrated the ability to measure metabolite levels with high spatial coverage in the brain

Due to the widening of the frequency spread and increased chemical shift artifact, spatial suppression becomes more difficult as the main field strengthens. Outer volume suppression using very selection saturation (VSS) pulses has been used in conjunction with spectroscopy to produce selection volumes with sharp edges (Tran et al. 2000). Once again, for high spatial selectivity, the peak RF power requirements must be overcome for high field studies. New strategies of RF design using quadratic phase (Le Roux et al. 1998; Schulte et al. 2004) or manipulating roots of the B(z) polynomial (Shinnar 1994) of the SLR RF pulse slice profile (Pauly et al. 1991) have made the use of VSS possible at 7 T. Although SAR is also generally very high and potentially problematic in cases of multiple saturation bands, it can be managed by extending the TR, which, as already mentioned reduces unwanted T_1 weighting but may in part compromise the SNR advantage of high field.

3 Metabolites Detectable by 7 T MR Spectroscopy

As stated earlier, the advantage of higher magnetic field is higher SNR and wider spectral separation for the detection of previously overlapped or low concentration metabolites (Tkac et al. 2001; Xu et al. 2008;

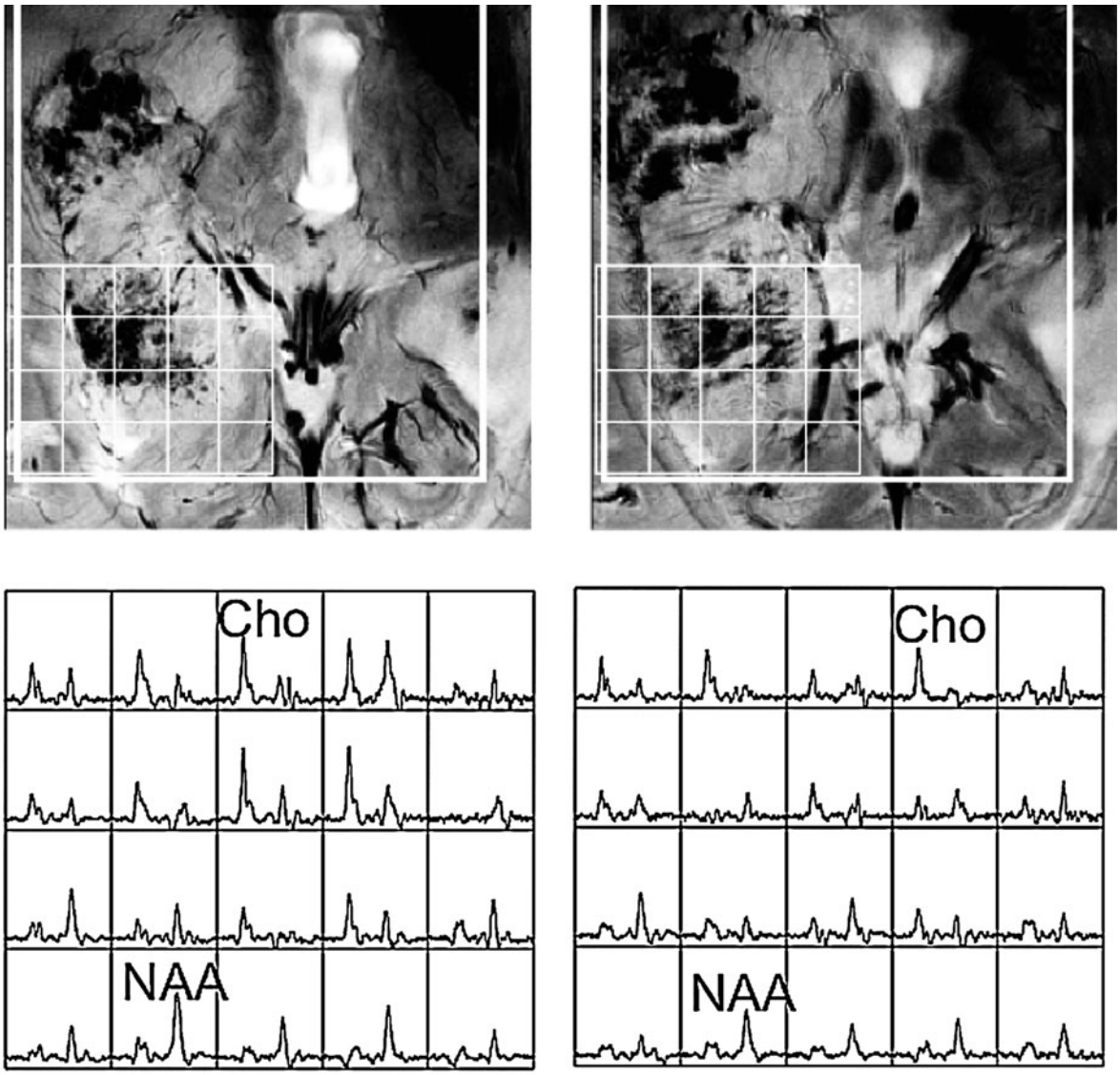

Fig. 3 3D MRSI with 0.5 cm^3 spatial resolution and TE/TR = 144/2,000 ms was obtained from a glioma patient in a 7 T MR scanner. The spectra are overlaid on high resolution gradient echo images showing non-uniform contrast within the cancerous region, confirmed by elevated choline and reduced NAA levels in the tumor and high NAA/reduced choline in the adjacent brain tissue. Courtesy of Drs. Sarah Nelson and Janine Lupo from the University of California San Francisco

Mekle et al. 2009; Choi et al. 2009; Ugurbil et al. 2003). At the same time, higher SNR aids in the detection of metabolites with J-modulation with enhanced editing techniques. As demonstrated in the figures below, the wealth of additional metabolites, which can be measured, is tremendous and still waiting to be fully explored for clinical analyses. Due to the long 180° refocusing pulses of the PRESS acquisition, the minimum TE obtainable is around 20–30 ms. By using a single voxel stimulated echo acquisition mode (STEAM) approach in combination with surface transmit and receive coils, human in vivo spectra with TE of 6 ms (Tkac et al. 2001) have been acquired using a 7 T MR scanner as shown in Fig. 6. Mekle et al. similarly demonstrated TE of 6 ms single voxel acquisition with excellent spectral quality (Mekle et al. 2009). These measurements had been performed with surface coils and are limited to brain areas close to the skull. The short TE greatly increases the number of metabolite resonances and the SNR of the spectrum as

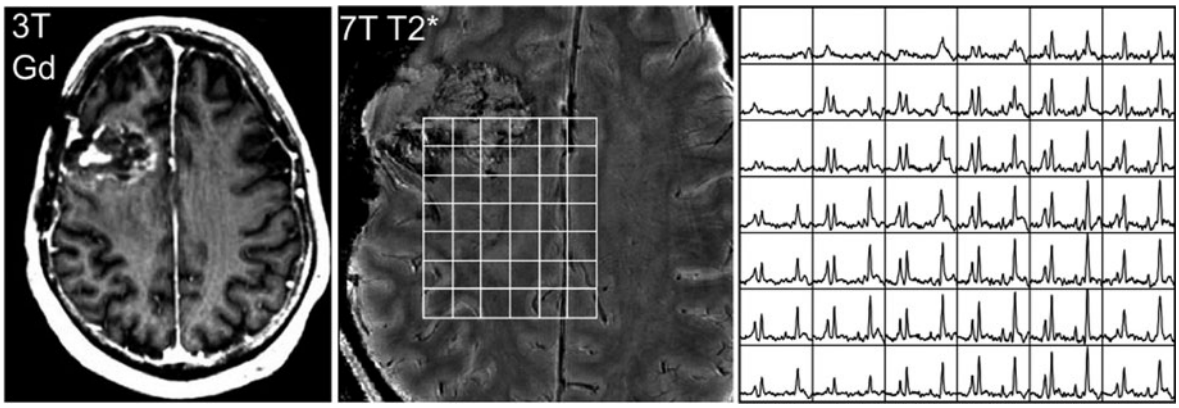

Fig. 4 A 3D MRSI of 0.5 cm^3 resolution, acquired at 7 T using long TE of 144 ms, is shown with a 3 T contrast enhanced T_1-weighted image as well as a high resolution 7 T gradient echo image for a brain tumor patient following surgical resection and radiation therapy. In this case only minimal choline levels were detected in the treated lesion. Courtesy of Drs. Sarah Nelson and Janine Lupo from the University of California San Francisco

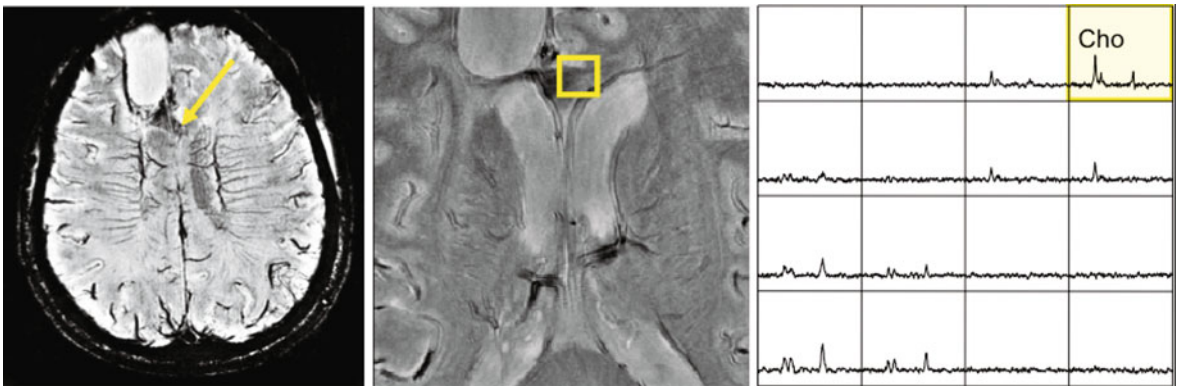

Fig. 5 The high spatial resolution (0.5 cm^3) of 7 T MRSI allowed detection of elevated choline levels in the corpus callosum in this glioma patient following resection and radiation indicating the spread of recurrent/residual cancer. The spatial resolution was twice as fine as that used routinely at 3 T thereby improving the detection of small regions of tumor. Courtesy of Drs. Sarah Nelson and Janine Lupo from the University of California San Francisco

the metabolites do not have time to dephase due to J-coupling and signal decay through T_2 relaxation. Although theoretically T_2 should not shorten as the field strength increases, the measured T_2 values of metabolites have been shown to decrease slightly as measured T_2 of water does for most tissues. This is due to incomplete refocusing and increased inhomogeneity in the field. Therefore, a small TE increase results in a significant SNR reduction. The spectrum shown in Fig. 6 demonstrates high SNR and excellent spectral quality. It demonstrates the ability to detect the resonances of a large number of cellular metabolites in the brain including: ascorbate (Asc), aspartate (Asp), creatine (Cr), phosphocreatine (PCr), γ-aminobutyric acid (GABA), glutamate (Glu), glutamine (Gln), glutathione (GSH), glycerophosphorylcholine (GPC), phosphorylcholine (PCho), inositol (Ins), lactate (Lac), N-acetylaspartate (NAA), and taurine (Tau).

At short TE, another challenge is water suppression. The water signal not only distorts the baseline but incomplete saturation can often result in water sidebands that render the spectrum unusable. In Fig. 6, VAPOR water suppression was employed with excellent results as demonstrated by the minuscule amount of residual water (Tkac et al. 2001). The more commonly available CHESS water suppression method can also be utilized. However, with the increased spectral width and variable T_1 of different

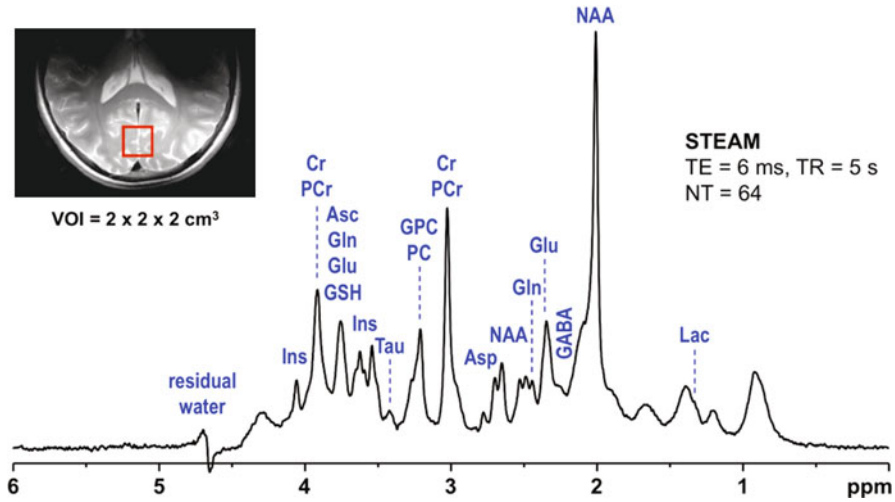

Fig. 6 A short TE single voxel 8 cc spectroscopic acquisition using STEAM. Multiple additional metabolites are seen in comparison with lower field MRS acquisitions, enabled by higher SNR, wider spectral separation, and varying J-modulation. VAPOR water suppression and OVS pulses were used. Courtesy of Dr. Ivan Tkac from the University of Minnesota

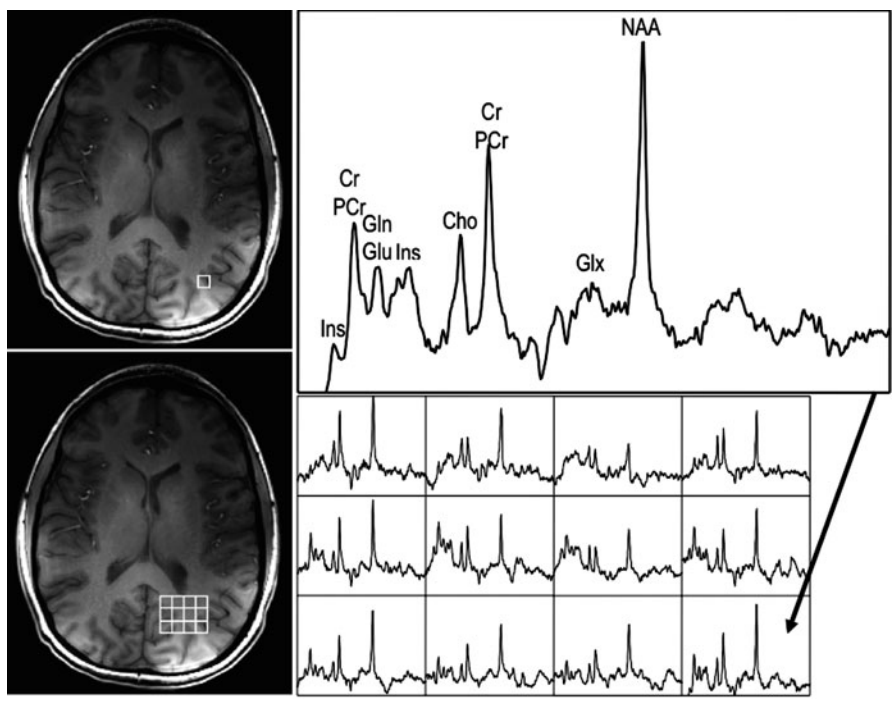

Fig. 7 This 8 × 8 × 8 MRSI spectral array of 0.7 cm isotropic (0.34 cm^3) was acquired in just over 17 min with TR/TE of 2200/35 ms and CHESS water suppression. This demonstrates multiple metabolic peaks with improved spectral separation and much higher spatial resolution than is typically attainable at lower fields

components of water, an increased number of CHESS pulses maybe needed in order to obtain a similar level of suppression in comparison to lower fields.

Although short TE spectra yield tremendous amounts of information, their use remains challenging for various reasons. The most obvious one is the quantification of metabolites. Early MRS studies have used metabolite to Cr ratio to quantify the results. On the other hand, methods for absolute quantification of the metabolite concentrations have also been proposed, using the non-suppressed water signal from the same voxel as intensity references. LCModel (Provencher 1993) is a widely used method (Tkac et al. 2001; Mangia et al. 2007), in which the spectrum is numerically fitted with spectra of predetermined, known quantity of metabolic compounds. In comparison, longer TE acquisitions with fewer peaks can also be studied using peak heights (Nelson 2001), or a combination of peak heights ratios and previously measured concentration (Choi et al. 2009).

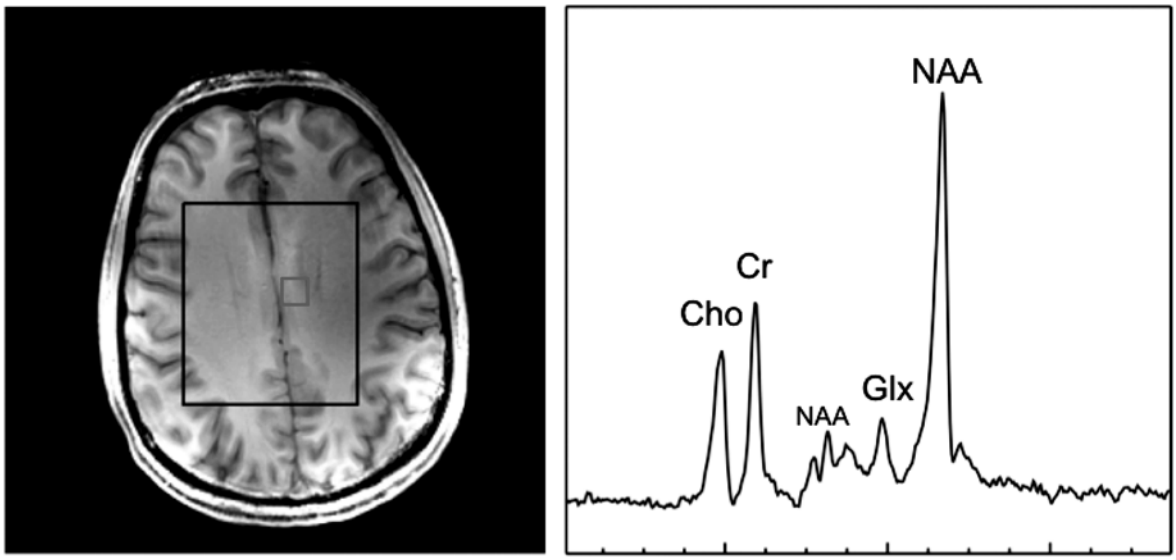

Fig. 8 A selected voxel from a 3D PRESS sequence acquired using SSRF with TE 144 ms and TR 2 s of a healthy volunteer. As is typical with long TE acquisitions, the baseline is relatively clean with fewer peaks

4 MR Spectroscopic Imaging at 7 T

Though single voxel acquisitions can provide outstanding metabolic information from a single region, MR spectroscopic imaging (MRSI) allows the simultaneous acquisition of multiple regions in arrays of spectra. Figure 7 demonstrates a TE = 35 ms 3D MRSI spectra, acquired using PRESS in 17 min. Avdievich et al. have also performed 3D MRSI with a short echo time TE = 15 ms showing glutamate and glutamine as well as lactate in tumor patients (Avdievich et al. 2009).

In acquisitions with longer TE, spectral spatial pulses can be employed to reduce the amount of water. This has the advantage of providing the ability to control the amounts of remaining water signal (Schricker et al. 2001), mentioned previously, and may be useful in quantification using water as an internal reference. In addition, broad signals from macromolecules that lead to large baseline variations in short TE spectra are reduced due to T_2 decay in longer echo time spectra. Therefore, long TE spectra generally have flatter baselines but also fewer metabolic peaks since low concentration metabolites don't yield enough signal. However, at high field, due to the SNR increase, J-modulation and spectral excitation profiles, some of the previously difficult to detect metabolites can now be visualized readily. For example, in the TE 144 ms PRESS acquisition using SSRF pulses noted by Xu et al., a prominent glutamine/glutamate (Glx) peak can be visualized (Xu et al. 2008). Simulations have confirmed this predominately glutamate peak (Xu et al. 2007) (Fig. 8).

5 Spectral Editing Techniques

Not all metabolites with J-modulation can be easily resolved using specialized pulses or just by going to higher magnetic field. Editing techniques are necessary to quantify and characterize those metabolites. These techniques also benefit from the linear gain in SNR at 7 T. Choi et al. used additional RF pulses within the PRESS acquisition to obtain serine levels in the brain (Choi et al. 2009). 2D J-resolved methods can be used, e.g. to quantify glutamate levels as well as measure T_2 relaxation times (Xu et al. 2007; Hurd et al. 2004). Srinivasan et al. used the BASING editing scheme (Star-Lack et al. 1997) for the detection of glutathione at 7 T (Srinivasan et al. 2010). Many of these methods are adopted from high resolution NMR spectroscopy and have been applied at 3 T, albeit with long measurement times. Application at higher field can reduce the acquisition times significantly and therefore facilitate more widespread

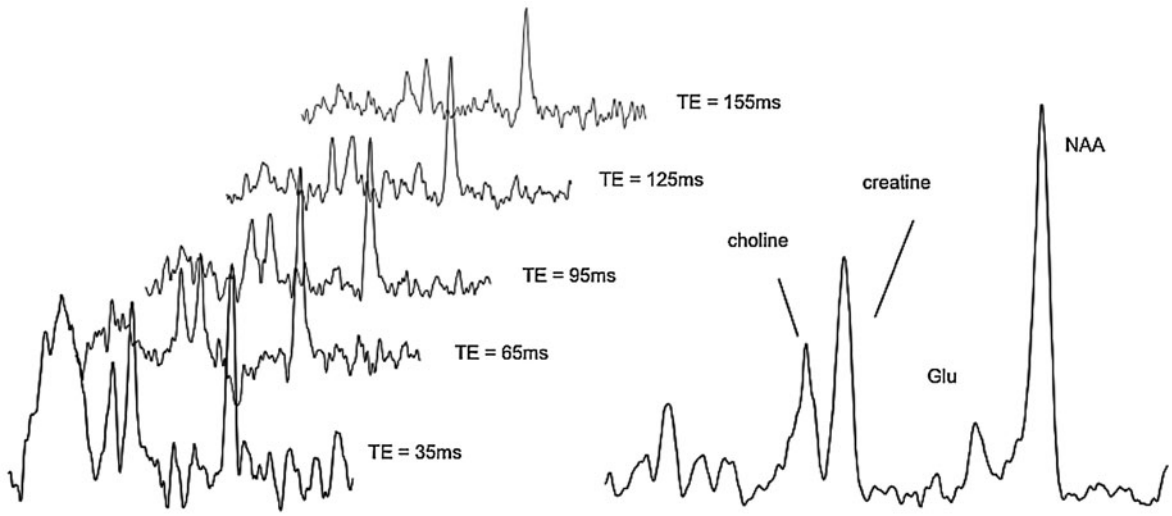

Fig. 9 Representative spectra at selected echo times from occipital white matter in a healthy volunteer at 7 T. TE-averaged spectra from TE = 35 ms through TE = 275 ms (48 steps from 35 ms at 5 ms increments) are presented

application of these methods. The accurate quantitation of these metabolites may have future clinical impact, as Srinivasan et al. demonstrate reduced glutathione levels in white matter lesion of patients with multiple sclerosis (Srinivasan et al. 2010). Figure 9 demonstrates a TE-averaged, single voxel acquisition from white matter at 7 T. The TE averaged sequence does not only allow the investigation of J-modulated species such as glutamate but it also provides a method for measuring T_2. Changes in metabolic relaxation times may allow the assessment of tissue abnormalities. However, a number of spectral editing methods that employed sophisticated RF excitation procedures currently suffer at 7 T due to the stronger B_1 inhomogeneity and therefore must rely on a more homogeneous and efficient RF excitation at 7 T.

6 Brain Tumors

Primary brain tumors are very aggressive with five-year survival rates of approximately 36% according to the American Cancer Society. Treatment strategies often include a combination of chemotherapy, surgical resection, and radiation. For surgical and radiation interventions, accurate delineation of brain tumor extent is critical for guiding therapy and for monitoring treatment response. Anatomic imaging alone is often not adequate for providing such reliable detection of the spatial extent of brain tumors even with the application of contrast agent. Thus metabolic assessment with ^{1}H MR spectroscopy has been used to detect differences in metabolite levels between normal brain and tumor (Luyten et al. 1990; Demaerel et al. 1991; Fulham et al. 1992; Negendank et al. 1996; Preul et al. 1996; Nelson et al. 1999) and has been applied for treatment planning (Nelson et al. 2002) and for monitoring therapeutic response (Chan et al. 2004; Park et al. 2007; Rock et al. 2002). Metabolite resonances that correlate with the changes due to tumor progression include levels of choline-containing compounds (Cho), creatine (Cr), *N*-acetylaspartate (NAA), lactate (Lac), and lipid (Lip). The intensity of the Cho signal reflects changes in membrane synthesis and turnover that are associated with cell proliferation and remodeling. The creatine peak is often used as a reference for normalizing the intensity of other metabolites and includes both creatine and phosphocreatine. NAA is a marker of normal brain tissue that is typically assumed to correspond to the presence of actively functioning neurons. Lactate is an end product of anaerobic metabolism and may therefore reflect ischemia and/or hypoxia.

While MR spectroscopic imaging of brain tumors has been applied in many clinical studies using 1.5 and 3 T MR scanners, only recently has the sensitivity of 7 T MRSI been used to detect the presence and

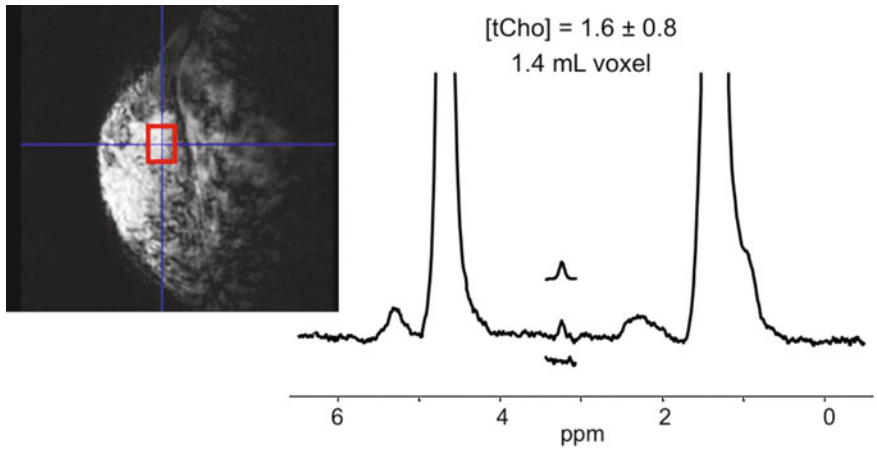

Fig. 10 7 T spectrum obtained in a patient with invasive ductal carcinoma detecting elevated choline using specialized RF excitation and TE averaging (47–193 ms) in 128 steps. Courtesy of Dr. Patrick Bolan from the University of Minnesota

extent of neoplastic lesions in the brain with high resolution. In Fig. 3, MRSI spectral arrays demonstrate the detection of high choline levels consistent with increased cell proliferation in a glioma at a two-fold smaller voxel size (0.5 cm^3) than routinely acquired at lower fields (1.0 cm^3). In Figs. 4 and 5, this high field MRSI technique was applied to study glioma patients following surgical resection and radiation treatment. For the patient in Fig. 4, only spectra consistent with necrosis and gliosis were observed. The high spatial resolution of 7 T MRSI detected highly elevated choline, indicative of tumor cellular proliferation localized to the corpus callosum consistent with recurrent/residual cancer (Fig. 5).

7 Other Tissues

As high field MR scanners have become more technologically advanced, in vivo spectroscopy studies have become no longer limited to the brain and recently researchers have investigated its use in other tissue such as the breast, prostate, bone, and muscle (Haddadin et al. 2009; Klomp et al. 2009; Wang et al. 2009; Ren et al. 2008). However some of these regions remain difficult to study due to the need of specialized receive coils or demand of high RF power.

7.1 Breast

Just as in brain tumor studies, the increase in SNR and spectral separation allows the reduction in voxel size and better characterization of the metabolites. Breast MRS has been predominately studied using the single voxel technique and quantitation of total choline. Dr. Bolan's group at the University of Minnesota has demonstrated that higher field can improve the detection of total choline, decrease measurement errors, and study smaller lesions (Haddadin et al. 2009). They have interestingly noted that at 7 T, normal healthy subjects have detectable choline, which has not been reported at 1.5 T. The reduction in voxel size enables visualization of smaller cancers, which is afforded by the gain of SNR. The choline peak is also better separated from water and lipid due to wider spectral separation. These two main advantages can be seen in Fig. 10. Another study (Stanwell et al. 2005) has indicated that in healthy subjects, the choline resonance includes contributions from taurine, myo-inositol, or glycerophosphocholine as opposed to predominately phosphocholine in breast cancers.

7.2 Prostate

In the prostate, citrate, choline, and polyamines are used to characterize the clinical status of the tissue. Previous studies have demonstrated that due to J-modulation, specialized CPMG refocusing RF trains were needed at 3 T to maintain in-phase citrate signal at a short TE. This is difficult to achieve at higher field strength due to SAR limitations. Extension of the TE or other spectral optimization techniques will be required. Prostate tumors have been investigated with the aid of adiabatic pulses, custom built endorectal coils and specially designed pulse sequence

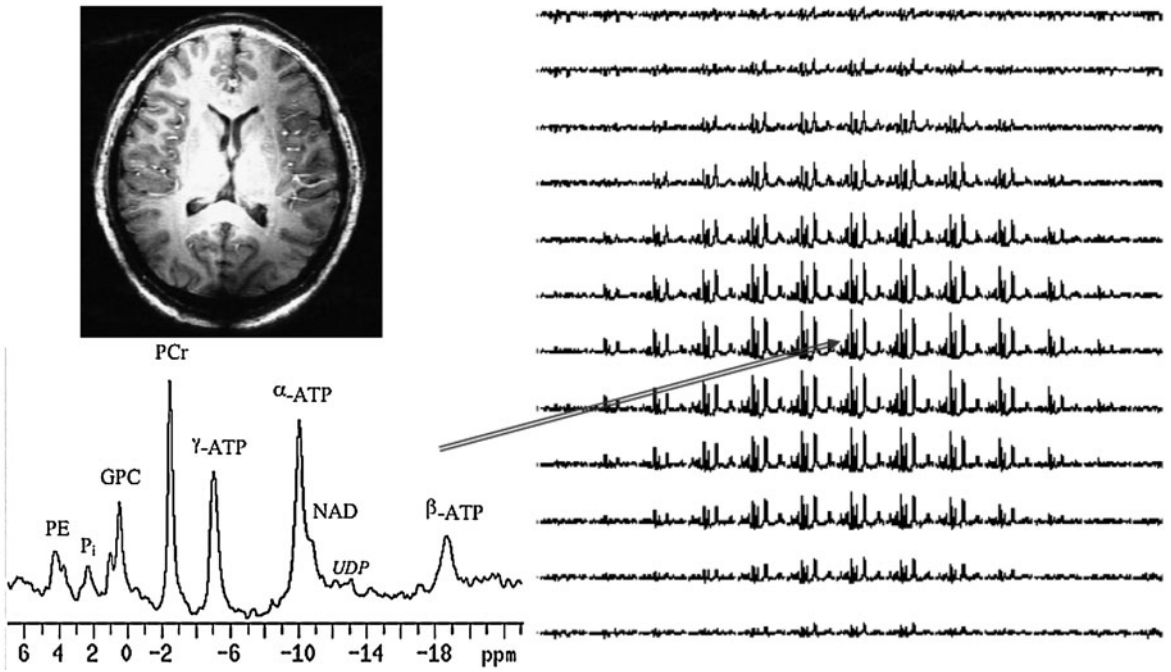

Fig. 11 7 T Human head MRI/MRS study with a double-tuned TEM volume coil. T_1 weighted ^1H image in axial orientation is shown in the *upper left*. Imaging parameters: TR = 8 ms, TE = 3.2 ms, NEX = 1, slice thickness = 2 mm, matrix = 128 × 128, FOV = 20 × 20 cm^2. An axial slice of the 3D ^{31}P spectroscopic imaging acquisition from the same subject is shown on the *right*. Total acquisition time was 18.2 min. SNR of PCr peak of center voxels was 70:1. The voxel size was 15.5 cc. An enlarged display of one spectrum demonstrates the various metabolites detected in this exam. Courtesy of Dr. Xiaoliang Zhang at the University of California San Francisco and Dr. Wei Chen at the University of Minnesota

(Klomp et al. 2009). A relatively short TE of 56 ms was achieved to yield high SNR while demonstrating distinct separation of spermine and choline, which may improve diagnosis of prostate tumors by better quantifying the amount of polyamines. However, due to the challenging location of the prostate that is also affected strongly by physiological motion, the full potential of the spectral separation between the polyamines and choline by 7 T has not yet been realized. Therefore, this application remains to be a continuing challenge.

7.3 Musculoskeletal Applications

Imaging adipose tissue has long been an interest for the groups studying muscle and bones. The application of 7 T for the determination of the composition of triglycerides in calf subcutaneous tissue as well as tibial bone marrow has been explored (Ren et al. 2008). It was concluded that the use of 7 T spectroscopy to determine lipid composition is a simple and robust way of monitoring changes in lipid. More recently, Ramadan et al. described in vivo 1D and 2D correlation spectroscopy of the soleus muscle at 7 T (Ramadan et al. 2010). Correlation spectroscopy is generally not performed in vivo due to long scan times and limited SNR. At 7 T, with customized hardware and carefully placed regions of interest, metabolite levels and T_1/T_2 relaxation values were acquired. While not used clinically, the authors are optimistic that the improved resolution and sensitivity at ultra-high field MRS would enable better characterization of diseases in muscle.

8 ^{31}P MR Spectroscopy at 7 T

In vivo ^{31}P MRS allows the noninvasive assessment of many fundamental, biochemical, physiological, and metabolic processes by detecting important bioenergetic metabolites such as adenosine triphosphate

(ATP), phosphocreatine (PCr) and inorganic phosphate (Pi) and key physiological parameters including intracellular pH and intracellular free magnesium concentration (Shulman et al. 1979; Ackerman et al. 1980). Phosphorus MRS studies at 7 T have been conducted to investigate the performance improvement with higher magnetic field (Lei et al. 2003; Qiao et al. 2006; Du et al. 2007) and representative brain ^{31}P MRSI are shown in Fig. 11.

In vivo ^{31}P spectra of human occipital lobe acquired at 4 and 7 T under similar experimental conditions have shown that in vivo ^{31}P sensitivity was significantly improved at 7 T compared with 4 T (Qiao et al. 2006). Moreover, the line-width of the PCr resonance peak showed less than a linear increase with increased B_0, which leads to a significant improvement in ^{31}P spectral resolution. These findings demonstrate the advantage of ultra-high magnetic field strength to improve in vivo ^{31}P MRS quality in both sensitivity and spectral resolution.

References

Ackerman JJ et al (1980) Mapping of metabolites in whole animals by ^{31}P NMR using surface coils. Nature 283(5743):167–170

Avdievich NI et al (2009) Short echo spectroscopic imaging of the human brain at 7 T using transceiver arrays. Magn Reson Med 62(1):17–25

Balchandani P, Pauly J, Spielman D (2008) Interleaved narrowband PRESS sequence with adiabatic spatial-spectral refocusing pulses for 1H MRSI at 7 T. Magn Reson Med 59(5):973–979

Chan AA et al (2004) Proton magnetic resonance spectroscopy imaging in the evaluation of patients undergoing gamma knife surgery for Grade IV glioma. J Neurosurg 101(3): 467–475

Choi C et al (2009) In vivo detection of serine in the human brain by proton magnetic resonance spectroscopy (1H-MRS) at 7 Tesla. Magn Reson Med 62(4):1042–1046

Demaerel P et al (1991) Localized ^{1}H NMR spectroscopy in fifty cases of newly diagnosed intracranial tumors. J Comput Assist Tomogr 15(1):67–76

Du F et al (2007) Efficient in vivo 31P magnetization transfer approach for noninvasively determining multiple kinetic parameters and metabolic fluxes of ATP metabolism in the human brain. Magn Reson Med 57(1):103–114

Fulham MJ et al (1992) Mapping of brain tumor metabolites with proton MR spectroscopic imaging: clinical relevance. Radiology 185(3):675–686

Garwood M, DelaBarre L (2001) The return of the frequency sweep: designing adiabatic pulses for contemporary NMR. J Magn Reson 153(2):155–177

Goelman G et al (2007) Chemical-shift artifact reduction in Hadamard-encoded MR spectroscopic imaging at high (3 T and 7 T) magnetic fields. Magn Reson Med 58(1): 167–173

Haddadin IS et al (2009) Metabolite quantification and high-field MRS in breast cancer. NMR Biomed 22(1):65–76

Hetherington HP et al (2010) RF shimming for spectroscopic localization in the human brain at 7 T. Magn Reson Med 63(1):9–19

Hurd R et al (2004) Measurement of brain glutamate using TE-averaged PRESS at 3 T. Magn Reson Med 51(3): 435–440

Klomp DW et al (2009) Proton spectroscopic imaging of the human prostate at 7 T. NMR Biomed 22(5):495–501

Le Roux P et al (1998) Optimized outer volume suppression for single-shot fast spin-echo cardiac imaging. J Magn Reson Imaging 8(5):1022–1032

Lei H et al (2003) In vivo 31P magnetic resonance spectroscopy of human brain at 7 T: an initial experience. Magn Reson Med 49(2):199–205

Luyten PR et al (1990) Metabolic imaging of patients with intracranial tumors: H-1 MR spectroscopic imaging and PET. Radiology 176(3):791–799

Mangia S et al (2007) Sustained neuronal activation raises oxidative metabolism to a new steady-state level: evidence from 1H NMR spectroscopy in the human visual cortex. J Cereb Blood Flow Metab 27(5):1055–1063

Mekle R et al (2009) MR spectroscopy of the human brain with enhanced signal intensity at ultrashort echo times on a clinical platform at 3 T and 7 T. Magn Reson Med 61(6):1279–1285

Metzger GJ et al (2008) Local B_1+ shimming for prostate imaging with transceiver arrays at 7 T based on subject-dependent transmit phase measurements. Magn Reson Med 59(2):396–409

Negendank WG et al (1996) Proton magnetic resonance spectroscopy in patients with glial tumors: a multicenter study. J Neurosurg 84(3):449–458

Nelson SJ (2001) Analysis of volume MRI and MR spectroscopic imaging data for the evaluation of patients with brain tumors. Magn Reson Med 46(2):228–239

Nelson SJ, Vigneron DB, Dillon WP (1999) Serial evaluation of patients with brain tumors using volume MRI and 3D ^{1}H MRSI. NMR Biomed 12(3):123–138

Nelson SJ et al (2002) In vivo molecular imaging for planning radiation therapy of gliomas: an application of 1H MRSI. J Magn Reson Imaging 16(4):464–476

Park I et al (2007) Patterns of recurrence analysis in newly diagnosed glioblastoma multiforme after three-dimensional conformal radiation therapy with respect to pre-radiation therapy magnetic resonance spectroscopic findings. Int J Radiat Oncol Biol Phys 69(2):381–389

Pauly J et al (1991) Parameter relations for the Shinnar-Leroux selective excitation pulse design algorithm. IEEE Trans Med Imaging 10(1):53–65

Preul MC et al (1996) Accurate, noninvasive diagnosis of human brain tumors by using proton magnetic resonance spectroscopy. Nat Med 2(3):323–325

Provencher SW (1993) Estimation of metabolite concentrations from localized in vivo proton NMR spectra. Magn Reson Med 30(6):672–679

Qiao H et al (2006) In vivo 31P MRS of human brain at high/ultrahigh fields: a quantitative comparison of NMR detection sensitivity and spectral resolution between 4 T and 7 T. Magn Reson Imaging 24(10):1281–1286

Ramadan S et al (2010) In vivo 1D and 2D correlation MR spectroscopy of the soleus muscle at 7 T. J Magn Reson 204(1):91–98

Ren J et al (2008) Composition of adipose tissue and marrow fat in humans by 1H NMR at 7 Tesla. J Lipid Res 49(9):2055–2062

Rock JP et al (2002) Correlations between magnetic resonance spectroscopy and image-guided histopathology, with special attention to radiation necrosis. Neurosurgery 51(4):912–919 discussion 919–20

Ross BD et al (1992) Spatially localized in vivo 1H magnetic resonance spectroscopy of an intracerebral rat glioma. Magn Reson Med 23(1):96–108

Scheenen TW, Heerschap A, Klomp DW (2008) Towards 1H-MRSI of the human brain at 7 T with slice-selective adiabatic refocusing pulses. MAGMA 21(1–2):95–101

Schricker AA et al (2001) Dualband spectral-spatial RF pulses for prostate MR spectroscopic imaging. Magn Reson Med 46(6):1079–1087

Schulte RF et al (2004) Equi-ripple design of quadratic-phase RF pulses. J Magn Reson 166(1):111–122

Setsompop K et al (2008) Slice-selective RF pulses for in vivo B_1+ inhomogeneity mitigation at 7 Tesla using parallel RF excitation with a 16-element coil. Magn Reson Med 60(6):1422–1432

Shinnar M (1994) Reduced power selective excitation radio frequency pulses. Magn Reson Med 32(5):658–660

Shulman RG et al (1979) Cellular applications of 31P and 13C nuclear magnetic resonance. Science 205(4402):160–166

Snyder J, Wilman A (2010) Field strength dependence of PRESS timings for simultaneous detection of glutamate and glutamine from 1.5 to 7 T. J Magn Reson 203(1):66–72

Spielman DM, Adalsteinsson E, Lim KO (1998) Quantitative assessment of improved homogeneity using higher-order shims for spectroscopic imaging of the brain. Magn Reson Med 40(3):376–382

Srinivasan R et al (2010) MR spectroscopic imaging of glutathione in the white and gray matter at 7 T with an application to multiple sclerosis. Magn Reson Imaging 28(2):163–170

Stanwell P et al (2005) Specificity of choline metabolites for in vivo diagnosis of breast cancer using ^{1}H MRS at 1.5 T. Eur Radiol 15(5):1037–1043

Star-Lack J et al (1997) Improved water and lipid suppression for 3D PRESS CSI using RF band selective inversion with gradient dephasing (BASING). Magn Reson Med 38(2):311–321

Tkac I et al (2001) In vivo ^{1}H NMR spectroscopy of the human brain at 7 T. Magn Reson Med 46(3):451–456

Tran TK et al (2000) Very selective suppression pulses for clinical MRSI studies of brain and prostate cancer. Magn Reson Med 43(1):23–33

Ugurbil K et al (2003) Ultrahigh field magnetic resonance imaging and spectroscopy. Magn Reson Imaging 21(10):1263–1281

Wang L et al (2009) Relaxation times of skeletal muscle metabolites at 7 T. J Magn Reson Imaging 29(6):1457–1464

Xu D et al (2006) Time efficient flip angle measurement at 7 T. In: 14th Annual Scientific Meeting of International Society of Magnetic Resonance in Medicine. Seattle, Washington, USA

Xu D et al (2007) 2D J-Resolved Spectroscopy at 7 T. In: Annual Meeting of Society of Magnetic Resonance in Medicine. Berlin, Germany

Xu D et al (2008) Phased array 3D MR spectroscopic imaging of the brain at 7 T. Magn Reson Imaging 26(9):1201–1206

Molecular and Translational Research

Dominik von Elverfeldt, Wilfried Reichardt, and Laura Harsan

Contents

Abstract

MR imaging and spectroscopy of small animals has been around for more than 3 decades and in fact preceded clinical MR in humans. With the advance of 'molecular imaging', the field has taken a new twist by strengthening the link of research on animal models with molecular biology at one side and with applications in translational research on humans on the other side. Given the wealth of research in small animal MR over the past and especially the explosive and very heterogeneous growth of the field today, it would be futile to attempt to present a comprehensive overview in a single book chapter. The authors have therefore limited the scope to some illustrative examples from their own research focusing on translational aspects and examples, where small animal MR has a direct link and implication to UHF-MR in humans. The rather eclectic selection is thus not meant to be representative and the omission of important topics like MR spectroscopy, functional imaging or research into brain ischemia—to name just a few—by no means meant to derogate the relevance of the extremely lively research efforts by the large variety of laboratories working in this field.

1 Introduction

Magnetic field strengths in small bore magnets for small animal MR are typically much higher compared to large magnets used for humans. 7 T has been the standard field strength for animal MR for years, and

D. von Elverfeldt (✉) · W. Reichardt · L. Harsan
Department of Medical Physics,
University Hospital Freiburg,
Breisacher Straße 60a, 79106 Freiburg, Germany
e-mail: dominik.elverfeldt@uniklinik-freiburg.de

J. Hennig and O. Speck (eds.), *High-Field MR Imaging,* Medical Radiology. Diagnostic Imaging,
DOI: 10.1007/174_2010_132, © Springer-Verlag Berlin Heidelberg 2011

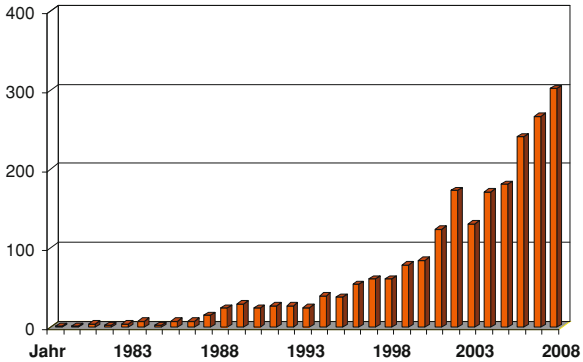

Fig. 1 PubMed search on animal model, rat/mice and MRI, total hits 2,426

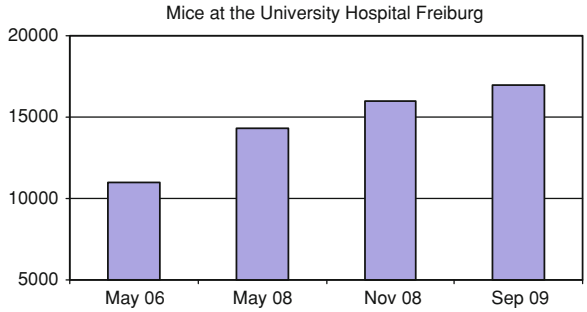

Fig. 2 Total numbers of mice used in experiments at the university hospital Freiburg

11.7 T systems are proliferating rapidly and there are a few installations of horizontal bore systems at even higher fields of up to 16 T. Scaling factors in MR are highly nonlinear, so some issues of major concern for UHF-MR in humans are irrelevant for MR of mice and rats. This is mainly true for issues related to the RF-field (see Radiofrequency coils and Safety), where even at the highest available field strengths, one safely stays in the near-field regime, and B_1-inhomogeneities and SAR considerations are of secondary concern. Main technological and methodological issues for high field small animal imaging are susceptibility effects, which pose severe (but not insurmountable) challenges for sequences like EPI, balanced SSFP, and all nonrectilinear scans like radials, spirals, and others. The jagged landscape of susceptibility-induced background fields not only leads to image distortions and artifacts. Even slight motion in steep local gradients leads to severe transient misencoding and therefore to strong image artifacts. Therefore, imaging of live animals becomes increasingly challenging, and applications on non-moving specimen and dead animals are becoming more and more prevalent with increasing field strength. MR on animals has been successfully applied in a wide range of sizes and species including insects, spiders, small and large fish, shrimps, rodents, monkeys, minipigs, pigs, dolphins, tigers, and horses. For translational research, the application market is cornered by mice and rodents, for which genetically modified animal models for a broad range of diseases are reasonably easily accessible (see Fig. 1).

Animal models of human pathologies help to learn about the origin, progression, symptoms, and possible treatment approaches. Given modern genetic engineering techniques, the number of animal models is steadily increasing. Most of these are in rats and especially mice as these are easily genetically modified, bred, and sustained. Therefore, preclinical research is predominantly performed in rodents. The commercial breeder Charles River™ to date has 31 rat and 30 mouse strains in stock of standard animal models for various diseases including but not limited to obesity, nephropathy, diabetes mellitus, and cardiovascular disease (Charles River Laboratories International 2010). In 2009, our institution at the University Medical Center Freiburg housed a total of 17,000 mice for experimental purposes only, excluding breeding of new strains (See Fig. 2).

This number has risen from 11,000 in 2006 and its rising has been recently somewhat slowed down due to housing capacity limitations. With 76 animal experiment licenses, applications covering a total of 39,600 mice have been approved (see Fig. 3) by active and approved IRBs.

This increase in animal models leads to an increasing request for preclinical imaging. Amongst other imaging modalities like microCT, miniSPECT, miniPET, and optical imaging, MR offers the unique opportunity to provide insight into function or molecular expression together with anatomical information. Beyond exquisite morphological imaging, MR can measure diffusion, perfusion, brain function, tissue oxygenation, metabolic profiles as well as microstructural parameters like vessel size index and neuronal fiber orientation, to name some examples. In addition to its potential for multiparametric and functional characterization, MR allows repetitive longitudinal studies in individual animals, which lead to a significant reduction in animals

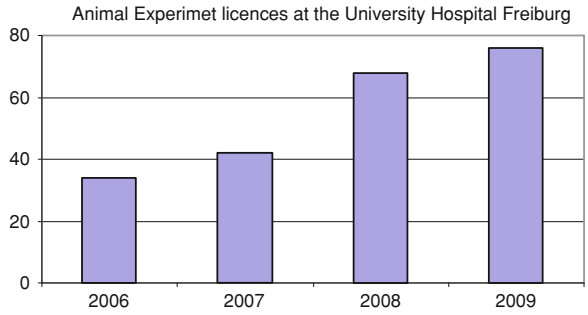

Fig. 3 Number of granted animal experiment licenses applications

needed in e.g. therapy monitoring. This allows accelerated development by replacing conventional experimental setups where animals have to be killed at each time point. Follow-up on individual animals increases statistical fidelity at a dramatic decrease in the number of killed animals. MR imaging thus supports the widely accepted ethical framework named "the three R's" for conducting scientific experiments using animals that requests to aim for: Replacement, Refinement and Reduction (Russel and Burch 1959).

When considering MRI of rodents as a model for human disease, the changes in scale on both the overall size of the subjects as well as the physiological relevant structures have to be considered. For example, in visualizing the germinal centers in the mouse spleen responsible for B lymphocytes production, the scale of the imaging target is similar to that in humans (300–500 μm). Contrary to that, the spleen itself scales down from approximately 12 × 8 × 4 cm to 1.5 × 0.4 × 0.2 cm from men to mice, a volume reduction of a factor 3,200. Thus, depending on the specific question addressed, the MRI measurement must consider the addressed task and not simply the scale of the animal alone. Nevertheless, the loss of signal-generating volume needs to be accounted for if imaging small animals.

Small animals allow for small receiving coils, magnets with small bore sizes, and field gradient systems with less volume to cover. Close placement and matching size of the coil to the target organ increases the filling factor and thus the SNR of the measurement. For an optimal match of coil to the given task, a gain in SNR by a factor of 4–10 can be easily reached compared to standard coil setups. Animal MR centers are characterized by a large zoo of coils for specific applications.

The higher field strength achievable in small magnets leads to an increase in SNR, which can be used to at least partially compensate for the increased spatial resolution necessary to match anatomical resolution. An image resolution of 0.2 mm × 0.2 mm × 0.5 mm is easily achievable at 9.4 T at short measurement times (1–3 min). Finally, the small size of the animals also permits the use of very strong imaging gradients ranging above 1,000 mT/m without any detrimental neuronal stimulation effects (Balaban 2001) (see Safety).

The following chapter represents an eclectic overview on the scope of high field MRI in translational and molecular preclinical research. It demonstrates examples from different types of examinations typically used in translational research. Given the confined available space, a structure according to different methodological approaches has been chosen with examples from a broad range of application fields including oncology, neurodisease, and other pathologies.

The most straightforward application of small animal MR in translational research is the performance of standard morphological imaging as used in standard MRI in humans. Apart from minor variations in image contrast due to field dependence of contrast parameters like T_1, T_2, and MT, images of close to identical contrast and anatomical resolution can be acquired. This allows for direct comparison of animal models to findings in humans. Given the opportunity for histological work-up and verification in animal models, this allows a straightforward understanding of the physiological and pathophysiological changes underlying observed changes in diagnostic examinations in humans. The one-to-one correspondence between animal and human images also allows straightforward assessment, whether a chosen animal model truly represents the human situation—which more often than not is not or only partially the case.

The following examples of morphological imaging show the potential in supporting histology and phenotyping as well as in longitudinal therapy monitoring in tumor therapy. This is exemplified in results from a mouse kidney study on cystic mouse kidneys in Sect. 2.3 and the physiological imaging of tumor progression and treatment response done by dynamic contrast-enhanced MRI in Sect. 3.2. Examples of physiological imaging include diffusion-weighted imaging(DWI) in Sect. 3.1 as well as DCE-MRI in

tumor models in Sect. 3.2 Both techniques are widely used in patient studies and diagnostic applications. Experiments in animal models allow understanding the underlying pathophysiological mechanisms and assessing the validity of animal models.

Section 4 demonstrates the use of diffusion tensor imaging in mouse brain as a valid tool in neuroscientific research on models for white matter disease. Direct and individual comparison of fiber tracks generated by DTI with histological staining also allows to validate fiber tracking algorithms used to translate diffusion anisotropy information into fiber tracts.

The last two subchapters are dedicated to describe examples of targeted imaging with molecular labels used for tracking of dendritic cells (Sect. 5) and for selective labeling of thrombolithic platelets (Sect. 6).

2 Preclinical High Resolution MRI

One of the most valuable features of high field animal MR imaging is the possibility to show anatomical details in rodents on a level that is equivalent to imaging in humans. It is therefore possible to study the interaction of anatomic and physiologic properties in animal models, with high correlation to human data and clinical settings. Once a new model for a disease is generated, the morphological characterization of the model is of great relevance to study the efficacy and adverse effects of experimental treatments of the underlying human disease. Ultrahigh resolution μMRI is achieved in ex vivo scans with a resolution below 30 μm (Schneider et al. 2003a, b; Schneider et al. 2004) that would typically run overnight, or even below 20 μm (Petiet et al. 2007; Driehuys et al. 2008) within 3-h scan time, involving a more sophisticated staining protocol (Petiet et al. 2007). However, since morphologic properties of different tissues change ex vivo and especially for longitudinal observations, morphological imaging is preferably performed in vivo.

2.1 Mouse Brain Magnetic Resonance Histomorphology

In neuroscience research, the use of genetically modified organisms, and in particular mice, has become indispensable for testing biological hypotheses and for advancing our knowledge of the brain and its diseases. Along with the development of gene targeting approaches and the increasing number of animal models that mimic human brain disorders, neuroimaging plays an increasingly important role. Magnetic resonance imaging (MRI) has emerged as an important approach to study noninvasively brain development and pathology. Despite the fact that the mouse brain is approximately 1,000 times smaller than the human brain, MRI methods have advanced to a degree that the effective neuroanatomical resolution is exceeding that of human brain MRI (Johnson et al. 2007; Badea et al. 2009a, b). In mouse brain, high resolution MRI from ex vivo samples approaches the limits of 10 μm imposed by water diffusion. High resolution mouse brain atlases were generated from data acquired with 20–60 μm isotropic resolution. This approaches the thickness of a histological slice. Whereas the histological preparation requires intensive, time-consuming labor, a high resolution 3D scan (i.e. 21.5 μm isotropic) of a fixed mouse brain could be obtained in less than 2 h (Badea et al. 2007; Kim et al. 2009). Although the in-plane resolution of MR is still far lower than that of a histological slide, the spatial resolution and contrast of MR is sufficient for characterization of changes induced by pathologies and interventions and for phenotyping of animal models. The recent progress was also due to new developments in specimen preparation, such as the use of the paramagnetic contrast agents delivered transcardially during the perfusion and fixation procedures. Gadolinium (Gd)-, Manganese (Mn)-, or Iron (Fe)-based contrast agents are routinely employed for better delineation of different brain components. Figure 4 shows the hippocampus layers demarcated on a 53-μm isotropic resolution image, after perfusion with Gd-DTPA.

These "staining" procedures combined with adapted acquisition settings and improved acquisition hardware allowed the "genetic dissection" and segmentation of small mouse brain structures (Badea et al. 2009a, b). This methodology provides a means for the creation of data banks and atlases, useful for correlation of morphological features with physiological and behavioral phenotypes, or comparison between mouse strains. The obtained contrast between small, subtle brain regions (such as thalamic nuclei) insure the feasibility of automatic segmentation and size quantification of up to 40 (Sharief et al. 2008)

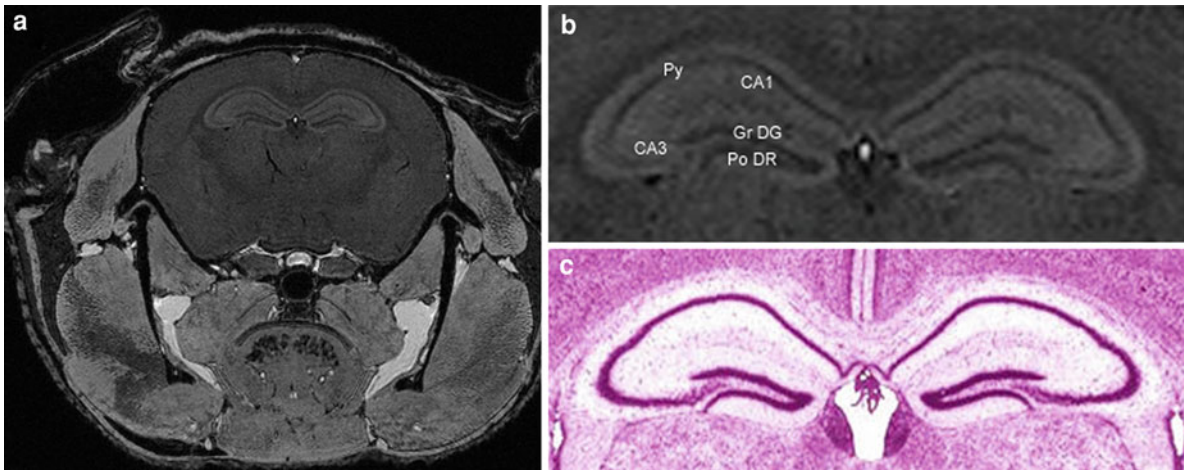

Fig. 4 Ex-vivo mouse brain MR image (**a**), showing the hippocampus layers (**b**) in comparison with the Nissl staining (High resolution mouse brain atlas: http://www.hms.harvard.edu/research/brain/intro.html) (**c**). Imaging was performed at 9.4 T with a 53 μm isotropic resolution

or 62 (Dorr et al. 2008) structures. The sensitivity of high field MR microscopy to quantify subtle variations was further highlighted while analyzing the brain of isogenic mice (clone of identical twins) housed in identical environmental conditions (Johnson et al. 2007; Sharief et al. 2008).

Direct observation of cortical layers in vivo was recently demonstrated (Boretius et al. 2009a, b) at high field strength (9.4 T). Data with a T_2-weighted fast spin echo sequence and a resolution down to $30 \times 30 \times 300$ μm^3 unravel up to 5 different layers in the cerebral cortex and demonstrate the internal structure of the hippocampus, cerebellum, and olfactory bulb lamination. The study emphasized the importance of physiological monitoring to avoid motion artifacts by respiratory movement. Mice were intubated and placed in a special designed animal bed for stabilization.

A breakthrough for high resolution imagining of small animal brains is given by the latest developments in coil technology using superconductive cryoprobes. Cryoprobes afford an increased sensitivity by a factor of 2–3 compared to standard room temperature RF-coils in routine imaging applications. Images of the mouse cerebellum assessed in vivo in about 30 min with 30 μm in-plane resolution using the cryoprobe showed micro structures comparable to ex vivo histology (Nissl staining) (Baltes et al. 2009). Purkinje cell layer of the cerebellum (25–30 μm) and molecular layer (150–200 μm) could be clearly delineated. Moreover, three-dimensional acquisitions with isotropic coverage ($60 \times 60 \times 60$ μm^3) of the mouse cerebral cortex enabled the identification of small intracerebral structures in 45 min of scanning time. The high signal to noise ratio obtained with the MRI cryoprobe also enables high resolution angiography showing tiny branch vessels in the mouse brain in 30-min acquisition time.

2.2 Mouse Phenotyping of Animal Dystrophic Epidermolysis Bullosa (DEB) Model

Dystrophic epidermolysis bullosa (DEB) is a debilitating disease characterized by the formation of blisters in the skin, which is extremely fragile.

The generation of new animal models allows for gaining insights into the pathogenesis and new potential treatment options. In this animal model (Fritsch et al. 2008), a hypomorphic mouse was generated that features a pathophysiology that closely resembles the human disease DEB. The developed collagen VII hypomorphic mouse has 10% of the normal collagen VII levels in the skin and develops all the symptoms of severe RDEB. It also survives to adulthood and has a normal immunocompetence, which makes it ideally suited for analysis of molecular pathogenesis of DEB and evaluation of novel therapeutic strategies. The MR images shown in Fig. 5 resemble the appearance of the

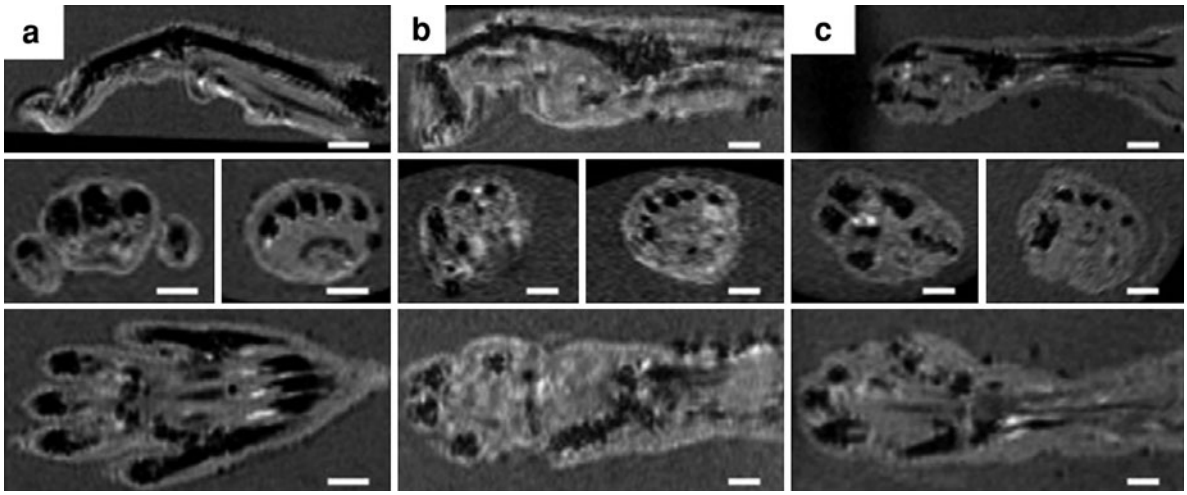

Fig. 5 High resolution MRI in sagittal (*top panels*), transversal (*middle panels*), and coronal (*bottom panels*) orientation in mildly (**b**) and strongly affected (**c**) *Col7a1flNeo/flNeo* mice as well as *Col7a1WT/WT* mice (**a**) revealed the extent of deformities and thickening of the soft tissues. *Scale bars*: 1 mm (**a–c**)

disease. The model was also demonstrated to be useful for therapy monitoring.

2.3 Mouse Kidney Imaging and Therapy Monitoring

Next to the transition of novel technologies from preclinical to clinical research, translational research also works in the opposite direction. Already established clinical protocols for specific diseases can be investigated by preclinical evaluation or preclinical drug testing. New drugs or therapeutical approaches can then be evaluated in animal models using the same modality as in a clinical trial, which enhances the significance of the preclinical data (Fig. 6).

Excessive proliferation of renal epithelial cells and the transformation from an absorbing to a secreting epithelium lead to cyst propagation and enlargement that eventually replaces most of the normal surrounding tissue and is accompanied by higher apoptosis rates (Calvet and Grantham 2001; Wilson 2004).

So far, magnetic resonance imaging (MRI) is the preferred modality for monitoring of the disease progression as well as most precise modality to monitor changes that are induced by therapeutic interventions. Recent developments demonstrated the possibility of pharmaceutical treatment of ADPKD to decelerate the growth of the cyst, protracting the onset of hemodialysis (Shillingford et al. 2006; Walz 2006). The clinical course and morphology of the slowly growing murine kidneys resemble the human adult form of polycystic kidney disease. Fluid-filled renal cysts can be identified in all segments of the nephron and collecting duct and are progressively enlarged with age. MRI has already proven to be a reliable method to measure renal volumetric indices in preclinical (Sun et al. 2002; Kobayashi et al. 2004; Shillingford et al. 2006) and clinical studies (Grantham 2006; Grantham et al. 2006). As dedicated animal scanners have not been widely available in the past, only renal volume had been used in animal models to monitor treatment effects. Because of their superior signal to noise ratio, high field MRI scanners have the potential to generate clinically relevant information. There are several animal models for PKD in mice (Takahashi et al. 1986; Liu et al. 2002) and rats (Lager et al. 2001).

Figure 7 shows the effect of treatment on the progress of the disease in the animal model longitudinally by using high field animal MRI. Because it is possible to use different statistical evaluations, these longitudinal studies are enabling drug treatment studies with less animals than traditional setups.

Next to treatment studies, it is also possible to characterize different genotypes and the influence of gene-directed therapies, which are based on the understanding of cystic growth.

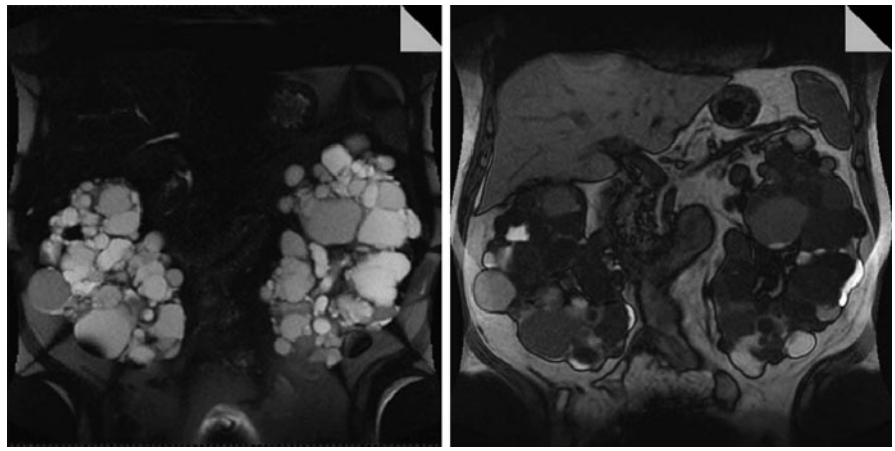

Fig. 6 A: T_2-weighted HASTE images showing the typical morphology of the human ADPKDB: OPP-phase-FLASH image of the same patient

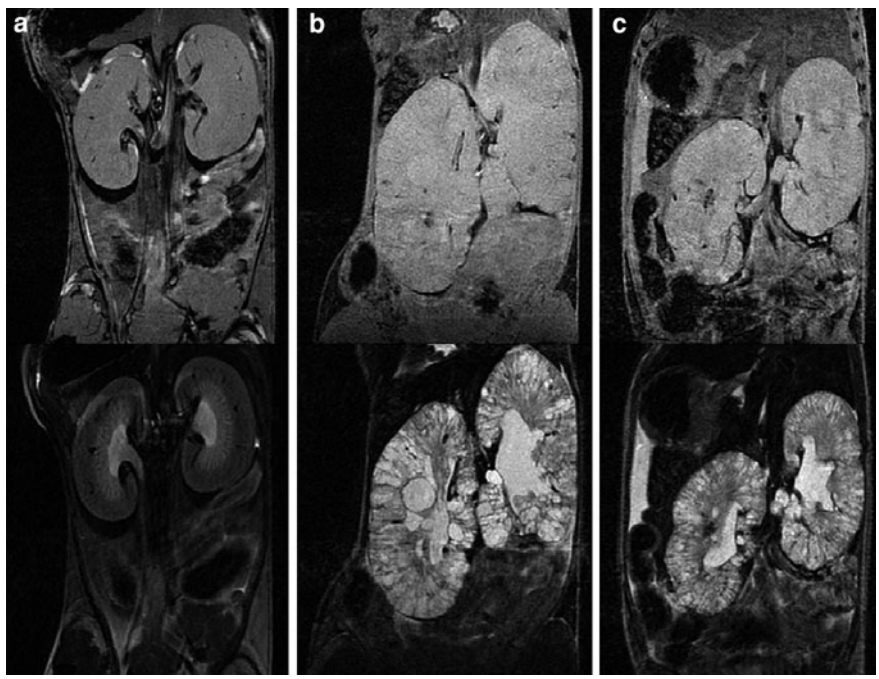

Fig. 7 *Upper row*: FLASH images with TE = 5.4 ms; *Lower row*: RARE images with TEeff = 36 ms. Colum (**a**) depicts wild type mice, (**b**) the untreated pcy-mouse model, and (**c**) the rapamycin treated pcy-mouse model

2.4 High Resolution Animal MRI in Oncology

The research and development of novel treatment approaches is a major current goal in oncological research. Testing and evaluation of potential new drugs in animal models is an important part of the development in this field. Small animal MR is extensively used in preclinical oncology research, because it allows the monitoring of treatment effects and the disease progression with techniques that are applicable in preclinical and clinical studies alike.

Combined application of parametric measurements has been shown to be a promising tool for therapeutic monitoring and imaging phenotyping of animal models. The pathologic behavior of the primary tumor and its metastasis requires interactions between the malignant cells and normal tissues as occurs in invasion into blood and lymph vessels, extravasation, migration, and neovascularization (Coussens et al.

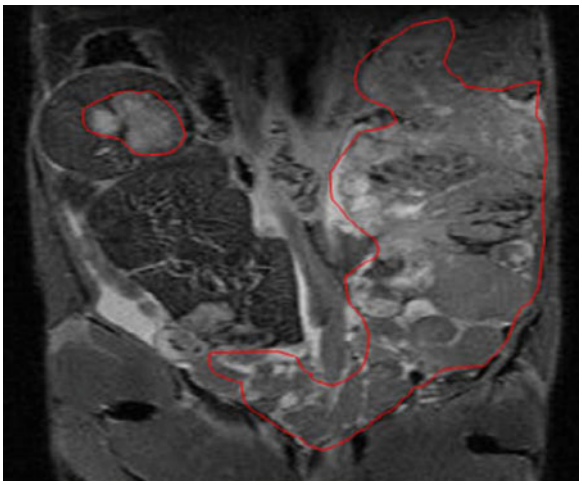

Fig. 8 TRAMP-model of prostatic cancer in the mouse. The mass of the Tumor is depicted in *red*

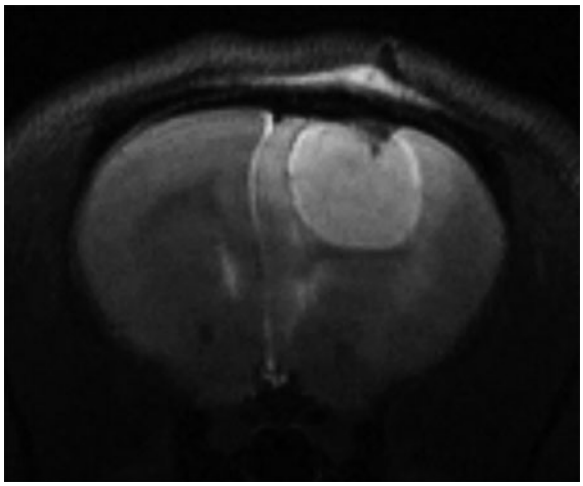

Fig. 9 Shows a model for gliomas using U87 rat glioma cells that are implanted into the right putamen via stereotactic intervention into the brain of nude rats

1996). While individual steps in these processes may be modeled in cell culture assays, assessment of the interactive processes of tumor cell motility requires the context of living animals.

2.4.1 Orthotopic Model for Prostate Cancer

In recent years, a number of newly developed orthotopic tumor models were applied in oncology research and drug development. In contrast to the nonorthotopic tumor models, the microenvironment of orthotopic models is much closer to the physiological situation in humans compared to subcutaneous tumor implantations. However, since the tumors are not easily visible and accessible for measurements, it is mandatory to closely follow the progression and potential treatment options for these tumors.

Figure 8 shows the MR image of the TRAMP (*t*ransgenic *a*denocarcinoma of the *m*ouse *p*rostate) mouse model. In this model, male mice express the SV40 large T antigen under the control of a prostate-specific androgen-dependent rat probasin promoter leading to prostate cancer during their development that has been developed for the evaluation of novel therapeutic approaches like DNA vaccination (Greenberg et al. 1995). Male TRAMP mice exhibit consistent prostate-specific patterns of expression and develop prostatic intraepithelial neoplasia that will become invasive and metastasize primarily to the lymph nodes and lungs. By using high field animal imaging, it is possible to test new therapeutic approaches on prostate cancer using this orthotopic model.

2.4.2 Orthotopic Model for Glioma

In the case of gliomas, an orthotopic model is also of special interest, since the specific properties of the brain and brain tumors, like the blood brain barrier, are important for the pathological behavior of the tumors and their treatment. The preclinical evaluation of these models is therefore of special significance in the development of new therapeutical approaches (Fig. 9).

2.5 High Resolution Imaging of the Mouse Spleen

Animal MRI at high fields can provide deeper insights into anatomy on a histomorphological level. This is especially the case where anatomical structures in mice are of similar size as in humans. The mean size of germinal centers in lymph nodes is about 300–500 μm. Germinal centers (also known as B-lymphatic follicles) are sites within lymph nodes or lymph nodules in peripheral lymph tissues where intense mature B lymphocytes rapidly proliferate, differentiate, mutate through somatic hypermutation, and class switch during antibody responses. They

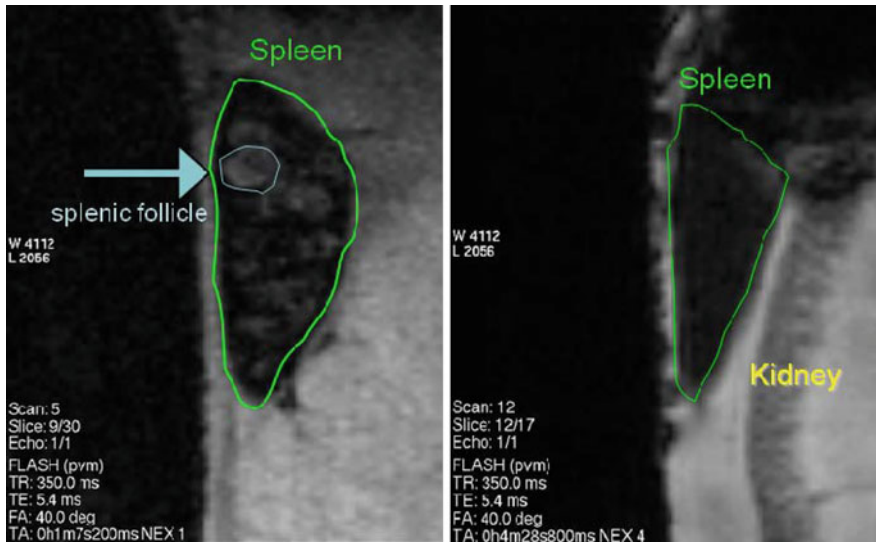

Fig. 10 Shows a splenic follicle (approx. 500 μm) in a BL6 wild-type mouse (*left*). The right picture shows the absence of lymphatic follicles in an immunodeficient mouse strain (BalbC)

develop dynamically after the activation of B cells by T-dependent antigen. Histologically, the GCs describe microscopically distinguishable parts in lymphoid tissues. Germinal centers are less perfused compared to the rest of the spleen. They are therefore well depicted in gradient echo sequences because of their different blood content. Figure 10 shows the spleen in C57BL6 mice and in immunocompromised BalbC mice. As the BalbC mice lack the activation of B cells, they fail to develop germinal centers in the spleen as it is shown in the picture. Up to now, germinal centers cannot be imaged in humans, but due to technical improvements (transmit-sense) and higher field strengths used for human systems, this seems possible in the future.

3 Physiological Imaging in Tumor Models

The use of imaging biomarkers for the detection and characterization of cancers as well as for monitoring the response to therapy is extremely valuable. With ongoing technological developments, novel imaging methodologies appear rapidly and their utility requires systematic evaluation. One of the great advantages of MRI is that in addition to morphology and volumetry, a broad spectrum of physiological processes can be quantitatively imaged. Next to perfusion and the microscopic mobility of water (diffusion), the hemodynamic properties of a tumor or the tumor vasculature are of great interest. High field MRI offers the possibility to measure these physiological processes in small animal models with the required sensitivity.

3.1 Diffusion-Weighted Imaging (DWI)

Diffusion-weighted imaging (DWI) depends on the microscopic mobility of water. This mobility is due to thermal agitation and is highly influenced by the cellular environment of water. Therefore, findings on DWI could be an early indication of biologic abnormality. The most established clinical indication for DW-MRI is the assessment of cerebral ischemia where DWI findings precede all other MR techniques (Johnston et al. 2007).

Current general oncologic imaging already incorporates diffusion-weighted MRI because of its high sensitivity (Thoeny and De Keyzer 2007; Patterson et al. 2008). DW-MRI does not require intravenous contrast media and thus can be used in patients with reduced renal function at little extra cost. DWI can be used for improved tissue characterization (differentiating benign from malignant lesions), for monitoring treatment response after chemotherapy or radiation, for differentiating post-therapeutic changes from residual active tumor, and for detecting recurrent cancer. Potential additional roles include predicting treatment outcomes (before and soon after starting therapy) and for tumor staging.

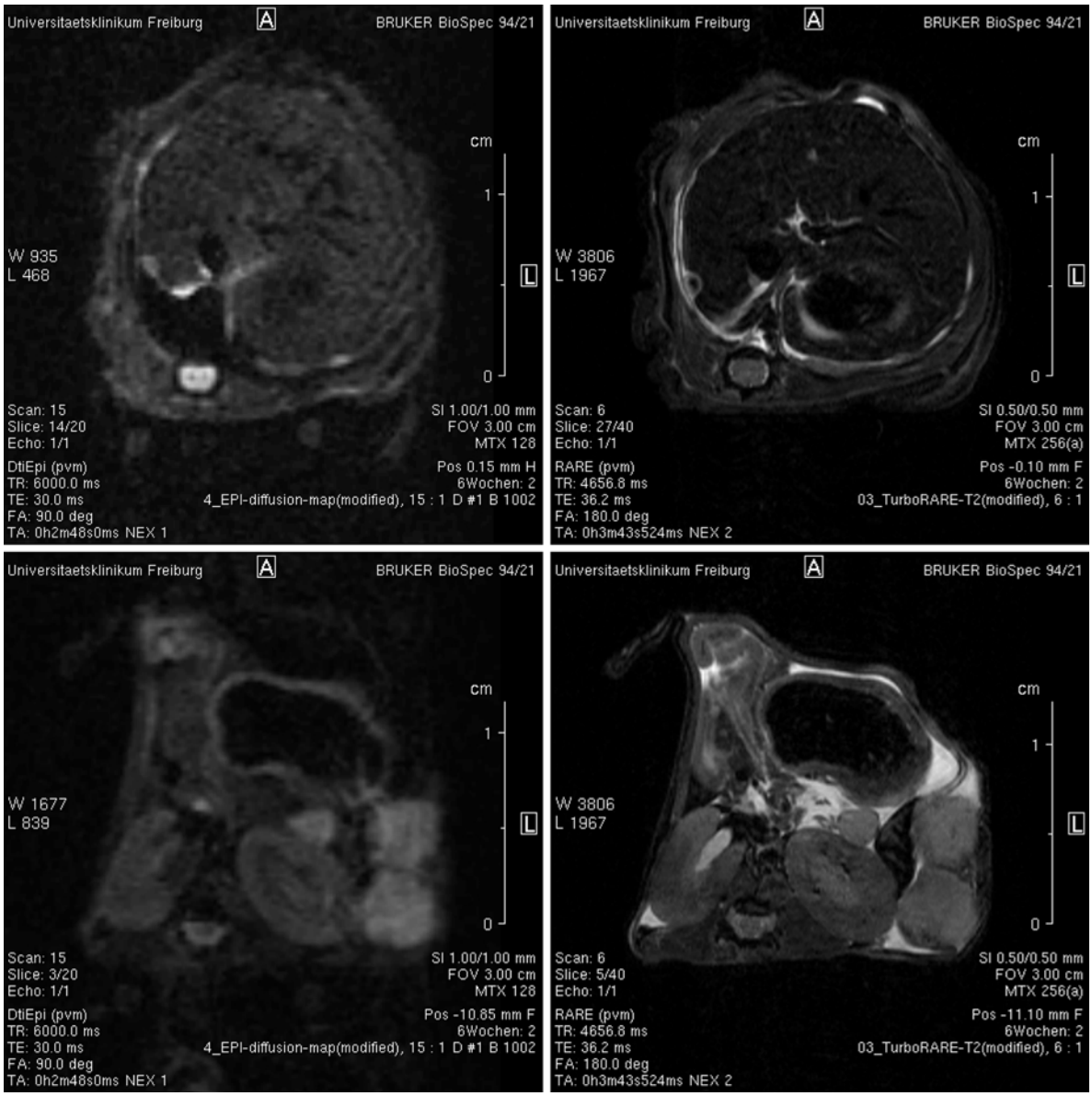

Fig. 11 In this picture, an animal model for pancreas carcinoma is shown. In the *upper row* a liver metastasis is visible (*arrow*), which is more clearly depicted by the diffusion-weighted image (*b*-value: 1,002). *Lower row*: in this picture the primary tumor is clearly visible in both sequences. However, the signal intensity depicts the neoplastic tissue visibly from the surrounding tissue in the diffusion-weighted image

Evidence from preclinical and clinical studies in oncologic imaging suggests that DWI is linked to lesion aggressiveness and tumor response, although the biophysical basis for this is not yet completely understood. Quantitative parameters derived from DWI like the apparent diffusion coefficient (ADC) are appealing as imaging biomarkers because the acquisition is noninvasive, does not require any exogenous contrast agents, does not use ionizing radiation, and can be obtained relatively rapidly and is easily incorporated into routine patient evaluations (Fig. 11).

Malignant tumors are characterized by reduced ADC values. The reasons for these findings are poorly

understood. Possible hypothesis include a combination of higher cellularity, tissue disorganization, and increased extracellular space tortuosity, all contributing to reduced motion of water. Correlations with cellularity have been found for some primary and secondary neoplasms (Squillaci et al. 2004; Hayashida et al. 2006; Humphries et al. 2007) but not for all tumors such as adenocarcinomas and necrotic lesions that correlate only weakly (Hayashida et al. 2006; Yoshikawa et al. 2008). Diffusion-weighted MRI is able to differentiate between benign and malignant focal hepatic lesions in many cases based on the higher ADC of benign lesions compared with malignant lesions (Taouli et al. 2003).

3.2 DCE-MRI

DCE-MRI provides the possibility to characterize tissue vasculature noninvasively including the anti-angiogenic response of tumor tissue during therapeutic intervention. It provides insight into tumor perfusion and capillary permeability and hence allows the evaluation of treatment response earlier than the delayed assessments of morphologic changes of the tumor. It is therefore widely used to evaluate clinical (Morgan et al. 2003) and preclinical (Maxwell et al. 2002; Strecker et al. 2003; Rudin et al. 2005) settings of anti-angiogenic treatment in animal models.

However, the implementation of DCE-MRI at high field in animal models is challenging. High magnetic fields afford a better signal/noise ratio (SNR) and consequently a better spatial resolution in a shorter acquisition time, but on the other hand, the primarily used sequences (TrueFISP) are more prone to artifacts because of the higher field strength. They are caused by the stronger field inhomogeneity in high field animal systems compared to magnets used in the clinical routine. Furthermore, the large discontinuities in bulk magnetic susceptibility, like the ones occurring at tissue interfaces, cause geometric distortions and image intensity variations. In addition to time-invariant off-resonance effects such as B_0 field inhomogeneities, dynamic field variations induced by eddy currents may further contribute to the observed image distortions.

DCE-MRI is based on measuring the temporal profile of a paramagnetic contrast agent after intravenous injection in the vascular and tissue compartment by dynamic T_1 mapping. Using tracer kinetic models, several parameters including vessel wall permeability, tumor blood volume, and extracellular, extravascular leakage space can be derived (Weidensteiner et al. 2006). These factors are associated with specific histopathological features of the tumor (Hashizume et al. 2000), with more aggressive tumors commonly exhibiting a more rapid and intense enhancement and washout, representing a higher vascular density and strong expression of VEGF. In response to therapy, it is often observed that the vascular permeability is reduced in the neoangiogenic vessels and this is reflected by a decrease in the rate of enhancement.

Also encouraging is the ability of DCE-MRI to visualize the heterogeneity in angiogenic properties within an individual tumor. This is crucial in assessing early therapy response and individualizing treatment regimes as it may allow for identification of a small subpopulation of tumor cells that remain after treatment.

3.2.1 Matrigel Implants as Model of Angiogenesis

One of the main goals of preclinical research is to improve the translational value of the animal models for a variety of disease. In a recent paper (Alajati et al. 2008), a method was demonstrated on how to establish a functional three-dimensional network of human neovessels connected to the mouse vascular system when implanted subcutaneously. The grafted human vasculature matures and connects to the mouse blood vascular system. This assay allows studying a fully humanized vasculature in mice. Since DCE-MRI is well established as a modality to study the effect of antiangiogenic therapies in vivo in clinical studies, this technique can provide substantial information on the newly formed human vasculature under therapy (Fig. 12).

4 Diffusion Tensor MRI and Fiber Tracking of the Mouse Brain

4.1 Introduction

Neuronal tissues in general and the white matter in particular are complex tissue structures and their detailed characterization represents an ambitious task.

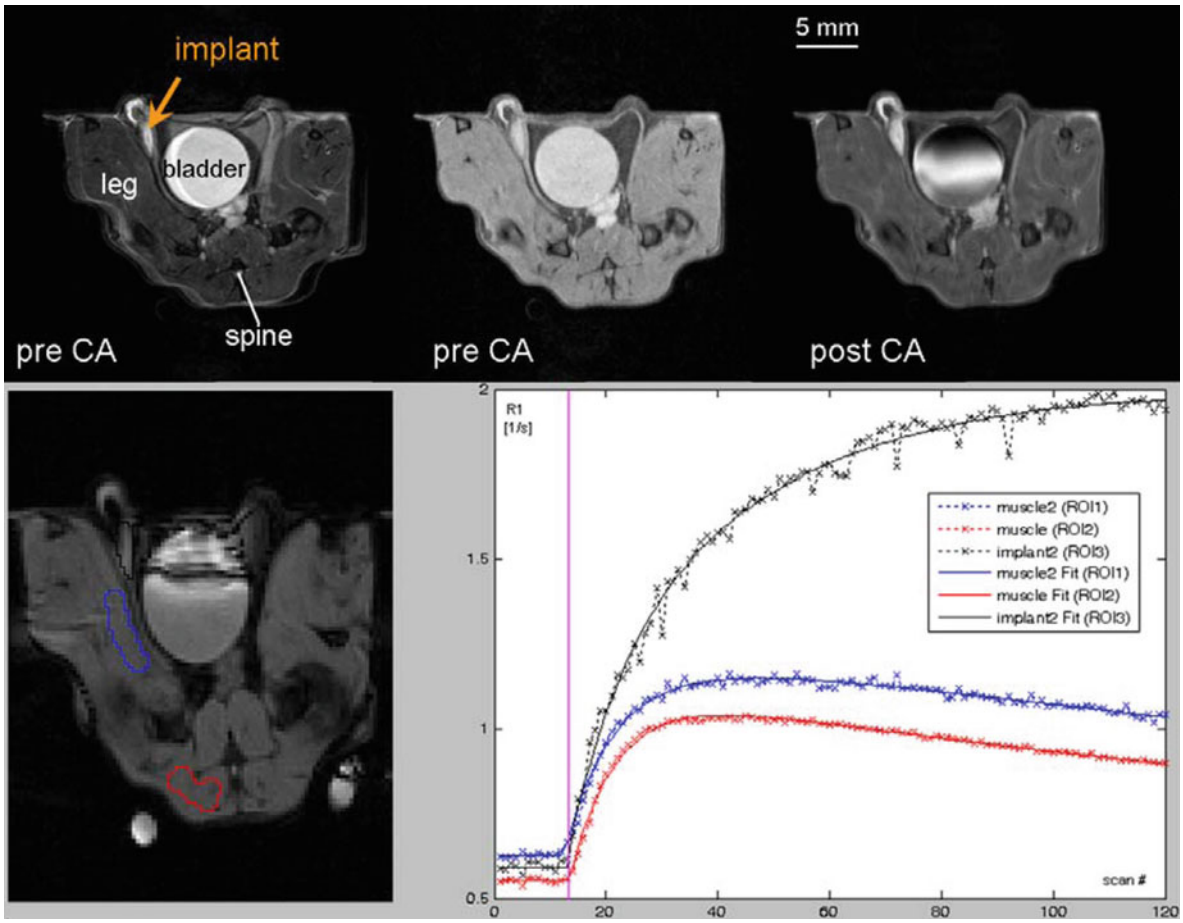

Fig. 12 Anatomical MR images of Matrigel plugs in vivo. *Top row*: T_2-weighted axial MR image acquired prior to contrast agent (CA) injection showing the implanted matrix plugs (*orange arrows*, T_1-weighted axial MR image acquired after CA injection. (in-plane spatial resolution 0.1 mm). *Lower row*: *Left*: T_1w RARE image post-CA showing the Matrigel plug (*black*) and the reference region dorsal muscle and legmuscle (*blue*). *Right*: R-Relaxivity curve acquired with DCE-MRI in the Matrigel plug vs. muscle

The majority of standard MR techniques are now able to provide an accurate representation of the brain's macroscopic anatomy and to give a good contrast between the gray and white matter. However, they fail to capture the fiber architecture, to identify connectivity pathways, or to provide specific markers of the axonal or myelin changes. Diffusion tensor magnetic resonance imaging (DT-MRI) is capable to address these issues because of its ability to describe and quantify maturation (Baloch et al. 2009) and pathological patterns, such as the formation of axonal projections, modifications in myelination and axonal state, or variations in regional connectivity. Very sensitive to water molecule motion, DT-MRI enables tissue structure to be probed and imaged to a microscopic scale, providing details of the fine cytoarchitecture of the nervous tissue (Le Bihan 2003). The structural mapping of such networks during health and disease states is essential in fundamental neuroscience for understanding the brain functioning, and DT-MRI is the only noninvasive technique capable so far to provide such information.

4.2 Application Studies

Current state-of-the-art DT-MRI techniques enable in vivo experiments that are evidencing detailed

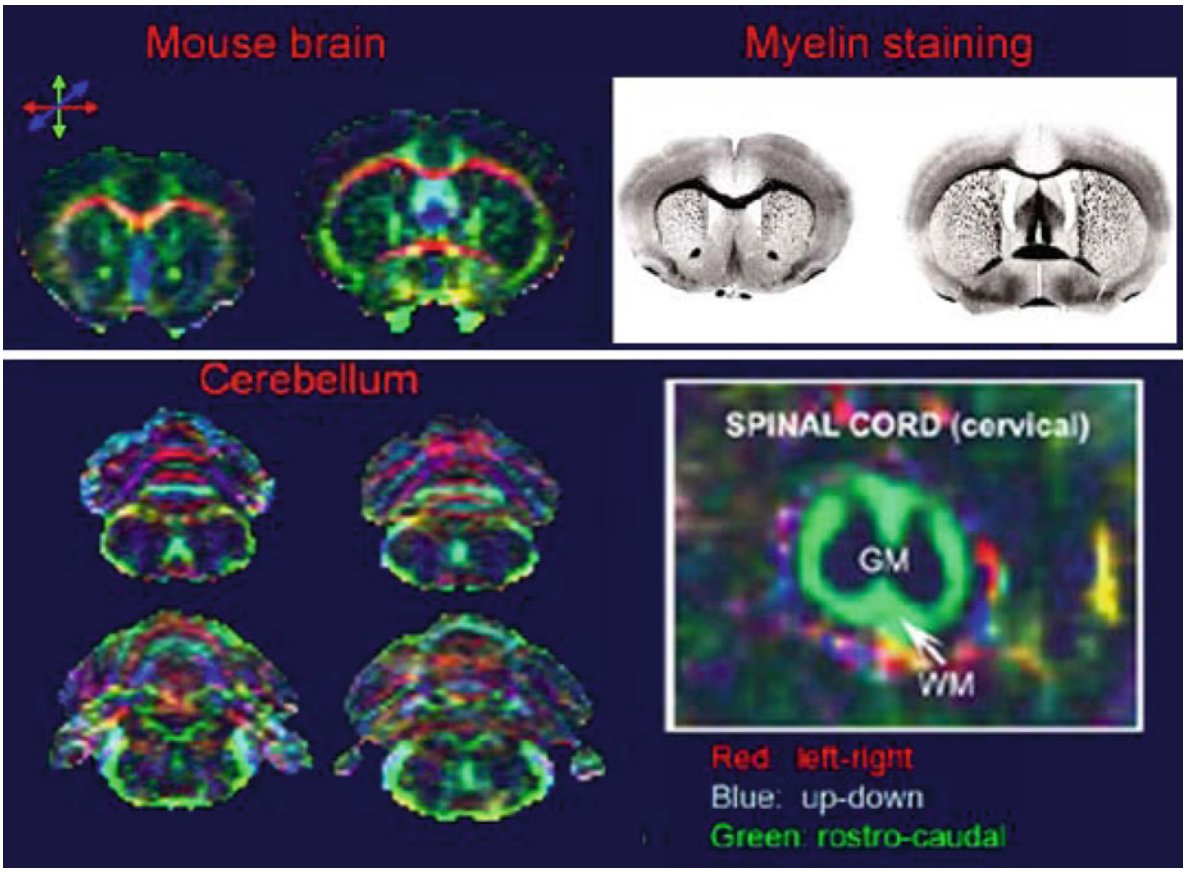

Fig. 13 Color-coded maps obtained with from in vivo DT-MRI are giving comparable information about the morphology of the mouse brain as the histological staining of the white matter (High resolution mouse brain atlas: http://www.hms.harvard.edu/research/brain/intro.html). Cerebellar lamination is also nicely highlighted and a very good contrast between *white* (WM) and *gray* (GM) matter is obtained in the spinal cord. Unlike histology, DT-MRI is also providing the supplementary information about the fibers orientation

mouse brain and spinal cord morphology (Fig. 13) in health or disease states. Rodent models of neurological diseases studied with DT-MRI have been very valuable in elucidating disease processes and since recently in evaluating quantitatively therapeutical strategies (Harsan et al. 2008), especially applied to white matter disorders. DT-MRI performed at high field allowed the development of so-called "diffusion tensor microscopy", and a number of studies elegantly demonstrated the utility of this method for understanding the intricate connectivity of the mouse brain and to delineate the developing anatomy (Zhang et al. 2005b; Baloch et al. 2009). To date, most of the literature dealing with mouse brain DT-MRI reports data from ex vivo analysis of the brain (Song et al. 2005; Verma et al. 2005; Zhang et al. 2005b; Tyszka et al. 2006; Wang et al. 2006) with only few attempts to perform in vivo DT-MRI (Lin et al. 2005; Harsan et al. 2006; Boretius et al. 2007; Boska et al. 2007; Chahboune et al. 2007; Grundmann et al. 2007; Larvaron et al. 2007).

The ex vivo *imaging* was able to capture embryonic structures such as the neuroepithelium, cortical plate (Fig. 14), or the forming axonal trees (Zhang et al. 2005a). DT-MRI convincingly showed also its potential to evidence the organization of unmyelinated white and gray matter structures of postnatal developing mouse brain (Zhang et al. 2005b).

The best resolution so far obtained with DT-MRI on the mouse brain is of 43-μm isotropic resolution (Jiang and Johnson 2010). This is far less than histology, but the situation changes when there is the

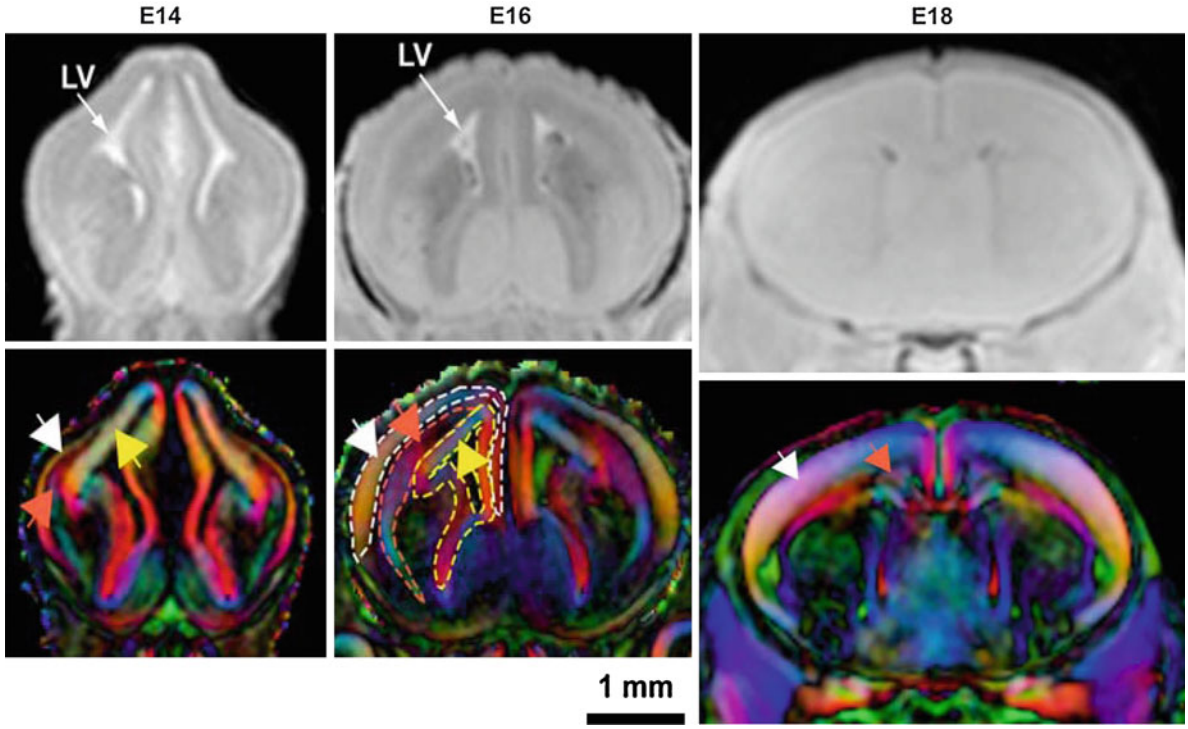

Fig. 14 Ex-vivo high resolution T_2-weighted (*top*) and diffusion tensor color map (*bottom*) images of embryonic day 14 (E14), E16, and E18 mouse brains show the drastic anatomical changes in the mouse brain during this time period. While the overall brain and lateral ventricle (LV) can be delineated in the T_2-weighted images, more detailed anatomical structures can only be visualized by DTI. For example, the cortical plate (indicated by the *white arrows*), intermediate zone (*orange arrows*), and ventricular zone (*yellow arrows*) can be appreciated in the E14 mouse brain. From E14 to E18, the cortical plate, the precursor of the adult cortex, gradually increases in its thickness, while the ventricular zone diminishes over time. The cortical plate is the precursor of the cortex, and the axon in the intermediate zone later forms the external capsule in the postnatal and adult mouse brains. The boundaries of the three structures are outlined in the E16 mouse brain images. The color scheme in the diffusion tensor color map images are *red*, left–right axis; *green*: anterior-posterior axis; *blue*: superior-inferior axis. Courtesy of Dr. Jiangyang Zhang, *F.M. Kirby Research Center for Functional Brain Imaging*, *Department of Radiology,* Johns Hopkins University, Baltimore, MD

requirement of 3D examination of the sample. With histological procedures, it is practically impossible to obtain consecutive slices free of artifacts through the entire sample and to estimate the volume changes. Tissue deformation and damage caused by tissue sectioning as well as the labor demanding staining procedures represent serious drawbacks for 3D investigations. Diffusion tensor microscopy provides measures of the 3D anatomy and gives additional quantitative information about the underlying tissue integrity (Verma et al. 2005). Generation of fractional anisotropy, radial and axial diffusivity maps allows to quantitatively assess the microstructural variations of the brain tissue, related to normal or pathological modifications. This type of evaluation can potentially capture genetic mutation effects, demyelination, axonal damage, etc.

All these aspects of DT-MRI technique are particularly valuable for in vivo *longitudinal studies* for a wide range of applications, especially in animal models of neurodegenerative disorders. In vivo examination refines the quality of the data allowing monitoring of individual animals and making possible the correlation with the behavioral or functional assessment (Budde et al. 2009). In vivo DT-MRI was applied to investigate different aspects of development (Larvaron et al. 2007), aging or pathology (Song et al. 2004; Sun et al. 2005; Sun et al. 2006) in the mouse brain. In clinical and experimental neuroscience, DT-MRI became a powerful tool for studying in vivo the white

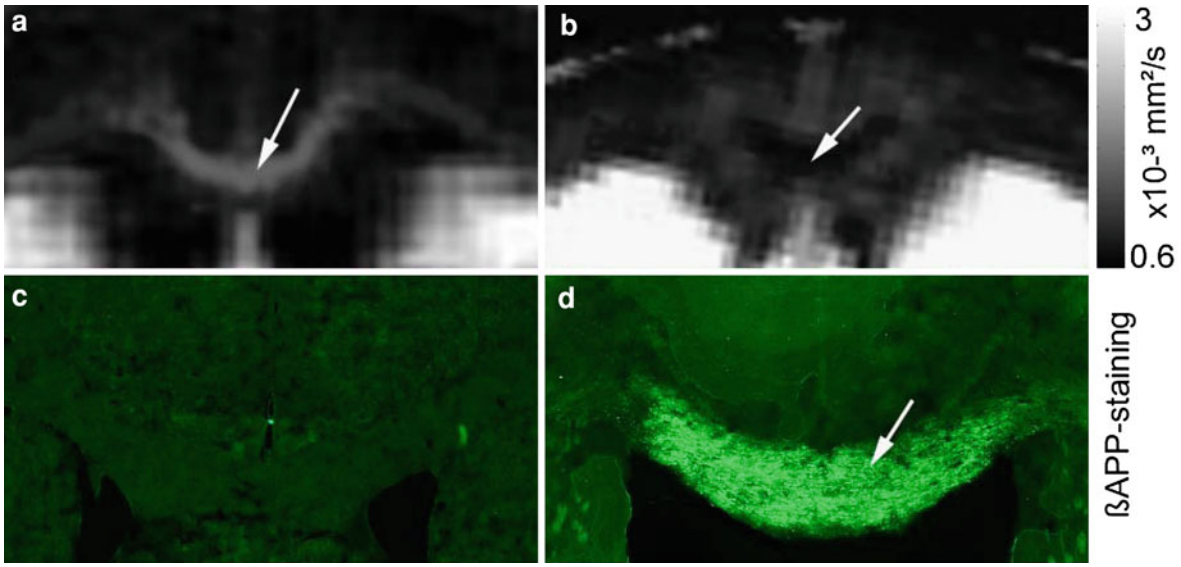

Fig. 15 Decreased axial diffusivity in demyelinated mice (**b**) is correlating with the axonal damage (strong ß APP staining) detected trough histopathology (**d**). Comparatively, high values of axial diffusivity are noticed in the corpus callosum of the control mouse (arrow a). the absence of ßAPP staining accounts for intact axonal tracts in the same animal. Imaging data were acquired at 9.4 T using a 4-shot DT-EPI sequence with 45 gradient diffusion directions, (**a**) depicts wild type mice, (**c**) the rapamycin treated pcy-mouse model

matter tissue, and the following chapter will focus on this aspect of the application: the noninvasive exploration of white matter pathologies.

4.2.1 DT-MRI in Animal Models of White Matter Disorders

Comprised of densely packed myelinated axons interconnecting gray matter regions and forming extensive networks, white matter microstructure imposes a preferential diffusion of water molecules, along the axons. Any modifications of tissue properties, as seen during pathology, can influence the diffusion anisotropy. Such modifications are often seen in the case of multiple sclerosis (MS), one of the most frequent and debilitating neurological disease. Myelin loss, changes in axonal density and caliber, axonal cytoskeleton rearrangements, or inflammatory reactions represent the typical hallmark of the MS lesions. Animal models are widely used to gain a better understanding of the underlying pathophysiology of MS. Commonly employed rodent models include the experimental autoimmune encephalomyelitis (EAE), Theiler's murine encephalitis virus, or chemical-induced demyelination using lysolecithin or cuprizone. The cuprizone (bis-cyclohexanone-oxaldihydrazone) is a well-known neurotoxic agent acting as selective and sensitive copper chelator. Several papers reported that mice fed with 0.2% cuprizone develop a demyelinating pathology. The model raised particular interest because it underlies the evolution of demyelination from acute to chronic state if the cuprizone insult is maintained for 12 weeks (Ludwin 1978; Matsushima and Morell 2001; Harsan et al. 2008). The treatment alters the well functioning of the mitochondria in the brain oligodendrocytes (Venturini 1973), and long-term cuprizone diet (for 12 weeks) induces a chronic severe pathology. Oligodendroglia is not regenerating spontaneously within chronically demyelinated regions due to the progenitor's injury and possibly due to axonal injury (Mason et al. 2004; Sun et al. 2006).

Recent studies have suggested that axonal damage, and not demyelination, is the primary cause of long-term neurological impairment in multiple sclerosis (Bjartmar and Trapp 2001). Therefore, the cuprizone mouse represents a suitable model for testing biological and imaging paradigms. The development of a noninvasive biological marker that is capable of detecting and differentiating axonal and myelin damage would have significant clinical

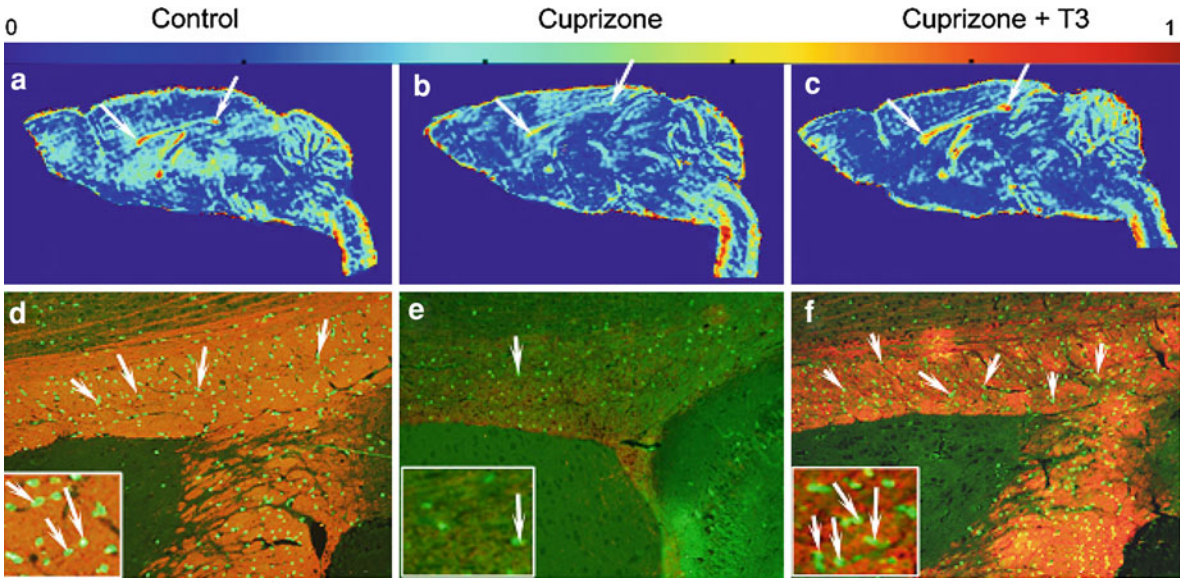

Fig. 16 **a–c** Mouse brain fractional anisotropy (FA) maps. **a** Normal mouse brain. **b** Cuprizone-demyelinated mouse brain, without T3 treatment. Low values of FA anisotropy are observed all along the corpus callosum—flashes. **c** Recovery of FA values in the corpus callosum is observed in cuprizone mice that received T3 treatment flashes. **d–f** Corresponding histopathological investigation of female brains imaged in (**a–c**), respectively. Double labeling procedure stained the myelin in red (anti-Myelin Basic Protein antibody) and the oligodendrocytes in *green* (anti carbonic anhydrase II antibody) in female mouse brains. DT-MRI and histology were performed 12 weeks after cuprizone treatment arrest in (**b** and **c**) mice

implications. DT-MRI has shown promise as a non-invasive marker of specific pathology. The technique is able to provide images of rotational invariant parameters of the diffusion tensor, such as fractional anisotropy (FA), volume ratio (VR), axial (λ_1), and radial [$(\lambda_2 + \lambda_3)/2$] diffusivity. These parameters are used for quantitative evaluation of microstructural modifications in developmental and pathological conditions. Of great interest is the evaluation of the radial and axial diffusivities derived after the diffusion tensor calculation in the brain of cuprizone-treated mice. Results from our studies (Harsan et al. 2006; Harsan et al. 2008) and from other groups (Song et al. 2005; Budde et al. 2009) suggest that increased radial diffusivity could serve as a surrogate marker of demyelination, while the reduced values of axial diffusivity are observed in brain areas of axonal damage. DT-MRI histology comparison emphasizes this correlation (Fig. 15).

The observation has great importance for the development of therapeutic strategies, designed to trigger specifically the remyelination, neuroprotection, or to combat the inflammation. The effects of the selected therapy could be further assessed in a quantitative manner in longitudinal studies. Among the potential remyelinating treatments, the thyroid hormone (T3) efficacy for inducing oligodendrogenesis and remyelination was followed in a longitudinal DT-MRI study in cuprizone-demyelinated mice (Harsan et al. 2008). The increased radial diffusivity values correlated with severe demyelination observed during the cuprizone diet. However, the values progressively diminish to control values along with the myelin recovery in mice receiving T_3-based remyelinating treatment. Besides the usefulness of radial and axial diffusivities to quantitatively estimate the demyelination and the recovery, fractional anisotropy values seem to be modulated by the myelination state.

Figure 16 illustrates the sensitivity of this parameter to changes in white matter microstructure.

In practice, one has also to keep in mind that the anisotropy values are also varying with the diffusion time used for the acquisition. The influence of barriers, such as myelin sheaths, become more visible at long diffusion times (Nair et al. 2005) yielding an increase in the anisotropy. Moreover, besides the myelin and axonal pathologic modifications, the white matter disorders are often accompanied by reactive gliosis,

hypertrophy of the astrocytes, or modifications of the blood–brain barrier permeability. Each of these features might influence to some extent the water diffusion coefficients (Harsan et al. 2007). It is however clear that measurement of water diffusion coefficients and their directionality allows an indirect measure of the white matter microstructure. Therefore, DT-MRI would be the methodology of choice for longitudinal studies to depict the evolution of the disease but also for the quantitative follow-up of therapeutic treatments. This imaging technique can also delineate the fiber tract organization in the brain (tractography) and can examine the extent of lesions three dimensionally (Mori and van Zijl 2002), predicting the possible functional deficits.

4.2.2 Fiber Tracking of the Mouse Brain

Neuronal connectivity has been a major scientific focus of neurologists and neuroanatomists since circuitry is highly correlated with brain function under normal conditions, or to dysfunction under pathological circumstances (Seung 2009). Methods for tracing connections in the fixed brain have a long history and evolved from silver stains (Nauta 1952, 1993) of serial sections to high resolution technologies using viral and genetic tracers (Wickersham et al. 2007; Young et al. 2008). Exploiting the active transport mechanisms along the axons, the histological tract-tracing methods are able to give insight into the neural architecture and to determine connectivity fingerprints at the cellular level. Although of extreme value in addressing neuroanatomical questions in experimental animals, the histological visualization of the transported substance is highly invasive and requires killing of the animal. Moreover, the difficulties associated with sectioning and recovering contiguous slices from the entire brain make impossible a large 3D representation of the brain connectivity pathways. DT-MRI and fiber tracking provide a window into the brain architecture that was not available previously. Various fiber tracking algorithms have emerged in the last few years, providing reproducible visualization of axonal projections in human and animal brains.

The fiber assignment by continuous tracking (FACT) method (Mori et al. 1999) is the most popular approach for axonal fiber tracking and was employed also for the reconstruction of the mouse fiber pathways in very few in vivo (Boretius et al. 2009b; Harsan et al. 2010b) and ex vivo studies (Jiang and Johnson 2010; Wang et al. 2006; Ren et al. 2007). For each voxel of the image, the diffusion tensor describes the magnitude and directionality (anisotropy) of the water movement. This information is used for tractography, but several acquisition parameters could influence the accuracy of the reconstructed path. Among them, the number of gradient diffusion directions is important for a robust estimation of tensor orientation (main diffusion direction) and mean diffusivity. Monte Carlo simulations showed that a minimum of 30 diffusion encoding directions are necessary for high quality fiber tracking (Jones 2004). For in vivo mouse brain imaging, the acquisition of high angular resolution diffusion (HARDI) data requires the use of fast sequences that limit the anesthesia time. At high field, the major white matter tracts were reconstructed from in vivo acquisitions at 7 T and 9.4 T. Boretius et al. (2007) visualized the main white matter fiber tracts by using an MR acquisition scheme that employed 12 gradient diffusion directions. The authors employed a half-Fourier diffusion-weighted single-shot STEAM MRI sequence. This strategy bears certain advantages (less prone to field inhomogeneity effects), but it requires the use of a high number of signal averages to overcome the poor signal to noise ratio (38 averages at 7 T), which increase subsequently the acquisition time (176 min). The same acquisition protocol was used at 9.4 T to demonstrate the disorganization of callosal and septal fibers with an almost complete lack of interhemispheric connectivity of mice lacking Pax6 transcription factor (Pax6cKO) (Boretius et al. 2009b). The findings are very similar with the brain connectivity changes observed in patients with heterozygous Pax6 mutations.

More recently, a measurement procedure based on a diffusion-weighted spin echo (SE) 4-shot echo-planar imaging (EPI) acquisition sequence has been adapted for in vivo mouse brain imaging at 9.4 T (Harsan et al. 2010b). The use of an EPI-based diffusion protocol reduced the acquisition time to 91 min for 30 gradient diffusion directions at a resolution of $156 \times 156 \times 500\ \mu m^3$. Different types of prominent and less prominent axonal fiber pathways were identified and tracked three dimensionally using the FACT algorithm, with high accuracy when compared to standard atlases.

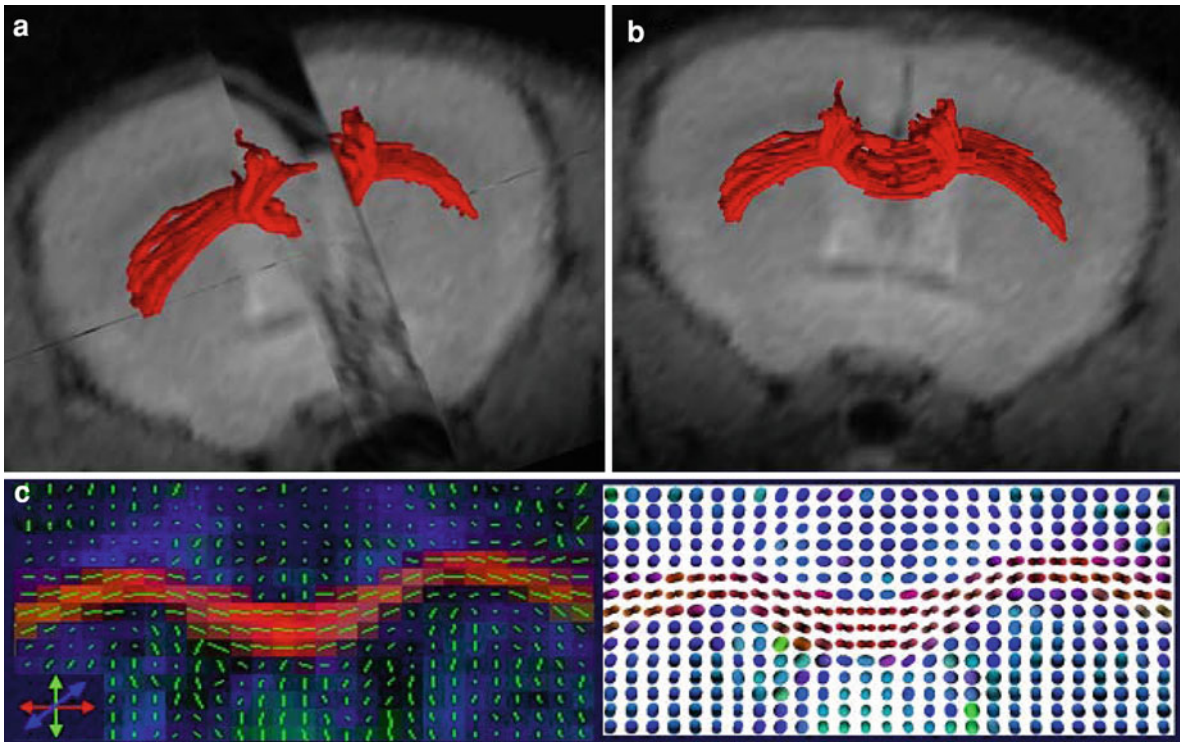

Fig. 17 FACT tracking of the major white matter fibers. **a** and **b** Views of the bundles running laterally through the genu of the corpus callosum (gcc) and toward the frontal part of the cerebral cortex, forming the forceps minor (fmi). **c** A high magnification view of the genu of the corpus callosum in a color-coded map is displayed in the *left panel*. The orientation of the main eigenvector is also represented in each voxel of the image as an oriented segment. In the *right panel*, tensor representations in each voxel are given for the ROI corresponding to the gcc

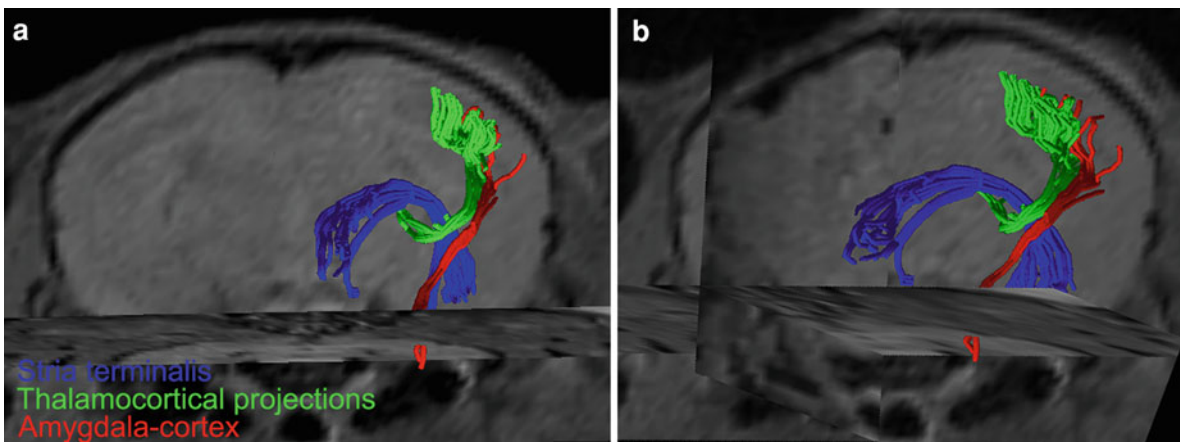

Fig. 18 Reconstructed mouse brain fibers from in vivo DT-MRI acquisition at 9.4 T. **a** Frontal view, **b** Lateral view. *Blue:* stria terminalis. *Red:* Amygdala-cortex. *Green*: Thalamocortical projections

Beside the reconstruction of the major white matter bundles (Fig. 17), fine grained mapping of rich axonal projections crossing gray matter regions could be revealed (Fig. 18). The study performed comparative deterministic and probabilistic tractography to investigate connectivity pathways in brain regions

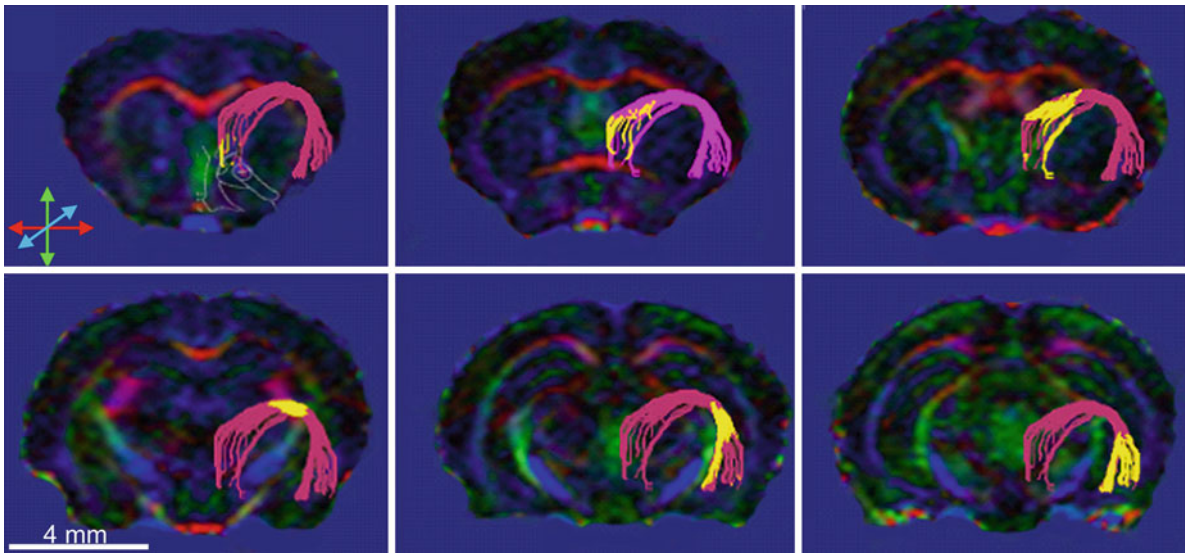

Fig. 19 Slice by slice visualization of the mouse stria terminalis, a major output projection of the amigdala. Fiber tracts are overlaid on color-coded orientation maps of contiguous slices, with *yellow* fibers accounting for the bundles cutting the image plane. Starting and ending points could be easily identified

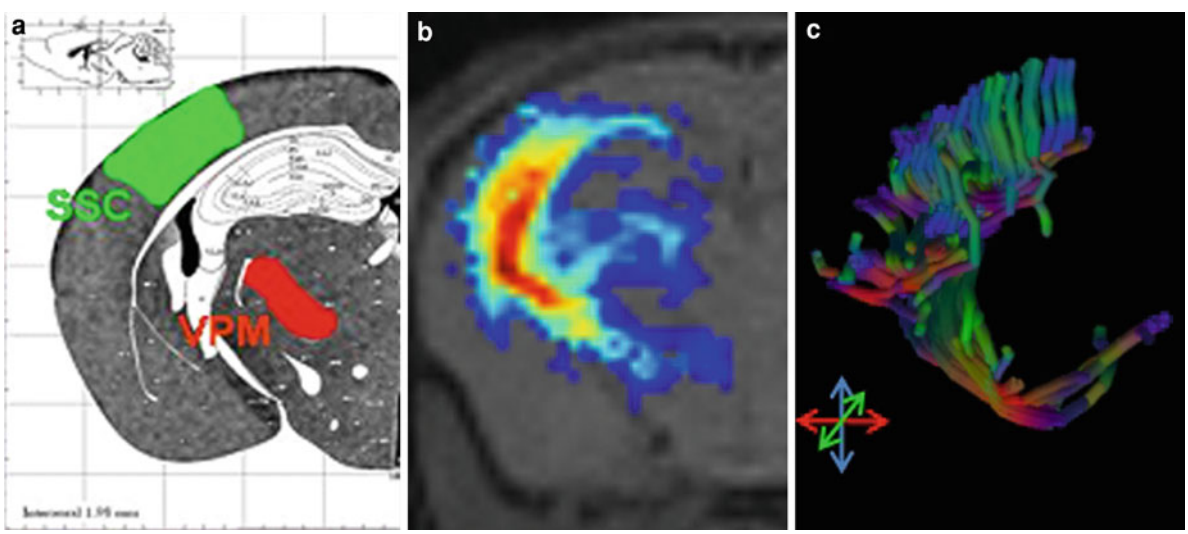

Fig. 20 Comparative mouse brain tractography of thalamo-cortical projections. **a** The seed points were located into the thalamus (VPM) and cortex (SSC). Probabilistic maps of connectivity (**b**) and FACT generated fiber tracts (**c**) were obtained after data acquisition using a 4-shot DT-EPI sequence with 30 gradient diffusion directions

belonging to the limbic or sensory systems. Figure 18 demonstrates the projection pathways from the core structure of the limbic system, the amygdala, to the mouse cortices and to the bed nucleus of stria terminalis. Revealing in vivo this type of neural pathways represents a breakthrough for studies related to depression, fear, or addiction behavior in rodents.

The feasibility of such studies in mice is determined by the possibility to identify and distinguish point-to-point structural connectivity. For example,

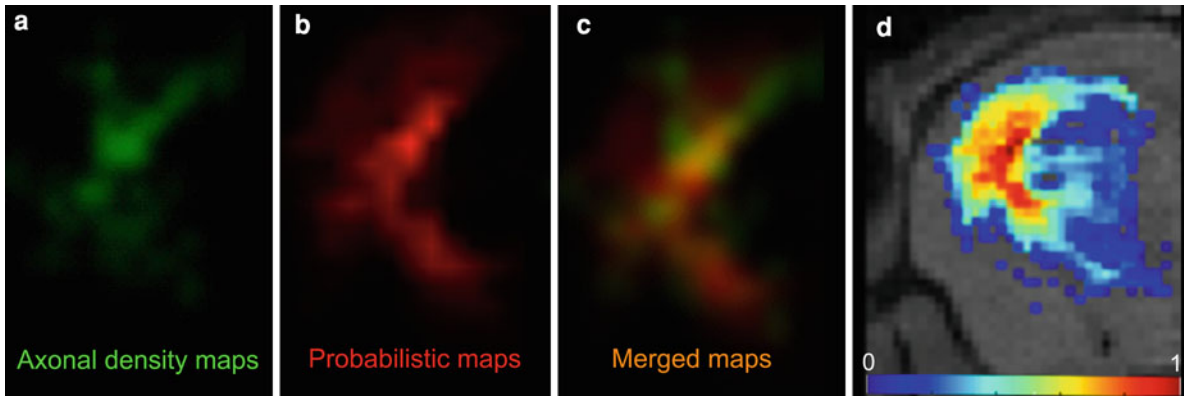

Fig. 21 Quantitative histological validation of probabilistic tractography in the living mouse brain. **a** Axonal density maps generated after counting the axons forming the thalamocortical projections. The axons were labeled with *Phaseolus vulgaris*-leucoagglutinin (PHA-L) histological tracer, injected in the posteromedial thalamic nucleus (VPM). **b, d** Probabilistic tractography of the thalamocortical projections reconstructed from in vivo DT-MRI data. MRI and histological sections were coregistered using landmarks (brain contour and the white matter tracts). **c** Colocalization algorithms show good agreement between (**a**) and (**b**) (overlap of 75%)

the stria terminalis is a major output pathway, projecting from the corticomedial division of the amygdala, running along the lateral margin of the ventricular surface of the thalamus, to target the bed nucleus of stria terminalis and the hypothalamus (Fig. 19).

As in the case of the amygdala, the thalamus, another gray matter region, sends axonal projections to the cerebral cortex. Figure 20 shows the architecture of the thalamocortical projections in wild-type mice. Comparatively, the probabilistic tractography (Fig. 20b) also identified the most probable pathway of connectivity between the ventral posteromedial thalamic nucleus (VPM) and the somatosensory cortex (SSC).

The probabilistic algorithm propagates a large number of pathways from the seed point, and the direction in which to step next was drawn from a distribution of possible orientations. The method required two processing steps. In the first step, probability maps were generated separately for each seed region. In these maps, the visiting frequency of a voxel reflects the degree of connectivity to the seed region. The second step consisted of combining the previously generated maps to derive the most probable direct pathway between the corresponding seed regions. The end result is a map that attempts to quantify the confidence level that a pathway can be found between each putative target voxel and the seed point, therefore probability maps of connectivity. This method does not require a priori knowledge about the projections' trajectories and is shown to be efficient even if the investigated pathway is long (i.e. lateral olfactory pathways—see Ref. Harsan et al. 2010a) or three-dimensionally complex (i.e. thalamocortical projections).

4.2.3 Fiber Tracking Validation

Although it seems clear that DT-MRI is able to reveal gross white matter connectivity as seen in human and animal brain atlases, the validation of the fiber tracking algorithms for identifying fine axonal trajectories is still scarce. In particular, validation of sensitive DT-MRI protocols and FT algorithms applied to depict in vivo subtle connection pathways in the small animal's brain would be of high value, given the high number of mouse models that mimic brain disorders. Like most techniques, tractography is susceptible to false positives or false negatives and a quantitative evaluation of its reliability is needed. A direct comparison of structural connectivity revealed through DTI tractography and histological neural tract was tried for the macaque (Dauguet et al. 2007) and pig brains (Dyrby et al. 2007). For the mouse brain, a rigorous validation of DT-MRI and deterministic and probabilistic tractography with correlative histological axonal tracing was recently performed (Harsan et al. 2010a). DT-MRI data were tested for fine-grained mapping of the

thalamocortical connectivity, and more precisely the connectivity between the ventral posteromedial thalamic nucleus (VPM) and the mouse somatosensory cortex. 3D reconstructions of the thalamocortical projections derived from DT-MRI were co-registered and correlated with 3D reconstructions of the fibers labeled with *Phaseolus vulgaris*-leucoagglutinin (PHA-L) histological tracer, injected in the VPM of the same animal. Two aspects of the tractography were explored: the connection pathways and the correlation between the values derived from probability maps of connectivity and the density of axons labeled with the histological tracer. Image correlation algorithms were applied giving information about the overlap of the pathways derived from FT and histological tracing (Fig. 21). An example of such colocalization is given in Fig. 21, and the calculated overlap (75%) shows a statistically significant agreement between results from the tractography and histological tracing.

In vivo DT-MRI tractography and axonal tracing were further compared in the case of the reeler mutant brain. The reeler mouse is a well-characterized model of disorganized cerebral lamination (D'Arcangelo 2005). Due to the impaired neuronal positioning, the reconstructed thalamocortical projections were distorted, less compacted, and thinner than normal. The study was able to assess the potential of in vivo DT-MRI and FT techniques for identifying and characterizing the subtle connection pathways in the living mouse brain, giving quantitative information about the confidence that one can assign to the reconstructed pathway. Tractography holds therefore the capabilities for reliable 3D longitudinal investigation of the impact of genetic mutations or neurodegenerative disorders on brain connectivity. Validation of tractography in the presence of brain abnormalities is important, since its use in the case of brain pathology is perhaps the most exciting application. The MRI investigations of adult mouse mutants stand as examples of preclinical studies that may contribute to bridge the gap between basic research and clinical application.

4.3 Technical Challenges of the Mouse Brain DT-MRI

Although, the final biological answer obtained with DT-MRI in preclinical studies is always highlighted, performing longitudinal in vivo mouse brain imaging is not a trivial task.

The primary technical challenge in DT-MRI of the mouse brain is to achieve high spatial resolution while preserving satisfactory signal to noise ratio (SNR). Due to the signal attenuation by diffusion sensitizing gradients, the acquisition of a complete data set with sufficient SNR in DT-MRI requires much longer scanning times than conventional T_1, T_2-based techniques. Therefore, most mouse brain DT-MRI experiments have been performed on high field systems with custom-made coils. However, the use of high field magnets has several disadvantages that have to be overcome.

The first one is the stronger field inhomogeneity when compared to classical 1.5 Tesla or 3 Tesla magnets used in clinical routine. High field systems have also the effect of shortening the tissue T_2 and T_2* while prolonging the T_1. The short T_2 and the higher inhomogeneity make the implementation of diffusion tensor echo-planar imaging (DT-EPI) type of acquisition difficult on high field animal systems. The large discontinuities in bulk magnetic susceptibility, such as those occurring at tissue/bone or tissue/air interfaces, produce geometric distortions and image intensity variations (signal brightening or dropout) while using DT-EPI. For mouse brain imaging, localized shimming procedures on a volume of interest placed inside the mouse brain sensitively improved the quality of the DT-EPI experiment (Harsan et al. 2010b) while maintaining an adapted acquisition time for in vivo studies.

In addition to time-invariant off-resonance effects such as B_0 field inhomogeneities, dynamic field variations induced by eddy currents may further contribute to the observed image distortions. Several methods to overcome limitations of geometric image distortions can be found in literature (Jezzard and Balaban 1995; Reber et al. 2002) but unfortunately, EPI distortion correction in animal MR imaging has received limited attention of the research community. Techniques based on the field mapping approach—though elegant and intuitive—face implementation difficulties related to the need for phase unwrapping, particularly at high fields and when imaging small objects.

The point spread function (PSF)-based approach for distortion correction (DiCo) by Robson et al. is often used in MRI, and its implementation and efficacy were recently demonstrated on a high field

animal scanner (Paul et al. 2009). Using an extended EPI acquisition with an additional gradient encoding on the phase encoding (PE) axis, the PSF can be measured and calculated for each point in image space. Based on the PSF information, a pixel shift map (PSM) can be calculated and applied to conventional DT-EPI data for image distortion correction. While the PSF data acquisition is directly integrated into the EPI method, the DiCo postprocessing is performed offline. The methodology is even more valuable because of its capabilities to correct the distortions created by the eddy currents induced by the long diffusion gradients. The eddy current artifacts can also be significantly reduced by adjusting the gradient pre-emphasis.

Moreover, because of the large diffusion gradients used to deliberately sensitize the sequences to diffusion, the DT-MRI technique is particularly prone to motion artifacts. Several types of movements might be the causes of these artifacts for in vivo studies: the global movement of the animal under examination or the motion related to physiological functions: breathing or heart beat, or even brain pulsations. These inconveniences may be partially overcome by cardiac and respiratory triggering during the acquisition, at the expense of longer acquisition time.

4.4 Practical Aspects of Data Acquisition

Sequences: DT-MRI pulse sequences are combining two parts: the diffusion preparation and the signal acquisition. For mouse brain imaging, most of the studies are using the spin echo preparation (Song et al. 2005; Harsan et al. 2006; Sun et al. 2006; Budde et al. 2007; Sizonenko et al. 2007; Harsan et al. 2008) but stimulated echo schemes were also used for different applications (Boretius et al. 2007; Boretius et al. 2009b), especially if long acquisition times are desired (Nair et al. 2005).

Many of the DT-MRI studies of the mouse brain employ the classical Stejskal-Tanner spin echo diffusion-sensitized sequence. The sequence is very sensitive to motion-induced artifacts but avoids the distortions observed when employing fast acquisition readouts, such as EPI. However, the minimum of 7 images needed to generate the diffusion tensor prolongs the scanning time, and the use of data sets with minimum number of gradient diffusion directions limits the tractographic possibilities. For in vivo studies, the long acquisition times, especially in animals already affected by different pathologies, might be very constraining. Therefore, fast acquisition schemes are desirable for in vivo experiments. EPI-based acquisition was avoided so far at high field, but the use of localized shimming procedures and distortion correction algorithms make it a promising choice for diffusion tensor experiments on animal scanners (Paul et al. 2009; Harsan et al. 2010b). A good tradeoff between imaging efficiency and image quality in terms of good spatial and temporal resolution and good SNR could be also obtained using DT rapid acquisition with relaxation enhancement (DT-RARE). This method has less B_0 and eddy current–related artifacts (e.g. at border regions) as well as fewer chemical shift artifacts and can be implemented with less-intensive gradient requirements than EPI-based acquisitions. However, artifacts can arise from imperfect refocusing pulses. The employment of twin navigator schemes positioned at the end of the echo trains could correct the phase differences between even and odd echoes and avoid this type of artifacts (Reese et al. 2003).

Several other parameters are important when performing DT-MRI and most of them depend on the application type and the biological question that has to be answered.

The *b factor* is one of the key parameters. The typical b values for in vivo brain and spinal cord experiments in small animals are in the range of 700–1,000 s/mm^2 (Song et al. 2002; Sun et al. 2006; Harsan et al. 2010b), most of the studies using 1,000 s/mm^2. Larger b values are used to probe small diffusion distances but one has to consider that stronger diffusion sensitization implies also reduced SNR. Because the water diffusion is much higher in immature, not completely myelinated brain and spinal cord tissues, lower b values are generally used. For ex vivo studies, it is generally suitable to increase the b factor values to more than 1,000 s/mm^2 (Jiang and Johnson 2010; Zhang et al. 2005a, b).

Another important parameter when exploring with DT-MRI the brain tissue is the *diffusion time* (t_{diff}). The root-mean-squared (rms) displacement in diffusion measurement is dependent on diffusion time. Most studies use relatively short diffusion times (t_{diff}), typically ranging from 15 to 60 ms in animal models, in order to minimize signal loss due to T_2 decay. For a

t_{diff} of 20 ms, the rms displacement is ~10 μm in vivo, while the mean axonal caliber in the mouse brain is 1.2 μm. The use of longer t_{diff} was shown to increase the diffusion measurements sensitization in myelin-deficient mice (Nair et al. 2005) and to improve the fiber tracking results (Rane et al. 2010).

In practice, the mentioned parameters and many others have to be adapted for particular hardware equipment and/or applications. Additionally, the in vivo data acquisitions require special attention for monitoring the physiological parameters, such as temperature or respiration rate. For reliable measurements, free of motion-related artifacts, respiratory gating is mandatory.

5 Cell tracking

To track cells in vivo by using magnetic resonance imaging (MRI) requires cell-labeling strategies with contrast agents that are suitable for MRI. Next to temporo-spatial localization of labeled cells, a major focus is the investigation of functional cell status since it allows studies of functional cell dynamics. In principle, there are two major approaches to reach this goal: first, the use of responsive contrast agents and second, the generation of transgenic cell lines. Looking at the rapid development in the field of cell biology, the interest to explore the therapeutic potentials of implanted cells has markedly increased. It is mandatory to gain further insight into the dynamics of cell migration and differentiation after implantation into the host organ, because it is needed for the assessment of the therapeutic possibilities. In this context, the access to noninvasive imaging modalities, which allow monitoring in individual subjects over time, is of special interest.

During the last few years, the availability of high field magnetic resonance imaging for animals has provided a much more effective platform for the in vivo detection of labeled cells. This has been achieved mostly by labeling with iron oxide nanoparticles, ultrasmall paramagnetic iron oxides (USPIOs), or superparamagnetic iron oxides (SPIOs) because they show the highest sensitivity. The particles are incorporated into the cells, thus producing a strong signal loss in T_2*-weighted MRI and susceptibility differences to the adjacent environment.

5.1 Dual Modality Tracking of Dendritic Cells

In preclinical settings, it is often beneficial to employ additional modalities to track cells. While MRI studies of a specific region can provide more information on the localization of labeled cells in the anatomical context in a noninvasive manner, the determination of that anatomical area is more easily done using bioluminescence imaging (BLI). Since intracellular nanoparticles are diluted when cells divide, MRI is particularly suitable for the tracking of dendritic cells (DC) because these cells have a low proliferative capacity and are efficient in Ag uptake. Figure 22 shows the visualization of dendritic cells in an animal model for allogeneic hematopoietic cell transplantation. (Reichardt et al. 2008). Following the path of the cells in vivo can be done with BLI at a high sensitivity and throughput, while a closer look on the anatomical context is provided by MRI.

6 Targeted Agents

Despite its comparably low sensitivity, preclinical high field MRI was able to prove its large potential and has its legitimate place in molecular imaging along with other techniques as SPECT, PET, or BLI. Especially the use of contrast agents enables minimal invasive options for cell tracking as described previously, and targeted agents supported detection of specific cell surface structures. Research in this field focuses mainly on contrast agents based on Gadolinium chelates, iron oxides, Fluorine (^{19}F), and Manganese (^{55}Mn).

Gadolinium chelates yield a positive contrast in T_1-weighted MRI and hold the potential of simplified translation toward human applications. This is because different types are already FDA approved as for example Multihance^{TM} or the blood pool agent variation binding to albumin Vasovist^{TM}. Their drawback however is the comparably low sensitivity if targeting aims for small volumes or limited receptor densities. Several approaches to increase the Gadolinium-induced contrast are under investigation (Delikatny and Poptani 2005). These include for example lipid-surfactant monolayers loaded with over 10,000 Gd chelates (Winter et al. 2003) or dendrimers ranging up to 128 Gd chelates or even more (Bryant et al. 2002).

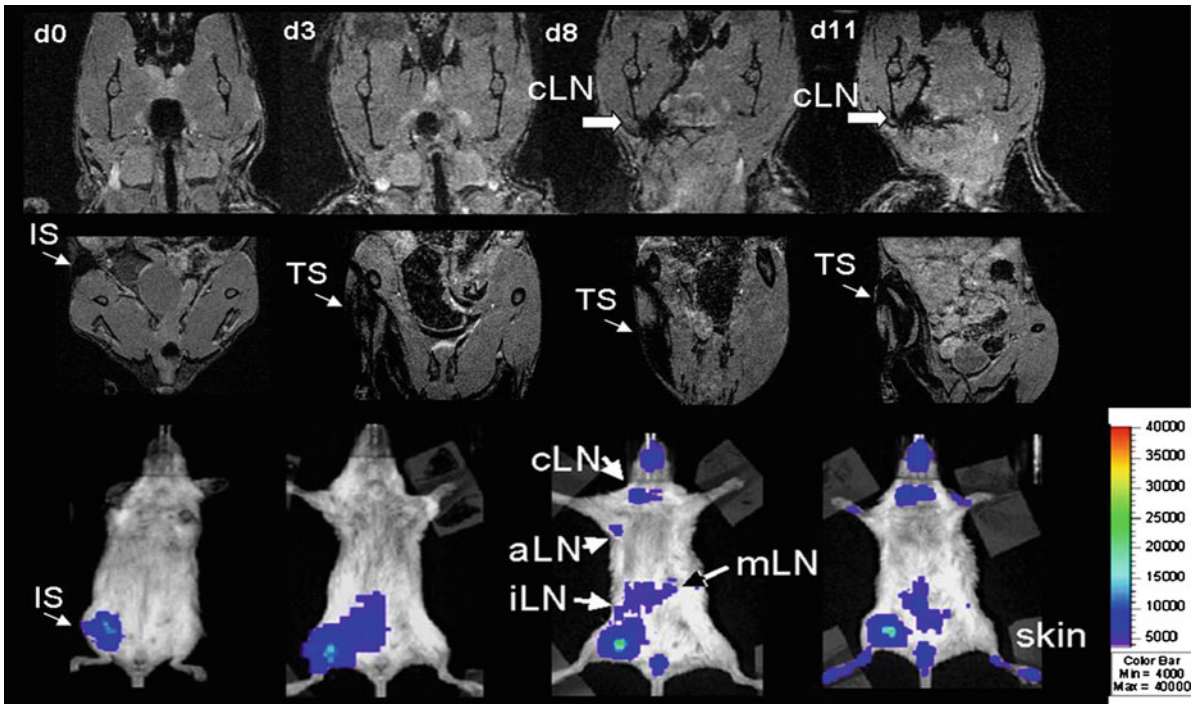

Fig. 22 In vivo imaging to track labeled DCs after injection. *Upper Row* MRI of the cervical region, showing signal voids in the region of the cLN as indicated on d8 + d11. *Middle row*: Signal void at the injection site (d0) and in the surrounding tissue (d3, 8, 11) as expected from the corresponding BLI. *Lower row*: Local injection of luc + SPIO + CD11c + cells in the right proximal leg on the day of BMT (C57B/6 and Balb/c). Trafficking is monitored with BLI on the indicated days with: injection site = IS, cLN = cervical lymph node, aLN = axillary lymph node, iLN = inguinal lymph node, mLN = mesenteric lymph node, TS = Tissue

A recent example for successfully targeting the folate receptor on tumors with a fluorescein-labeled dendrimer and dynamic contrast-enhanced MRI was demonstrated in (Chen et al. 2010). Louie et al. developed an impressive Gd chelate with a galactose cap on the 9th coordination site. In this state, the contrast agent is inactive and reveals close to no water relaxation at all unless in contact with the commonly used marker enzyme b-galactosidase that removes the cap and activates the contrast agent (Louie et al. 2000).

Super-paramagnetic iron oxides create strong local field gradients that dephase surrounding water protons leading to T_2 and T_2* relaxation and a potentially strong signal reduction (Bulte et al. 2001). These contrast agents with cores of iron oxide exist in a large variety of sizes altering their name as for example VSOP, with 4–8 nm, USPIO with 20–40 nm, SPIO with 60–150 nm, and used as magnetic separation agents e.g. dynabeads, which are in the range of 1–3 μm also named MPIO. In addition, the particles are usually coated with low-molecular-weight polymers in order to avoid aggregation. Common are dextran, polyethanol, and silica-coated particles. In clinical routine, these particles are often used as blood pool agents for detection of lymph nodes or liver metastases and brain tumor delineation (Harisinghani et al. 2003; Hahn and Saini 1998; Enochs et al. 1999), whereas in molecular imaging, they enable stem cell detection and tracking if internalized (Modo et al. 2002); (Heyn et al. 2005; Liu et al. 2007; Walczak et al. 2007) into the cells as well as when functionalized with various antibodies or peptides applications in targeting numerous cell types from tumors (Allport and Weissleder 2001) to ischemic heart tissue (Hoehn et al. 2002).

One advantage of Fluor (^{19}F) as a contrast agent is that there is no natural MRI visible Fluor in organic tissue and ^{19}F MRI therefore yields a contrast similar to PET imaging just revealing the location of the

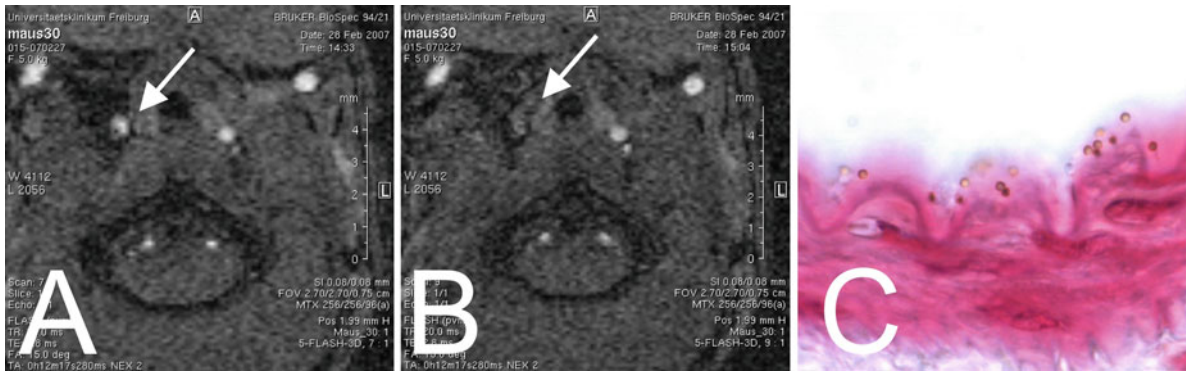

Fig. 23 An axial image of the mouse neck depicts the common carotid arteries *left* and *right* of the trachea. The *white arrow* points to the right carotid artery (**A**) bearing the thrombus. Note the blood signal void after contrast agent application in **B**. In **C**, a washed histological cut of the artery wall with bound contrast agent MPIOs demonstrates the binding capacities of the anti body

contrast agent. In combination with standard morphological ^{1}H MRI, these locations can directly be matched with the anatomical position. ^{19}F is commonly used in the form of fluorinated carbon hydrides (PFC) as these are chemically inert, therefore biologically harmless and carry multiple fluorine atoms per molecule. Similar to the other contrast agents, PFC-filled nano particles as micelle emulsions or liposomes are used for cell tracking (Ahrens et al. 2005; Srinivas et al. 2007) or for detecting ischemic tissue (Flogel et al. 2008).

The contrast effect of Manganese is similar to Gd. It enhances the water signal in T_1-weighted sequences. In its ionic form, Mn^{2+} can use the calcium channels in neurons and is therefore dedicated for neuronal applications. Watanabe et al. were among the first using this MEMRI (manganese-enhanced magnetic resonance imaging) called technique to prove on the optical tract (Watanabe 2001) that it can be used to map neuronal connections. It was shown by Aoki et al. (2002) that the uptake of Mn^{2+} is activation dependent. And both insights were impressively applied in a study investigating the brain plasticity of a song bird in changes of morphology, activity, and connectivity depending on seasonal, hormonal, auditory stimuli (Van der Linden et al. 2004).

A prominent field for targeted agent applications is detection of atherosclerotic plaque. This is of highest interest as ruptured plaque is the leading cause of death in the western world, and therefore, numerous research laboratories work on approaches for an early and specific detection of vulnerable plaque.

Existing approaches use particles of iron oxide as well as gadolinium (Gd) preparations (Flacke et al. 2001; Ruehm et al. 2001; Winter et al. 2003). Conjugation of Gd-containing paramagnetic particles to antibodies or peptidomimetics has been used to selectively image cellular receptors expressed in various disease conditions. For instance, this approach allowed imaging of angiogenesis in early-stage atherosclerosis with $\alpha v\beta 3$-integrin-targeted Gd nanoparticles (Kooi et al. 2003; Winter et al. 2003) and of fibrin for intravascular thrombus detection (Flacke et al. 2001; Spuentrup et al. 2005). Shapiro et al. used microparticles of iron oxide (MPIOs) for cellular imaging and tracking. These MPIOs convey a payload of iron that is many orders of magnitude greater than iron nanoparticles and cause local magnetic field inhomogeneity extending for a distance exceeding the physical diameter of the microparticle by far (Shapiro et al. 2004). Another approach using these MPIOs as markers to state a proof of principle aims directly at visualization of freshly agglomerating platelets and is described as an example in the following chapter.

6.1 Platelet-Targeted Thrombosis Imaging

Upon rupture of vulnerable plaques, initial aggregation and activation of platelets plays a pivotal role, mediating further activation of the coagulation cascade. As one possible way to allow in vivo imaging of in wall-adherent arterial thrombosis, an MRI contrast

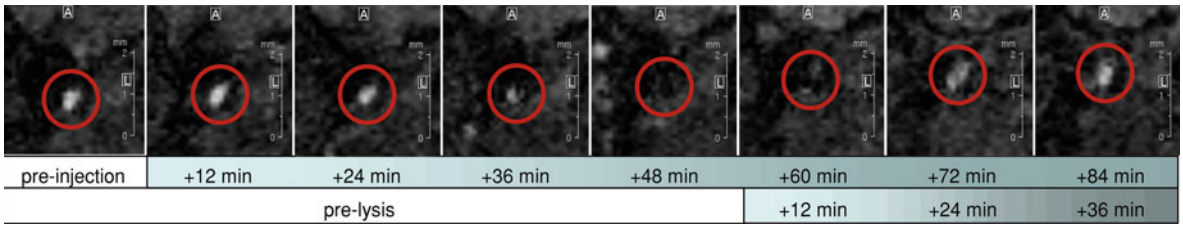

Fig. 24 Blood signal over time of the right common carotid artery of a mouse. A total signal void is visible 48 min after injection of the platelet targeted contrast agent. A lysis removes the thrombus and the signal reappears

agent targeting activated platelets directly has been successfully used in mice (von zur Muhlen et al. 2008).

The targeting part of the contrast agent used in this work is a single-chain antibody designed to bind to the GPIIb/IIIa-receptor (Schwarz et al. 2004). This receptor is expressed on the outside of blood platelets. It changes its conformation once activated and binds fibrin leading to thrombus formation. When changing its structure, the target- an epitope of GPIIB/IIIa called ligand-induced binding site- is expressed. This restricts binding of the antibodies to activated platelets only. As MR contrast agent, von zur Muhlen et al. used 1-µm-sized iron oxide particles linked to the antibodies via a histidine tag. These MPIOs lead to strong signal attenuation and voids and turned out to be well detectable in a slightly modified 3D FLASH sequence. With a flip angle of 15°, a short TR of 20 ms and a TE of 2.8 ms at a resolution of 100 µm a strong blood to tissue contrast similar to ToF was achieved nicely depicting the carotid blood vessels of a mouse.

In the applied mouse model, a nonocclusive wall-adherent thrombosis was induced by short application of a ferric chloride moistened blotting paper on the vessel during surgery.

Von zur Muhlen et al. could sensitively detect small platelet amounts in a wall-adherent thrombosis within the common carotid artery (see Fig. 23).

Furthermore, they were able to verify a quantitative contrast agent determination based on the known relaxivity values of the contrast agent and signal attenuation through counting MPIO particles in histological slices. Counted particles always ranged below the values calculated from MR. This was accounted to the processing of the histological slice. Nevertheless, with highest deviations of −50%, rough quantifications on the basis of signal attenuations seem reliable.

The breakdown of the thrombus can clearly be observed through the reappearance of the blood signal. This could be an important characteristic for future clinical applicability of such a platelets-based MRI contrast agent.

References

Ahrens ET, Flores R et al (2005) In vivo imaging platform for tracking immunotherapeutic cells. Nat Biotechnol 23(8): 983–987

Alajati A, Laib AM et al (2008) Spheroid-based engineering of a human vasculature in mice. Nat Methods 5(5):439–445

Allport JR, Weissleder R (2001) In vivo imaging of gene and cell therapies. Exp Hematol 29(11):1237–1246

Aoki I, Tanaka C et al (2002) Dynamic activity-induced manganese-dependent contrast magnetic resonance imaging (DAIM MRI). Magn Reson Med 48(6):927–933

Badea A, Nicholls PJ et al (2007) Neuroanatomical phenotypes in the reeler mouse. Neuroimage 34(4):1363–1374

Badea A, Johnson GA et al (2009a) Genetic dissection of the mouse brain using high-field magnetic resonance microscopy. Neuroimage 45(4):1067–1079

Badea A, Johnson GA et al (2009b) Genetic dissection of the mouse CNS using magnetic resonance microscopy. Curr Opin Neurol 22(4):379–386

Balaban RS (2001) Challenges in small animal noninvasive imaging. ILAR J 42(3):248–263

Baloch S, Verma R et al (2009) Quantification of brain maturation and growth patterns in C57BL/6 J mice via computational neuroanatomy of diffusion tensor images. Cereb Cortex 19(3):675–687

Baltes C, Radzwill N et al (2009) Micro MRI of the mouse brain using a novel 400 MHz cryogenic quadrature RF probe. NMR Biomed 22(8):834–842

Bjartmar C, Trapp BD (2001) Axonal and neuronal degeneration in multiple sclerosis: mechanisms and functional consequences. Curr Opin Neurol 14(3):271–278

Boretius S, Kasper L et al (2009a) MRI of cellular layers in mouse brain in vivo. Neuroimage 47(4):1252–1260

Boretius S, Michaelis T et al (2009b) In vivo MRI of altered brain anatomy and fiber connectivity in adult Pax6 deficient mice. Cereb Cortex 19(12):2838–2847

Boretius S, Wurfel J et al (2007) High-field diffusion tensor imaging of mouse brain in vivo using single-shot STEAM MRI. J Neurosci Methods 161(1):112–117

Boska MD, Hasan KM et al (2007) Quantitative diffusion tensor imaging detects dopaminergic neuronal degeneration in a murine model of Parkinson's disease. Neurobiol Dis 26(3):590–596

Bryant LH Jr, Jordan EK et al (2002) Pharmacokinetics of a high-generation dendrimer-Gd-DOTA. Acad Radiol 9(1): S29–S33

Budde MD, Kim JH et al (2007) Toward accurate diagnosis of white matter pathology using diffusion tensor imaging. Magn Reson Med 57(4):688–695

Budde MD, Xie M et al (2009) Axial diffusivity is the primary correlate of axonal injury in the experimental autoimmune encephalomyelitis spinal cord: a quantitative pixelwise analysis. J Neurosci 29(9):2805–2813

Bulte JW, Douglas T et al (2001) Magnetodendrimers allow endosomal magnetic labeling and in vivo tracking of stem cells. Nat Biotechnol 19(12):1141–1147

Calvet JP, Grantham JJ (2001) The genetics and physiology of polycystic kidney disease. Semin Nephrol 21(2):107–123

Chahboune H, Ment LR et al (2007) Neurodevelopment of C57B/L6 mouse brain assessed by in vivo diffusion tensor imaging. NMR Biomed 20(3):375–382

Charles River Laboratories International I (2010) www.criver.com

Chen WT, Thirumalai D et al (2010) Dynamic contrast-enhanced folate-receptor-targeted MR imaging using a Gd-loaded PEG-dendrimer-folate conjugate in a mouse xenograft tumor model. Mol Imaging Biol 12(2):145–154

Coussens LM, Hanahan D, Arbeit JM (1996) Genetic predisposition and parameters of malignant progression in K14-HPV16 transgenic mice. Am J Pathol 149:1899–1917

D'Arcangelo G (2005) The reeler mouse: anatomy of a mutant. Int Rev Neurobiol 71:383–417

Dauguet J, Peled S et al (2007) Comparison of fiber tracts derived from in vivo DTI tractography with 3D histological neural tract tracer reconstruction on a macaque brain. Neuroimage 37(2):530–538

Delikatny EJ, Poptani H (2005) MR techniques for in vivo molecular and cellular imaging. Radiol Clin North Am 43(1):205–220

Dorr AE, Lerch JP et al (2008) High resolution three-dimensional brain atlas using an average magnetic resonance image of 40 adult C57Bl/6 J mice. Neuroimage 42(1):60–69

Driehuys B, Nouls J et al (2008) Small animal imaging with magnetic resonance microscopy. Ilar J 49(1):35–53

Dyrby TB, Sogaard LV et al (2007) Validation of in vitro probabilistic tractography. Neuroimage 37(4):1267–1277

Enochs WS, Harsh G et al (1999) Improved delineation of human brain tumors on MR images using a long-circulating, superparamagnetic iron oxide agent. J Magn Reson Imaging 9(2):228–232

Flacke S, Fischer S et al (2001) Novel MRI contrast agent for molecular imaging of fibrin: implications for detecting vulnerable plaques. Circulation 104(11):1280–1285

Flogel U, Ding Z et al (2008) In vivo monitoring of inflammation after cardiac and cerebral ischemia by fluorine magnetic resonance imaging. Circulation 118(2):140–148

Fritsch A, Loeckermann S et al (2008) A hypomorphic mouse model of dystrophic epidermolysis bullosa reveals mechanisms of disease and response to fibroblast therapy. J Clin Invest 118(5):1669–1679

Grantham JJ (2006) CRISP: opening a new frontier in the diagnosis and treatment of PKD. Nephrol News Issues 20(9):29–30

Grantham JJ, Torres VE et al (2006) Volume progression in polycystic kidney disease. N Engl J Med 354(20):2122–2130

Greenberg NM, DeMayo F et al (1995) Prostate cancer in a transgenic mouse. Proc Natl Acad Sci USA 92(8): 3439–3443

Grundmann K, Reischmann B et al (2007) Overexpression of human wildtype torsinA and human DeltaGAG torsinA in a transgenic mouse model causes phenotypic abnormalities. Neurobiol Dis 27(2):190–206

Hahn PF, Saini S (1998) Liver-specific MR imaging contrast agents. Radiol Clin North Am 36(2):287–297

Harisinghani MG, Barentsz J et al (2003) Noninvasive detection of clinically occult lymph-node metastases in prostate cancer. N Engl J Med 348(25):2491–2499

Harsan L-A, Paul D et al (2010b) In vivo diffusion tensor magnetic resonance imaging and fiber tracking of the mouse brain. NMR Biomed 23(7):884–896

Harsan LA, Poulet P et al (2006) Brain dysmyelination and recovery assessment by noninvasive in vivo diffusion tensor magnetic resonance imaging. J Neurosci Res 83(3):392–402

Harsan LA, Poulet P et al (2007) Astrocytic hypertrophy in dysmyelination influences the diffusion anisotropy of white matter. J Neurosci Res 85(5):935–944

Harsan LA, Steibel J et al (2008) Recovery from chronic demyelination by thyroid hormone therapy: myelinogenesis induction and assessment by diffusion tensor magnetic resonance imaging. J Neurosci 28(52):14189–14201

Harsan L-A, Reisert M, Schnell S, Hennig J, von Elverfeldt D, Staiger JF (2010a) Validation of in vivo mouse brain fiber tracking with correlative axonal tracing in wild-type and reeler animals. ISMRM precedings

Hashizume H, Baluk P et al (2000) Openings between defective endothelial cells explain tumor vessel leakiness. Am J Pathol 156(4):1363–1380

Hayashida Y, Yakushiji T et al (2006) Monitoring therapeutic responses of primary bone tumors by diffusion-weighted image: initial results. Eur Radiol 16(12):2637–2643

Heyn C, Bowen CV et al (2005) Detection threshold of single SPIO-labeled cells with FIESTA. Magn Reson Med 53(2):312–320

Hoehn M, Kustermann E et al (2002) Monitoring of implanted stem cell migration in vivo: a highly resolved in vivo magnetic resonance imaging investigation of experimental stroke in rat. Proc Natl Acad Sci USA 99(25):16267–16272

Humphries PD, Sebire NJ et al (2007) Tumors in pediatric patients at diffusion-weighted MR imaging: apparent diffusion coefficient and tumor cellularity. Radiology 245(3): 848–854

Jezzard P, Balaban RS (1995) Correction for geometric distortion in echo planar images from B_0 field variations. Magn Reson Med 34(1):65–73

Jiang Y, Johnson GA (2010) Microscopic diffusion tensor imaging of the mouse brain. Neuroimage 50(2):465–471

Johnson GA, Ali-Sharief A et al (2007) High-throughput morphologic phenotyping of the mouse brain with magnetic resonance histology. Neuroimage 37(1):82–89

Johnston KC, Wagner DP et al (2007) Validation of an acute ischemic stroke model: does diffusion-weighted imaging lesion volume offer a clinically significant improvement in prediction of outcome? Stroke 38(6):1820–1825

Jones DK (2004) The effect of gradient sampling schemes on measures derived from diffusion tensor MRI: a monte carlo study. Magn Reson Med 51(4):807–815

Kim S, Pickup S et al (2009) Enhanced delineation of white matter structures of the fixed mouse brain using Gd-DTPA in microscopic MRI. NMR Biomed 22(3):303–309

Kobayashi H, Kawamoto S et al (2004) Micro-MRI methods to detect renal cysts in mice. Kidney Int 65(4):1511–1516

Kooi ME, Cappendijk VC et al (2003) Accumulation of ultrasmall superparamagnetic particles of iron oxide in human atherosclerotic plaques can be detected by in vivo magnetic resonance imaging. Circulation 107(19):2453–2458

Lager DJ, Qian Q et al (2001) The pck rat: a new model that resembles human autosomal dominant polycystic kidney and liver disease. Kidney Int 59(1):126–136

Larvaron P, Boespflug-Tanguy O et al (2007) In vivo analysis of the post-natal development of normal mouse brain by DTI. NMR Biomed 20(4):413–421

Le Bihan D (2003) Looking into the functional architecture of the brain with diffusion MRI. Nat Rev Neurosci 4(6):469–480

Lin CY, Sun SW et al (2005) Unsupervised identification of white matter tracts in a mouse brain using a directional correlation-based region growing (DCRG) algorithm. Neuroimage 28(2):380–388

Liu W, Dahnke H et al (2007) In vivo MRI using positive-contrast techniques in detection of cells labeled with superparamagnetic iron oxide nanoparticles. NMR Biomed 21(3):242–250

Liu S, Lu W et al (2002) A defect in a novel Nek-family kinase causes cystic kidney disease in the mouse and in zebrafish. Development 129(24):5839–5846

Louie AY, Huber MM et al (2000) In vivo visualization of gene expression using magnetic resonance imaging. Nat Biotechnol 18(3):321–325

Ludwin SK (1978) Central nervous system demyelination and remyelination in the mouse: an ultrastructural study of cuprizone toxicity. Lab Invest 39(6):597–612

Mason JL, Toews A et al (2004) Oligodendrocytes and progenitors become progressively depleted within chronically demyelinated lesions. Am J Pathol 164(5):1673–1682

Matsushima GK, Morell P (2001) The neurotoxicant, cuprizone, as a model to study demyelination and remyelination in the central nervous system. Brain Pathol 11(1):107–116

Maxwell RJ, Wilson J et al (2002) Evaluation of the anti-vascular effects of combretastatin in rodent tumours by dynamic contrast enhanced MRI. NMR Biomed 15(2):89–98

Modo M, Cash D et al (2002) Tracking transplanted stem cell migration using bifunctional, contrast agent-enhanced, magnetic resonance imaging. Neuroimage 17(2):803–811

Morgan B, Thomas AL et al (2003) Dynamic contrast-enhanced magnetic resonance imaging as a biomarker for the pharmacological response of PTK787/ZK 222584, an inhibitor of the vascular endothelial growth factor receptor tyrosine kinases, in patients with advanced colorectal cancer and liver metastases: results from two phase I studies. J Clin Oncol 21(21):3955–3964

Mori S, van Zijl PC (2002) Fiber tracking: principles and strategies—a technical review. NMR Biomed 15(7–8):468–480

Mori S, Crain BJ et al (1999) Three-dimensional tracking of axonal projections in the brain by magnetic resonance imaging. Ann Neurol 45(2):265–269

Nair G, Tanahashi Y et al (2005) Myelination and long diffusion times alter diffusion-tensor-imaging contrast in myelin-deficient shiverer mice. Neuroimage 28(1):165–174

Nauta WJ (1952) Selective silver impregnation of degenerating axons in the central nervous system. Stain Technol 27(3):175–179

Nauta WJ (1993) Some early travails of tracing axonal pathways in the brain. J Neurosci 13(4):1337–1345

Patterson DM, Padhani AR et al (2008) Technology insight: water diffusion MRI–a potential new biomarker of response to cancer therapy. Nat Clin Pract Oncol 5(4):220–233

Paul D, Zaitsev M et al (2009) Implementation and application of PSF-Based EPI Distortion correction to high field animal imaging. Int J Biomed Imaging 2009:946271

Petiet A, Hedlund L et al (2007) Staining methods for magnetic resonance microscopy of the rat fetus. J Magn Reson Imaging 25(6):1192–1198

Rane S, Nair G et al (2010) DTI at long diffusion time improves fiber tracking. NMR Biomed 23(5):459–465

Reber PJ, Wong EC et al (2002) Comparing the brain areas supporting nondeclarative categorization and recognition memory. Brain Res Cogn Brain Res 14(2):245–257

Reese TG, Heid O et al (2003) Reduction of eddy-current-induced distortion in diffusion MRI using a twice-refocused spin echo. Magn Reson Med 49(1):177–182

Reichardt W, Durr C et al (2008) Impact of mammalian target of rapamycin inhibition on lymphoid homing and tolerogenic function of nanoparticle-labeled dendritic cells following allogeneic hematopoietic cell transplantation. J Immunol 181(7):4770–4779

Ren T, Zhang J et al (2007) Diffusion tensor magnetic resonance imaging and tract-tracing analysis of Probst bundle structure in Netrin1- and DCC-deficient mice. J Neurosci 27(39):10345–10349

Rudin M, McSheehy PM et al (2005) PTK787/ZK222584, a tyrosine kinase inhibitor of vascular endothelial growth factor receptor, reduces uptake of the contrast agent GdDOTA by murine orthotopic B16/BL6 melanoma tumours and inhibits their growth in vivo. NMR Biomed 18(5):308–321

Ruehm SG, Corot C et al (2001) Magnetic resonance imaging of atherosclerotic plaque with ultrasmall superparamagnetic particles of iron oxide in hyperlipidemic rabbits. Circulation 103(3):415–422

Russel WMS, Burch RL (1959) The principles of humane experimental technique. London, Methuen

Schneider JE, Bamforth SD et al (2003a) Rapid identification and 3D reconstruction of complex cardiac malformations in transgenic mouse embryos using fast gradient echo sequence magnetic resonance imaging. J Mol Cell Cardiol 35(2):217–222

Schneider JE, Bamforth SD et al (2003b) High-resolution, high-throughput magnetic paragraph sign resonance imaging of mouse embryonic paragraph sign anatomy using a fast gradient-echo sequence. Magma 16(1):43–51

Schneider JE, Bose J et al (2004) Identification of cardiac malformations in mice lacking Ptdsr using a novel high-throughput magnetic resonance imaging technique. BMC Dev Biol 4:16

Schwarz M, Katagiri Y et al (2004) Reversibility versus persistence of GPIIb/IIIa blocker-induced conformational change of GPIIb/IIIa (alphaIIbbeta3, CD41/CD61). J Pharmacol Exp Ther 308(3):1002–1011

Seung HS (2009) Reading the book of memory: sparse sampling versus dense mapping of connectomes. Neuron 62(1):17–29

Shapiro EM, Skrtic S et al (2004) MRI detection of single particles for cellular imaging. Proc Natl Acad Sci USA 101(30):10901–10906

Sharief AA, Badea A et al (2008) Automated segmentation of the actively stained mouse brain using multi-spectral MR microscopy. Neuroimage 39(1):136–145

Shillingford JM, Murcia NS et al (2006) The mTOR pathway is regulated by polycystin-1, and its inhibition reverses renal cystogenesis in polycystic kidney disease. Proc Natl Acad Sci USA 103(14):5466–5471

Sizonenko SV, Camm EJ et al (2007) Developmental changes and injury induced disruption of the radial organization of the cortex in the immature rat brain revealed by in vivo diffusion tensor MRI. Cereb Cortex 17(11):2609–2617

Song SK, Sun SW et al (2002) Dysmyelination revealed through MRI as increased radial (but unchanged axial) diffusion of water. Neuroimage 17(3):1429–1436

Song SK, Kim JH et al (2004) Diffusion tensor imaging detects age-dependent white matter changes in a transgenic mouse model with amyloid deposition. Neurobiol Dis 15(3): 640–647

Song SK, Yoshino J et al (2005) Demyelination increases radial diffusivity in corpus callosum of mouse brain. Neuroimage 26(1):132–140

Spuentrup E, Buecker A et al (2005) Molecular magnetic resonance imaging of coronary thrombosis and pulmonary emboli with a novel fibrin-targeted contrast agent. Circulation 111(11):1377–1382

Squillaci E, Manenti G et al (2004) Correlation of diffusion-weighted MR imaging with cellularity of renal tumours. Anticancer Res 24(6):4175–4179

Srinivas M, Morel PA et al (2007) Fluorine-19 MRI for visualization and quantification of cell migration in a diabetes model. Magn Reson Med 58(4):725–734

Strecker R, Scheffler K et al (2003) DCE-MRI in clinical trials: data acquisition techniques and analysis methods. Int J Clin Pharmacol Ther 41(12):603–605

Sun Y, Zhou J et al (2002) Magnetic resonance imaging assessment of a murine model of recessive polycystic kidney disease. Comp Med 52(5):433–438

Sun SW, Song SK et al (2005) Detection of age-dependent brain injury in a mouse model of brain amyloidosis associated with Alzheimer's disease using magnetic resonance diffusion tensor imaging. Exp Neurol 191(1):77–85

Sun SW, Liang HF et al (2006) Noninvasive detection of cuprizone induced axonal damage and demyelination in the mouse corpus callosum. Magn Reson Med 55(2):302–308

Takahashi H, Ueyama Y et al (1986) A new mouse model of genetically transmitted polycystic kidney disease. J Urol 135(6):1280–1283

Taouli B, Vilgrain V et al (2003) Evaluation of liver diffusion isotropy and characterization of focal hepatic lesions with two single-shot echo-planar MR imaging sequences: prospective study in 66 patients. Radiology 226(1):71–78

Thoeny HC, De Keyzer F (2007) Extracranial applications of diffusion-weighted magnetic resonance imaging. Eur Radiol 17(6):1385–1393

Tyszka JM, Readhead C et al (2006) Statistical diffusion tensor histology reveals regional dysmyelination effects in the shiverer mouse mutant. Neuroimage 29(4):1058–1065

Van der Linden A, Van Meir V et al (2004) Applications of manganese-enhanced magnetic resonance imaging (MEMRI) to image brain plasticity in song birds. NMR Biomed 17(8):602–612

Venturini G (1973) Enzymic activities and sodium, potassium and copper concentrations in mouse brain and liver after cuprizone treatment in vivo. J Neurochem 21(5):1147–1151

Verma R, Mori S et al (2005) Spatiotemporal maturation patterns of murine brain quantified by diffusion tensor MRI and deformation-based morphometry. Proc Natl Acad Sci USA 102(19):6978–6983

von zur Muhlen C, von Elverfeldt D et al (2008) Magnetic resonance imaging contrast agent targeted toward activated platelets allows in vivo detection of thrombosis and monitoring of thrombolysis. Circulation 118(3):258–267

Walczak P, Kedziorek DA et al (2007) Applicability and limitations of MR tracking of neural stem cells with asymmetric cell division and rapid turnover: the case of the shiverer dysmyelinated mouse brain. Magn Reson Med 58(2):261–269

Walz G (2006) Therapeutic approaches in autosomal dominant polycystic kidney disease (ADPKD): is there light at the end of the tunnel? Nephrol Dial Transplant 21(7):1752–1757

Wang Y, Zhang J et al (2006) Axonal growth and guidance defects in Frizzled3 knock-out mice: a comparison of diffusion tensor magnetic resonance imaging, neurofilament staining, and genetically directed cell labeling. J Neurosci 26(2):355–364

Watanabe T (2001) Mapping of retinal projections in the living rat using high-resolution 3D gradient-echo MRI with Mn 2+-induced contrast. Magn Reson Med 46(3):424

Weidensteiner C, Rausch M et al (2006) Quantitative dynamic contrast-enhanced MRI in tumor-bearing rats and mice with inversion recovery TrueFISP and two contrast agents at 4.7 T. J Magn Reson Imaging 24(3):646–656

Wickersham IR, Lyon DC et al (2007) Monosynaptic restriction of transsynaptic tracing from single, genetically targeted neurons. Neuron 53(5):639–647

Wilson PD (2004) Polycystic kidney disease: new understanding in the pathogenesis. Int J Biochem Cell Biol 36(10):1868–1873

Winter PM, Morawski AM et al (2003) Molecular imaging of angiogenesis in early-stage atherosclerosis with alpha(v)beta3-integrin-targeted nanoparticles. Circulation 108(18):2270–2274

Yoshikawa MI, Ohsumi S et al (2008) Relation between cancer cellularity and apparent diffusion coefficient values using diffusion-weighted magnetic resonance imaging in breast cancer. Radiat Med 26(4):222–226

Young P, Qiu L et al (2008) Single-neuron labeling with inducible Cre-mediated knockout in transgenic mice. Nat Neurosci 11(6):721–728

Zhang J, Chen YB et al (2005a) Magnetic resonance diffusion tensor microimaging reveals a role for Bcl-x in brain development and homeostasis. J Neurosci 25(8):1881–1888

Zhang J, Miller MI et al (2005b) Mapping postnatal mouse brain development with diffusion tensor microimaging. Neuroimage 26(4):1042–1051

Index

J. Hennig and O. Speck (eds.), *High-Field MR Imaging,* Medical Radiology. Diagnostic Imaging,
DOI: 10.1007/978-3-540-85090-8, © Springer-Verlag Berlin Heidelberg 2011